

MATER. TEHNOL.	LETNIK VOLUME	50	ŠTEV. NO.	4	STR. P.	467–636	LJUBLJANA SLOVENIJA	JULY–AUG. 2016
-------------------	------------------	----	--------------	---	------------	---------	------------------------	-------------------

VSEBINA – CONTENTS

Predgovor urednika/Editor's preface

Matjaž Torkar 469

*IZVIRNI ZNANSTVENI ČLANKI – ORIGINAL SCIENTIFIC ARTICLES***Organosoluble xanthone-based polyimides: synthesis, characterization, antioxidant activity and heavy-metal sorption**Organsko topni poliamidi na osnovi ksantona: sinteza, karakterizacija, antioksidativna aktivnost in sorpcija težkih kovin
M. M. Lakouraj, G. Rahpaima, R. Azimi 471**Correlation of the heat-transfer coefficient at sprinkled tube bundle**Korelacija koeficienta prenosa toplote pri potresenem snopu cevi
P. Kracik, L. Šnajdarek, M. Lisý, M. Baláš, J. Pospíšil 479**Mathematical modeling of a cement raw-material blending process using a neural network**Matematično modeliranje postopka mešanja sestavin cementa s pomočjo nevronske mreže
A. Egrisogut Tiryaki, R. Kozan, N. Gokhan Adar 485**Possibilities of determining the air-pore content in cement composites using computed tomography and other methods**Možnosti določanja vsebnosti zračnih por v cementnih kompozitih z uporabo računalniške tomografije in drugih metod
B. Moravcová, P. Pössl, P. Misák, M. Blažek 491**Material and technological modelling of closed-die forging**Materialno-tehnološko modeliranje kovanja v zaprtem utopu
I. Vorel, Š. Jeniček, H. Jirková, B. Mašek 499**Investigation of wear behavior of borided AISI D6 steel**Preiskava obrabe boriranega jekla AISI D6
I. Gunes, S. Kanat 505**Investigation of Portevin-Le Chatelier effect of hot-rolled Fe-13Mn-0.2C-1Al-1Si TWIP steel**Preiskava Portevin-Le Chatelier učinka pri vročem valjanju Fe-13Mn-0.2C-1Al-1Si TWIP jekla
B. Aydemir, H. Kazdal Zeytin, G. Guven 511**The influence of surface coatings on the tooth tip deflection of polymer gears**Vpliv površinskih prevlek na poves vrha zoba polimernih zobnikov
B. Trobentar, S. Glodež, J. Flašker, B. Zafošnik 517**Vapour-phase condensed composite materials based on copper and carbon**Kompoziti na osnovi bakra in ogljika, kondenzirani iz plinske faze
V. Bukhanovsky, M. Rudnytsky, M. Grechanyuk, R. Minakova, C. Zhang 523**Homogenization of an Al-Mg alloy and alligating failure: influence of the microstructure**Homogenizacija Al-Mg zlitine in krokodiljenje: vpliv mikrostrukture
E. Romhanji, T. Radetić, M. Popović 531**Metal particles size influence on graded structure in composite Al₂O₃-Ni**Vpliv velikosti kovinskih delcev na gradientno strukturo kompozita Al₂O₃-Ni
J. Zygmuntowicz, A. Miazga, K. Konopka, W. Kaszuwara 537**Static and dynamic tensile characteristics of S420 and IF steel sheets**Statične in dinamične natezne lastnosti pločevine iz S420 in IF jekla
M. Mihaliková, V. Girman, A. Lišková 543**Acoustic and electromagnetic emission of lightweight concrete with polypropylene fibers**Akustična in elektromagnetna emisija lahkega betona s polipropilenskimi vlakni
R. Štoudek, T. Trčka, M. Matysik, T. Vymazal, I. Pišková 547**Multi-criteria analysis of synthesis methods for Ni-based catalysts**Večkriterijska analiza sinteznih metod na osnovi Ni katalizatorja
V. Nikolić, B. Agarski, Ž. Kamberović, Z. Andić, I. Budak, B. Kosec 553

Influence of structural defects on the magnetic properties of massive amorphous $Fe_{60}Co_{10}Mo_2W_xY_8B_{20-x}$ ($x = 1, 2$) alloys produced with the injection casting method Vpliv strukturnih napak na magnetne lastnosti masivne amorfne zlitine $Fe_{60}Co_{10}Mo_2W_xY_8B_{20-x}$ ($x = 1, 2$), izdelane z metodo litja z vbrižgavanjem J. Gondro, K. Bloch, M. Nabiałek, S. Garus	559
Possibilities of NUS and Impact-Echo methods for monitoring steel corrosion in concrete Možnosti metod NUS in Udarec-odmev za kontrolo korozije jekla v betonu K. Timčaková-Šamárková, M Matysík, Z. Chobola	565
Characterization of heterogeneous arc welds through miniature tensile testing and Vickers-hardness mapping Karakterizacija heterogenih zvarov s pomočjo miniaturnih nateznih preizkusov in matričnimi meritvami trdote po Vickersu S. Hertelé, J. Bally, N. Gubeljak, P. Štefane, P. Verleysen, W. De Waele	571
Overcooling in overlap areas during hydraulic descaling Podhladitev in prekrivanje področij med hidravličnim razškajanjem M. Pohanka, H. Votavová	575
Investigation of the mechanical properties of a cork/rubber composite Raziskava mehanskih lastnosti kompozita pluta/guma R. Kottner, J. Kocáb, J. Heczko, J. Krystek	579
Fabrication and properties of SiC reinforced copper-matrix-composite contact material Izdelava in lastnosti s SiC utrjenega kompozitnega materiala na osnovi bakra G. F. Celebi Efe, M. İpek, S. Zeytin, C. Bindal	585
Investigation of the cutting forces and surface roughness in milling carbon-fiber-reinforced polymer composite material Preiskava sil rezanja in hrapavosti površine pri rezkanju kompozitnega polimernega materiala, ojačanega z ogljikovimi vlakni S. Bayraktar, Y. Turgut	591
Development of aluminium alloys for aerosol cans Razvoj aluminijevih zlitin za aerosol doze S. Kores, J. Turk, J. Medved, M. Vončina	601
STROKOVNI ČLANKI – PROFESSIONAL ARTICLES	
Computer tools to determine physical parameters in wooden houses Določanje fizikalnih parametrov z računalniškimi orodji v lesenih hišah D. Bečkovský, F. Vajkay, V. Tichomirov	607
Impression relaxation and creep behavior of Al/SiC nanocomposite Sprostitev vtisa in obnašanje Al/SiC nanokompozita pri lezenju Y. S. Kakhki, S. Nategh, T. S. Mirdamadi	611
Microstructure and properties of the high-temperature (HAZ) of thermo-mechanically treated S700MC high-yield-strength steel Mikrostruktura in lastnosti visoko temperaturnega območja zvara (HAZ) termo-mehansko obdelanega jekla S700MC z visoko mejo plastičnosti J. Górká	617
New concept for manufacturing closed die forgings of high strength steels Nov koncept izdelave odkovkov iz visokotrnostnih jekel v zaprtih utopih K. Ibrahim, I. Vorel, D. Bublíková, B. Mašek	623
PREGLEDNI ČLANEK – REVIEW ARTICLE	
Helium atom scattering – a versatile technique in studying nanostructures Sipanje atomov helija – vsestranska tehnika za študij nanostruktur G. Bavdek, D. Cvetko	627

PREDGOVOR UREDNIKA

Ideja o dejavniku vpliva (Impact factor – IF) se je pojavila že leta 1955. Kasneje pa se je dejavnik vpliva uveljavil kot eno od ključnih meril za določanje znanstvene kakovosti revije in hkrati predstavlja enega od ključnih kriterijev pri oceni raziskovalcev. Poenostavljeno: dejavnik vpliva predstavlja število citatov revije, preračunano na število objavljenih člankov v zadnjih dveh letih. Ker gre za matematični izračun, je teoretično mogoče nanj delno vplivati tudi z uredniško politiko. Vsi taki, sicer neetični, poskusi v preteklosti so se izjalovili. Urednik ne sme vplivati na avtorje in jih ne sme spodbujati, da citirajo članke iz urednikove revije. To kontrolira tudi Thomson Reuters, ki dopušča kot etično, maksimalno 20 % samocitatov in s tem omejuje možno vplivanje urednikov na gibanje dejavnika vpliva. Etično sprejemljivo je, če je urednikov vpliv omejen na izbiro kvalitetnih člankov priznanih avtorjev za katere je več možnosti, da bodo po objavi tudi citirani.

Za revije, ki so vrhunske in imajo tudi najvišji dejavnik vpliva je značilno, da objavljajo dela priznanih, uveljavljenih avtorjev in predvsem pregledne članke, kar skupaj lahko največ prispeva k dvigu dejavnika vpliva.

V sredini vsakega leta Thomson Reuters objavlja nove vrednosti dejavnika vpliva za preteklo obdobje, ki ga uredniki pričakujemo z nestrpnostjo. Uredništvo revije *Materials in tehnologije* je v preteklih letih dalo več možnosti mladim, še neveljavljenim avtorjem, kar se je takoj odrazilo na zmanjšani vrednosti dejavnika vpliva.

V zvezi s tem se postavlja več dilem in vprašanj glede prihodnje uredniške politike. Ali je res nujno potrebno, da se dejavnik vpliva stalno povišuje? Ali je smiselno, da se daje možnost objave tudi manj priznanim mladim raziskovalcem, ki se lahko v prihodnje razvijejo v vrhunske znanstvenike? Ali naj uredništvo zaostri pogoje sprejemanja člankov v objavo? Ali je zmanjšanje dejavnika vpliva znak za slabo uredniško politiko?

Večina teh vprašanj nima enostavnega odgovora, zato ostaja dejavnik vpliva trd oreh tako dosedanjih kot tudi bodočih urednikov.

Ob prenehanju opravljanja funkcije glavnega in odgovornega urednika se zahvaljujem vsem avtorjem, uredniškemu odboru in vsem sodelavcem, ki skrbijo za revijo *Materials in tehnologije/Materials and Technology*, ki bo v letu 2017 praznovala častitljivo, že 50. obletnico izhajanja.

Glavni in odgovorni urednik
Dr. Matjaž Torkar

EDITOR'S PREFACE

The idea of impact factor (IF) first appeared in 1955. Since then, IF has established itself as one of the key criteria for determining the ranking of a journal, as well as an indicator of a researcher's scientific quality. The IF is derived from the number of citations of the journal, recalculated to take account of the number of published articles in the past two years. Because of its mathematical basis it can be influenced by editorial politics. However, all such unethical experiments have failed in the past. The editor should not put pressure on the authors, and they should not be encouraged to cite the editor's journal. This is also controlled by Thomson Reuters, which allows up to 20 % of self-citations, and so limits the possible influence of editors. It is, however, ethically acceptable for editors to choose quality papers by well-known authors, which are more likely to be cited after their publication.

It is also typical for the journals with the highest IFs to publish review papers by renowned, established authors, which tend to contribute to a higher IF.

In the middle of every year Thomson Reuters publishes its new values for journal IFs, something editors wait impatiently for. As the editor of *Materials and Technology*, in recent years I gave more chances to young, not-yet-established authors, which was immediately reflected in a lower IF. There are clearly a number of questions that future editors must consider. Is it really necessary for IFs to keep on increasing? Does it make sense to encourage young, less-established researchers who may yet develop into world-class scientists? Should the editor toughen the conditions for the acceptance of articles for publication? Is a lower IF really a sign of poor editorial policy?

Most of these questions have no simple answer, and for this reason the IF remains as a difficult problem for current and future editors.

As I step down from my position as Editor in Chief, I would like to thank all the authors, the Editorial Board and my co-workers, all of whom care about the journal *Materials in tehnologije/Materials and Technology*, which will celebrate its 50th anniversary in 2017.

Editor in Chief
Dr. Matjaž Torkar

ORGANOSOLUBLE XANTHONE-BASED POLYIMIDES: SYNTHESIS, CHARACTERIZATION, ANTIOXIDANT ACTIVITY AND HEAVY-METAL SORPTION

ORGANSKO TOPNI POLIAMIDI NA OSNOVI KSANTONA: SINTEZA, KARAKTERIZACIJA, ANTIOKSIDATIVNA AKTIVNOST IN SORPCIJA TEŽKIH KOVIN

Moslem Mansour Lakouraj¹, Ghasem Rahpaima², Razieh Azimi¹

¹University of Mazandaran, Faculty of Chemistry, Department of Polymer Chemistry, Babolsar, Iran

²Islamic Azad University, Department of Chemistry, Lamerd Branch, Lamerd, Iran
lakouraj@umz.ac.ir

Prejem rokopisa – received: 2013-10-15; sprejem za objavo – accepted for publication: 2015-08-25

doi:10.17222/mit.2013.250

To improve the solubility, thermal properties and processability of polyxanthenes, a new class of polyxanthenes, poly(xanthone-imide)s (PXIs), with a high yield was prepared using a two-step chemical imidation of 2,7-diaminoxanthone with pyromellitic dianhydride (PMDA), 3,3',4,4'-benzophenone tetracarboxylic dianhydride (BTDA) and 2,2'-bis-(3,4-dicarboxyphenyl) hexafluoropropane dianhydride (6-FDA)). These PXIs were characterized with FT-IR and ¹H NMR spectroscopies. They presented a good solubility in aprotic polar solvents such as N,N-dimethyl acetamide (DMAc), N,N-dimethyl formamide (DMF), N-methyl pyrrolidone (NMP) and dimethyl sulfoxide (DMSO), and showed inherent viscosities in a range of 0.34–0.58 dL/g. These PXIs exhibited lower glass-transition temperatures than the original polyxanthenes and a high thermal stability. The obtained results of the UV-vis absorption and photoluminescence indicated that the maximum absorption and fluorescence emission of PXIs were in the range of 300–304 nm and 432–510 nm, respectively. The antioxidant activity of PXIs was evaluated with a DPPH assay. The antioxidant values for PXIs were greater than for the parent xanthone (X). The polyimides were investigated for the extraction of environmentally noxious metal ions such as Cr (VI), Co (II), Ni (II), Cu (II), Pb (II) and Cd (II) from aqueous solutions.

Keywords: poly(xanthone-imide)s, antioxidant activity, fluorescence, organosolubility, heavy metals

Za izboljšanje topnosti, toplotnih lastnosti in predelovalnost poliksantonov je bila pripravljena nova vrsta poliksantonov, poli(ksanton-imidov) (PXIs) z visokim izkoristkom, z uporabo dvostopenjske kemijske sinteze 2,7-diaminoksantona z piro-melitim dianhidridom (PMDA), 3,3',4,4'-benzofenon tetrakarboksiličnega dianhidrida (BTDA) in 2,2'-Bis-(3,4-Dikarbofenil) heksafluoropropan dianhidrida (6-FDA)). Ti PXI-ji so bili karakterizirani s FT-IR in ¹H NMR-spektroskopijo. Predstavljajo dobro topnost v aprotičnih polarnih topilih, kot je N,N-dimetil acetamid (DMAc), N,N-dimetil formamid (DMF), N-metil piroolidon (NMP) in dimetil sulfoksid (DMSO) in kažejo nespremenljivo viskoznost v območju 0,34–0,58 dL/g. Ti PXI-ji kažejo nižjo temperaturo prehoda v steklasto stanje kot originalni poliksantoni ter veliko termično stabilnost. Dobljeni rezultati UV-absorpcije in fotoluminiscence kažejo, da je maksimalna absorpcija in emisija fluorescenca PXI-jev v območju 300–304 nm, oziroma 432–510 nm. Antioksidativna aktivnost PXI-jev je bila ocenjena z DPPH preizkusom. Vrednost protioksidativnosti za PXI-je je bila večja kot pri matičnem ksantonu. Poliamidi so bili preiskovani za ekstrakcijo okoljsko škodljivih kovinskih ionov, kot so Cr (VI), Co (II), Ni (II), Cu (II), Pb (II) in Cd (II) iz vodnih raztopin.

Gljučne besede: poli(ksanton-imidi), antioksidacijska aktivnost, fluorescenca, organska topnost, težke kovine

1 INTRODUCTION

Xanthenes have a conjugated planar ring system consisting of two benzene rings bridged through a carbonyl group and an oxygen atom. This unique structure shows an admirable thermo-oxidative and hydrolytic stability with numerous potential beneficial properties such as antioxidant,^{1,2} antihistamine,^{3,4} anti-inflammatory,^{5,6} antibacterial,^{7,8} antifungal,⁹ antiviral^{10,11} and anticancer^{12,13} effects. Consequently, it seems to have a great potential as a structural pattern in high-performance polymers. Although several different synthetic and natural xanthenes were introduced^{14–18} few of such biologically active compounds were investigated in a polymer synthesis.¹⁹

Polyxanthenes can be used for high-temperature applications and as electrical insulating materials due to their excellent solvent and chemical resistance, good physical and electrical properties even at high temperatures. However, a poor processability of the polymers is the main drawback as they have high glass or melting temperatures and are often insoluble in common organic solvents.^{20,21}

On the other hand, due to oxidative-degradation reactions that may occur during various stages of the polymer lifecycle including the manufacturing, processing and end-use stages, it is essential to place antioxidant building block in polymer matrices. These polymers, whose antioxidant moieties are covalently attached to the backbone of a polymer, have unique advantages: they are

non-volatile and they do not penetrate into the skin and tissue.

Aromatic polyimides are well-known high-performance polymers that have a high thermal stability, excellent mechanical and chemical properties. Due to these advantageous properties, polyimides are widely used as adhesives, films, composite matrices, coatings, membranes, and in the electronic-packaging industry.²²⁻²⁵

Therefore, in continuation of our ongoing work on polyxanthenes²⁶ and also in order to improve the physical properties of polyxanthenes, in the present study, we attempted to insert a xanthone unit into the backbone of a polyimide to develop new organosoluble polyxanthenes. For this purpose, at first, 2,7-diaminoxanthone was prepared and then used for a polymerization with pyromellitic dianhydride (PMDA), 3,3', 4,4'-benzophenone tetracarboxylic dianhydride (BTDA) and 2,2'-bis-(3,4-dicarboxyphenyl) hexafluoropropane dianhydride (6-FDA). The structures of the resulting poly(xanthone-imide)s were characterized with NMR and FT-IR spectroscopies. The physical properties of these PXIs, including their viscosity, solubility, thermal stability, morphology, and their spectroscopic properties such as ultraviolet-visible absorption and fluorescence emission were studied. In addition, PXIs were also evaluated for their antioxidant activities with a 2,2-diphenyl-1-picrylhydrazyl (DPPH) assay. Furthermore, their ability to eliminate environmentally toxic heavy-metal ions such as Pb (II), Cd (II), Co (II), Ni (II), Cu (II) and Cr (VI) were studied in aqueous media.

2 EXPERIMENTAL WORK

2.1 Materials

N-methyl-2-pyrrolidone (NMP), N,N-dimethylacetamide (DMAc), acetic anhydride and pyridine were purchased from Merck and purified with distillation under a reduced pressure over calcium hydride and stored above a 4° A molecular sieve. Pyromellitic dianhydride (PMDA), 3,3',4,4'-benzophenone tetracarboxylic dianhydride (BTDA) and 2,2'-bis-(3,4-dicarboxyphenyl) hexafluoropropane dianhydride (6-FDA) were dried in a vacuum oven at 110 °C for 5 h. All the other materials and solvents, such as DMF, pyridine and DMSO were purchased from TCI Chemical Co., Fluka Chemical Co. (Buchs, Switzerland) and Merck Chemical Co. and used as received.

2.2 Measurements

A Bruker Tensor 27 spectrometer (Bruker, Karlsruhe, Germany) and a 400-MHz Bruker Avance DRX spectrometer in DMSO-d₆ were used for recording FT-IR, ¹H and ¹³C NMR spectra, respectively. Inherent viscosities (*h_{inh}*) of the polymers were determined in NMP at 0.5 g per 100 mL concentration, with an Ubbelohde viscometer (Schott-Gerate, Hofheim, Germany) at 25 °C. A thermogravimetric analysis (TGA) was conducted

with a TA Instruments TGA-50 (Shimadzu, Kyoto, Japan) in a temperature range of 50–650 °C at a heating rate of 10 °C/min under nitrogen atmosphere.

Glass-transition temperatures (*T_g*) of the polymers were determined with a Perkin-Elmer Pyris 6 differential scanning calorimeter at a heating rate of 10 °C/min under nitrogen atmosphere. The UV-visible absorption and fluorescence emission spectra were recorded on Cecil 5000 and Perkin-Elmer LS-3B spectrophotometers in an NMP solution, respectively. X-ray powder diffraction patterns were performed at room temperature (about 25 °C) with an X-ray diffractometer (GBC MMA instrument) with Be-filtered Cu-K_α (0.15418 nm) operating at 35.4 kV and 28 mA. The 2θ scanning range was set between 4° and 50° at a scan rate of 0.05° per s. The concentration of metal cations in the liquid phase was determined with an atomic-absorption instrument (BRAIC WFX-130 AA).

2.3 Monomer synthesis

As illustrated in **Figure 1**, the 2,7-dinitroxanthone (DNX) and 2,7-diaminoxanthone (DAX) were prepared according to our published article.²²

2.4 Polymer synthesis

The general synthetic route used to produce the PXIs was as follows. A 100-mL two-necked, round-bottomed flask equipped with a magnetic stirrer bar, nitrogen-gas inlet tube and calcium chloride drying tube was charged with 0.226 g (1.0 mmol) of diamine (DAX) and 10 mL of dry NMP. The mixture was stirred at room temperature for 0.5 h. Then 1.0 mmol of a dianhydride was added and the mixture was again stirred at room temperature for 24 h, forming a viscous solution of a poly(amic acid) (PAA) precursor in NMP. The PAA was converted into polyimide with the chemical-imidization process.²⁷ The chemical imidization was carried out by adding 3 mL of a mixture of acetic anhydride/pyridine (6:4, v/v) into the PAA solution, while stirring it at room temperature for 1 h. Then the mixture was stirred at 130 °C for 12 h to yield a homogeneous solution. The polymer solution was slowly poured into methanol to form a precipitate. The precipitate was then filtered, washed thoroughly with hot methanol and dried overnight under vacuum at 80 °C.

PXI-a. A yield of 97 %, FTIR (KBr, cm⁻¹): 3020 (aromatic C-H stretching), 1775 (C=O asymmetric stretching), 1714 (C=O symmetric stretching), 1658 (C=O stretching of the carbonyl group), 1466 (C=C stretching), 1375 (C-N stretching), 1145 (C-O stretching). ¹H NMR (400 MHz, DMSO-d₆): δ 7.52–8.84 (8 H, aromatic protons).

PXI-b. A yield of 96 %, FTIR (KBr, cm⁻¹): 3050 (aromatic C-H stretching), 1780 (C=O asymmetric stretching), 1705 (C=O symmetric stretching), 1660 (C=O stretching of the carbonyl group), 1470 (C=C stretching),

1370 (C-N stretching), 1155 (C-O stretching). ^1H NMR (400 MHz, DMSO-d_6): δ 7.61–8.52 (12 H, aromatic protons).

PXI-c. A yield of 93 %, FTIR (KBr, cm^{-1}): 3010 (aromatic C-H stretching), 1785 (C=O asymmetric stretching), 1755 (C=O symmetric stretching), 1658 (C=O stretching of the carbonyl group), 1475 (C=C stretching), 1385 (C-N stretching), 1140 (C-O stretching). ^1H NMR (DMSO-d_6): δ 7.29–7.79 (12H Aromatic).

2.5 Antioxidant activities

The antioxidant activity of the compounds (PXI-a, b and c) was determined spectrophotometrically, using a stable 2,2-diphenyl-1-picrylhydrazyl (DPPH) radical according to the already reported method, with a slight modification.²⁸ A stock solution of the PXIs (0.5 mg/mL) was prepared in DMSO, and 50 μL of the prepared PXI solution was added to 5 mL of a 0.004 % ethanol solution of the DPPH radical. After 30 min of incubation in dark at room temperature, the absorbance was observed against a blank at 517 nm. The assay was carried out in triplicate and the percentage of inhibition was calculated using the following formula:

$$\% \text{ inhibition} = (\text{AB} - \text{AA}) / \text{AB} \times 100$$

where AB = absorption of the blank and AA = absorption of the test.

2.6 Water absorption

Two examination methods were investigated for the water-absorption capacity of poly(xanthone-imide)s. Method I: the polymer (0.2 g) was poured in 30 mL water at 25 °C for 24 h, followed instantly by weighing. Method II: a polymer powder was boiled in water at 100 °C for 30 min, and its weight difference was determined with the measurements before and after the insertion.

2.7 Adsorption capability

Solid-liquid extractions of Cd (II), Cu (II), Co (II) and Ni (II) as their chloride salts, Pb (II) as nitrate salt and Cr (VI) as $\text{Cr}_2\text{O}_7^{2-}$ ($\text{K}_2\text{Cr}_2\text{O}_7$) were carried out either

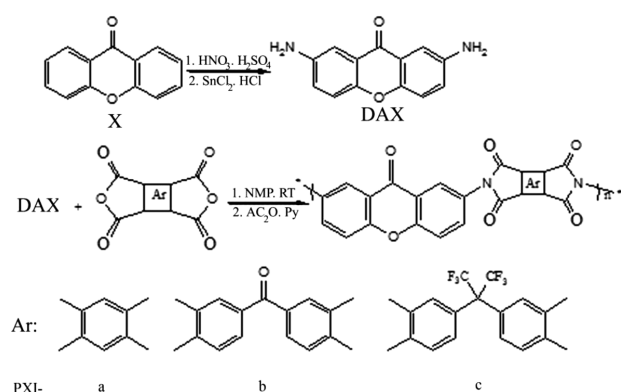


Figure 1: Synthesis and designations of poly(xanthone-imide)s (PXIs)
Slika 1: Sinteza in oznaka poli(ksanton-imidov) (PXI-jev)

individually or in the mixture. Approximately 10 mg of the appropriate polymer powder was shaken with 10 mL of an aqueous solution of the metal salt for 3 d at 25 °C. The initial concentration of the salts was 10 mg L^{-1} . After filtration, the concentration of each metal cation in the liquid phase was determined with the atomic-absorption technique, and direct information regarding the extraction percentage of metal ions by the polymer was obtained using a calibration curve, made for each metal ion from the standard solutions of (5, 10, and 20) $\mu\text{g/g}$.

3 RESULTS AND DISCUSSION

3.1 Polyimide synthesis and characterization

Three polyimides containing a xanthone group were prepared in high yields (90–97 %) with a polycondensation of equal molar amounts of the diamine with commercially available aromatic dianhydrides, such as PMDA, BTDA and 6-FDA, as shown in **Figure 1**. The polycondensation was carried out in NMP at room temperature for 24 h to form poly(amic acid)s, followed by chemical imidization with acetic anhydride and pyridine. The inherent viscosity of the polymers, as a suitable criterion for evaluating the molecular weight, was measured at a concentration of 0.5 g/dL in NMP at 25 °C. The inherent viscosities of the polyimides were in a range of 0.34–0.58 dL/g, indicating moderate molecular weights. All the polymers were characterized using the FT-IR and ^1H NMR techniques. In **Figure 2**, the FT-IR spectrum of the PXI-b is shown as a representative polyimide. The FT-IR spectra of the PXI-b exhibited characteristic absorption bands of the five-membered imide ring at 1780 and 1705 cm^{-1} (typical of the imide carbonyl asymmetric and symmetric stretching), 1660 cm^{-1} (C=O stretching of the xanthone carbonyl group), 1470 cm^{-1} (C=C stretching), 1370 cm^{-1} (C-N stretching), together with a strong absorption band at 1155 cm^{-1} (C-O stretching). ^1H NMR spectra for the poly(xanthone-imide), PXI-b, is shown in **Figure 3**. The spectrum showed characteristic resonance signals of aromatic protons in the region of 7.61–8.52 $\mu\text{g/g}$.

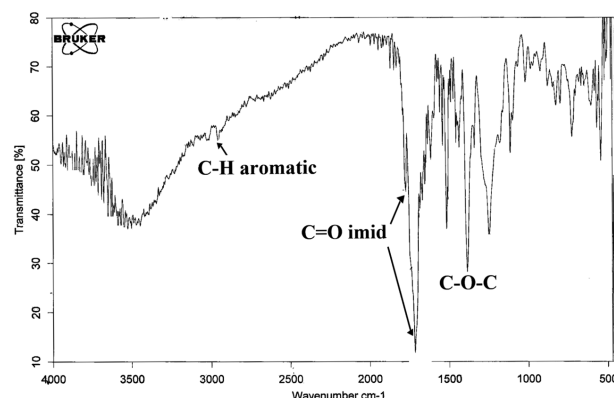


Figure 2: FT-IR spectrum of PXI-b
Slika 2: FT-IR spekter PXI-b

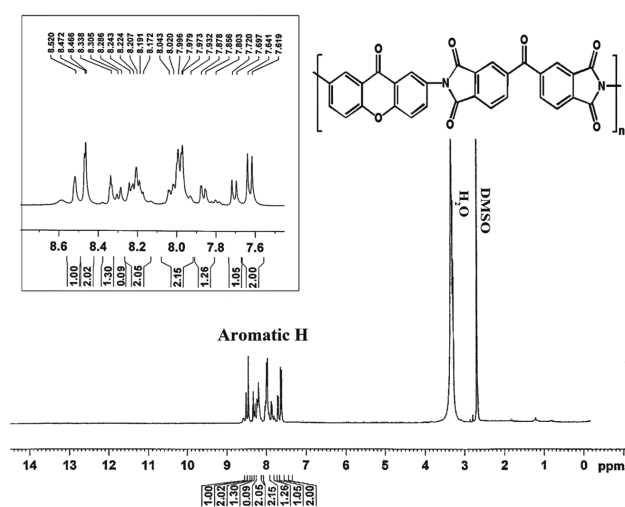


Figure 3: ^1H NMR spectrum of PXI-b
Slika 3: ^1H NMR spekter PXI-b

3.2 Solubility and viscosity

The solubility behavior of the poly(xanthone-imide)s depended on their chain-packing ability and intermolecular interactions, which were affected by the rigidity, symmetry and regularity of the molecular backbone. The solubility behavior of the PXIs was experienced in several organic solvents using a 5 % (w/v) concentration at room temperature, and the results are tabulated in **Table 1**. These poly(xanthone-imide)s had a higher solubility than the earlier reported polyxanthenes.²¹ The solubility of these polyimides varies depending on the dianhydride used. A comparison of the solubility values for PXIs shows that the presence of carbonyl and hexafluoroisopropylidene groups in the PXI-b and PXI-c enhances their solubility at room temperature. However, the solubility of these poly(xanthone-imide)s could be improved by attaching bulky trifluoromethyl ($-\text{CF}_3$) groups onto the polymer chain.

The enhancement in solubility is clearly attributed to the additional effect arising from the bulky $-\text{CF}_3$ unit, which increased the disorder in the chains, causing a less close chain packing, thus facilitating the distribution of solvent molecules among the macromolecule chains. These PXIs showed a good solubility in polar aprotic solvents such as DMF, DMAc, DMSO and NMP at room temperature, while the corresponding polyxanthone homopolymers have no solubility in such solvents at

Table 1: Solubility behavior and inherent viscosities of poly(xanthone-imide)s

Tabela 1: Topnost in nespremenljiva viskoznost poli(xsanton-imidov)

PXIs code	NMP	DMF	DMSO	DMAc	THF	Acetone	ETOH	Inherent viscosity (dL/g)
PXI-a	+	+	+	+	-	-	-	0.58
PXI-b	++	++	++	++	-	-	-	0.43
PXI-c	++	++	++	++	-	-	-	0.34

(DMAc: N,N-dimethyl acetamide; DMF: N,N-dimethyl formamide; NMP: N-methyl pyrrolidone; DMSO: dimethyl sulfoxide; THF: tetrahydrofuran; ETOH: ethanol); ++: soluble at room temperature; +: soluble during heating at 60 °C; -: insoluble)

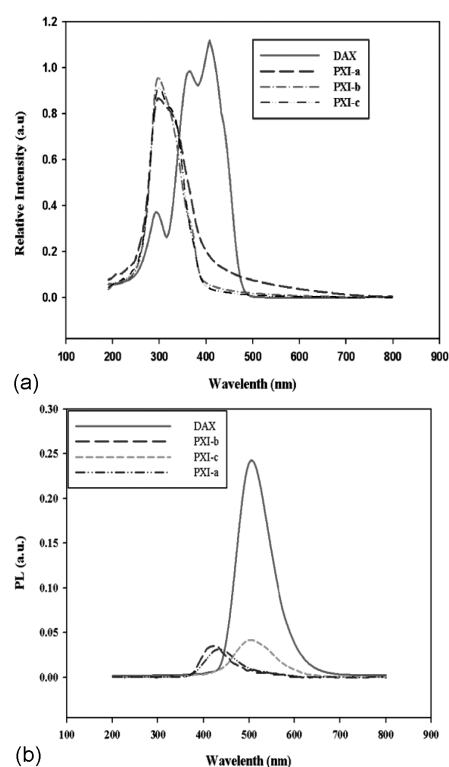


Figure 4: a) UV-vis absorption spectra and b) fluorescence emission spectra of the DAX and PXIs in NMP solution

Slika 4: a) UV absorpcijski spekter in b) emisijski spekter fluorescence DAX in PXI-jev v NMP raztopini

ambient temperature. This suggests that these polymers have potential applications in the areas such as film formation or casting process where the temperature is a determining factor.

3.3 Optical properties

Several classes of xanthone compounds were successfully used for protecting light-sensitive materials, controlling the harmful influence of light, especially of UV irradiation. The photophysical properties of the monomer and PXIs were examined with UV-visible and fluorescence spectroscopies in an NMP solution. The UV-vis absorption of the monomer and poly(xanthone-imide)s (**Figure 4a**) showed a strong absorption at 355 and 300–304 nm, respectively, in the NMP solutions due to the $\pi-\pi^*$ transition of the aromatic chromophores of a xanthone ring. In comparison with the parent xanthone,

the UV spectra of the corresponding poly(xanthone-imide)s were slightly blue shifted and broadened. The fluorescence emission spectra of the PXIs exhibited peak positions with the maxima at 413–510 nm (Figure 4b).

3.4 Thermal properties

The thermal behavior of the poly(xanthone-imide)s was evaluated with a thermogravimetric analysis (TGA) and differential scanning calorimetry (DSC) at a heating rate of 10 °C min⁻¹ and the results obtained from these thermograms are summarized in Table 2. DSC thermograms of the polyimides are shown in Figure 5. As indicated in Figure 5, the T_g values of these PXIs are in a range of 213–285 °C, while the reported values of T_g for the bare polyxanthenes were found to be higher than 370 °C.²¹ The results showed that the T_g values of these PXIs depend on the structure of the dianhydride component and they decrease with the increasing flexibility of the dianhydride structure.

Table 2: Characteristic thermal data of poly(xanthone-imide)s
Tabela 2: Podatki o toplotni značilnosti poli(ksanton-imidov)

Compound	T_g (°C)	T_5 (°C)	T_{10} (°C)	Char. yield (%)
PXI-a	285	415	460	60
PXI-b	218	380	400	61
PXI-c	213	370	394	46

T_g : glass-transition temperature; T_5 : temperature for a 5% weight loss; T_{10} : temperature for a 10% weight loss; Char. yield: weight of the polymer, kept at 700 °C

The polyimide derived from PMDA exhibits the highest T_g because of a rigid backbone, while the PXI-c obtained from 6-FDA showed the lowest T_g owing to the bulky CF₃ groups between the phthalimide units, which might be a result of reduced chain-to-chain charge-transfer interactions and poor chain packing of the bulky pendant -CF₃ groups. Indeed, the difference in T_g of the

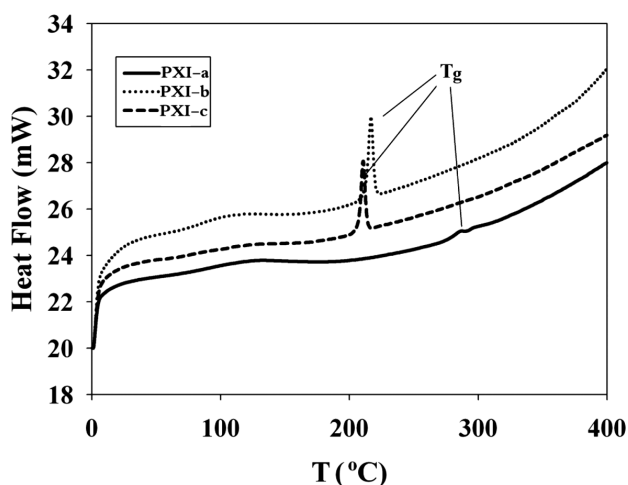


Figure 5: DSC thermograms of PXIs
Slika 5: DSC-krivulja za PXI-je

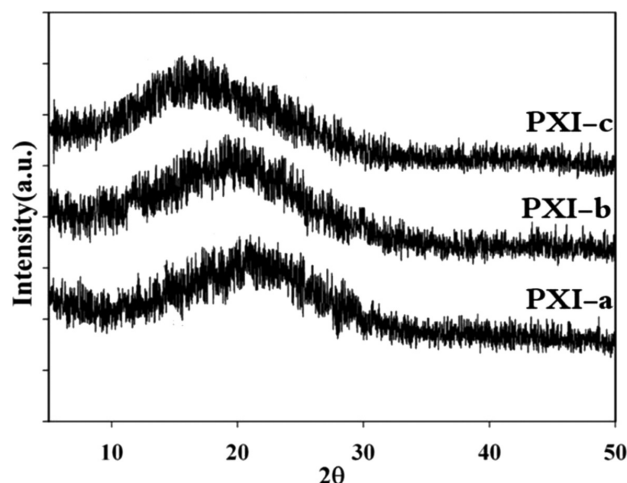


Figure 6: X-ray diffraction patterns of PXIs
Slika 6: Rentgenska difrakcija PXI-jev

PXIs can be attributed to the rigidity and close packing of the polymer chains. No melting endotherm or sign of a crystalline formation was observed in the DSC traces of the poly(xanthone-imide)s as confirmed by their WAXD patterns (Figure 6).

These observations disclose an amorphous nature of the polymers. The thermal stabilities of these poly(xanthone-imide)s were evaluated with TGA (Figure 7). The TGA data indicated a good thermal stability of the PXIs up to 460 °C with a weight loss of 10%. Also, the char yields of the poly(xanthone-imide)s at 600 °C were in a range of 46–67% implying that these polymers possess a good thermal stability. Summing up, it can be deduced that the PMDA-derived polyimide (PXI-a) has the highest thermal stability among those investigated, which can be related to the incorporation of rigid PMDA units. The introduction of hexafluoroisopropylidene units appears to reduce the packing density of molecular chains, which is strongly affected by the intermolecular interactions.

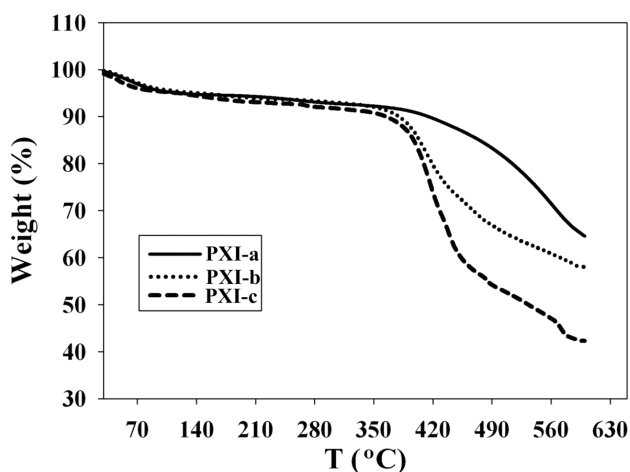


Figure 7: TGA thermograms of PXIs
Slika 7: TGA-krivulja PXI-jev

3.5 Antioxidant activity

Antioxidant polymers, both externally doped and chemically bounded, are extensively utilized in the field of polymeric materials showing antioxidant properties. In recent years, this research area has grown rapidly because antioxidant polymers have many industrial applications including materials science, biomedicine, pharmaceuticals, cosmetics and food packaging. Generally, chemically bounded polymeric antioxidants have unique advantages: they are non-volatile and do not penetrate into the skin and tissue. Consequently, the use of polymeric antioxidants, in which the antioxidant species are covalently bonded to the backbone of the polymer, especially in biocompatible materials, can be a key step toward a healthy life. The antioxidant activities of the parent xanthone (X) and PXIs were evaluated with a DPPH assay and the results are given in **Table 3**. The inhibition percentages determined with the DPPH assay for the monomeric diaminoxanthone was 27.07 %, whereas those of the PXIs were in a range of 47.80–61.30 %. It is evident that the polyxanthones exhibit a higher antioxidant activity than the xanthone itself. As illustrated in **Figure 8**, this behavior can be related to a more extended π -conjugation of the xanthone ring with imide nitrogen of poly(xanthone-imide).

Table 3: Antioxidant inhibition percentages of X and PXIs

Tabela 3: Protioksidativni odstotek inhibicije X in PXI-jev

Compound	Inhibition percentage
X	27.0
PXI-a	49.4
PXI-b	61.3
PXI-c	47.8

The PXI-b, obtained from BTDA, exhibited the highest antioxidant activity because of the presence of the carbonyl group between two phenyl rings, which increases the stability of radicals due to further conjugation. On the contrary, the PXI-c, obtained from 6-FDA, exhibited the lowest antioxidant activity because of the saturated carbon in the $C(CF_3)_2$ groups between the phthalimide units, which can effectively interrupt the conjugation. Thus, placing a xanthone unit into the polymer backbone is a simple way of preparing macromolecular systems with a high antioxidant power that may have the potential for use as biomaterials in biological media.

3.6 Water absorption

The water uptake affects the final application of these high-performance materials, especially in the sorption of heavy metals in water. Though the absorbed water reduces the physical properties such as the mechanical, electrical and dielectrical properties and T_g , it also provides for a better presentation in the other high-tech fields such as the membrane technology. The polymers dealt with in this study have two imide groups and one

xanthone moiety per repeating unit; the polar groups interact with water, which leads to partly hydrophilic materials. Two methods described in the literature²⁹ were used for the water-absorption measurement of the PXIs: at 25 °C for 24 h and at 100 °C for 30 min. As can be seen in **Table 4**, the PXI-b derived from BTDA showed a higher percentage of water absorption (up to 5.4 %) in comparison with the water absorption of the PXI-a and PXI-c based on PMDA and 6FDA (up to 5.0 and 4.8 %, respectively). This is probably due to the existence of the carbonyl group in the backbones of BTDA-based polymers.

Table 4: Water absorption of PXIs

Tabela 4: Absorpcija vode PXI-jev

Compound	Method 1(%)	Method 2(%)
PXI-a	4.7	5.0
PXI-b	5.1	5.4
PXI-c	4.4	4.8

3.7 Adsorption capability

The PXI-b (10 mg) was dissolved in 10 mL of an aqueous solution of heavy metals such as Co (II), Pb (II), Cd (II), Ni (II), Cu (II) and Cr (VI). The mixtures were agitated magnetically at reasonable min^{-1} for 3 d and the solids were separated with filtration. The concentration of metal ions in the filtrate was analyzed via atomic absorption spectroscopy. The quantity of the adsorbed metal ions was calculated with the following equation:

$$Q_t = (C_0 - C_A) \times V/w$$

where Q_t is the amount of metal ions adsorbed into the unit of the composites (mg g^{-1}), C_0 and C_A are the concentrations of metal ions in the initial solution and in the aqueous phase after the adsorption, respectively (mg mL^{-1}). V is the volume of the aqueous phase (mL) and w is the weight of the polymer (mg). The effectiveness of the metal-ion adsorption from the solution (% R) was calculated using the following equation:

$$R = (C_i - C_e) / C_i \times 100$$

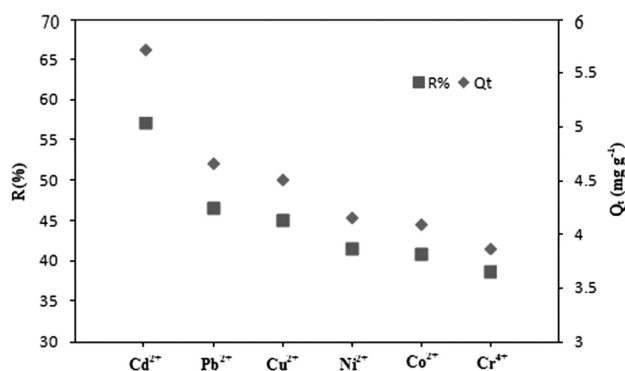


Figure 8: Sorption of transition-metal cations in water using PXIs

Slika 8: Sorpcija kationov prehodnih kovin v vodi z uporabo PXI-jev

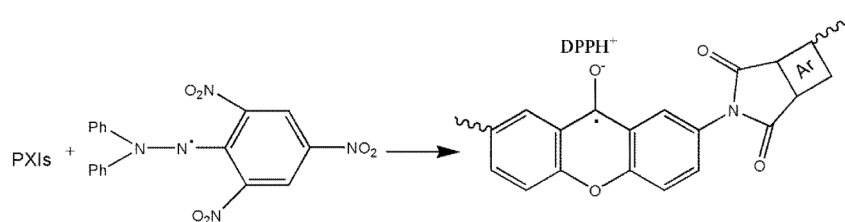
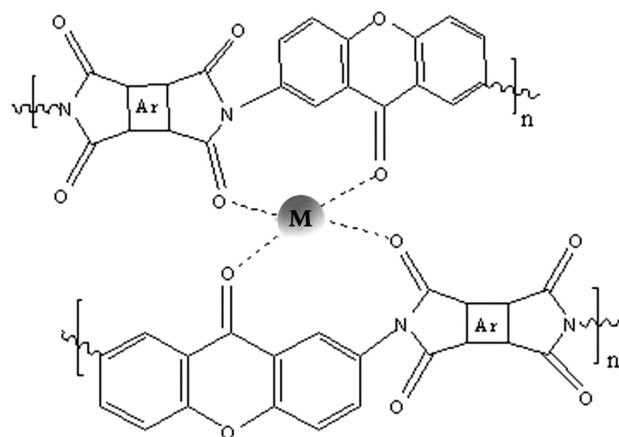


Figure 9: Proposed DPPH radical-scavenging mechanism

Slika 9: Predlagani radikalni splakovalni mehanizem DPPH

where C_i and C_e are the initial concentration and the concentration at the equilibrium of metal ions in the solution, respectively.

Figure 9 depicts the solid-liquid extraction results for the elimination of individual metal cations from the aqueous solution at 25 °C. As can be seen in **Figure 9**, both parameters, Q_i and $\%R$, increased in the order of Cd (II) > Pb (II) > Cu (II) > Ni (II) > Co (II) > Cr (VI), which is comparable with the order of their ionic radii. In **Figure 9**, the extraction for the smallest metal ion Cr (VI) is about 39 % and for the largest metal ion Pb (II), it increases up to 47 %, while the extraction for Cd (II) has the highest quantity; these results were compared with those of poly(azoxanthone-esters)³⁰ in **Table 5**. Therefore, it can be suggested that the carbonyl functional groups along the polymer chains provide a coordinating site to chelate with the metal ions (**Figure 10**).



M: Cr (VI), Co (II), Cu (II), Pb (II), Ni (II), Cd (II)

Figure 10: Chelation of PXIs with metal cations

Slika 10: Kelacija PXI-jev s kovinskimi kationi

Table 5: Heavy-metal sorption capability (%) of PXI-b in comparison with poly(azoxanthone-ester)

Tabela 5: Sposobnost sorpcije težkih kovin (%) PXI-jev v primerjavi s poli(azoksanton-estra)

Compound	Cd ²⁺	Pb ²⁺	Cu ²⁺	Ni ²⁺	Co ²⁺	Cr(VI)
PAXEO	59.7	48.8	45	44.2	43.6	40
PXI-b	57.3	47	45.2	42	41.1	39

4 CONCLUSION

A series of organosoluble poly(xanthone-imide)s with an antioxidant activity was prepared through a two-step chemical imidation of 2,7-diaminoxanthone with commercially available dianhydrides and they it was characterized using different spectroscopic techniques. These polyxanthones showed an amorphous nature with lower glass-transition temperatures (T_g) and a higher solubility than the previously reported polyxanthones. These polymers indicated inherent viscosities in a range of 0.34–0.58 dL/g, showing a moderate molecular weight and being soluble in polar aprotic solvents such as DMF, NMP, DMSO and DMAc at room temperature. The T_{10} values and high char yields for the poly(xanthone-imide)s indicate their good thermal stability. The introduction of a xanthone ring to the main chains of the polyimides imparts advantageous properties of the xanthone nucleus to the polyimides.

The UV-vis absorption spectra of the monomer and poly(xanthone-imide)s exhibited a strong absorption at

355 nm and 300–304 nm, respectively, and the fluorescence emission spectra of the PXIs exhibited peak positions with the maxima at 413–510 nm in the NMP solutions.

The antioxidant capacities of the PXIs were investigated. Good antioxidant activities were obtained for all the poly(xanthone-imide)s. Interestingly, the results showed that antioxidant activities were enhanced after an insertion of xanthone into the polymeric chain.

Also, the solid-liquid extractions were carried out in an aqueous solution and the results showed that the PXIs are effective for eliminating risky heavy metals such as Co (II), Pb (II), Cd (II), Ni (II), Cu (II) and Cr (VI) from wastewaters.

Summing up, an insertion of the xanthone structure into the polymer backbone provides for a high antioxidant activity of polyxanthone imides that may have a potential for application in pharmaceutical and food industries, and also in the solid-phase extraction of environmentally risky cations.

Acknowledgements

We wish to express our gratitude to the Research Council of the University of Mazandaran for partial financial support of this work.

5 REFERENCES

- ¹ M. Kondo, L. Zhang, H. Ji, Y. Kou, B. Ou, Bioavailability and Antioxidant Effects of a Xanthone-Rich Mangosteen (*Garcinia mangostana*) Product in Humans, *Journal of Agricultural and Food Chemistry*, **57** (2009), 8788–8792, doi:10.1021/jf901012
- ² A. Martínez, E. Hernández-Marin, A. Galano, Xanthenes as antioxidants: A theoretical study on the thermodynamics and kinetics of the single electron transfer mechanism, *Food and Function*, **3** (2012), 442–450, doi:10.1039/C2FO10229C
- ³ N. Chairungsrilerd, K. Furukawa, T. Ohta, S. Nozoe, Y. Ohizumi, Histaminergic and serotonergic receptor blocking substances from the medicinal plant *Garcinia mangostana* Linn, *Planta Medica*, **62** (1996), 471–472, doi:10.1055/s-2006-957943
- ⁴ K. Nakatani, M. Atsumi, T. Arakawa, K. Oosawa, S. Shimura, N. Nakahata, Y. Ohizumi, Inhibitions of Histamine Release and Prostaglandin E₂ Synthesis by Mangosteen, a Thai Medicinal Plant, *Biological and Pharmaceutical Bulletin*, **25** (2002), 1137–1141, doi:10.1248/bpb.25.1137
- ⁵ S. L. Crockett, B. Poller, N. Tabanca, E. M. Pferschy-Wenzig, O. Kunert, D. E. Wedge, F. Bucar, Bioactive xanthenes from the roots of *Hypericum perforatum* (common St John's wort), *Journal of Science and Food Agriculture*, **91** (2011), 428–434, doi:10.1002/jsfa.4202
- ⁶ K. Nakatani, T. Yamakuni, N. Kondo, T. Arakawa, K. Oosawa, S. Shimura, H. Inoue, Y. Ohizumi, Biological Activities and Bioavailability of Mangosteen Xanthenes: A Critical Review of the Current Evidence, *Molecular Pharmacology*, **66** (2004), 667–674, doi:10.3390/nu5083163
- ⁷ Y. Sakagami, M. Iinuma, K. G. Piyasena, H. R. Dharmaratne, Antibacterial activity of alpha-mangostin against vancomycin resistant Enterococci (VRE) and synergism with antibiotics, *Phytomedicine*, **12** (2005), 203–208, doi:10.1016/j.phymed.2003.09.012
- ⁸ G. Franklin, L. F. R. Conceição, E. Kombrink, A. C. P. Dias, Xanthone biosynthesis in *Hypericum perforatum* cells provides antioxidant and antimicrobial protection upon biotic stress, *Phytochemistry*, **70** (2009), 65–73, doi:10.1016/j.phytochem.2008.10.016
- ⁹ E. Pinto, C. Afonso, S. Duarte, L. Vale-Silva, E. Costa, E. Sousa, M. Pinto, Antifungal Activity of Xanthenes: Evaluation of their Effect on Ergosterol Biosynthesis by High-Performance Liquid Chromatography, *Chemical Biology and Drug Design*, **77** (2011), 212–222, doi:10.1111/j.1747-0285.2010.01072.x
- ¹⁰ V. Reutrakul, N. Anantachoke, M. Pohmakotr, T. Jaipetch, S. Sophasan, C. Yoosook, J. Kasisit, C. Napaswat, T. Santisuk, P. Tuchinda, Cytotoxic and anti-HIV-1 caged xanthenes from the resin and fruits of *Garcinia hanburyi*, *Planta Medica*, **73** (2007), 33–40, doi:10.1055/s-2006-951748
- ¹¹ A. Groweiss, J. H. Cardellina, M. R. Boyd, HIV-Inhibitory prenylated xanthenes and flavones from *Maclura tinctoria*, *Journal of Natural Products*, **63** (2000), 1537–1539, doi:10.1021/np000175m
- ¹² P. Moongkarndi, N. Kosem, O. Luanratana, S. Jongsomboonkusol, N. Pongpan, Polyphenols from the mangosteen (*Garcinia mangostana*) fruit for breast and prostate cancer, *Fitoterapia*, **75** (2004), 375–377, doi:10.3389/fphar.2013.00080
- ¹³ M. K. Schwaebe, T. J. Moran, J. P. Whitten, Total synthesis of psorospermin, *Tetrahedron Letters*, **46** (2005), 827–829, doi:10.1016/j.tetlet.2004.12.006
- ¹⁴ F. M. Hauser, W. A. Dorsch, General and Expedient Synthesis of 1,4-Dioxygenated Xanthenes, *Organic Letters*, **5** (2003), 3753–3754, doi:10.1021/ol201910v
- ¹⁵ Z. H. Zhang, H. J. Wang, X. Q. Ren, Y. Y. Zhang, A facile and efficient method for synthesis of xanthone derivatives catalyzed by HBF₄/SiO₂ under solvent-free conditions, *Monatshefte für Chemie*, **140** (2009), 1481–1483, doi:10.1007/s00706-009-0204-9
- ¹⁶ D. H. A. Rocha, D. C. G. A. Pinto, A. M. S. Silva, T. Patonay, J. A. S. Cavaleiro, A New Synthesis of 5-Arylbenzo[c]xanthenes from Photoinduced Electrocyclisation and Oxidation of (E)-3-Styrylflavones, *Synlett*, **4** (2012), 559–564, doi:10.1055/s-0031-1290355
- ¹⁷ J. Zhao, C. R. Larock, One-Pot Synthesis of Xanthenes and Thioxanthenes by the Tandem Coupling-Cyclization of Arynes and Salicylates, *Organic Letters*, **7** (2005), 4273–4275, doi:10.1021/ol0517731
- ¹⁸ S. Boonsr, C. Karalai, C. Ponglimanont, A. Kanjana-opas, K. Chantapromma, Antibacterial and cytotoxic xanthenes from the roots of *Cratogeomys formosum*, *Phytochemistry*, **67** (2006), 723–727, doi:10.1016/j.phytochem.2006.01.00
- ¹⁹ J. L. Patel, H. S. Patel, Xanthone Polymers Derived from Salicylic Acid-Formaldehyde Polymers, *Journal of Macromolecular Science Part A*, **23** (1986), 285–294, doi:10.1080/00222338608063391
- ²⁰ R. Darms, Fairfax, Wilmington, Del., Polyxanthenes, United States Patent Office, 1970, 3546167
- ²¹ H. M. Colquhoun, D. F. Lewis, D. J. Williams, Synthesis of Dixanthenes and Poly(dixanthone)s by Cyclization of 2-Aryloxybenzotrioles in Trifluoromethanesulfonic Acid, *Organic Letters*, **3** (2001), 2337–2340, doi:10.1021/ol010097+
- ²² M. Ghaemy, M. Bazzar, Synthesis of soluble and thermally stable polyimides from 3,5-diamino-*N*-(4-(8-quinolinoxy) phenyl) aniline and various dianhydrides, *Journal of Applied Polymer Science*, **119** (2011), 983–988, doi:10.1002/app.32817
- ²³ S. Zhang, Y. Li, D. Yin, X. Wang, X. Zhao, Y. Shao, S. Yang, Study on synthesis and characterization of novel polyimides derived from 2,6-Bis(3-aminobenzoyl) pyridine, *European Polymer Journal*, **41** (2005), 1097–1107, doi:10.1016/j.eurpolymj.2004.11.014
- ²⁴ T. Lee, J. Lim, I. Chung, I. Kim, C. S. Ha, Preparation and characterization of polyimide/modified β -cyclodextrin nanocomposite films, *Macromolecular Research*, **18** (2010), 120–128, doi:10.1007/s13233-009-0120-1
- ²⁵ H. S. Jin, J. H. Chang, Synthesis and Characterization of Colorless Polyimide Nanocomposite Films Containing Pendant Trifluoromethyl Groups, *Macromolecular Research*, **16** (2008), 503–509, doi:10.1007/BF03218551
- ²⁶ M. M. Lakouraj, G. Rahpaima, M. Mohseni, Synthesis, characterization, and biological activities of organosoluble and thermally stable xanthone-based polyamides, *Journal of Materials Science*, **48** (2013), 2520–2528, doi:10.1007/s10853-012-7041-7
- ²⁷ J. P. Chen, A. Natanoshn, Synthesis and characterization of novel carbazole-containing soluble polyimides, *Macromolecules*, **32** (1999), 3171–3177, doi:10.1021/ma981609b
- ²⁸ M. Kumar, K. Sharma, R. M. Samarth, A. Kumar, Synthesis and antioxidant activity of quinolinobenzothiazinones, *European Journal of Medical Chemistry*, **45** (2010), 4467–4472, doi:10.1016/j.ejmech.2010.07.006
- ²⁹ K. Xie, S. Y. Zhang, J. G. Liu, M. H. He, S. Y. Yang, Synthesis and characterization of soluble fluorine-containing polyimides based on 1,4-bis(4-amino-2-trifluoromethylphenoxy)benzene, *Journal of Polymer Science, Part A: Polymer Chemistry*, **39** (2001), 2581–2590, doi:10.1002/pola.1235
- ³⁰ M. M. Lakouraj, G. Rahpaima, M. Mohseni, Synthesis, characterization, metal sorption, and biological activities of organosoluble and thermally stable azoxanthone-based polyester, *Polymer for Advanced Technology*, **26** (2015), 234–244, doi:10.1002/pat.3446

CORRELATION OF THE HEAT-TRANSFER COEFFICIENT AT SPRINKLED TUBE BUNDLE

KORELACIJA KOEFICIENTA PRENOSA TOPLOTE PRI POTRESENEM SNOPU CEVI

Petr Kracík, Ladislav Šnajdárek, Martin Lisý, Marek Baláš, Jiří Pospíšil

Brno University of Technology, Institute of Power Engineering, Faculty of Mechanical Engineering,
Technická 2896/2, 616 69 Brno, Czech Republic
kracik@fme.vutbr.cz

Prejem rokopisa – received: 2014-07-23; sprejem za objavo – accepted for publication: 2015-07-08

doi:10.17222/mit.2014.115

The paper presents a research on the heat-transfer coefficient at the surface of a sprinkled tube bundle, using a boiling simulation. A tube bundle consists of thirteen copper tubes divided into two rows and it is located in a low-pressure chamber where vacuum is generated by an exhaustor via an ejector. The liquid tested was water at the absolute pressure in the chamber of 96.8–12.3 kPa and at a thermal gradient of 55–30 °C between the cooled liquid flowing upwards inside the exchanger and the heated falling film liquid. The flow of the falling film liquid ranged from 0–17 L/min. Two types of tubes were tested, a smooth one and a sandblasted one. The correlation of the average heat-transfer coefficient at the surfaces of both tube types was identified.

Keywords: sprinkled, water, under-pressure, heat transfer

Članek predstavlja raziskavo koeficienta prenosa toplote na površini potresenega snopa cevi s simulacijo vrenja. Snop cevi sestoji iz trinajstih bakrenih cevi, razporejenih v dve vrsti in se nahaja v nizko tlačni komori, kjer se ustvarja vakuum s pomočjo aspiratorja preko ejetorja. Preizkusna tekočina je bila voda pri absolutnem tlaku v komori med 96,8 kPa do 12,3 kPa in toplotnim gradientom 55 °C do 30 °C med ohlajeno tekočino, ki je tekla znotraj izmenjevalca navzgor in padajočo tanko plastjo segrete tekočine. Tok padajoče tekočine je bil med 0 L/min in 17 L/min. Preizkušeni sta bili dve vrsti cevi, gladka in peskana. Postavljena je bila korelacija povprečnega koeficienta prenosa toplote na površini obeh vrst cevi.

Ključne besede: posuto stanje, voda, podtlak, prenos toplote

1 INTRODUCTION

On a horizontal tube bundle sprinkled with a liquid at a low flow rate, a thin liquid film is formed that facilitates an effective heat transfer. The liquid flowing through the bundle may form three basic sprinkle modes visible in **Figure 1**. These are: a) the droplet mode, b) the jet mode and c) the membrane (sheet) mode.¹

The transition from the droplet into the jet mode is defined with at least one stable water column among the droplets. The transition from the jet into the membrane mode is defined with the columns' connections and their creation of small triangular sheets. In this mode, columns and sheets exist side by side. The type of mode depends

mainly on the tube pitch at a horizontal tube bundle, the flow rate and physical properties of the liquid.

2 ANALYSIS

This paper presents the results of the heat-transfer coefficient at the surface of a sprinkled tube bundle situated in a low-pressure environment, where the water flowing outside the bundle has not yet reached the boiling point. For the practical use of the experimental results and their generalisation for a wide range of operational parameters, Chun and Seban² suggested the mathematical dependence of the Nusselt number (Nu [-]) on the Reynolds number (Re [-]) that expresses the falling-film-liquid flow, the Prandtl number (Pr [-]) that is functionally dependent mainly on the falling-film-liquid temperature and the pressure in the surroundings of the liquid, and, in the case that the surface of the sprinkled tube boils, it also includes the thermal flow density. The Nusselt number for a non-boiling liquid can be generally defined as:

$$Nu = \alpha_0 \cdot \sqrt[3]{\frac{v^2}{g \cdot \lambda^2}} = a_1 \cdot Re^{a_2} \cdot Pr^{a_3} \quad (1)$$

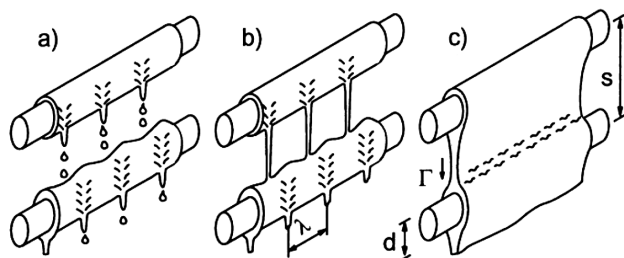


Figure 1: Sprinkle modes:¹ a) droplet, b) jet, c) membrane
Slika 1: Načini potresenja:¹ a) kapljica, b) curek, c) zavesa

where α_0 [$\text{W m}^{-2} \text{K}^{-1}$] is the heat-transfer coefficient at the sprinkled tube surface, ν ($\text{m}^2 \text{s}^{-1}$) is the kinematic viscosity, g (m s^{-2}) is the gravitational acceleration, λ ($\text{W m}^{-1} \text{K}^{-1}$) is the thermal conductivity and the values a_1 to a_3 are empirically derived constants.

W. H. Parken et al.⁴ published the results of their experiments where they always sprinkled one brass, electrically heated tube. The experiments were conducted in the temperature range of the falling film liquid between 49 °C and 127 °C, in an input range of 30–80 kW/m^2 and at a falling-film-liquid mass flow related to the tube length (Γ) of 0.135–0.366 $\text{kg}/(\text{s m})$. The measured data for water that was not boiling at the tube surface were used to derive empirical equations for the average heat-transfer coefficient for tube diameters of 25.4 mm (1") and 50.8 mm (2") based on Equation (1):

$$\alpha_0 = 0.042 \cdot \sqrt[3]{\frac{\lambda^3 \cdot g}{\nu^2}} \cdot \left(\frac{4\Gamma}{\mu}\right)^{0.15} \cdot \left(\frac{\nu}{a}\right)^{0.53} \quad (2)$$

$$\alpha_0 = 0.038 \cdot \sqrt[3]{\frac{\lambda^3 \cdot g}{\nu^2}} \cdot \left(\frac{4\Gamma}{\mu}\right)^{0.15} \cdot \left(\frac{\nu}{a}\right)^{0.53} \quad (3)$$

where μ (Pa s) is the dynamic viscosity, a ($\text{m}^2 \text{s}^{-1}$) is the thermal diffusivity and the water properties were determined with the average temperature of the tube-wall temperature and the input falling-film-liquid temperature. When determining Equation (2) for the tube diameter of 25.4 mm, the relative error reached seven percent and seven data points out of fifty-two deviated by more than 10 %. With Equation (3), derived for the tube diameter of 50.8 mm, the relative error reached the maximum of 8 %.

W. L. Owens³ published the results of his research on the heat-transfer coefficient at the surface of one smooth stainless-steel tube of one- and two-inch diameters that was sprinkled with both water boiling at the tube surface and non-boiling water, in a Reynolds-number range of 120–10⁴ [-]. In comparison with K. R. Chun's and R. A. Seban's² equations that already formed the basis for a derivation of the empirical dependencies of the above-mentioned W. A. Parken and al.⁴, W. L. Owens reached the conclusion that the Nusselt number (or the heat-transfer coefficient at the tube surface) is not, at all conditions, dependent on the Reynolds number. However, eventually he added to his equations the dimensionless ratio of the distance between the sprinkling and the sprinkled tube to the sprinkled-tube diameter, the total of this raised to the power of one tenth.

When assessing and determining the empirical dependence, W. L. Owens³ used dispersion diagrams, which proved the necessity of the extraction of the root of the Prandtl number by the second power, helping to achieve a linearization in relation to the rest of the parameters in the following equations of the Nusselt-number calculation with a relatively low value dispersion (all the equation deviations were determined at 10 %). The final empirical dependence of the heat-transfer coefficient of

non-boiling water for the laminar mode lies in Equation (4) and for the turbulent mode in Equation (5):

$$\alpha_{0,\text{lam}} = 2.2 \cdot \sqrt[3]{\frac{\lambda^3 \cdot g}{\nu^2}} \cdot \left(\frac{s-D}{D}\right)^{0.1} \cdot \frac{1}{\sqrt[3]{Re}} \quad (4)$$

$$\alpha_{0,\text{tur}} = 0.185 \cdot \sqrt[3]{\frac{\lambda^3 \cdot g}{\nu^2}} \cdot \left(\frac{s-D}{D}\right)^{0.1} \cdot \sqrt{Pr} \quad (5)$$

where s (m) is the pitch pipe, D (m) is the tube diameter and the transition between these modes was determined by W. L. Owens³ in Equation (6):

$$Re_{tr} = 1.68 \cdot \frac{1}{Pr^{1.5}} \quad [-] \quad (6)$$

In the case of boiling occurring at the tube surface, Owens³ assumed a fully developed turbulent flow, for which the following heat-transfer-coefficient equation stands:

$$\alpha_{0,\text{tur}} = 0.175 \cdot \left(\frac{s-D}{D}\right)^{0.1} \cdot \sqrt[3]{\dot{q}} \cdot \sqrt{Pr} \quad (7)$$

Should the temperature of the tube wall be higher than the temperature of the saturated liquid flowing around the tube, although the liquid does not reach this temperature, the so-called undercooled boiling may occur. This generalised assumption can be deepened by the criterion that undercooled boiling can be viewed at the tube where the bubbles appear. The temperature at the bubble surface is higher or equal to the temperature of the saturated liquid, corresponding to the pressure inside the bubbles. This phenomenon was studied by Sernas⁵ who published the results of his experiments when he sprinkled, in each case, one brass electrically heated tube with water. Experiments were conducted in a falling-film-liquid temperature range of 44.9–117 °C, in an input range of 47–79 kW/m^2 and a mass flow related to the tube length of 0.133–0.292 $\text{kg}/(\text{s m})$. He derived empirical equations of the average heat-transfer coefficient for a tube of 25.4 mm (8) and 50.8 mm (9) diameters from the measured data:

$$\alpha_0 = 0.1925 \cdot \sqrt[3]{\frac{\lambda^3 \cdot g}{\nu^2}} \cdot Re^{0.24} \cdot Pr^{0.66} \quad (8)$$

$$\alpha_0 = 0.1725 \cdot \sqrt[3]{\frac{\lambda^3 \cdot g}{\nu^2}} \cdot Re^{0.24} \cdot Pr^{0.66} \quad (9)$$

where the mean quadratic deviation equalled 3.1 % at the smaller diameter and 3.3 % at the larger diameter and only one point out of 33 exceeded such a deviation at the smaller diameter and 4 points out of 39 at the larger diameter, which makes about 10 %.

3 EXPERIMENTAL DEVICE

For the purposes of examining the heat transfer at sprinkled tube bundles, a test apparatus was constructed at the Brno University of Technology (**Figure 2**). The

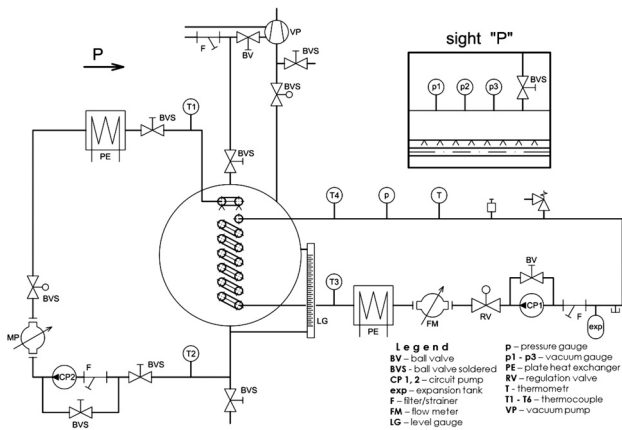


Figure 2: Low-pressure stand diagram
Slika 2: Diagram stanja pri niskem tlaku

tube bundle, at which both boiling and condensation can be simulated, is placed in a vessel where a low pressure is created by an exhauster through an ejector.

The low-pressure stand chamber is a cylindrical vessel, 1.2 m in length, with three apertures, in which the tube bundle of an examined length of 940 mm is inserted. The tube bundle is installed in two fitting metal sheets, which define the sprinkled area. The bundle is divided into two rows and consists of 13 (7 and 6) copper tubes of a 12-mm diameter with a tube pitch of 25 mm. The bundle is U-shaped and the flow in the loop is uninterrupted.

Two closed loops are connected to the chamber; a sprinkled one and a sprinkling one. The sprinkled loop is designed for an overpressure of up to 1.0 MPa and it functions as a cooling/heating liquid conveyor. There are a pump, a regulation valve, a flow meter and a plate heat exchanger attached to both loops. The plate heat exchanger can be connected to a boiler or a gas boiler with hot water designated for the liquid heating-up or cooling water in the case of cooling. In order to enable visual control, the sprinkled loop also includes a manometer and a thermometer. The thermal status in individual loops is measured with wrapped unearthed T-type thermocouples on the agents' input and output from the vessel. There are three vacuum gauges measuring the low pressure. The first vacuum gauge is designed for the visual control and it is a mercury meter; the second digital vacuum gauge, Baumer TED6, enables the measuring within the whole desired low-pressure range, but it is less accurate with lower pressure values. To allow accurate measuring of the low spectrum, the third digital vacuum gauge with a range of 2.0–0 kPa is used. The accuracy of the vacuum gauge, providing the results for the assessment, is 0.5 % of the measured range, i.e., ± 0.5 kPa.

Electromagnetic flow meters Flomag 3000 attached to both loops measure the flow rate. The measuring range of the flow meters is 0.0078–0.9424 L s⁻¹, where the accuracy is 0.5 % of the measured range, i.e., ± 0.00467 L s⁻¹. All the examined quantities are scanned

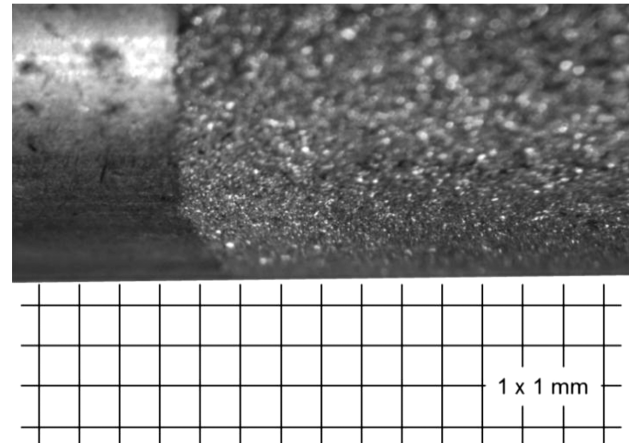


Figure 3: Sprinkled-tube surface types (smooth on the left and sandblasted on the right)
Slika 3: Vrsta površine na cevi (gladka na levi in peskana na desni)

with a frequency of 0.703 Hz, using measuring cards DAQ 56 either directly (thermocouples) or via transducers.

Apart from the influence of the sprinkled and sprinkling temperature media, the absolute pressure in the vessel and the medium flow for the studied heat-transfer coefficient at the tube surface, the influence of the tube surface type is also investigated. The illustration of the tested tube surfaces can be found in Figure 3. The sandblasted surface was treated with a blast-furnace slag to make it coarser, but the reduction of the material was insignificant, so the effect of this technology modification is negligible.

The evaluation of the measured data is based on the thermal balance between the sprinkled and sprinkling loop according to the law of conservation of energy. The transferred heat comprises convection, conduction and radiation. At lower temperatures, the heat transferred by radiation is negligible; therefore, it is excluded from further calculations. The calculation of the studied heat-transfer coefficient is based on Newton's heat-transfer law and Fourier's heat-conduction law.

4 RESULTS

The final dependence of the heat-transfer coefficient on the smooth tube surface is shown with blue points in Figure 4. In this mode, hot water flows inside the tubes with the average input temperature of 55.2 °C, with a statistical deviation of four tenths of a degree and with the average flow rate of 12.4 \pm 0.5 L min⁻¹. The exchanger is sprinkled with cool water with the average input temperature of 29.9 \pm 0.5 °C and the sprinkling-liquid flow rate ranges from 1.0 L to 15.8 L min⁻¹. This mode was tested at a pressure level of 96.8–12.9 kPa (atmospheric pressure at the time of measurement). The same diagram displays the dependence of the heat-transfer coefficient on the sandblasted tubes with red points. In this mode, the average temperature of the closed-loop input was 55.1 °C, having a statistical deviation of half a

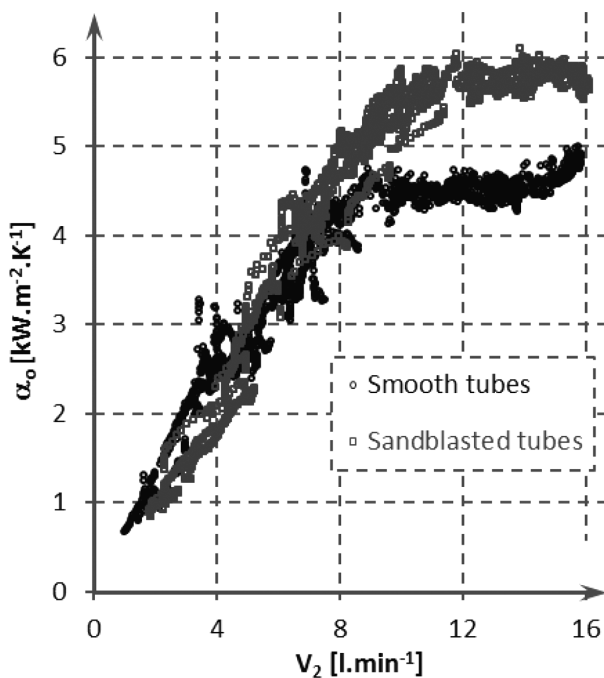


Figure 4: Dependence of heat-transfer coefficient on falling-film-liquid volumetric flow rate

Slika 4: Odvisnost koeficienta prenosa toplote od volumetrične hitrosti padajoče tekočine

degree and the average flow rate of $13.7 \pm 0.3 \text{ L min}^{-1}$. The exchanger is sprinkled with cool water with the average input temperature of $29.8 \pm 0.5 \text{ }^\circ\text{C}$ and the sprinkling-liquid flow rate ranges from 1.8 to 16.1 L min^{-1} . This mode was tested at a pressure level of $96.7\text{--}12.3 \text{ kPa}$ (atmospheric pressure at the time of measurement).

Considering the total sprinkled length, only the jet mode was achieved with the maximum flow rate. It changed into the droplet-jet mode at a flow rate of approximately 14.0 L min^{-1} and into the full droplet mode at a flow rate of approximately 6.0 L min^{-1} or below this value. **Figure 4** clearly shows the final trends of the heat-transfer coefficient in dependence on the increasing falling-film-liquid volumetric flow rate and the convenience of individual surface types. Up to a flow rate of approximately 5.0 L min^{-1} the smooth surface is more convenient, as smooth tubes enable the heat-transfer coefficient to improve by at least 45 %. In a flow-rate range of approximately $5.0\text{--}7.0 \text{ L min}^{-1}$ no surface proves better, and at a flow rate of 9.0 L min^{-1} and higher the sandblasted surface is more convenient. The difference against the smooth surface is up to 22 %. The measuring-device error recalculated into the heat-transfer coefficient fluctuated around the average value of 3.8 % for the smooth tubes and around 5.3 % for the sandblasted tubes.

For the purpose of a comparison with the other authors, analogy criteria and the functional dependence between them were used, as visible on **Figure 5**, where the points indicating "smooth", including the curve

connecting the points, stand for the resulting Nusselt number, which is the function of the Reynolds number and it is derived from the first section of Equation (1). The same applies to the points indicating "sandblasted". The average measuring-device error related to the heat-transfer coefficient at the tube-bundle surface is displayed at individual points; it is recalculated into the Nusselt number and it is the same, in relative values, as for the heat-transfer coefficient. This figure does not display all the measured points, but only the above-mentioned selected points. Status variables used in the equations defined by other authors and displayed in the same figure were taken from these particular points.

The results of the measurement are compared with two other authors and one author team. The first comparison is with Parken et al.⁴, displaying the points (a) for the tube diameter of 25.4 mm according to Equation (2) and the points (b) for the tube diameter of 50.8 mm according to Equation (3). Another comparison is with Sernas⁵, displaying the points for the same diameters according to Functions (8) and (9). The last author whose points are included in the figure is Owens³, who defined the functions for various diameters, i.e., the functions for a laminar and a turbulent flow. With respect to the high Prandtl number, with which the transit Reynolds number is determined according to Equation (6), the case is considered to be a turbulent flow in the entire measured range. Therefore, the points are displayed according to Equation (5). The points are connected by a conveniently selected curve to highlight the trend.

Figure 5 presents two major intersections of the given waveforms with the compared curves. The values

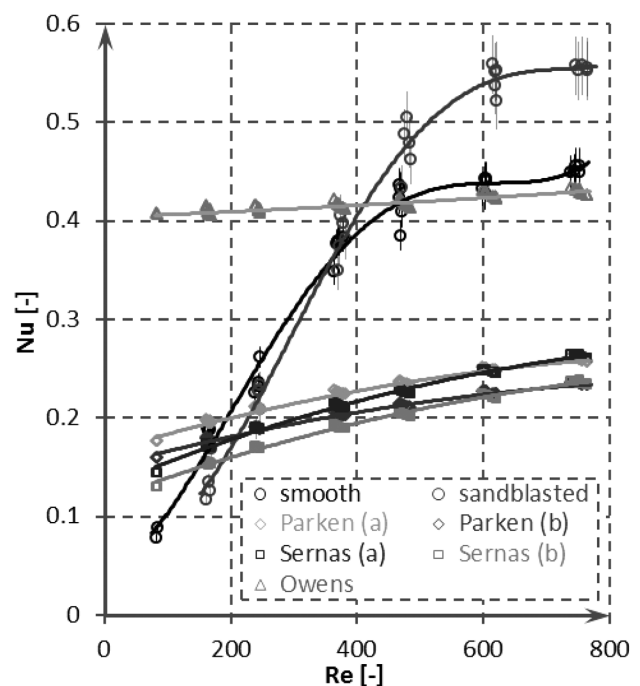


Figure 5: Comparison of obtained results with other authors

Slika 5: Primerjava dobljenih rezultatov z rezultati drugih avtorjev

of the first one are determined according to Parken and Sernas, in a Reynolds number range of approximately 150–240, i.e., a Nusselt-number range of 0.08–0.17, and the values of the second one are displayed according to Owens, in a Reynolds-number range of approximately 410–470, where the Nusselt number is approximately 0.42.

The functions according to Parker and Sernas were determined for the mass flow related to a length unit from $0.135 \text{ kg}\cdot\text{s}^{-1}\cdot\text{m}^{-1}$, which corresponds to the end of the studied Reynolds number range. The function defined by Owens, calculated with the value of the outer tube diameter of 12.0 mm, covers approximately 40 % of the studied volumetric flow-rate range, in which the correspondence with the results for the smooth tubes is quite strong, starting already at the value of the Reynolds number of 380.

Criterial functions were derived for the whole statistical collection of the measured data for the bundles of smooth or sandblasted tubes. When determining the criterial equation, the recommended Chun's and Seban's² Equation (1) was not effective, although it is most frequently applied by many authors. Within the regression analysis the given trend was best expressed with a linear combination of power functions:

$$Nu = \alpha_0 \cdot \sqrt[3]{\frac{\mu^2}{g\rho^2\lambda^3}} \quad (10)$$

$$Nu = a + b \cdot (Re)^c + d \cdot (Re)^e + f \cdot (Re)^g + h \cdot (Pr)^i$$

where coefficients c, e, g, i were estimated on the basis of the function parameters and the other coefficients were calculated with a statistical software. All the coefficients for the smooth and sandblasted tubes are given in **Table 1**.

Table 1: Coefficients for equation (10)

Tabela 1: Koeficienti za enačbo (10)

	<i>a/b</i>	<i>c/d</i>	<i>e/f</i>	<i>g/h</i>	<i>i</i>
Smooth	1.5344	1.35	5.3	4.8	0.3
	0.000134	$1.992 \cdot 10^{-15}$	$-6.332 \cdot 10^{-14}$	-0.9692	
Sand-blasted	2.4086	1.48	3.2	0	0.3
	0.000066	$-3.6894 \cdot 10^{-15}$	0	-1.547	

Both forms of derived equation were tested comparatively against the originally calculated values of the Nusselt number; in the case of smooth tubes, it was 2483 points. For this statistical collection, a relative error of 4.25 % and a relative mean quadratic deviation of 4.72 % were set; they are below 5 % that is generally considered as the limit for a well-defined regression function. In the case of sandblasted tubes, 1874 points were measured (calculated) which, in comparison with the derived function, showed a relative error of 4.50 % and a relative mean quadratic deviation of 4.63 %, which are also below the 5 % limit.

5 CONCLUSIONS

This paper presents a research on the heat-transfer coefficient at the surface of a sprinkled tube exchanger where the falling film liquid was heated. This tube bundle was tested in a low-pressure chamber, in a pressure range of 96.8–12.3 kPa(abs) and at a thermal gradient of 55–30 °C with various falling-film-liquid flow rates. Two different types of the tube-bundle surface were studied, i.e., a smooth one and a sandblasted one, while the geometries of the heat exchangers were identical. Correlations of the mean heat-transfer coefficient at the tube surface were determined for both heat-exchanger types and these were compared with the other authors who conducted research on the heat-transfer coefficient in a sprinkled tube with water as the falling film liquid that did not reach the boiling point.

When comparing the results with the other authors, it is necessary to consider the difference as merely orientational, due to the following reasons. The studied tube bundle was made of copper tubes with a 12 mm diameter and the total bundle length of 12.22 m. The other authors studied the heat-transfer coefficient at a single short smooth tube with a 1-m length, and 1" and 2" diameters; in Sernas and Parken's case, the tubes were made of brass and in Owens's case, they were made of stainless steel. In spite of that, a significant correspondence of the Nusselt number occurred in the case of the tube bundle with a smooth surface where the Reynolds number was higher than approximately 400 [-].

Acknowledgment

The presented results were obtained in the frame of project NETME CENTRE PLUS (LO1202), created with the financial support from the Ministry of Education, Youth and Sports of the Czech Republic under the National Sustainability Programme I.

6 REFERENCES

- 1 R. Armbruster, J. Mitrovic, Evaporative cooling of a falling water film on horizontal tubes, *Experimental Thermal and Fluid Science*, 18 (1998) 3, 183–194, doi:10.1016/S0894-1777(98)10033-X
- 2 K. R. Chun, R. A. Seban, Heat Transfer to Evaporating Liquid Films, *Journal of Heat Transfer*, 93 (1971) 4, 391–396, doi:10.1115/1.3449836
- 3 W. L. Owens, Correlation of thin film evaporation heat transfer coefficients for horizontal tubes, *Proceedings of the Fifth Ocean Thermal Energy Conversion Conference*, Miami Beach, Florida, 1978, 71–89
- 4 W. H. Parken, L. S. Fletcher, V. Sernas, J. C. Han, Heat Transfer Through Falling Film Evaporation and Boiling on Horizontal Tubes, *Journal of Heat Transfer*, 112 (1990) 3, 744–750, doi:10.1115/1.2910449
- 5 V. Sernas, Heat Transfer Correlation for Subcooled Water Films on Horizontal Tubes, *Journal of Heat Transfer*, 101 (1979) 1, 176–178, doi:10.1115/1.3450913

MATHEMATICAL MODELING OF A CEMENT RAW-MATERIAL BLENDING PROCESS USING A NEURAL NETWORK

MATEMATIČNO MODELIRANJE POSTOPKA MEŠANJA SESTAVIN CEMENTA S POMOČJO NEVRONSKE MREŽE

Aysun Egrisogut Tiryaki, Recep Kozan, Nurettin Gokhan Adar

Sakarya University, Department of Mechanical Engineering, 54187, Sakarya, Turkey
aysune@sakarya.edu.tr

Prejem rokopisa – received: 2014-08-01; sprejem za objavo – accepted for publication: 2015-06-30

doi:10.17222/mit.2014.156

Raw-material blending is an important process affecting cement quality. The aim of this process is to mix a variety of materials such as limestone, shale, sandstone and iron to produce cement raw meal for the kiln. One of the fundamental problems in cement manufacture is ensuring the appropriate chemical composition of the cement raw meal. A raw meal with a good fineness and well-controlled chemical composition by a control system can improve the cement quality. The first step in designing a control system for the process is obtaining an appropriate mathematical model. In this study, Linear and Nonlinear Neural Network models were investigated for the raw-material blending process in the cement industry and their results were compared with the experimental data. The results showed that the nonlinear model has a higher predictive accuracy.

Keywords: mathematical modeling, cement, raw material blending, neural network

Mešanje sestavin je pomemben postopek, ki vpliva na kvaliteto cementa. Naloga tega postopka je zmešati različne materiale, kot so: apnenec, škrlavec, peščenjak, železo in drugi; da se dobi surovino za cement za rotacijsko peč. Ena od osnovnih težav pri izdelavi cementa je zagotoviti primerno kemijsko sestavo surovine za cement. Kontrolni sistem za surovino z dobro zrnatostjo in dobro kontrolirano kemijsko sestavo, lahko izboljša kvaliteto cementa. Prvi korak pri postavitvi kontrole procesa je postavitev primerne matematičnega modela procesa. V študiji sta bila preiskovana linearni in nelinearni model nevronske mreže za postopek mešanja v cementni industriji in rezultati so bili primerjani z eksperimentalnimi podatki. Rezultati so pokazali, da ima nelinearni model večjo točnost napovedovanja.

Ključne besede: matematično modeliranje, cement, mešanje surovin, nevronska mreža

1 INTRODUCTION

Cement is the world's most widely used construction material and is a key ingredient in concrete. The cement manufacturing process includes the raw-materials blending process as well as the burning process, the cement clinker grinding process, and the packaging process. One of the main processes that effects cement quality is the raw-material blending process. The task of this process is to mix a variety of materials such as limestone, shale, sandstone, and iron, to produce cement raw meal for the kiln. Raw meal mainly contains four oxides: calcium oxide or lime (CaO), silica (SiO_2), alumina (Al_2O_3) and iron oxide (Fe_2O_3). The oxide compositions of the raw meal significantly affect the quality and the properties of cement clinker. On the other hand, the chemical compositions of the raw materials vary from time to time and the feeder tanks do not contain chemically homogeneous raw materials. That is why blend estimating systems with computer control are needed to obtain the correct composition of the blend.

The approaches to the solution of this fundamental blending problem have varied widely. Stochastic modeling, which uses experimental process data and the characteristics of the various disturbances, and self-tuning control of a continuous cement raw-material

mixing system were presented in ¹. A recursive estimation of the cement raw-material feedstream oxide concentrations was presented by using information from the output raw meal X-ray analysis.² L. Keviczky et al.³ modified the self-tuning (ST) minimum variance (MV) regulator algorithm developed for a multiple input multiple output (MIMO) system presented with the required average for finite time (RAFT). P. Lin et al.⁴ proposed a two-level adaptive control policy combined with a heuristic auxiliary system for the robustness of the raw mix control system. A new generic optimal controller structure, which is equivalent to those used at internal model principal or pole placement technique, was dealt with in ⁵. C. Ozsoy et al.⁶ presented a constrained self-tuning composition control algorithm for a MIMO system. The identification and control of the cement raw-material blending system in a cement factory were examined and in the identification part of the studies, three different linear multivariable stochastic time-series models (ARX) in which the inputs are the feed ratios of the raw-material components (low grade and iron ore) and the outputs are the iron oxide and/or the lime module of the raw meal, were constructed.⁷ K. Kizilaslan et al.⁸ modeled the raw-material blending process in the cement industry using intelligent techniques and the results are compared with

classic system-identification methods. A fuzzy controller is proposed to improve the real-time performance in the blending process.⁹ An adaptive control framework was presented for the raw-material blending process, and the corresponding optimal control structure was discussed too.¹⁰ A fuzzy neural network with particle-swarm optimization FNN-PSO methods was applied to establish and optimize the cement raw-material blending process in¹¹. The ingredient ratio optimization problem was analyzed using the general nonlinear time-varying (G-NLTV) model for the cement raw-material blending process under various conditions by X. Li et al.¹²

The first step in applying an adaptive and dynamic control strategy to this kind of process is obtaining an appropriate mathematical model of the process. This paper is concerned with modeling the raw-material blending process in cement industry by using neural networks. Linear and Nonlinear Neural Network models were developed and the results were compared with the experimental data.

2 CEMENT RAW-MATERIAL BLENDING PROCESS

The cement -manufacturing process consists broadly of mining, crushing and grinding, burning, and grinding with gypsum. In the dry process of cement production, the raw materials are proportioned, stored, ground, mixed, pulverized, and fed into the kiln in a dry state. Inside the kiln the raw mix will undergo a sequence of reactions. Sintering takes place at the final stage of the reaction, i.e., at 1400–1450 °C, and a substance called clinker, having its own physical and chemical properties, is formed. The clinker is cooled, crushed, and mixed with a predetermined percentage of gypsum to regulate the setting time of the cement. Finally, the finished pro-

duct, known as Portland cement, is stored in large storage bins called silos, from which it is fed to an automatic packing machine.⁸

The original cement materials are obtained from a natural mine, thus the chemical composition is time-varying function. Composition fluctuation is inevitable and it may contain randomness. Therefore, modeling of the cement raw-material blending process becomes more important and a challenge.

In this study, the raw material blending process in the Nuh Cement Factory in Turkey was investigated. Here, three different feed streams, which are low grade, high grade and iron ore, are controlled by weigh feeders and, after mixing on a conveyor belt, fed to the raw mill. A simplified schematic diagram of the raw mill blending process is shown in **Figure 1**.

Mixing on a conveyor belt is fed to the raw mill by weight-feeders, before being thoroughly ground and mixed in the raw mill. In this study, two feed streams containing low grade and iron ore were modeled, because the values of all the measurements are a percentage. A sample of this raw mix is collected at the input of the raw mill grinder by an auto sampler and analyzed every five seconds and the average of twelve analyses is sent to the computer through a data-communication line by PGNA (Prompt Gamma Neutron Activation Analyzers). These data are utilized and manipulated for the raw meal feed stream. Thus, the desired blend is supplied continuously. The measurements consist of the output concentrations of the four basic oxides (CaO, SiO₂, Fe₂O₃ and Al₂O₃). The raw meal is transferred to homogenization basins where further continuous mixing decreases the magnitude of the concentration variations about the silo average values. The complete filling of a basin requires a unit batch time of 16 h.

The quality of raw meal depends on the relative rates of CaO, SiO₂, Fe₂O₃ and Al₂O₃. The relative rates can be expressed by the so-called modulus values:^{8,12}

Lime standard (or modulus):

$$ML = \frac{100CaO}{2.8SiO_2 + 1.1Al_2O_3 + 0.8Fe_2O_3} \quad (1)$$

Aluminum modulus:

$$MA = \frac{Al_2O_3}{Fe_2O_3} \quad (2)$$

Silica modulus:

$$MS = \frac{SiO_2}{Al_2O_3 + Fe_2O_3} \quad (3)$$

A high *ML* requires a high heat consumption for the clinker burning inside the kiln and thus gives more strength to the cement. A higher *MS* decreases the liquid-phase content, which impairs the burn ability of the clinker and reduces the cement setting time. The

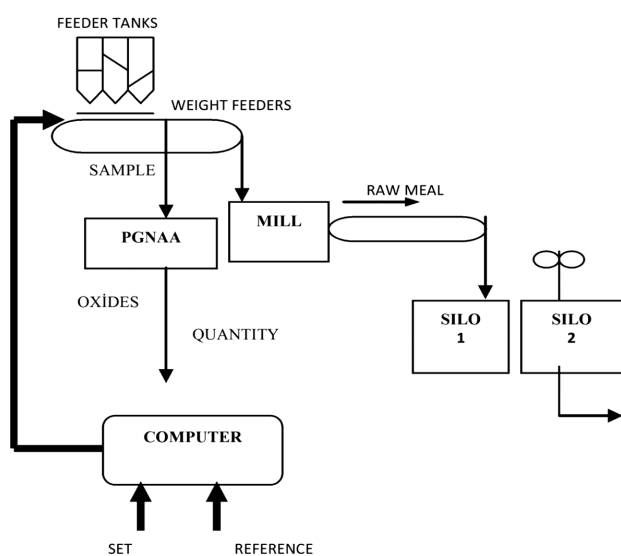


Figure 1: Simple schema of the raw-material blending in the Nuh Cement Factory

Slika 1: Preprosta shema mešanja surovin v tovarni cementa Nuh

value of *MA* determines the composition of the liquid phase of the clinker. The goal is to achieve a desired level of *ML*, *MS* and *MA* of the raw mix, to produce a particular quality of the cement by controlling the mix proportions of the raw materials. To achieve an appropriate raw mix proportion is very difficult due to the inconsistencies in the chemical composition of the raw material.⁸

3 ARTIFICIAL NEURAL NETWORK APPROACH

The Artificial Neural Network (ANN) has been developed by a generalization of the mathematical model of the human brain's ability and neural biology. The ANN, which is relatively new modeling technique, has shown remarkable performance when used to model complex linear and non-linear relationships. Neural Networks (NN) have been successfully applied to model complicated processes in many engineering applications: electronics, manufacturing, robotics, materials science and physical metallurgy, automotive, defense, and telecommunications. An ANN is a set of processing elements, or neurons, and connections with adjustable weights. A multi-layer neural network consists of an input layer, one or more hidden layers, and an output layer. The input layer is the first layer and accepts symptoms, signs, and experimental data. The layers that are placed between the input and output layers are called hidden layers. The hidden layer processes the data it receives from the input layer, and sends a response to the output layer. The output layer accepts all the responses from the hidden layer and produces an output vector.

Figure 2 shows the structure of the ANN.

Each layer has a certain number of processing elements that are connected by links with adjustable weights. These weights are adapted during the training process, most commonly through the backpropagation algorithm, by presenting the neural network with examples of input-output pairs exhibiting the relationship the network is attempting to learn.

The total input to the layer neuron *i*, x_i , is the summation of the weight (w_{ij}), which is associated with the connection between the neuron *i* and the neuron *j*,

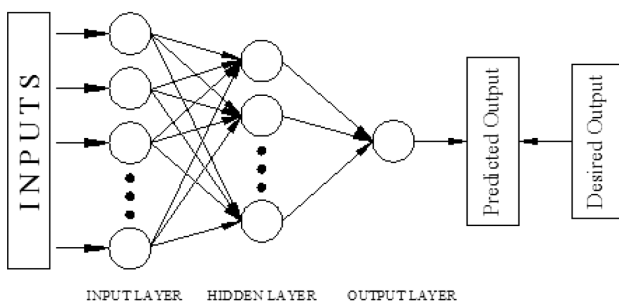


Figure 2: The structure of the ANN
Slika 2: Struktura ANN

multiplied by the input value received from the preceding layer neuron, x_j , for each connection path:¹³

$$x_i = w_{i0} + \sum_{j=1}^N w_{ij} \times x_j \tag{4}$$

where *N* is the number of inputs, w_{i0} is the bias of the neuron.

The output from neuron *i*, V_i , is given by:

$$V_i = f(x_j) \tag{5}$$

where *f* is the activation function.

During training, *Q* sets of input and output data are given to the neural network. An iterative algorithm adjusts the weights so that the outputs (y_k) according to the input patterns will be as close as possible to their respective desired output patterns (d_k). Considering a neural network with *K*, which is the total number of outputs, the Mean Squared Error (*MSE*) function is to be minimized:

$$MSE = \frac{1}{Q \cdot K} \cdot \sum_{q=1}^Q \sum_{k=1}^K [d_k(q) - y_k(q)]^2 \tag{6}$$

The backpropagation algorithm is the most widely used to minimize *MSE* by adjusting the weights of the connection links. The equation for calculating the updated weights and bias is:

$$w_{ij}^{t+1} = w_{ij}^t + \Delta w_{ij}^{t+1} \tag{7}$$

Where Δw_{ij}^{t+1} is the (\pm) incremental change in the weight. The weight change is determined by an optimization method.¹³

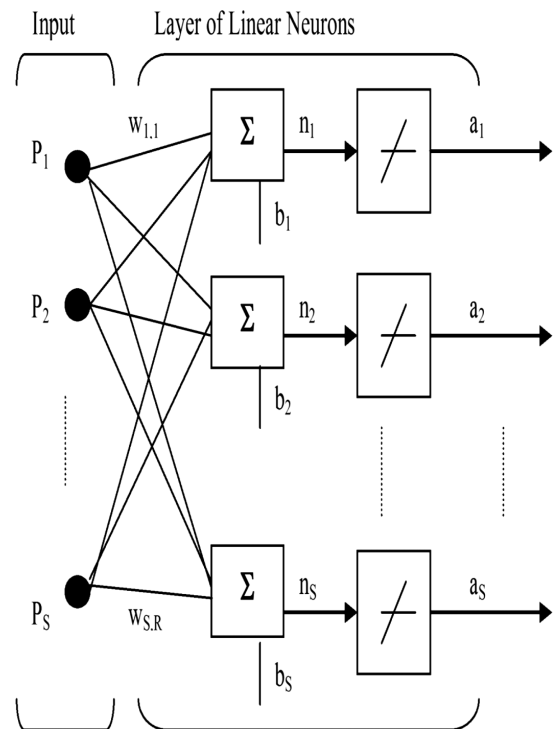


Figure 3: The linear network structure¹⁴
Slika 3: Struktura linearne mreže¹⁴

4 ANN MODEL

Linear and Nonlinear Neural Network models were developed for the raw-material blending process in cement manufacture. The inputs of both the models are low grade and iron ore, and the outputs are Fe₂O₃ and Lime Modulus.

4.1 Linear ANN

The linear network (ADALINE network) shown in Figure 3 has one layer of *S* neurons connected to *R* inputs through a matrix of weights *W*.¹⁴

The linear network has the same basic structure as the perceptron network. The only difference is that the linear neuron uses a linear transfer function. This transfer function is shown in Figure 4. The linear transfer function calculates the neuron's output by simply returning the value passed to it. This neuron can be trained to learn an affine function of its inputs, or to find a linear approximation to a nonlinear function. A linear network cannot, of course, be made to perform a nonlinear computation.¹⁴

A nonlinear relationships between the inputs and the targets cannot be represented exactly by a linear network. Under se circumstances, backpropagation might be a good alternative.

4.2 Nonlinear ANN

The nonlinear network is shown in Figure 5.¹⁴ In this study a feed-forward backpropagation network was designed. A log-sigmoid transfer function was used in a hidden layer and the output layer. Because, generally, a natural incident resembles the structure of a log-sigmoid function, using this function has given better results. A log-sigmoid transfer function is shown in Figure 6.¹⁴ The inputs to the system determine the neuron number in the input layer of the network and its outputs determine the neuron number in output layer of network. Eight neurons were used in the hidden layer of the model.

A neural network requires that the range of the both input and output values should be between 0.1 and 0.9

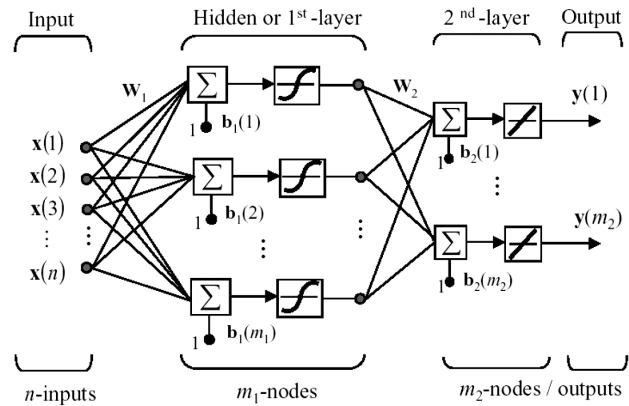


Figure 5: The nonlinear network structure¹⁴
Slika 5: Struktura nelinearne mreže¹⁴

due to the restriction of the sigmoid function, consequently, the data must be unified.

$$\text{Normalize data} = \frac{\text{Actual value} - \text{Minimum value}}{\text{Maximum value} - \text{Minimum value}} \times (\text{High} - \text{Low}) + \text{Low}$$

is a widely employed method in unification.¹⁵

In this study, the backpropagation network training function updates the weight and bias values according to the Levenberg-Marquardt optimization. The performance index was determined by the mean squared error. The Levenberg-Marquardt algorithm is very well suited to neural network training where the performance index is the mean squared error.

5 RESULTS

The input-output data set for the neural network training and testing were obtained from experiments in the Nuh Cement Factory. A data set of 455 samples was used to train the neural network model. A data set of 200 samples was utilized to test the network model.

The input and output data were used by the network in the training stage and the network learned the process. After the network was trained, the Fe₂O₃ and Lime Modulus for different combinations of low grade and

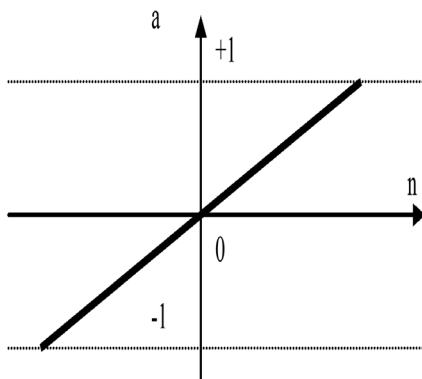


Figure 4: Linear transfer function¹⁴
Slika 4: Linearna prenosna funkcija¹⁴

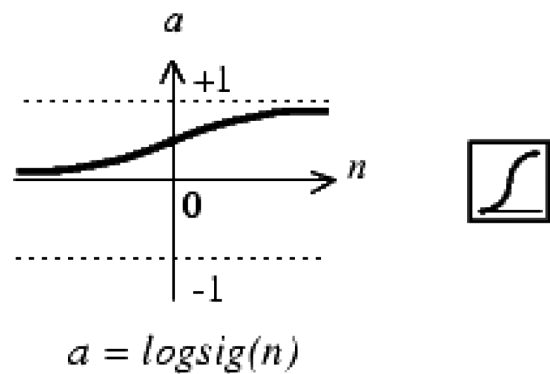


Figure 6: Log-Sigmoid transfer function¹⁴
Slika 6: Log-Sigmoid prenosna funkcija¹⁴

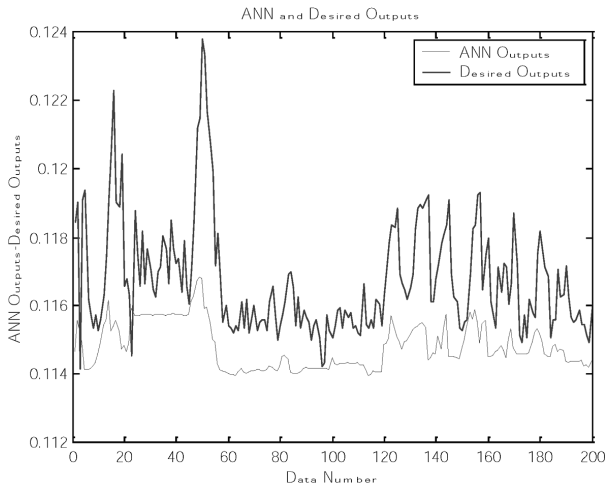


Figure 7: Comparison of the linear neural network prediction with the experimental data (for Fe_2O_3)

Slika 7: Primerjava napovedi linearne nevronske mreže z eksperimentalnimi podatki (za Fe_2O_3)

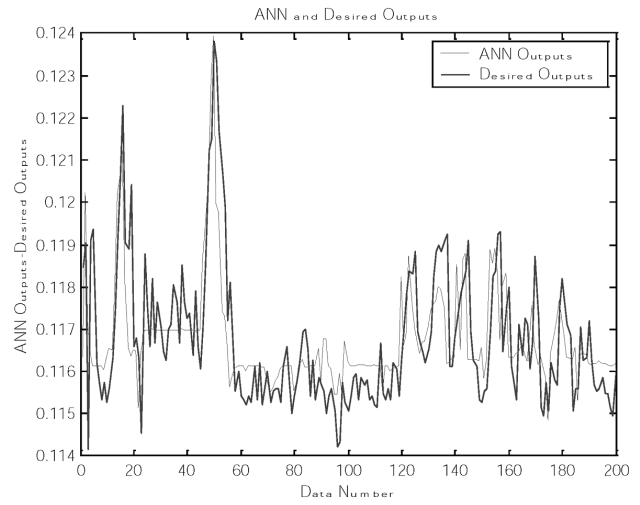


Figure 9: Comparison of the nonlinear neural network prediction with the experimental data (for Fe_2O_3)

Slika 9: Primerjava napovedi z nelinearno nevronske mreže z eksperimentalnimi podatki (za Fe_2O_3)

iron ore from the test data set were predicted. **Figures 7 and 8** show a comparison of the linear neural network prediction with the experimental data. The comparison of the nonlinear neural network prediction with the experimental data is shown in **Figures 9 and 10**.

During training, the mean squared errors were recomputed using next updated weights and the performance graphic was obtained for the nonlinear network in **Figure 11**. The goal in the figures is the target value of the MSE and the performance is the MSE value obtained from the ANN training result. As shown in **Figure 11**, the error decreases rapidly in the next iterations.

The Fe_2O_3 prediction of the models indicated that the maximum error between the linear neural network results and desired outputs is about 7.5×10^{-3} and maximum error between nonlinear neural network results and the desired outputs is about 4×10^{-3} . For the Lime Modulus

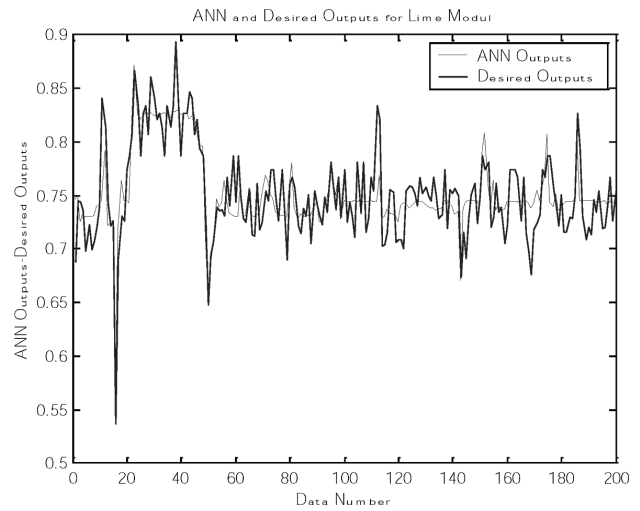


Figure 10: Comparison of the nonlinear neural network prediction with the experimental data (for Lime Modulus)

Slika 10: Primerjava napovedi nelinearne nevronske mreže z eksperimentalnimi podatki (za module z apnom)

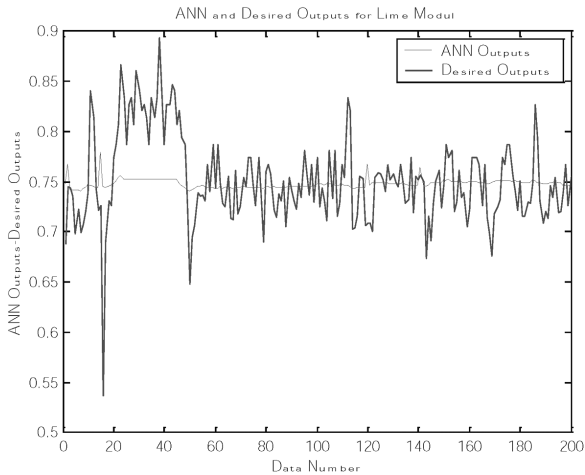


Figure 8: Comparison of the linear neural network prediction with experimental data (for Lime Modulus)

Slika 8: Primerjava napovedi linearne nevronske mreže z eksperimentalnimi podatki (za module z apnom)

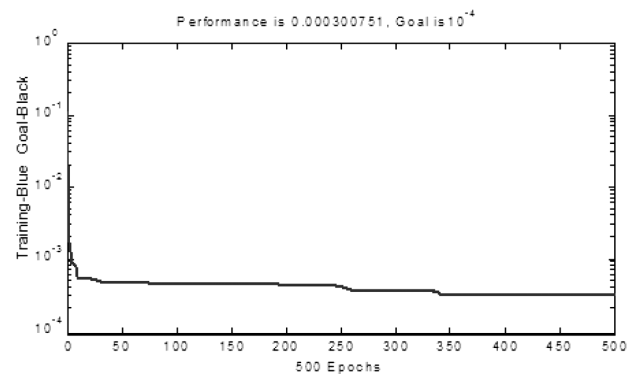


Figure 11: Performance of the nonlinear neural network

Slika 11: Uspešnost nelinearne nevronske mreže

output of the models, the maximum error of the linear neural network is about -0.21 and the maximum error of the nonlinear neural network is about 0.095 . Furthermore, the training performance (*MSE*) of the nonlinear neural network reached 3.00751×10^{-4} at 500 epochs. The meaning of the *MSE* being very small is that the desired outputs and the ANN's outputs for the training set have become very close to each other.

6 CONCLUSION

In this study the raw-material blending process in a cement factory was examined and two different mathematical models were developed using linear and nonlinear neural networks. In this modeling the experimental data were used from a controlled process under varying operating conditions in the Nuh Cement Factory in Turkey. Good parametric multivariable models having the minimum number of parameters were obtained. The inputs are the feed ratios of the raw materials (low grade and iron ore) and the outputs are iron oxide and/or the lime module values of the raw meal.

The developed linear and nonlinear neural network predictions were compared with the experimental results. The network test showed that the nonlinear neural network has a higher predictive accuracy and convergence for the raw-material blending process. The linear-model-based prediction shows a greater deviation than the nonlinear model. The mathematical model that is established by the nonlinear neural network is a suitable model for the blending process of cement raw material.

Finally, this multi-input, multi-output model has made possible the control of the iron oxide and the lime module together, instead of using parallel-working single-loop controllers. In this case only the lime module or the iron oxide could have been controlled, depending on the choice in the Nuh Cement Factory with the available control package, designed models give the opportunity for these outputs to be controlled together by using a two-input, two-output process model. Furthermore, stable operating conditions can predict the process with these models.

7 REFERENCES

- ¹ K. T. Westerlund, H. Toivenon, K. E. Nyman, Stochastic modelling and self-tuning control of a continuous cement raw material mixing system, Proceeding of the 18th IEEE Conference on Decision and Control, Fort Lauderdale, Florida 1979, 610–615, doi:10.1109/CDC.1979.270255
- ² M. Hubbard, T. Dasilva, Estimation of feedstream concentrations in cement raw material blending, *Automatica*, 18 (1982) 5, 595–606, doi:10.1016/0005-1098(82)90011-5
- ³ L. Keviczky, J. Hetthéssy, M. Hilger, J. Kolostori, Self-Tuning adaptive control of cement raw material blending, *Automatica*, 14 (1978) 6, 525–532, doi:10.1016/0005-1098(78)90042-0
- ⁴ P. Lin, Y. S. Yun, J. P. Barbier, P. Prevot, Intelligent tuning and adaptive control for cement raw meal blending process, Proceedings of the IFAC Intelligent Tuning and Adaptive Control, Singapore 1991, 301–306, doi:10.1016/B978-0-08-040935-1.50053-3
- ⁵ A. K. Swain, Material mix control in cement plant automation, *IEEE Transactions on Automatic Control*, 15 (1995) 4, 23–27, doi:10.1109/37.408464
- ⁶ C. Ozsoy, A. Kural, M. Cetinkaya, S. Ertug, Constrained MIMO self-tuning composition control in cement industry, 7th International Conference on Emerging Technologies and Factory Automation 20–22, Barcelona 1999, 1021–1027, doi:10.1109/ETFA.1999.813103
- ⁷ A. Kural, C. Ozsoy, Identification and control of the raw material blending process in cement industry, *Int. J. Adapt. Control Signal Process*, 18 (2004) 5, 427–442, doi:10.1002/acs.805
- ⁸ K. Kizilaslan, S. Ertugrul, A. Kural, C. Ozsoy, A comparative study on modeling of a raw material blending process in cement industry using conventional and intelligent techniques, In: *IEEE Conference on Control Applications* 1, June 23–25 Istanbul 2003, 736–741, doi:10.1109/CCA.2003.1223529
- ⁹ G. Bavdaz, J. Kocijan, Fuzzy controller for cement raw material blending, *Transactions of the Institute of Measurement and Control*, 29 (2007) 1, 17–34, doi:10.1177/0142331207070362
- ¹⁰ C. Banyasz, L. Keviczky, I. Vajk, A novel adaptive control system for raw material blending, *IEEE Control Systems Magazine*, 23 (2003) 1, 87–96, doi:10.1109/MCS.2003.1172832
- ¹¹ X. Wu, M. Yuan, H. Yu, Soft-sensor modeling of cement raw material blending process based on fuzzy neural networks with particle swarm optimization, *Proceedings of the International Conference on Computational Intelligence and Natural Computing*, 2009, 158–161, doi:10.1109/CINC.2009.186
- ¹² X. Li, H. Yu, M. Yuan, Modeling and Optimization of Cement Raw Materials Blending Process, *Mathematical Problems in Engineering*, (2012), 1–30, doi:10.1155/2012/392197
- ¹³ R. Kazan, M. Firat, A. E. Tiryaki, Prediction of springback in wipe-bending process of sheet metal using neural network, *Materials and Design*, 30 (2009) 2, 418–423, doi:10.1016/j.matdes.2008.05.033
- ¹⁴ M. H. Beale, M. T. Hagan, H. B. Demuth, *Neural network design*, 2008
- ¹⁵ I. A. Basheer, M. Hajmeer, *Artificial Neural Networks: Fundamentals, Computing, Design, and Application*, *Journal of Microbiological Methods*, 43 (2000) 1, 3–31, doi:10.1016/S0167-7012(00)00201-3

POSSIBILITIES OF DETERMINING THE AIR-PORE CONTENT IN CEMENT COMPOSITES USING COMPUTED TOMOGRAPHY AND OTHER METHODS

MOŽNOSTI DOLOČANJA VSEBNOSTI ZRAČNIH POR V CEMENTNIH KOMPOZITIH Z UPORABO RAČUNALNIŠKE TOMOGRAFIJE IN DRUGIH METOD

Bronislava Moravcová, Petr Póssl, Petr Misák, Michal Blažek

Brno University of Technology, Faculty of Civil Engineering, Veveří 331/95, 602 00 Brno, Czech Republic
BlazekM7@study.fce.vutbr.cz

Prejem rokopisa – received: 2014-08-13; sprejem za objavo – accepted for publication: 2015-08-24

doi:10.17222/mit.2014.193

The aim of the paper is to outline the possibilities and predictive values of the selected methods for determining air-pore characteristics in concrete and cement composites in general. Four samples (mixtures) of cement concrete without additives or admixtures were chosen for the measurement, differing in cement content while maintaining the consistency of fresh concrete S3 according to EN 206. Both standardized and non-standardized methods are used in Europe, therefore providing a possibility of comparing their outcomes.

Keywords: concrete, durability, porosity, surface, covering layer, X-ray computed micro-tomography

Namen članka je prikazati možnosti za splošno napovedovanje izbranih metod za določanje značilnosti zračnih por v betonu in v kompozitih iz cementa. Za meritve so bili izbrani štirje vzorci (mešanice) betona brez dodatkov in primesi z različno vsebnostjo cementa ob zadržanju konsistence svežega betona S3, skladno z EN 206. Standardizirane in nestandardizirane metode se uporabljajo v Evropi in zato omogočajo primerjavo rezultatov.

Ključne besede: beton, zdržljivost, poroznost, površina, prekritje, rentgenska računalniška mikro-tomografija

1 INTRODUCTION

The durability of cement composites has been a topic of increasing importance. It is illustrated by the fact that the requirement for the durability of concrete structures has become part of CPR (Construction Products Regulation).¹ The content, size and distribution of air pores, i.e., porosity, influence not only on the durability but also the physical/mechanical properties of cement composites and thus concrete structures in general.²

Recently, there have been claims that concrete air entrainment in percent is not sufficiently informative as both the air-entrained concrete and the traditional concrete contain a broad spectrum of air voids (**Figure 1**). Not all the pores are beneficial for the required property. Recent investigations argue that an effective entrainment (a pore diameter of 1 μm –1000 μm) above 2 % can significantly increase the resistance to water and chemical thawing agents.^{3–5}

The pores can be divided, according to their characters³, into gel, capillary, entrained and entrapped ones, or by their size⁴, into micropores (<1.25 nm), mesopores (1.25–25 nm), macropores (25–5000 nm) and other large pores (5000–50000 nm).

Figure 1 shows a detailed diagram of the division of pores and the possibilities of their detection by means of the methods discussed below.

In connection with what was mentioned above, four methods for determining various pore characteristics dealing with the air-void content in concrete (total air content, micropore air content, average pore diameter and specific surface of an air-void system) were chosen. Out of these, two are used for determining the properties of fresh concrete (the pressure method and the air-void analyser) and the remaining two for determining the properties of hardened concrete (a microscopic analysis and CT).

The goal is to determine the air-pore-system characteristics using the above-mentioned methods and to

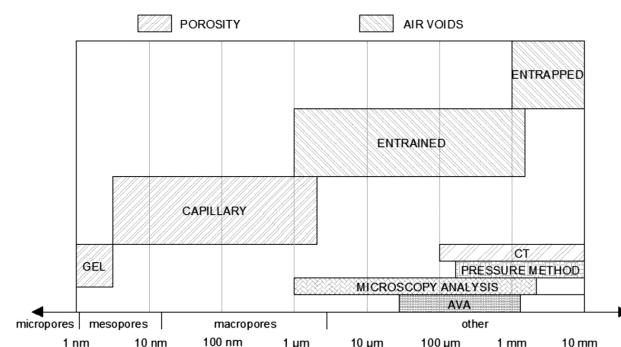


Figure 1: Example of pore size in concrete

Slika 1: Primer velikosti por v betonu

select the optimum method for determining the characteristics of specific types of the air-pore system in concrete.

2 METHODS USED IN THE EXPERIMENT

There is a number of situations where there is a need to have information about the pore distribution in concrete. This paper is concerned with the determination of concrete-cover porosity, which has a significant influence on the quality of the concrete and thus the durability of the whole structure.² This experiment determines the concrete cover to be 40–60 mm, taken from the surface of the specimen.

The following paragraphs describe standardised and non-standardised methods for the above-specified properties of fresh and hardened concrete, used in the experimental part of the research.

It must be emphasised that the results of the methods differ because of their different abilities to detect the pore size, due to the physical nature of the methods and differently sized specimens used for each method.

2.1 Pressure method

The method is applied for determining the air content in compacted fresh concrete made of dense or heavy-weight aggregate. It is based on the Boyle-Mariotte law, which says that the product of the pressure and volume of a gas is constant. This method uses an air meter according to EN 12350-7⁵ (Figure 2).



Figure 2: Concrete pressure-air meter
Slika 2: Merilnik tlaka zraka v betonu

2.2 Air-void analyser (AVA)

For the analysis of the air-void structure in fresh concrete, AVA (an air-void analyser, Figure 3) was used.^{6,7} Its advantages are the possibility of taking samples directly from the vibrated mixture without any further processing and, as in the case of the previous method, the possibility of performing a measurement in situ. The apparatus also detects the content of microscopic air pores A_{300} , but it is necessary to note that it cannot detect pores smaller than 50 μm .

It was discovered that, under certain conditions, the air pores in a cement mixture can be transported into a liquid without affecting their content or size.⁸ Successful transport depends on the viscosity and hydrophilic character of the liquid. Once air bubbles have exited the cement paste, they start to rise through the liquid. The function of the air-bubble movement can be described with reversed Stokes' law, according to which larger bubbles rise faster than smaller ones. The total distribution of an air-void structure can be calculated by recording the amount of air that has risen up to a given level over the elapsed time. The number of pores escaping the cement paste is observed through the changes in the mass of an upside-down Petri dish placed just below the surface of the liquid.

The principle is that the apparatus determines the amount and size of air pores and thus enables an assessment of the spacing and the specific air-void surface. The method is primarily used for air-entrained concretes. However, even for non-entrained concretes, it is better at determining the air-void characteristics than method 2.1 as it can be used also for the determination of other characteristics, not just the total air content.

The following characteristics can be determined using this method:

- spacing factor,
- micro-air-void content (A_{300}),



Figure 3: Air Void Analyzer (AVA)
Slika 3: Analizator praznin (AVA)

- total air content,
- specific surface of an air-void system.

2.3 Determining air-void characteristics in hardened concrete according to EN 480-11

A stereoscopic microscope was used for the observation of the air-void diameter and distribution in hardened concrete according to the standard EN 480-11.⁹ This device detects pores of 1–4000 μm and is able to identify microscopic air pores (A_{300}). Prior to its use, the specimens need to be prepared from a concrete cured for a minimum of 7 d. The measurement results can be recorded manually or automatically. Both procedures differ depending on human errors (the subjectivity of an evaluation) during pore detections (e.g., mistaking a hollow after a missing piece of the aggregate for an air pore).

The ability to detect air pores depends on the human ability to recognise a pore based on the contrast in the adapted specimen. During an automatic assessment, the factor is the resolution, at which a specimen is examined.

The following values can be determined using this method:

- spacing factor,
- micro-air-void content (A_{300}),
- total air content,
- specific surface of an air-void system,
- average pore diameter.

2.4 Computed tomography

Computed tomography (CT) is a method, which enables us to look inside the specimens non-destructively. CT detects differences in the material density. A 3D visualisation of a specimen can be constructed through the processing of several consecutive slices.¹⁰

Using special SW, the following characteristics can be determined on a 3D image of a specimen:

- spacing factor,
- micro-air-void content (A_{300}),
- total air content,
- specific surface of an air-void system,
- average pore diameter.

3 EXPERIMENTAL PART

The goal of this experiment was to compare the results of the selected methods used for the determination of air-pore characteristics in concrete and, at the same time, to ascertain whether the outputs of these methods correspond to one another. Four mixtures of cement concrete without additives or admixtures were chosen for the measurement, differing in the water/cement ratio while maintaining the consistency of fresh concrete S3 according to EN 206.¹¹ The components of the concretes identified as *R* (0/1, 0/2 and 0/3) are in **Table 1**. The

components in individual concretes were identical, i.e., of the same type of aggregate from the same location, one type of cement from the same mill.

The relevant properties of the concrete components were monitored according to EN 196-6¹², EN 933¹³, and EN 1097¹⁴ (**Table 2**). Samples were taken according to EN 12350-1.¹⁵ Properties of fresh concrete were determined according to EN 12350-2, 5, 6 and 7.^{5,16–18}

Although some of the methods are intended primarily for air-entrained concrete (2.2 and 2.3), it should be noted that, in terms of the entrained-air-void content, even non-entrained concretes contain voids corresponding, in size, to the entrained-air pores in air-entrained concrete.

Table 1: Composition of individual mixtures

Tabela 1: Sestava posameznih mešanik

Component	Aggregates (kg)			Cement 42,5 R, Mokrá (kg)	Water (kg)	Water ratio (-)
	0 – 4 Bratčice	4 – 8 Olbra- movice	8 – 16 Olbra- movice			
Concrete mixture R - C12/15 X0 S3 D16						
	978	177	693	255	206	0.81
Concrete mixture 0/1 - C20/25 X0 S3 D16						
	927	182	698	309	202	0.65
Concrete mixture 0/2 - C30/37 X0 S3 D16						
	892	175	695	358	192	0.54
Concrete mixture 0/3 - C35/45 (45/55) X0 S3 D16						
	888	202	692	402	203	0.50

Table 2: Characteristics of fresh concrete for individual mixtures

Tabela 2: Značilnosti svežega betona posameznih mešanik

Concrete	Characteristics			
	Flow table test (mm)	Density of fresh con- crete (kg/m ³)	Total air content (%) (pressure method)	Micro air content A_{300} (%) (AVA)
<i>R</i>	435	2250	2.7	0.2
				0.1
0/1	410	2315	2.7	0.0
0/2	385	2315	2.5	0.1
0/3	420	2290	2.5	0.1

For method 2.1, the specimen volume was 8 dm³. This method enables a detection of pores > 300 μm. It is the most commonly used method; however, its disadvantage is that it only allows a determination of the total air content and gives no information the on pore distribution and size.

In the case of method 2.2, the specimen volume was approximately 50 cm³. As it was a relatively small specimen, obtained with an impact drill, it was highly probable that it contained only smaller-sized pores (< 2 mm).

For the procedure according to 2.3, the specimen was a concrete slab of 100 mm × 100 mm. The evaluation was performed in two ways, i.e., manually and automatically, both of which have their drawbacks, see 2.3. Automatic evaluation took place at a resolution of 1 μm



Figure 4: Phoenix v|tome|x L 240¹⁹
Slika 4: Naprava Phoenix v|tome|x L 240¹⁹

per pixel, which corresponds to the minimum size of a detectable pore.

For the measurement with method 2.4, cylindrical specimens of 50 mm in diameter and 60 mm in height were used. All the cylinders were obtained from larger specimens, using a core drill. The drilling was performed perpendicular to the surface of the concrete and each specimen was cut to a length of 60 mm in order to represent the concrete cover. At this specimen size, the device was able to detect the pores of above 100 μm.

Each cylinder was scanned in consecutive slices using device Phoenix v|tome|x L 240 (Figure 4).¹⁹ All the data was recorded and subsequently processed in the laboratory of the Central European Institute of Technology – Brno University of Technology (CEITEC BUT). A module of VG Studio MAX was used for the pore analysis.²⁰

Table 3: Characteristics of air voids for concrete R
Tabela 3: Značilnosti zračnih por v betonu R

	Used methods				
	Fresh concrete		Hardened concrete		
	Pressure method	Air-void analyser	Microscopy analysis spacing		Computer tomography
manual			automatic		
Total air content A (%)	2.7	$\bar{x} = 1.1$ $s = 0.3$	$\bar{x} = 2.86$ $s = 0.21$	$\bar{x} = 10.72$ $s = 0.49$	1.69
Micro air content A ₃₀₀ (%)	–	$\bar{x} = 0.15$ $s = 0.05$	$\bar{x} = 1.20$ $s = 0.11$	$\bar{x} = 5.58$ $s = 0.67$	0.05
Spacing factor L (mm)	–	1.13	$\bar{x} = 0.11$ $s = 0.00$	$\bar{x} = 0.08$ $s = 0.01$	0.70
Average pore diameter D (μm)	–	–	–	$\bar{x} = 114.50$ $s = 6.50$	320.0
Specific surface of air-void system α (mm ⁻¹)	–	7.5	$\bar{x} = 57.65$ $s = 1.65$	$\bar{x} = 35.04$ $s = 1.95$	11.48

4 RESULTS AND DISCUSSION

Tables 3 to 6 show the air-pore characteristics obtained with the selected methods for fresh and hardened concrete. Figures 5 to 9 show the method outputs. In the cases, where the measurement was performed on more specimens, the tables include their average values and standard diversions. The number of decimal places in the tables is based on the output of individual methods.

Table 4: Characteristics of air voids for concrete 0/1
Tabela 4: Značilnosti zračnih por v betonu 0/1

	Used methods				
	Fresh concrete		Hardened concrete		
	Pressure method	Air-void analyser	Microscopy analysis spacing		Computer tomography
manual			automatic		
Total air content A (%)	2.7	0.9	1.48	$\bar{x} = 4.44$ $s = 0.15$	1.85
Micro air content A ₃₀₀ (%)	–	0.0	0.27	$\bar{x} = 1.93$ $s = 0.01$	0.02
Spacing factor L (mm)	–	1.80	0.27	$\bar{x} = 0.13$ $s = 0.01$	1.01
Average pore diameter D (μm)	–	–	–	$\bar{x} = 99.00$ $s = 12.00$	416.0
Specific surface of air-void system α (mm ⁻¹)	–	6.0	31.80	$\bar{x} = 41.06$ $s = 5.13$	7.82

Table 5: Characteristics of air voids for concrete 0/2
Tabela 5: Značilnosti zračnih por v betonu 0/2

	Used methods				
	Fresh concrete		Hardened concrete		
	Pressure method	Air-void analyser	Microscopy analysis spacing		Computer tomography
manual			automatic		
Total air content A (%)	2.5	1.0	1.76	$\bar{x} = 2.90$ $s = 0.33$	1.95
Micro air content A ₃₀₀ (%)	–	0.1	0.39	$\bar{x} = 1.33$ $s = 0.36$	0.01
Spacing factor L (mm)	–	1.28	0.28	$\bar{x} = 0.14$ $s = 0.04$	1.16
Average pore diameter D (μm)	–	–	–	$\bar{x} = 86.50$ $s = 18.50$	406.0
Specific surface of air-void system α (mm ⁻¹)	–	8.1	29.1	$\bar{x} = 48.68$ $s = 10.47$	6.68

Table 6: Characteristics of air voids for concrete 0/3

Tabela 6: Značilnosti zračnih por v betonu 0/3

	Used methods				
	Fresh concrete		Hardened concrete		
	Pressure method	Air-void analyser	Microscopy analysis spacing		Computer tomography
manual			automatic		
Total air content A (%)	2.5	1.0	2.48	$\bar{x} = 3.51$ $s = 0.78$	1.70
Micro air content A_{300} (%)	–	0.1	0.26	$\bar{x} = 1.69$ $s = 0.44$	0.01
Spacing factor L (mm)	–	1.26	0.40	$\bar{x} = 0.13$ $s = 0.03$	0.93
Average pore diameter D (μm)	–	–	–	$\bar{x} = 88.5$ $s = 10.5$	445.0
Specific surface of air-void system α (mm^{-1})	–	8.4	18.20	$\bar{x} = 45.8$ $s = 5.45$	9.20

When determining the total air content in fresh concrete, the AVA method gave lower values than the pressure method (Figure 5), which could have been caused by the amount of fresh concrete being tested.

Different values of manual and automatic microscopy may have been caused by the ability/inability to distinguish between an air pore and a hollow created by a particle of the aggregate forced out during the cutting or grinding of the specimen. The differences may have also been caused by the operator during the manual measurement of the factor. During automatic measurement, the

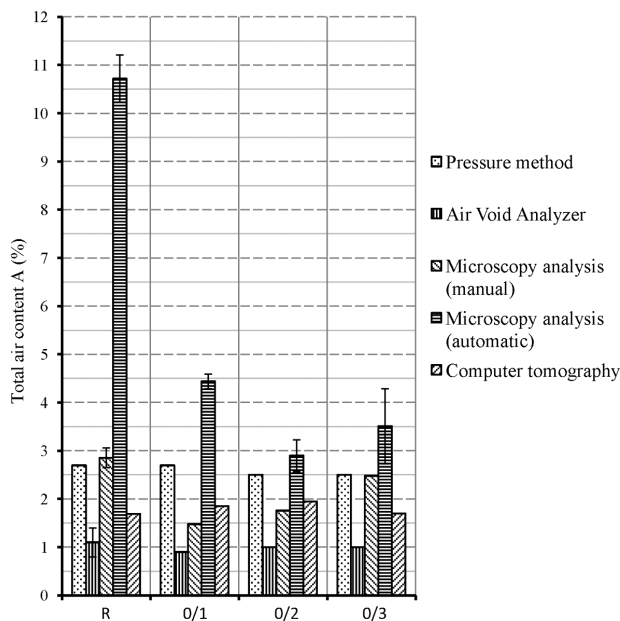


Figure 5: Results of total air content for individual concretes
Slika 5: Rezultati vsebnosti vsega zraka v posameznem betonu

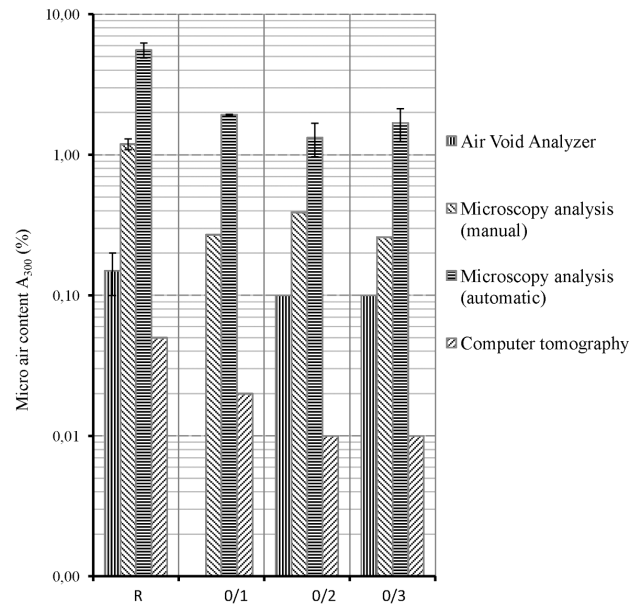


Figure 6: Results of micro-air-void content A_{300} for individual concretes

Slika 6: Rezultati vsebnosti zraka v mikroporah A_{300} pri posameznih betonih

ability to detect a pore depends on the resolution (in our case, $1\mu\text{m}$ per pixel), while during manual measurement, this ability lies with the technician performing the test.

Figure 6 shows that out of all the methods used, the measurement results obtained with CT and AVA corresponded most closely to each other. A small difference between these results was probably caused by different abilities to detect air voids at the bottom threshold of the detection: AVA (at $50\mu\text{m}$), CT (at $100\mu\text{m}$).

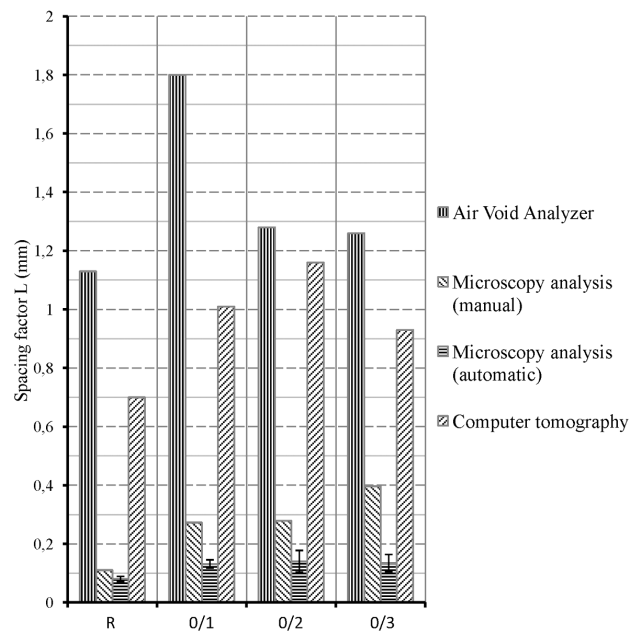


Figure 7: Results of spacing factor for individual concretes
Slika 7: Rezultati faktorja ločljivosti pri posameznih betonih

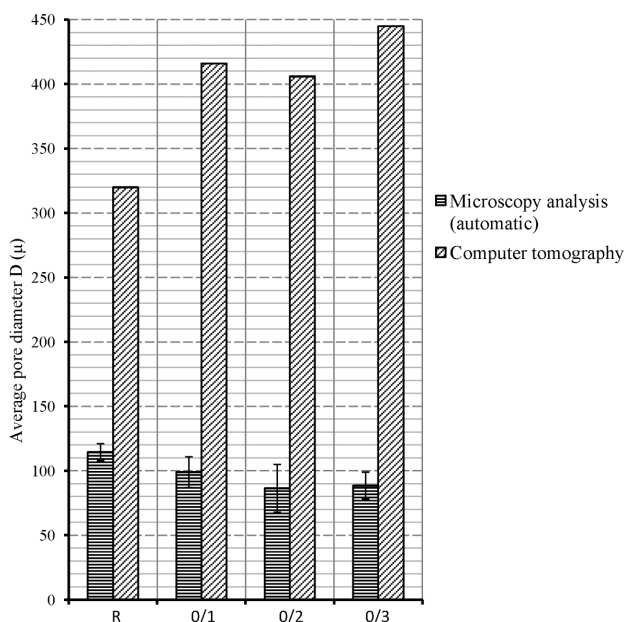


Figure 8: Results of average pore diameter for individual concretes
Slika 8: Rezultati povprečne velikosti por pri posameznih betonih

In general terms, it can be stated that, in determining the A_{300} value, a comparison of the results of individual methods was very demanding. All the methods exhibited a trend of a decrease in the resulting values of A_{300} dependent on the increasing cement content in the individual concretes; however, each method displayed significantly different absolute values of A_{300} .

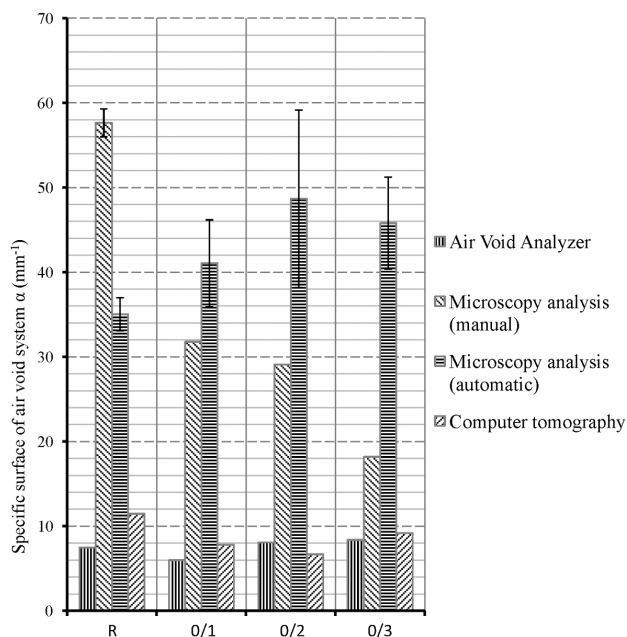


Figure 9: Results of specific surface of air-void system for individual concretes

Slika 9: Rezultati specifične površine sistema zračnih por pri posameznih betonih

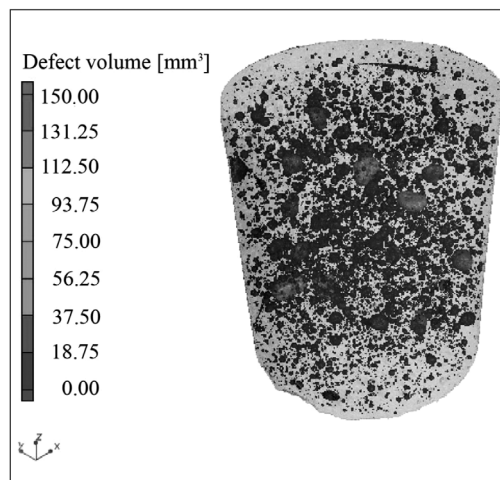


Figure 10: Volume of air-void system – 3D
Slika 10: Volumen sistema zračnih por – 3D

Based on the results shown in **Figure 7**, it could be stated that a comparison of the outcomes of the methods was again very demanding. The results that at least partially corresponded to each other were the values from the measurement using manual and automatic microscopy.

No conclusive proof was found for the premise that the spacing-factor results obtained with CT and the microscope would differ only minimally. This fact may have been caused by a difference in the mathematical model of the calculation between the microscope and CT. In the case of the microscope, the spacing factor was calculated from 2D scanning of the specimen, while in the case of CT, it was calculated from 3D scanning.

All the used methods displayed significantly different values of the average pore size for different concretes, as shown in **Figure 8**. The cause of the higher values in case of CT was probably its measurement range, where the bottom threshold was defined at 100 μm and the top threshold was not defined in this experiment; therefore,

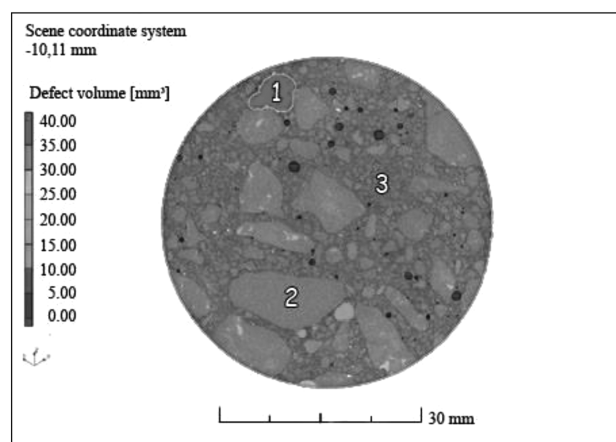


Figure 11: Volume of air-void system – cross-section: 1 – air void, 2 – aggregate particle, 3 – cement paste

Slika 11: Volumen sistema zračnih por – presek: 1-zračna pora, 2 – delec agregata, 3 – cementna osnova

possible air voids may have also been included in the calculation. On the other hand, the microscope had its range limited to the maximum pore diameter of 4000 μm .

The measurements using CT and AVA displayed lower final values of the specific surface of the air-void system, while the results obtained with microscopy were significantly higher. It was nearly impossible to find any correlation between these results (**Figure 9**).

A possible cause for this great difference in the results may have been, much like in the case of most of the other properties, a different range of the diameter of the air pores being measured with the above methods and, in the case of CT, also the detection of possible air voids.

Some outcomes of the measurement with CT (the pore distribution and volume) are shown in **Figures 10** and **11**.

5 CONCLUSION

The performed measurements allowed the following conclusions:

- The results of the used methods are difficult to compare. The main causes for this difficulty are probably different air-pore measurement ranges and the measurement of different types of pores (**Figure 1**). The characteristics determined with the individual methods performed on the concretes hardly correspond to one another. If one method indicates a certain trend in the results based on the cement content in the concrete, the other methods do not generally follow the trend or they even contradict it.
- A conclusive comparison of the results of the methods for determining the air content in concrete would require us to include, in the calculation, only the pore diameters within the intersection of the measurement ranges of the all the methods used (**Figure 1**).
- When measuring according to EN 480-11, differences are found in the results for the pores recorded manually and automatically. Possible causes are the inability of automatic recording to differentiate between an air pore and a missing particle of the aggregate and different abilities of detecting a pore at the bottom resolution threshold during each method of evaluation.
- AVA and stereoscopic microscope are primarily intended for determining the pore characteristics of aerated concretes. Based on the obtained results, it can be concluded that these methods probably give lower predictive values when used for non-aerated concretes.
- CT is a modern method for determining the concrete porosity with a great potential lying in the possibility of rendering the complete pore structure of a concrete specimen in 3D. Given the fact that it is demanding

to set up the device along with the evaluation software, it appears that a correct interpretation of results is rather difficult. The results include possible voids, which would have to be filtered out of the chosen algorithm, thus increasing the accuracy of the predictive values.

- The results of this experiment may have been influenced by the small number of the specimens used, e.g., in the case of CT, each type of concrete was represented by one specimen only.
- CT appears to be a very suitable method for measuring air-pore characteristics in concrete; it is, however, necessary to tackle the above-mentioned flaws (filtering possible voids, a correct set-up of the device). When these problems are removed, the outputs of CT can be used as a benchmark for the results of the other methods measuring the pore structure in concrete, mainly thanks to detailed 3D mapping.
- During the determination of concrete-pore characteristics, it is necessary to consider the types and sizes of the pores being examined, which are the key factors for the purpose and characteristics of a pore system. It is then possible to choose the most suitable method of their determination in line with **Figure 1**.

Acknowledgement

This paper was elaborated with the financial support of the Czech Science Foundation, project GA13-18870S, and Junior Specific Research FAST-J-15-2703.

6 REFERENCES

- ¹ Regulation (EU) No 305/2011 of the European parliament and of the council of 9 March 2011 laying down harmonised conditions for the marketing of construction products and repealing Council Directive 89/106/EEC, <http://eur-lex.europa.eu/legal-content/EN/TXT/?uri=celex:32011R0305>
- ² B. Kucharczyková, P. Misák, T. Vymazal, Determination and evaluation of the air permeability coefficient using Torrent Permeability Tester, Russian Journal of Nondestructive Testing, 46 (2010) 3, 226–233, doi:10.1134/S1061830910030113
- ³ M. Golová, Relationship between the basic properties of aerated concrete and its resistance to influence of environment, Diploma Thesis, Technical University of Ostrava, Ostrava 2012
- ⁴ F. Collins, J. G. Sanjayan, Effect of pore size distribution on drying shrinking of alkali-activated slag concrete, Cement and Concrete Research, 30 (2000) 9, 1401–1406, doi:10.1016/S0008-8846(00)00327-6
- ⁵ EN 12350-7 Testing fresh concrete – Part 7: Air content – Pressure methods, ÚNMZ, 2009
- ⁶ Apparatus for analysis of air pore structure: Quality Guarantee of air pores in concrete, <http://www.avas-concrete.com>, 23.07.2015
- ⁷ J. Distlehorst, G. Kurgan, Development of Precision Statement for Determining Air Void Characteristics of Fresh Concrete with Use of Air Void Analyzer, Transportation Research Record: Journal of the Transportation Research Board, 2020 (2007), 45–49, doi:10.3141/2020-06
- ⁸ AVA – Air Void Analyzer, <http://www.germann.org/>, 18.08.2015

- ⁹ EN 480-11, Admixtures for concrete, mortar and grout – Test methods – Part 11: Determination of air void characteristics in hardened concrete, ÚNMZ, 2005
- ¹⁰ J. Kaiser, M. Holá, M. Galiová, K. Novotný, V. Kanický, P. Martinec, J. Ščučka, F. Brun, N. Sodini et al., Investigation of the microstructure and mineralogical composition of urinary calculi fragments by synchrotron radiation X-ray microtomography: a feasibility study, *Urological Research*, 39 (2011) 4, 259–267, doi:10.1007/s00240-010-0343-9
- ¹¹ EN 206 Concrete - Specification, performance, production and conformity, ÚNMZ, 2013
- ¹² EN 196-6 Methods of testing cement - Part 6: Determination of fineness, ÚNMZ, 2010
- ¹³ EN 933 Tests for geometrical properties of aggregates, ÚNMZ, 2012
- ¹⁴ EN 1097 Tests for mechanical and physical properties of aggregates, ÚNMZ, 2011
- ¹⁵ EN 12350-1 Testing fresh concrete - Part 1: Sampling, ÚNMZ, 2009
- ¹⁶ EN 12350-2 Testing fresh concrete - Part 2: Slump test, ÚNMZ, 2009
- ¹⁷ EN 12350-5 Testing fresh concrete - Part 5: Flow table test, ÚNMZ, 2009
- ¹⁸ EN 12350-6 Testing fresh concrete - Part 6: Density, ÚNMZ, 2009
- ¹⁹ V|tome|x L 240 Brochure, GE Measurement & Control, 2014, http://www.ge-mcs.com/download/x-ray/phoenix-x-ray/GEIT_31205_flyer_vtomex_L_EN_1213.pdf, 23.7.2015
- ²⁰ VG studio MAX software, <http://www.volumegraphics.com/en/products/vgstudio-max>

MATERIAL AND TECHNOLOGICAL MODELLING OF CLOSED-DIE FORGING

MATERIALNO-TEHNOLOŠKO MODELIRANJE KOVANJA V ZAPRTEM UTOPU

Ivan Vorel, Štěpán Jeníček, Hana Jirková, Bohuslav Mašek

University of West Bohemia, Research Centre of Forming Technology – FORTECH, Univerzitní 22, Plzeň, Czech Republic
Stepan.Jenicck@seznam.cz

Prejem rokopisa – received: 2014-09-06; sprejem za objavo – accepted for publication: 2015-07-28

doi:10.17222/mit.2014.220

In the forging industry, as in other sectors, opportunities are sought for a continuous improvement in the manufacturing productivity. The solution can be found predominantly in optimizing the existing manufacturing processes or developing new ones. However, suspending the production in order to verify optimization proposals often results in substantial financial losses to the company. The present paper describes a design of a comprehensive material/technological model of a production sequence of real-world forging, including the heat treatment in continuous furnaces. A forging used in automotive applications is made of the C45 steel by closed-die forging. A material/technological model of this forging was developed using data gathered in the real-world forging production and with the aid of a FEM simulation. Good agreement between the specimen processed according to the model and the real-world forging was confirmed with a metallographic observation and tension testing. In both cases, the microstructure consisted of ferrite and pearlite. The ultimate strength of the forging was 676 MPa and its elongation reached 28 %. In the material processed according to the model, the ultimate strength was 655 MPa and the elongation level was 32 %. The results will be used as the basis for the material/technological modelling in an effort to develop and optimize a controlled cooling sequence to replace the existing heat-treatment process.

Keywords: material/technological model, FEM, simulation, production optimization

V kovaški industriji, tako kot v drugih sektorjih, stalno iščejo priložnosti za izboljšave in povečanje produktivnosti proizvodnje. Rešitev je v optimiranju obstoječega procesa ali v razvoju novega. Vendar pa opustitev proizvodnje pri preverjanju predloga optimizacije v podjetju pogosto povzroči občuten izpad prihodka. Članek opisuje celovit materialno-tehnološki model zaporedja proizvodnje realnega kovanja, vključno s toplotno obdelavo v kontinuirnih pečeh. Odkovek, ki se uporablja v avtomobilski industriji, je izdelan iz jekla C45 s kovanjem v zaprtem utopu. Materialno-tehnološki model tega kovanja je bil razvit z uporabo zbranih podatkov v proizvodnji med kovanjem in s pomočjo FEM-simulacije. Dobro ujemanje med vzorci izdelanimi po modelu in realnimi odkovki je bilo potrjeno z metalografijo in z nateznimi preskusi. V obeh primerih sta mikrostrukturo sestavljala ferit in perlit. Natezna trdnost odkovkov je bila 676 MPa, raztezek pa 28 %. Material, izdelan skladno z modelom, je imel natezno trdnost 655 MPa, raztezek pa je bil 32 %. Rezultati bodo uporabljeni kot osnova za materialno-tehnološko modeliranje z namenom razvoja in optimizacije faze kontroliranega ohlajanja, ki bi nadomestilo sedanjo toplotno obdelavo.

Ključne besede: materialno-tehnološki model, FEM, simulacija, optimizacija proizvodnje

1 INTRODUCTION

In response to current trends in a wide range of sectors of the industry, virtually all companies strive to increase their productivity and cut production costs, while maintaining high quality of products. In the forging industry, the production chain consists predominantly of forming operations, which impart the shape to products, and heat-treatment operations, which impart the desired properties for the intended use of the forgings. Forging and heat treatment of the parts require substantial investments, equipment, labour costs and, in particular, energy costs. In order to manage the costs of these operations, parameters of various treatment processes must be known. A purposeful alteration to the process or a change to a particular parameter can then yield the desired savings. This field has not been fully mapped yet. It is therefore open for material/technological modelling, a tool for obtaining the optimum results.

Material/technological modelling is a technique for studying the processing of materials. It relies on a small amount of material but delivers optimum results, which can be applied to real-world operations. The model uses a small volume of the actual material. The material is processed in a thermomechanical simulator. The simulator applies the desired forming parameters to a specimen and performs heat treatment with very short response times. By this means, a real-world process is simulated.¹⁻³ The output is a specimen processed according to the actual processing sequence. The processing parameters can be easily modified and the effect of such changes on the resulting properties can be studied without interfering with the real-world operation.

For the first stage of the investigation, a forging from 42CrMoS4 steel was selected to find the agreement between the real-world forging and the model constructed from the measured data.⁴

2 EXPERIMENTAL WORK

The data for the material-technological modelling was gathered in a production where the forgings are processed using conventional forging sequences and where the subsequent heat treatment comprises normalizing or quenching and tempering in continuous heat-treatment lines. With regard to the accuracy of the acquired data, four extensive measurement sessions were undertaken. The purpose was to find the temperature profiles and times for individual operations. The temperatures during forming were measured by means of pyrometers. The times of forming operations were retrieved from the time data log for the press ram. When the forgings were cooling down on cooling conveyors after the forming, the temperature profiles were measured with pyrometers and monitored with a thermal imaging camera. During the heat treatment, the temperature-profile data were gathered via eight thermocouples. Seven of them were placed on the surface of the forgings in the transport container. One was used to monitor the temperature in the furnace (**Figure 1**).⁴

To ensure that the data gathered is as accurate as possible and to avoid thermocouples running through the continuous furnaces, a thermally insulated box was developed. Equipped with a data-logging device, the box followed the same route as the transport container with forgings. Deformation and temperature profiles that are virtually impossible to measure were found with the FEM simulations conducted in the DEFORM software.⁵ This simulation also used the input data obtained from an in-situ measurement in the production. With the data obtained in this manner, the material/technological model was constructed.

Referring to the experience gained during the construction of the previous model, an effort was made to use the real-world processing data from the forging line and the heat-treatment line in developing the material/technological model of the forging from the C45 steel (**Table 1**). The forging serves as a semi-finished product for a functional part used in the automotive industry (**Figure 2**).

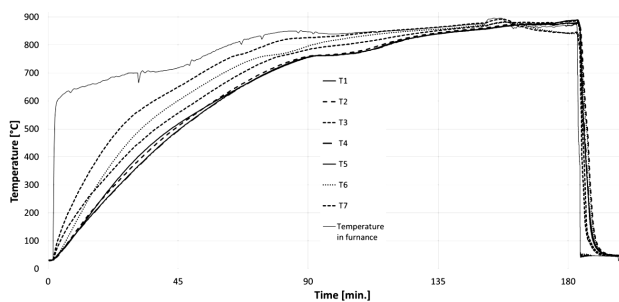


Figure 1: Temperature profile during heat treatment of forgings in a production plant. The curves were measured in various locations of the container (T1-T7).

Slika 1: Temperaturni profil med toplotno obdelavo odkovkov v proizvodnji. Krivulje so bile izmerjene na različnih lokacijah (T1-T7).

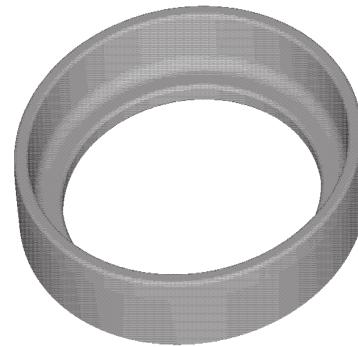


Figure 2: Forged part
Slika 2: Odkovke

Its manufacturing route comprises the forming operations of upsetting, blocking, finish forging and flash trimming. They are followed by normalizing to impart the desired properties. The model was constructed as a tool for further optimization of the forming and heat-treating sequences in order to achieve cost savings.

Table 1: Chemical composition of C45 steel

Tabela 1: Kemijska sestava jekla C45

C	Si	Mn	Cr	Ni	P	S
0.4-0.5	0.4	0.50.8	0.4	0.4	0.03	0.035

The specimens with threaded ends had a diameter of 8 mm. Their gauge length was 16 mm. For the purpose of the material/technological modelling, they were held in the grips of a thermomechanical simulator – Flex Test SE MTS 810 Material Test System (**Figure 3**). The simulator allows precise control and short response times



Figure 3: Test specimen in the clamping device of the thermomechanical simulator

Slika 3: Preizkušavec v čeljustih termomehanskega simulatorja

when performing the thermomechanical treatment, even at high strain rates and in demanding thermal schedules. The specimens were heated with a combination of induction and resistive heating. The strain rate was 0.35 m/s. The agreement between the model and the real-world forging was evaluated by means of light microscopy, HV hardness test and tension test.

3 RESULTS AND DISCUSSION

Using the data measured on the real-world forging, FEM simulations of deformation and temperature profiles at various points of the forging were created. The material/technological model was developed for the point denoted as P10 (Figure 4). This point was chosen because of its importance in terms of the technology of the production.

At this point, the total strain, according to the FEM simulation, was $\varphi = 3.6$ (Figure 5a). The largest increase in the strain was found in the first upsetting operation: 67 % of the total strain. In order to impart to the test specimen (when processed according to the material/technological model), the strain corresponding to the upsetting operation, the deformation, must be split into tension/compression modes. Otherwise, the deformation applied to the test specimen could amount to a 90 % reduction in the gauge length. This is not possible if the requirement for a uniform distribution of the strain is met. Another reason for dividing the total strain, which is normally imparted in a single forming operation, into the tension/compression strokes is the lateral spreading of the test specimen. With the heating method used here and beyond a certain spread of the specimen, the temperature increase due to deformation heating cannot be compensated. If that was to occur, the desired temperature field could not be attained.

The temperature profile at the above-defined point during the cooling after the forming was examined using the FEM simulation. Based on the previous experiments and measurement, the temperature profile during the

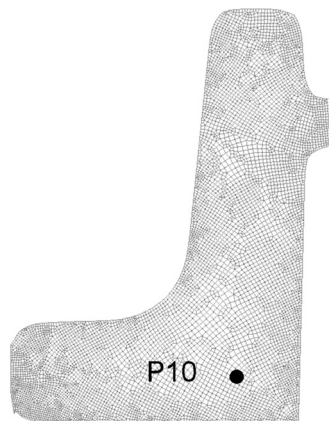


Figure 4: Cross-section of the FEM model of the forging
Slika 4: Presek FEM-modela odkovka

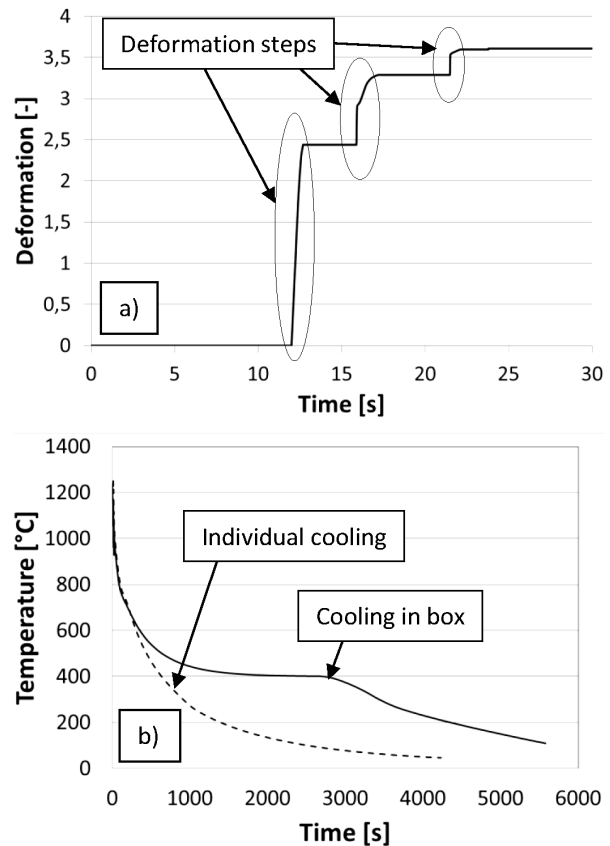


Figure 5: a) Deformation profile during forging of the workpiece, b) temperature profile during cooling after forming

Slika 5: a) Profil deformacije med kovanjem odkovka, b) profil temperature med ohlajanjem po kovanju

cooling was determined for a separately handled forged part and for a forging placed with other forgings into the container (Figure 5b). As the way of the cooling has a significant impact on the properties of the forging, the configuration of the spot where the forging is placed, together with the others, into the container was selected for the next modelling experiments as derived from the previous research.

The plot from the thermomechanical simulator shows that the actual temperature slightly deviates from the prescribed temperature during the simulated upsetting.

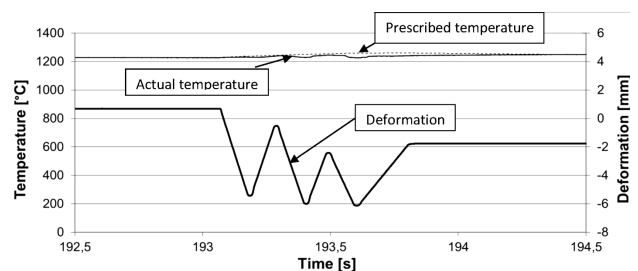


Figure 6: Deformation and temperature profiles during experimental forming of the specimen in the simulator: point P10

Slika 6: Profila deformacije in temperature med eksperimentalnim kovanjem vzorca v simulatorju: točka P10

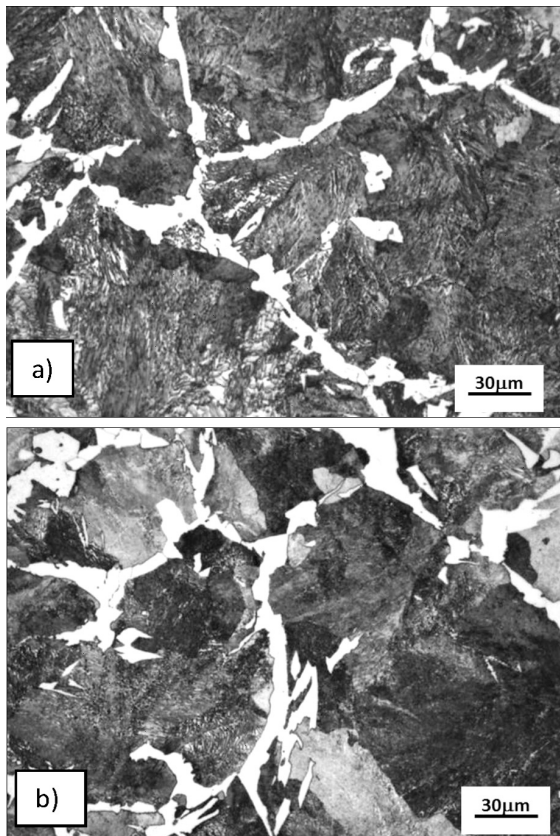


Figure 7: Microstructures of the real-world forging and the specimen after heat treatment – point P10: ferrite-pearlite: a) real-world forging, b) specimen processed according to the material/technological model
Slika 7: Mikrostruktura realnega odkovka in vzorca po toplotni obdelavi – točka P10: ferit-perlit : a) realni odkovek, b) vzorec, obdelan skladno z materialno-tehnološkim modelom

This is due to deformation heating. The prescribed and actual deformation plots are in agreement (Figure 6).

The microstructures of the specimen and the real-world forging at the P10 point are in excellent agreement (Figures 7a and 7b). The specimen was processed according to the material/technological model of the conditions at the corresponding point of the forging. The specimen and the real-world forging contained a mixture of ferrite and pearlite. The hardnesses of the specimen

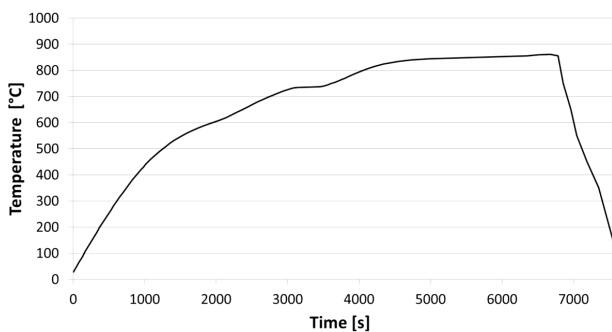


Figure 8: Temperature profile of the real-world forging during normalisation

Slika 8: Profil temperature realnega odkovka med normalizacijo

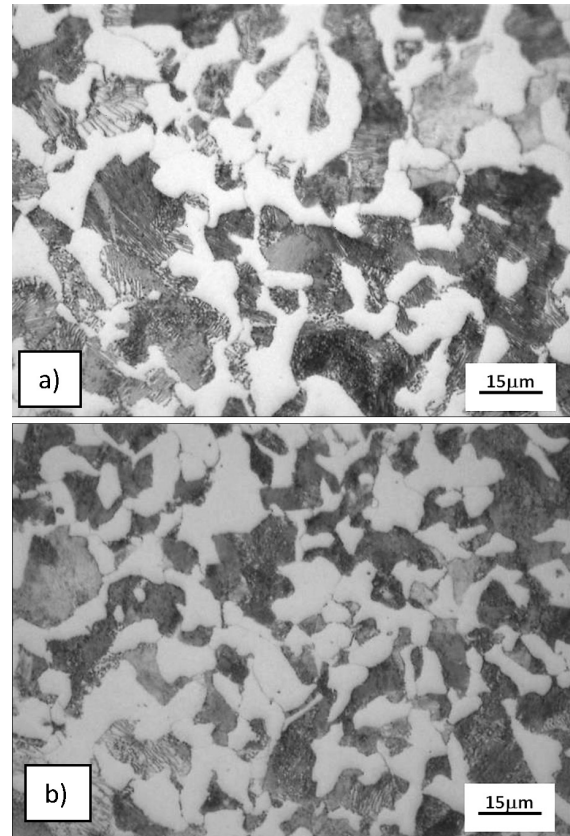


Figure 9: Microstructures of the real-world forging and the specimen after heat treatment – point P10: ferrite-pearlite: a) real-world forging, b) specimen processed according to the material/technological model
Slika 9: Mikrostrukturi realnega odkovka in vzorca po toplotni obdelavi- točka P10: ferit-perlit: a) realni odkovek, b) vzorec, obdelan skladno z materialno-tehnološkim modelom

and the forging were 226 HV10 and 221 H10, respectively.

The effect of heat treatment on the final properties of the forging was examined for the purpose of further experiments. The material/technological model was modified using the data from the FEM simulations and the values measured in the real-world heat-treatment process. The forging was normalised at 860 °C for 120 min (Figure 8).

The comparison between the microstructures of the real-world forging and the specimen processed according to the model showed that they were in agreement again (Figures 9a and 9b). In both cases, the microstructure consisted of ferrite and pearlite. The hardnesses of the forging and the specimen were 189 HV10 and 192 HV10, respectively.

Table 2: Mechanical properties of the real-world forging and the specimen processed according to the model: point 10

Tabela 2: Mehanske lastnosti realnega odkovka in vzorca izdelanega po modelu: točka 10

	HV10	R_m (MPa)	A_{5mm} (%)
Real-world forging	189	675	28
Specimen	192	655	32

The table of mechanical properties upon heat treatment (**Table 2**) shows that the ultimate strength and elongation at the point of interest of the real-world forging were 675 MPa and 28 %, respectively. The specimen, processed according to the model describing the same region of the forging, showed the strength and elongation of 655 MPa and 32 %, respectively.

4 CONCLUSION

Using the data gathered during the production in an actual forging plant and the results of FEM simulations, a material/technological model of a forging was developed. The material/technological model represented the point of the forging, which was very important in terms of the technology of the production. It comprised the forming operations and the subsequent normalising treatment. The validity of the model was examined using specimens of the material. The application of the model of forming led to a significant agreement between the microstructure of the specimen and the corresponding region of the real-world forging. In both cases, a ferrite-pearlite microstructure was obtained. The hardnesses of the specimen and the forging were 226 HV10 and 221 HV10, respectively. The testing of the model of heat treatment also led to a significant agreement between the microstructure of the specimen and the corresponding region of the real-world forging. In both cases, a ferrite-pearlite microstructure was obtained. The hardnesses of the specimen and the forging were 192 HV10 and 189 HV10, respectively. By the same token, mechanical properties were found to be in agreement. The strength and elongation of the specimen were 655 MPa and 32 %, respectively. In the real-world forging, these were 675 MPa and 28 %, respectively. These results represent a great success in fitting material/technological models to the real-world manufacturing processes. Thanks to the

good agreement between the model and the real-world process, opportunities for reducing energy costs and shortening the cycle times can be sought by adjusting the parameters of the model.

Acknowledgement

This paper includes the results achieved within the project TA02010390 Innovation and Development of New Thermo-Mechanical and Heat Treatment Processes of Die Forgings by the Transfer of Findings Obtained from Material-Technological Modelling. The project belongs to the ALFA Programme and is subsidised from the specific resources of the state budget for research and development through the Technology Agency of the Czech Republic. The paper was also supported from the project SGS-2013-028 Support of Student Research Activities in Materials Engineering Field.

5 REFERENCES

- ¹ B. Mašek, H. Staňková, J. Malina, L. Skálová, L. W. Meyer, Physical modelling of microstructure development during technological processes with intensive incremental deformation, *Key Engineering Materials*, 345–346 (2007), 943–946, doi:10.4028/www.scientific.net/KEM.345-346.943
- ² B. Mašek, H. Jirková, L. Kučerová, A. Ronešová, J. Malina, Material-Technological Modelling of Real Thin Sheet Rolling Process, *METAL 2011, Ostrava 2011*, 216–220
- ³ B. Mašek, H. Staňková, A. Ronešová, D. Klauberova, Modelling Structure Development with High Gradient of the Changes in Physical Parameters, *Conference on Advances in Heterogeneous Material Mechanics ICHMM-2008, Huangshan, China 2008*, 390–393
- ⁴ V. Pileček, F. Vančura, H. Jirková, B. Mašek, Material-Technological Modelling of Die Forging of 42CrMoS4 Steel, *Mater. Tehnol.*, 48 (2014) 6, 869–873
- ⁵ M. Fedorko, L. Maleček, Construction of Numerical Model of Forging Process of Four-Pole Rotor Shaft, *Hutnické listy, LXV* (2012) 4

INVESTIGATION OF WEAR BEHAVIOR OF BORIDED AISI D6 STEEL

PREISKAVA OBRABE BORIRANEGA JEKLA AISI D6

Ibrahim Gunes¹, Salih Kanat²

¹Afyon Kocatepe University, Faculty of Technology, Department of Metallurgical and Materials Engineering, 03200 Afyonkarahisar, Turkey

²Afyon Kocatepe University, Institute of Natural and Applied Sciences, Department of Metallurgical and Materials Engineering,
03200 Afyonkarahisar, Turkey
igunes@aku.edu.tr

Prejem rokopisa – received: 2014-11-09; sprejem za objavo – accepted for publication: 2015-07-02

doi:10.17222/mit.2014.279

We have investigated the effect of the boriding process on the wear behavior of AISI D6 steel. The boride layer was characterized by light microscopy, X-ray diffraction and micro-Vickers hardness testing. The X-ray diffraction analysis of the boride layers on the surface of the steels revealed the existence of the FeB, Fe₂B, CrB and Cr₂B compounds. Depending on the chemical composition of the substrates, the boride-layer thickness on the surface of the AISI D6 steel was found to be 164.42 μm. The hardness of the boride compounds formed on the surface of the steels ranged from 1672 HV_{0.05} to 2118 HV_{0.05}, whereas the Vickers hardness value of the untreated steels was 584 HV_{0.05}. The wear tests were carried out using a ball-disc arrangement under dry-friction conditions at room temperature with an applied load of 10 N and a sliding speed of 0.3 m/s for a sliding distance of 1000 m. It was observed that the wear rate of the borided and unborided AISI D6 steel ranged from 1.28 × 10⁻⁶ to 81.2 × 10⁻⁶ mm³/Nm.

Keywords: AISI D6, boriding, micro-hardness, friction coefficient, wear rate

V študiji je bil preiskovan vpliv postopka boriranja na obrabo jekla AISI D6. Borirana plast je bila pregledana s svetlobno mikroskopijo, z rentgensko difrakcijo in izmerjena je bila mikrotredota po Vickersu. Rentgenska difrakcijska analiza borirane plasti je pokazala prisotnost spojin FeB, Fe₂B, CrB in Cr₂B. Odvisno od kemijske sestave podlage je bila debelina borirane plasti na jeklu AISI D6 164,42 μm. Trdota boridov, nastalih na površini jekla, je bila med 1672 HV_{0.05} do 2118 HV_{0.05}, pri čemer je bila trdota neobdelanega jekla po Vickersu 584 HV_{0.05}. Preizkusi obrabe so bili izvedeni na sestavu kroglica-plošča, pri pogojih suhega trenja pri sobni temperaturi, z uporabljenim obremenitvijo 10 N, s hitrostjo drsenja 0,3 m/s in potjo drsenja 1000 m. Ugotovljeno je, da je hitrost obrabe boriranega in neboriranega jekla AISI D6 v območju od 1,28 × 10⁻⁶ do 81,2 × 10⁻⁶ mm³/Nm.

Ključne besede: AISI D6, boriranje, mikrotredota, koeficient trenja, hitrost obrabe

1 INTRODUCTION

Boriding is a thermochemical surface-hardening process that occurs with the diffusion of boron atoms into a variety of metals; including ferrous, non-ferrous and some superalloy surfaces between 973 K and 1373 K for a period of time ranging from 0.5 h to 12 h. Boriding can be performed in numerous ways, including plasma, paste, gas, molten salt, electrolysis, and pack boriding. Depending on the boriding parameters and the chemical composition of the substrate, the diffusion of boron atoms into their substrates leads to the formation of iron and metallic borides. The produced layers provide an extremely high hardness, good tribological properties and anti-corrosion resistance of the treated surfaces.¹⁻¹⁰

One of the most important reasons for machine parts to suffer damage and fail is wear. The surfaces of tool steel, dies and the majority of the machine parts (pumps, crankshafts, rolls and heavy gears, motor and car construction) are commonly subjected to higher stresses, wear and corrosive damage. In these types of working conditions, surface properties are often the most important for a reliable and long economic service life. In order to reduce this loss, the properties of the surfaces

should be improved. The diffusion of boron atoms into the surface of the materials is a common boriding treatment to improve the surface properties of industrial mechanical parts and tools. Among these surface-hardening treatments, boriding is a highly effective method for increasing the surface hardness, wear resistance, corrosion resistance and high-temperature oxidation resistance.¹¹⁻¹³

The wear behavior of borided steels has been evaluated by a number of investigators.¹⁴⁻¹⁹ However, there is no information about the friction and wear behaviors of borided AISI D6 steel. The main objective of this study was to investigate the effect of the boriding process on the wear behavior of borided D6 steel. The structural and tribological properties were investigated using light microscopy, XRD, SEM, EDS, microhardness tests and a ball-on-disc tribotester.

2 EXPERIMENTAL PROCEDURES

2.1 Boriding and characterization

The AISI D6 steel contained 2.08 % of mass fractions of C, 12.3 % of mass fractions of Cr, 0.6 % of mass

fractions of W, 0.16 % of mass fractions of Ni, 0.36 % of mass fractions of Mn and 0.25 % of mass fractions of Si. The test specimens were cut into $\varnothing 28 \times 10$ mm dimensions, ground up to 1200 G and polished using a diamond solution. The boriding heat treatment was carried out in a solid medium containing an Ekabor-II powder mixture placed in an electrical resistance furnace operated at 1123 K and 1323 K for 2 and 8 h under atmospheric pressure. The microstructures of the polished and etched cross-sections of the specimens were observed under a Nikon MA100 light microscope. The presence of borides formed in the coating layer was confirmed by means of X-ray diffraction equipment (Shimadzu XRD 6000) using $\text{Cu-K}\alpha$ radiation. The hardness measurements of the boride layer on each steel and untreated steel substrate were made on cross-sections using a Shimadzu HMV-2 Vickers indenter with a 50 g load.

2.2 Friction and wear

To perform the friction and wear of borided samples, a ball-on-disc test (ASTM G99-05) device was used.²⁰ In this equipment, the bottom part is movable and the top pin or ball is stationary. In the present study, the bottom movable flat surface was the borided steel and the upper fixed surface was the WC-Co ball with a diameter of 8 mm. The wear experiments were carried out in a ball-disc arrangement under dry friction conditions at room temperature with an applied load of 10 N and with a sliding speed of 0.3 m/s for a sliding distance of 1000 m. Before and after each wear test, each sample and abrasion element was cleaned with alcohol. After the test, the wear volumes of the samples were quantified by multiplying the cross-sectional areas of the wear by the width of the wear track obtained from the Taylor-Hobson Rugosimeter Surtronic 25 device. The wear rate was calculated with the Equation (1):

$$W_k = \frac{W_v}{M \cdot S} \text{ mm}^3/\text{Nm} \quad (1)$$

where W_k is the wear rate, W_v is the worn volume, M is the applied load and S is the sliding distance. Friction coefficients, depending on the sliding distance, were obtained through a friction-coefficient program. The surface profiles of the wear tracks on the samples and surface roughness were measured with a Taylor-Hobson Rugosimeter Surtronic 25. The worn surfaces were investigated by scanning electron microscopy (SEM), energy-dispersive X-ray spectroscopy (EDS) and with a Nanovea ST-400 non-contact optical profiler.

3 RESULTS AND DISCUSSION

3.1 Characterization of boride coatings

The cross-sections of the optical micrographs of the borided AISI D6 steel at 1123 K and 1323 K for 2 h and 8 h are shown in **Figure 1**. It is clear that the borides formed on the AISI D6 substrate have a saw-tooth morphology. It was found that the coating/matrix interface and matrix could be easily distinguished and the boride layer had a columnar structure. Depending on the chemical composition of the substrates, boriding time and temperature the boride layer thickness on the surface of the AISI D6 steel ranged from 13.54 μm and 164.42 μm in **Figure 2**.

Figure 3 gives the XRD pattern obtained from the surface of borided AISI D6 steel at 1123 K and 1323 K for treatment times of 2 h and 8 h. The XRD patterns show that the boride layer consists of borides such as SB and S_2B (S=Metal; Fe, Cr). The XRD results show that the boride layers formed on the AISI D6 steel contained the FeB, Fe_2B , CrB and Cr_2B phases in **Figure 3**.

Micro-hardness measurements were carried out from the surface to the interior along a line in order to see the

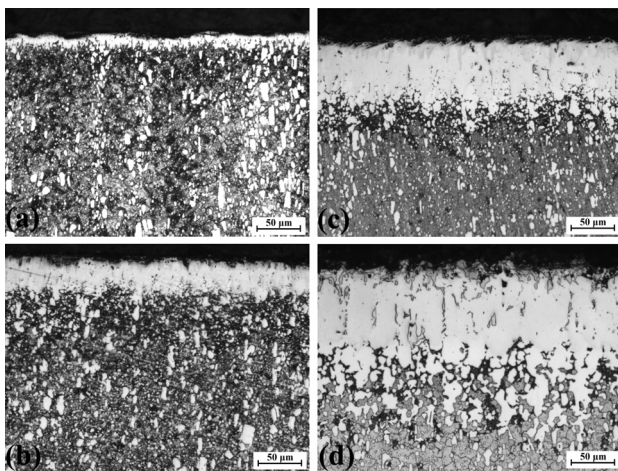


Figure 1: Cross-section of the borided AISI D6 steel: a) 1123 K – 2 h, b) 1123 K – 8 h, c) 1323 K – 2 h, d) 1323 K – 8 h

Slika 1: Presek boriranega jekla AISI D6: a) 1123 K – 2 h, b) 1123 K – 8 h, c) 1323 K – 2 h, d) 1323 K – 8 h

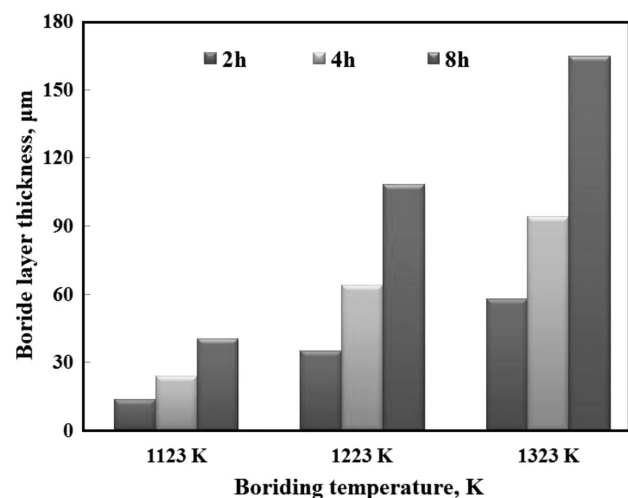


Figure 2: Thickness values of boride layers with respect to boriding time and temperatures

Slika 2: Debelina borirane plasti glede na čas in temperaturo boriranja

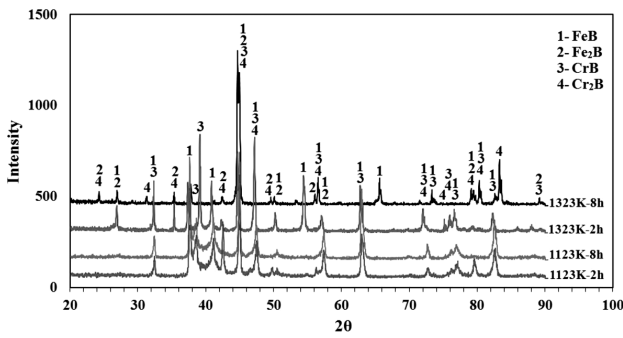


Figure 3: X-ray diffraction patterns of borided AISI D6 steel
Slika 3: Rentgenska difrakcija boriranega jekla AISI D6

variations in the boride layer hardness, transition zone and matrix. The micro-hardness of the boride layers was measured at 10 different locations at the same distance from the surface and the average value was taken as the hardness. Micro-hardness measurements were carried out on the cross-sections from the surface to the interior along a line (Figure 4). The hardness of the boride layer formed on the AISI D6 steel varied between 1672 HV_{0.05} and 2118 HV_{0.05}. On the other hand, the Vickers hardness values were 584 HV_{0.5}, for the untreated AISI D6 steel. When the hardness of the boride layer is compared with the matrix, the boride layer hardness is approximately four times greater than that of the matrix.

3.2 Friction and wear behavior

Figure 5 shows the surface roughness values of the borided and unborided AISI D6 steel. For the AISI D6 steel it was observed that the surface-roughness values increased with the boriding treatment. C. Li²¹ and S. Sahin²² solid borided different steels and reported that surface-roughness values increased with an increase in the boriding temperature. On the other hand, the friction coefficients of the unborided and borided AISI D6 steel varied from 0.39 to 0.62, as can be seen in Table 1. With the boriding treatment, a slight reduction was observed in the friction coefficients of the borided steels.

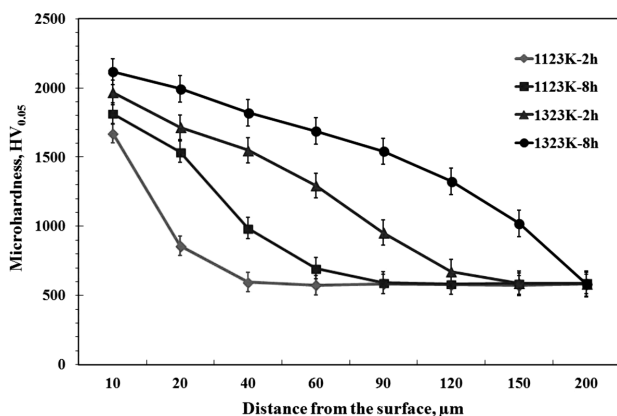


Figure 4: Variation of hardness depth in the borided AISI D6 steel
Slika 4: Spreminjanje trdote po globini boriranega jekla AISI D6

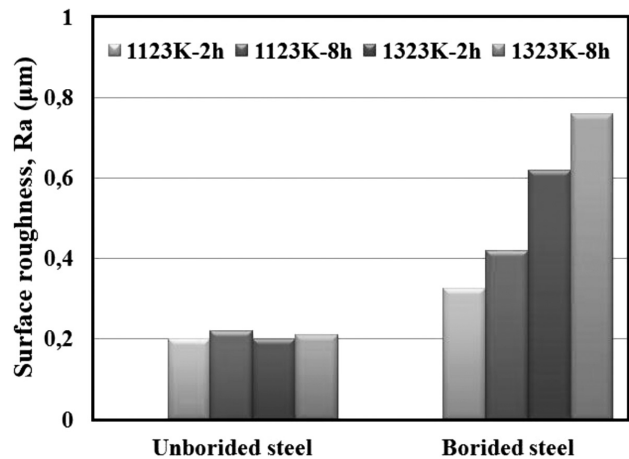


Figure 5: Surface-roughness values of the unborided and borided AISI D6 steel

Slika 5: Vrednosti površinske hrapavosti neboriranega in boriranega jekla AISI D6

Table 1: Friction coefficients of the unborided and borided AISI D6 steel

Tabela 1: Koeficient trenja neboriranega in boriranega jekla AISI D6

Unborided	Borided			
	1123 K – 2 h	1123 K – 8 h	1323 K – 2 h	1323 K – 8 h
0.62	0.39	0.47	0.51	0.58

Figure 6 shows the wear rate of the unborided and borided AISI D6 steel. Reductions in the wear rates of the borided steels were observed according to the unborided steels. Due to the toughness of the FeB, Fe₂B, CrB and Cr₂B phases, the steel showed more resistance to wear. While the highest wear rate is observed for the unborided AISI D6 steel ($81.2 \times 10^{-6} \text{ mm}^3/\text{Nm}$), the lowest wear rate was found for the borided AISI D6 steel at 1323 K for 8 h ($1.28 \times 10^{-6} \text{ mm}^3/\text{Nm}$). The wear test results indicated that the wear resistance of the borided steels increased considerably with the boriding treatment

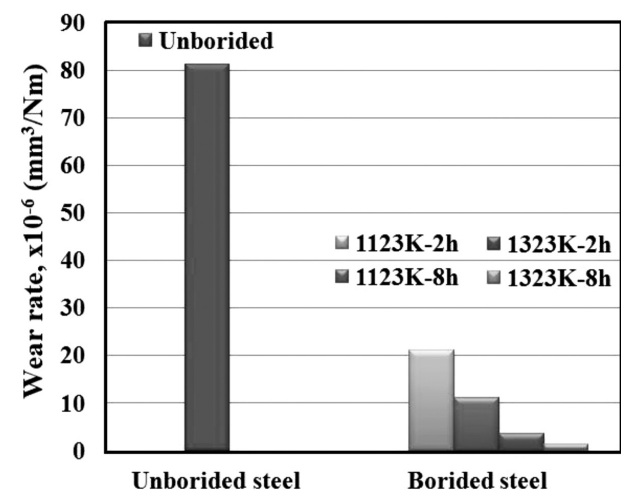


Figure 6: Wear rate of unborided and borided AISI D6 steel

Slika 6: Hitrost obrabe neboriranega in boriranega AISI D6 jekla

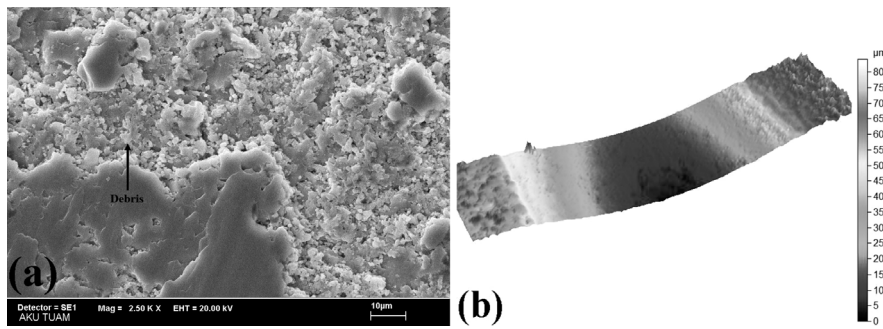


Figure 7: SEM micrograph and cross-sectional surface of the worn-out surfaces of the unborided AISI D6 steel: a) unborided, b) cross-sectional surface (CS)

Slika 7: SEM posnetek površine in presek obrabljene površine neboriranega jekla AISI D6: a) neborirano, b) presek obrabljene površine (CS)

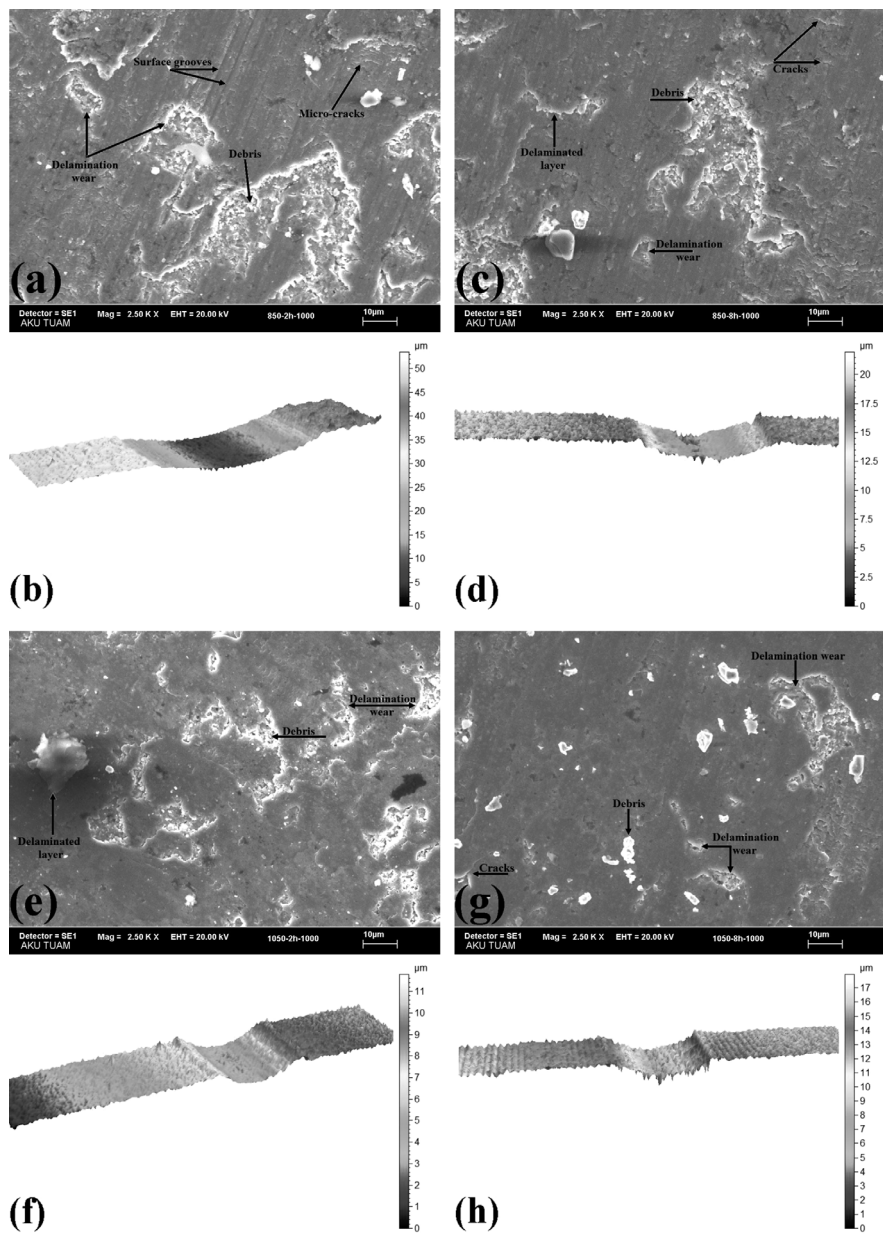


Figure 8: SEM micrographs and cross-sectional surface of the worn-out surfaces of the borided AISI D6 steel: a) 1123 K – 2 h, b) 1123 K – 2 h CS, c) 1123 K – 8 h, d) 1123 K – 8 h CS, e) 1323 K – 2 h, f) 1323 K – 2 h CS, g) 1323 K – 8 h, h) 1323 K – 8 h CS

Slika 8: SEM posnetek površine in presek obrabljene površine na boriranem jeklu AISI D6: a) 1123 K – 2 h, b) 1123 K – 2 h CS, c) 1123 K – 8 h, d) 1123 K – 8 h CS, e) 1323 K – 2 h, f) 1323 K – 2 h CS, g) 1323 K – 8 h, h) 1323 K – 8 h CS

and time. It is well known that the hardness of the boride layer plays an important role in the improvement of wear resistance. As shown in **Figures 4** and **6**, the relationship between the surface microhardness and the wear resistance of the borided samples also confirms that the wear resistance was improved with the increasing hardness. This is in agreement with the reports of previous studies.^{17–22} Comparing the wear rate of the borided steel with the unborided steel, the wear rate of the borided steels is approximately four times lower. The wear rate of the unborided sample was $81.2 \times 10^{-6} \text{ mm}^3/\text{Nm}$; however, this value dropped to $1.28 \times 10^{-6} \text{ mm}^3/\text{Nm}$ (1323 K – 8 h) as a result of the boriding process.

The SEM micrographs of the worn surfaces of the unborided and borided AISI D6 steel are illustrated in **Figures 7** and **8**. **Figure 7a** shows the SEM micrographs of the wear surfaces and **Figure 7b** shows the cross-sectional surface (CS) of the wear mark obtained from the wear region of the unborided AISI D6 steel. In **Figure 7a**, the worn surface of the unborided steel was rougher and coarser wear-debris particles were present. The wear region of the borided steel, debris, delamination wear, surface grooves and cracks on the surface can be seen (**Figure 8**). There were micro-cracks, abrasive particles and small holes on the worn surface of the boride coatings. In the wear region of the borided AISI D6 steel there were cavities probably formed as a result of layer fatigue (**Figure 8**) and the cracks concluded in delaminating wear. **Figure 8** shows the wear surfaces, and the cross-sectional surface (CS) of the wear mark obtained from the wear region by analyzing multiple profilometry surface line scans using a Nanovea ST-400 non-contact optical profiler. It was observed that the depth and the width of the wear trace on the surfaces of the samples decreased with an increase in the boriding temperature and time (**Figures 7b, 7d, 7f** and **7h**). When the SEM image of the worn surfaces of the unborided sample is examined, it can be seen that the wear marks in **Figure 7a** are larger and deeper.

4 CONCLUSIONS

In this study the wear behavior and some of the mechanical properties of borides on the surface of borided AISI D6 steel were investigated. Some of the conclusions are as follows.

- The boride layer thickness on the surface of the AISI D6 steel was obtained, depending on the chemical composition of the substrates, 13.54–164.42 μm .
- The multiphase boride coatings that were thermochemically grown on the AISI D6 steel were made up of the FeB, Fe₂B, CrB and Cr₂B phases.
- The surface hardness of the borided steel was in the range 1672–2118 HV_{0.05}, while for the untreated steel substrate it was 584 HV_{0.05}.
- The coefficient-of-friction values for the borided samples (between 0.39 and 0.58) were lower than the

coefficient-of-friction values (0.62) for the unborided steel sample.

- The lowest wear rate was obtained for the steel borided at 1323K for 8 hours, while the highest wear rate was obtained for the unborided steel.
- The wear rate of the borided steel was found to be approximately four times lower than the wear rate of the unborided steel.

Acknowledgement

The authors are grateful to the Scientific Research Project (14.FEN.BİL.49) Council of Afyon Kocatepe University. This article was based on Salih Kanat's master's thesis.

5 REFERENCES

- 1 A. G. von Matuschka, Boronizing, Heyden and Son Inc., Philadelphia, USA 1980, 11
- 2 A. K. Sinha, Boriding (Boronizing), ASM Handbook, Vol. 4, J. Heat Treating, ASM International, OH, USA 1991, 437–447
- 3 M. Keddami, S. M. Chentouf, A diffusion model for describing the bilayer growth (FeB/Fe₂B) during the iron powder-pack boriding, Applied Surface Science, 252 (2005), 393–399, doi:10.1016/j.apsusc.2005.01.016
- 4 I. Gunes, Tribological behavior and characterization of borided cold-work tool steel, Mater. Tehnol., 48 (2014), 765–769
- 5 I. Gunes, Kinetics of borided gear steels, Sadhana, 38 (2013), 527–541, doi:10.1007/s12046-013-0138-0
- 6 M. Hudakova, M. Kusy, V. Sedlicka, P. Grac, Analysis of the boronized layer on K 190 PM tool steel, Mater. Tehnol., 41 (2007) 2, 81–84
- 7 M. Keddami, M. Kulka, N. Makuch, A. Pertek, L. Maldzinski, A kinetic model for estimating the boron activation energies in the FeB and Fe₂B layers during the gas-boriding of Armco iron: Effect of boride incubation times, Applied Surface Science, 298 (2014), 155–163, doi:10.1016/j.apsusc.2014.01.151
- 8 I. Gunes, S. Taktak, Surface characterization of pack and plasma paste boronized of 21NiCrMo2 steel, Journal of the Faculty of Engineering and Architecture of Gazi University, 27 (2012), 99–108
- 9 G. Kartal, O. Kahvecioglu, S. Timur, Investigating the morphology and corrosion behavior of electrochemically borided steel, Surface Coatings Technology, 200 (2006), 3590–3593, doi:10.1016/j.surfcoat.2005.02.210
- 10 R. Matsumoto, K. Osakada, Development of warm forging method for magnesium alloy, Materials Transactions, 45 (2004) 9, 2838–2844, doi:10.2320/matertrans.45.2838
- 11 I. Gunes, M. Erdogan, A. G. Çelik, Corrosion behavior and characterization of plasma nitrided and borided AISI M2 steel, Materials Research, 17 (2014) 3, 612–618, doi:10.1590/S1516-14392014005000061
- 12 W. Muhammad, Boriding of high carbon high chromium cold work tool steel, Materials Science and Engineering, 60 (2014), 1–6, doi:10.1088/1757-899X/60/1/012062
- 13 I. Ozbek, S. Sen, M. Ipek, C. Bindal, S. Zeytin, H. A. Ucisik, A mechanical aspect of borides formed on the AISI 440C stainless-steel, Vacuum, 73 (2004), 643–648, doi:10.1016/j.vacuum.2003.12.083
- 14 M. Erdogan, I. Gunes, Corrosion Behavior and Microstructure of Borided Tool Steel, Revista Matéria, 20 (2015), 523–529, doi:10.1590/S1517-707620150002.0052
- 15 C. Bindal, A. H. Ucisik, Characterization of boriding of 0.3% C, 0.02% P plain carbon steel, Vacuum, 82 (2008), 90–94, doi:10.1016/j.vacuum.2007.04.039

I. GUNES, S. KANAT: INVESTIGATION OF WEAR BEHAVIOR OF BORIDED AISI D6 STEEL

- ¹⁶ I. Gunes, Tribological properties and characterisation of plasma paste borided AISI 5120 steel, *Journal of the Balkan Tribological Association*, 20 (2014), 351–361
- ¹⁷ M. Tabur, M. Izciler, F. Gul, I. Karacan, Abrasive wear behavior of boronized AISI 8620 steel, *Wear*, 266 (2009), 1106–1112, doi:10.1016/j.wear.2009.03.006
- ¹⁸ C. Martini, G. Palombarini, G. Poli, D. Prandstraller, Sliding and abrasive wear behaviour of boride coatings, *Wear*, 256 (2004), 608–613, doi:10.1016/j.wear.2003.10.003
- ¹⁹ I. Gunes, Investigation of tribological properties and characterization of borided AISI 420 and AISI 5120 steels, *Transactions of the Indian Institute of Metals*, 67 (2014), 359–365, doi:10.1007/s12666-013-0356-5.
- ²⁰ S. Taktak, M. S. Baspinar, Wear and friction behaviour of alumina/mullite composite bysol-gel infiltration technique, *Materials and Design*, 26 (2005), 459–464, doi:10.1016/j.matdes.2004.07.012
- ²¹ C. Li, B. Shen, G. Li, C. Yang, Effect of boronizing temperature and time on microstructure and abrasion wear resistance of Cr12Mn2V2 high chromium cast iron, *Surface and Coatings Technology*, 202 (2008), 5882–5886, doi:10.1016/j.surfcoat.2008.06.170
- ²² S. Sahin, Effects of boronizing process on the surface roughness and dimensions of AISI 1020, AISI 1040 and AISI 2714, *Journal of Mater. Process. Tech.*, 209 (2009), 1736–1741, doi:10.1016/j.jmatprotec.2008.04.040

INVESTIGATION OF PORTEVIN-LE CHATELIER EFFECT OF HOT-ROLLED Fe-13Mn-0.2C-1Al-1Si TWIP STEEL

PREISKAVA PORTEVIN-LE CHATELIER UČINKA PRI VROČEM VALJANJU Fe-13Mn-0.2C-1Al-1Si TWIP JEKLA

Bulent Aydemir¹, Havva Kazdal Zeytin², Gokhan Guven²

¹Tubitak National Metrology Institute (UME), P.K. 54, Gebze, Kocaeli 41470, Turkey

²Tubitak MRC, Materials Institute, P.K. 21, Gebze, Kocaeli 41470, Turkey
bulent.aydemir@tubitak.gov.tr

Prejem rokopisa – received: 2015-02-07; sprejem za objavo – accepted for publication: 2015-07-08

doi:10.17222/mit.2015.034

This study was undertaken to investigate the microstructure and mechanical properties of hot rolled Fe-13Mn-0.2C-1Al-1Si TWIP steel. Tensile tests were carried out at different strain rates to determine the Portevin-Le Chatelier (PLC) effect during deformation. Subsequently, the samples were investigated by light microscopy and SEM. The sample microstructures revealed inhomogeneous dislocation zones, deformation twinning and twin-dislocation interactions. Consequently, the PLC effect during deformation was determined to be responsible for the excellent mechanical properties of the TWIP steel.

Keywords: TWIP steel, mechanical properties, microstructure, Portevin Le Chatelier effect

V študiji je bila preiskovana mikrostruktura in mehanske lastnosti vroče valjanega Fe-13Mn-0.2C-1Al-1Si TWIP jekla. Natezni preizkusi so bili izvedeni pri različnih hitrostih obremenjevanja. Kot rezultat nateznega preizkusa je bil ugotovljen učinek Portevin-Le Chatelier (PLC) med deformacijo. Vzorci so bili nato preiskani s svetlobnim mikroskopom in s SEM. Mikrostruktura vzorcev kaže nehomogena področja dislokacij, deformacijske dvojčke in interakcije dvojčkov z dislokacijami. Ugotovljeno je, da so odlične mehanske lastnosti TWIP jekla posledica vpliva PLC med deformacijo.

Gljučne besede: TWIP jeklo, mehanske lastnosti, mikrostruktura, vpliv Portevin Le Chatelier

1 INTRODUCTION

Higher automotive safety standards have led to a strong interest in advanced high strength steel and "super tough", high manganese steel characterized by Twinning-Induced Plasticity (TWIP). The high-manganese austenitic TWIP steels present excellent properties, combining a very large strain-hardening rate and ductility. The TWIP effect is responsible for the observed high maximum stress (600 MPa – 1100 MPa) and good elongation (50 % – 95 %).^{1,2} Extensive research has already investigated on high Mn TWIP steels with slightly different compositions. For example: Fe18Mn0.6C, Fe22Mn0.6C, Fe–17Mn–0.6C, Fe–17Mn–0.8C etc.^{1–9}

TWIP steels have a high manganese (Mn) content. Manganese tends to stabilize austenite, although its role in the TWIP microstructure is still a subject of active research. Twinning promotes retention of the austenitic microstructure but competes with dislocation glide by impeding dislocation motion at twin boundaries and other dislocation-dislocation interactions (e.g. forest hardening). Twin formation is associated with Stacking Fault Energy (SFE) at room temperature. Deformation twinning in low SFE austenitic steels leads to high strain-hardening and improved ductility of TWIP steel. In low SFE austenitic steels, the increased partial dislocation separation results in ease of twin nucleation. With applied deformation, the grains are progressively

subdivided by the twinning process, and the internal twin boundaries increase the strain hardening. Though the actual twinning strain is limited, and the twin formation itself may actually cause softening, the twin boundaries decrease the dislocation slip distances progressively and promote dislocation accumulation and storage, especially at grain boundaries.¹ This dynamic Hall–Petch effect may not be the only cause for the observed strain hardening of TWIP steel. In fact, the mechanism leading to high strain hardening in TWIP steel is still a matter of debate.

Austenitic steels usually reveal dynamic strain aging (DSA); a form of unstable plastic flow found in the dilute metal alloys.^{10–13} Portevin-Le Chatelier bands (or the PLC effect) and serrated flow curves are usual manifestations of DSA, which occurs over a large temperature range.¹⁴ The bands, which are regions of localized plasticity, are commonly divided in three groups. As: Type A (continuously propagates across the gage length of a tensile specimen); Type B (discontinuous propagation or "hop"); and Type C (no spatial correlation). A common explanation of DSA in metals centers on dislocation-solute interactions in which solute atoms diffuse to dislocations temporarily arrested at obstacles (or trapped by the local energy landscape in the lattice) thereby increasing the stress required to release the dislocations.¹⁰ With aging, the dislocations are suddenly released, and

the process repeats elsewhere. There have been many publications on dynamic strain aging and the PLC effect in TWIP steels.^{15–17} The microstructure and mechanical properties of the hot rolled Fe-13Mn-0.2C-1Al-1Si TWIP Steel is investigated in this study. The conclusion of the study was expected to be an aid for future industrial manufacture of TWIP steel.

2 MATERIAL AND EXPERIMENTAL PROCEDURE

The chemical composition of the newly developed Fe-13Mn-0.2C-1Al-1Si TWIP steel is given in **Table 1**. The TWIP steel was melted by induction melting under an inert gas atmosphere in a furnace. Then, it was cast in a ceramic mold with a thickness of about 20 mm. The ingot was homogenized at 1200 °C for 6 h and then hot-rolled to a thickness of 5 mm i.e. a total deformation of 75 % by thickness. In addition, no annealing was carried out.

Table 1: Chemical composition of investigated alloy in mass fractions, (wt%)

Tabela 1: Kemijska sestava preiskovane zlitine, v masnih odstotkih (wt%)

C	Mn	Si	Cr	N	Al
0.23	12.73	1.08	0.12	0.10	0.95

The tensile samples were prepared mechanically in accordance with the EN ISO 6892 Standard.¹⁸ The experiments were conducted with a Zwick Z250 tensile tester at the Material Institute in TUBITAK. The force

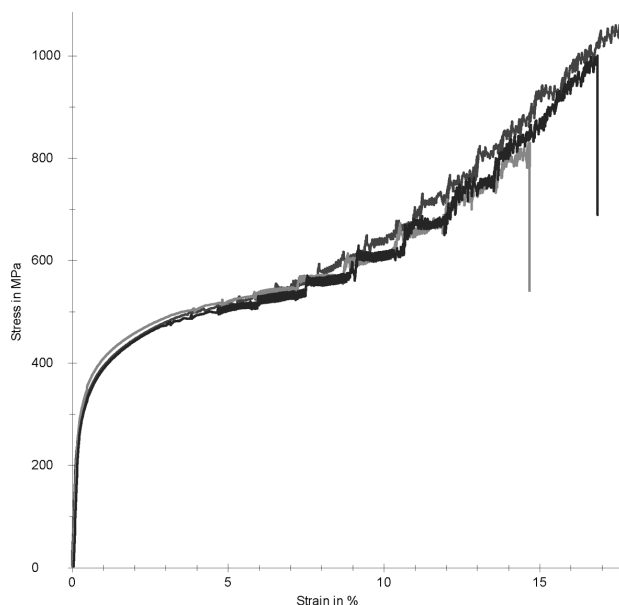


Figure 1: Stress-strain curves of Fe-13Mn-0.2C-1Al-1Si TWIP steel at different test speeds at room temperature (2 mm/min, 5 mm/min, 10 mm/min)

Slika 1: Krivulje napetost-raztezek Fe-13Mn-0.2C-1Al-1Si TWIP jekla pri različnih hitrostih preizkusa, pri sobni temperaturi (2 mm/min, 5 mm/min, 10 mm/min)

accuracy class of the machine was "class 0.5" according to EN ISO 7500-1 standard.¹⁹ The extensometer was used together with a strain measurement system. The extensometer accuracy class of the machine was "class 0.5" according to EN ISO 9513 standard.²⁰ All tests were performed at 23±1 °C and 50±10 % humidity. The specimen was gripped by jaws and preload applied. Then, the extensometer was automatically attached to the specimen. The gage length of the applied extensometer was 50 mm. The tensile test was carried out with test speeds of (2, 5 and 10) mm/min. In addition, the Charpy impact energy of 3 samples was tested at room temperature by Charpy V-notch measurements on 55 mm × 10 mm × 5 mm specimens.

The samples' microstructures were examined by light (Nikon) and scanning electron microscopes (SEM-Jeol-JSM 6335F-Japan). The samples for microstructure investigations were cut suitably and mounted, mechanically polished, and etched using a nital solution.

3 RESULTS AND DISCUSSION

Figure 1 shows a typical room temperature stress-strain curve of the Fe-13Mn-0.2C-1Al-1Si TWIP steel at different test speeds. Mechanical property values obtained from the data in **Figure 1** are listed in **Table 2**. Average Charpy impact energy values in Joules are given in **Table 2**. **Figure 2** presents the tensile true stress-true strain curves at different test speeds.

There isn't a yield point nor a yield plateau observed on the stress-strain curve, though some remarkable serrated flows are found at strains above 5 %. As can be seen the steel retains high strength and elongation without necking at these strain rates. The main differences between the stress-strain curves are the morphologies of

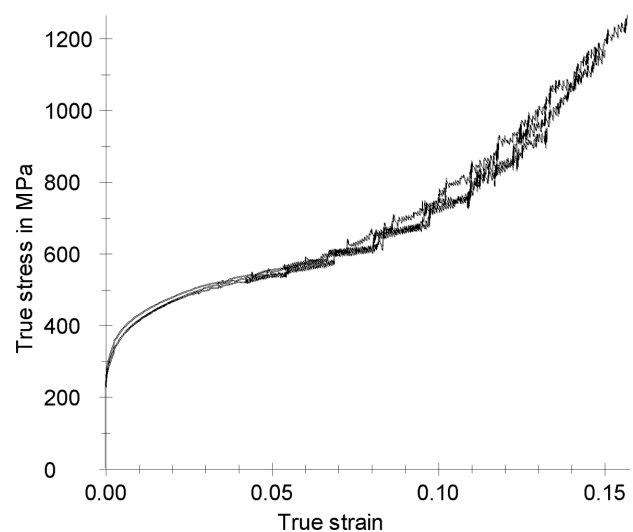


Figure 2: True stress-true strain curves of Fe-13Mn-0.2C-1Al-1Si TWIP steel at different test speeds at room temperature

Slika 2: Prava krivulja napetost-raztezek TWIP jekla Fe-13Mn-0.2C-1Al-1Si pri različnih hitrostih preizkusa na sobni temperaturi

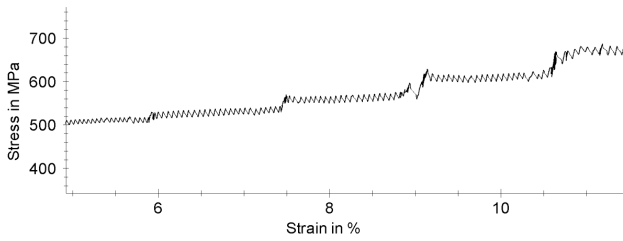


Figure 3: The room-temperature tensile response (magnified) of Fe-13Mn-0.2C-1Al-1Si TWIP steel at 10 mm/min test speed

Slika 3: Povečan odziv pri nateznem preiskusu Fe-13Mn-0.2C-1Al-1Si TWIP jekla pri hitrosti preiskusa 10 mm/min na sobni temperaturi

the serrations. The fluctuations on the stress-strain curve result from the dynamic strain aging (DSA) which is consistent with earlier work on cold-rolled TWIP steel.^{21–23}

Table 2: Mechanical properties of Fe-13Mn-0.2C-1Al-1Si TWIP steel at room temperature

Tabela 2: Mehanske lastnosti Fe-13Mn-0.2C-1Al-1Si TWIP jekla pri sobni temperaturi

Test speed (mm/min)	$R_p 0.2$ (MPa)	R_m (Mpa)	A (%)	E_{impact} (J)
10	308	1075	17	23,9
5	307	844	14	
2	306	999	16	

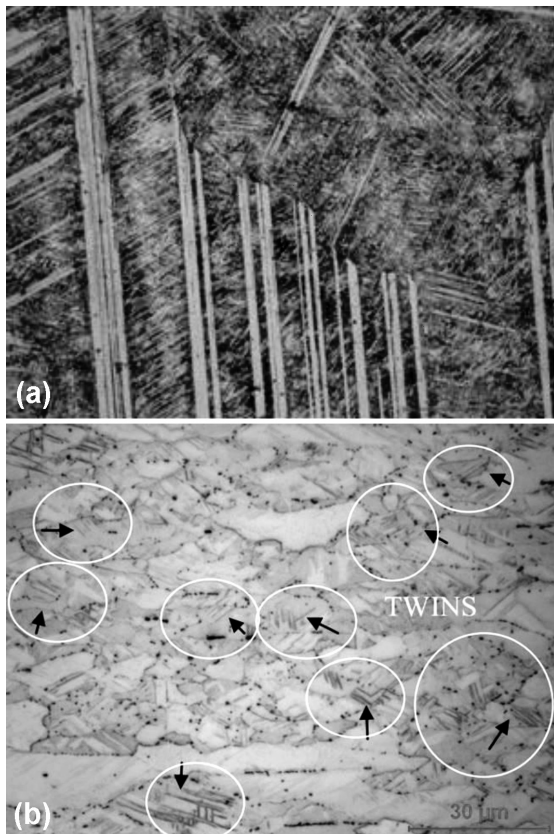


Figure 4: Microstructure of the TWIP steel: a) as cast, b) hot rolled

Slika 4: Mikrostruktura TWIP jekla: a) lito, b) vroče valjano

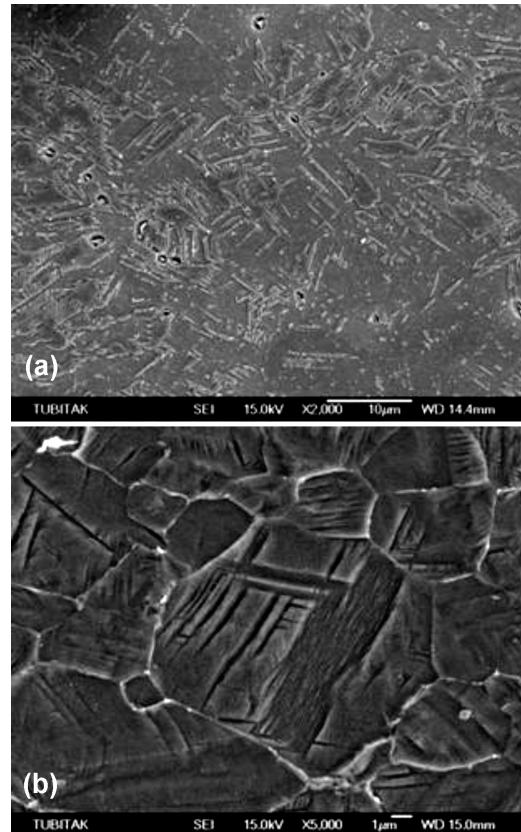


Figure 5: Microstructure of the TWIP steel (SEM): a) 2000x, b) 5000x

Slika 5: Mikrostruktura TWIP jekla (SEM): a) 2000 x, b) 5000 x

Evidence of the appearance of deformation bands and the coherent evolution of the serration is seen at room temperature. In **Figure 3** the magnified stress–strain curve at 10 mm/min test speed is shown. The stress–strain curve shows clear stress jumps and dips of the same type described by K. Renard et al.¹⁷ The observed serrations correspond to those of type A i.e. the bands propagate continuously after nucleation.

An image of the hot rolled Fe-13Mn-0.2C-1Al-1Si TWIP Steel obtained with a Nikon L150 light microscope is given in **Figure 4**. The microstructure shows

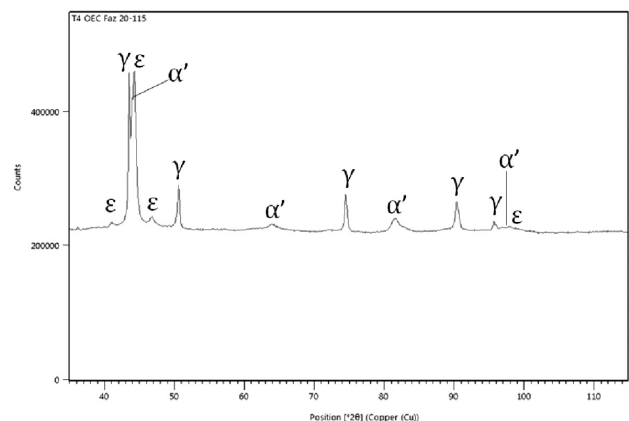


Figure 6: Diffraction pattern of the TWIP steel

Slika 6: Rentgenogram vzorca TWIP jekla

austenite grains containing a secondary precipitate phase. The precipitates are mostly observed at grain boundaries. Hot-rolling of the TWIP steel resulted in annealing of the austenite grain twins, presenting as mechanical twins. Deformation twins and twin-dislocation interactions are observed in the deformed TWIP steel. This twinning produces high strain hardening and

higher ductility, and is responsible for the excellent mechanical properties of the hot-rolled TWIP steel.

SEM images of this sample are shown in **Figure 5**. Analysis of secondary precipitated phases observed at the grain boundaries yields ϵ and α' particles. A secondary phase precipitated within austenite matrix is also seen. The ϵ and α' martensite transformations occurred

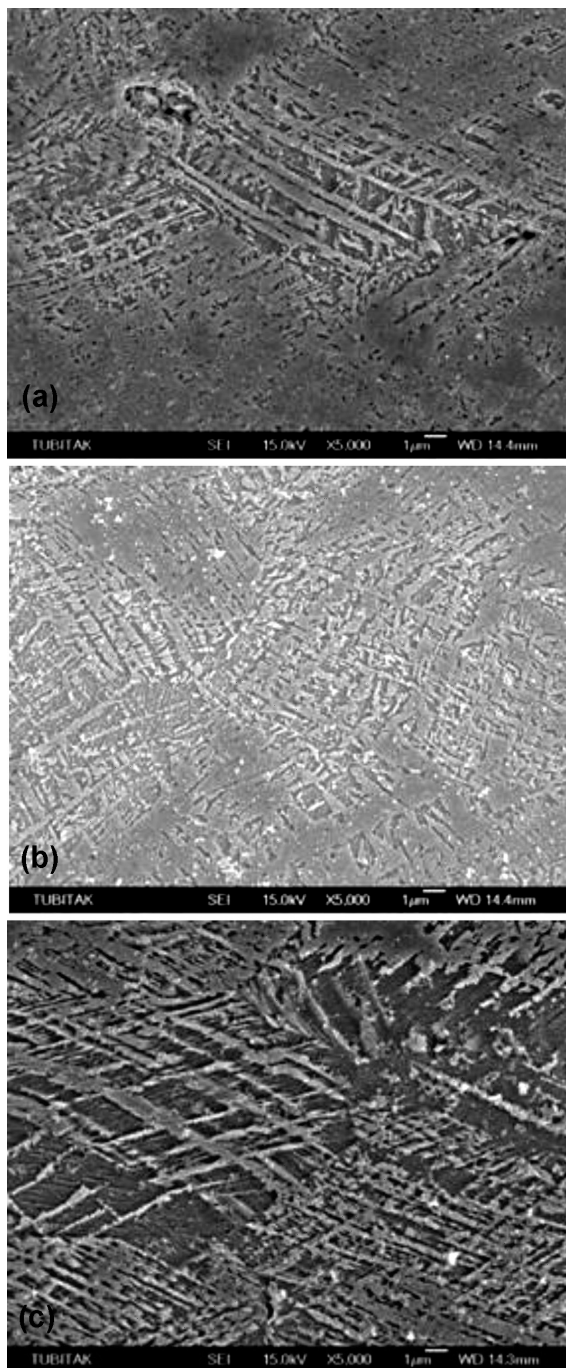


Figure 7: Microstructure of the TWIP steel necked region after applying the tensile test at different speeds: a) 2 mm/min, b) 5 mm/min, c) 10 mm/min

Slika 7: Mikrostruktura područja vratu pri TWIP jeklu, po nateznom preizkusu pri različitim hitrostih preizkusa: a) 2 mm/min, b) 5 mm/min, c) 10 mm/min

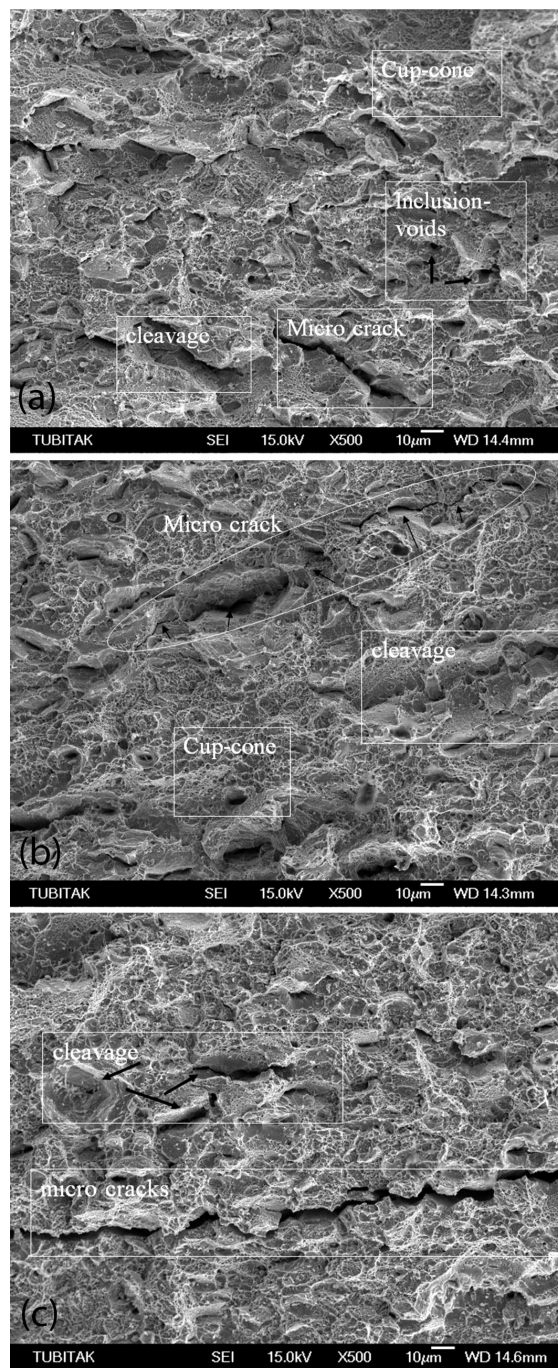


Figure 8: Microstructure of the TWIP steel necked region after applying the tensile test with test speed: a) 2 mm/min, b) 5 mm/min, c) 10 mm/min

Slika 8: Mikrostruktura područja vratu pri TWIP jeklu po nateznom preizkusu s hitrostjo preizkusa: a) 2 mm/min, b) 5 mm/min, c) 10 mm/min

after hot rolling. In the present work, the steel is cooled in air after being hot rolled. Large parallel laths crossing the micrograph correspond to ε martensite, with α' martensite also forming. With a relatively low stability, the austenite transformation proceeds by $\gamma \rightarrow \varepsilon \rightarrow \alpha'$ martensitic transformations, resulting in a high work-hardening rate. Stability against the $\gamma \rightarrow \varepsilon$ martensite transformation is usually considered to imply stability against the $\gamma \rightarrow \alpha'$ martensite transformation since ε martensite laths form as an intermediate phase.^{8,24} The Diffraction Pattern is given in **Figure 6**.

I. Gutierrez-Urrutia and D. Raabe²⁵ in their study of FeMnAlC steels, and many other researchers, reported a form of carbides at the grain boundaries in the sediments, the k-carbides (Fe, Mn)₃AlC.^{24,25} SEM images of the second phase are precipitated in the grain boundary (Fe,Mn)₃AlC phase. This phase is reported in the austenite grain boundaries of FeMnAl steel with high carbon content after hot-rolling, and is deposited after an aging process. Optical microscopy, SEM, and XRD studies show the k-carbides to be precipitated in the austenite grain boundary phase.

The microstructures of this TWIP steel at the necked region in parallel with the tension force direction after applying the tensile test with (2, 5, and 10) mm/min test speed were analyzed. These fracture surface images are shown in **Figures 7 and 8**. The cleavage regions in the fracture surface images increased with test speed increases, and there was a growth of cracks. SEM photos clearly demonstrate the typical ductile pattern of surface fracture. Cleavage fracture areas and micro-cracks in the grain developed when the test speed increases. Unfilled areas formed by pouring of inclusions can be observed on the fracture surface.

Figure 8 shows a local deformation region with many parallel deformation twins. Moreover, the high dislocation density found in the micro-scale mechanical twins, indicate that the twin boundaries could play a similar role to grain boundaries as short range obstacles for gliding dislocations and strongly delay the necking of the sample. Thus the samples in this study showed high strength and moderate elongation.

This evolution of the serrations with the strain level is the commonly expected behavior in a classical PLC scheme. This reflects an increase of DSA effectiveness due to a rise in the dislocation density when the strain increases. The evolution of the serration type with strain rate is also a characteristic of DSA. Indeed, when the strain rate decreases, that is, the waiting time of the dislocations increases, the magnitude of the serrations was enhanced. As a consequence, the jerky flow was mostly of type A when the test speed was sufficiently large, as was the case at 10 mm/min. Finally, DSA should be avoided in sheets during manufacturing as it gives rise to non-homogeneous plastic flow during sheet forming processes and may lead to surface defects on formed parts.

4 CONCLUSIONS

This study investigated the microstructure and mechanical properties of hot rolled Fe-13Mn-0.2C-1Al-1Si TWIP steel. The conclusions are summarized in the following:

- The hot-rolled Fe-13Mn-0.2C-1Al-1Si TWIP steel exhibited excellent mechanical properties with an ultimate strength of 1075 MPa and an elongation of 17 %.
- Many deformation twins and twin-dislocation interactions were observed in the deformed TWIP steel microstructure. This is due to the influence of the PLC effect. The PLC effect during deformation was determined to be responsible for the excellent mechanical properties of the hot-rolled TWIP steel.
- From a technological point of view the PLC effect, and hence DSA, must be avoided. DSA gives rise to non-homogeneous plastic flow during sheet forming processes and may lead to surface defects on formed parts.

5 REFERENCES

- S. Allain, J. P. Chateau-Cornu, O. Bouaziz, A physical model of the twinning-induced plasticity effect in a high manganese austenitic steel, *Mater. Sci. Eng. A*, 387–389 (2004), 143, doi:10.1016/j.msea.2004.01.060
- L. Chen, H. S. Kim, S. K. Kim, B. C. De Cooman, On the Transition of Internal to External Selective Oxidation on CMnSi TRIP, *Metallurgical and Materials Transactions A*, 47 (2007) 12, 1804–1812, doi:10.2355/issijinternational.47.1804
- Y. N. Dastur, W. C. Leslie, Mechanism of work hardening in Hadfield manganese steel, *Metal. Trans. A*, 12A (1981) 5, 749–759, doi:10.1007/BF02648339
- O. Grassel, L. Krüger, G. Frommeyer, L. W. Meyer, Int. J. Plast., Microstructure–deformation relationships in fine grained high manganese TWIP steel—the role of local texture, *International Journal of Materials Research*, 16 (2000) 10–11, 1391, doi:10.1016/S0749-6419(00)00015-2
- M. Koyama, T. Sawaguchi, T. Lee, C. S. Lee, K. Tsuzaki, Work hardening associated with ε -martensitic transformation deformation twinning and dynamic strain aging in Fe–17Mn–0.6C and Fe–17Mn–0.8C TWIP steels, *Materials Science and Engineering A*, 528 (2011), 7310–7316, doi:10.1016/j.msea.2011.06.011
- I. Karaman, H. Sehitoglu, K. Gall, Y. I. Chumlyakov, H. J. Maier, Deformation of single crystal Hadfield steel by twinning and slip, *Acta Mater.*, 48 (2000), 1345, doi:10.1016/S1359-6454(99)00383-3
- S. Kibey, J. B. Liu, M. J. Curtis, D. D. Johnson, H. Sehitoglu, Effect of nitrogen on generalized stacking fault energy and stacking fault widths in high nitrogen steels, *Acta Mater.*, 54 (2006), 2991, doi:10.1016/j.actamat.2006.02.048
- E. Bayraktar, F. A. Khalid, C. Levaillant, *J. Mater.*, Deformation and fracture behaviour of high manganese austenitic steel, *Process. Technol.*, 147 (2004), 145, doi:10.1016/j.jmatprotec.2003.10.007
- B. X. Huang, X. D. Wang, Y. H. Rong, L. Wang, L. Jin, Mechanical behavior and martensitic transformation of an Fe–Mn–Si–Al–Nb alloy, *Mater.Sci. Eng. A*, A438–440 (2006), 306, doi:10.1016/j.msea.2006.02.150
- L. G. Hector, P. D. Zavattieri, Nucleation And Propagation Of Portevin-Le Chatelier Bands In Austenitic Steel With Twinning Induced Plasticity, *Proceedings of the SEM Annual Conference, Indianapolis, USA 2010*

- ¹¹ S. Kumar, E. Pink, Dynamic strain aging in a tungsten heavy metal, *Scripta Mat.*, 35 (1996), 1047–1052, doi:10.1016/1359-6462(96)00262-X
- ¹² J. M. Robinson, M. P. Shaw, Microstructural and mechanical influences on dynamic strain aging phenomena, *Int. Materials Reviews*, 39 (1994), 113–121, doi:10.1179/imr.1994.39.3.113
- ¹³ J. A. Yakes, C. C. Li, W. C. Leslie, The Effect of Dynamic Strain Aging on the Mechanical Properties of Several HSLA Steel, *SAE Trans.*, SAE 790009 (1980), 44–59
- ¹⁴ B. Skoczen, J. Bielski, S. Sgobba, D. Marcinek, Constitutive Model of Discontinuous Plastic Flow at Cryogenic Temperature, *Int. J. Plasticity*, (2010), doi:10.1016/j.ijplas.2010.02.003
- ¹⁵ P. Zavattieri, V. Savic, L. G. Hector Jr., J. R. Fekete, W. Tong, Y. Xuan, Spatio-temporal characteristics of the Portevin-Le Châtelier effect in austenitic steel with twinning induced plasticity, *Int. J. Plasticity*, 25 (2009), 2298–2330, doi:10.1016/j.ijplas.2009.02.008
- ¹⁶ B. C. De Cooman, L. Chen, S. Kim, H. S. Estrin, Y. Kim, S. K. State-of-the-Science of High Manganese TWIP Steels for Automotive Applications, Springer, # 2010, 165–183
- ¹⁷ K. Renard, S. Ryelandt, P. J. Jacques, Characterization of the Portevin-Le Chatelier effect affecting an austenitic TWIP steel based on digital image correlation, *Mat. Sci. Eng. A*, 527 (2010), 2969–2977, doi:10.1016/j.msea.2010.01.037
- ¹⁸ EN ISO 6892-1:2009, Metallic materials – Tensile testing –Part 1: Method of test at room temperature
- ¹⁹ EN ISO 7500-1:2015 Metallic materials – Verification of static uniaxial testing machines – Part 1: Tension/compression testing machines – Verification and calibration of the force-measuring system
- ²⁰ EN ISO 9513:2012 Metallic materials - Calibration of extensometer systems used in uniaxial testing
- ²¹ L. Zhang, X. H. Liu, K. Y. Shu, Microstructure and Mechanical Properties of Hot-Rolled Fe-Mn-C-Si TWIP Steel, *J. Iron. Steel. Res. Int.*, 18 (2011) 12, 45–48, 64, doi:10.1016/S1006-706X(12)60008-9
- ²² O. Bouaziz, S. Allain, C. Scott, Effect of grain and twin boundaries on the hardening mechanisms of twinning-induced plasticity steels, *Scripta Mater.*, 58 (2008) 6, 484, doi:10.1016/j.scriptamat.2007.10.050
- ²³ D. Barbier, N. Gey, S. Allain, N. Bozzolo, M. Humbert, Analysis of the tensile behavior of a TWIP steel based on the texture and microstructure evolutions, *Mater. Sci.*, 500 (2009) 1–2, 196, doi:10.1016/j.msea.2008.09.031
- ²⁴ S. S. F., De Dafé, F. L. Sicupira, F. C. S. Matos, N. S. Cruz, D.R. Moreira, D.B. Santos, Effect of cooling rate on (ϵ , α') martensite formation in twinning/transformation-induced plasticity Fe-17Mn-0.06C steel, *Mat. Res.*, 16 (2013) 6, 1229–1236, doi:10.1590/S1516-14392013005000129
- ²⁵ I. Gutierrez-Urrutia, D. Raabe, High strength and ductile low density austenitic FeMnAlC steels: Simplex and alloys strengthened by nanoscale ordered carbides, *Materials Science and Technology*, 30 (2014) 9, 1099, doi:10.1179/1743284714Y.0000000515
- ²⁶ Y. Minamino, Y. Koizuma, N. Tsujia, N. Hirohataa, K. Mizuuchib, Y. Ohkandab, Microstructures and mechanical properties of bulk nanocrystalline Fe–Al–C alloys made by mechanically alloying with subsequent spark plasma sintering, *Science and Technology of Advanced Materials*, (2004) 5, 133–143, doi:10.1016/j.stam.2003.11.004

THE INFLUENCE OF SURFACE COATINGS ON THE TOOTH TIP DEFLECTION OF POLYMER GEARS

VPLIV POVRŠINSKIH PREVLEK NA POVES VRHA ZOBA POLIMERNIH ZOBNIKOV

Boštjan Trobentar¹, Srečko Glodež¹, Jože Flašker¹, Boštjan Zafošnik²

¹University of Maribor, Faculty of Mechanical Engineering, Smetanova ulica 17, 2000 Maribor, Slovenia

²Prometheus, Boštjan Zafošnik s.p., Tacenska cesta 125 E, 1000 Ljubljana, Slovenia
bostjan.trobentar@gmail.com

Prejem rokopisa – received: 2015-03-09; sprejem za objavo – accepted for publication: 2015-07-29

doi:10.17222/mit.2015.056

When designing gear drives made of polymer, the tooth tip deflection is a crucial parameter in respect to the proper gear drive operation. Excessive tooth tip deflection can lead to serious disturbances of gear meshing and consequently to increased noise and wear of the teeth flanks. In such cases the tooth tip deflection can be reduced through the use of stiff surface coatings on the tooth flanks. In this paper the influence of different coating materials and thicknesses on the tooth tip deflection of polymer gears is analysed using comprehensive finite element computational analysis. The numerical results obtained are then used to define an approximate equation for the calculation of gear tooth tip deflection for the coating material used and the thickness of the surface coating layer. The results show that the tooth tip deflection decreases with large values of the coating material Young's modulus and with the coating layer thickness.

Keywords: polymer gears, surface coatings, tooth deflection, numerical analysis

Pri konstruiranju zobniških dvojic s polimernimi zobniki je poves vrha zoba zobnika eden ključnih dejavnikov, ki vpliva na pravilno delovanje zobniške dvojice. Prevelik poves vrha zoba namreč vodi do resnih motenj pri ubiranju zobniške dvojice, kar povzroči večji hrup in tudi večjo obrabo zobnih bokov. V takšnih primerih lahko poves vrha zoba zobnika zmanjšamo z uporabo togih površinskih prevlek. V predloženem prispevku je predstavljena obsežna numerična analiza po metodi končnih elementov, ki zajema vpliv materiala trde prevleke in debeline prevleke na poves vrha zoba zobnika. Numerični rezultati so nato uporabljeni za določitev aproksimativne enačbe za izračun povesa vrha zoba zobnika v odvisnosti od izbranega materiala prevleke in njene debeline. Končni rezultati kažejo, da se poves vrha zoba zmanjšuje z večanjem modula elastičnosti prevleke in debeline utrjenega površinskega sloja zobnih bokov.

Ključne besede: polimerni zobniki, površinske prevleke, poves zoba, numerične analize

1 INTRODUCTION

The primary function of gears is to transmit rotary or linear motion. The design for the kinematics of a gear set is geometrically controlled when the deflections of gear teeth during the gear drive operation are taken into account. Therefore, the selection of appropriate gear material is crucial in the design process. Recently, the development of new materials and technologies have resulted in increased use of engineering polymers for machine elements (e.g. gears) due to benefits such as low cost for injection moulding, light weight, resilience and their ability to operate under dry, unlubricated conditions.¹ Polymer gears, when used in moderate power transmission applications without lubrication may have potentially conflicting tribological properties (low friction, high resistance to wear) and mechanical properties (stiffness, fracture strength). This situation is further complicated by the complex loading and contact phenomena that change throughout the meshing cycle. As the transmissible power levels increase, problems of surface temperatures arise due to the frictional losses between mating gear teeth.^{2,3}

Most of these coatings are based on zinc and aluminium, which are mainly used for radio frequency shielding and electrical conductivity where the mechanical properties of the coatings are not of prime importance. The use of polymer with good strength to weight ratio as a base material is an alternative to metallic components. The main disadvantage is the poor wear resistance of contact surfaces. Recent research work regarding these problems has indicated that thermal spray coatings on polymers can be applied in many engineering applications. Careful selection of material combinations and the use of special process parameters can produce relatively thick metal, ceramic or carbide coatings which can be machined or ground.⁴

It is very important to optimize the gear design before the tools for manufacturing and experimental testing are made to decrease their cost. Traditionally, the gear designer had a limited number of analytical tools as well as his own experience to achieve this goal. Some of the most well known analytical tools for the prediction of gear tooth strength are the procedures according to ISO, VDI and AGMA standards.⁵⁻⁷ As noted earlier, the tooth tip deflection becomes important for gears made of

materials with low stiffness (e.g. polymers) as it can lead to disturbances in gear meshing in the case of excessive tooth tip deflection. The procedure of gear meshing considering the deflection effect is described in the VDI 2736 standard,⁷ where spur gear tooth tip deflection is influenced by the force, tooth face width and material stiffness, which is represented by the Young's modulus and the gear geometrical parameters. It is known that the Young's modulus of polymer materials is much smaller than that of steels, which are often used as gear materials. Furthermore polymer stress-strain behaviour is also affected by changes in the temperature.

Lately, thermoplastic polymers are widely used in manufacturing polymer gears. They have different stress-strain behaviour in the tensile than in the compression region which leads to different values of the Young's modulus in both regions. Furthermore, polymers can also show nonlinear behaviour in the elastic region which cannot be described with a Young's modulus. Therefore, the different stress-strain behaviour in tensile/compression regions and the nonlinear behaviour in an elastic region have to be described with an appropriate constitutive model using an appropriate computational approach (e.g. Finite Element Method). P. Wyluda and V. Wolf¹ performed an elastic-plastic finite element analysis of meshing of two acetal copolymer spur gears under quasi-static loading conditions. Their computational results were in a relative good agreement with the experimental data. The effect of PTFE on the tribological behaviour of polymers in rolling sliding contact has been investigated for two of the most widely used polymers – PA 66 and polyacetal. The experimental results showed that the friction and wear performance of the PTFE filled polymers was superior to that of the unfilled polymers. In addition, the surface cracking found in unfilled PA66 and thought to be responsible for the premature fracture of components such as gear teeth was suppressed by the PTFE. It is suggested that a combination of high surface temperature and high surface tensile stress, produced by friction, is required to initiate these cracks and that PTFE inhibits crack formation by reducing friction.⁸

In general, the gear tooth tip deflection can be decreased using a stiffer material with higher Young's modulus. If a gear is made of low stiffness material (e.g. polymer) the gear tooth stiffness can be increased using a stiff surface coating. Because the standard VDI procedure for the determination of gear tooth deflection includes only homogenous material properties, it is not possible to determine the deflection of a coated gear tooth using the equations available in the above quoted standards.⁷ For this reason, an appropriate computational model to analyse the tooth tip deflection of coated polymer spur gears with different coating materials is presented in this paper.

2 MATERIALS AND METHODS

Polymer materials have low stiffness that can lead to greater deflection of elements made of such materials. Excessive deflection can lead to serious problems in the meshing of polymer gears and consequently the additional loading of the gear teeth. According to the VDI 2736⁷ the deflection of the tooth tip of a spur gear in the circumferential direction can be approximately calculated from Equation (1):

$$\lambda = \frac{\frac{F_t}{b}}{\frac{2E_1 E_2}{c' \cdot \frac{E_1 + E_2}{E_{\text{steel}}}}} \quad (1)$$

where F_t is the tangential force in N, b is the face width in mm, c' is the maximum tooth stiffness per unit face width (single stiffness) of a tooth pair in $\text{N/mm} \times \mu\text{m}^2$, E_{steel} is the modulus of elasticity of steel ($E_{\text{steel}} = 210000$ MPa) and $E_{1,2}$ are the elastic moduli of gears 1 and 2 in MPa at room temperature. The maximum tooth stiffness per unit face width can be expressed in the Equations (2) and (3)⁶:

$$c' = c'_{th} \cdot C_M \cdot C_R \cdot C_B \cdot \cos \beta \quad (2)$$

$$c'_{th} = \frac{1}{q'} \quad (3)$$

Equation (2) uses the theoretical single tooth stiffness c'_{th} as given by Equation (3), where q' is the minimum value for the flexibility of a gear pair. Individual factors in Equation (2) can be determined as described in the ISO 6336 standard: C_M is the correction factor that takes into account the difference between theoretical and actual values for solid disc gears ($C_M = 0.8$ according to the standard ISO 6336); gear blank factor C_R takes into account flexibility of gear rims and webs ($C_R = 1.0$ for a solid disc according to the standard ISO 6336); the factor C_B reflects the influence of deviation from the gear basic rack profile according to standards ISO 6336 and ISO 53.^{6,9}

The deflection of the tooth tip λ determined with Equation (1) must be smaller than the estimated permissible deformation $\lambda_P = 0.07 \cdot m_n$, where m_n is the normal module in mm. Overcoming of the permissible deflection λ_P can lead to serious disturbances of the meshing gear teeth and consequently to higher noise and a shorter service life of the gear pair.⁷

As mentioned above, Equation (1) cannot be used for calculation of the tooth tip deflection of coated gears. Therefore, an appropriate numerical model should be used in that case. The first step in developing a numerical model for the simulation of tooth tip deflection of coated gears was the creation of a numerical model that will yield proper results to be verified by analytical or experimental solutions, or solutions taken from standardised procedures. For this purpose a two dimensional

plane strain model with homogeneous material properties (Hooke's law) and static load was generated. The stress-strain behaviour of the polymer material used in this paper consists of linear and non-linear regions (**Figure 1**). The assumption of using Hooke's law for polymer gears was verified by comparison of the tooth tip deflections based on material models that consider linear elastic material properties.

The static load used in the present model is based on the assumption that the number of loading cycles during the service life of the gear is small and that the gear is used only for partial rotation (e.g. application of the four bar mechanism and for slow motion of the gear rack). This is necessary due to the presence of polymer hysteresis during loading and unloading. If the material is viscoelastic, the path of loading is not coincident with the path of unloading, which occurs when the material changes significantly in volume and is experiencing large deformations. Furthermore, it is assumed that there is enough time for strain recovery and a permanent set effect of the polymer can be neglected.¹¹

An accurate two-dimensional model of the benchmark gear was developed and imported into the ABAQUS software. The contact position of engaging gear tooth flanks was chosen to be on the outer point of single engagement, where the bending load is highest. Contact between engaging teeth was prescribed as a standard surface to surface contact, with the master surface set on the driving gear and the slave surface on the driven pinion gear. Assuming good lubrication, contact interaction was modelled as tangentially frictionless with finite sliding with no adjustments or smoothing between the surfaces. The influence of coating wear during the service life and consequently its influence on tooth toughness and deflection were not considered.

The pinion in **Figure 2a** was fully constrained in the centre bore, while displacements were only constrained in the gear, and the rotations remained free. The load was applied by torque load in the centre of the gear.

The material properties of the pinion were defined as hyper-elastic in the core and as linearly elastic in various coatings. The mesh was generated with CPS4R-type elements with locally controlled element size at tooth flanks (**Figure 2b**) and with at least ten elements in the

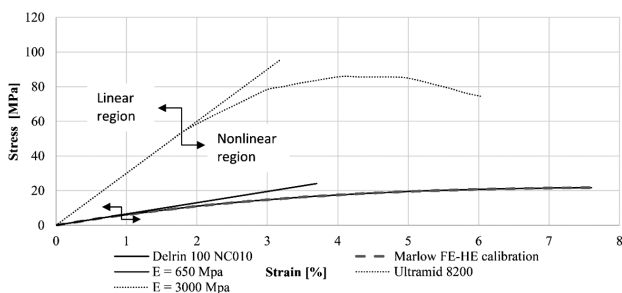


Figure 1: Material properties of pinion core^{10,11,13}

Slika 1: Materialne lastnosti jedra pastorka^{10,11,13}

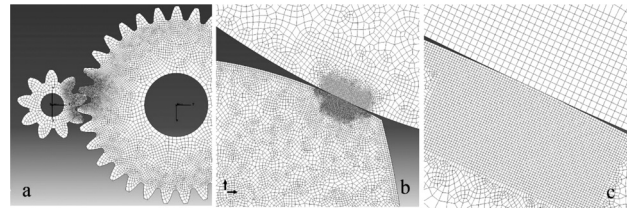


Figure 2: a) Numerical model, b) locally adjusted mesh on gear teeth and c) coating model on pinion

Slika 2: a) Numerični model, b) lokalna zgostitev mreže na zobu in c) prikaz sloja na pastorku

coating layer thickness direction (**Figure 2c**). The numerical model was also tested for convergence analysis. **Figure 3** shows a significant improvement when the number of elements in contact was increased from 467 to 3456. An increase to 5538 elements had no influence on the results or calculation time.

Our workflow was combined from several steps. First, the gear deflection according to VDI 2736⁷ and ISO 6336⁶ standards are calculated. The analysed gears (gear and pinion presented in Table 1) have properties of the steel and the polymer material. Young's modulus and Poisson's ratio for the steel gear was $E = 206000$ MPa and $\nu = 0.33$, respectively, while the polymer material was described with the properties for POM (**Figure 1**) and $\nu = 0.35$. A reference tooth tip deflection was calculated according to Equation (1). In the next step, a model with a coated polymer gear was generated. The pinion gear was partitioned between a coating layer (**Figure 2c**) and core material. Different models were created for different types of coatings and their thicknesses. Two different core material properties from DuPont and BASF (POM Delrin 100 NC010¹² and PA Ultramid® 8202¹³) and several different materials used for coating

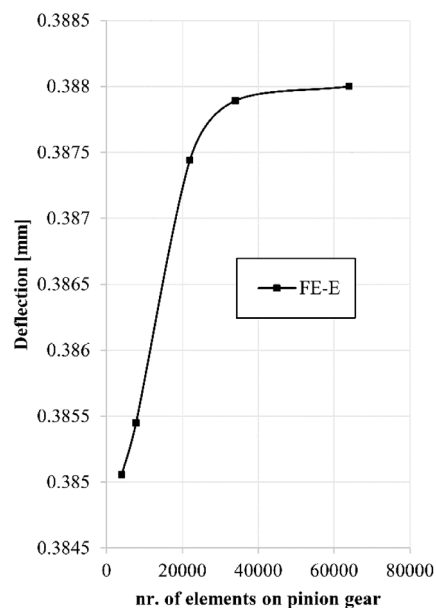


Figure 3: Mesh converge of pinion gear

Slika 3: Konvergenca mreže pastorka

were studied; Polytetrafluoroethylene – PTFE ($E=560$ MPa), aluminium – Al ($E = 70$ GPa), Boron nitride – BN ($E = 33.85– 85.91$ GPa) and Molybdenum disulphide – MoS₂ ($E = 210–400$ GPa) with various Young’s moduli between 560 MPa and 210 GPa.¹⁴ Four different thickness of the coating were modelled on the pinion: $t = 25 \mu\text{m}$, $50 \mu\text{m}$, $75 \mu\text{m}$ and $100 \mu\text{m}$.

Table 1: Details of gear pairs

Tabela 1: Podatki zobniških dvojic

Parameter	Gear pair 1, 2, 3		Gear pair 4, 5	
	Pinion	Gear	Pinion	Gear
Module m (mm)	4		4	
Centre distance a (mm)	80		100	
Pressure angle α (°)	25		20	
Width b (mm)	25	25	25	25
Number of teeth z (-)	9	31	23	27
Profile shift x (mm)	0.4871	-0.4871	0	0
Addendum height h_{aP} (mm)	4.750	2.000	4	4
Dedendum Height h_{fP} (mm)	3.051	6.949	5	5
Root radius profile ρ (mm)	1.24	48	1.83	1.78
Material	POM	42CrMo4	POM/PA	42CrMo4
Young’s modulus E (MPa)	560	206000	560/3000	206000
Poisson’s ratio ν (-)	0.35	0.33	0.35/0.35	0.33

The computational results based on the numerical procedure as described above have then been used to determine the appropriate mathematical formulation where the tooth tip deflection λ is expressed according to the Young’s modulus of the coating material E and the coating thickness t . Several forms of polynomials were used to find the best fit, however the best correlation was found using the following Equation (4):

$$\lambda = A + B \cdot E + C \cdot t + D \cdot \ln t + F \cdot \ln E \quad (4)$$

The computational parameters A , B , C , D and F were calculated using the least squares method. The large value of the coating material’s Young’s modulus and large coating thickness cause a minimum deflection λ , and vice versa. This fact can lead to verification of the model and the derivation of extreme values. Using the global optimization method, the coating material Young’s modulus E and coating thickness t parameters were determined, yielding the minimum and maximum deflections. Equation (4) is valid for general nonlinear elastic base materials.

3 COMPUTATIONAL RESULTS

As described in section 2, the computational analysis of a gear without coating has been carried out first to compare the numerical results with the results of the

analytical procedure as described in VDI 2736.¹⁵ The first finite element analysis (FE-E model) using the standard Young’s modulus and with torque $T = 10$ Nm (tangential force $F_t = 555.6$ N) results in a tooth tip deflection of the uncoated pinion $\lambda = 0.388$ mm, while the standardised VDI calculation gives a value $\lambda = 0.361$ mm. Using a modified computational model (FE-HE model), the tooth tip deflections are also determined for coated gears with different Young’s moduli of coating materials and constant coating thickness $t = 0.1$ mm. As shown in **Figure 3**, the tooth tip deflection of the coated pinion is reduced compared to the tooth tip deflection of an uncoated gear and is for a tangential force, $F_t = 555.6$ N, inside the permissible limit according to VDI 2736. It is evident from **Figure 4** that a reasonably thick coating of $t = 0.1$ mm can have a significant influence on the deflection values of polymer gears.

Combining the computational results with Equation (4), valid parameters for treated Gear pair 1 with regression $R = 0.991$ are determined:

$$A = 0.5173140, B = 8.42502 \cdot 10^{-8}, C = -0.236158, D = 0.000644889 \text{ and } F = -0.0251878.$$

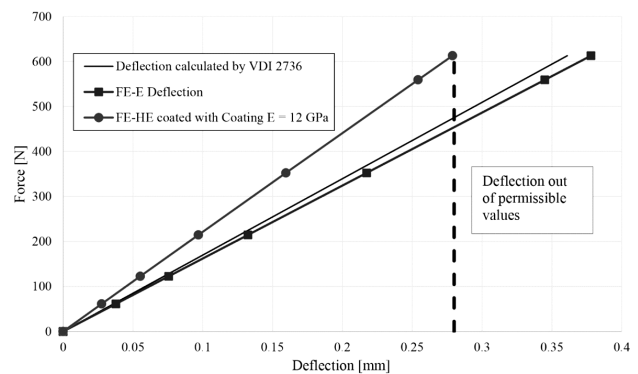


Figure 4: Comparison of gear tooth tip deflection with and without coating (Gear pair 1)

Slika 4: Primerjava povesa vrha zoba zobnika z in brez prevleke (zobniška dvojica 1)

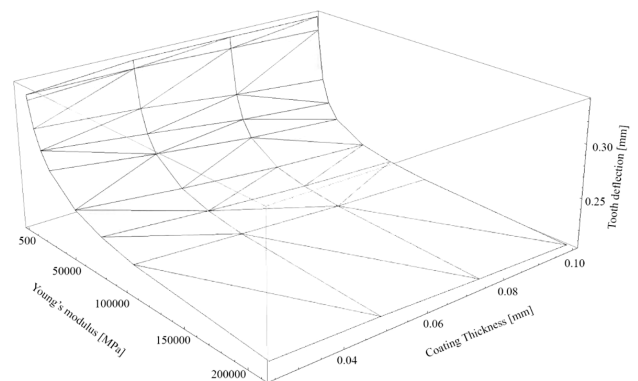


Figure 5: The effect of Young’s modulus and coating thickness on the tooth tip deflection for gear pair 1 and $R = 0.991$

Slika 5: Vpliv modula elastičnosti in debeline prevleke na povese vrha zoba za zobniško dvojico 1 in $R = 0,991$

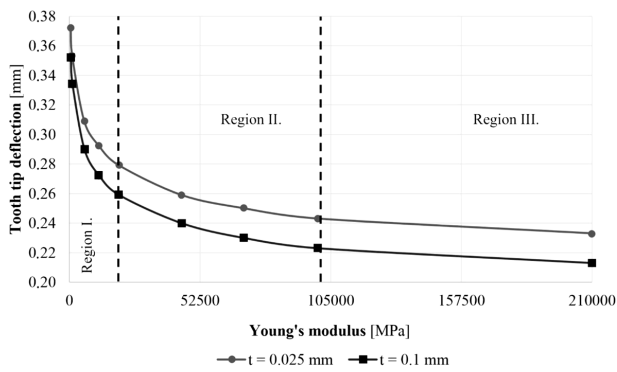


Figure 6: Comparison of tooth tip deflection for two coating thicknesses on gear pair 1

Slika 6: Primerjava povesa vrha zoba za dve debelini prevlek na zobniški dvojici 1

For different gear pairs we obtained the coefficients A, B, C, D, F (Table 3) and with different regression values R which can be found in Table 2. The effect of the Young's modulus E and coating thickness t on the tooth tip deflection according to Equation (4) is presented in Figure 5. The minimum tooth tip deflection $\lambda_{min} = 0.2132$ mm is observed for Young's modulus $E = 210$ GPa and a coating thickness $t = 0.1$ mm, with the maximum tooth tip deflection $\lambda_{max} = 0.3717$ mm seen for Young's modulus is $E = 560$ MPa and coating thickness $t = 0.025$ mm.

The influence of Young's modulus on the tooth tip deflection for minimum ($t = 0.025$ mm) and maximum ($t = 0.1$ mm) coating thicknesses is presented in Figure 6. In region I it can be seen that an increase of the Young's modulus of the surface coating can significantly reduce the tooth tip deflection of the treated gear (about 26.4 % relative to that of Young's modulus $E = 560$ MPa and $E = 20000$ MPa). A somewhat smaller decrease of the tooth tip deflection with increase of Young's modulus is observed in region II (about 13 % relative to that of at $E = 20000$ MPa and $E = 105000$ MPa), while in region III the tooth tip deflection drops only about 6.1 %.

Similar results to those described above are also found when the tooth tip deflection is studied for two given Young's moduli (560 MPa and 210 GPa) and different surface coating thickness (Figure 7). For uncoated gears ($t = 0$) a tooth tip deflection of 0.388 mm is observed. When a surface coating is applied, the significant drop of tooth tip deflection is observed especially for harder surface coatings. In region I (up to coating thickness of 0.025 mm) the decrease of tooth tip

Table 3: Equation coefficients for equation 4

Tabela 3: Koeficienti za enačbo 4

Gear	A	B	C	D	F
Gear pair 1 $i = 9/31$	0.5173140	8.42502E-08	-0.236158000	0.000644889	-0.025187800
Gear pair 2 $i = 9/31$	0.2407840	3.56586E-08	0.053658500	-0.004475320	-0.012522600
Gear pair 3 $i = 9/31$	0.0463095	7.10510E-09	0.000250842	-0.001774000	-0.002599930
Gear pair 4 $i = 23/27$	0.1549290	3.23817E-08	-0.009230920	-0.006828120	-0.010816000
Gear pair 5 $i = 23/27$	0.0304427	-1.67453E-08	-0.009067370	-0.000983624	-0.001365980

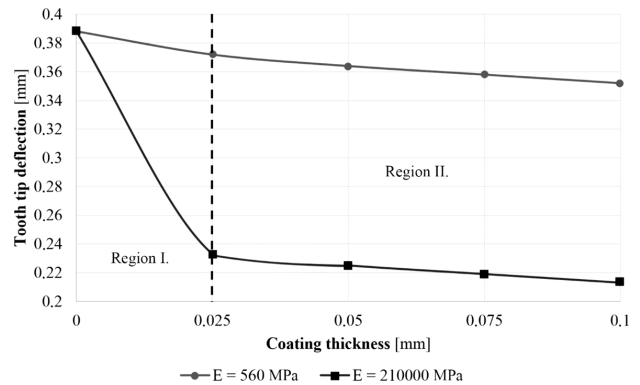


Figure 7: Comparison of tooth tip deflection for two different coating materials on gear pair 1

Slika 7: Primerjava povesa vrha zoba za dva tipa prevlek na zobniški dvojici 1

deflection is about 40 %, while in region II this value is only 9 %.

The deflection behaviour of five gear pairs was examined at the given operating conditions (Table 2). Two distinct geometries were tested with different core materials. Table 2 shows the values for regression of all five cases. The largest deflection has been found in the gear pair 1, with torque 10 Nm and POM as the core material. The smallest deflection was observed in gear pair 5, with torque 10 Nm and PA as a core material.

Table 2: Fitting of equation with FE values

Tabela 2: Ujemanje enačbe z MKE rezultati

Gear	Torque (Nm)	Material	Regression R
Gear pair 1 $i = 9/31$	10	Delrin 100 NC010	0.9910
Gear pair 2 $i = 9/31$	5	Delrin 100 NC010	0.9806
Gear pair 3 $i = 9/31$	1	Delrin 100 NC010	0.9790
Gear pair 4 $i = 23/27$	10	Delrin 100 NC010	0.9781
Gear pair 5 $i = 23/27$	10	Ultramid® 8202	0.9650

In Table 3, the A, B, C, D and F coefficients are given for different gear pairs. It is evident that by reducing force or increasing the stiffness of the base material (gear pair 5), these coefficients approach zero. This is a direct consequence of the fact that the tooth tip deflection decreases with stiffer materials and/or reduced

torque. For gear pair 1 (the weakest material and the largest torque) the maximum coefficient deviations and consequently the highest tooth tip deflection was observed.

4 CONCLUSION

The influence of different coating materials and coating thicknesses on the tooth tip deflection of polymer gears made of POM and PA is presented in this paper. The tooth tip deflection was determined numerically using a finite element model. Here, the mechanical properties of the core material were defined using the Marlow hyperelastic material model while the coating materials' mechanical properties were defined using the linearly elastic Hooke's law. The computational results obtained have then been used to define the approximate analytical equation, where linear and logarithmic terms of Young's modulus and coating layer thickness were used. The obtained analytical equation form describes the tooth tip deflection. It is valid for coating material Young's moduli in the range from 560 MPa to 210 GPa, coating thicknesses between 0.025 mm to 0.1 mm, different loads, different nonlinear elastic base materials and different geometries. The final results showed that the use of stiff surface coatings on polymer gears significantly reduce the tooth tip deflection and consequently improve the operation of such gear pairs.

Further investigations for coated polymer gears should cover the potential cracking of hard coatings in the case where the core material stiffness is too low. The coating layer wear due to the relative sliding of gear flanks and its influence on the tooth tip deflection should also be studied. To confirm the computational results, the experimental testing of bending behaviour of coated polymer elements should be carried out.

Acknowledgement

The doctoral study of the first author is partly co-financed by the European Union through the European Social Fund. Co-financing is carried out within the framework of the Operational Programme for Human Resources Development for the period 2007–2013, 1. Development priorities for Promoting entrepreneurship and adaptability; policy priority. 3: Scholarship Scheme.^{15–19}

5 REFERENCES

- ¹ P. Wyluda, D. Wolf, Examination of finite element analysis and experimental results of quasi-statically loaded acetal copolymer gears, Axcel Products, Inc., http://www.axelproducts.com/downloads/FEA_gears_copolymer.pdf, 7.6.2016
- ² E. Letzelter, M. Guingand, J. P. de Vaujany, P. Schlosser, A new experimental approach for measuring thermal behaviour in the case of nylon 6/6 cylindrical gears, *Polymer Testing*, 29 (2010) 8, 1041–1051, doi:10.1016/j.polymertesting.2010.09.002
- ³ C. J. Hooke, S. N. Kukureka, P. Liao, M. Rao, Y. K. Chen, The friction and wear of polymers in non-conformal contacts, *Wear*, 200 (1996) 1-2, 83–94, doi:10.1016/s0043-1648(96)07270-5
- ⁴ D. Petrov, K. Dearn, D. Walton, R. Banks, The Influence Of Surface Coatings On The Wear Of Polyamide Gears, Proceedings of I International Conference – Process Technology And Environmental Protection (PTEP 2011), 2011, 9
- ⁵ AGMA, AGMA 1006-A97: Tooth Proportions for Plastic Gears
- ⁶ Cylindrical gears. Calculation of service life under variable load. Conditions for cylindrical gears in accordance with ISO 6336, BSI British Standards, doi:10.3403/01383565
- ⁷ VDI, VDI 2736 Blatt 2: Thermoplastic gear wheels - Cylindrical gears - Calculation of the load-carrying capacity, Postfach 10 11 39, 40002 Dusseldorf
- ⁸ M. Rao, C. J. Hooke, S. N. Kukureka, P. Liao, Y. K. Chen, The effect of PTFE on the friction and wear behavior of polymers in rolling-sliding contact, *Polymer Engineering & Science*, 38 (1998) 12, 1946–1958, doi:10.1002/pen.10364
- ⁹ ISO, ISO 53: Cylindrical gears for general and heavy engineering - Standard basic rack tooth profile
- ¹⁰ DuPont, DuPont Engineering Polymers, <<http://plastics.dupont.com/plastics/pdf/lit/americas/markets/gears.pdf>> (accessed 4 2015)
- ¹¹ V. A. Beloshenko, Y. E. Beigel'zimer, V. N. Varyukhin, Y. V. Voznyak, Strain hysteresis of polymers, *Dokl Phys Chem*, 409 (2006) 1, 207–209, doi:10.1134/s0012501606070086
- ¹² C. datasheet DuPont, Delrin® 100 NC010 - POM DuPont Engineering Polymers, <<http://www.campusplastics.com/campus/en/datasheet/Delrin%C2%AE+100+NC010/DuPont/52/6fc48544>>, (accessed 4 2015)
- ¹³ BASF, Ultramid® 8202 Polyamide 6, <<http://iwww.plasticsportal.com/products/dspdf.php?type=iso¶m=Ultramid+8202>> (accessed 6 2015)
- ¹⁴ J. Shackelford, W. Alexander (Eds.), *CRC Materials Science and Engineering Handbook*, Third Edition, Informa UK Limited, doi:10.1201/9781420038408
- ¹⁵ B. Trobentar, S. Glodež, B. Zafošnik, Gear tooth deflection of spur polymer gears, in *International Gear Conference*, Lyon, 2014, 129–137, doi:10.1533/9781782421955.129
- ¹⁶ A. Version, 6.12 Documentation Collection, ABAQUS/CAE User's Manual, 2013
- ¹⁷ A. B. Cropper, *The failure mode analysis of plastic gears*, University of Birmingham, 2003
- ¹⁸ D. Petrov, K. Dearn, D. Walton, R. Banks, Some Experimental Results Concerning The Influence Of Surface Coatings On The Wear Of Poly-Ether-Ether-Ketone (PEEK) Polymeric Gears, *Annals of the University Dunarea de Jos of Galati: Fascicle: VIII, Tribology*, 17 (2011) 1, 5–10
- ¹⁹ D. Petrov, K. Dearn, D. Walton, R. Bancs, Some Experimental Results Concerning The Influence Of Surface Coatings From Solid Lubricants On The Wear Of Polymeric Gars, *Journal of the Technical University Sofia, branch Plovdiv Fundamental Sciences and Applications Vol. 16* (2011), 6

VAPOUR-PHASE CONDENSED COMPOSITE MATERIALS BASED ON COPPER AND CARBON

KOMPOZITI NA OSNOVI BAKRA IN OGLJIKA, KONDENZIRANI IZ PLINSKE FAZE

Viktor Bukhanovsky¹, Mykola Rudnytsky¹, Mykola Grechanyuk², Rimma Minakova³, Chengyu Zhang⁴

¹National Academy of Science of Ukraine, Pisarenko Institute for Problems of Strength, 2 Tymiryazevska str., 01014 Kyiv, Ukraine

²Eltekhmash (Gekont) Science & Technology Company, Vinnitsa, Ukraine, Vatutina str. 25, 21011 Vinnitsa, Ukraine

³National Academy of Science of Ukraine, Frantsevich Institute for Problems of Materials Science, 3 Krzhizhanovskogo str., 03680, Kyiv, Ukraine

⁴Northwestern Polytechnical University, Xi'an, China, 710072 Xi'an, China
victan@ipp.kiev.ua

Prejem rokopisa – received: 2015-03-10; sprejem za objavo – accepted for publication: 2015-07-28

doi:10.17222/mit.2015.057

The production technology, structure, electrical conductivity, coefficient of friction, hardness, strength, and plasticity over a temperature range of 290–870 K of copper-carbon composites with laminated structures and carbon contents from 1.2 to 7.5 % of volume fractions for sliding electrical contacts of current-collecting devices obtained by electron-beam evaporation and vapor condensation are studied. Thermodynamic activation analysis of the hardness and strength of the composites was carried out. Correlations between the hardness and strength of the composites were established.

Keywords: condensed composites, electron-beam technology, electrical, tribotechnical and mechanical characteristics, correlation

Študirana je tehnologija izdelave, struktura, električna prevodnost, koeficient trenja, trdota, trdnost in plastičnost v temperaturnem območju 290–870 K kompozita baker-ogljik s plastovito strukturo in vsebnostjo ogljika od 1,2 do 7,5 % volumenskega deleža, za drsne električne kontakte za prenos tokov, dobljene z izparevanjem v elektronskem curku in s kondenzacijo par. Izvedena je bila analiza termodinamične aktivacije trdote in trdnosti kompozitov.

Ključne besede: kondenzirani kompoziti, tehnologija elektronskega curka, električne, tribotehnične in mehanske značilnosti, korelacija

1 INTRODUCTION

Nowadays composite materials (CMs) based on copper and carbon are widely used as electrocontact materials for current-collecting devices.^{1–6} In addition to the conventional powder metallurgy processes for producing these materials, they are also obtained by high rate electron beam evaporation of copper and carbon from individual water cooled crucibles, with layer by layer condensation of the mixed vapour flow on a rotating steel disk.^{7–13} The technology of high rate electron beam evaporation-condensation is the alternative to powder metallurgy: the thermal dispersion of the liquid melt and consolidation of dispersed particles flow (without special molding to obtain a high-density material state) with a limited amount of admixtures within a closed space. The apparent advantages of the electron-beam technology, which makes the development of a new generation of composite materials for electrical contacts possible, are as follows:

- the possibility of mixing the vapor flows of substances that do not dissolve well within each other at the atomic and molecular levels, to create composite materials and coatings (facing layers) with the

desired structure, chemical composition and performance characteristics, which cannot be obtained by other methods;

- simplicity and efficiency compared to powder metallurgy, as the material is formed in one technological cycle;
- the possibility to create gradient structures by varying the deposition rate of the components being evaporated in the course of the process;
- the possibility to obtain laminated composite materials, which is practically impossible to achieve using traditional methods;
- ecological purity, as this technology eliminates all atmospheric emissions.

Electron beam evaporation and condensation technology is used to produce electrical contact Cu-C CMs with specific laminated structures and chemistries within one production cycle. The composition determines its unique physical-mechanical and operational properties. Condensed copper-carbon composite materials with carbon contents from 1.2 to 7.5 % of volume fractions in the form of sheets of 3 to 5 mm in thickness were produced by the Gekont (Eltekhmash) Science &

Technology Company and, at present, these materials are in series production in Ukraine. These sheet materials are used in current-collecting devices as the operating floors of copper contact clips which are attached to them by brazing.

The present paper covers data on the production technology and experimental investigations of the structure, electrical and tribotechnical characteristics, strength, hardness, and plasticity of condensed laminated composite materials of the Cu-C system for current-collecting devices with carbon contents from 1.2 to 7.5 % of volume fractions over a temperature range of 290–870 K.

2 MATERIALS AND EXPERIMENTS

One of the advantages of copper-carbon CMs is the potential to vary their electroconductive and tribotechnical properties over a wide range by changing the copper and carbon contents in the composite. High-speed electron beam evaporation and condensation is regarded here as the most common and easily implemented manufacturing method.

However, there are almost insurmountable difficulties with obtaining Cu-C CMs using the aforementioned production process, i.e. a lack of physicochemical interaction between copper and carbon, a very high melting temperature of carbon, and the difficulty of its transformation into a vapor state. Taking these issues into consideration, the original electron-beam technology of carbon evaporation through a molten tungsten mediator was designed by the Eltechmash (Gekont) Science & Technology Company, and experimental industrial specimens of Cu-C CMs with the carbon contents within a particular range were obtained.

The principle of the method of evaporation through a molten tungsten mediator is as follows. Tungsten carbide is formed upon contact between molten tungsten and carbon, which is thermodynamically unstable under the given temperature conditions, decomposing into atomic

tungsten and carbon on the surface of the molten tungsten mediator. As the elasticity of the carbon vapour is two orders of magnitude lower than the elasticity of the tungsten vapour, it is mainly carbon which evaporates from the surface. This process ensures the atomic transfer of carbon to the rotating steel substrate and makes it possible to obtain the condensed Cu-C CMs with the specified laminated structure.

The materials for study were condensed composites of the Cu-C system, which were created using electron-beam technology with carbon contents of (1.2, 3.5, 5.0 and 7.5) % of volume fractions.

The Cu-C composites condensed from the vapor phase were obtained using the L5 electron-beam facility designed at the Eltechmash (Gekont) Science & Technology Company. The physical configuration and a schematic diagram of the equipment are given in **Figures 1** and **2**, respectively. The equipment comprises work chamber 1 (**Figure 2**), which on its side wall has gun chamber 2 connected to it, which contains electron-beam heaters 3, 4, 5 and 6. The vacuum system, comprised of two fore pumps, two booster pumps and two high-vacuum units, serves to provide a dynamic vacuum in the evaporation and condensation chambers.

On the upper flange of the work chamber 1 there is mechanism 15 (**Figure 2**) that rotates the 800 mm diameter steel substrate 14. The mechanism design allows it

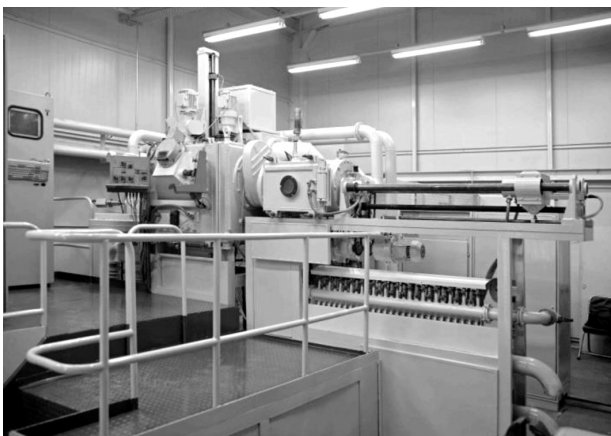


Figure 1: Physical configuration of the L5 electron-beam facility designed at the Eltechmash (Gekont) Science&Technology Company
Slika 1: Konfiguracija naprave z L5 elektronskim curkom, postavljena v Eltechmash (Gekont) Science&Technology podjetju

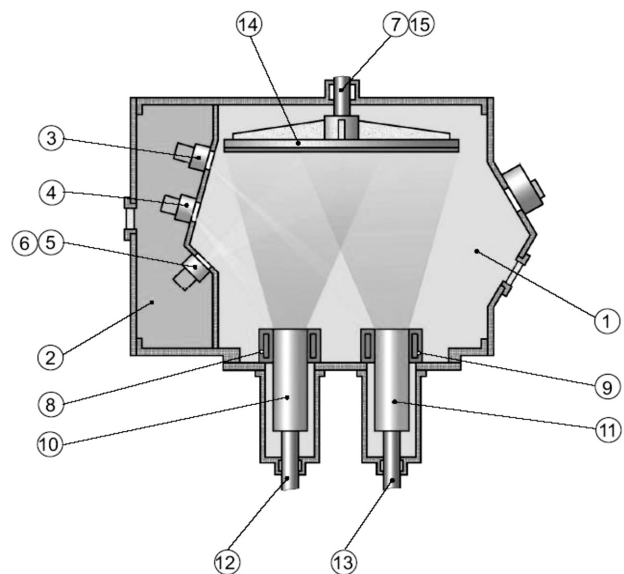


Figure 2: Scheme of the L5 electron-beam facility. Designations: 1 – work chamber; 2 – gun chamber; 3, 4, 5 and 6 – electron-beam heaters; 7 – substrate rotation rod; 8 – crucible for evaporation of copper; 9 – crucible for evaporation of carbon; 10, 11 – ingots of copper and carbon, respectively; 12, 13 – mechanisms for introducing ingots into the vapor flow zone; 14 – steel substrate for condensation of copper and carbon vapor flows; 15 – substrate rotation mechanism
Slika 2: Shema L5 naprave z elektronskim curkom. Oznake: 1 – delovna komora; 2 – komora s puško; 3, 4, 5 in 6 – grelci elektronskega curka; 7 – palica za vrtenje podlage; 8 – lonček za izparevanje bakra; 9 – lonček za izparevanje ogljika; 10, 11 – ingota bakra in ogljika; 12, 13 – mehanizma za podajanje ingotov v področje toka par; 14 – podlaga iz jekla za kondenzacijo par bakra in ogljika; 15 – mehanizem za rotacijo podlage

to be operated for a long time at a temperature of 870 ± 50 K without destroying the vacuum. The substrate, fixed to the rotating rod 7 was heated to the required temperature by 40 kW electron-beam heaters 5 and 6. The original material was heated to evaporation by 100 kW electron-beam heaters 3 and 4. All heaters have independent cathode-glow and electron-beam controls.

The evaporation unit has crucibles 8 and 9 with diameters of 100 and 70 mm for evaporation of copper and carbon, ingots 10 and 11 for evaporation, and mechanisms 12 and 13 that allow the ingots to be put in the evaporation zone.

In the present study, the copper-carbon condensates are obtained by means of copper and carbon evaporation from separate crucibles followed by their precipitation on a rotating steel substrate coated with a layer of calcium fluoride. The steel substrate was heated to a temperature of 935–965 K. The original materials were M0 grade copper ingots, 100 mm in diameter, after electron-beam remelting, and GMZ grade carbon ingots with a diameter of 70 mm.

The process of carbon evaporation involves the following stages. A batch of VA grade tungsten of 400 g weight was placed on the surface of the carbon ingot. When a vacuum level in the region of $1.3\text{--}4.0 \times 10^{-3}$ Pa is reached in the work chamber, electron-beam heating of the substrate to a temperature of 950 ± 15 K is performed. Simultaneously, the surfaces of both ingots are electron beam heated to the melting temperature of the base metal – copper, and intermediate for the carbon – tungsten with a current of 1.15–1.3 A. The melt pools became homogeneous after 15–20 min of heating. A layer from the copper evaporation crucible was the first to be precipitated on the substrate. At the production stage, evaporation from both crucibles was performed simultaneously at a beam current of 2.2–2.4 A for copper and 2.6–3.8 A for carbon under an acceleration voltage of 20 kV. By varying the beam current one can readily regulate the evaporation rate of carbon and its concentration in the composite over wide ranges.

By maintaining the substrate temperature in the range 935 K to 965 K, the re-evaporation of copper from the surface of the condensed material is prevented. The condensation rate of the tempered vapour flow was 20 $\mu\text{m}/\text{min}$. The resulting condensed materials were 2–3 mm thick disks of 800 mm in diameter.

At the end of the technological process, the condensed composite material was separated from the substrate. The condensed material obtained was annealed in a vacuum furnace at 1170 K for three hours to relieve internal stresses, stabilise the structure, and enhance its ductility.

In this study, the authors used the characterisation techniques that include macro- and microstructure analysis using optical and scanning electron microscopy, electrical resistance methods, tribotechnical tests, mechanical tensile tests at room and high temperatures, and hot hardness measurements. The carbon and copper

contents were determined using the mortar method (volumetric analysis).

The structure of the composite materials was investigated by light and scanning electron microscopy using a Neophot-2 light microscope and a Jeol Superprobe 733 raster electron microscope. Specimens for metallographic analysis were prepared using chemical etching in a 40 % hydrochloric acid solution and ion etching in a glow discharge. The authors studied the specimen surfaces and cross sections perpendicular to the substrate.

The electrical conductivity of the Cu-C CMs was determined by indirect bridge method measurements according to GOST 7229-76.¹⁴

The coefficient of friction of Cu-C CMs with copper was determined by the measurement of moment of friction and the determination of adhesion bond strength at the contact of copper specimen rotating under load with a composite counter-specimen according to GOST 27640-88.¹⁵

The mechanical characteristics were determined at ambient (outdoor) and elevated temperatures up to 870 K (in vacuum not below 0.7 mPa) from the results of mechanical tensile tests on standard flat fivefold proportional specimens with a gauge length of 15 mm, 3 mm width and ~ 2 mm thickness, using a 1246-R unit¹⁶ according to ISO 6892¹⁷ and ISO 783¹⁸, respectively. The specimens were cut from ~ 2 mm thick composite material after vacuum annealing at 1170 K for 3 h. The carbon content in the composites varied from 1.2 to 7.5 % of volume fractions. Three to five specimens were tested at each temperature. The deformation rate was 2 mm/min, which corresponded to a relative strain rate of $\sim 2.2 \times 10^{-3} \text{ s}^{-1}$. During the tests deformation diagrams were recorded to determine the proof strength $R_{p0.2}$, the ultimate strength R_m , the percentage elongation after fracture A , and the percentage non-proportional elongation at the maximum force A_g . In addition, the percentage reduction of cross-sectional area Z was evaluated.

The Cu-C composite hardness was estimated in the temperature range from 290 K to 870 K by Vickers indentation in the plane parallel to the surface of condensation. The pyramidal indenter was made of a synthetic corundum single crystal. Indentation loads were 10 N. The tests were carried out at a pressure no more than 0.7 mPa on a UVT-2 unit^{19,20} according to DSTU 2434-94.²¹

3 RESULTS AND DISCUSSION

The electron-beam process provides a particular laminated composite structure with alternating copper layers, containing dispersed carbon particles, of 150 μm to 300 μm in thickness with carbon layers of 6 to 8 μm thickness (Figure 3). The copper grain size is 0.1–0.3 μm . The mean size of the dispersed carbon particles in the copper matrix does not exceed 20 nm.

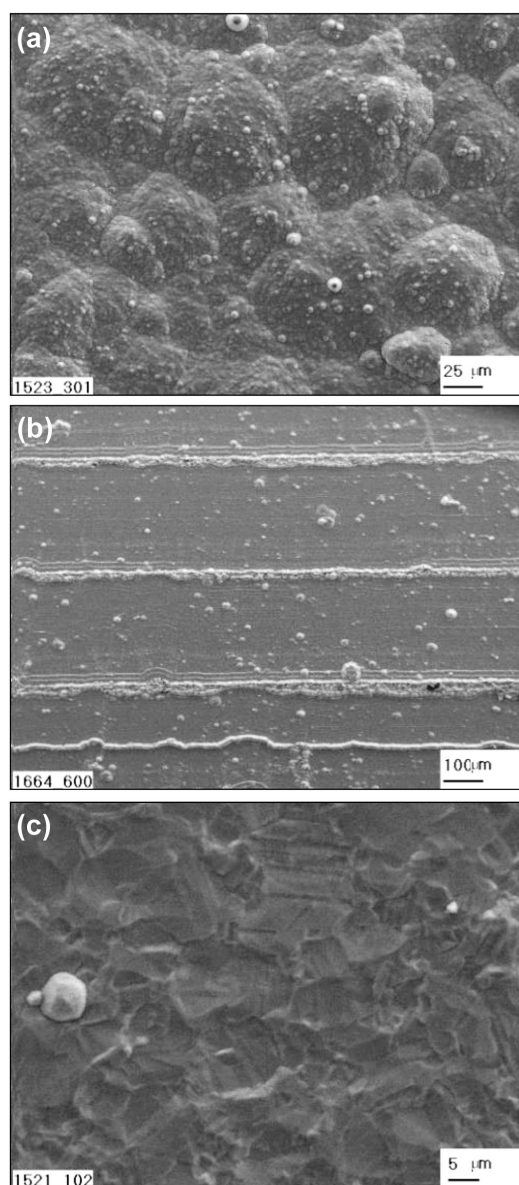


Figure 3: Microstructure of the Cu-5.0 % of volume fractions of C composite (scanning electron micrograph): a) composite surface microstructure (without etching), b) micro-layer structure of the composite, observed after ion etching (wide dark layers – copper, narrow light layers and spots – carbon), c) polygonal structure of the layers, observed after ion etching

Slika 3: SEM posnetek mikrostrukture kompozita Cu-5,0 % volumenskega deleža C; a) mikrostruktura površine kompozita (brez jedkanja), b) struktura kompozita z mikro plastmi, opažena po ionskem jedkanju (širok temni pas je baker, ozke svetlejšje plasti in točke so ogljik), c) poligonalna struktura plasti, opažena po ionskem jedkanju

The electrical conductivity of the CMs with carbon contents from 7.5 to 1.2 % of volume fractions varies in the range from 3.49×10^7 to $4.07 \cdot 10^7$ S/m, which is 60 to 70 % of that of copper. Generally the electrical conductivity of the condensed CMs is almost one and a half times that of the many known Cu-C powder compositions.¹⁻⁶ The maximum magnitude of the transferred current (up to 3000 A) for the condensed Cu-C CMs is two times higher than that of silver.

The results of the investigation of the tribotechnical characteristics of the condensed Cu-C CMs together with a copper contact wire show that the friction coefficient for the composites with 4.0 – 7.0 % of volume fractions of C decreases by 3 – 4 times as compared with the tough-pitch copper.

In operation, current-collecting device materials are subjected not only to intensive wear and electrical erosion, but also to mechanical loads at elevated temperatures. Therefore, studies on their mechanical properties over the operating temperature ranges are of clear scientific and practical interest.

Hardness, strength and plasticity characteristics of the copper-carbon composites over the temperature range 290 – 870 K are presented in **Table 1**. From **Table 1**, the hardness and strength losses due to heating are continuous. With increasing temperature, the hardness decreases monotonically from maximum values of 805–951 MPa at room temperature to minimum values of 74–138 MPa at 870 K. The tensile strength and proof

Table 1: Strength and plasticity characteristics of the Cu-C composites in the 290–870 K temperature range

Tabela 1: Značilnosti trdnosti in plastičnosti kompozita Cu-C, v temperaturnem področju 290–870 K

T, K	HV (MPa)	R _m (MPa)	R _{p 0,2} (MPa)	A (%)	A _g (%)	Z (%)
Composite Cu = 1.2 % of volume fractions of C						
290	951	260	235	27.8	20.2	70.5
370	783	233	196	21.0	15.2	59.0
470	579	194	153	16.7	11.3	40.0
570	389	165	136	14.9	9.0	34.4
670	290	127	107	20.7	12.0	35.0
770	186	93	86	29.3	4.8	36.5
870	138	60	53	40.4	20.2	40.2
Composite Cu = 3.5 % of volume fractions of C						
290	926	257	225	24.7	20.3	42.3
370	724	216	186	20.0	16.4	35.4
470	571	185	145	16.5	12.1	34.5
570	381	145	128	14.5	10.0	33.0
670	263	107	100	11.3	7.8	30.5
770	177	83	75	10.5	3.2	27.0
870	127	50	47	9.2	2.0	23.2
Composite Cu = 5.0 % of volume fractions of C						
290	828	253	186	8.5	5.5	28.2
370	666	213	173	6.7	4.3	24.6
470	552	167	140	4.6	4.1	22.0
570	373	127	117	4.5	4.2	20.2
670	252	104	96	6.0	3.2	18.3
770	174	65	59	6.6	2.0	17.4
870	122	37	34	8.2	2.5	17.0
Composite Cu = 7.5 % of volume fractions of C						
290	805	250	180	7.5	4.5	25.0
370	618	210	167	5.7	4.0	22.5
470	526	155	133	4.1	3.7	20.0
570	359	107	100	4.0	3.6	19.2
670	211	95	90	4.5	3.0	17.3
770	126	55	49	5.5	2.5	16.4
870	74	30	32	7.0	2.0	16.0

strength of the material decrease from 250–260 MPa and 180–235 MPa at room temperature to 30–60 MPa and 32–53 MPa at 870 K, respectively. Moreover, the hardness and the strength of Cu-C condensed CMs decrease with increasing carbon content in the composite over the entire temperature range.

The temperature dependences of CMs plastic properties are of a more complicated nature, with peaks caused by hot brittleness typical of copper and its alloys. In particular, a sharp decrease in plasticity values is observed at 570 K. An increase of the carbon content in composites facilitates the decrease of their plastic characteristics at all investigated temperatures.

Owing to their particular structure the condensed CMs surpass the tough-pitch cast copper and most of known Cu-C powder composites of similar composition in mechanical characteristics (including strength, plasticity and hardness).¹⁻⁶

Thermodynamic activation analysis of the composites was used to estimate its strength and hardness variations with temperature by a procedure presented earlier.^{20,22} To establish basic strength variation patterns over the temperature range under study, the exponential equations describing temperature dependences of strength and hardness were used:

$$R = A' \exp\left(\frac{U}{3kT}\right) \quad (1)$$

$$H = cA' \exp\left(\frac{U}{3kT}\right) \quad (2)$$

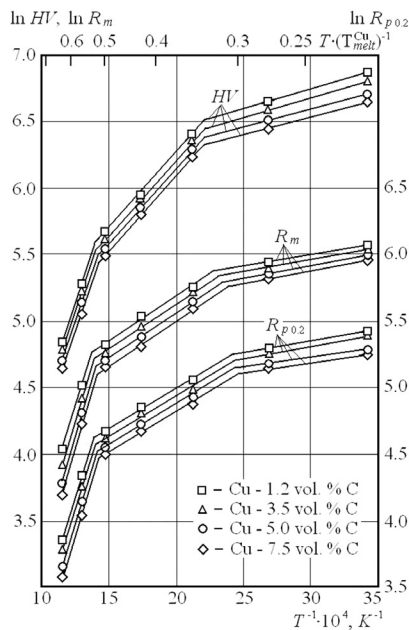


Figure 4: Temperature dependences of the hardness HV , the tensile strength R_m , and the proof strength $R_{p0.2}$ of copper-carbon composites over the temperature range 290–900 K

Slika 4: Temperaturna odvisnost trdote HV , natezne trdnosti R_m in meje plastičnosti $R_{p0.2}$ kompozita baker-ogljik v območju 290–900 K

where R is strength characteristic, MPa; HV is Vickers hardness, MP; T is the temperature, K; U is the activation energy (enthalpy) of plastic strain, eV; k is the Boltzmann constant; A' is a constant function of the material parameters and strain rates, and c is the proportionality constant, $c = H/R$.

In **Figure 4** the data obtained are presented as a function of $\ln R_{p0.2}$, $\ln R_m$, $\ln HV-1/T$ coordinates. As is seen, the temperature dependences of strength and hardness of Cu-C CMs consist of several regions, corresponding to the temperature intervals 290–460 K, 460–710 K, and 710–900 K, which are (0,20–0,35), (0,35–0,52), and (0,52–0,65) T_{melt}^{Cu} . Within these intervals they parameters vary linearly, obeying Equations (1) and (2). Moreover, within each of the intervals the temperature dependences of strength and hardness are parallel to each other for all the composites studied.

Each of these regions corresponds to a certain plastic strain mechanism. Equations (1) and (2) were used to determine the activation energies of plastic strains from experimental strength and hardness data for different temperature intervals in the range from 0.20 to 0.65 T_{melt}^{Cu} . They correspond to average strain rates of $10^{-3} s^{-1}$ under applied stresses, exceeding a 10^{-4} shear modulus. As is clear from **Table 2**, the values of activation energy obtained for all the investigated Cu-C CMs within each assigned temperature interval virtually coincide, and are in a range from 1.5 to 3 times lower than those of tough-pitch copper. The latter is evidence for the fact that the intensity of thermal softening of Cu-C system composites decreases significantly in comparison with that of tough-pitch copper, in particular at temperatures higher than 0,52 T_{melt}^{Cu} .

Table 2: Activation energies of plastic strains of a Cu-C composites and commercially pure copper

Tabela 2: Aktivacijske energije plastične deformacije kompozita Cu-C in komercialno čistega bakra

Material	Strength characteristic	U , eV in the temperature interval (K)		
		290...460	460...710	710...900
Cu-1.2 % of volume fractions of C	HV	0,03	0,12	0,30
	R_m	0,02	0,07	0,31
	$R_{p0.2}$	0,02	0,07	0,30
Cu-3.5 % of volume fractions of C	HV	0,03	0,12	0,30
	R_m	0,02	0,07	0,33
	$R_{p0.2}$	0,02	0,06	0,32
Cu-5.0 % of volume fractions of C	HV	0,03	0,11	0,30
	R_m	0,02	0,07	0,33
	$R_{p0.2}$	0,02	0,06	0,32
Cu-7.5 % of volume fractions of C	HV	0,03	0,11	0,34
	R_m	0,02	0,07	0,34
	$R_{p0.2}$	0,02	0,06	0,33
Cu ^{14, 17}	HV	0,05	0,22	0,91
	R_m	0,03	0,14	0,93
	$R_{p0.2}$	0,03	0,13	0,90

In this respect, the plots of the strength and hardness temperature dependences are diagrams of the Ashby

deformation mechanisms²³. According to Ashby, for bcc metals of group IB under the conditions investigated, the mechanisms of dislocation sliding are acting at temperatures below $0.5 T_{melt}$ and the mechanisms of dislocation creep at higher temperatures. At present, the concept of thermally activated dislocation motion across the local barriers is commonly accepted as a mechanism which controls the rate of the plastic flow process for many types of crystalline solid bodies. During deformation of commercially pure copper in the temperature range from 0.2 to $0.3 T_{melt}$, the process of blocking dislocations by impurities takes place. In the temperature range from 0.35 to $0.55 T_{melt}$, the strength of copper is governed by the processes of release of Cottrell and Suzuki atmospheres.²⁴

The analysis and comparison of activation energies of plastic strains in copper and copper-based composites (Table 2) as well as earlier theoretical and experimental work on deformation, internal friction, creep, and self-diffusion of copper^{21,22} allow a conclusion about plastic flow development accompanied by significant activation energy variations in passing from one temperature interval to another. This result points to a progressive change of active (controlling), thermally activated plastic strain mechanisms. Possible dominant mechanisms for metals are presented in²²⁻²⁴. The patterns of strength-temperature and hardness-temperature curves are similar, obeying general relationships in their variations with temperature.

The analysis of experimental and calculated data demonstrated that the above strength characteristics were

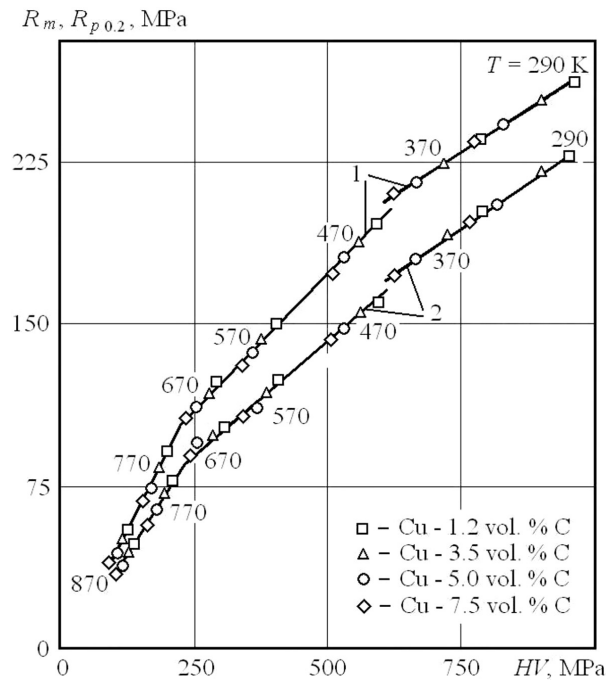


Figure 5: Correlation field and strength-hardness regression lines for Cu-C composites at different temperatures: 1 – $R_m \rightarrow HV$; 2 – $R_{p0.2} \rightarrow HV$

Slika 5: Korelacijsko polje regresijskih linij trdnost-trdota za kompozit Cu-C pri različnih temperaturah: 1 – $R_m \rightarrow HV$; 2 – $R_{p0.2} \rightarrow HV$

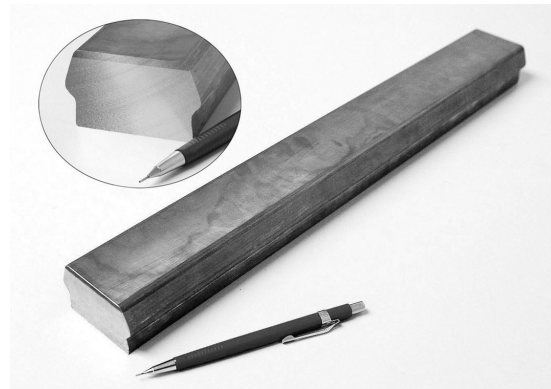


Figure 6: Production specimen of sliding contact for current-collecting device in electric transport made with Cu-C condensed CMs
Slika 6: Izdelan vzorec drsnega kontakta za napravo za zbiranje toka v električnem transportu, narejen na osnovi kondenziranih Cu-C kompozitov

controlled by the same plastic strain mechanisms and their temperature intervals were coincident. Therefore, correlations between strength characteristics should be established within the temperature intervals where strength is controlled by the same mechanisms or at least the latter do not change (for Cu-C composites these intervals are 290–460 K, 460–710 K, and 710–900 K).

The correlation analysis is aimed at establishing the functional relation between the hardness HV , the tensile strength R_m , and the proof strength $R_{p0.2}$ of Cu-C composites. Empirical distributions of R_m and $R_{p0.2}$ (Figure 5) are the aggregate of points on the plane whose coordinates correspond to the values of the above characteristics at different fixed temperatures.

As is seen, correlation fields possess several regions that are adequately described by the linear regression function. This function is common for all the investigated Cu-C CMs within each region. Such a form of the function is in full agreement with theoretical calculations of the linear hardness-strength relation. Temperature intervals for these regions, as expected, are coincident with the intervals of dominant plastic strain mechanisms.

The results of calculations of the correlation and regression coefficients of the linear function $y = ax + b$ or $R_m (R_{p0.2}) = aHV + b$ describing the empirical distribution areas, are summarized in Table 3.

Table 3: Empirical regression coefficients a and b for strength-hardness correlation of a Cu-C composites

Tabela 3: Empirična regresijska koeficienta a in b za korelacijo trdnost-trdota kompozita Cu-C

Correlation	T (K)	a	b	Correlation coefficient
$R_m \rightarrow HV$	290...460	0.14	125	1.0
	460...710	0.22	63	0.99
	710...900	0.51	-10	1.0
$R_{p0.2} \rightarrow HV$	290...460	0.16	71	1.0
	460...710	0.15	63	0.99
	710...900	0.42	-6	1.0

Due to excellent tribotechnical, electrotechnical, mechanical and operating characteristics, the condensed Cu-C CMs produced by the Eltechmash (Gekont) Science & Technology Company are used for the manufacture of sliding contacts for current-collecting devices in electric transport (**Figure 6**). These materials exhibit excellent operating characteristics and are successfully used in Ukraine.

4 CONCLUSIONS

1) An original technology for obtaining condensed laminated composite materials of the Cu-C system by means of high-speed electron-beam evaporation-condensation was developed. Condensed Cu-C composites with a thickness of 2–3 mm and carbon content from 1.2 to 7.5 % of volume fractions were obtained using electron-beam technology for the first time.

2) The electrical conductivity of Cu-C CMs varies with the carbon content in the range from 3.49×10^7 S/m for Cu-7.5 % of volume fractions of C to 4.07×10^7 SC/m for Cu-1.2 % of volume fractions, which is from 60 % to 70 % of that of copper. Generally the electrical conductivity of the CMs is almost one and a half times that of the many known Cu-C powder compositions.

3) The friction coefficient of Cu-C composites with 4.0 – 7.0 % of volume fractions of C with a copper contact wire decreases by 3 – 4 times compared with tough-pitch copper.

4) Owing to their particular structure the CMs surpass tough-pitch cast copper and many known Cu-C powder composites of similar composition in mechanical characteristics (including strength, plasticity and hardness).

5) Static strength and hardness variation behaviour and correlations between these properties were experimentally established over a wide temperature range .

6) Thermodynamic activation analysis of hardness and strength characteristics were carried out. The variation of the tensile strength, proof strength, and hardness of composites upon heating is controlled by the same mechanisms, with their temperature intervals being coincident.

7) The coefficients of regression equations relating hardness to other strength characteristics of Cu-C composites were determined for each temperature interval.

8) The CMs developed are very promising materials for sliding contacts in current-collecting devices for electric transport.

List of notation:

A – percentage elongation after fracture, %
 A_g – percentage non-proportional elongation at maximum force, %
 H – hardness, MPa
 HV – Vickers hardness, MPa

R – strength characteristics, MPa

R_m – the tensile strength, MPa

$R_{p0.2}$ – the proof strength, MPa

T – thermodynamic temperature, K

T_{melt} – melting temperature, K

$T_{\text{melt}}^{\text{Cu}}$ – melting temperature of copper, K

U – activation energy (enthalpy) of plastic strain, eV

Z – percentage reduction of area, %

A' – constant being the function of material parameters and strain rates

a, b – regression coefficients

c – proportionality constant

k – Boltzmann constant

5 REFERENCES

- G. G. Gnesin (Ed.), Sintered materials for electrical and electronic applications, Handbook, Metallurgy, Moscow 1981, 343
- V. I. Rakhovsky, G. V. Levchenko, O. K. Teodorovich, Interrupting contacts of electric appliances, Energy, Moscow-Leningrad 1966, 293
- T. Shubert, T. Weisgarber, B. Kieback, Fabrication and Properties of Copper/Carbon Composites for Thermal Management Applications, Advanced Materials Research, 59 (2008), 169–172, doi:10.4028/www.scientific.net/AMR.59.169
- Q. Hong, M. W. Li, J. Z. Wie et al., New Carbon-Copper Composite Materials Applied in Rail-Type Launching System, IEEE Transactions on Magnetics, 43 (2007), 137–140, doi:10.1109/TMAG.2006.887534
- T. S. Koltsova, L. I. Nasibulina, I. V. Anoshkin et al., Direct Synthesis of Carbon Nanofibers on the Surface of Copper Powder, Journal of Materials Science and Engineering B, 2 (2012) 4, 240–246
- E. P. Shalunov, V. Y. Berent, Uniform Current-Collecting Elements of Dispersion-Hardened Copper with Graphitic Lubrication for Current Collectors of Heavy-Duty and High-Speed Electric Trains, Electrical Contacts and Electrodes, Frantsevich Institute of Materials Science Problems, National Academy of Sciences of Ukraine, Kiev, 2004, 202–210
- B. A. Movchan, I. S. Malashenko, Vacuum-Deposited Heat-Resistant Coatings, Naukova Dumka, Kiev 1983
- N. Grechanyuk, I. Mamuzić, P. Shpak, Modern electron-beam technologies of melting and evaporation of materials in vacuum, used by Gekont Company, Ukraine, Metalurgija, 41 (2002) 2, 125–128
- N. I. Grechanyuk, I. Mamuzić, V. V. Bukhanovsky, Production technology and physical, mechanical, and performance characteristics of Cu-Zr-Y-Mo finely-dispersed microlayer composite materials, Metalurgija, 46 (2007) 2, 93–96
- N. I. Grechanyuk, V. A. Osokin, I. N. Grechanyuk, R. V. Minakova, Vapour-Phase Condensed Materials Based on Copper and Tungsten for Electrical Contacts, Structure, Properties, Technology, Current Situation and Prospects for Using Electron Beam Physical Vapour Deposition Technique to Obtain Materials for Electrical Contacts, First Announcement, Modern Electrometallurgy, (2005) 2, 28–35
- N. I. Grechanyuk, V. A. Osokin, I. N. Grechanyuk, R. V. Minakova, Basics of Electron Beam Physical Vapour Deposition Technique Used to Obtain Materials for Electrical Contacts, Structure and Properties of Electrical Contacts, Second Announcement, Modern Electrometallurgy, (2006) 2, 9–19
- V. V. Bukhanovsky, N. P. Rudnitsky, I. Mamuzich, The Effect of Temperature on Mechanical Characteristics of Copper-Chromium Composite, Materials Science and Technology, 25 (2009) 8, 1057–1061, doi:10.1179/174328408 X365829

- ¹³ V. V. Bukhanovsky, N. I. Grechanyuk, R. V. Minakova et al., Production Technology, Structure and Properties of Cu-W Layered Composite Condensed Materials for Electrical Contacts, *International Journal of Refractory Metals and Hard Materials*, 29 (2011) 5, 573–581, doi:10.1016/j.ijrmhm.2011.03.007
- ¹⁴ Cables, Wires and Cords, Method of Measurement of Electrical Resistance of Conductors, GOST 7229-76
- ¹⁵ Engineering materials and lubricants, Experimental evaluation of coefficient of friction, GOST 27640-88
- ¹⁶ V. V. Klyuev, Test Equipment, Handbook, vol. 2., Mashinostroenie, Moscow 1982
- ¹⁷ ISO 6892:1998(E), Metallic Materials – Tensile Testing at Ambient Temperature, 1998
- ¹⁸ ISO 783:1999(E), Metallic Materials – Tensile Testing at Elevated Temperature, 1999
- ¹⁹ M. M. Aleksyuk, V. A. Borisenko, V. P. Krashchenko, Mechanical Tests at High Temperatures, Naukova Dumka, Kiev 1980
- ²⁰ V. A. Borisenko, Hardness and Strength of Refractory Materials at High Temperatures, Naukova Dumka, Kiev 1984
- ²¹ Method of Determining High-Temperature Hardness by Pyramidal and Bicylindrical Indentation, DSTU 2434-94, 1995
- ²² V. A. Borisenko, V. P. Krashchenko, Temperature dependences of hardness of group IB Metals, *Acta Met.*, 25 (1977) 3, 251–256, doi:10.1016/0001-6160(77)90143-2
- ²³ V. P. Krashchenko, V. E. Statsenko, Temperature and deformation rate effects on basic processes controlling copper strength, *Probl. Prochn.*, (1981) 4, 78–83
- ²⁴ E. P. Pechkovskii, Physical substantiation of the true strain-temperature diagram for polycrystalline bcc metals, *Strength Mater.*, 32 (2000) 4, 381–390, doi:10.1023/A:1026617020771

HOMOGENIZATION OF AN Al-Mg ALLOY AND ALLIGATORING FAILURE: INFLUENCE OF THE MICROSTRUCTURE

HOMOGENIZACIJA Al-Mg ZLITINE IN KROKODILJENJE: VPLIV MIKROSTRUKTURE

Endre Romhanji, Tamara Radetić, Miljana Popović

University of Belgrade, Faculty of Technology and Metallurgy, Department of Metallurgical Engineering, Karnegijeva 4,
POB 35-03, 11 120 Belgrade, Serbia
endre@tmf.bg.ac.rs

Prejem rokopisa – received: 2015-06-01; sprejem za objavo – accepted for publication: 2015-06-12

doi:10.17222/mit.2015.111

In this study the influence of the microstructure of Al-5.1Mg-0.7Mn alloy on the propensity towards an alligating failure was evaluated. The morphology of the constituent particles appears to be the key factor, with dissolution and fragmentation of fibrous Mg-Si-Sr and transformation of the $Al_6(Fe,Mn)$ into more compact shapes taking place at homogenization temperatures above 520 °C, contributing to improved ductility and diminished propensity towards alligating. Homogenization at temperatures below 500 °C gave rise to a non-uniform precipitation of the dispersoids. Such a microstructure favored localized slip that induced stress concentration at the grain boundaries and triggered grain boundary embrittlement.

Keywords: Al-Mg alloy, homogenization, microstructure, localized slip, alligating

V študiji je bil ocenjen vpliv mikrostrukture zlitine Al-5.1Mg-0.7Mn na pojav krokodiljenja. Izgleda, da je morfologija delcev ključna, ker sta raztapljanje in drobljenje vlaknastih Mg-Si-Sr ter pretvorba $Al_6(Fe,Mn)$ v bolj kompaktno oblike, kar se dogaja med homogenizacijo pri temperaturah nad 520 °C, prispevala k izboljšanju duktilnosti in k odpravi krokodiljenja. Homogenizacija pri temperaturah pod 500 °C povzroči povečanje neenakomernega izločanja delcev. Taka mikrostruktura pospešuje lokalno drsenje ki povzroči koncentracijo napetosti na mejah zrn in sproži pojav interkristalne krhkosti.

Ključne besede: zlitina Al-Mg, homogenizacija, mikrostruktura, lokalno drsenje, krokodiljenje

1 INTRODUCTION

Fabrication of high strength Al-Mg sheet products requires careful design of the thermo-mechanical process to avoid hot fracture.¹ In the first part of this study, we report on the effect of homogenization temperature on failure by alligating during hot rolling of the Al-5.1Mg-0.7Mn alloy.²

Alligating has been studied mostly from the aspect of rolling process optimization¹ while microstructural factors influencing the occurrence of alligating are far less understood. However, there is evidence that the microstructure contributes to a propensity to alligating. Cold rolling of spheroidized 1020, 1045 and 1090 steels failed due to the alligating only in the last alloy, which has greatest density and length of linear inclusions.³ Another study on a steel⁴ showed that the occurrence of the alligating was influenced by the presence of MnS inclusions. The high density of coarse Mn-based constitutive particles increased the susceptibility to alligating in Al-Mg alloys.⁵

The aim of this work was to evaluate the effect of homogenization temperature and resultant microstructures on the occurrence of alligating in Al-5.1Mg-0.7Mn alloy during hot rolling experiments.

2 EXPERIMENTAL WORK

The Al-5.1Mg-0.7Mn alloy studied had higher Mg and Zn contents compared to the standard AA 5083 alloy. The exact chemical composition was given in ².

The industrial cast alloy was hot rolled in the laboratory. Prior to hot rolling, the plates were homogenized. Three homogenization regimes were applied, with a difference in the homogenization temperature. Regime I corresponded to the homogenization temperature of 460 °C, Regime II to 520 °C and Regime III to 550 °C. Details of the homogenization treatment and hot rolling procedure were given in ².

Microstructural characterization involved light microscopy and Scanning Electron Microscopy (SEM). Specimens were prepared by fine mechanical polishing of sections of interest. SEM characterization was conducted in JEOL JSM-6610LV at 20 kV equipped with an Energy-Dispersive X-ray Spectroscopy (EDS) detector. Specimens for light microscopy were examined in the as-polished state and after electrolytic etching with Barker's reagent.

3 RESULTS

3.1 Microstructure around the alligator crack tip

A cross-section of an alligator crack tip in the fractured plate interior is shown in **Figure 1a**. A number of cracks and micro-cracks was observed in its vicinity (**Figures 1** and **1b**). The micro-cracks were associated with a fracture (**Figures 1c** and **1d**) of the constituent particles. The alligator crack propagated in the intergranular manner (**Figure 2a**), but some deviations, most likely following the slip bands, were observed.

In a number of grains, bands with coloration different from the surrounding matrix were observed (**Figure 2b**). Barker's etch has a sensitivity toward changes in the crystallographic orientation, so the bands were most likely slip bands introduced by intensive localized slip. The bands were present in plates homogenized at 460 °C

(Regime I) and 520 °C (Regime II), but in the latter case they were finer and more evenly distributed.

3.2 Microstructure

Microstructure of the as-cast state consisted of constituent particles and Al matrix.⁶ Products of solidification, coarse constituent particles were mostly situated along the dendrite boundaries that, to a large extent, overlapped with grain boundaries. The constituent particles were identified as $Al_6(Fe,Mn)$, Mg_2Si and Mg-Si phase enriched in Sr (Sr is present as a trace element in the alloy)^{2,6} and $Al_6(Fe,Mn)$ phase with a Chinese script morphology. Thin, fibrous Mg-Si-Sr phase with attached rectangular Mg_2Si lined the grain boundaries. Homogenization induced rounding of the sharp facets of the constitutive particles.⁶

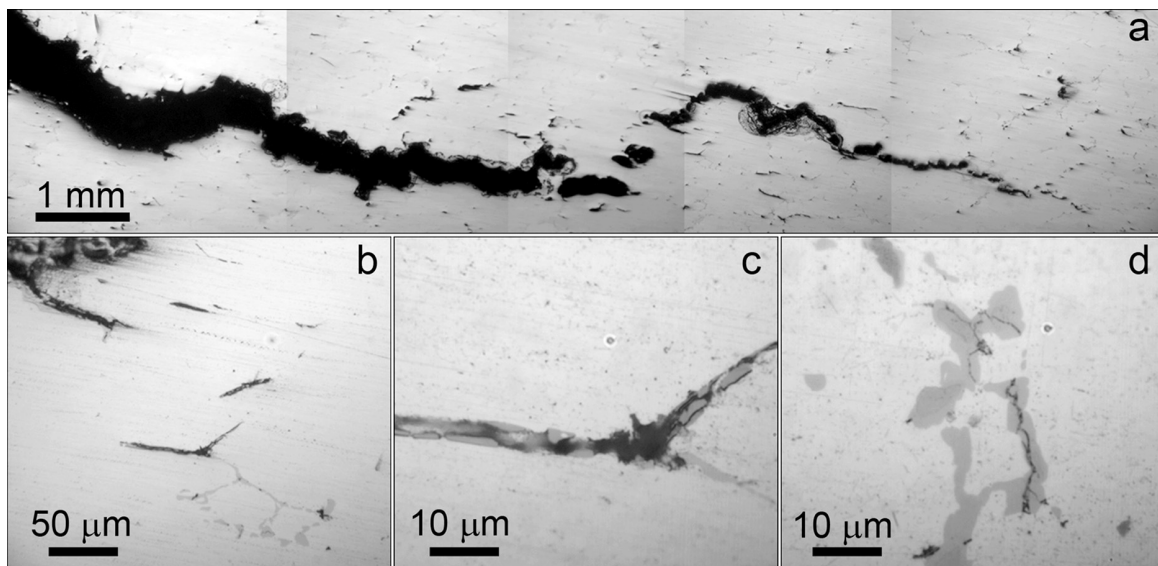


Figure 1: Light micrographs of: a) the tip of alligator crack, b) to d) microcracks and fractured constitutive particles in a plate homogenized at 460 °C

Slika 1: Svetlobni posnetki: a) vrh krokodilje razpoke, od b) do d) mikrorazpoke in prelom delcev v plošči, homogenizirani pri 460 °C

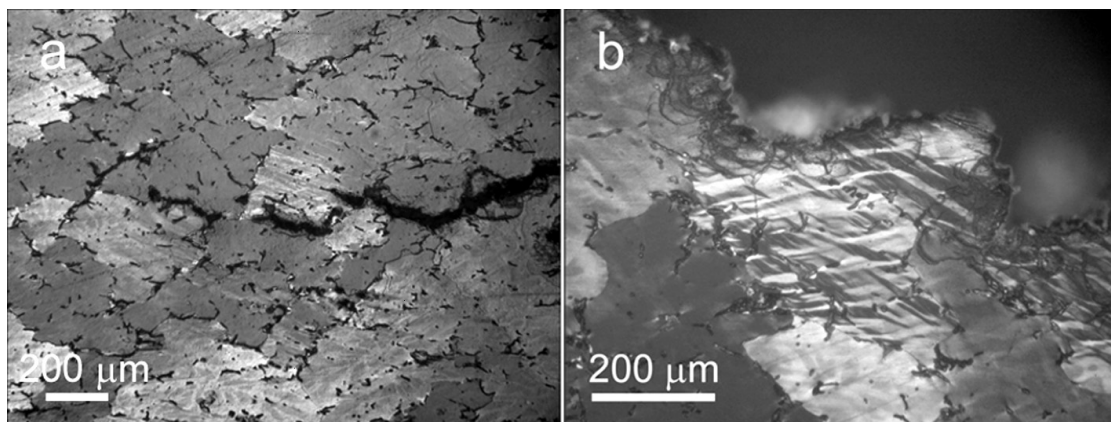


Figure 2: Light micrographs of the plates etched with Barker's reagent: a) intergranular propagation of the alligator crack (homogenization at 520 °C - Regime II), b) slip bands (homogenization at 460 °C - Regime I)

Slika 2: Svetlobna posnetka plošče, jedkane z Barker jedkalom: a) napredovanje aligatorske razpoke med zrni (homogenizacija pri 520 °C - Režim II), b) trakovi drsenja (homogenizacija pri 460 °C - Režim I)

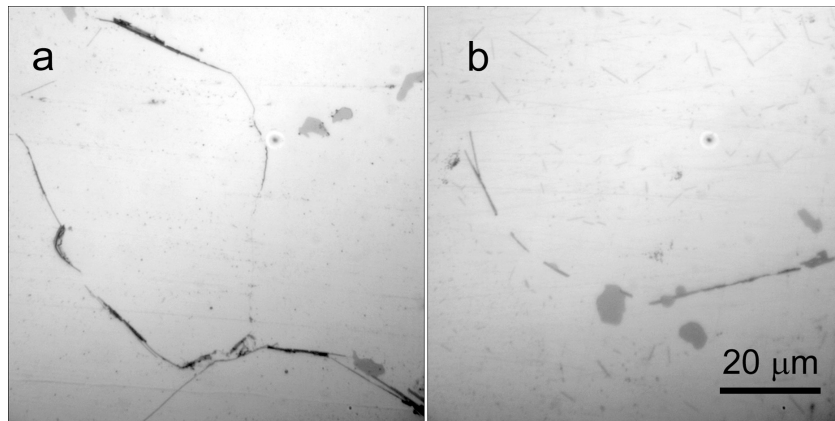


Figure 3: Light micrographs of the fibrous Mg-Si-Sr/Mg₂Si constitutive particles: a) 460 °C (Regime I), b) 550 °C (Regime III)
Slika 3: Svetlobna posnetka vlaknastih delcev Mg-Si-Sr/Mg₂Si: a) 460 °C (Režim I), b) 550 °C (Režim III)

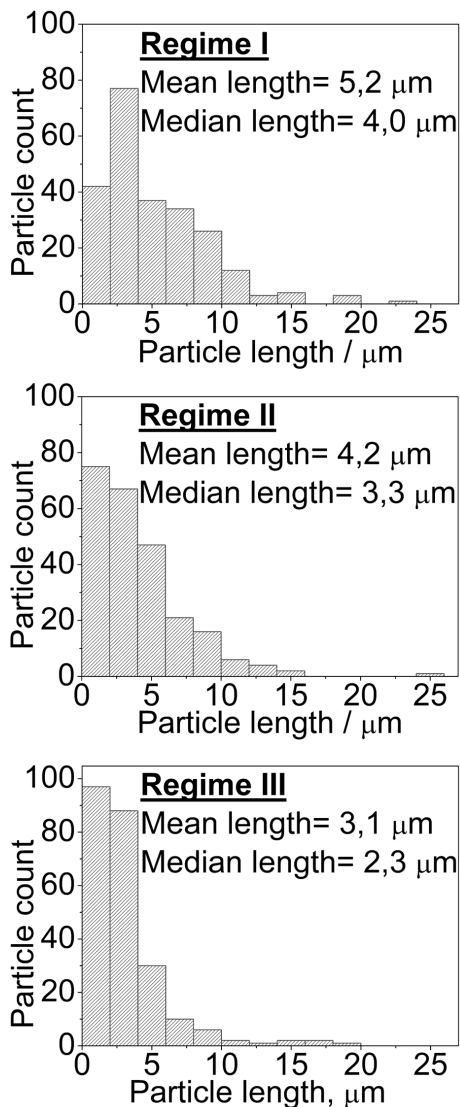


Figure 4: Size distribution (length) of fibrous Mg-Si-Sr constitutive particles. The total number of measured particles (240), was the same for each histogram.

Slika 4: Razporeditev velikosti (dolžine) vlaknastih Mg-Si-Sr delcev. Celotno število izmerjenih delcev (240), je bilo enako za vsak histogram

During homogenization at 460 °C (Regime I), growth and precipitation of Mg₂Si phase took place at interfaces of the constitutive particles with the aluminum matrix (**Figure 3a**).

At homogenization temperatures above 500 °C, Mg-Si rich phases appear to dissolve as the fibers shortened (**Figure 4**). Clusters of the fibers delineating grain boundaries were still present after the homogenization at 520 °C (Regime II), but had almost completely vanished

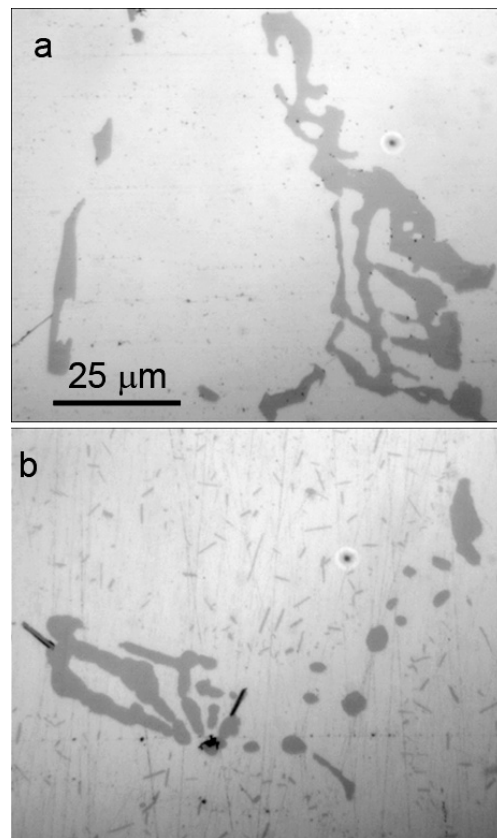


Figure 5: Light micrographs of the Al₆(Fe,Mn) constitutive particles: a) 460 °C (Regime I), b) 550 °C (Regime III)

Slika 5: Svetlobna posnetka delcev Al₆(Fe,Mn): a) 460 °C (Regime I), b) 550 °C (Regime III)

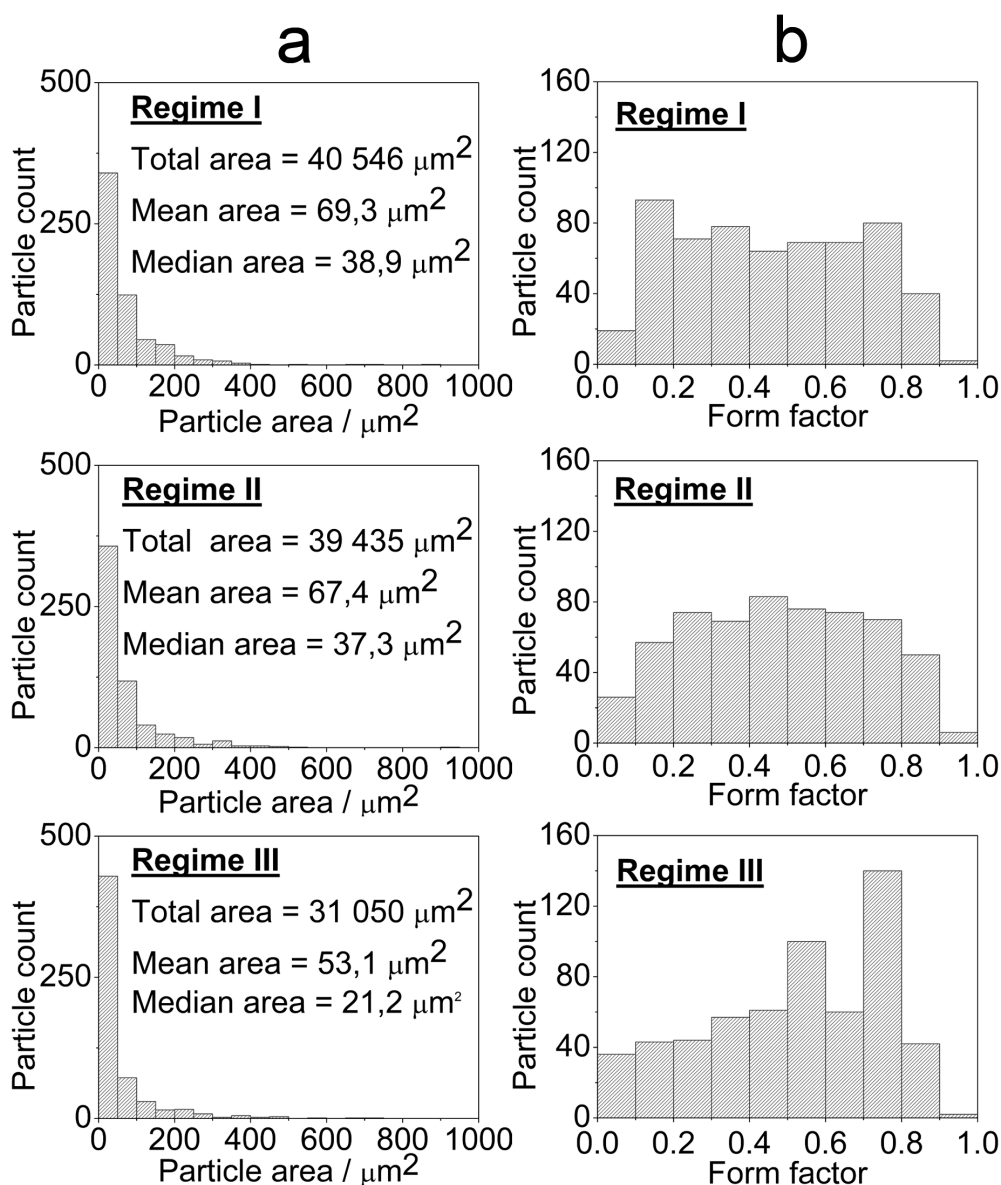


Figure 6: a) Size and b) form factor distribution of $\text{Al}_6(\text{Fe},\text{Mn})$ constitutive particles. The form factor is defined as $F = 4\pi \cdot \text{Area} / \text{Perimeter}^2$ and reflects the particle shape. It is equal to 1 for a perfect circle and < 1 for less regular shapes. The total number of measured particles (585), was the same for each histogram.

Slika 6: a) Velikost in b) faktor oblike razporeditve delcev. Faktor oblike je določen kot: $F = 4\pi \cdot \text{površina} / \text{obseg}^2$ in odraža obliko delcev. Enak je 1 pri popolnoma okroglih delcih in je < 1 pri manj pravilnih oblikah. Celotno število delcev (585), je bilo enako pri vseh histogramih.

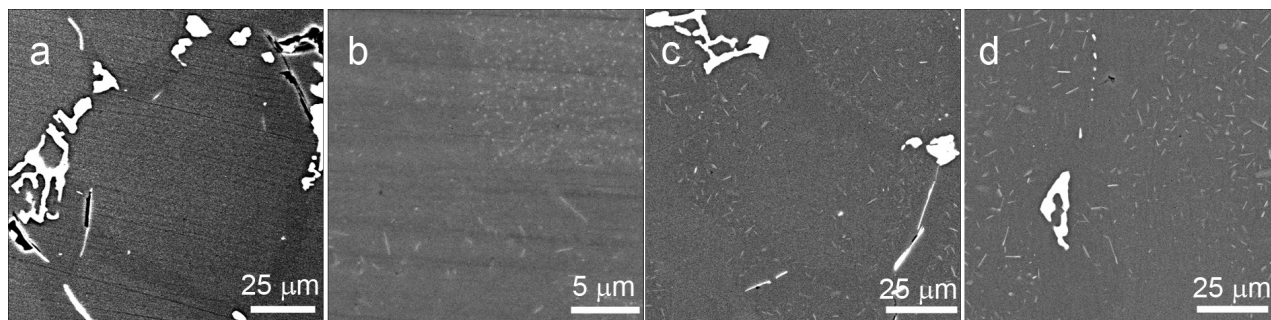


Figure 7: Backscattered SEM electron images of the microstructure after the homogenization anneal: a), b) 460 °C (Regime I), c) 520 °C (Regime II) and d) 550 °C (Regime III)

Slika 7: SEM-posnetek, s povratno sipanimi elektroni, mikrostrukture po homogenizacijskem žarjenju: a), b) 460 °C (Režim I), c) 520 °C (Režim II) in d) 550 °C (Režim III)

after homogenization at 550 °C (Regime III) while the few remaining fibers were fragmented (**Figure 3b**).

Annealing at higher temperatures (Regimes II and III) resulted in a partial dissolution and break down of the branches of the $Al_6(Fe,Mn)$ phase to more compact forms. The process was particularly advanced after the homogenization at 550 °C (Regime III) as can be seen from **Figures 5** and **6**.

Homogenization in a temperature range of 430–500 °C resulted in the precipitation of dispersoids in the dendrite cores (**Figure 7a**). Dendrite cores, with a high density of dispersoids, were surrounded by channels that were almost dispersoid free (**Figure 7b**). The width of the channels was in the range of 4–25 μm .

Precipitation of coarser, rod- and plate-shaped Al-Mn-Fe particles took place during homogenization above 500 °C. The precipitation occurred in the "precipitate free" channels formed during the first homogenization stage (annealing at 430 °C) of Regimes II and III. After homogenization at 520 °C (Regime II), the distinction between the regions was preserved (**Figure 7c**). The homogenization at 550 °C (Regime III) resulted in more uniform precipitation of coarser Al-Mn-Fe particles (**Figure 7d**).

Cooling down to the hot rolling onset temperature (500 °C) caused further precipitation of dispersoids.

4 DISCUSSION

Non-heat treatable Al-Mg alloys contain two types of the particles, dispersoids and constitutive particles. The domination of ductile intergranular fracture in the alligatored plates points out the important role of constitutive particles in the failure. The tendency toward break-up of the constitutive particles is dependent on their morphology, i.e. complex and plate-like shapes are more prone to break-up than compact morphologies.⁷ In this study, the increase in the homogenization temperature led to changes in the constitutive particles that improved the ductility of the alloy. Thin plates of Mg-Si-Sr phase enveloping grains comprised the majority of the broken particles filling the dimples of the fractured plates which had been homogenized at 460 °C (Regime I). Their fraction decreased with a partial dissolution at 520 °C (Regime II). Homogenization at the highest temperature, 550 °C, lead not only to almost complete dissolution of the Mg-Si-Sr phase, but also to a change in the size and shape of the $Al_6(Fe,Mn)$ phase. $Al_6(Fe,Mn)$ transformed into more compact morphologies (**Figures 5** and **6**) resulting in an alloy with a good hot ductility that did not alligator during the hot deformation.

The primary function of the other type of particles in the alloy, dispersoids, is to limit grain growth during hot deformation. It is also known that they can contribute to the homogenization of slip⁸ and to reduction of the tendency toward intergranular embrittlement in Al-Mg-Si alloys.^{9,10} However, in the studied alloy, homogenization

below 500 °C resulted in non-uniform precipitation of the dispersoids and formation of broad precipitate free channels (**Figure 7b**). Such a microstructure strongly promoted localized slip. Impingement of the dislocation pile-ups at the grain boundaries or large constituent particles could create significant local stresses triggering grain boundary decohesion and embrittlement² as well as break-up of the constituent particles (**Figure 1**). Absence of the brittle intergranular fracture in the plates homogenized at 520 °C (Regime II)² indicates that precipitation of the rod-like dispersoids in the "precipitate free" channels decreased the extent of the slip localization that was the cause of the grain boundary decohesion.

Apparently, homogenization affected both types of particles present in the Al-5,1Mg-0,7Mn alloy. The increase in the homogenization temperature led to a more uniform distribution of the dispersoids and, hence, more uniform slip, as well as the reversal of the morphology of the constituent particles toward a more break-up resistant shape. The result was that the microstructure developed during the homogenization Regime III showed high resistance toward intergranular fracture and the absence of alligating.

5 CONCLUSION

The microstructure of the plates homogenized at 460 °C (Regime I) with well-defined precipitate rich and free zones promoted localized slip and inhomogeneous deformation resulting in brittle and ductile intergranular fracture. Precipitation of rod-like dispersoids into the precipitate free channels during homogenization at 520 °C (Regime II) contributed to the more uniform distribution of slip and only the ductile variant of intergranular fracture was observed. During homogenization at 550 °C (Regime III), fairly uniform distribution of the dispersoids, dissolution of Mg-Si-Sr phase and reversal of $Al_6(Fe,Mn)$ constituent particles toward more compact morphology contributed to the development of a ductile material that did not show a proclivity toward alligating.

Acknowledgement

This research was supported by Ministry of Education, Science and Technological Development, Republic of Serbia, and Impol-Seval Aluminium Rolling Mill, Sevojno, under contract grant TR 34018.

6 REFERENCES

- ¹ J. G. Lenard, Workability and Process Design in Rolling, In: G. Dieter, H. A. Kuhn, S. L. Semiatin (eds.), Handbook of Workability and Process Design, ASM International, Materials Park, Ohio, USA 2003, 258–277, doi:10.1361/hwpd2003p258
- ² E. Romhanji, T. Radetić, M. Popović, Homogenization of an Al-Mg alloy and alligating failure Part I: alloy ductility and fracture, Mater. Tehnol. 50 (2016) 3, 403–407, doi:10.17222/mit.2015.110

- ³ L. Xu, G. S. Daehn, Alligating and Damage in the cold rolling of spheroidized steels, *Metallurgical and Materials Transactions A*, 25 (1994) 3, 589–598, doi:10.1007/BF02651600
- ⁴ H. Kim, M. Kang, S. Y. Shin, S. Lee, Alligating phenomenon occurring during hot rolling of free-machining steel wire rods, *Materials Science and Engineering A*, 568 (2013), 8–19, doi:10.1016/j.msea.2013.01.018
- ⁵ M. R. Cappucci, An investigation of the workability of Al-8.5% Mg alloys, Report MTL TR 89-33, U.S. Army Materials Technology Laboratory, Watertown, Massachusetts, <http://www.dtic.mil/cgi-bin/GetTRDoc?AD=ADA209451>
- ⁶ A. Halap, T. Radetić, M. Popović, E. Romhanji, Study of homogenization treatments of cast 5xxx series Al-Mg-Mn alloy modified with Zn, In: C. E. Suarez (Ed.), *Light Metals 2012*, John Wiley & Sons, Inc., Hoboken, NJ, USA 2012, 387–392, doi:10.1002/9781118359259.ch65
- ⁷ N. Moulin, E. Parra-Denis, D. Jeulin, C. Ducottet, A. Bigot, E. Boller, E. Maire, C. Barat, H. Klöcker, Constituent particle break-up during hot rolling of AA 5182, *Advanced Engineering Materials*, 12 (2010) 1–2, 20–29, doi:10.1002/adem.200900241
- ⁸ J. M. Dowling, J. W. Martin, The influence of Mn additions on the deformation behaviour of Al-Mg-Si alloy, *Acta Metallurgica*, 24 (1976) 12, 1147–1153, doi:10.1016/00016160(76)90032-8
- ⁹ K. C. Prince, J. W. Martin, The effect of dispersoids on micro-mechanisms of crack propagation, *Acta Metallurgica*, 27 (1979) 8, 1401–1408, doi:10.1016/0001-6160(79)90209-8
- ¹⁰ J. D. Evensen, N. Ryum, J. D. Embury, The intergranular fracture of Al-Mg-Si alloys, *Materials Science and Engineering*, 18 (1975) 2, 221–229, doi:10.1016/0025-5416(75)90173-1

METAL PARTICLES SIZE INFLUENCE ON GRADED STRUCTURE IN COMPOSITE Al₂O₃-Ni

VPLIV VELIKOSTI KOVINSKIH DELCEV NA GRADIENTNO STRUKTURO KOMPOZITA Al₂O₃-Ni

**Justyna Zygmuntowicz, Aleksandra Miazga, Katarzyna Konopka,
Waldemar Kaszuwara**

University of Technology, Faculty of Materials Science and Engineering, Woloska St. 141, 02-507 Warsaw, Poland
justyna.zygmuntowicz@inmat.pw.edu.pl

Prejem rokopisa – received: 2015-06-15; sprejem za objavo – accepted for publication: 2015-07-28

doi:10.17222/mit.2015.120

The aim of this study was to investigate the effect of the nickel particle size on the changes in metallic phase content in the graded structure in the Al₂O₃-Ni composites. Centrifugal slip casting was chosen as the method of composite fabrication. This method allows the creation of a graded distribution of Ni particles in the hollow cylinder composite sample. Functional graded materials were prepared in the vertical rotation axis. In the experiments the following powders were used: α -Al₂O₃ TM-DAR from Taimei Chemicals (Japan) of an average particle size 0.133 μ m and density 3.96 g/cm³ and Ni powders from Sigma-Aldrich of average particle sizes 3 μ m and 8.5 μ m. Aqueous slurries containing alumina (50 % of volume fractions of solid phase volume content) and nickel powders (10 % of volume fractions) were tested. Deflocculates diammonium citrate (p.a., Aldrich) and citric acid (p.a., POCH Gliwice) were also added. Final sintering was conducted on all the specimens at 1400 °C in a reducing atmosphere (N₂/H₂). The obtained samples were characterized by X-ray diffraction (XRD) and scanning electron microscopy (SEM). In addition, quantitative analyses of the Ni particles distribution were made. In the fabricated samples the graded structure were characterized by zones with different Ni particles concentration. The size of the Ni particles influences the width of these zones. Vickers indentation was used to determine the hardness of the materials.

Keywords: functionally graded material (FGM), centrifugal slip casting (CSC), Al₂O₃-Ni system

Namen študije je bil preiskati vpliv velikosti delcev niklja na spreminjanje vsebnosti kovinske faze v gradientni strukturi kompozita Al₂O₃-Ni. Centrifugalno oblikovalno ulivanje je bilo izbrano kot metoda za izdelavo kompozita. Ta metoda omogoča stopenjsko razporeditev delcev Ni v votlem cilindričnem kompozitem vzorcu. Funkcionalno razporejen material je bil izdelan na vertikalni rotacijski osi. Za preizkuse so bili uporabljeni naslednji prahovi: α -Al₂O₃ TM-DAR iz Taimei Chemicals (Japan) s povprečno velikostjo delcev 0.133 μ m in gostoto 3.96 g/cm³ ter prah Ni iz Sigma-Aldrich, s povprečno velikostjo delcev 3 μ m in 8.5 μ m. Preizkušena je bila na vodi osnovana mešanica (z vsebnostjo 50 % volumenskega deleža trdne faze), ki je vsebovala prah glinice in niklja (10 % volumenskega deleža). Uporabljeni deflokulant je bil sestavljen iz diamonium citrata (p.a., Aldrich) in citronske kisline (p.a., POCH Gliwice). Končno sintranje je bilo pri vseh vzorcih na 1400 °C, v reduktivni atmosferi (N₂/H₂). Dobljeni vzorci so bili pregledani z rentgensko difrakcijo (XRD) in vrstično elektronsko mikroskopijo (SEM). Poleg tega je bila izvedena tudi kvantitativna analiza razporeditve Ni delcev. V vzorcih je bila analizirana gradientna struktura po področjih z različno koncentracijo Ni delcev. Velikost Ni delcev vpliva na širino teh področij. Določena je bila trdota materiala po Vickersu.

Ključne besede: funkcionalno gradientni material (FGM), centrifugalno oblikovalno ulivanje (CSC), Al₂O₃-Ni sistem

1 INTRODUCTION

Novel ceramic-metal composites should have a combination of properties such as good strength, high hardness together with high fracture toughness, wear and thermal resistance as well as chemical inertness, among others. Such demands may be fulfilled by functional graded materials (FGM). These materials are characterized by a variation in composition and structure gradually over volume, resulting in corresponding changes in the chemical and physical properties of the composite.^{1,2}

The concept of graded materials was shown for the first time in 1971 in an article entitled "Preliminary work on Functionally Graded Materials".³ These materials can be prepared by a variety of methods. Currently, among the most popular techniques for producing FGM are powder technology methods, inter alia: dry powder compaction,^{3,4} tape casting,^{1,3,5-7} self-propagating high – tem-

perature synthesis – SHS,^{7,8} slip casting and filtration.^{1,9-13} However, other in-situ techniques such as: spray forming,^{14,15} centrifugal casting^{1,16-19} and the deposition methods of Electrophoretic Deposition (EDP)²⁰⁻²⁶ and Pulsed Laser Deposition (PLD)^{27,28} have also gained broad attention.

Ceramic-metal composites with a gradient concentration of the metal particles are an example of FGM materials. Typical scheme of ceramic-metal FGM composites is shown in **Figure 1**. Such composites can be used as functional materials, and also as structural materials in the aerospace industry.

The principal advantage of ceramic matrix composites with metal particle concentration gradients is an increase of the fracture toughness with respect to the ceramic matrix.²⁹⁻³¹ The literature data indicate that the particle size and amount of the metal phase essentially affect crack propagation.³² Modification of the particle

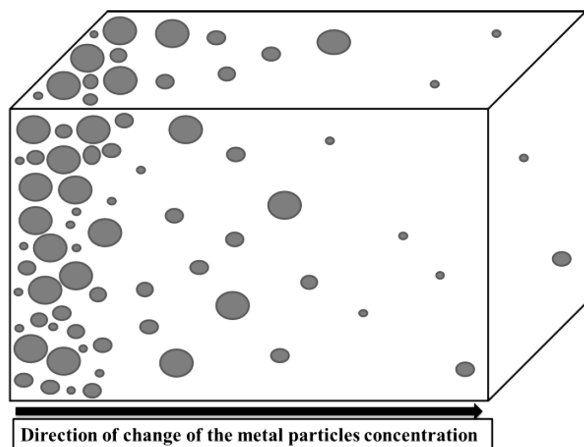


Figure 1: Schema of ceramic-metal FGM composite, dark-grey – metal particles

Slika 1: Shema kompozita keramika-kovina FGM, temno sivo – delci kovine

size of metal in the composite enables precise control of the material properties.

In the present work, Al₂O₃-Ni composites with a concentration gradient of the metal particles were fabricated using centrifugal slip casting. This method allows fabrication of a graded distribution of Ni particles in a hollow cylinder composite sample. The aim of this study was to investigate the effect of the nickel particles size on the metallic phase content in graded Al₂O₃-Ni composites.

2 EXPERIMENTAL PART

2.1 Materials and methods

In the tests the following powders were used: α -Al₂O₃ TM-DAR from Taimei Chemicals (Japan) of an average particle size $D_{50} = 0.133 \mu\text{m}$ and density 3.96 g/cm^3 and Ni powders from Sigma-Aldrich of average particle sizes $D_{50} = 3 \mu\text{m}$ and $D_{50} = 8.5 \mu\text{m}$. For both Ni particle sizes a series of composite samples were prepared. Aqueous slurries containing alumina (with 50 % of volume fractions content of solid phase) and nickel powder (10 % of volume fractions with respect to total volume) were tested. Deflocculates diammonium citrate (p.a., Aldrich) and citric acid (p.a., POCH Gliwice) were also added. **Figure 2** shows the scanning electron microscopy images of α -Al₂O₃ and the two Ni powders.

The components were homogenized in a planetary mill with a rotation speed of 300 min^{-1} for 90 min. Afterwards, the air absorbed on the particle surfaces was removed in a THINKY ARE-250 Mixer and Degassing Machine for 15 min at a speed of 900 min^{-1} . The equipment allows the removal of bubbles above $1 \mu\text{m}$. The ceramic water-based slurries were cast into thick-walled tubes using a plaster mold. A stirrer with a vertical rotation axis was used in the centrifugal slip casting process. The process parameters were first chosen by set of trials. The dimensions of the fabricated tubes are as

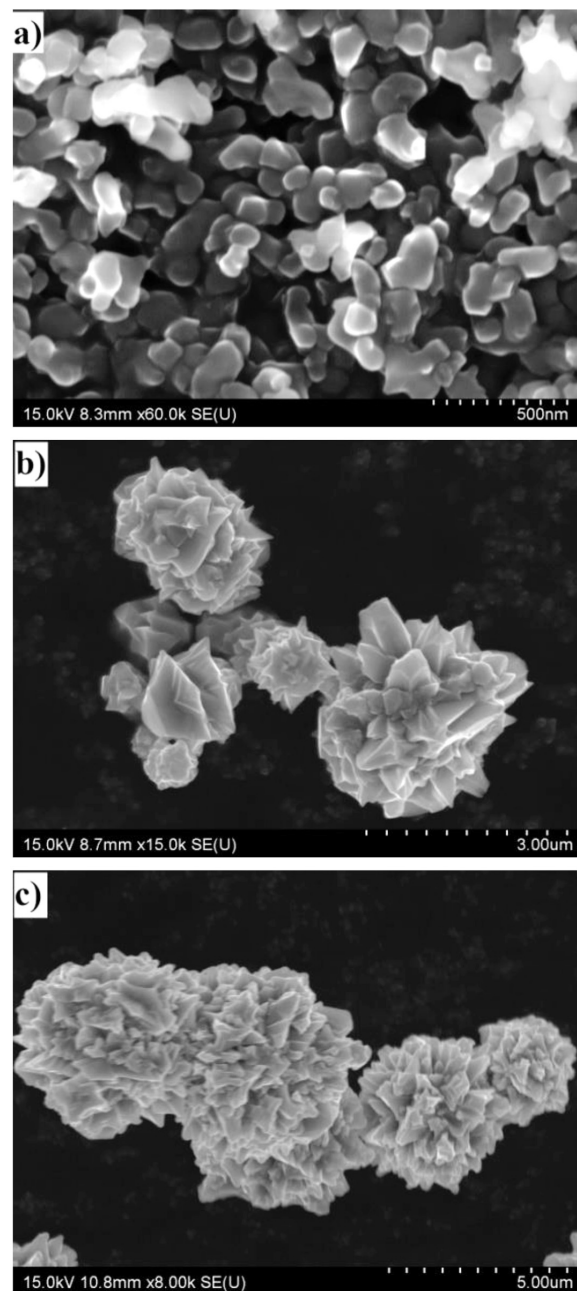


Figure 2: Electron micrographs of: a) α -Al₂O₃, b) Ni powder, ($D_{50} = 3 \mu\text{m}$), c) Ni powder ($D_{50} = 8.5 \mu\text{m}$)

Slika 2: SEM posnetki: a) α -Al₂O₃, b) prah Ni ($D_{50} = 3 \mu\text{m}$), c) prah Ni ($D_{50} = 8.5 \mu\text{m}$)

follows: the outer radius is 20 mm, the length 40 mm and thickness 18 mm. Thereafter, the samples were dried and removed from the plaster mold. The final step was sintering which was conducted on all specimens at $1400 \text{ }^\circ\text{C}$ in a reducing atmosphere (N₂/H₂).

An X-ray Rigaku MiniFlex X-ray diffractometer II was used to study the structure of the composites. The data were recorded using the "step-scanning" method in the 2θ mode with Cu- $K_{\alpha 1.54}$ radiation.

The Al₂O₃-Ni composites microstructures were characterized using a SEM HITACHI SU-70 scanning

electron microscope. Quantitative analysis of the graded region microstructures from SEM images was carried out using the Micrometer computer image analysis program.³³

The hardness of the microstructures from outer sample to inner sample were measured with a Vickers hardness tester. The hardness measurements were made under a load of 49.03 N.

3 RESULTS AND DISCUSSION

Figure 3 shows typical examples of fabricated tubes before and after sintering. Using the Archimedes method, it was found that the average sintering shrinkage was about 13 %. A tube having a post-sintering diameter of 17 mm, inner radius 6.5 mm and 40 mm could be fabricated successfully (i.e. without breakage of the cast tubes during subsequent drying and sintering) with a relatively high consolidation (> 98.8 % of relative density). No damage in the form of cracks or voids on the surface of samples were noticed. The X-ray data from the surfaces and the cross-sections of composites confirmed the presence of the two phases Ni and Al₂O₃. **Figure 4** presents a typical diffraction pattern.

In **Figure 5** the graded distribution of metal particles in Al₂O₃-Ni composites is shown. The grey area is Al₂O₃ and the bright area is Ni. Three zones of Ni particles of the samples can be distinguished in the cross-section. A quantitative analysis of the photomicrographs using the Micrometer computer image analysis program^{33,34} yielded the compositional profile variations shown in **Figure 6**. The measurements show that in area A, the nickel particle content was equal to 12 % of volume fractions per 1 mm width in both samples. Between areas A and B there is a mild increase in nickel particles. In area B there was a maximum of nickel particles in both composites. In the case of the nickel powder with the larger particle size ($D_{50} = 8.5 \mu\text{m}$) it was observed that zone B is narrower than zone A. In area B there was a

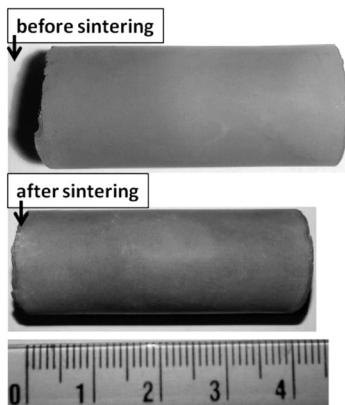


Figure 3: Views of composite sample prepared using a Ni powder ($D_{50} = 8.5 \mu\text{m}$) before and after sintering

Slika 3: Izgled kompozitnega vzorca, pripravljenega z uporabo prahu Ni ($D_{50} = 8,5 \mu\text{m}$), pred in po sinteranju

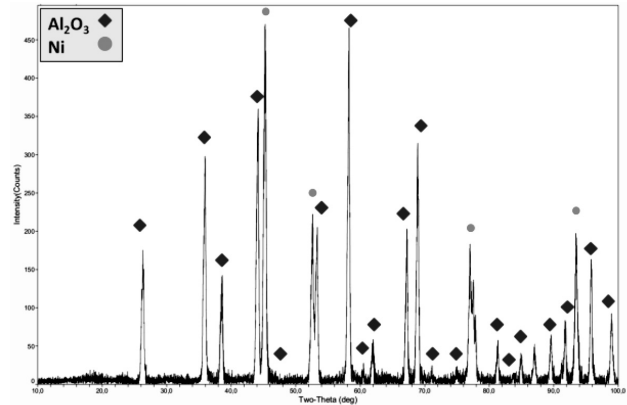


Figure 4: Diffraction patterns of the sample prepared using a Ni powder ($D_{50} = 8.5 \mu\text{m}$)

Slika 4: Rentgenogram vzorca, izdelanega z uporabo prahu Ni ($D_{50} = 8,5 \mu\text{m}$)

maximum of nickel particles equal to about 28 % of volume fractions per 560 μm wide for the sample prepared using Ni $D_{50} = 8.5 \mu\text{m}$ powder. In contrast, the sample prepared using a Ni powder ($D_{50} = 3 \mu\text{m}$) was contained 25 % of volume fractions per 840 μm . Then there was a sharp decline in nickel particles. However, in area C there was a mild decrease, down to 0 % of volume fractions, in the percentage of nickel particles.

The motion of metal particles in a slurry under centrifugal force can be determined by Stokes' law.³⁵ According to this law the velocity of the particles is proportional to the square of the particles' diameter. Therefore the migration distance is greater in the case of larger particles. For this reason the width of zone B is smaller in the case of samples prepared with 8.5 μm Ni than for composites with 3 μm Ni powder.

The hardness values measured from the outer to the inner periphery are shown in **Figure 7**. It has been found that the hardness profiles for both series (3 μm and 8.5 μm Ni powders) have similar behaviour (**Figure 8**). In region A hardness values in the range 1000-1300 HV are found for both series. Region A results from the removal

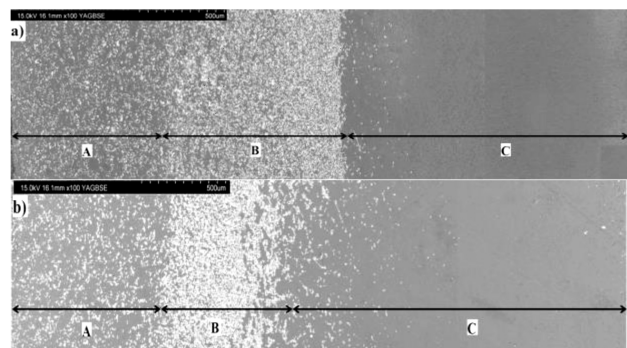


Figure 5: SEM photo of cross-section of composite: a) the sample prepared using a Ni powder ($D_{50} = 3 \mu\text{m}$) and b) the sample prepared using a Ni powder ($D_{50} = 8.5 \mu\text{m}$)

Slika 5: SEM-posnetek preseka kompozita: a) vzorec, pripravljen z uporabo prahu Ni ($D_{50} = 3 \mu\text{m}$) in b) vzorca, pripravljenega z uporabo prahu Ni ($D_{50} = 8,5 \mu\text{m}$)

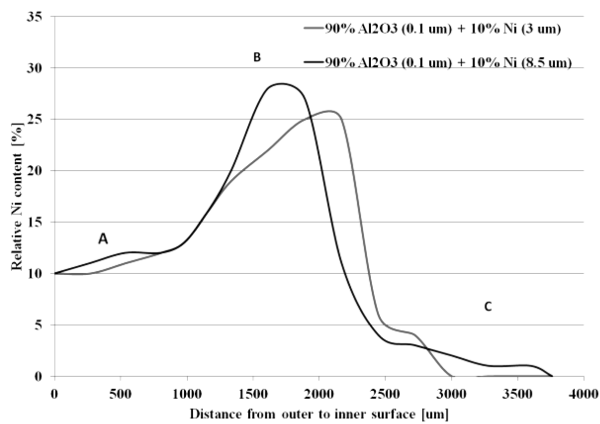


Figure 6: Changes in Al₂O₃-Ni composites metallic phase content from outer zone to inner

Slika 6: Spreminjanje vsebnosti kovinske faze v kompozitu Al₂O₃-Ni od zunanega področja v notranjost

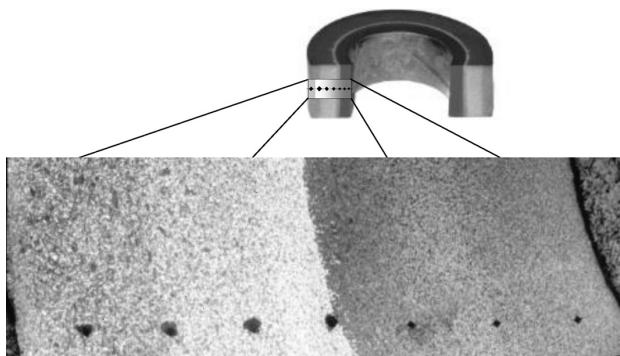


Figure 7: Scheme of hardness testing

Slika 7: Prikaz meritve trdote

of fluid through capillary action in the plaster mold. In **Figure 7** a slightly lower hardness is observed in the area between A and B due to the increase of nickel particles in the composite. The maximum amount of nickel particles in the region B corresponds to the lowest hardness values. This part of the sample was produced as a result of centrifugal acceleration. As expected, in both series of samples the maximum hardness values are observed in region C, at the inner edge of the casting due to the absence of nickel particles. The area C in both samples corresponds to hardness values in the range 1800-1920 HV.

4 CONCLUSIONS

Al₂O₃-Ni FGM ceramic matrix composites with a graded distribution of Ni particles have been successfully produced by the centrifugal slip casting method.

Quantitative analysis of the graded microstructure in the composites revealed that the graded zones depend on the size of the starting metal particles in the slurry.

By changing the content of the metallic phase it is possible to control the hardness profile. As a result of the

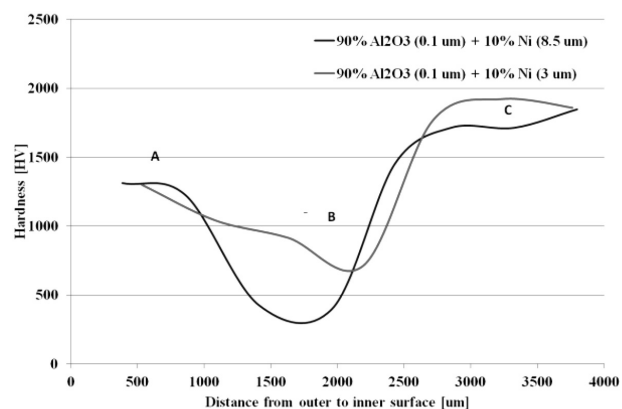


Figure 8: Variation in hardness from the outer edge of Al₂O₃-Ni functionally graded composites

Slika 8: Spreminjanje trdote od zunanega roba funkcionalno stopenjskega kompozita Al₂O₃-Ni

centrifugal slip casting method used, the packing of the powder particles prevents grain growth.

Acknowledgments

The authors would like to thank Professor M. Szafran and his Team from the Faculty of Chemistry of Warsaw University of Technology for help in preparing the samples. The results presented in this paper were obtained as part of the the Polish National Science Centre (NCN) project No. 2013/11/B/ST8/0029.

5 REFERENCES

- 1 T. Ogawa, Y. Watanabe, H. Sato, I. S. Kim, Y. Fukui, Theoretical study on fabrication of functionally graded material with density gradient by a centrifugal solid-particle method, *Composites: Part A*, 37 (2006), 2194–2200, doi:10.1016/j.compositesa.2005.10.002
- 2 Y. Fukui, Fundamental Investigation of Functionally Gradient Material Manufacturing System using Centrifugal Force, *JSME international Journal*, 34 (1991), 144–148, doi:10.1299/jsmec.1988.34.144
- 3 A. Neubrand, J. Neubrand, Gradient materials: an overview of a novel concept, *Zeitschrift für Metallkunde*, 88 (1997), 358–371
- 4 D. Delfosse, B. Ilschner, Pulvermetallurgische Herstellung von Gradientenwerkstoffen, *Matt.-wiss.*, 23 (1992), 235–240, doi:10.1002/mawe.19920230705
- 5 J. G. Yeo, S. C. Choi, Zirconia-stainless steel functionally graded material by tape casting, *Journal of the European Ceramic Society*, 18 (1998), 1281–1285, doi:10.1016/S0955-2219(98)00054-5
- 6 Y. P. Zeng, D. L. Jiang, T. Watanabe, Fabrication and properties of tape-casting laminated and functionally gradient alumina-titanium carbide materials, *Journal of American Ceramic Society*, 83 (2000), 2999–3003, doi:10.1111/j.1151-2916.2000.tb01673.x
- 7 A. L. Dumont, J. P. Bonnet, T. Chartier, J. Ferreira, MoSi₂/Al₂O₃ FGM: elaboration by tape casting and SHS, *Journal of the European Ceramic Society*, 21 (2001), 2353–2360, doi:10.1016/S0955-2219(01)00198-4
- 8 S. S. Tjong, Z. Ma, Microstructural and mechanical characteristics of in situ metal matrix composite, *Materials Science and Engineering*, 29 (2000) 3–4, 49–114, doi:10.1016/S0927-796X(00)00024-3
- 9 A. Tomsia, E. Saiz, H. Ishibashi, M. Diaz, J. Requena, J. Moya, Powder processing of Mullite/Mo functionally graded materials, *Journal of the European Ceramic Society*, 18 (1998), 1365–1371, doi:10.1016/S0955-2219(98)00066-1

- ¹⁰ A. Mortensen, S. Suresh, Functionally graded metals and metal-ceramic composites: Part I. Processing, *International Materials Reviews*, 40 (1995), 239–265, doi:10.1179/imr.1995.40.6.239
- ¹¹ B. Marple, J. Boulanger, Graded casting of materials with continuous gradients, *Journal of American Ceramic Society*, 77 (1994) 10, 2747–2750, doi:10.1111/j.1151-2916.1994.tb04670.x
- ¹² A. J. Sanchez-Herencia, K. Morinaga, J. S. Moya, Al₂O₃/Y-TZP Continuous Functionally Graded Ceramics by Filtration-Sedimentation, *Journal of the European Ceramic Society*, 17 (1997), 1551–1554, doi:10.1016/S0955-2219(97)00003-4
- ¹³ J. Chu, H. Ishibashi, K. Hayashi, H. Takebe, K. Moriga, Slip casting of continuous functionally graded material, *Journal of the Ceramic Society of Japan*, 101 (1993), 818–820
- ¹⁴ A. Lawley, R. Doherty, ASM handbook A, powder metal technologies and applications, unit: Spray forming, 1998, 408–419
- ¹⁵ P. Grant, I. Palmer, I. Stone, Spray formed aerospace alloys, *Materials World*, 7 (1999) 6, 331–333
- ¹⁶ S. Oike, Y. Watanabe, Development of in-situ Al-Al₃Cu functionally graded materials by a centrifugal method, *International Journal of Materials and Product Technology*, 16 (2001), 40–49, doi:10.1504/IJMPT.2001.005394
- ¹⁷ S. Nai, M. Gupta, C. Lim, Synthesis and wear characterization of Al based, free standing functionally graded materials: effect of different matrix compositions, *Composites Science and Technology*, 63 (2003), 1895–1909, doi:10.1016/S0266-3538(03)00158-1
- ¹⁸ K. Yamagiwa, Y. Watanabe, Y. Fukui, P. Kapranos, Novel recycling system of aluminum and iron wastes in-situ Al-Al₃Fe functionally graded material manufactured by a centrifugal method, *Materials Transactions*, 44 (2003) 12, 2461–2467
- ¹⁹ Y. Watanabe, R. Sato, K. Matsuda, Evaluation of particle size and particle shape distributions in Al-Al₃Ni FGMS fabricated by a centrifugal in-situ method, *Science and Engineering of Composite Materials*, 11 (2004), 2–3
- ²⁰ J. Vleugels, G. Anné, S. Put, O. van der Biest, Thick plate-shaped Al₂O₃/ZrO₂ composites with continuous gradient processed by electrophoretic deposition, *Materials Science Forum*, 423 (2003) 4, 171–176, doi:10.4028/www.scientific.net/MSF.423-425.171
- ²¹ P. Sarkar, S. Datta, P. Nicholson, Functionally graded ceramic/ceramic and metal/ceramic composites by electrophoretic deposition, *Composites Part B*, 28 (1997) 1–2, 49–56
- ²² Y. Chen, T. Li, J. Ma, A functional gradient ceramic monomorph actuator fabricated using electrophoretic deposition, *Ceramics International*, 30 (2004) 5, 683–687, doi:10.1016/j.ceramint.2003.08.008
- ²³ A. Boccaccini, I. Zhitomirsky, Application of electrophoretic and electrolytic deposition techniques in ceramic processing, *Current Opinion in Solid State and Material Science*, 6 (2002), 251–260
- ²⁴ S. Put, G. Anné, J. Vleugels, Functionally graded hard metals with a continuously graded symmetrical profile, *Materials Science Forum*, 423 (2003) 4, 33–38, doi:10.4028/www.scientific.net/MSF.423-425.33
- ²⁵ S. Put, G. Anné, J. Vleugels, Gradient profile prediction in functionally graded materials processed by electrophoretic deposition, *Acta Materialia*, 51 (2003) 20, 6303–6317, doi:10.1016/S1359-6454(03)00463-4
- ²⁶ A. Ruys, J. Kerdic, C. Sorrel, Thixotropic casting of ceramic-metal functionally gradient materials, *Journal of Materials Science*, 31 (1996) 16, 4347–4355, doi:10.1007/BF00356459
- ²⁷ J. Lackner, W. Waldhauser, R. Ebner, B. Major, T. Schöberl, Structural, mechanical and tribological investigations of pulsed laser deposited titanium nitride coatings, *Thin Solid Films*, 453-454 (2004), 195–202, doi:10.1016/j.tsf.2003.11.106
- ²⁸ P. Willmott, J. Huber, Pulse laser vaporization and deposition, *Reviews of Modern Physics*, 72 (2000), 315–328, doi:10.1103/RevModPhys.72.315
- ²⁹ L. S. Sigl, P. A. Mataga, B. J. Dalgleish, R. M. Mc Meeking, A. G. Evans, On the toughness of brittle materials reinforce with a ductile phase, *Acta Metall.*, 36 (1998) 4, 945–953, doi:10.1016/0001-6160(88)90149-6
- ³⁰ O. Sbaizero, G. Pezzoti, Influence of the metal particle size on toughness of Al₂O₃/Mo composite, *Acta Mater.*, 48 (2000), 985–992, doi:10.1016/S1359-6454(99)00349-3
- ³¹ X. Su, J. Yeomans, Microstructure and fracture toughness of nickel particle toughened alumina, *Journal of Materials Science*, 31 (1996), 875–880, doi:10.1007/BF00352885
- ³² M. Szafran, K. Konopka, E. Bobryk, K. J. Kurzydłowski, Ceramic matrix composites with gradient concentration of metal particles, *Journal of the European Ceramic Society*, 27 (2007), 651–654, doi:10.1016/j.jeurceramsoc.2006.04.046
- ³³ J. Michalski, T. Wejrzanowski, R. Pielaszek, K. Konopka, W. Łojkowski, K. J. Kurzydłowski, Application of image analysis for characterization of powders, *Materials Science Poland*, 23 (2005) 1, 79–86
- ³⁴ J. Zygmuntowicz, A. Miazga, K. Konopka, W. Kaszuwara, M. Szafran, Forming graded microstructure of Al₂O₃-Ni composite by centrifugal slip casting, *Composites Theory and Practice*, 15 (2015) 1, 44–47
- ³⁵ Y. Watanabe, K. Kawamoto, K. Matsuda, Particle Size Distributions of Functionally Graded Materials Fabricated by Centrifugal Solid-Particle Method, *Composite Science and Technology*, 62 (2002), 881–888, doi:10.1016/S0266-3538(02)00023-4

STATIC AND DYNAMIC TENSILE CHARACTERISTICS OF S420 AND IF STEEL SHEETS

STATIČNE IN DINAMIČNE NATEZNE LASTNOSTI PLOČEVINE IZ S420 IN IF JEKLA

Mária Mihaliková¹, Vladimír Girman², Anna Lišková³

¹Technical University of Košice, Faculty of Metallurgy, Department of Materials Science, Letná 9, 042 00 Košice, Slovakia

²P. J. Šafarik University in Košice, Faculty of Science, Department of Condensed Matter Physics, 042 00 Košice, Slovakia

³Technical University of Košice, Faculty of Metallurgy, Department of Materials Science, Letná 9, 042 00 Košice, Slovakia
maria.mihalikova@tuke.sk

Prejem rokopisa – received: 2015-06-22; sprejem za objavo – accepted for publication: 2015-07-27

doi:10.17222/mit.2015.125

Two automotive steels were investigated; the Interstitial Free Steel (IF) HSLA (High Strength Low Alloy) and the S420 micro-alloyed steel. The properties of these materials were determined by static 10^{-3} s^{-1} and dynamic 10^3 s^{-1} rate stress experiments. The plastic properties were determined after static and dynamic tests. The aim of examination of substructures was to determine the distribution of dislocations for various types of stress. The hardness of all the tested materials was higher at a slow rate of deformation. The greater strain hardening of the materials was confirmed by the dislocation distributions.

Keywords: IF steel, micro alloyed steel (S420), dynamic tensile test, hardness (HV1), dislocation structure

Preiskovani sta bili dve jekli iz avtomobilske industrije: jeklo brez intersticij (IF) HSLA (visko trdnostno nizko legirano jeklo) in mikro-legirano jeklo S420. Namen študije je bil določiti spremembe lastnosti teh materialov pri statični hitrosti 10^{-3} s^{-1} in dinamični hitrosti 10^3 s^{-1} obremenjevanja. Plastičnost je bila določena na vzorcih po statičnih in dinamičnih preizkusih. Namen preiskave podstruktur je bil določiti razporeditev dislokacij pri različnih vrstah obremenjevanja. Skladno z izmerjenimi vrednostmi in s podatki iz literature je bila trdota vseh preizkušenih materialov višja pri manjši hitrosti deformacije. Večje napetostno utrjevanje materialov je bilo potrjeno z razporeditvijo dislokacij.

Ključne besede: IF jeklo, mikro legirano jeklo (S420), statični natezni preskus, dinamični natezni preskus, trdota (HV1), dislokacijska mikrostruktura

1 INTRODUCTION

Strain rate, as a modifier of internal structure, is a significant external factor that influences the material behaviour in the forming process. In practice, an understanding of the behaviour of steel under extreme loading conditions is essential for the accurate prediction of material response when a material is subjected to a combination of severe load scenarios such as in collisions. Presently sheets of different qualities are used in the automotive industry. Therefore it is necessary to create research and development for innovation capabilities which could facilitate the rapid development of materials and their cost reduction. The strain rate influences the strength properties through the internal structure and thus affects the material function.¹⁻³ Special attention in research is paid to progressive IF Steels and Micro-Alloyed Steels. Interstitial Free Steel (IF) contains only a small amount of carbon (C <0.005%) and has very good deep-ductility, as result of its low yield strength (YS= 100–310 MPa). On the other hand, good deep-ductility requires higher ultimate tensile strength (UTS =140–450 MPa). The material ability to plastically deform without breaking is determined by the ratio R_e/R_m .⁴⁻⁶ Micro-Alloyed Steels have a fine-grained ferrite-pearlite microstructure with small quantities

(max. 0.15%) of precipitates of Al, Ti, Nb and V bound to C and N.⁷ The micro-alloying effects are related to the solubility of carbides (TiC, NbC, NC), nitrides (TiN, AlN) and carbonitrides (Ti (C, N)) in austenite and ferrite.^{7,8} An increase of strength can be obtained by grain refinement and precipitation hardening. High strength steels are considered as steels with a nominal yield stress equal to or above 420 MPa. The mechanical properties of the Micro-Alloyed Steels are largely a result of a microstructure which depends on the chemical composition and the processing method.^{9,10}

2 EXPERIMENTAL MATERIALS AND METHODS

Two steel materials, IF Steel and S420 steel with chemical compositions presented in **Table 1** were investigated. Tensile testing at the specified strain rates was performed with a Zwick 1387 servo-hydraulic machine with a load capacity of 1000 kN (accuracy $\pm 0.005 \%$ of load capacity). In **Figure 1** the size and shape of the test bars is depicted. Static tensile testing was carried out according to the EN ISO 6892-1 standard at three traverse speed loads.¹¹ The strain rate was calculated according to Equation (1):¹²

Table 1: Chemical composition of IF and S420 steel (in mass fractions, w/%)

Tabela 1: Kemična sestava IF in S420 jekla (v masnih odstotkih, w/%)

Material	C	S	N	Mn	P	Si	Al	Nb	V	Ti
IF	0.0013	0.0105	0.0017	0.82	0.011	0.006	0.055	0.001	0.002	0.04
S420	0.12	0.002	-	1.44	0.009	0.05	0.046	0.035	0.2	0.016

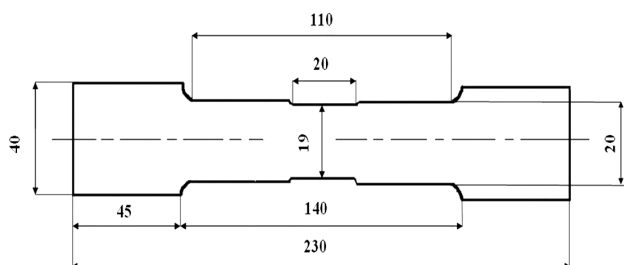


Figure 1: Size of the transverse test bars
Slika 1: Velikost testnih prečnih preizkušancev

$$\dot{\epsilon} = \frac{\epsilon}{t} = \frac{v}{L_0} \quad (1)$$

Where: ϵ – relative deformation, t – duration of the deformation, L_0 – working length of the test bar, v – speed of the load

The dynamic tests were performed according to ISO 26203-1 and ISO 26203-2 standards on the rotary hammer RSO^{13,14} with the data evaluated using the Scope 4 program. **Figures 2 and 3** show the effect of strain rate on yield stress and ultimate tensile strength of IF and S420 steels sheets. In **Figure 4** the elongation of both steels (IF and S420) by quasi-static and dynamic conditions is given. The S420 steel demonstrated an increase of 48 % tensile strength at a strain rate of 100 s⁻² showing its better formability by sheet metal forming.

2.1 Substructure

The substructure evolution was investigated on samples formed at a static strain rate of 8.33.10⁻³ s⁻¹ and

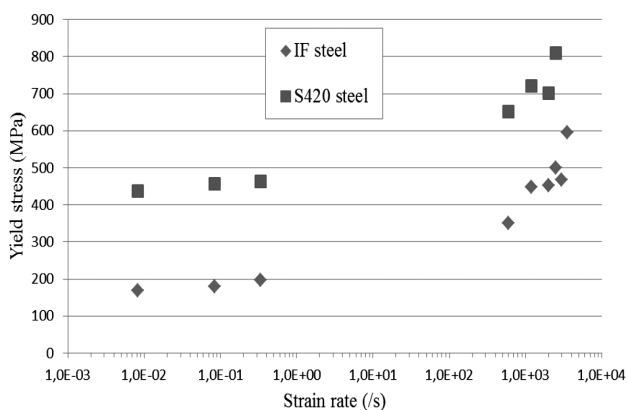


Figure 2: Dependence of yield stress with strain rate of IF and S420 steel sheets

Slika 2: Odvisnost med hitrostjo deformacije jeklenih plošč IF in S420 ter mejo plastičnosti

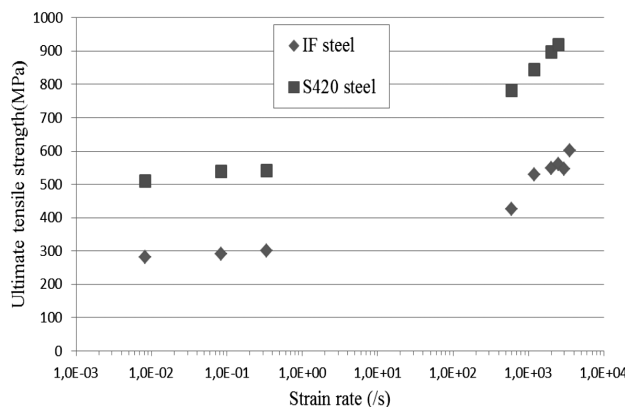


Figure 3: UTS dependence on strain rate of IF and S420 steel sheets
Slika 3: Odvisnost hitrosti deformacije jeklenih plošč IF in S420 ter razržno trdnostjo

dynamic strain rates of (600, 2000, 3000 and 4000) s⁻¹. Samples were imaged in a JEOL 2100F transmission electron microscope at 300 kV with STEM detector.¹⁵ Mechanically ground thin plates of 0.1 mm thickness were then punched out as discs with a diameter of 3 mm. The discs were then electrolytically polished using a double jet device (TenuPol5) in a solution of acetic acid and perchloric acid to obtain specimens for TEM investigation¹⁵ of dislocations. In **Figure 5** planar structures are mainly observed. Such stacking faults and planar dislocation structures (regular dislocation pile-ups, planar tangled bundles) were often observed. After dynamic strain of $\dot{\epsilon} = 4000$ s⁻¹, the dislocations were still mainly present as more evenly distributed planar structures (**Figure 6**), with stacking faults less often observed.¹⁶ **Figure 7** shows the S420 steel after static strain with numerous dislocation arrangements close to a

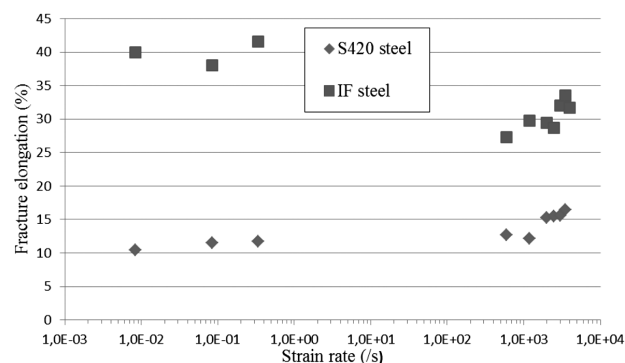


Figure 4: Influence of loading rate on fracture elongation of IF and S420 steel sheets

Slika 4: Vpliv hitrosti deformacije na raztezek pri prelomu IF in S420 jeklenih plošč

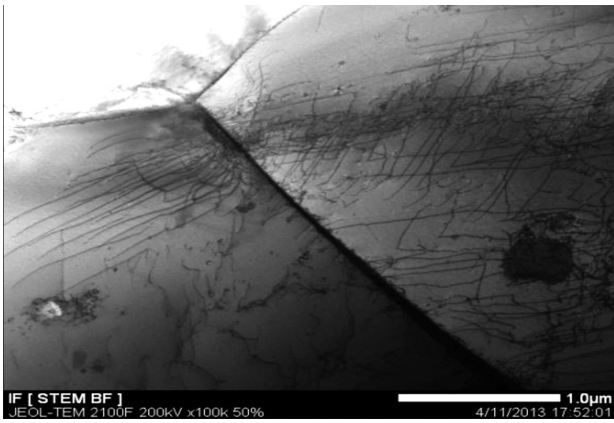


Figure 5: Dislocation structure of IF steel in the static condition ($\dot{\epsilon} = 8.33 \cdot 10^{-4} \text{ s}^{-1}$)

Slika 5: Struktura dislokacij v statičnem stanju IF jekla ($\dot{\epsilon} = 8.33 \cdot 10^{-4} \text{ s}^{-1}$)

grain boundary, whereas the dislocations in the middle of the same grain were much fewer. After dynamic strain $\dot{\epsilon} = 3000 \text{ s}^{-1}$, the dislocation density was much higher than that of the static condition, with the dislocations distributed homogeneously (**Figure 8**).

3 RESULTS AND DISCUSSION

The experimental results indicate that the strain rate affects the basic mechanical properties of tested steels. The change of properties is greater by at higher strain rates (**Figure 2**) and potentially lead to a change in deformation properties (**Figure 4**).¹⁶⁻¹⁹ The dependence of the strength properties on the strain rates for the steels tested in the range from 10^{-3} to 10^3 s^{-1} is described by parametric Equations (2) and (3):²⁰

$$R_{\dot{\epsilon}\dot{\epsilon}} = R_{\dot{\epsilon}\dot{\epsilon}_0} + A \cdot \ln \frac{\dot{\epsilon}}{\dot{\epsilon}_0} \quad (2)$$

$$R_{m\dot{\epsilon}} = R_{m\dot{\epsilon}_0} + B \cdot \ln \frac{\dot{\epsilon}}{\dot{\epsilon}_0} \quad (3)$$

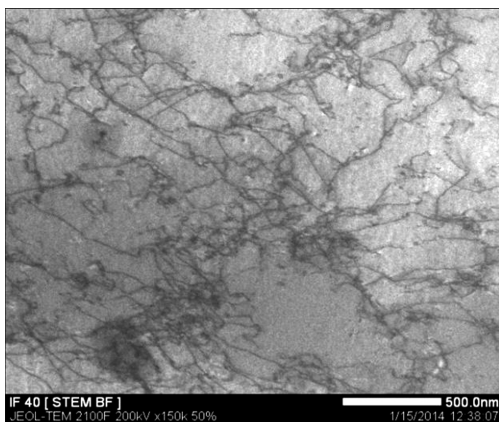


Figure 6: Dislocation structure of IF steel in the dynamic condition ($\dot{\epsilon} = 4000 \text{ s}^{-1}$)

Slika 6: Struktura dislokacij pri dinamičnem stanju IF jekla ($\dot{\epsilon} = 4000 \text{ s}^{-1}$)

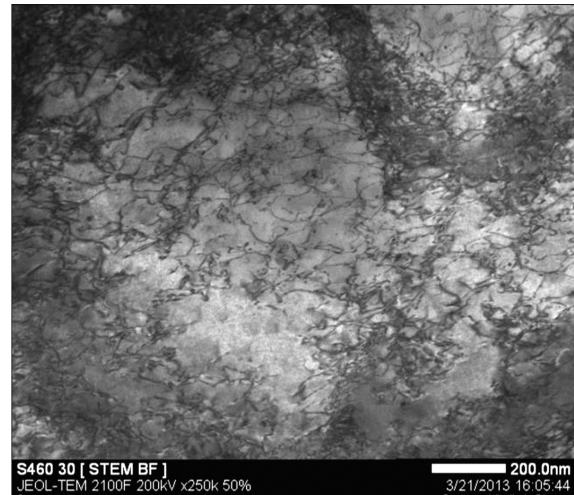


Figure 7: Dislocation structure of S420 steel in the static condition ($\dot{\epsilon} = 8.33 \cdot 10^{-4} \text{ s}^{-1}$)

Slika 7: Struktura dislokacij pri statičnem stanju jekla S420 ($\dot{\epsilon} = 8,33 \cdot 10^{-4} \text{ s}^{-1}$)

Where:

$R_{\dot{\epsilon}\dot{\epsilon}}$ and $R_{m\dot{\epsilon}_0}$ are the yield stress and ultimate tensile strength at a given strain rate $\dot{\epsilon}$.

$R_{\dot{\epsilon}\dot{\epsilon}_0}$ and $R_{m\dot{\epsilon}_0}$ are the yield stress and ultimate tensile strength at a static deformation rate (10^{-3} s^{-1}).

The parameters A and B are material constants and express the steel sensitivity to strain rate. With higher A and B parameters, the steel is more sensitive to strain rate, presenting less obstruction to dislocation motion. A and B values of 24.1 and 20.4, respectively, were determined for the IF steel and 16.61 and 24.9, respectively, for the S420 steel.²⁰

The greater increase of the strength properties by dynamic stress than by static stress could be explained by increasing lattice resistance to the movement of dislocations. The assumption is if the deformation is dynamic

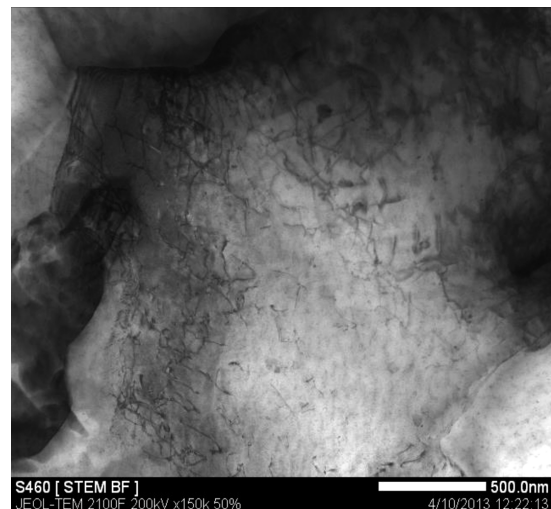


Figure 8: Dislocation structure of S420 steel in the dynamic condition ($\dot{\epsilon} = 3000 \text{ s}^{-1}$)

Slika 8: Struktura dislokacij pri dinamičnem stanju jekla S420 ($\dot{\epsilon} = 3000 \text{ s}^{-1}$)

there is not sufficient time for it to pass through the best-oriented lattice planes and slip planes yielding higher critical shear stresses and greater stress is required for deformation.^{21,22}

4 CONCLUSION

The experimental results and calculations support the following conclusions:

- The strength properties of tested steels increase with strain rate.
- The dynamic yield strength is increased substantially with respect to quasi static strain. In an uninterrupted tensile test at a strain rate of 1 s^{-1} the yield strength ($Y_S = 0.2 \%$) is increased by 16 % for IF steel and by 6 % for S420. With a strain rate 10 s^{-1} , the yield strength was increased by 98 % for IF steel and 49 % for S420. The tensile strength also increased with increased strain rate.
- IF steel with the coarse-grained ferritic structure was more sensitive to strain rate. For yield strength the sensitivity coefficient $A = 24.1$.
- S420 steel with the fine-grained ferritic – pearlitic structure and precipitates had a lower sensitivity to the strain rate and the sensitivity coefficient for yield stress is $A = 16.6$.
- The dynamic response can be associated with the regrouping of dislocations.
- It is concluded that the IF steel had fewer barriers to the movement of dislocations than the S420 steel. The effect of strain rate reflects the resistance of lattice against the motion of dislocations and was more pronounced in dynamic load conditions.

Acknowledgement

This study was supported by the Grant Agency of Slovak Republic, grant project VEGA 1/0549/14.

5 REFERENCES

- ¹ S. I. Kim, S. H. Choi, Y. C. Yoo, Influence of boron on mechanical properties and microstructures of hot-rolled interstitial free steel, *Materials, Science Forum*, 495–497 (2005) 537–542, doi:10.4028/www.scientific.net/MSF.495-497
- ² S. K. Paul, A. Raj, P. Biswas, G. Manikandan, R. K. Verma, Tensile flow behavior of ultra low carbon, low carbon and micro alloyed steel sheets for auto application under low to intermediate strain rate, *Mater. & Des.*, 57 (2014) 211–217, doi:10.1016/j.matdes.2013.12.047
- ³ S. Oliver, T. B. Jones, G. Fourlaris, Dual phase versus TRIP strip steels: Microstructural changes as a consequence of quasi-static and dynamic tensile testing, *Mater. Character.*, 58 (2007) 390–400, doi:10.1016/j.matchar.2006.07.004
- ⁴ N. Kamikawa, N. Tsuji, Y. Minamino, Microstructure and texture through thickness of ultralow carbon IF steel sheet severely deformed by accumulative roll-bonding, *Scien. and Techn. of adv. Mater.*, 5 (2004) 163–172, doi:10.1016/j.stam.2003.10.018
- ⁵ M. Jahazi, B. Eghbali, The influence of hot forging conditions on the microstructure and mechanical properties of two microalloyed steels, *Journal of Materials Processing Technology*, 113, 1–3 (2001) 594–598, doi:10.1016/S0924-0136(01)00599-4
- ⁶ N. D. Beynon, G. Fourlaris, T. B. Jones, Effect of high strain rate deformation on microstructure of strip steels tested under dynamic tensile conditions, *Mater. Sci. Techn.*, 21 (2005) 103–112, doi:10.1007/s 11661-008-9495-4
- ⁷ M. Cabibbo, A. Fabrizi, M. Merlin, G. L. Garagnani, Effect of thermo-mechanical treatments on the microstructure of micro-alloyed low-carbon steels, *J. Mater. Sci.*, 43 (2008) 6857–6865, doi:10.1007/s10853-008-3000-8
- ⁸ M. Mihaliková, M. Németh, V. Girman, DP 600 steel research of dynamic testing, *Metalurgija*, 54 (2015), 211–213
- ⁹ H. Huh, J. H. Lim, S. H. Park, High speed tensile test of steel sheets for the stress-strain curve at the intermediate strain rate, *International Journal of Automotive Technology*, 10 (2009) 2, 195–204, doi:10.1007/s12239-009-0023-3
- ¹⁰ A. Kovalčíková, P. Kurek, P. Balko, et. al., Effect of the counterpart material on wear characteristics of silicon carbide ceramics, *J. of Refr. Metal and Hard Mater.*, 44 (2014) 12–18, doi:10.1016/j.ijrmhm.2014.01.006
- ¹¹ ISO 6892-1. Metallic materials-tensile testing-Part 1: method of test at room temperature; (2009)
- ¹² M. Mihaliková, M. Németh, M. Vojtko, Impact of strain rate on microalloyed steel sheet fracturing, *Acta Polytechnica*, 54 (2014) 281–284, doi:10.14311/AP.2014.54.0281
- ¹³ M. Mihaliková, M. Ambriško L. Pešek, Videoextensometric measuring of deformation processes in automotive steel sheets at two strain rate levels, *Kovov. Mater.*, 49 (2011) 2, 137–141, doi:10.4149/km-2011-2-137
- ¹⁴ ISO 26203-2 Tensile testing at high strain rates – Part 2: Servo-hydraulic and other test systems; (2011)
- ¹⁵ J. Lis, A. K. Lis, C. Kolan, Processing and properties of C-Mn steel with dual-phase microstructure, *Journal of Materials Processing Technology*, 162–163 (2005), 350–354, doi:10.1016/j.jmatprotec.2005.02.105
- ¹⁶ R. R. Balokhonov, V. A. Romanova, S. Schmauder, Finite-element and finite-difference simulations of the mechanical behavior of austenitic steels at different strain rates and temperatures, *Mechanics of Materials*, 41 (2009) 12, 1277–1287, doi:10.1016/j.mechmat.2009.08.005
- ¹⁷ W. Wang, X. Wei, The effect of martensite volume and distribution on shear fracture propagation of 600-1000 MPa dual phase sheet steels in the process of deep drawing, *Inter. Jour. of Mechan. Scien.*, 67 (2013) 100–107, doi:10.1016/j.ijmecsci.2012.12.011
- ¹⁸ B. Peeters, S. R. Kalidindi, C. Teodosiu, P. V. Houtte, E. Aernoudt, A theoretical investigation of the influence of dislocation sheets on evolution of yield surfaces in single-phase B.C.C. polycrystals, *Jour. of Mech. and Phys. of Solids.*, 50 (2002) 4, 783–807
- ¹⁹ J. Slota, M. Jurčičin, E. Spišák, T. Slezziak, An investigation of springback in sheet metal forming of high strength steels, *Applied Mechanics and Materials*, 693, (2014) 370–375, doi:10.4028/www.scientific.net/AMM.693.370
- ²⁰ J. Michelf, M. Buršák, The influence of strain rate on the plasticity of steel sheets, *Komunikacie*, 12 (2010) 4, 27–32
- ²¹ M. Suliga, Analysis of the heating of steel wires during high speed multipass drawing process, *Archives of Metallurgy and Materials*, 59 (2014) 4, 1475–1480, doi:10.2478/amm-2014-0251
- ²² P. Zubko, M. Vojtko, L. Pešek, M. Németh, P. Bekeč, Changes in mechanical properties and microstructure after quasi-static and dynamic tensile loading, *Materials Science Forum*, 782 (2014), 215–218, doi:10.4028/www.scientific.net/MSF.782.215

ACOUSTIC AND ELECTROMAGNETIC EMISSION OF LIGHTWEIGHT CONCRETE WITH POLYPROPYLENE FIBERS

AKUSTIČNA IN ELEKTROMAGNETNA EMISIJA LAHKEGA BETONA S POLIPROPILENSKIMI VLAKNI

**Richard Štoudek¹, Tomáš Trčka², Michal Matysík¹, Tomáš Vymazal¹,
Iveta Plšková¹**

¹Brno University of Technology, Faculty of Civil Engineering, Veveří 331/95, 602 00 Brno, Czech Republic

²Brno University of Technology, Faculty of Electrical Engineering and Communication, Technická 3058/10, 616 00 Brno, Czech Republic
matysik.m@fce.vutbr.cz

Prejem rokopisa – received: 2015-06-29; sprejem za objavo – accepted for publication: 2015-07-08

doi:10.17222/mit.2015.138

This paper is focused on failure monitoring in lightweight concrete (special high-performance concrete that contains porous aggregate with a low bulk density) with high-strength polypropylene fibers under mechanical loading. The aim was to determine how the cracks' generation intensity in the tested concrete samples depends on the fibers' length and quantity. Our diagnostic method is based on a measurement of the acoustic and electromagnetic emission signals, which occur when solid dielectric materials are mechanically stressed. Several groups of lightweight concrete samples with various types and concentrations of high-strength polypropylene fibers were prepared for our experiment. We made two-channel measurements of the concrete samples from each group for defined loading conditions. The first channel was electromagnetic emission (EME) and the second was acoustic emission (AE). The electromagnetic emission and acoustic emission methods are promising methods to study the generation and behavior of cracks. The main advantage of EME and AE is their ability to be detected already in the stressed stage, which prevents macroscopic deterioration in solids. From the obtained results it can be concluded that the generated cracks' intensity is significantly affected by the presence of polypropylene fibers and by their length and dosage.

Keywords: acoustic emission, electromagnetic emission, lightweight concrete, fibers

Članek je usmerjen na pregled poškodb pri mehanskem obremenjevanju lahkega betona (poseben visoko zmogljiv beton, ki vsebuje porozne sestavine z majhno gostoto), z visokotrdnostnimi polipropilenskimi vlakni. Namen je bil ugotoviti, kako je intenziteta nastanka razpok odvisna od dolžine in količine vlaken. Diagnostična metoda je temeljila na merjenju akustičnih signalov in signalov elektromagnetne emisije, ki se pojavijo kadar je trden dielektrični material mehansko obremenjen. Za eksperiment je bilo pripravljenih več vrst lahkih betonov z različno vrsto in koncentracijo visokotrdnostnih polipropilenskih vlaken. Pri določenih pogojih obremenitve smo izvršili dvokanalne meritve vzorcev betona iz vsake skupine. Prvi kanal je bila elektromagnetna emisija (EME), drugi pa akustična emisija (AE). Metodi elektromagnetne emisije in akustične emisije sta obetajoči metodi za študij nastanka in obnašanja razpok. Glavna prednost EME in AE je, da ju je mogoče odkriti že med stanjem napetosti, kar prepreči lokalne makroskopske poškodbe v trdnem stanju. Iz dobljenih rezultatov je mogoče zaključiti, da je intenzivnost nastajanja razpoke močno odvisna od prisotnosti polipropilenskih vlaken, od njihove dolžine in odmerka.

Ključne besede: akustična emisija, elektromagnetna emisija, lahki beton, vlakna

1 INTRODUCTION

Cracks very often generate in the structures of both normal and lightweight concrete. They can interfere only with the surface of the concrete body, or penetrate the whole volume. In both cases these cracks have a highly negative affect, not only on the static and deformation characteristics of the concrete, and thus the static behavior of the structure as a whole, but also lead to an intensive reduction of the durability. The source of these cracks can be the volume changes of the concrete (plastic shrinkage and settlement, heat of hydration, autogenous shrinkage, drying) or by external strain (cracks from bending and shearing stress).¹

When a solid is exposed to mechanical stress, emission of electrons, ions, ground-state and excited neutrals, free radicals, electromagnetic emission in the frequency range from tenths of Hz up to gamma radiation and acoustic emission may take place under certain condi-

tions. This phenomenon is generally termed fracto-emission. Fracto-emission may be due to several kinds of mechanical stress: tensile, compression, and torsional stress. Furthermore, it may be induced by friction, shock, drilling, splitting, scaling, grinding, skimming etc.^{2,3} This phenomenon is particularly strong in composite materials. In the frequency domain these processes are characterized as a flicker noise, especially in the low-frequency range. Several authors put forward a physical interpretation directly connected with particular non-homogeneous structures.⁴

Electromagnetic emissions in the radio-frequency region (EME) make up one of very important fracto-emission components for material research in physics as well as in engineering. In the past, great attention was paid to the application of EME from rocks and minerals being exposed to a mechanical stress, both in connection with earthquake and volcanic activity predictions and in rock mechanics.⁵⁻⁷ Although there are a number of

experimental papers dealing with various aspects of EME, the physical origin of this phenomenon is not sufficiently known for the time being.

Our diagnostic method designed for experimental examinations of EME signals in composite materials is based on an experimental fact, namely, that the formation of cracks in an electrically non-conducting material is accompanied by the generation of an electromagnetic field.⁸ The cracks' generation in solids is accompanied by the redistribution of the electric charge. The crack walls are electrically charged and their vibrations produce time-variable electrical dipole moments. Hence, the individual cracks become electromagnetic field sources, which can be measured with the appropriate sensors.⁸

The signal of the acoustic emission (AE) is generated simultaneously with the EME signal. Acoustic emission appears due to the release of elastic energy during this process and it is in the frequency range of ultrasonic waves.⁹

The electromagnetic emission and acoustic emission methods are promising methods for studying the generation and behavior of cracks. The main advantage of EME and AE is their ability to be detected already in the stressed stage, which prevents the macroscopic deterioration in solids. A suitably designed methodology of EME and AE signals measurement, processing and evaluation allows us to observe the response of stressed materials to an applied mechanical load continuously and also allows us to obtain useful information about the processes taking place in the cracks' formation in solids.¹⁰⁻¹² For the time being, the EME method is the only method suitable for studying the time development of crack growth (crack-propagation speed, crack-face movement speed, crack length and size, etc.).^{13,14}

2 EXPERIMENTAL PART

For EME and AE observations the automatic measurement system was developed. It is schematically shown in **Figure 1**. The adjustable hydraulic press is controlled by computer via a voltage that is set by card NI PCI-6014. A press provides a mechanical load in the range from 10 kN up to 110 kN. The measurement card acquires the output voltage of the Wheatstone bridge with a sensitive load cell that measures the mechanical load. A deformation meter is used to measure the sample's contraction during a compressive stress application. The data from the deformation meter are read and processed by computer.

For the EME detection we used capacitance sensors. Our capacitance sensor was formed by a specially made adjustable bracket with two electrodes, into which we can easily insert the rectangular samples from the studied material.

For AE capturing the piezoelectric sensors were used. These sensors meet the requirements of the AE frequency band (at least up to 1 MHz). Beeswax was applied for

good mechanical coupling between the sensors and the specimen.

The EME measurement channel consists of a capacitance sensor, the dielectric of which is composed of the stressed sample, a high-pass-filter-type load impedance Z_L , a low-noise preamplifier PA31, and an amplifier AM22 with a set of filters. The total EME channel gain is 60 dB, the frequency range is from 30 kHz to 1.2 MHz and the sampling rate is 5 MHz.

The AE channel consists of a piezoelectric acoustic sensor (30 kHz ~ 1 MHz), the low-noise preamplifier PA31 and the amplifier AM22 with a set of filters. The total AE channel gain is 40 dB, while the frequency range is from 30 kHz to 1.2 MHz.

EME and AE Preamplifiers and Amplifiers:

- Preamplifier (3S SEDLAK PA31): This low-noise preamplifier exhibits a bandwidth from 20 Hz to 10 MHz, a high input impedance 10 M Ω /20 pF, a variable gain of 6/20/40 dB and a noise voltage < 1.8 nV/vHz.
- Amplifier (3S SEDLAK AM22): This low-noise amplifier exhibits a bandwidth from 0.3 Hz to 1.2 MHz, a set of high-pass and low-pass filters, an input impedance of 1 M Ω /50 pF and a noise voltage < 3 nV/vHz.

Both signals of the EME and AE are acquired by the NI PCI 6111 card and stored in the PC. The stored data is processed using our software. The whole measurement system is controlled by a computer with the software developed in LabVIEW. The software makes it possible to find the typical events in the EME and AE. The evaluation process for these parameters and the measurement process are provided in real time and simultaneously.

Our study is focused on lightweight concrete with polypropylene fibers. Classical lightweight concrete (without polypropylene fibers) has been used as a reference sample. This fresh concrete mixture was prepared from Liapor 4-8/600 lightweight aggregates (LWA), heavyweight aggregates (HWA) of a 0-4-mm fraction, CEM I - 42.5 R cement, fly ash, plasticizer and water. The water and lightweight aggregates of a 4-8-mm fraction were dosed by volume, the remaining components

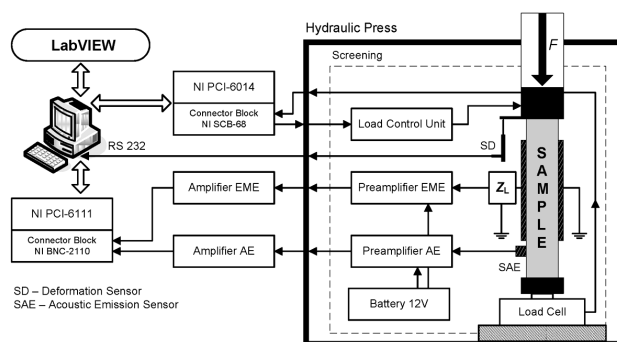


Figure 1: Experimental set-up
Slika 1: Eksperimentalni sestav

by weight. The composition of the fresh concrete mixture is in **Table 1**.

Table 1: Composition of fresh concrete mixture (reference sample)
Tabela 1: Sestava sveže mešanice betona (referenčni vzorec)

Components	Units	Quantities per 1 m ³
LWA Liapor 4-8/600	L	440
HWA 0-4 mm Bratčice	kg	580
Cement 42.5 R	kg	400
Fly ash Trinec	kg	50.0
Plasticizer Sika Viscocrete 1035	kg	5.00
Water	L	206

Table 2: Dosage of polypropylene fibers, additional water and plasticizer. The length of the fibers is shown in brackets.

Tabela 2: Odmerek polipropilenskih vlaken, dodatka vode in plastifikatorja. Dolžina vlaken je prikazana v oklepajih.

Components	Quantities per 1 m ³ (kg)					
Forta Ferro (54 mm)	–	9.0		6.0	4.0	2.0
Forta Econo-Net (38 mm)	–	–	9.0	1.5	1.0	0.5
Forta Econo-Net (19 mm)	–	–	–	1.5	1.0	0.5
Additional water	–	60	40	60	20	–
Additional plasticizer	–	–	–	0.8	0.8	0.8
Designation of the mixture						

We also made five mixtures of fiber-lightweight concrete, which are mutually of a different type and amount of polypropylene fibers. The compositions of these concretes were based on the reference lightweight concrete – to the basic components was added an appropriate dose of fibers and the consistency of the mixtures was adjusted by adding water, possibly plasticizer. The dosage of the fibers, additional water and plasticizer, for the individual mixtures is shown in **Table 2**.

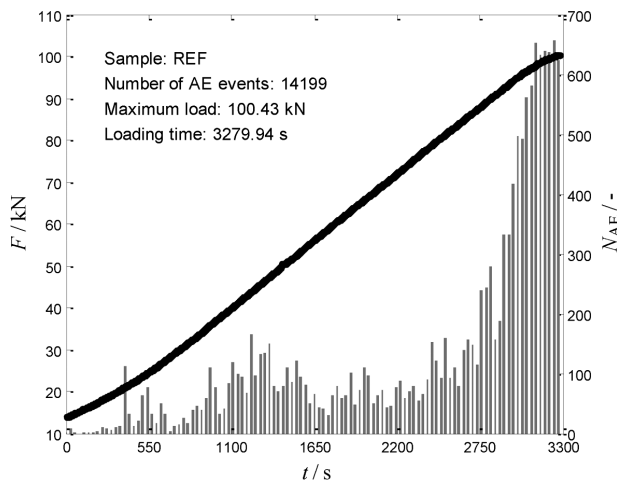


Figure 2: Applied mechanical load and the distribution of the fracture events (triggered by the AE signals) in time, sample REF

Slika 2: Uporabljena mehanska obremenitev in časovna razporeditev pojavov loma (sproženega z AE signali), vzorec REF

3 RESULTS AND DISCUSSION

Six groups of lightweight concrete samples with various types and amounts of fibers were prepared for a two-channel (EME and AE) measurement on our experimental set-up. The measured specimens were concrete blocks of overall dimensions 100 mm × 100 mm × 100 mm. These blocks from each of the prepared groups were measured for defined loading conditions (linearly increasing the uniaxial compression up to a load of 110 kN with a rate of 27 N/s.). The steel rods with a square cross-section of 8 mm × 8 mm were inserted between the specimens and the hydraulic press jaws.

Figure 2 shows an example of the REF specimens' loading conditions, the curve of the applied mechanical load and the histogram describing the distribution of the fracture events (triggered by the AE signals) with time. Each bar in this chart describes the number of AE events during a time interval of 30 s. The number of fracture events in individual time intervals is almost constant below the applied load of approximately 85 kN. The number of fracture events exponentially increases above this load level. The peak in the maximum value corresponds to the start of the whole sample destruction. In **Figure 2** we can also see that the force versus time is linear only for the range of 20 kN to 95 kN. This is due to the hydraulic press.

Figures 3 and 4 show examples of the measured signals that contain only separated EME and AE events.

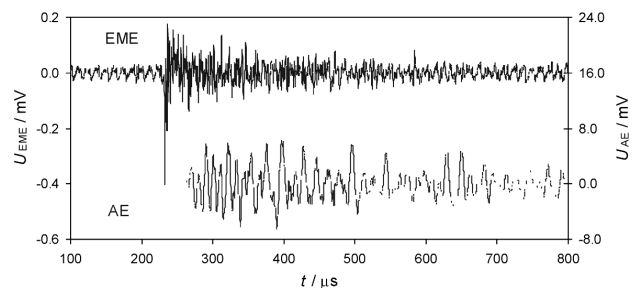


Figure 3: Separated EME and AE events, mechanical load 64.33 kN, sample MIX2

Slika 3: Ločeni EME in AE dogodki, mehanska obremenitev 64,33 kN, vzorec MIX2

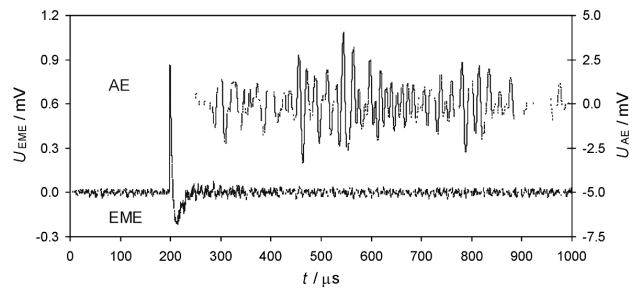


Figure 4: Separated EME and AE events, mechanical load 107.06 kN, sample MIX2

Slika 4: Ločeni EME in AE dogodki, mehanska obremenitev 107,06 kN, vzorec MIX2

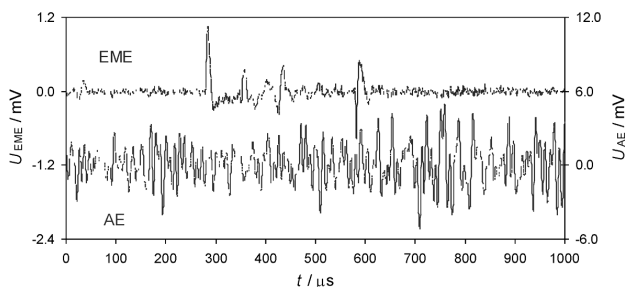


Figure 5: Continuous EME and AE events, mechanical load 76.23 kN, sample EN38

Slika 5: Nprekinjeni EME in AE dogodki, mehanska obremenitev 76,23 kN, vzorec EN38

The time delay between both signals is caused by the different propagation velocities of the acoustic and electromagnetic signals in the sample under examination. The AE signal time latency to the EME signal arrival provides information about the distance of the crack from the AE sensor. In the case of the AE signal multi-

channel measurement, we can get useful information about the crack's position in the stressed material.^{12,13} The formation of the continuous EME and AE signals (**Figure 5**) occurs just before the total destruction of the whole sample. In the case of the EN38 sample, the maximum load (before the sample destruction) was approximately 82 kN.

The curves of the applied force versus sample deflection (contraction) for the individual measured concrete samples are in **Figures 6 to 11**. The histograms in these figures illustrate the distribution of the AE fracture events depending on the increasing sample contraction. The numbers of AE and EME events, the maximum force and the maximum strain of the measured samples are shown in **Table 3**. The cumulative numbers of detected AE events for a defined applied force are in **Figure 12**. **Figure 13** shows the dependence of the cumulative number of AE events on the total dosage of polypropylene fibers in 1 m³ of lightweight concrete mixture for a defined mechanical load.

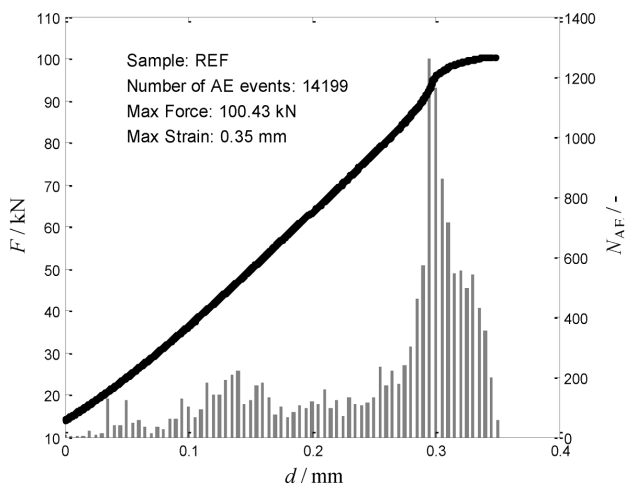


Figure 6: Sample REF – AE intensity
Slika 6: Vzorec REF – intenzivnost AE

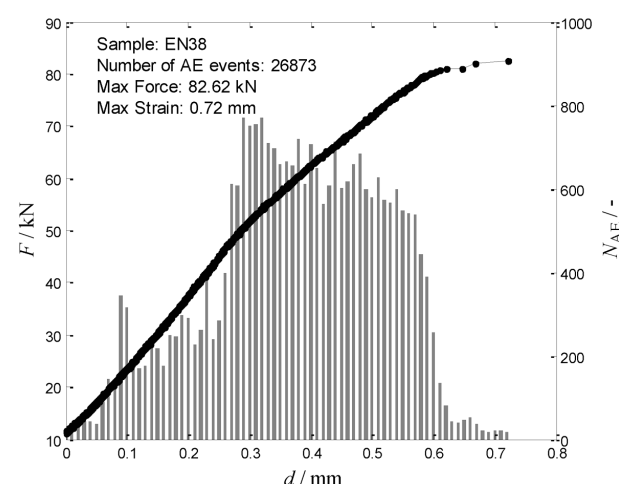


Figure 8: Sample EN38 – AE intensity
Slika 8: Vzorec EN38 – intenzivnost AE

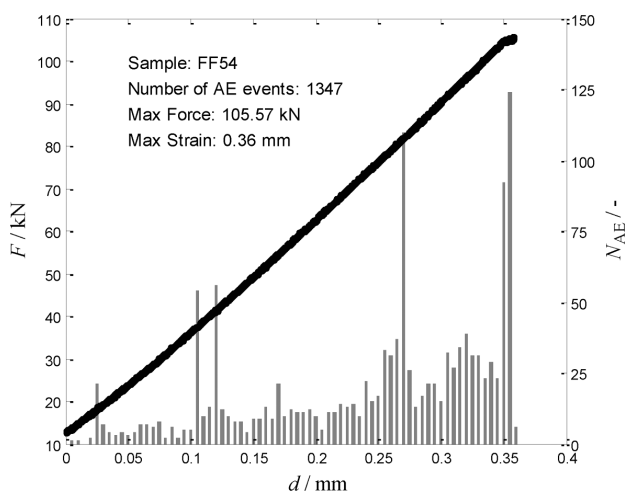


Figure 7: Sample FF54 – AE intensity
Slika 7: Vzorec FF54 – intenzivnost AE

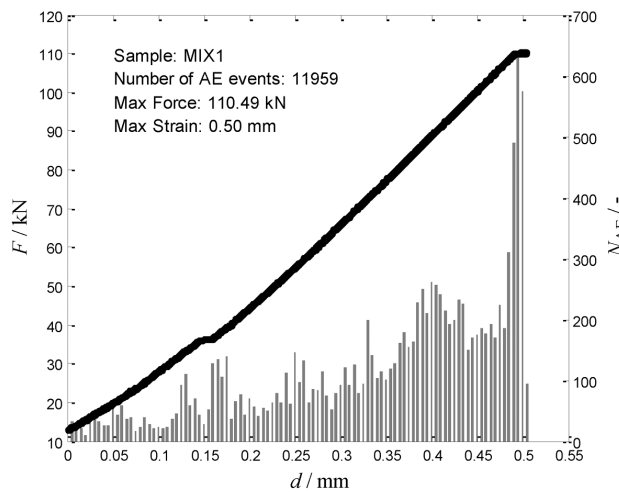


Figure 9: Sample MIX1 – AE intensity
Slika 9: Vzorec MIX1 – intenzivnost AE

Table 3: Numbers of AE and EME events, maximum force and maximum strain of measured samples

Tabela 3: Števila dogodkov AE in EME, maksimalna sila in maksimalna napetost izmerjenih vzorcev

Designation of the mixture	REF	FF54	EN38	MIX1	MIX2	MIX3
Number of AE events	14199	1347	26873	11959	7123	16644
Number of EME events	25	4	166	13	113	96
Maximum force (kN)	100.43	105.57	82.62	110.49	107.90	108.09
Maximum strain (mm)	0.348	0.358	0.723	0.504	0.475	0.437

4 CONCLUSIONS

For the EN38 sample it is evident that the intensity of the detected AE signals increases from the beginning of the mechanical loading (Figure 6) and the cumulative number of AE events for a defined load reaches signifi-

cantly higher values compared to the rest of the samples. This is only valid for a mechanical load of approximately 83 kN, during which the EN38 sample was destroyed (Figure 12). By contrast, for the sample FF54 we recorded the lowest value of AE events for every load. We can see in Figure 12 that the REF sample (without polypropylene fibers) is located between the FF54 and EN38 samples. The low strength and the high AE activity of sample EN38 is probably due to pulping fiber bundles and their re-clustering already during mixing. In the production of this sample we observed a noticeable increase in the volume of the mixture.

From the cumulative number of AE events (Figure 12) we can plot the dependence of the total number of AE events on the total dosage of polypropylene fibers for a defined mechanical load (Figure 13). In this figure we can see only the REF sample and the samples with mixtures of fibers. There is a clear minimum of AE activity

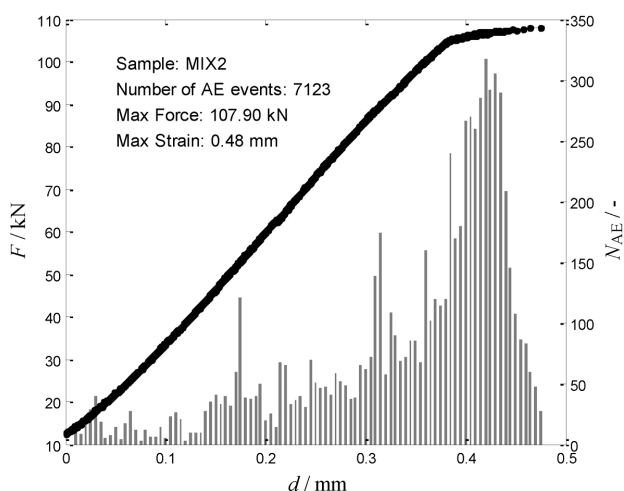


Figure 10: Sample MIX2 – AE intensity
Slika 10: Vzorec MIX 2 – intenzivnost AE

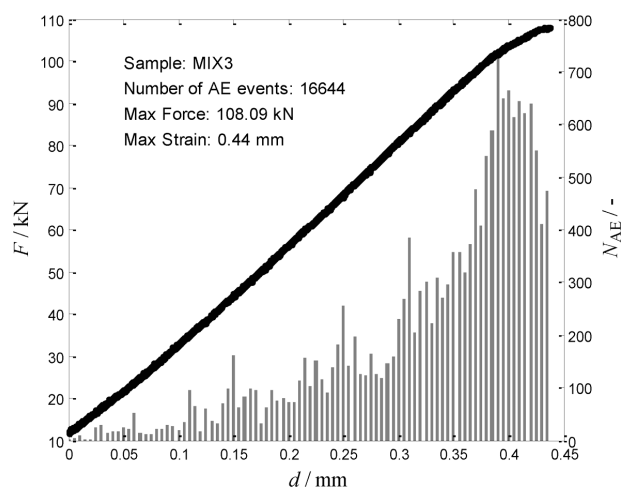


Figure 11: Sample MIX3 – AE intensity
Slika 11: Vzorec MIX3 – intenzivnost AE

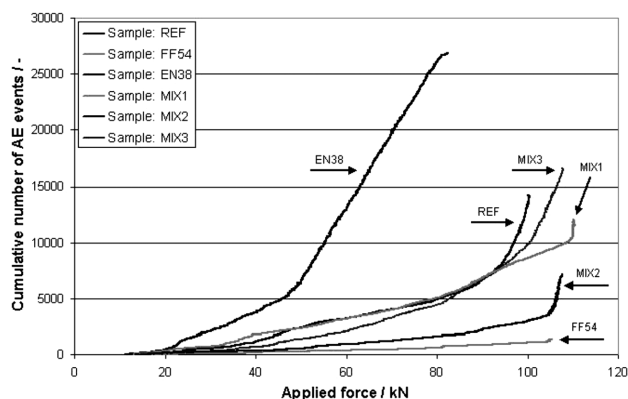


Figure 12: Cumulative numbers of detected AE events for a defined applied force
Slika 12: Kumulativno število zabeleženih dogodkov AE pri določeni uporabljeni sili

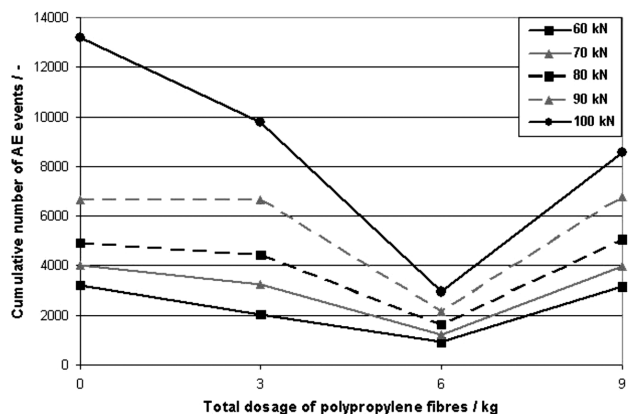


Figure 13: Dependence of the cumulative number of AE events on the total dosage of polypropylene fibers in 1 m³ of lightweight concrete mixture for a defined mechanical load (REF – 0 kg, MIX3 – 3 kg, MIX2 – 6 kg, MIX1 – 9 kg)

Slika 13: Odvisnost kumulativnega števila dogodkov pri AE od celotnega odmerka polipropilenskih vlaken v 1 m³ mešanice lahkega betona pri določeni mehanski obremenitvi (REF – 0 kg, MIX3 – 3 kg, MIX2 – 6 kg, MIX1 – 9 kg)

for the sample MIX2 (a total of 6 kg of polypropylene fibers in 1 m³ of concrete mixture). A smaller dosage of fibers does not have such a big impact – sample MIX3 (total 3 kg) and a larger dosage seems to be reflected again in the clustering of polypropylene fibers – sample MIX1 (total 9 kg).

In the case of electromagnetic emission the largest total detected EME event was again for the EN38 sample (**Table 3**). But the number of these events in all the samples is too small for any conclusions to be drawn.

From the obtained results it can be concluded that the generated cracks' intensity is significantly affected by the total dosage of polypropylene fibers and by their length (and type). More detailed studies would require additional measurements on a larger number of lightweight concrete samples with defined compositions.

Acknowledgments

This paper has been written as part of the project No. LO1408 "AdMaS UP – Advanced Materials, Structures and Technologies", supported by Ministry of Education, Youth and Sports under the "National Sustainability Programme I" and under the project of Czech Science Foundation project GA13-18870S and specific research program at Brno University of Technology, project No. FAST-S-13-2149.

5 REFERENCES

- ¹ B. Kucharczykova, Z. Kersner, O. Pospichal, P. Misak, T. Vymazal, Influence of freeze–thaw cycles on fracture parameters values of lightweight concrete, *Procedia Engineering*, 2 (2010) 1, 959–966, doi:10.1016/j.proeng.2010.03.104
- ² J. T. Dickinson, M. K. Park, E. E. Donaldson, L. C. Jensen, Fracto-emission accompanying adhesive failure, *Journal of Vacuum Science & Technology A Vacuum Surfaces and Films*, 20 (1982) 3, 436–439, doi:10.1116/1.571327
- ³ J.T. Dickinson, E.E. Donaldson, M.K. Park, The emission of electrons and positive ions from fracture of materials, *Journal of Materials Science*, 16 (1981) 10, 2897–2908, doi:10.1007/BF00552976
- ⁴ R. Macku, P. Koktavy, Analysis of fluctuation processes in forward-biased solar cells using noise spectroscopy, *Physica Status Solidi*, 207 (2010) 10, 2387–2394, doi:10.1002/pssa.201026206
- ⁵ V. Hadjicontis, G.S. Tombras, D. Ninos, C. Mavromatou, Memory effects in EM emission during uniaxial deformation of dielectric Crystalline materials, *Geoscience and Remote Sensing Letters IEEE*, 2 (2005) 2, 118–120, doi:10.1109/LGRS.2004.842472
- ⁶ Y. Mori, K. Sato, Y. Obata, K. Mogi: Acoustic emission and electric potential changes of rock samples under cyclic loading, *Proc. of the International Acoustic Emission Symposium, Kamuela, Hawaii, 1998*, S45–S52, ISSN: 0730-0050
- ⁷ P. Koktavy, J. Pavelka, J. Sikula, Characterization of acoustic and electromagnetic emission sources, *Measurement Science and Technology*, 15 (2004) 5, 973–977, doi: 10.1088/0957-0233/15/5/028
- ⁸ P. Koktavy, Experimental study of electromagnetic emission signals generated by crack generation in composite materials, *Measurement Science and Technology*, 20 (2009) 1, 1–8, doi:10.1088/0957-0233/20/1/015704
- ⁹ P. Koktavy, T. Trcka, B. Koktavy: Noise diagnostics of advanced composite materials for structural applications, *Proc. of the 21st International Conference on Noise and Fluctuations, Toronto, 2011*, 88–91, doi:10.1109/ICNF.2011.5994391
- ¹⁰ L. Topolar, L. Pazdera, V. Bilek, L. Dedeckova: Acoustic Emission Method Applied on Four Point Loading of Concrete Structures with and without Small Wires, *Proc. of the 50th Annual Conference on Experimental Stress Analysis, Prague, 2012*, 477–484, ISBN 978-80-01-05060-6
- ¹¹ T. Trcka, P. Koktavy, P. Tofel, Electromagnetic and Acoustic Emission Signals Real-Time Measurement, Processing and Data Evaluation, *Key Engineering Materials*, 465 (2011), 318–321, doi:10.4028/www.scientific.net/KEM.465.318
- ¹² P. Sedlak, Y. Hirose, S. Khan, M. Enoki, J. Sikula, New automatic localization technique of acoustic emission signals in thin metal plates, *Ultrasonics*, 49 (2009) 2, 254–262, doi:10.1016/j.ultras.2008.09.005
- ¹³ P. Sedlak, J. Sikula, T. Lokajicek, Y. Mori, Acoustic and electromagnetic emission as a tool for crack localization, *Measurement Science and Technology*, 19 (2008) 4, 1–7, doi:10.1088/0957-0233/19/4/045701
- ¹⁴ L. Pazdera, L. Topolar, Application acoustic emission method during concrete frost resistance, *Russian Journal of Nondestructive Testing*, 50 (2014) 2, 127–132, doi:10.1134/S1061830914020065

MULTI-CRITERIA ANALYSIS OF SYNTHESIS METHODS FOR Ni-BASED CATALYSTS

VEČKRITERIJSKA ANALIZA SINTEZNIH METOD NA OSNOVI Ni KATALIZATORJA

Vesna Nikolić¹, Boris Agarski², Željko Kamberović³, Zoran Anđić⁴, Igor Budak²,
Borut Kosec⁵

¹University of Belgrade, Innovation Center of the Faculty of Technology and Metallurgy, 4 Karnegijeva Street, 11120 Belgrade, Serbia

²University of Novi Sad, Faculty of Technical Sciences, 6 Trg Dositeja Obradovića Street, 21000 Novi Sad, Serbia

³University of Belgrade, Faculty of Technology and Metallurgy, 4 Karnegijeva Street, 11120 Belgrade, Serbia

⁴University of Belgrade, Innovation Center of the Faculty of Chemistry, 12-16 Studentski Trg Street, 11000 Belgrade, Serbia

⁵University of Ljubljana, Faculty of Natural Sciences and Engineering, 12 Aškerčeva Street, 1000 Ljubljana, Slovenia
vnikolic@tmf.bg.ac.rs

Prejem rokopisa – received: 2015-06-30; sprejem za objavo – accepted for publication: 2015-07-28

doi:10.17222/mit.2015.147

Catalysts based on the Ni/Al₂O₃ system are used in a variety of catalytic processes. Catalysts are commonly synthesized through thermochemical routes (impregnation, precipitation, coprecipitation and others). The authors prepared a Ni-Pd/Al₂O₃ catalyst supported by a ceramic foam, using a novel method, whereby the foam was impregnated with aerosol. This paper evaluates the synthesis methods for the experimentally obtained Ni-Pd/Al₂O₃ catalyst in comparison with other Ni-based catalysts, using three multi-criteria analysis methods (SAW, TOPSIS and PROMETHEE II). The synthesis methods for Ni-based catalysts were compared with respect to the following parameters: preparation method, addition of the precipitation agent during preparation, forming and mixing precursors, filtration, drying procedure, calcination, reduction, and the presence of NiAl₂O₄. The final results indicate that the synthesis method for the Ni-Pd/Al₂O₃ catalyst is the best ranked in comparison with the others.

Keywords: catalysts, multi-criteria analysis, Ni-Pd/Al₂O₃, ceramic foam, aerosol method

Katalizatorji na osnovi sistema Ni/Al₂O₃ se uporabljajo v številnih katalitičnih procesih. Katalizatorji so običajno sintetizirani po termokemijski poti (impregnacija, izločanje, koprecipitacija in drugi). Avtorji so pripravili Ni-Pd/Al₂O₃ katalizator, podprt s keramično peno z uporabo nove metode, kjer je bila pena impregnirana z aerosolom. Članek ocenjuje sintezne metode eksperimentalno dobljenega Ni-Pd/Al₂O₃ katalizatorja z drugimi katalizatorji na osnovi Ni, z uporabo treh večkriterijskih analizičnih metod (SAW, TOPSIS, and PROMETHEE II). Sintezne metode katalizatorjev na osnovi Ni, so bile primerjane po naslednjih parametrih: metoda priprave, dodatek izločevalnega sredstva med pripravo, oblikovanje in mešanje prekurzorjev, filtracija, postopek sušenja, kalcinacija, redukcija in prisotnost NiAl₂O₄. Končni rezultati kažejo, da je, v primerjavi z drugimi, najvišje uvrščena metoda sinteze katalizatorja Ni-Pd/Al₂O₃.

Ključne besede: katalizator, večkriterijska analiza, Ni-Pd/Al₂O₃, keramična pena, metoda aerosola

1 INTRODUCTION

While metal-processing technologies can have significant impact on human health, the synthesis of metal/ceramic catalysts is conducted in a laboratory environment with a small risk on human health.¹ Composite metal/ceramic catalysts are used in a wide range of heterogeneous catalytic processes, including reforming of hydrocarbons. Hydrocarbons are reformed in order to obtain H₂ or a synthesis gas (CO+H₂), which are highly efficient energy sources.^{2,3} The most common catalysts for this purpose are based on the Ni/Al₂O₃ system.^{4,5} Despite high catalytic properties of noble-metal-based catalysts, their application is not economically favorable in industrial conditions.^{6,7} Ni is an effective alternative for noble metals due to its low price, good catalytic activity and selectivity. In order to prevent a deactivation of active Ni particles, a low amount of an activity modifier, such as 0.1 % of mass fractions of Pd, is added.^{2,3}

Conventional thermochemical methods for the Ni/Al₂O₃ catalyst synthesis are impregnation, precipitation, coprecipitation and others. Oxide precursors for Ni that are supported by an Al₂O₃ powder are obtained from aqueous solutions of nickel salts and calcination in air. Also, both Al₂O₃ and oxide precursors for Ni can be prepared from the aqueous solutions of the corresponding metal salts. Calcination is carried out to form mixed oxides. Catalysts are then obtained with a hydrogen reduction and they are usually in the form of a powder. During the calcination procedure, undesirable and hardly reducible NiAl₂O₄ is commonly formed. In order to reduce this phase to Ni, high reduction temperatures are required.^{4,8,9}

There are novel methods for the catalyst synthesis, which include aerosol generation in order to form the precursors for active metals. In a previous research¹⁰, authors synthesized a monolithic Ni-Pd/Al₂O₃ catalyst supported by a Al₂O₃-based foam, using a novel method. The foam was prepared according to the previously

presented procedure¹¹ and then impregnated with ultrasonically generated aerosols of chlorides of Ni and Pd. The calcination step was eliminated and the catalyst was reduced at a very low temperature, which allowed a simplification of the synthesis process and energy savings. The obtained catalyst was intended for dry methane reforming, where the synthesis gas is produced from CH₄ and CO₂.^{10,12}

Considering the work of the previous authors on the catalyst-synthesis methods, it can be concluded that none of the studies compared the catalyst-synthesis methods using a multi-criteria analysis. In this research, the novel synthesis method for the Ni-Pd/Al₂O₃ catalyst is compared with the other Ni-based catalyst-synthesis methods using three multi-criteria analysis methods.

2 MATERIALS AND METHODS

Parameters (criteria) for assessing the catalyst-synthesis methods are:

P1 – Preparation method [-], expressed with a five-point scale. Impregnation is carried out by soaking the Al₂O₃ powder in a Ni(NO₃)₂ aqueous solution. With respect to the precipitation, the Al₂O₃ powder is immersed into the Ni(NO₃)₂ solution and a precipitation agent is added. Coprecipitation involves mixing the Al(NO₃)₃ solution (this salt is the precursor for Al₂O₃) and the Ni(NO₃)₂ solution, and then the precipitation agent is added.

P2 – Addition of the precipitation agent during the preparation [-], expressed with a two-point scale: without the addition – 0 points, with the addition – 1 point. Impregnation is used to deposit Ni ions to the Al₂O₃ surface. During the precipitation, the initial precursor for Ni is deposited into Al₂O₃ from the salt solution, by increasing its pH value with the precipitation agent. During the coprecipitation, the initial precursors for both Ni and Al₂O₃ are formed by increasing the pH value of the mixed salt solution.

P3 – Forming and mixing the precursors [Kh], expressed by temperature (K) × time (h). The conventional thermochemical routes require a long time. The mixing of appropriate solutions with the Al₂O₃ powder during the impregnation and precipitation is usually performed at 293 K for 24 h. During the coprecipitation, solutions are stirred between 313–358 K for 1–10 h.

P4 – Filtration [-], expressed with a five-point scale. The solid deposit and the liquid phase are separated with filtration. After the impregnation, the deposit is only filtered and dried in an oven. However, after the precipitation and coprecipitation, the deposit is first filtered, dried and rinsed, usually with distilled water. Then, the drying procedure is repeated.

P5 – Drying procedure [Kh], expressed with temperature (K) × time (h). The drying of the solid deposit is carried out between 353–383 K for 10 h.

P6 – Calcination parameters [Kh], expressed with temperature (K) × time (h). Dried deposits are calcined in air atmosphere, commonly between 873–973 K for 3–6 h, to prepare mixed oxides.

P7 – Reduction parameters [Kh], expressed with temperature (K) × time (h). To activate the catalysts, mixed oxides are reduced by H₂, usually between 873–973 K for 1–3 h. Metallic Ni is obtained from an oxide precursor and Al₂O₃ remains as the oxide.

P8 – Presence of NiAl₂O₄ [-], expressed with a two-point scale: not present – 0 points, present – 1 point. The NiAl₂O₄ spinel phase, which occurs during the calcination, is highly undesirable due to a low reducibility. Its presence causes a lower amount of the active metallic Ni and lower catalyst performances.

The considered catalyst-synthesis methods are:

CSM1 – Ni/Al₂O₃, 15 % Ni – impregnation – Powder γ -Al₂O₃ and aqueous Ni(NO₃)₂ solution were stirred at room temperature for 24 h and filtered. The deposit was dried at 383 K for 10 h and calcined at 873 K for 3 h. Reduction was performed at 873 K for 2 h.⁴

CSM2 – Ni/Al₂O₃, 15 % Ni – precipitation – The Ni(NO₃)₂ solution was added to the solution of the precipitating agent (Na₂CO₃), which contained the γ -Al₂O₃ powder. After stirring the mixture for 24 h, the deposit was filtered, dried at 353 K for 10 h, then rinsed with distilled water and dried again at 383 K for 10 h. The obtained deposit was calcined at 873 K for 3 h and reduced at 873 K for 2 h.⁴

CSM3 – Ni/Al₂O₃, 15 % Ni – coprecipitation – A solution of Ni(NO₃)₂ and Al(NO₃)₃ was added drop-wise into the Na₂CO₃ solution. After constant stirring at 313 K, the resulting deposit was additionally stirred for 1 h. The filtered deposit was dried at 353 K for 10 h, rinsed with distilled water and then dried at 383 K for 10 h. Calcination parameters were 873 K and 3 h. Reduction was performed at 873 K for 2 h.⁴

CSM4 – Ni/Al₂O₃, 20 % Ni – sequential precipitation – Separate solutions of Ni(NO₃)₂ and Al(NO₃)₃ were prepared. First, a NH₄OH solution was added to the Al(NO₃)₃ solution in order to form a white deposit. Then, the NH₄OH and Ni(NO₃)₂ solutions were slowly added to the solution with the white deposit until a blue deposit was obtained. The resulting product was kept at 293 K for 24 h. The separation of the deposit from the liquid was followed by rinsing with ethanol, drying at 373 K for 10 h, calcination at 973 K for 5 h and reduction at 973 K for 3 h.¹³

CSM5 – Ni/Al₂O₃, 50 % Ni – coprecipitation – Dissolved Ni(NO₃)₂ and Al(NO₃)₃ were mixed with urea (the precipitation agent) and stirred at 358 K for 10 h. The deposit was washed, filtered and dried at 383 K for 10 h. Calcination was carried out at 923 K for 6 h and the catalyst was reduced at 973 K for 1 h.⁹

CSM6 – Ni/Al₂O₃, 50 % Ni – coprecipitation – This catalyst was prepared according to the *CSM5* procedure,

Table 1: Performance matrix: properties of synthesis methods for Ni-based catalysts

Tabela 1: Matrika uspešnosti: lastnosti metod sinteze katalizatorjev na osnovi Ni

Parameter/ catalyst	P1				P2	P3	P4				P5	P6	P7	P8
	DM1	DM2	DM3	Sum			DM1	DM2	DM3	Sum				
CSM1	3	2	3	8	0	7032	3	3	3	9	3830	2619	1746	1
CSM2	4	3	5	12	1	7032	1	1	2	4	7360	2619	1746	0
CSM3	2	1	1	4	1	313	1	1	2	4	7360	2619	1746	1
CSM4	4	3	5	12	1	7032	3	2	3	8	3730	4865	2919	1
CSM5	2	1	1	4	1	3580	3	2	3	8	3830	5538	973	0
CSM6	2	1	1	4	1	3580	3	2	3	8	3830	5538	973	1
CSM7	3	5	4	12	0	473	5	5	5	15	473	0	799,5	0

with the same calcination and reduction conditions. K_2CO_3 was used as the precipitation agent.⁹

CSM7 – Ni-Pd/Al₂O₃, 20 % Ni, 0.1 % Pd – The authors synthesized this catalyst with a novel method, that involved an impregnation of Al₂O₃-based foams with an ultrasonically generated aerosol of chlorides of Ni and Pd. Impregnation was performed for 1 h at 473 K. Afterwards, the chlorides deposited onto the foam were dried at 473 K for 1 h. Calcination was eliminated and the reduction of the chlorides was carried out for 1.5 h at a very low temperature – 533 K. The chlorides were nearly completely reduced and their reduction degree was 98.2 % of mass fractions.¹⁰

The performance matrix, the properties of the catalysts based on system Ni/Al₂O₃ synthesized with different methods, is given in **Table 1**. Parameters P1 and P4 represent the decision makers' preference according to their experience, expressed with points in the range of one to five. The final parameter values for P1 and P4 are obtained as the sum of all decision makers' preferences. The five-point rating scale was used for evaluating parameters P1 and P4, where one point represents the least desirable and five points represent the most desirable solution.

SAW (Simple Additive Weighting), TOPSIS (Technique for Order Preference by Similarity to Ideal Solution) and PROMETHEE II (Preference Ranking Organization METHod for Enrichment Evaluation) methods were used for a multi-criteria assessment of the catalyst-synthesis methods.

SAW is a simple method that usually provides results similar to the ones obtained with more complex methods.¹⁴ After assigning the parameter weighting factors w_j using Equation (1) for every alternative, the total value S_i is calculated, where the best alternative has the largest S_i value:

$$S_i = \sum_{j=1}^m w_j b_{ij}; i=1,2,\dots,n \quad (1)$$

$$\sum_{j=1}^m w_j = 1; \quad 0 \leq w_j \leq 1$$

Normalized performance-matrix elements b_{ij} are calculated with Equations (2) and (3):

$$b_{ij} = \frac{a_{ij} - a_j^-}{a_j^* - a_j^-} \quad (2)$$

for the parameters that have to be maximized,

$$b_{ij} = 1 - \frac{a_{ij} - a_j^-}{a_j^* - a_j^-} \quad (3)$$

for the parameters that have to be minimized,

where: S_i – rating of i th-alternative (alternative rank), w_j – parameter weighting factor, b_{ij} – normalized matrix element, a_{ij} – performance matrix element, a_j^* – j -parameter ideal solution (the maximum value), a_j^- – j -parameter anti-ideal solution (the minimum value), n – number of alternatives, m – number of parameters.

The basic principle of the TOPSIS method is that the chosen alternative should have the shortest distance from the ideal solution and the farthest distance from the negative-ideal solution.¹⁵ The TOPSIS procedure consists of six steps:

1. *Normalization of the performance matrix.* The performance matrix $X_{(n,m)}$, where each matrix row corresponds to one alternative, and each column to a single criterion, is normalized with the following Equation (4):

$$r_{ij} = \frac{x_{ij}}{\sqrt{\sum_{i=1}^n x_{ij}^2}} \quad i = 1, \dots, n, j = 1, \dots, m \quad (4)$$

2. *Calculation of the weighted normalized performance matrix.* Weighted normalized performance-matrix values v_{ij} are calculated in Equation (5) as:

$$v_{ij} = w_j r_{ij} \quad (5)$$

where w_j is the parameter weight and $\sum w_j = 1$.

3. *Determining the ideal and anti-ideal solutions.* The ideal solution A^+ and anti-ideal solution A^- are determined with Equations (6) and (7):

$$A^+ = \{(\max v_{ij} | j \in G), (\min v_{ij} | j \in G^c), i=1, \dots, n\} = \{v_1^+, v_2^+, \dots, v_m^+\} \quad (6)$$

$$A^- = \{(\min v_{ij} | j \in G), (\max v_{ij} | j \in G^c), i=1, \dots, n\} = \{v_1^-, v_2^-, \dots, v_m^-\} \quad (7)$$

where:

$G = \{j = 1, 2, \dots, m \mid j \text{ parameters that have to be maximized}\}$

$G' = \{j = 1, 2, \dots, m \mid j \text{ parameters that have to be minimized}\}$

4. Calculations of the distances from the ideal and anti-ideal solutions.

$$D_i^+ = \sqrt{\sum_{j=1}^m (v_{ij} - v_j^+)^2}, i=1, \dots, n \quad (8)$$

$$D_i^- = \sqrt{\sum_{j=1}^m (v_{ij} - v_j^-)^2}, i=1, \dots, n \quad (9)$$

5. Calculation of relative closeness (RC) to ideal solution.

$$RC_i^+ = \frac{D_i^-}{D_i^+ + D_i^-}, i = 1, \dots, n \quad (10)$$

where $0 \leq RC_i^+ \leq 1$.

6. Ranking of alternatives. Alternatives are ranked by descending values of RC_i^+ .

The PROMETHEE I method provides a partial ranking, while PROMETHEE II provides a complete ranking of alternatives.^{16,17} The main feature of the PROMETHEE method is the fact that for each parameter, the decision maker assigns one of the six predefined preference functions provided in^{16,17}. Only the two preference functions, which are used in this paper, are described here. The usual preference function (Equations (11) and (12)) is used for qualitative criteria (P1 and P4), while a V-shape preference function (Equations (13) and (14)) is used for quantitative criteria (P2, P3, P5, P6, P7, and P8):

$$P_{\text{usual}}(a, b) = \begin{cases} 0, & d(a, b) \leq 0 \\ 1, & d(a, b) > 0 \end{cases} \quad (11)$$

parameters that have to be maximized

$$P_{\text{usual}}(a, b) = \begin{cases} 0, & d(a, b) > 0 \\ 1, & d(a, b) \leq 0 \end{cases} \quad (12)$$

parameters that have to be minimized

$$P_{\text{V-shape}}(a, b) = \begin{cases} \frac{|d(a, b)|}{p}, & d(a, b) \leq p \\ 1, & d(a, b) > p \end{cases} \quad (13)$$

parameters that have to be maximized

$$P_{\text{V-shape}}(a, b) = \begin{cases} \frac{|d(a, b)|}{p}, & d(a, b) > p \\ 1, & d(a, b) \leq p \end{cases} \quad (14)$$

parameters that have to be minimized

where $d_j(a, b)$ is a deviation in the assessment of alternative a over alternative b for each parameter, and p is the preference threshold.

PROMETHEE II can be calculated through the following five steps:

1. Defining the deviations according to pairwise comparisons,

$$d_j(a, b) = g_j(a) - g_j(b) \quad (15)$$

where $d_j(a, b)$ is the deviation in the assessment of alternative a over alternative b for each parameter.

2. Applying the preference functions,

$$P_j(a, b) = F_j[d_j(a, b)]; j=1, 2, \dots, m \quad (16)$$

where $P_j(a, b)$ is the preference of alternative a over alternative b for each parameter, as function $d_j(a, b)$.

3. Calculating the total preference index,

$$\forall a, b \in A, \pi(a, b) = \sum_{j=1}^m P_j(a, b)w_j \quad (17)$$

where $\pi_j(a, b)$, from a to b (from 0 to 1), is defined with the weighted sum $P_j(a, b)$ for each j -parameter, and w_j is the weighting factor of j -parameter.

4. Calculating the positive (ϕ^+) and negative flows (ϕ^-) – PROMETHEE I partial ranking,

$$\phi^+(a) = \frac{1}{n-1} \sum_{x \in A} \pi(a, x) \quad (18)$$

$$\phi^-(a) = \frac{1}{n-1} \sum_{x \in A} \pi(x, a) \quad (19)$$

5. Calculating the net flow (ϕ) – PROMETHEE II complete ranking,

$$\phi(a) = \phi^+(a) - \phi^-(a) \quad (20)$$

Parameter preferences of the decision makers (parameter weight, type, PROMETHEE preference function and preference threshold) for MCA are provided in **Table 2**. Parameter weighting factors (in this case DM1, DM2 and DM3) are assigned by the decision makers, who are experts in field of Nickel-based catalysts, for

Table 2: Parameter preferences

Tabela 2: Nastavitve parametrov

Parameter preferences	P1	P2	P3	P4	P5	P6	P7	P8
Parameter weight (DM1)	1	2	3	2	6	9	7	6
Parameter weight (DM2)	2	2	6	2	8	10	9	6
Parameter weight (DM3)	1	1	5	1	5	9	6	8
Final parameter weight	0.0333	0.0426	0.1204	0.0426	0.1611	0.2407	0.1870	0.1741
Parameter type	Max	Min	Min	Max	Min	Min	Min	Min
PROMETHEE Pref. function	Usual	Usual	V-shape	Usual	V-shape	V-shape	V-shape	Usual
PROMETHEE Pref. threshold	–	–	6000	–	6000	5000	2000	–

each parameter on a ten-point scale. The final, aggregated weighting factor is calculated with the following Equation (21):

$$w_{F,j} = \frac{1}{k} \sum_{k=1}^l \frac{w_{DM,k,j}}{\sum_{j=1}^m w_{DM,k,j}}, j=1, \dots, m; k=1, \dots, l \quad (21)$$

where $w_{F,j}$ is the final weighting factor, $w_{DM,k}$ is the weighting factor of k -th decision maker, m is the number of parameters, l is the number of decision makers.

3 RESULTS AND DISCUSSION

According to the decision makers' preferences (Table 2), parameters P6, P7, P5, and P8 were considered as the most important. The qualitative parameters, obtained on the basis of the decision makers' preferences on the five-point scale, P1 and P4, were considered as the least important by the decision makers. After the decision makers expressed their preferences about the parameters for the catalyst-synthesis methods from Table 2, three MCA methods (SAW, TOPSIS, and PROMETHEE II) were applied in order to obtain the results shown in Figures 1 and 2.

The normalization results of the TOPSIS method (vector normalization), shown in Figure 1, show the "default scenario" without the decision makers' preferences. From Figure 1 it is clear that catalyst Ni-Pd/Al₂O₃ (CSM7) stands out from the rest. The normalization results for catalyst Ni-Pd/Al₂O₃ are affected by the fact that in the performance matrix (Table 1) catalyst Ni-Pd/Al₂O₃ has the best values (ideal solution) for parameters P2, P4, P5, P6 and P7.

As in the normalization results, the results for all three MCA methods (SAW, TOPSIS, PROMETHEE II) shown in Figure 2, indicate that the best ranked catalyst is Ni-Pd/Al₂O₃. When the decision makers' weighting factors are included in the three MCA methods (Figure 2), Ni-Pd/Al₂O₃ is even more distinguished from the other catalysts than in the normalization results (Figure

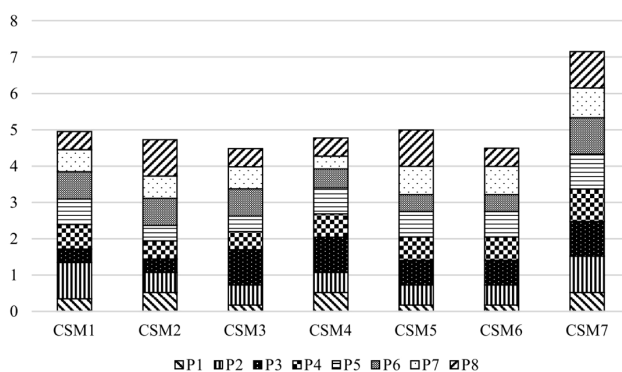


Figure 1: Normalization results (vector normalization) in TOPSIS
Slika 1: Rezultati normalizacije (vektorska normalizacija TOPSIS)

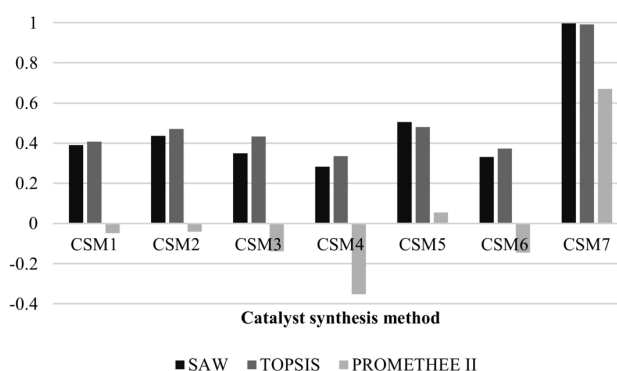


Figure 2: Ranking of catalyst-synthesis methods
Slika 2: Razvrstitev metod sinteze katalizatorja

1). On the other hand, catalyst-synthesis methods CSM3, CSM4 and CSM6 are ranked as the poorest.

4 CONCLUSION

The best ranked catalyst-synthesis method is the novel method for obtaining the Ni-Pd/Al₂O₃ catalyst according to the normalization results (Figure 1) and the results for all three MCA methods (SAW, TOPSIS, PROMETHEE II) (Figure 2). For a multi-criteria analysis, it is common that the results of different methods differ to some extent, as in this case. However, all three methods indicated the Ni-Pd/Al₂O₃ catalyst as the best solution, which is a strong proof that the novel catalyst-synthesis method stands out from the rest.

The Ni-Pd/Al₂O₃ catalyst was synthesized with a novel method, which includes impregnation of Al₂O₃ based foams with an ultrasonically generated aerosol of metal chlorides. The method enabled elimination of the calcination step and the chloride precursors were almost completely reduced (98.2 % of mass fractions) at a very low temperature of 533 K. This may provide economic and technological benefits in the catalyst production process.

Future research will be focused on the life-cycle analysis of the synthesis method for the Ni-Pd/Al₂O₃ catalyst, where the consumption of natural resources and energy sources in the production phase will be analyzed. Assessment results for the life-cycle impact will provide more information about the synthesis method for the Ni-Pd/Al₂O₃ catalyst and environmental impacts on impact categories such as human health, natural resources and ecosystem quality.

Acknowledgement

This research was financially supported by the Ministry of Education, Science and Technological Development of the Republic of Serbia and it is a result of projects Nos. 34033 and 35020.

5 REFERENCES

- ¹ M. Ilić, I. Budak, B. Kosec, A. Nagode, J. Hodolič, The Analysis of Particles Emission During the Process of Grinding of Steel EN 90MnV8, *Metalurgija*, 53 (2014), 189–192
- ² A. N. Fatsikostas, D. I. Kondarides, X. E. Verykios, Production of hydrogen for fuel cells by reformation of biomass-derived ethanol, *Catalysis Today*, 75 (2002), 145–155, doi:10.1016/S0920-5861(02)00057-3
- ³ L. P. R. Profeti, J. A. C. Dias, J. M. Assaf, E. M. Assaf, Hydrogen production by steam reforming of ethanol over Ni-based catalysts promoted with noble metals, *Journal of Power Sources*, 190 (2009), 525–533, doi:10.1016/j.jpowsour.2008.12.104
- ⁴ A. J. Akande, R. O. Idem, A. K. Dalai, Synthesis, characterization and performance evaluation of Ni/Al₂O₃ catalysts for reforming of crude ethanol for hydrogen production, *Applied Catalysis A: General*, 287 (2005), 159–175, doi:10.1016/j.apcata.2005.03.046
- ⁵ A. J. Zhang, A. M. Zhu, J. Guo, Y. Xu, C. Shi, Conversion of greenhouse gases into syngas via combined effects of discharge activation and catalysis, *Chemical Engineering Journal*, 156 (2010), 601–606, doi:10.1016/j.cej.2009.04.069
- ⁶ M. A. Goula, S. K. Kontou, P. E. Tsiakaras, Hydrogen production by ethanol steam reforming over a commercial Pd/γ-Al₂O₃ catalyst, *Applied Catalysis B: Environmental*, 49 (2004), 135–144, doi:10.1016/j.apcatb.2003.12.001
- ⁷ D. K. Liguras, D. I. Kondarides, X. E. Verykios, Production of hydrogen for fuel cells by steam reforming of ethanol over supported noble metal catalysts, *Applied Catalysis B: Environmental*, 43 (2003), 345–354, doi:10.1016/S0926-3373(02)00327-2
- ⁸ J. Juan-Juan, M. C. Roman-Martinez, M. J. Illan-Gomez, Nickel catalyst activation in the carbon dioxide reforming of methane: Effect of pretreatments, *Applied Catalysis A: General*, 355 (2009), 27–32, doi:10.1016/j.apcata.2008.10.058
- ⁹ Y. Jung, W. Yoon, Y. Seo, Y. Rhee, The effect of precipitants on Ni-Al₂O₃ catalysts prepared by a co-precipitation method for internal reforming in molten carbonate fuel cells, *Catalysis Communications*, 26 (2012), 103–111, doi:10.1016/j.catcom.2012.04.029
- ¹⁰ V. Nikolić, Ž. Kamberović, Z. Anđić, M. Korać, M. Sokić, V. Maksimović, Influences of synthesis methods and modifier addition on the properties of Ni-based catalysts supported on reticulated ceramic foams, *International Journal of Minerals, Metallurgy, and Materials*, 21 (2014), 806–812, doi:10.1007/s12613-014-0974-x
- ¹¹ V. Nikolić, Ž. Kamberović, Z. Anđić, M. Korać, M. Sokić, Synthesis of α-Al₂O₃ based foams with improved properties as catalyst carriers, *Mater. Tehnol.*, 48 (2014), 45–50
- ¹² V. Nikolić, Ž. Kamberović, M. Korać, Z. Anđić, M. Sokić, A. Tomović, Ni-Pd/Al₂O₃ catalyst supported on reticulated ceramic foam for dry methane reforming, *Metallurgical and Materials Engineering*, 21 (2015), 57–63
- ¹³ J. G. Seo, M. H. Youn, D. R. Park, I. Nam, I. K. Song, Hydrogen production by steam reforming of liquefied natural gas (LNG) over Ni–Al₂O₃ catalysts prepared by a sequential precipitation method: Effect of precipitation agent, *International Journal of Hydrogen Energy*, 34 (2009), 8053–8060, doi:10.1016/j.ijhydene.2009.08.020
- ¹⁴ E. Triantaphyllou, *Multi-Criteria Decision Making: A Comparative Study*, Kluwer Academic Publishers (Springer), Dordrecht, The Netherlands 2000, 320
- ¹⁵ C. L. Hwang, K. Yoon, *Multiple Attribute Decision Making*, Lecture Notes in Economics and Mathematical Systems 186, Springer-Verlag, Berlin 1981
- ¹⁶ J. P. Brans, *L'ingenierie de la decision, Elaboration dinstruments daide a la decision, Methode PROMETHEE, Laide a la Decision: Nature, Instruments et Perspectives d'Avenir*, Presses de l'Université Laval, Québec, Canada, 1982, 183–214
- ¹⁷ J. P. Brans, B. Mareschal, *The PROMETHEE methods for MCDM, the PROMCALC, GAIA and Bankadviser Software*, Working Paper ST001224, Vrije Universiteit, Brussel 1989

INFLUENCE OF STRUCTURAL DEFECTS ON THE MAGNETIC PROPERTIES OF MASSIVE AMORPHOUS $\text{Fe}_{60}\text{Co}_{10}\text{Mo}_2\text{W}_x\text{Y}_8\text{B}_{20-x}$ ($x = 1, 2$) ALLOYS PRODUCED WITH THE INJECTION CASTING METHOD

VPLIV STRUKTURNIH NAPAK NA MAGNETNE LASTNOSTI MASIVNE AMORFNE ZLITINE $\text{Fe}_{60}\text{Co}_{10}\text{Mo}_2\text{W}_x\text{Y}_8\text{B}_{20-x}$ ($x = 1, 2$), IZDELANE Z METODO LITJA Z VBRIZGAVANJEM

Joanna Gondro, Katarzyna Bloch, Marcin Nabialek, Sebastian Garus

Institute of Physics, Faculty of Production Engineering and Materials Technology, Czestochowa University of Technology,
Al. Armii Krajowej 19, 42-200 Czestochowa, Poland
j.gondro@wp.pl

Prejem rokopisa – received: 2015-06-30; sprejem za objavo – accepted for publication: 2015-07-29

doi:10.17222/mit.2015.148

This paper presents the results of research pertaining to high-field magnetic properties, in relation to the theory of H. Kronmüller. Studies were performed on bulk amorphous alloys featuring composition $\text{Fe}_{60}\text{Co}_{10}\text{Mo}_2\text{W}_x\text{Y}_8\text{B}_{20-x}$ ($x = 1, 2$). Samples were produced in the form of plates with a thickness of 0.5 mm; they were prepared by injecting the molten alloy into a water-cooled copper mould. The influence of structural defects on the magnetization process was investigated within high magnetic fields known as the area of the approach to ferromagnetic saturation. For the investigated samples, the studies showed that, in the process of magnetization in high magnetic fields, rotation of the magnetization vector was mainly due to the presence of linear defects in the structure, i.e., quasidislocational dipoles. The density of quasidislocational dipoles in a sample with an addition of 1 % W was nearly twice as high as that of an alternative alloy.

Keywords: bulk amorphous alloy, metallic glasses, high magnetic fields, magnetization, structural defects, relaxation

Članek predstavlja rezultate raziskav, ki se nanašajo na visokomagnetne lastnosti, v povezavi s teorijo H. Kronmüllerja. Študije so bile izvedene na masivni amorfnih zlitini s sestavo $\text{Fe}_{60}\text{Co}_{10}\text{Mo}_2\text{W}_x\text{Y}_8\text{B}_{20-x}$ ($x = 1, 2$). Vzorci so bili izdelani v obliki ploščic debeline 0,5 mm, izdelane z vbrizgavanjem staljene zlitine v vodno hlajeno bakreno kokilo. Preiskovan je bil vpliv napak v strukturi na proces magnetizacije v visokomagnetnih poljih, poznanih kot področje približka k feromagnetnemu nasičenju. Za preiskovane vzorce so raziskave pokazale, da pri procesu magnetizacije v visoko magnetnih poljih pride do rotacije magnetnega vektorja predvsem zaradi prisotnosti linearnih napak v strukturi: to so kvazidislokacijski dipoli. Gostota dislokacijskih dipolov v vzorcu, z dodatkom 1 % W, je bila skoraj dvakrat višja kot pa pri drugi zlitini.

Ključne besede: masivna amorfn zlitina, kovinska stekla, visokomagnetno polje, magnetizacija, napake v strukturi, relaksacija

1 INTRODUCTION

Within the past decade, a group of materials known as ‘bulk amorphous alloys’ have been studied intensely;¹⁻⁴ This interest is associated with their excellent soft-magnetic and mechanical properties, which facilitate their application. The amorphous alloys can be classified into two categories: classic (in the form of thin ribbons with a thickness of up to 100 μm) and bulk amorphous alloys (with a thickness greater than 100 μm). The bulk amorphous alloys are characterised by properties, which are very difficult or even impossible to achieve in the classic, ribbon-shaped, amorphous alloys.^{5,6} The group of bulk amorphous alloys includes: ribbons with a thicknesses of approximately 100 μm , plates and rods with diameters of a few millimetres, and cores that can feature complex shapes.⁷

Although the finished amorphous alloys are in the solid state, the constituent particles are distributed in a chaotic way; their configuration is closer to that of the

liquid state.⁸ These alloys are characterised by a lack of a long-range order and they exist in a metastable state. If a sufficient quantity of energy is delivered to these metastable materials, the crystallisation process will be activated; therefore, this value of energy is called the activation energy. The barriers to their crystallisation, during the rapid-quenching process from the liquid state (10^4 – 10^6 K/s), are mainly their high viscosity and the presence of inclusions within their volumes.

The bulk amorphous alloys consist of more than three elements and they are based mostly on Pd, Zr, Ti, Al, Mg, Fe or Cu. The group with the highest prospects for applications is based on Fe. Given an appropriate composition of this type of alloy, it is possible to obtain a material with a stable structure and excellent magnetic properties – both hard and soft. These properties are often determined by local stresses in the structure, resulting from the existence of structural defects. In the case of crystalline materials, these irregularities are point and linear defects; their counterparts in the amorphous

materials are free volumes and quasidislocational dipoles.

Defects are usually the result of the production process itself, being a by-product of the rapid solidification, "freezing" the structure. The resulting free volumes facilitate short- and long-distance movement of the atoms within the systems of atomic pairs.^{8,9} The free volumes created in a relatively slow solidification process, below the glass transition temperature, have the ability to create cluster systems. These clusters are systems with a low stability and, as a result of the atomic movement, they disintegrate into simpler, two-dimensional systems called quasidislocational dipoles.^{10,11} A direct observation of the structural defects of an amorphous structure is very difficult; therefore, the indirect method is used. This method involves observation and analysis of the initial magnetisation curve, according to the H. Kronmüller theorem.¹² On the basis of the modified Brown micromagnetism theorem¹³, H. Kronmüller showed that structural defects in the ferromagnetic materials with soft magnetic properties are the source of internal stresses, causing a locally inhomogeneous distribution of the magnetisation vector. The presence of these stresses in an amorphous material prevents the achievement of the state of ferromagnetic saturation, even under the influence of a strong magnetic field.¹²

The magnetisation of the amorphous alloys within high magnetic fields, in the so-called "approach to the ferromagnetic saturation" region, could be described using the following Equation (1):⁹

$$\mu_0 M(H) = \mu_0 M_s \left[1 - \frac{a_{1/2}}{(\mu_0 H)^{1/2}} - \frac{a_1}{(\mu_0 H)^1} - \frac{a_2}{(\mu_0 H)^2} \right] + b(\mu_0 H)^{1/2} \quad (1)$$

where:

M_s – spontaneous magnetization; μ_0 – magnetic permeability of a vacuum; H – magnetic field; a_i – directional coefficients of the linear fit (free volumes and linear defects $i = 1/2, 1, 2$); b – directional coefficient of the linear fit.

The b coefficient is calculated on the basis of the spin-wave theorem and connected with the spin-wave stiffness parameter (D_{sp}) with the following relation:^{14–16}

$$b = 3.54 g \mu_0 \mu_B \left(\frac{1}{4\pi D_{sp}} \right)^{3/2} k_B T (g \mu_B)^{1/2} \quad (2)$$

where:

μ_B – Bohr magneton, k_B – Boltzmann constant, g – gyromagnetic coefficient, T – temperature.

The strongest influence on the stresses, connected with the existence of free volumes, is observed for the $a_{1/2}$ coefficient:

$$\frac{a_{1/2}}{(\mu_0 H)^{1/2}} = \mu_0 \frac{3}{20 A_{ex}} \left(\frac{1+r}{1-r} \right)^2 \cdot G^2 \lambda_s^2 (\Delta V)^2 N \left(\frac{2 A_{ex}}{\mu_0 M_s} \right)^{1/2} \frac{1}{(\mu_0 H)^{1/2}} \quad (3)$$

where:

N – volume density of point defects, ΔV – volume change caused by point defects, A_{ex} – exchange constant, r – Poisson number, G – transverse elasticity modulus, λ_s – saturation magnetostriction.

The elements $a_1/\mu_0 H$ and $a_2/(\mu_0 H)^2$ are connected with the linear, elongated agglomerates of free volumes, in which the internal stress field is equivalent to the field created by linear dislocation dipoles with a width of D_{dip} , the effective Burgers vector b_{eff} and the surface density of N . The stresses related to these defects cause a non-collinear distribution of the magnetic moments in their vicinity:¹⁷

$$\frac{a_1}{(\mu_0 H)} = 1.1 \mu_0 \frac{G^2 \lambda_s^2}{(1-V)^2} \frac{N b_{eff}}{M_s^2} D_{dip}^2 \frac{1}{(\mu_0 H)^2} \quad (4)$$

This situation exists, when $l_H^{-1} D_{dip} < 1$, and l_H is the exchange distance given with the following equation:^{18,19}

$$l_H = \left(\frac{2 A_{ex}}{\mu_0 H M_s} \right)^{1/2} \quad (5)$$

In the case where $l_H^{-1} D_{dip} > 1$, the dominant element influencing the magnetisation process, according to Equation (1), is $a_2/(\mu_0 H)^2$; this is described with Equation (6):

$$\frac{a_2}{(\mu_0 H)^2} = 0.456 \mu_0 \frac{G^2 \lambda_s^2}{(1-V)^2} \frac{N b_{eff}}{M_s^2} D_{dip}^2 \frac{1}{(\mu_0 H)^2} \quad (6)$$

In Equation (1), each separate element exerts a major influence on the magnetisation process in the approach to the ferromagnetic saturation region, in strictly defined ranges of the magnetic field. Therefore, it is possible to define the influence of structural defects, inherent in amorphous materials, on the magnetisation process within high magnetic fields. On the basis of "defined" defects, their packing density within the alloy volume can be calculated using Equations (3), (4) and (6).²⁰

2 MATERIALS AND METHODS

In this paper, results of investigations are presented for the samples obtained by injecting liquid alloy into a water-cooled copper die under a protective atmosphere of inert gas (Ar). The manufactured samples were in the form of plates with an approximate width of 10 mm and a thickness of 0.5 mm. The nominal compositions of the investigated alloys, $Fe_{60}Co_{10}Mo_2W_xY_8B_{20-x}$ ($x = 1, 2$), were obtained by weighing high-purity (99.9 %) components.

The structure of the resulting alloys was investigated by means of an X-ray diffractometer. The BRUKER "ADVANCE D8" X-ray diffractometer was equipped with a Cu- K_{α} radiation source. The samples were studied within a 2θ range of $30\text{--}120^{\circ}$ with a measurement step size of 0.02° and an exposure time of 5 s per step. Measurements of magnetization were performed over a magnetic field range of $0\text{--}2$ T using a vibrating sample magnetometer (VSM).

3 RESULTS AND DISCUSSION

X-ray diffraction (XRD) curves for the investigated alloys are presented in **Figure 1**. These curves feature only one broad maximum, as characteristic of amorphous materials.

Static hysteresis loops were found to exhibit shapes typical for ferromagnetic materials, which exhibit soft magnetic properties (**Figure 2**).

The value of the coercive field was obtained from an analysis of the static hysteresis loops, being 8705.57 A/m for the $\text{Fe}_{60}\text{Co}_{10}\text{W}_1\text{Mo}_2\text{Y}_8\text{B}_{19}$ alloy and 4610.88 A/m for $\text{Fe}_{60}\text{Co}_{10}\text{W}_2\text{Mo}_2\text{Y}_8\text{B}_{18}$ (**Figure 3**).

From an analysis of the magnetisation as a function of magnetic-field induction curves, it was found that the magnetisation process in the $\text{Fe}_{60}\text{Co}_{10}\text{W}_1\text{Mo}_2\text{Y}_8\text{B}_{19}$ alloy (**Figures 4 to 6**), where the domain structure is not

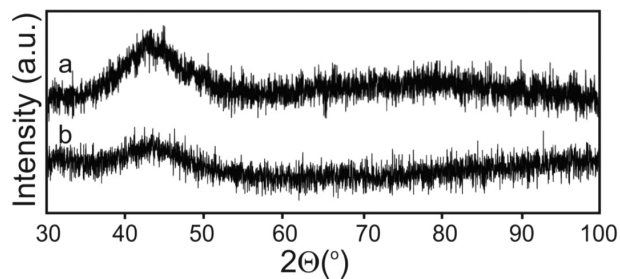


Figure 1: X-ray diffraction patterns for powdered as-quenched samples: a) $\text{Fe}_{60}\text{Co}_{10}\text{W}_1\text{Mo}_2\text{Y}_8\text{B}_{19}$ and b) $\text{Fe}_{60}\text{Co}_{10}\text{W}_2\text{Mo}_2\text{Y}_8\text{B}_{18}$

Slika 1: Rentgenska difrakcija kaljenih vzorcev prahu: a) $\text{Fe}_{60}\text{Co}_{10}\text{W}_1\text{Mo}_2\text{Y}_8\text{B}_{19}$ in b) $\text{Fe}_{60}\text{Co}_{10}\text{W}_2\text{Mo}_2\text{Y}_8\text{B}_{18}$

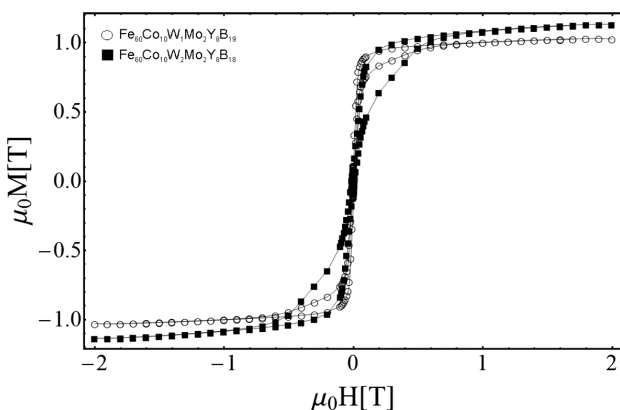


Figure 2: Static hysteresis loops obtained for the investigated alloys

Slika 2: Statične histerezne zanke, dobljene pri preiskovanih zlitinah

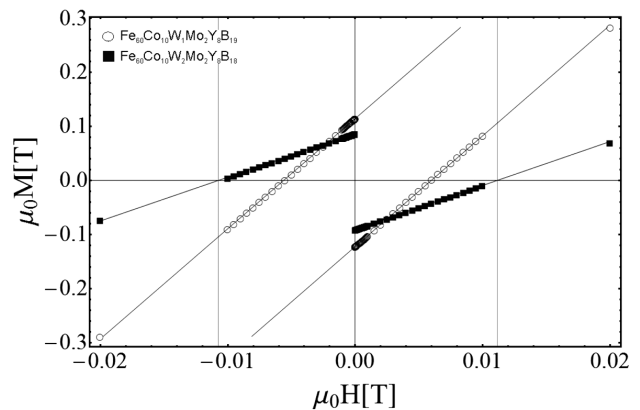


Figure 3: Coercive field obtained from the analysis of the static hysteresis loops for the investigated alloys

Slika 3: Koercitivno polje, dobljeno iz analize statičnih histereznih zank pri preiskovanih zlitinah

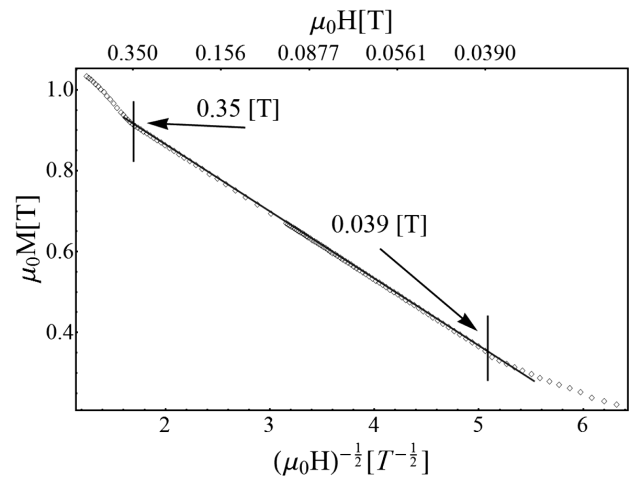


Figure 4: Curves of high-field magnetization as a function of $(\mu_0H)^{-1/2}$, for a plate-shaped sample of $\text{Fe}_{60}\text{Co}_{10}\text{W}_1\text{Mo}_2\text{Y}_8\text{B}_{19}$ alloy

Slika 4: Krivulje visokopoljske magnetizacije kot funkcija $(\mu_0H)^{-1/2}$ pri ploščatih vzorcih iz zlitine $\text{Fe}_{60}\text{Co}_{10}\text{W}_1\text{Mo}_2\text{Y}_8\text{B}_{19}$

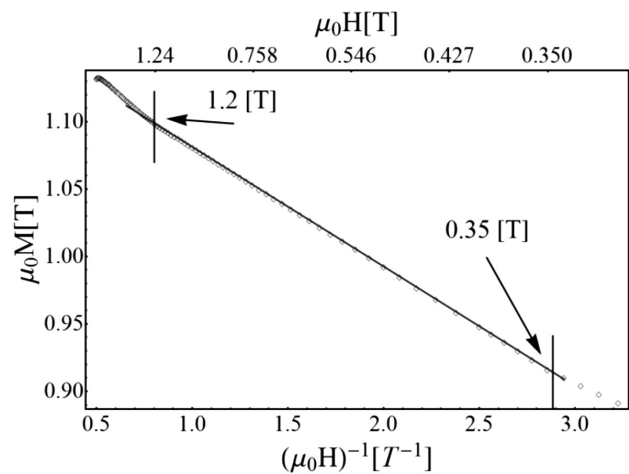


Figure 5: Curves of high-field magnetisation as a function of $(\mu_0H)^{-1}$, for a plate-shaped sample of $\text{Fe}_{60}\text{Co}_{10}\text{W}_1\text{Mo}_2\text{Y}_8\text{B}_{19}$ alloy

Slika 5: Krivulje visokopoljske magnetizacije kot funkcija $(\mu_0H)^{-1}$ pri ploščatih vzorcih iz zlitine $\text{Fe}_{60}\text{Co}_{10}\text{W}_1\text{Mo}_2\text{Y}_8\text{B}_{19}$

Table 1: Results of the analysis of magnetisation as a function of magnetic field to the powers of $^{-1/2}$, $^{-1}$ and $^{1/2}$; spin-wave stiffness parameter D_{spf} and N_{dip} – density of quasislational dipoles

Tabela 1: Rezultati preizkusa magnetizacije kot funkcije magnetnega polja na potenco $^{-1/2}$, $^{-1}$ in $^{1/2}$; parametra vrtilno-valovne togosti D_{spf} in gostote kvazidisllokacijskih dipolov N_{dip}

Composition	$a_{1/2}$ ($\text{T}^{-1/2}$)	a_1 (T^{-1})	b ($\text{T}^{-1/2}$)	D_{spf} (meVnm^2)	N_{dip} (10^{16}m^{-2})
$\text{Fe}_{60}\text{Co}_{10}\text{W}_1\text{Mo}_2\text{Y}_8\text{B}_{19}$	0.166	0.089	0.108	29	51
$\text{Fe}_{60}\text{Co}_{10}\text{W}_2\text{Mo}_2\text{Y}_8\text{B}_{18}$	0.611	0.040	0.085	34	30

present, is influenced by two types of defect: point defects, indicated, in **Figure 4**, by the linear relationship of magnetisation as a function of $(\mu_0 H)^{-1/2}$ over a magnetic field range of 0.039–35 T and linear defects (called quasislational dipoles), indicated, in **Figure 5**, by the linear relationship of magnetisation as a function of $(\mu_0 H)^{-1}$ over a magnetic field range of 0.35–1.2 T. In a strong magnetic field, i.e., greater than 1.2 T, a small increase in the magnetisation is connected with the

dumping of thermally induced spin waves by the strong magnetic field (**Figure 6**).

The high-field magnetisation curves for the $\text{Fe}_{60}\text{Co}_{10}\text{W}_2\text{Mo}_2\text{Y}_8\text{B}_{18}$ alloy are presented in **Figures 7 to 9**. Similarly, in the case of this alloy, the magnetisation process is connected with the rotation of magnetic moments around the point defects (**Figure 7**) and linear defects (**Figure 8**), for which the relationship $l_{\text{H}}^{-1} D_{\text{dip}} < 1$ was fulfilled. The further increase in the magnetisation is

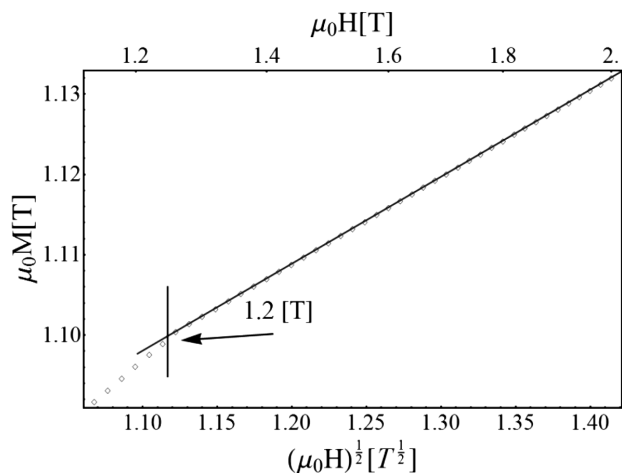


Figure 6: Curves of high-field magnetisation as a function of $(\mu_0 H)^{1/2}$, for a plate-shaped sample of $\text{Fe}_{60}\text{Co}_{10}\text{W}_1\text{Mo}_2\text{Y}_8\text{B}_{19}$ alloy
Slika 6: Krivulje visokopoljske magnetizacije, kot funkcija $(\mu_0 H)^{1/2}$ pri ploščatih vzorcih iz zlitine $\text{Fe}_{60}\text{Co}_{10}\text{W}_1\text{Mo}_2\text{Y}_8\text{B}_{19}$

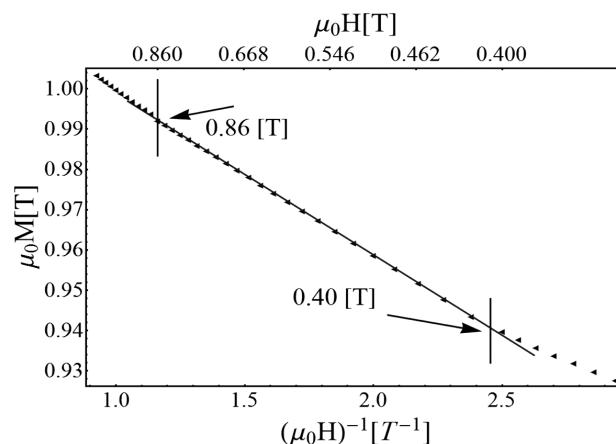


Figure 8: Curves of high-field magnetisation as a function of $(\mu_0 H)^{-1}$, for a plate-shaped sample of $\text{Fe}_{60}\text{Co}_{10}\text{W}_2\text{Mo}_2\text{Y}_8\text{B}_{18}$ alloy
Slika 8: Krivulje visokopoljske magnetizacije, kot funkcija $(\mu_0 H)^{-1}$ pri ploščatih vzorcih iz zlitine $\text{Fe}_{60}\text{Co}_{10}\text{W}_2\text{Mo}_2\text{Y}_8\text{B}_{18}$

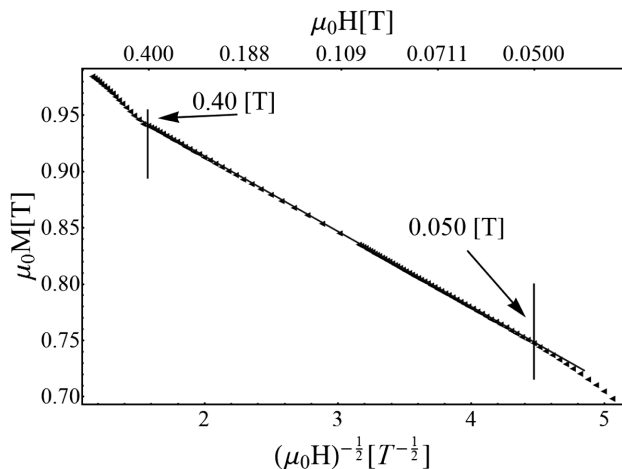


Figure 7: Curves of high-field magnetisation as a function of $(\mu_0 H)^{-1/2}$, for a plate-shaped sample of $\text{Fe}_{60}\text{Co}_{10}\text{W}_2\text{Mo}_2\text{Y}_8\text{B}_{18}$ alloy
Slika 7: Krivulje visokopoljske magnetizacije, kot funkcija $(\mu_0 H)^{-1/2}$ pri ploščatih vzorcih iz zlitine $\text{Fe}_{60}\text{Co}_{10}\text{W}_2\text{Mo}_2\text{Y}_8\text{B}_{18}$

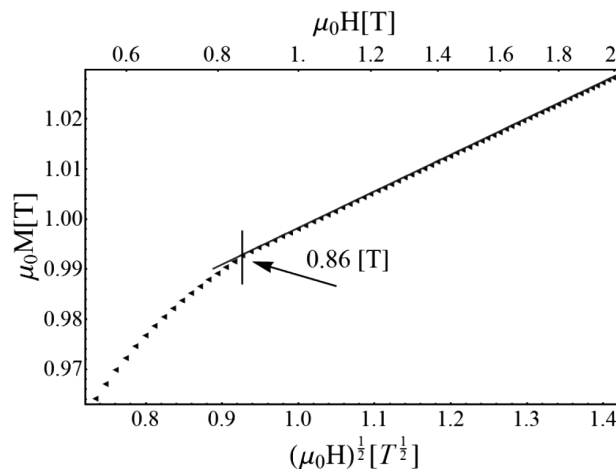


Figure 9: Curves of high-field magnetisation as a function of $(\mu_0 H)^{1/2}$, for a plate-shaped sample of $\text{Fe}_{60}\text{Co}_{10}\text{W}_2\text{Mo}_2\text{Y}_8\text{B}_{18}$ alloy
Slika 9: Krivulje visokopoljske magnetizacije, kot funkcija $(\mu_0 H)^{1/2}$ pri ploščatih vzorcih iz zlitine $\text{Fe}_{60}\text{Co}_{10}\text{W}_2\text{Mo}_2\text{Y}_8\text{B}_{18}$

related with the existence of the Holstein-Primakoff paraprocess (**Figure 9**).^{21,22}

The parameters obtained from the analysis of the high-field magnetization curves, obtained for both alloys, are presented in **Table 1**.

4 CONCLUSIONS

During the production process involving bulk amorphous alloys, structural relaxations occur, leading to a more stable structure. This process influences both topological (TSRO) and chemical (CSRO) short-range ordering. Changes in TSRO are irreversible and connected with the decreases in the volume and redistribution of free volumes.²³ As a result, the average distance between the atoms decreases and this, in turn, causes an increase in the atomic packing density.

On the basis of the obtained results of the current investigations, it could be stated that the investigated alloys are amorphous. The value of the coercivity for $\text{Fe}_{60}\text{Co}_{10}\text{W}_2\text{Mo}_2\text{Y}_8\text{B}_{18}$ is half the value for the other alloy.

On the basis of the magnetisation studies, carried out in strong magnetic fields, it was found that for both alloys the magnetisation process was influenced by the presence of point defects and quasidislocational dipoles. Also, the dumping of thermally induced spin waves by the magnetic field (Holstein-Primakoff paraprocess) has an influence on the magnetisation process. In the case of the $\text{Fe}_{60}\text{Co}_{10}\text{W}_2\text{Mo}_2\text{Y}_8\text{B}_{18}$ alloy, both the $a^{1/2}$, and a^1 coefficients are half the equivalent values found for the $\text{Fe}_{60}\text{Co}_{10}\text{W}_1\text{Mo}_2\text{Y}_8\text{B}_{19}$ alloy. Also, the value of the density of the quasidislocational dipoles N_{dip} is almost halved for the alloy with a higher tungsten content. These values indicate a higher atomic packing density in the $\text{Fe}_{60}\text{Co}_{10}\text{W}_2\text{Mo}_2\text{Y}_8\text{B}_{18}$ alloy. The analysis of the high-field magnetisation curves facilitated the calculation of the spin-wave stiffness parameter, D_{spf} , which is connected with the changes in the chemical and topological atomic ordering. The higher value of this parameter for the sample of the $\text{Fe}_{60}\text{Co}_{10}\text{W}_2\text{Mo}_2\text{Y}_8\text{B}_{18}$ alloy indicates a high concentration of magnetic atoms in a given volume and confirms that the alloy has a higher atomic packing density.

On the basis of the performed investigations, it can be stated that an addition of 1 % (by weight) of tungsten, replacing boron, caused a decrease in the number of defects present in the investigated material and an increase in the value of the spin-wave stiffness parameter D_{spf} . This indicates that, during the solidification process of the $\text{Fe}_{60}\text{Co}_{10}\text{W}_2\text{Mo}_2\text{Y}_8\text{B}_{18}$ alloy, structural relaxations caused more atoms to take locally ordered positions. In turn, this led to a decrease in the size of free volumes and an increase in the atomic packing density within the structure.

5 REFERENCES

- 1 T. Thomas, M. R. J. Gibbs, Anisotropy and magnetostriction in metallic glasses, *Journal of Magnetism and Magnetic Materials*, 103 (1992), 97–110, doi:10.1016/0304-8853(92)90242-G
- 2 K. Sobczyk, J. Świerczek, J. Gondro, J. Zbrozarczyk, W. Ciużyńska, J. Olszewski, P. Brągiel, A. Łukiewska, J. Rzącki, M. Nabiałek, Microstructure and some magnetic properties of bulk amorphous $(\text{Fe}_{0.61}\text{Co}_{0.10}\text{Zr}_{0.025}\text{Hf}_{0.025}\text{Ti}_{0.02}\text{W}_{0.02}\text{B}_{0.20})_{100-x}\text{Y}_x$ ($x=0, 2, 3$ or 4) alloys, *Journal of Magnetism and Magnetic Materials*, 324 (2012), 540–549, doi:10.1016/j.jmmm.2011.08.038
- 3 M. Hasiak, K. Sobczyk, J. Zbrozarczyk, W. Ciużyńska, J. Olszewski, M. Nabiałek, J. Kaleta, J. Świerczek, A. Łukiewska, Some magnetic properties of bulk amorphous Fe-Co-Zr-Hf-Ti-W-B-(Y) alloys, *IEEE Transactions on Magnetics*, 11 (2008), 3879–3882, doi:10.1109/TMAG.2008.2002248
- 4 A. Brand, Improving the validity of hyperfine field distributions from magnetic alloys: Part I: Unpolarized source, *Nuclear Instruments and Methods in Physics Research Section B*, B28 (1987), 398–416, doi:10.1016/0168-583X(87)90182-0
- 5 M. Nabiałek, Soft magnetic and microstructural investigation in Fe-based amorphous alloy, *Journal of Alloys and Compounds*, 642 (2015), 98–103, doi:10.1016/j.jallcom.2015.03.250
- 6 J. Olszewski, J. Zbrozarczyk, K. Sobczyk, W. Ciużyńska, P. Brągiel, M. Nabiałek, J. Świerczek, A. Łukiewska, Thermal stability and crystallization of iron and cobalt-based bulk amorphous alloys, *Acta Physica Polonica A*, 114 (2008) 6, 1659–1666
- 7 A. Inoue, Bulk amorphous alloys with soft and hard magnetic properties, *Materials Science and Engineering A*, A226–228 (1997), 357–363, doi:10.1016/S0921-5093(97)80049-4
- 8 H. Kronmüller, Micromagnetism and microstructure of amorphous alloys (invited), *Journal of Applied Physics*, 52 (1981), 1859–1864, doi:10.1063/1.329552
- 9 H. Kronmüller, Magnetization processes and the microstructure in amorphous metals, *Journal de Physique Colloques*, 41 (1980) C8, C8-618-C8-625, doi:10.1051/jphyscol:19808156. jpa-00220256
- 10 H. Kronmüller, J. Ulner, Micromagnetic theory of amorphous ferromagnets, *Journal of Magnetism and Magnetic Materials*, 6 (1977), 52–56, doi:10.1016/0304-8853(77)90073-7
- 11 K. Bloch, M. Nabiałek, The influence of heat treatment on irreversible structural relaxation in bulk amorphous $\text{Fe}_{61}\text{Co}_{10}\text{Ti}_3\text{Y}_6\text{B}_{20}$ alloy, *Acta Physica Polonica A*, 127 (2015) 2, 442–444, doi:10.12693/APhysPolA.127.442
- 12 H. Kronmüller, Micromagnetism in amorphous alloys, *IEEE Transactions on Magnetics*, 15 (1979) 5, 1218–1225, doi:10.1109/TMAG.1979.1060343
- 13 W. F. Brown Jr., *Micromagnetics*, Interscience Tracts on Physics and Astronomy, Interscience Publishers (John Wiley & Sons), New York, London 1963
- 14 O. Kohmoto, High-field magnetization curves of amorphous alloys, *Journal of Applied Physics*, 53 (1982), 7486–7490, doi:10.1063/1.330121
- 15 M. Nabiałek, P. Pietrusiewicz, M. Dośpiał, M. Szota, J. Gondro, K. Gruszka, A. Dobrzańska-Danikiewicz, S. Walters, A. Bukowska, Effect of manufacturing method on the magnetic properties and formation of structural defects in $\text{Fe}_{61}\text{Co}_{10}\text{Y}_8\text{Zr}_1\text{B}_{20}$ amorphous alloy, *Journal of Alloys and Compounds*, 615 (2015), S56–S60, doi:10.1016/j.jallcom.2013.12.236
- 16 M. Nabiałek, M. Dośpiał, M. Szota, P. Pietrusiewicz, Influence of Solidification Speed on Quality and Quantity of Structural Defects in $\text{Fe}_{61}\text{Co}_{10}\text{Zr}_{2.5}\text{Hf}_{2.5}\text{Y}_2\text{W}_2\text{B}_{20}$ Amorphous Alloy, *Materials Science Forum*, 654–656 (2010), 1074–1077, doi:10.4028/www.scientific.net/MSF.654-656.1074
- 17 M. Vázquez, W. Fernengel, H. Kronmüller, Approach to magnetic saturation in rapidly quenched amorphous alloys, *Physica Status Solidi A*, 115 (1989) 2, 547–553, doi:10.1002/pssa.2211150223

- ¹⁸ M. Hischer, R. Reisser, R. Würschum, H. E. Schaefer, H. Kronmüller, Magnetic after-effect and approach to ferromagnetic saturation in nanocrystalline iron, *Journal of Magnetism and Magnetic Materials*, 146 (1995), 117–122, doi:10.1016/0304-8853(94)01643-7
- ¹⁹ N. Lenge, H. Kronmüller, Low temperature magnetization of sputtered amorphous Fe-Ni-B films, *Physica Status Solidi A*, 95 (1986), 621–633, doi:10.1002/pssa.2210950232
- ²⁰ P. Pietrusiewicz, K. Błoch, M. Nabiałek, S. Walters, Influence of 1 % addition of Nb and W on the relaxation process in classical Fe-based amorphous alloys, *Acta Physica Polonica A*, 127 (2015) 2, 397–399, doi:10.12693/APhysPolA.127.397
- ²¹ T. Holstein, H. Primakoff, Field dependence of the intrinsic domain magnetization of a ferromagnet, *Physical Review Letters*, 58 (1940) 12, 1098–1113, doi:10.1103/PhysRev.58.1098
- ²² K. Błoch, M. Nabiałek, Approach to ferromagnetic saturation for the bulk amorphous alloy: $(\text{Fe}_{0.61}\text{Co}_{0.10}\text{Zr}_{0.025}\text{Hf}_{0.025}\text{Ti}_{0.02}\text{W}_{0.02}\text{B}_{0.20})_{97}\text{Y}_3$, *Acta Physica Polonica A*, 127 (2015) 2, 413–414, doi:10.12693/APhysPolA.127.413
- ²³ F. F. Marzo, A. R. Pierna, M. M. Vega, Effect of irreversible structural relaxation on the electrochemical behavior of $\text{Fe}_{78-x}\text{Si}_{13}\text{B}_9\text{Cr}_{(x=3,4,7)}$ amorphous alloys, *Journal of Non-Crystalline Solids*, 329 (2003), 108–114, doi:10.1016/j.jnoncrysol.2003.08.022

POSSIBILITIES OF NUS AND IMPACT-ECHO METHODS FOR MONITORING STEEL CORROSION IN CONCRETE

MOŽNOSTI METOD NUS IN UDAREC-ODMEV ZA KONTROLO KOROZIJE JEKLA V BETONU

Kristýna Timčaková-Šamárková, Michal Matysík, Zdeněk Chobola

Brno University of Technology, Faculty of Civil Engineering, Institute of Physics, Veverí 331/95, 602 00 Brno, Czech Republic
samarkova.k@fce.vutbr.cz

Prejem rokopisa – received: 2015-06-30; sprejem za objavo – accepted for publication: 2015-08-25

doi:10.17222/mit.2015.149

The corrosion of steel elements in reinforced concrete can cause considerable damage to civil-engineering structures. Early detection of rust is therefore very important. The aim of this paper is to evaluate the possibility of using nonlinear ultrasonic spectroscopy with a single exciting harmonic frequency and the impact-echo method for monitoring the corrosion of concrete-covered steel. For the research we manufactured concrete beams, reinforced with a standard reinforcing-steel bar passing through their centre. After concrete curing and drying, the samples were exposed to a 20 % carbon dioxide atmosphere. After the concrete pH decreased below 9.6 throughout the sample volume, the samples were immersed into a 5 % water solution of NaCl and subsequently placed into a drying oven. Measurements were carried out before the carbonation of the concrete, after it, and then after every 20th cycle of the accelerated degradation by chlorides. Nonlinear-ultrasonic-spectroscopy (NUS) methods are based on the fact that crack-induced nonlinearity makes a sensitive material-impairment indicator. The impact-echo method uses short-time mechanical impulses applied to the surface of a test sample, producing elastic waves. These waves spread throughout the sample and reflect from the surface but also from the microcracks and unobservable defects inside the sample. To verify the correctness of the NUS and impact-echo-method results, additional measurements were carried out (a confocal scanning microscope). It was proved that both methods could be used for monitoring the corrosion of concrete-covered steel.

Keywords: impact-echo, reinforced concrete, nonlinear ultrasonic spectroscopy, steel corrosion, confocal microscopy

Korozija jeklenih elementov v ojačanem betonu lahko povzroči občutne poškodbe v zgradbah. Zgodnje odkrivanje rje je zato zelo pomembno. Namen tega članka je oceniti možnosti uporabe nelinearne ultrazvočne spektroskopije z vzbujajočo harmonično frekvenco in metodo udarec-odmev za kontrolo korozije jekla, pokritega z betonom. Za preiskavo so bili izdelani betonski stebri, ki so bili ojačani s standardno rebričasto jekleno palico, nameščeno po sredini stebra. Po strjevanju in sušenju betona so bili vzorci izpostavljeni atmosferi 20 % ogljikovega dioksida. Ko se je pH betona zmanjšal pod 9.6 po vsem volumnu vzorca, so bili vzorci potopljeni v 5 % vodno raztopino NaCl in nato nameščeni v peč za sušenje. Meritve so bile izvedene pred karbonacijo betona, po njej in nato po vsakem 20 ciklu pospešene degradacije s kloridi. Metode nelinearne ultrazvočne spektroskopije (NUS) temeljijo na dejstvu, da zaradi razpoke povzročena nelinearnost povzroči indikator oslavitve materiala. Metoda udarec-odmev uporablja kratkotrajne mehanske udarce na površini preizkušanca, kar povzroči elastične valove. Ti valovi se širijo skozi vzorec in se odbijajo od površine in tudi od mikrorazpok in nevidnih napak znotraj vzorca. Za preverjanje pravilnosti rezultatov metode NUS in metode udarec-odmev so bile opravljene dodatne meritve s konfokalnim vrstičnim mikroskopom. Potrjeno je bilo, da sta obe metodi uporabni za kontrolo korozije z betonom pokritega jekla.

Ključne besede: metoda udarec-odmev, armiran beton, nelinearna ultrazvočna spektroskopija, korozija jekla, konfokalna mikroskopija

1 INTRODUCTION

Steel-reinforced concrete parts can be threatened by corrosion. The corrosion of steel elements in concrete decreases the lifetime of affected constructions and negatively changes their properties. Steel in concrete is usually in a non-corroding, passive condition. But if chloride moves into the concrete, it violates the passive layer protecting the steel, causing it to rust. Another reason for steel corrosion in concrete is carbonation. The alkaline environment in concrete protects steel from corrosion. However, a problem may activate carbon dioxide, which reduces the pH value of concrete. Under these conditions steel is no longer passive and can start to corrode.¹

This article describes the monitoring of corrosion, caused by carbonation of concrete and supported by active chlorides, using nonlinear ultrasonic spectroscopy

and the impact-echo method. The paper presents the results obtained for reinforced concrete samples with one steel rod passing through the centre.

The first method used for corrosion monitoring was nonlinear ultrasonic spectroscopy with one ultrasonic excitation signal. On the basis of nonlinear effect studies, new diagnostic and defectoscopic methods were designed. These methods are called the nonlinear ultrasonic spectroscopy. The nonlinear ultrasonic spectroscopy brings new perspectives into the acoustic non-destructive testing of material degradation. The material inhomogeneity and, sometimes, the shape complexity of some parts used in civil engineering heavily decrease the applicability of "classical" ultrasonic methods. These linear acoustic methods focus on the energy of waves, reflected by structural defects, variations in the wave-propagation velocity or changes in the wave amplitude.

However, none of these "linear" wave characteristics is as sensitive to structural defects as the specimen nonlinear response. In this way, nonlinear methods open up new horizons in non-destructive ultrasonic testing, providing high sensitivities, application speeds and an easy interpretation. One of the fields, in which a wide application range of nonlinear ultrasonic spectroscopy methods can be expected, is civil engineering. It is predicted that these advanced techniques can contribute a great deal to the improvement and refinement of defectoscopic and testing methods in the building-industry practice.^{2,3}

In this article, we focused on one type of the NUS methods – NUS with a single harmonic excitation ultrasonic signal. This method was used in the experimental part. In this case, where a single exciting frequency, f_1 , is used, the nonlinearity gives rise to other harmonic signals, whose frequencies f_n obey the Fourier series equations:

$$f_n = n f_1; \quad n = 0, 1, 2, \dots, \infty \quad (1)$$

In general, these frequency-component amplitudes decrease when the harmonic-order natural number, n , increases. If the nonlinearity effect is not entirely symmetrical, there can be changes in the amplitudes.³⁻⁵

The second method used for the corrosion monitoring was the impact-echo method. It is based on the acoustic properties of a material, which depend on its condition. A short-time mechanical impulse, usually caused by a hit of a hammer or a falling steel ball, spreads throughout the sample in the form of elastic waves. These waves are reflected from the surface of the sample and also from the micro-cracks and unobservable defects inside the sample and they are thus transformed. On another location on the sample surface, piezoelectric sensors subsequently detect these transformed waves as the response signal.⁶⁻⁸ The signal analysis within the impact-echo method is most frequently performed on the basis of the frequency spectra obtained from the fast Fourier transform. Usually we monitor the changes in the dominant frequency depending on the damage of the material structure. This method has a wide application in mechanical engineering, power engineering and in many industries as well as in civil engineering due to its simplicity and quick procedure.⁹⁻¹¹

In addition, the sample surface was observed using a confocal microscope. In the conventional microscopy, not only is the plane of focus illuminated, but much of the specimen above and below this point is also illuminated resulting in an out-of-focus blur from these areas. This out-of-focus light leads to a reduction in the image contrast and a decrease in the resolution. In the confocal microscope, all out-of-focus structures are suppressed during the image formation. The detection pinhole does not permit the rays of light from out-of-focus points to pass through it. The wavelength of the light, the numerical aperture of the objective and the diameter of the diaphragm (a wider detection pinhole reduces the confocal effect) affect the depth of the focal plane. To obtain

a full image, the point of light is moved across a specimen using scanning mirrors. The emitted/reflected light passing through the detector pinhole is transformed into electrical signals and processed by a computer.

2 EXPERIMENTAL SECTION

For the research, beams with dimensions of 50 mm × 50 mm × 330 mm were made. They were reinforced with one standard reinforcing bar with a 10 mm diameter and a length of 400 mm, passing through the centre of the sample. For the production of concrete, we used a mixture composed of 300 kg of cement CEM II/B – S 32.5, 1350 kg of sand with an aggregate fraction of 0–4 mm and 225 L of water. The concrete had a high water-cement ratio to allow an easy penetration of degradation agents into the concrete structure. After 24 h, when these samples were in the form, they were cured in water for the following 27 d and then they were dried to natural humidity at room temperature. Thus prepared samples were exposed to 20 % carbon dioxide at 80 % humidity and a temperature of 26 °C. The carbonation lasted for 60 d and the pH decreased below the value of 9.6 throughout the sample volume. Then the samples underwent an accelerated degradation by chlorides, when they were immersed into a 5 % water solution of NaCl for 16 h; subsequently, they were placed into a drying oven with an air temperature of 40 °C for 8 h. The measurement was carried out before the carbonation of the concrete, after the carbonation and after every 20th cycle of the accelerated degradation by chlorides. We performed a total of 100 degradation cycles.

The transmitting part for the NUS with a single harmonic ultrasonic signal consists of four functional blocks: a controlled-output-level harmonic-signal generator, a low-distortion 100 W power amplifier, an output low-pass filter to suppress higher harmonic components and ensure high purity of the exciting harmonic signal and a piezoceramic transmitter (actuator) to ensure the ultrasonic excitation.

The receiving section consists of a piezoceramic sensor, a low-noise preamplifier, an amplifier with band-pass filters, an oscilloscope and a computer. The measuring apparatus is schematically shown in **Figure 1**.

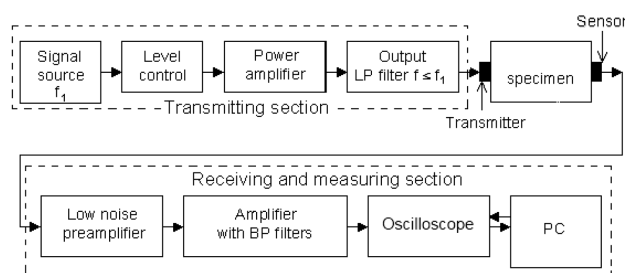


Figure 1: Scheme of non-linear ultrasonic spectroscopy with an ultrasonic-excitation-signal measuring apparatus

Slika 1: Shema nelinearne ultrazvočne spektroskopije z napravo za merjenje ultrazvočno zbujenega signala

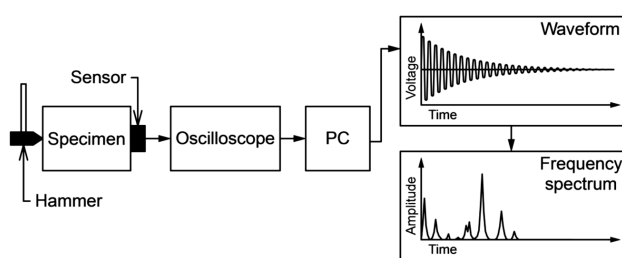


Figure 2: Scheme of the impact-echo method

Slika 2: Shema metode udarec – odmev

For the recorded data to be interpreted properly, each of the measuring instruments must meet the following criteria:

- High linearity of all the instruments (generators, amplifiers, sensor, transmitter, etc);
- High resolution in the frequency domain;
- High dynamic range (90–130 dB);
- Highly efficient filtration of detected signals;
- Frequency range of 10 kHz to 10 MHz;
- Optimized sensor and transmitter location.

We also constructed a measuring apparatus for the impact-echo method. In this case, a hanging hammer weighing 12 g was used and the hit was carried out from a predetermined height, which was the same for all the measurements. A MIDI piezoelectric sensor measured the signal response, which was fed to the input of a two-channel oscilloscope (TiePie engineering Handyscope HS3). The sensor was placed on the surface of concrete and the hit was carried out on uncovered reinforcement.^{12,13} A scheme of the impact-echo method is shown in **Figure 2**.

An Olympus LEXT 3100 laser confocal scanning microscope was used to study the surface and cracks of the specimens. The microscope uses an Ar laser blue-green spectral line with a wavelength of 488 nm, which makes it possible to gain very high-precision 3D imaging and measurement. The microscope resolution power is: superficial, 120 nm; sectional, 40 nm.

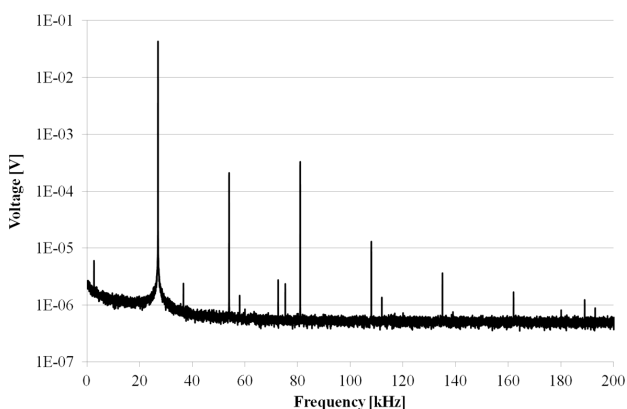


Figure 3: Frequency spectrum, obtained with the NUS method, for specimen C432 before carbonation

Slika 3: Spekter frekvenc, dobljen z metodo NUS na vzorcu C432 pred karbonacijjo

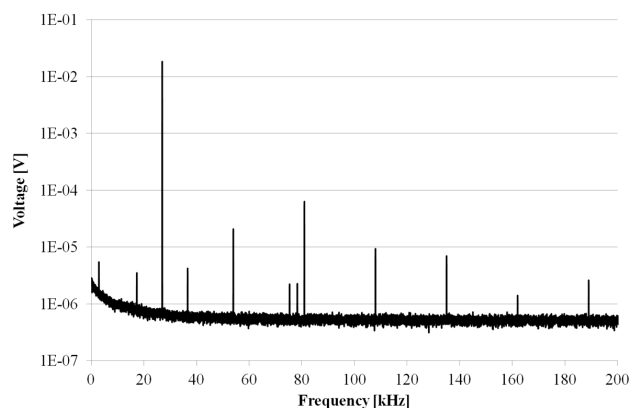


Figure 4: Frequency spectrum, obtained with the NUS method, for specimen C432 after carbonation

Slika 4: Spekter frekvenc, dobljen z metodo NUS na vzorcu C 432 po karbonaciji

3 RESULTS AND DISCUSSION

All the measurement results of individual methods are represented by sample C432 and sample C435. Pre-degradation measurements obtained with the NUS method for specimen C432 are shown in **Figure 3**. **Figure 4** shows the frequency spectrum of the same specimen after carbonation and **Figure 5** shows the frequency spectrum of specimen C432 after 100 cycles of the accelerated degradation by chlorides. We used the same exciting power and the same exciting frequency. The transmitter was on the steel bar, the sensor was mounted on the concrete. We could see a significant amplitude decrease in the first and especially in the third harmonic frequencies. There was also growth in the numbers and amplitudes of the non-harmonic frequencies, which was typical for this measurement configuration for all the specimens. As an example, we present specimen C435 too (**Figures 6 to 8**).

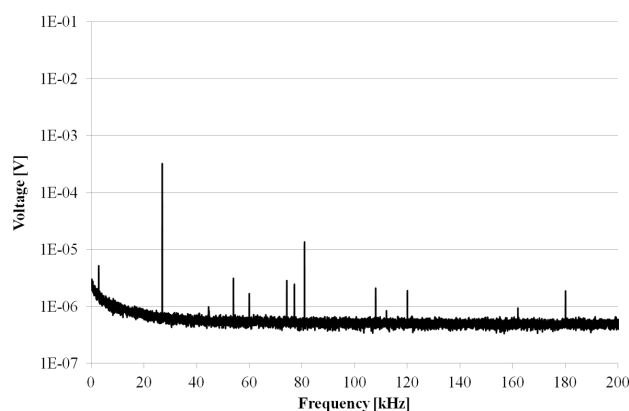


Figure 5: Frequency spectrum, obtained with the NUS method, for specimen C432 after 100 cycles of accelerated degradation by chlorides

Slika 5: Spekter frekvenc, dobljen z metodo NUS na vzorcu C432 po 100 ciklih pospešene degradacije s kloridi

The dominant frequency of the frequency spectrum obtained with the impact-echo method for sample C432 before the degradation by carbon dioxide was at position

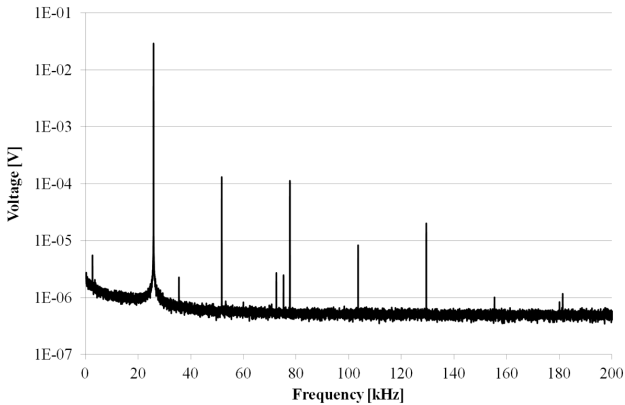


Figure 6: Frequency spectrum, obtained with the NUS method, for specimen C435 before carbonation

Slika 6: Spekter frekvenc, dobljen z metodo NUS na vzorcu C435 pred karbonacijo

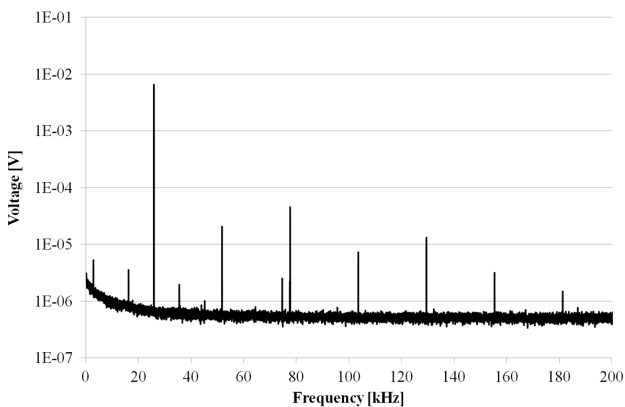


Figure 7: Frequency spectrum, obtained with the NUS method, for specimen C435 after carbonation

Slika 7: Spekter frekvenc, dobljen z metodo NUS na vzorcu C 435 po karbonaciji

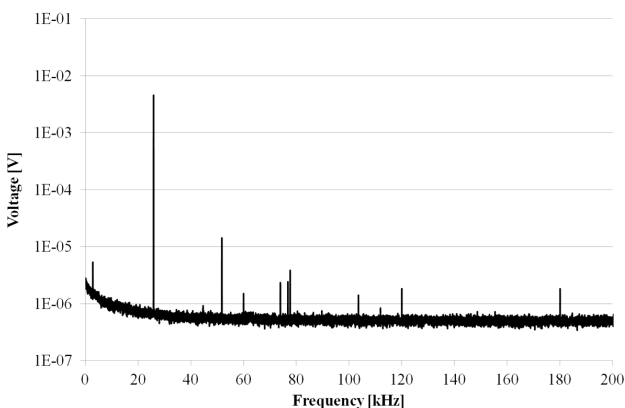


Figure 8: Frequency spectrum, obtained with the NUS method, for specimen C435 after 100 cycles of accelerated degradation by chlorides

Slika 8: Spekter frekvenc, dobljen z metodo NUS na vzorcu C435 po 100 ciklih pospešene degradacije s kloridi

10869 Hz. After the carbonation of the concrete, this frequency moved to 10 172 Hz and after 100 cycles of the accelerated degradation by chlorides, the value of this dominant frequency was 9950 Hz. These frequency

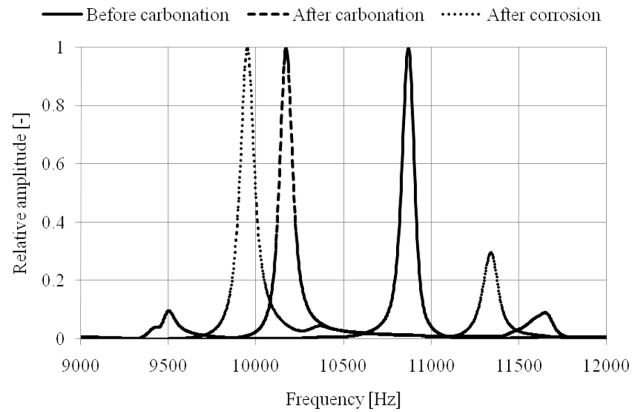


Figure 9: Frequency shifts during the degradation of specimen C432, obtained with the impact-echo method

Slika 9: Zamik frekvenc med degradacijo vzorca C432, dobljen z metodo udarec-odmev

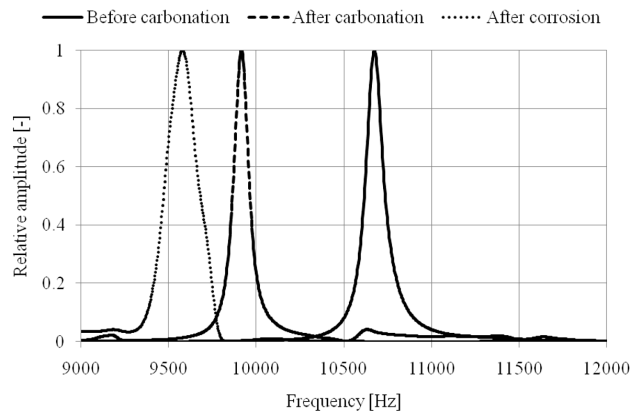


Figure 10: Frequency shifts during the degradation of specimen C435, obtained with the impact-echo method

Slika 10: Zamik frekvenc med degradacijo vzorca C435, dobljen z metodo udarec-odmev

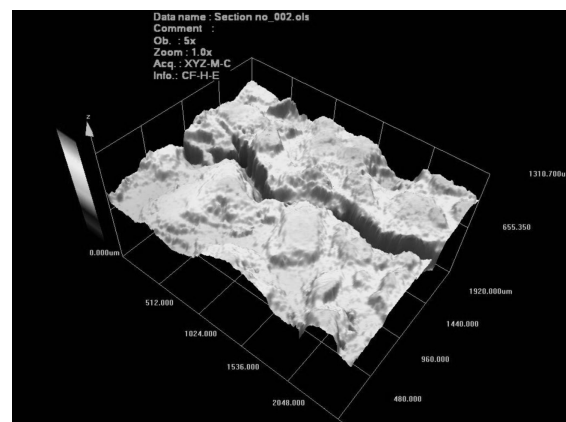


Figure 11: Crack in specimen C432 after 40 cycles of accelerated degradation by chlorides

Slika 11: Razpoka v vzorcu C432 po 40 ciklih pospešene degradacije s kloridi

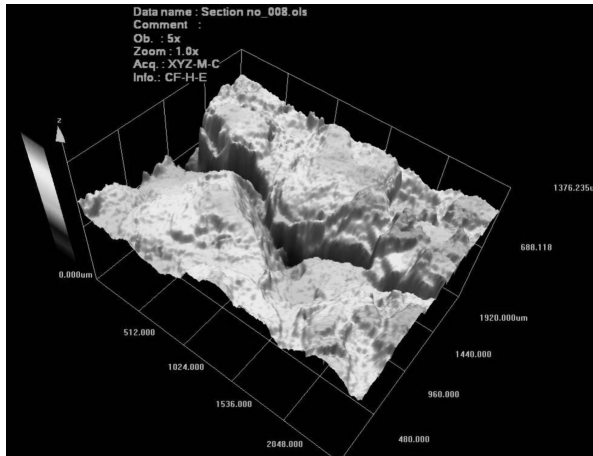


Figure 12: Crack in specimen C432 after 60 cycles of accelerated degradation by chlorides

Slika 12: Razpoka v vzorcu C432 po 60 ciklih pospešene degradacije s kloridi

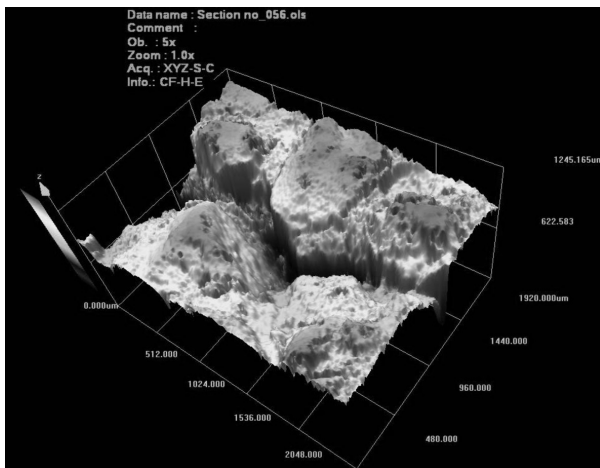


Figure 13: Crack in specimen C432 after 100 cycles of accelerated degradation by chlorides

Slika 13: Razpoka v vzorcu C432 po 100 ciklih pospešene degradacije s kloridi

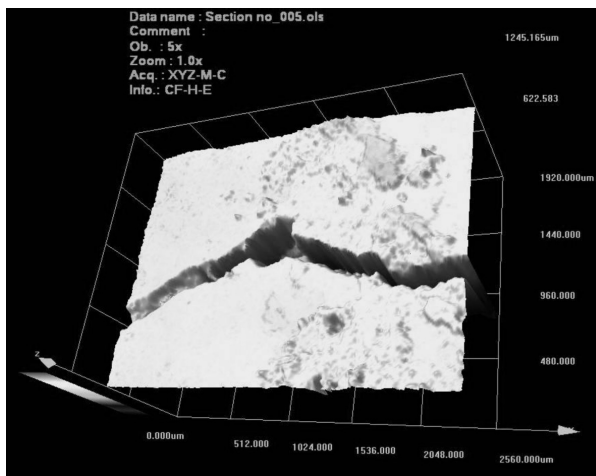


Figure 14: Crack in specimen C435 after 40 cycles of accelerated degradation by chlorides

Slika 14: Razpoka v vzorcu C435 po 40 ciklih pospešene degradacije s kloridi

shifts during the degradation are shown with the graph in **Figure 9**. **Figure 10** shows changes in the dominant frequency for sample C435. The development-frequency spectrum during the degradation of this sample has the same tendency as sample C432 and as all the other samples. The value of the dominant frequency before the carbonation of the concrete was 10677 Hz; after the carbonation, it was 9918 Hz and after the corrosion, it was 9579 Hz.

Using the confocal microscope LEXT 3100, we monitored the state of the surface and the cracks of the concrete samples during the degradation. We always scanned the same place on the surface. We were particularly interested in the growth of the cracks. In **Figures 11 to 13** (for sample C432) and in **Figures 14 to 16** (for sample C435) we can see a gradual expansion of the cracks during the degradation process.

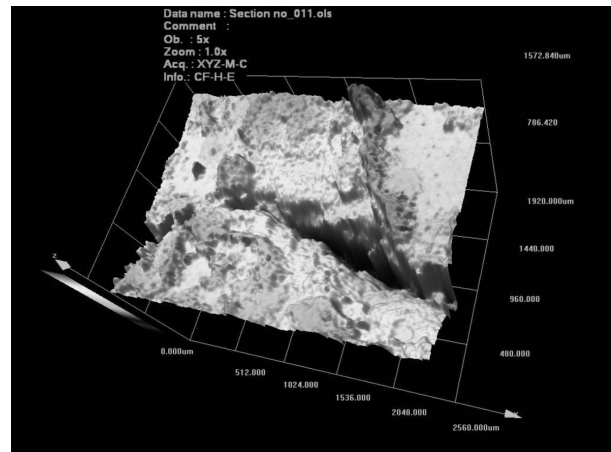


Figure 15: Crack in specimen C435 after 60 cycles of accelerated degradation by chlorides

Slika 15: Razpoka v vzorcu C435 po 60 ciklih pospešene degradacije s kloridi

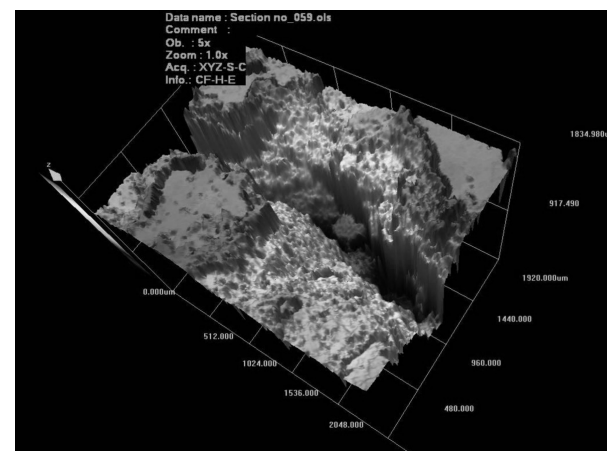


Figure 16: Crack in specimen C435 after 100 cycles of accelerated degradation by chlorides

Slika 16: Razpoka v vzorcu C435 po 100 ciklih pospešene degradacije s kloridi

4 CONCLUSIONS

This paper presents our results for monitoring the corrosion of concrete-covered steel by means of non-linear ultrasonic spectroscopy using a single exciting harmonic ultrasonic frequency and the impact-echo method.

For the NUS method, it is essential to minimize any harmonic distortion in the signal pick-up and amplification path by eliminating any interfering signals (noise, parasitic signal) from the measuring apparatus. A very good mechanical coupling must also be ensured between the exciter and the specimen and between the specimen and the piezoceramic sensor during the measurement. It was proved that structural defects, which are due to steel corrosion, give rise to non-linear effects. We can see significant amplitude changes, especially the third-harmonic amplitude changes and the growth of non-harmonic frequencies.

The results of the impact-echo method proved that this method is very sensitive to the damage of a concrete structure by carbonation and corrosion. The shifts of the dominant frequencies obtained with the fast Fourier transform from the response signal correspond with the changes in the structure during the degradation. It was shown that the deteriorating state of the structure has an effect on the reduction in the dominant frequencies.

The growth of the cracks was also proved with confocal microscopy. Based on this, we can say that both methods are very promising for monitoring steel corrosion in concrete.

Acknowledgments

This paper was completed within project No. LO1408 "AdMaS UP – Advanced Materials, Structures and Technologies", supported by the Ministry of Education, Youth and Sports under the "National Sustainability Programme I", project GA13-18870S of the Czech Science Foundation and specific research program at the Brno University of Technology, project No. FAST-S-15-2622.

5 REFERENCES

- ¹ M. Collepardi, *The New Concrete*, 1st ed, Tintoretto, 2006, 421, ISBN: 9788890146947
- ² K. E. Van Den Abeele, A. Sutin, J. Carmeliet, P. A. Johnson, *Micro-damage diagnostics using nonlinear elastic wave spectroscopy (NEWS)*, *NDT & E International*, 34 (2001) 4, 239–248, doi:10.1016/S0963-8695(00)00064-5
- ³ V. Zaitsev, V. Nazarov, V. Gusev, B. Castagnede, *Novel non-linear-modulation acoustic technique for crack detection*, *NDT & E International*, 39 (2006) 3, 184–194, doi:10.1016/j.ndteint.2005.07.007
- ⁴ L. Pazdera, L. Topolar, *Application acoustic emission method during concrete frost resistance*, *Russian Journal of Nondestructive Testing*, 50 (2014) 2, 127–132, doi:10.1134/S1061830914020065
- ⁵ L. Pazdera, L. Topolar, J. Smutny, V. Rodriguezova: *Modulus of Elasticity Determination from Cantilever Deflection*, *Proc. of the 50th Annual Conference on Experimental Stress Analysis*, Praha, 2012, 313–320, ISBN 978-80-01-05060-6
- ⁶ H. S. Limaye, R. J. Krause, *Nondestructive evaluation of concrete with impact-echo and pulse-velocity techniques*, *Materials Evaluation*, 49 (1991) 10, 1312–1315, doi:10.1016/S0963-8695(97)88984-0
- ⁷ M. T. Liang, P.J. Su, *Detection of the corrosion damage of rebar in concrete using impact-echo method*, *Cement and Concrete Research*, 31 (2001) 10, 1427–1436, doi:10.1016/S0008-8846(01)00569-5
- ⁸ M. Matysik, I. Plskova, Z. Chobola, *Estimation of Impact-Echo Method for the Assessment of Long-Term Frost Resistance of Ceramic Tiles*, *Advanced Materials Research*, 1000 (2014), 285–288, doi:10.4028/www.scientific.net/AMR.1000.285
- ⁹ G. Epasto, E. Proverbio, V. Venturi, *Evaluation of fire-damaged concrete using impact-echo method*, *Materials and Structures*, 43 (2010) 1–2, 235–245, doi:10.1617/s11527-009-9484-0
- ¹⁰ B. Kucharczykova, P. Misak, T. Vymazal, *Determination and evaluation of the air permeability coefficient using Torrent Permeability Tester*, *Russian Journal of Nondestructive Testing*, 46 (2010) 3, 226–233, doi:10.1134/S1061830910030113
- ¹¹ M. Krause, M. Barmann, R. Frielinghaus, *Comparison of pulse-echo methods for testing concrete*, *NDT & E International*, 30 (1997) 4, 195–204, doi:10.1016/S0963-8695(96)00056-4
- ¹² T. Vymazal, N. Zizkova, P. Misak, *Prediction of the risks of design and development of new building materials by fuzzy inference systems*, *Ceramics-Silikáty*, 53 (2009) 3, 216–224, ISSN 0862-5468
- ¹³ D. N. Boccaccini, M. Maioli, M. Cannio, M. Romagnoli, P. Veronesi, C. Leonelli, A. R. Boccaccini, *A statistical approach for the assessment of reliability in ceramic materials from ultrasonic velocity measurement: Cumulative Flaw Length Theory*, *Engineering Fracture Mechanics*, 76 (2009) 11, 1750–1759, doi:10.1016/j.engfractmech.2009.03.008

CHARACTERIZATION OF HETEROGENEOUS ARC WELDS THROUGH MINIATURE TENSILE TESTING AND VICKERS-HARDNESS MAPPING

KARAKTERIZACIJA HETEROGENIH ZVAROV S POMOČJO MINIATURNIH NATEZNIH PREIZKUSOV IN MATRIČNIMI MERITVAMI TRDOTE PO VICKERSU

**Stijn Hertelé¹, Jonas Bally¹, Nenad Gubelj², Primož Štefane²,
Patricia Verleysen³, Wim De Waele¹**

¹Ghent University, Department of Electrical Energy, Systems and Automation, Soete Laboratory, Technologiepark Zwijnaarde 903, 9052 Zwijnaarde, Belgium

²University of Maribor, Laboratory for Machine Parts and Structures, Smetanova 17, 2000 Maribor, Slovenia

³Ghent University, Department of Materials Science and Engineering, 9052 Zwijnaarde, Belgium
stijn.hertele@ugent.be

Prejem rokopisa – received: 2015-07-01; sprejem za objavo – accepted for publication: 2015-07-13

doi:10.17222/mit.2015.157

The heterogeneity of arc-welded connections is often ignored in structural assessments, giving rise to inaccuracies. Improved assessments taking into account heterogeneity require the characterization of local constitutive properties. We have compared two methods to do this: Vickers-hardness mapping and miniature tensile testing. Whereas the former is more straightforward to apply, the latter provides full-range stress-strain data. This paper discusses an experimental comparison of both methods on a heterogeneous arc weld. Miniature tensile tests were performed, using digital image correlation to measure the strain. The specimens were indented to compare their stress-strain response with Vickers hardness. Notwithstanding that small natural flaws invalidated some tests, reliable stress-strain curves were obtained. Vickers hardness testing is a convenient alternative if the yield and ultimate tensile strength are the only points of interest and the corresponding conversion inaccuracy is acceptable.

Keywords: arc weld, heterogeneity, hardness, miniature tensile testing, digital image correlation

Heterogenost obločno zvarjenega zvara pogosto ni upoštevana pri ocenjevanju celovitosti konstrukcij, kar je lahko razlog za nepravilno oceno. Za boljšo oceno, ki upošteva heterogenost, je potrebno določiti lokalne mehanske lastnosti. Avtorji članka so opravili primerjavo dveh metod za določanje lokalnih mehanskih lastnosti: matrično meritev mikrotrdote po Vickersu in miniaturni natezni preizkus. Za razliko od dosedanje prakse neposredne uporabe mejnih vrednosti, se danes uporablja celotna natezna krivulja napetost-deformacija. V članku je opravljena primerjava med obema eksperimentalno dobljenima skupinama podatkov za heterogeni zvarni spoj. Meritve deformacij na miniaturnih nateznih preizkušancih so bile opravljene s stereo optično digitalno merilno metodo. Na vsakemu od miniaturnih nateznih preizkušancev je bila opravljena meritev mikrotrdote po Vickersu, pri čemer so bile izmerjene vrednosti mikrotrdote primerjane z natezno krivuljo napetost-deformacija. Kljub dejstvu, da so bili preizkušanci z majhnimi napakami v zvarih izključeni iz analize, so bile dobljene verodostojne vrednosti meje tečenja in natezne trdnosti iz krivulje napetost-deformacija. Pokazalo se je, da je za hitro oceno natezne trdnosti in meje tečenja materiala zvara, matrična meritev mikrotrdote po Vickersu alternativna metoda nateznemu preizkušanju.

Ključne besede: obločni zvar, heterogenost, trdota, miniaturno natezno preizkušanje, digitalne optične meritve

1 INTRODUCTION

Arc welds are prone to defects of which the acceptability should be investigated from the viewpoint of structural integrity. The occurrence of different microstructures in a confined area implies potentially strong local variations of stress-strain behaviour (weld heterogeneity), leading to uncontrolled scatter in the accuracy of defect-tolerance predictions.¹ A first step in accounting for weld heterogeneity in an improved assessment is the experimental characterization of local stress-strain properties. This paper compares two techniques to do this: Vickers-hardness mapping and miniature tensile testing.

The first technique is to characterize the spatial distribution of hardness by applying a large number of

adjacent indents. This method indicates variations of strength², but is not linked to ductility and strain-hardening behaviour. When full-range information is desired, miniature tensile testing is an alternative. The associated test procedure, however, is characterized by a large number of technical challenges and requires a careful preparation, execution and analysis of the tests.³

The authors have developed and optimized a procedure for miniature tensile testing, and have compared the results of a test program with Vickers hardness data. This paper highlights the challenges that have been addressed to achieve reliable tensile test results, and the relation between hardness and local stress-strain properties.

2 MATERIAL

Test material was taken from the girth weld of a 914-mm-diameter steel pipeline having a nominal wall thickness of 10 mm, excavated from a natural-gas transmission grid after nearly five decades of operation. The specified minimum yield strength of the microalloyed steel was 415 MPa and the weld was constructed by multipass shielded metal arc welding (SMAW). This weld was selected for its severe heterogeneity, as witnessed by the 49 N Vickers (HV5) hardness map shown in **Figure 1**. Traversing from root to cap, the hardness increases by roughly 50 % of its minimum value. Similarly significant variations are to be expected for the yield and ultimate tensile strength given their approximate relation with hardness.

3 TEST PROGRAM

Miniature tensile specimens were sampled from the weld by means of electrical discharge machining (EDM) with a 0.25-mm-diameter wire electrode. This technique is suitable as no forces are applied to the vulnerable specimens. A dog-bone-shaped block, taken out in the welding direction, was divided into 0.7-mm-thick slices (**Figure 2**). Nine specimens were extracted. These were then ground on both sides to a thickness of 0.5 mm, thus removing the brittle heat-affected zone associated with the EDM. The specimens are numbered in a manner that indicates their through-thickness position, starting from the weld root (1) and heading towards the weld cap (9). The adopted dog-bone geometry has a nominal cross-sectional area of 1 mm². It was developed at the GKSS research centre (Helmholtz-Zentrum Geesthacht)⁴ and has been adopted by other institutions.^{5,6}

Note the prismatic section's ratio of length (9 mm) to width (2 mm), allowing us to measure strain using an extensometer whose gauge length is four times the specimen width, in accordance with the standards for conventional tensile testing of metallic materials.⁷ Note a filleted end corner having a radius of 1 mm, providing a unique reference for the specimen orientation with respect to the weldment.

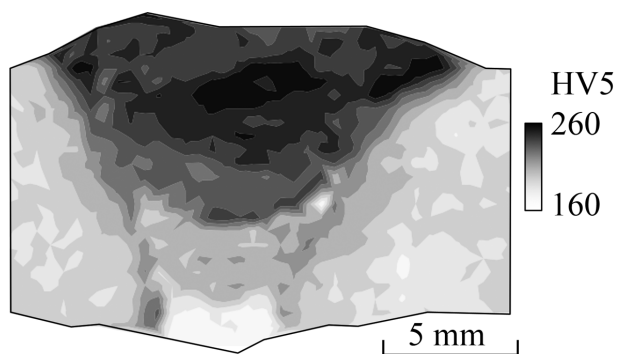


Figure 1: Hardness map of the investigated weld
Slika 1: Površinska porazdelitev trdote na analiziranem zvaru

Following grinding, the top and bottom surfaces were polished using 2000-grit sandpaper, on average reducing the roughness R_a (measured in a longitudinal track) from 0.26 μm to 0.026 μm . The side faces were also polished (using 1200-grit sandpaper) to remove the burrs resulting from the grinding process. Without this step, specimen-width measurements would have been biased, giving rise to an estimated error of 10 % on the stress calculation.

For all nine specimens, the net section width and thickness were measured at five equidistant positions. Small coefficients of variance were observed between all 45 values of the width (0.82 %) and thickness (1.74 %), indicating a sound dimensional repeatability of the specimen production. The specimen-specific coefficients of variance did not exceed 0.5 % for the width and 1.0 % for the thickness.

To examine the correlation between the Vickers macrohardness and the tensile-test characteristics, a total of twelve HV5 measurements were performed in the clamping faces of each specimen (six at either end of the specimen). ASTM E384⁸ was consulted to confirm that a specimen thickness of nominally 0.5 mm is sufficient to obtain valid HV5 indentations, and to ensure a sufficient spacing between the adjacent indentations.

After polishing and hardness testing, specimens were painted white, followed by applying black speckles for the purpose of monitoring strain by means of digital image correlation (DIC). This is an optical measurement technique that allows us to track full-field displacements by following the movements of a random pattern. Next, a 'virtual extensometer' measurement of strain can be output from the obtained displacement data. A stand-alone system provided by Limes GmbH, adopting the VIC3D software (version 2009) of Correlated Solutions Inc, was used for the DIC analysis.

Particularly challenging was the application of a high-quality speckle pattern. Optimal DIC accuracy requires an average speckle size of around 3×3 camera pixels.⁹ From the camera resolution and the dimensions

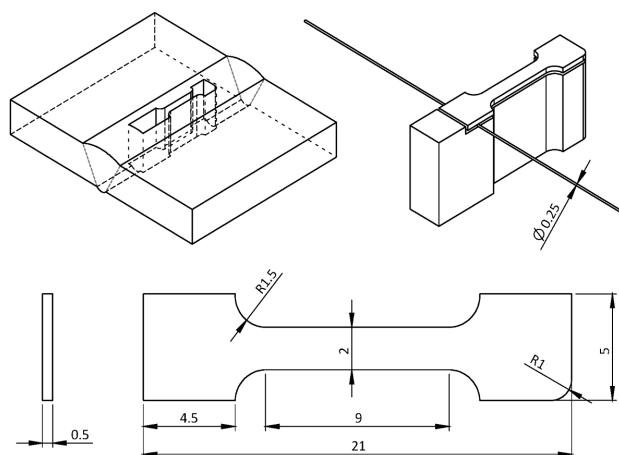


Figure 2: Sampling plan and geometry of miniature tensile specimens
Slika 2: Plan izreza vzorcev in geometrija

of the area of interest, a desired speckle size of $18 \times 18 \mu\text{m}$ followed. The literature indicated that such a speckle size can be achieved by non-conventional methods such as dispersing and heating graphite powder on the surface, or contact lithography.⁹ For this project, however, conventional painting was performed by means of an in-house-developed spray procedure using a nozzle airbrush. The optimization of paint viscosity, nozzle opening, airbrush pressure and spray angle eventually allowed us to create patterns having the desired speckle size with sufficient repeatability. **Figure 3** shows a speckled specimen and a close-up of the pattern at a pixel level, confirming the ability to obtain the desired fine speckle size.

The miniature tensile tests were executed using a 5-kN Deben stage, made available by TU Delft for the purpose of this study. Specimens were clamped between grips that were actuated at a fixed displacement rate, which was empirically tuned to limit the stress rate in the linear-elastic region to a value below 11.5 MPa/s (as required by ASTM E8M⁷ for the standard tensile testing of metallic materials). The tests were stopped upon fracture. The load was recorded and coupled with DIC images that were taken at a rate of 0.5 Hz. To obtain stress-strain data, the stress was calculated by dividing the tensile load by the average values of the net section width and thickness. The strain was obtained from DIC by means of a 'virtual extensometer' having a gauge length of 8 mm, as discussed above.

4 RESULTS AND DISCUSSION

This section focuses on three aspects of the test program: the validity of the miniature tensile test results, the observations related to weld heterogeneity, and the relation between the Vickers hardness and the strength characteristics.

Of all nine specimens, three specimens (3, 4 and 9) clearly showed an anomalous response, characterized by localized necking at unexpectedly low strain values. Post-mortem fractography revealed weld porosities in each of these specimens. The relative size of such porosi-

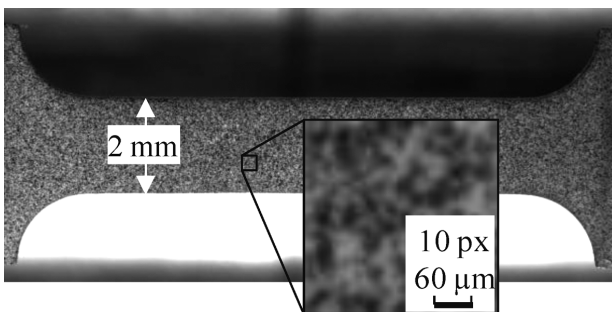


Figure 3: Speckle pattern for the strain analysis using digital image correlation

Slika 3: Raster za meritev deformacij z uporabo optične digitalne merilne tehnike

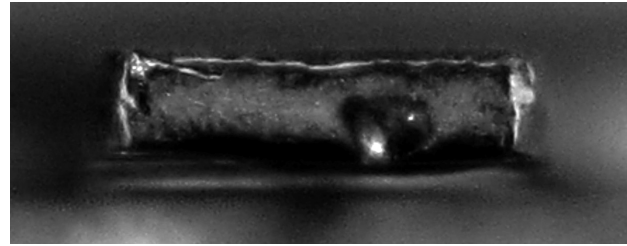


Figure 4: Weld porosities invalidated three miniature tensile test results

Slika 4: Pore v zvarnem spoju so povzročile odstopanje v rezultatih na nateznih preizkušancih

ties with respect to miniature tensile specimens is clearly sufficient to invalidate their test result (**Figure 4**).

No irregularities were observed on the fracture surfaces of the other specimens, which behaved in an expected manner. Their stress-strain curves are depicted in **Figure 5**. Weld heterogeneity is reflected in many aspects. Obviously, yield strength (expressed as 0.2 % proof stress $R_{p0.2}$) and tensile strength R_m vary considerably ($493 \text{ MPa} < R_{p0.2} < 672 \text{ MPa}$ and $570 \text{ MPa} < R_m < 794 \text{ MPa}$). In addition, there are strong variations in the ductility and strain-hardening behaviour. Comparing specimen 1 with 8, the former has a Lüders plateau and a uniform elongation (strain at R_m) of 10.1 %, whereas the latter shows round-house yielding and a uniform elongation of 4.3 %. The extent of the strain hardening is also variable, as reflected in the ratio $R_{p0.2}/R_m$, which varies between 0.80 and 0.89.

The variety of the stress-strain curve shapes in **Figure 5** indicates the limitation to the use of Vickers hardness as a unique number to characterize local properties. Nonetheless, the literature and standards suggest that hardness may be used to estimate $R_{p0.2}$ and R_m . For instance, the following Equation (1), proposed for steel weld metal in ISO 15653 (in MPa):³

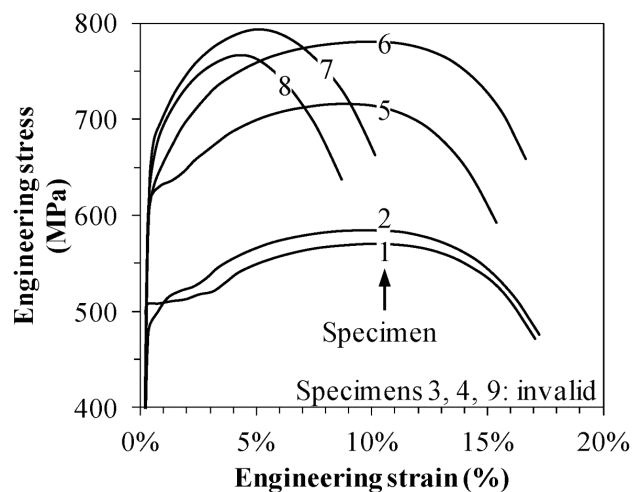


Figure 5: Test results indicate a significant heterogeneity of the constitutive properties

Slika 5: Rezultati nateznih preizkusov kažejo heterogenost v mehanških lastnostih

$$\begin{cases} R_{p0.2} = 2.35HV + 62.0 \\ R_m = 3.00HV + 22.1 \end{cases} \quad (1)$$

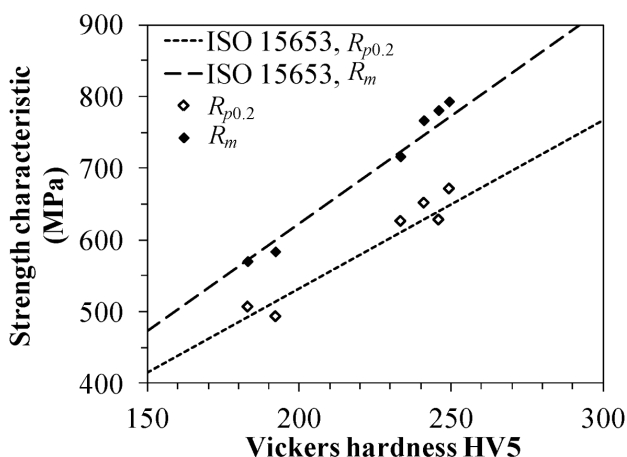


Figure 6: ISO 15653 describes the observed relations between hardness and strength

Slika 6: ISO 15653 kaže razmerje med trdoto in trdnostjo ter odstopanje od eksperimentalno dobljenih vrednosti

The six hardness values at one specimen end may significantly differ from those at the other end (up to 33 HV difference between the average values from either end). This observation indicates weld heterogeneity in the weld direction (perpendicular to the section shown in **Figure 1**). As the weakest cross-section governs the failure load of the tensile specimen, the average hardness value of the weakest specimen end was considered for a comparison with strength properties (**Figure 6**). Equation (1) succeeds in describing the observed relations between the hardness and the strength characteristics. For the six valid tests, predicting $R_{p0.2}$ and R_m from HV5 results in errors below 25 MPa. The prediction accuracy is higher for R_m than for $R_{p0.2}$ (average absolute value of error 14.5 MPa and 18.5 MPa, respectively).

5 CONCLUSIONS

This paper has shown the potential merit of miniature tensile testing to characterize weld stress-strain heterogeneity. The careful specimen preparation and execution of the tests are essential for this. The following attention points of the experimental procedure have been high-

lighted: specimen polishing, accurately measuring cross-section dimensions, and applying a suitable speckle pattern for optical strain monitoring. Test validity requires that the specimen is free of any natural weld defects such as porosities.

Comparing the miniature tensile test results with the Vickers hardness testing has pointed out the suitability of the latter (more straightforward) method, provided the desired information is limited to the evolution of the strength variations and, hereto, small strength estimation errors are allowed. Vickers hardness testing does not provide direct information with respect to the ductility or the nature of the strain hardening.

Acknowledgements

The authors wish to acknowledge the financial support of BOF UGent (grant BOF12/PDO/049), FWO Vlaanderen and ARRS Slovenia (joint FWO grant G.0609.15N), and the kind permission of TU Delft to use their 5-kN test stage.

6 REFERENCES

- M. Koçak, S. Webster, J. J. Janosch, R. A. Ainsworth, R. Koers (Eds.), *Fitness for service procedure, FITNET, MK8, Vol. 1: Procedure*, GKSS Research Centre, Geesthacht, Germany 2008
- ISO 15653: *Metallic materials – method for the determination of quasistatic fracture toughness of welds*, ISO, 2010
- D. A. LaVan, W. N. Sharpe, *Tensile testing of microsamples*, *Experimental Mechanics*, 39 (1999) 3, 210–216, doi:10.1007/BF02323554
- M. Koçak, *Structural integrity of welded structures: process – property – performance relationship*, 63rd Ann. Assembly & Int. Conf. Int. Instit. Weld., Istanbul 2010, 3–19
- D. Dobi, E. Junghans, *Determination of the tensile properties of specimens with small dimensions*, *Kovine zlitine tehnologije*, 33 (1999) 6, 451–457
- S. Hertelé, N. Gubelj, W. De Waele, *Advanced characterization of heterogeneous arc welds using micro tensile tests and a two-stage strain hardening ('UGent') model*, *International Journal of Pressure Vessels and Piping*, 119 (2014) 9, 87–94, doi:10.1016/j.ijpvp.2014.03.007
- ASTM E8M: *Standard test method for tension testing of metallic materials*, ASTM International, 2011
- ASTM E384: *Standard test method for Knoop and Vickers hardness of materials*, ASTM International, 2011
- M. A. Sutton, J. J. Orteu, H. W. Schreier, *Image correlation for shape, motion and deformation measurements*, Springer, USA 2009, doi:10.1007/978-0-387-78747-3

OVERCOOLING IN OVERLAP AREAS DURING HYDRAULIC DESCALING

PODHLADITEV IN PREKRIVANJE PODROČIJ MED HIDRAVLIČNIM RAZŠKAJANJEM

Michal Pohanka, Helena Votavová

Brno University of Technology, Faculty of Mechanical Engineering, Heat Transfer and Fluid Flow Laboratory,
Technická 2, 616 69 Brno, Czech Republic
pohanka@fme.vutbr.cz

Prejem rokopisa – received: 2015-07-01; sprejem za objavo – accepted for publication: 2015-07-28

doi:10.17222/mit.2015.164

The production and processing of high-quality grades of steel are connected with the oxidation at high temperatures. Unwanted scales are formed on the steel surface, which is usually heated to over 900 °C. These scales are often removed by hydraulic descaling during the production. In most cases where long, flat products are produced, one row of descaling nozzles is used. As these flat jet nozzles are arranged in a row, the water spray from one nozzle interferes with the spray from the neighboring nozzles. This zone is called an overlap area and often even more scales remain here after the descaling process. An increased amount of the scales left behind results in a lower quality of a final product. A typical configuration with an inclination and twist angle of 15° was studied. Heat-transfer coefficients (HTC) and surface temperatures were measured in the overlap area and compared with the values obtained from undisturbed areas. It was found that the overlap area is grossly overcooled. The results were compared with a new configuration, where the twist angle was changed to 0°, and it was found that the overcooling was significantly reduced. The temperature measurement showed that an increased thickness of the scales in the overlap area can also be caused by surface overcooling because the scales change the material properties with the temperature, and they are therefore more difficult to remove. The new configuration with the twist angle of 0° seems promising for improving the quality of hydraulic descaling.

Keywords: scales, steel, water, hydraulic descaling, overlapping, temperature, heat-transfer coefficient, surface

Proizvodnja in predelava visoko kvalitetnih jekel je povezana z oksidacijo pri visokih temperaturah. Nezaželjene škake nastajajo na površini jekla, ki se ga običajno segreva nad 900 °C. Te škake se med proizvodnjo pogosto odstranjujejo s hidravličnim razškajanjem. V večini primerov, ko se proizvaja dolge, ploščate proizvode, se uporablja ena vrsta razškajevalnih šob. Ker so šobe s ploščatim curkom razporejene v vrsti, vodni curek iz ene šobe vpliva na vodni curek sosednjih šob. To področje se imenuje področje prekrivanja in pogosto na tem področju ostane več škake po odškajanju. Povečan delež preostale škake pa povzroča slabšo kvaliteto končnega proizvoda. Analizirana je bila značilna postavitev z naklonom in kotom zasuka 15°. Na področju prekrivanja je bil izmerjen koeficient prenosa toplote (HTC) in temperatura površine ter primerjava s podatki iz neprizadetih področij. Ugotovljeno je, da so področja prekrivanja močno podhlajena. Rezultati so bili primerjani z novo konfiguracijo, kjer je bil kot zasuka 0° in ugotovljeno je, da se je podhladitev močno zmanjšala. Meritve temperature so pokazale, da je povečana debelina škake v področju prekrivanja lahko tudi posledica podhladitve površine, ker škaka s temperaturo spreminja lastnosti materiala in se jo zato tudi težje odstrani. Zdi se, da bo nova postavitev, s kotom zasuka 0°, omogočila izboljšanje kvalitete hidravličnega razškajanja.

Ključne besede: škaka, jeklo, voda, hidravlika, razškajanje, prekrivanje, temperatura, koeficient prenosa toplote, površina

1 INTRODUCTION

Hydraulic descaling (also called high-pressure water descaling) is a very common and effective way to remove unwanted scales on steel products before the hot-rolling process. However, this process is coupled with intense cooling.^{1,2} The intense cooling can also influence the final microstructure.³ J. W. Choi⁴ studied the correlation of the heat-transfer coefficient (HTC) with the impact pressure within a pressure range of 0.48–0.8 MPa and found the following relationship:

$$h = (44.265 \times IP + 7.3670) \times 10^4 \quad (1)$$

where h is the convective HTC ($\text{W m}^{-2} \text{K}^{-1}$) and IP is the impact pressure (MPa).

Published heat-transfer simulations assume a constant HTC across the width of a sprayed product.^{5,6} How-

ever, high-pressure flat-jet descaling nozzles are arranged in one or more rows because the product to be descaled is usually wider than the spray width of a single nozzle, and a more intense cooling occurs in the areas where the surface is sprayed with the water from more than one nozzle.^{7,8} This area is called the overlap area as water streams from two adjacent nozzles, overlapping in the direction parallel to the product movement. The overlap area is often problematic and it is the first place where more remaining scale can be found after descaling. This area is also overcooled. This paper focuses on overcooling in the overlap area for a typical descaling-nozzle configuration and compares the results with a new configuration. Measured surface-temperature inhomogeneities are presented as well as convective HTCs in both the undisturbed and overlap areas.

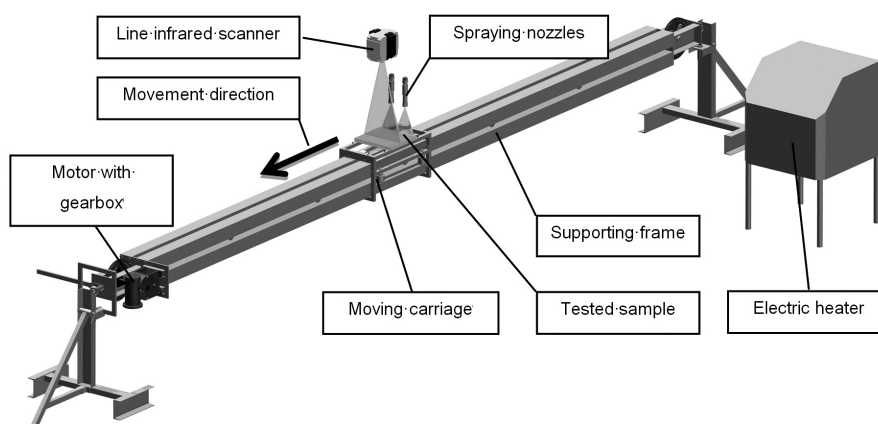


Figure 1: Experimental stand used for experiments
Slika 1: Stojalo uporabljeno pri preizkusih

2 MEASUREMENTS

The main purpose of the experiments was to simulate real descaling conditions with more than one spray nozzle and to obtain boundary conditions for numerical simulations.

The experiments were carried out on the experimental stand⁹ shown in **Figure 1**. An austenitic test plate of (320 × 300 × 25) mm was attached to a moving carriage and heated with an electric heater to over 900 °C. The feed-water pressure was adjusted and the heated test plate moved under the spray nozzles. The velocity of the movement was 0.5 m/s. The temperature history inside the test plate, the surface temperatures, and the information about the carriage position were recorded during the motion. The surface temperatures were measured using a Raytek RAYTMP501M line infrared scanner located 350 mm behind the spray nozzles. The temperatures inside the test plate were measured with shielded ungrounded type-K thermocouples. The outer diameter of the shield was 0.52 mm. They were placed in the holes drilled parallel with the surface. The distance of the measurement points from the cooled surface was 0.6 mm. Three thermocouples were installed in the test plate as shown in **Figure 2**. The thermocouple pitch was 25 mm and the middle one was in the overlap area.

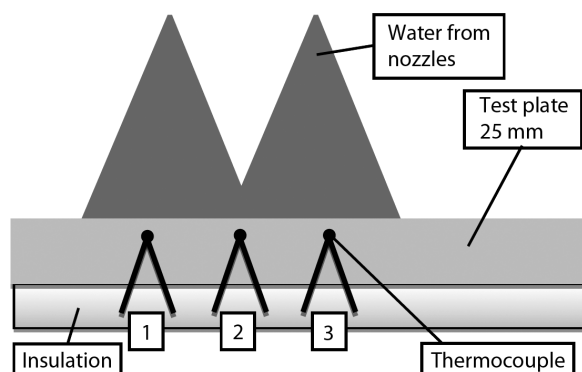


Figure 2: Thermocouple positions for HTC measurements
Slika 2: Položaji termoelementov pri HTC meritvah

The measured temperature history from each thermocouple is an input to the inverse computation.¹⁰ Computed results are the time-dependent HTC and the surface temperature of the cooled side of a test plate. The computed HTC is matched with the position information.

Two high-pressure descaling nozzles at a spray angle of 45° were used during the measurements. The water-flow rate for each nozzle was 58 L/min at 40 MPa. The spray height was 55 mm and the nozzle pitch was 43 mm. Two configurations were tested. The first one was with a 15° twist angle (**Figure 3**) and the second one was with a 0° twist angle (**Figure 4**).

3 RESULTS

It was found that the overlap area is extremely overcooled compared to the region cooled by only one spray nozzle. The computed maximum HTC rose from 21 kWm⁻² K⁻¹ to 37 kWm⁻² K⁻¹ in the overlap area for the 15° twist angle (**Figure 5**). The removed heat is even higher, by 99 %, at the T2 thermocouple position com-

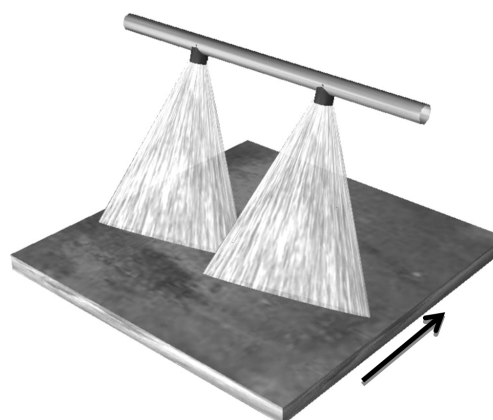


Figure 3: Visualization of the nozzle configuration with the 15° twist angle. The spray width of each nozzle is 47 mm and the overlap is 4 mm. The arrow indicates the plate movement direction.

Slika 3: Prikaz postavitve šob s kotom zasuka 15°. Širina curka je 47 mm pri eni šobi in prekrivanje je 4 mm. Puščica kaže smer gibanja plošče.



Figure 4: Visualization of the nozzle configuration with the 0° twist angle. The spray width of each nozzle is 49 mm and the overlap is 6 mm. The arrow indicates the plate movement direction.

Slika 4: Prikaz postavitve šob s kotom zasuka 0°. Širina curka je 49 mm pri eni šobi in prekrivanje je 6 mm. Puščica kaže smer gibanja plošče.

pared to thermocouple positions T1 and T3. It is also clear that the HTC for T1 is not aligned with the HTC for T3. This is because T1 and T2 are not exactly under the spray nozzles (Figure 2) and a non-zero twist angle is used. T1 first passes through the spray on the left, from the left spray nozzle (see the 3D view on Figure 3) and T3 later passes on the right, through the spray from the right nozzle. The HTC peak is much wider for T2. This is because it passes through two sprays from both nozzles in the overlap area. We should see two peaks in the HTC curve but, due to the limitation of the sequential inverse method for computing the HTC from the temperatures measured inside the test plate, the HTC curve is smoothed and these two peaks merge into one peak.

The computed HTC curves for the 0° twist angle are shown in Figure 6. The curves for T1 and T3 are almost equal to the curves for T1 and T3 from the experiment with the 15° twist angle. The only difference is that they are not shifted because of the 0° twist angle. The HTC curve for T2 is also aligned with the HTC curves for T1

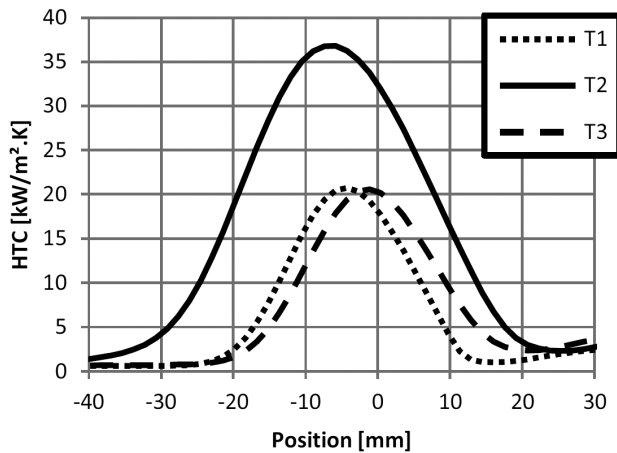


Figure 5: Measured HTC distribution for the 15° twist angle
Slika 5: Izmerjena razporeditev HTC pri kotu zasuka 15°

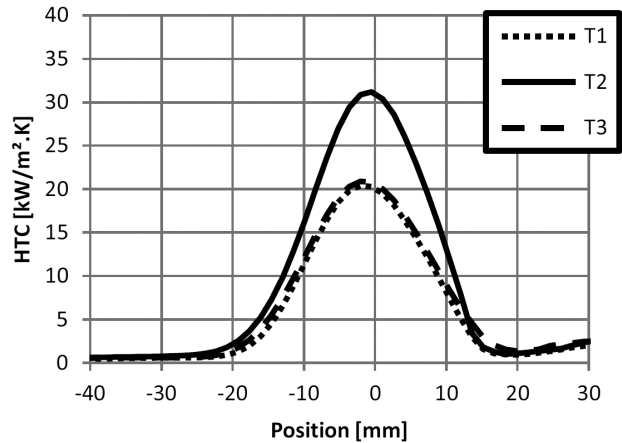


Figure 6: Measured HTC distribution for the 0° twist angle
Slika 6: Izmerjena razporeditev HTC pri kotu zasuka 0°

and T3 but it is higher by 52 %. The removed heat is higher by only 34 % for the T2 thermocouple position, compared to thermocouple positions T1 and T3.

Surface-temperature measurements for both configurations are compared in Figure 7. It is clear that the temperature drop for both configurations is almost the same at the T1 and T3 thermocouple positions. The temperature drop is approximately 40°C. The major difference is found in the overlap area where the temperature dropped by 79 °C for the 15° twist angle and by only 55 °C for the 0° twist angle. The measured temperature profile is slightly smoothed by the relatively large measuring point because the minimum diameter of the area measured with the line infrared scanner is about 10 mm.

4 CONCLUSION

Two descaling configurations were measured: a typical configuration with a 15° twist angle and one with a 0° twist angle. Heat-transfer coefficients for both undis-

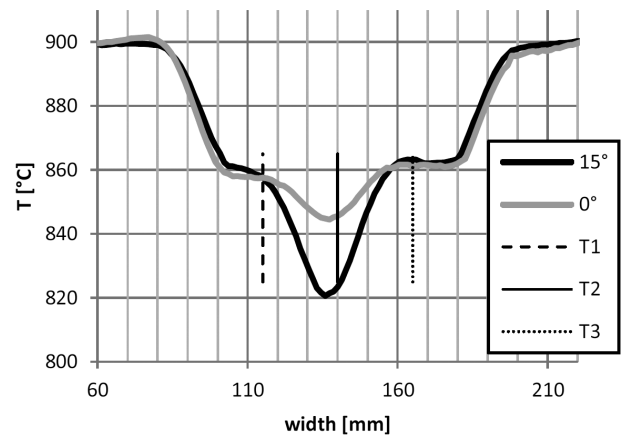


Figure 7: Measured surface temperature across the test plate, 350 mm behind descaling nozzles

Slika 7: Izmerjena temperatura površine preko plošče, 350 mm za razškaljevalno šobo

turbed and overlap areas were computed from the measurements as position-dependent values. To give a better idea of the cooling inhomogeneity across the test-plate surface, the temperature profile was measured 350 mm behind the descaling nozzles.

It was found that the overcooling in the overlap area was very high and the heat removed was almost double that of the typical descaling configurations with the 15° twist angle. The results from the experiments show that the overcooling can be significantly reduced, by 33 %, when the twist angle is set to 0°. In this case, the measured temperature drop was also reduced by 24 °C, which is 30 % of the maximum temperature drop.

The new configuration with the 0° twist angle seems to be very promising. It does not suffer from the washout effect⁸ and any overcooling is significantly reduced in the overlap area.

Acknowledgement

This work is an output of the research and scientific activities of project LO1202, with the financial support from the MEYS under the programme NPU I.

5 REFERENCES

- ¹ M. Čarnogurská, M. Příhoda, Z. Hajkr, R. Pyszko, Z. Toman, Thermal effects of a high-pressure spray descaling process, *Mater. Technol.*, 48 (2014) 3, 389–394
- ² D. C. J. Farrugia, C. Fedorciuc-Onisa, M. Steer, Investigation into mechanisms of heat losses and mechanical descalability during high pressure water descaling, *Steel Research International*, (2008), 397–402
- ³ F. Wang, L. Ning, Q. Zhu, J. Lin, T. A. Dean, An investigation of descaling spray on microstructural evolution in hot rolling, *International Journal of Advanced Manufacturing Technology*, 38 (2008) 1–2, 38–47, doi:10.1007/s00170-007-1085-x
- ⁴ J. W. Choi, Convective heat transfer coefficient for high pressure water jet, *ISIJ International*, 42 (2002) 3, 283–289, doi:10.2355/isijinternational.42.283
- ⁵ R. Colas, Modelling heat transfer during hot rolling of steel strip, *Modelling and Simulation in Materials Science and Engineering*, 3 (1995) 4, 437–453, doi:10.1088/0965-0393/3/4/002
- ⁶ M. Krzyzanowski, J. H. Beynon, Modelling the behaviour of oxide scale in hot rolling, *ISIJ International*, 46 (2006) 11, 1533–1547, doi:10.2355/isijinternational.46.1533
- ⁷ H. Votavová, M. Pohanka, Study of Water Jets Collision of High Pressure Flat Jet Nozzles for Hydraulic Descaling, *Applied Mechanics and Materials*, Switzerland, 821 (2015), 152–158, doi:10.4028/www.scientific.net/AMM.821.152
- ⁸ H. Votavová, M. Pohanka, P. Bulejko, Cooling homogeneity measurement during hydraulic descaling in spray overlapping area, 24th International Conference on Metallurgy and Materials METAL , Ostrava 2015, 1–6
- ⁹ J. Horský, M. Raudenský, M. Pohanka, Experimental study of heat transfer in hot rolling and continuous casting, *Materials Science, Testing and Informatics II*, *Materials Science Forum*, 473–474 (2005), 347–354, doi:10.4028/www.scientific.net/MSF.473-474.347
- ¹⁰ M. Pohanka, P. Kotrbáček, Design of Cooling Units for Heat Treatment, *Heat Treatment Conventional and Novel Applications*, InTech, Rijeka 2012, 1–20, doi:10.5772/50492

INVESTIGATION OF THE MECHANICAL PROPERTIES OF A CORK/RUBBER COMPOSITE

RAZISKAVA MEHANSKIH LASTNOSTI KOMPOZITA PLUTA/GUMA

Radek Kottner¹, Jiří Kocáb², Jan Heczko², Jan Krystek¹

¹University of West Bohemia, Faculty of Applied Sciences, European Centre of Excellence, NTIS – New Technologies for Information Society, Univerzitní 8, 306 14 Plzeň, Czech Republic

²University of West Bohemia, Faculty of Applied Sciences, Department of Mechanics, Univerzitní 8, 306 14 Plzeň, Czech Republic
kottner@kme.zcu.cz

Prejem rokopisa – received: 2015-07-01; sprejem za objavo – accepted for publication: 2015-07-28

doi:10.17222/mit.2015.172

This work was focused on the investigation of the mechanical properties of the ACM87 composite when subjected to a large strain. Simple tension, simple shear, simple compression, and volumetric compression tests were performed using a universal testing machine. Various strain rates were used. The material data necessary for the identification of the parameters of a finite-strain viscoelastic constitutive model, such as the Bergstrom-Boyce model, were obtained.

Keywords: cork, rubber, particle composite, Bergstrom-Boyce model, viscoelastic, large strain

Delo je usmerjeno v preiskavo mehanskih lastnosti kompozita ACM87, ki je bil izpostavljen veliki obremenitvi. Na univerzalnem preizkuševalnem stroju so bili izvršeni natezni, strižni, tlačni in volumetrični tlačni preizkusi. Uporabljene so bile različne hitrosti obremenjevanja. Dobljeni so bili podatki o materialu, ki so potrebni za postavitev parametrov konstitutivnega viskoelastičnega modela končne obremenitve, kot je Bergstrom-Boyceov model.

Ključne besede: pluta, guma, kompozitni delec, Bergstrom-Boyceov model, viskoelastičnost, velika obremenitev

1 INTRODUCTION

Cork/rubber composites are often used to damp vibrations before they are radiated as an acoustic noise and before they are transmitted to the other components of the system. An improvement of the damping properties of carbon-fibre reinforced plastics using an integration of the layers made of a cork/rubber composite or rubber, when subjected to small strain deformations, was proved.¹⁻³ In these works, cantilever flat bars and square tubes were experimentally analysed. Similar cantilever beams were applied in the structure of a machine tool. The influence of the hybrid composite lay-up on the stiffness and damping of the cantilever beams was numerically investigated.^{1,2} The Rayleigh damping was considered in the numerical simulations.

Since this work is motivated by an application of the ACM87 (AMORIM cork/rubber particle composite) as a damping layer with much larger deformations (e.g., in helmets), a more accurate material model, which would be possible to use for finite-strain simulations, has to be used. The Bergstrom-Boyce model⁴ is one of the models suitable for elastomer modelling. This micromechanics-inspired theory successfully captures many time-dependent characteristics. Since cork has a cellular structure similar to foam⁵ it does not exhibit incompressibility (in contradistinction to rubber). Therefore, the aim of this work is to obtain experimental data for the identification

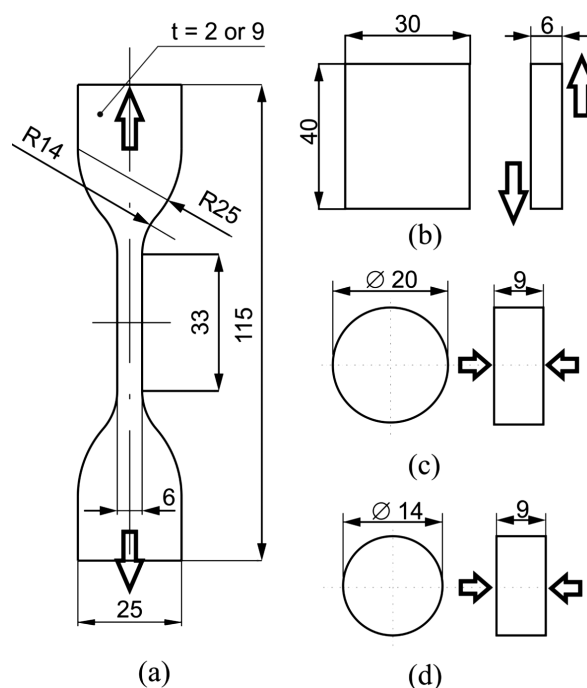


Figure 1: Experimental samples for: a) simple tension (T2 or T9), b) simple shear (S6), c) simple compression (C9), d) volumetric compression (V9)

Slika 1: Vzorci za preizkuse: a) enostaven nateg (T2 ali T9), b) enostavno striženje (S6), c) enostavno stiskanje (C9), d) volumetrično tlačenje (V9)

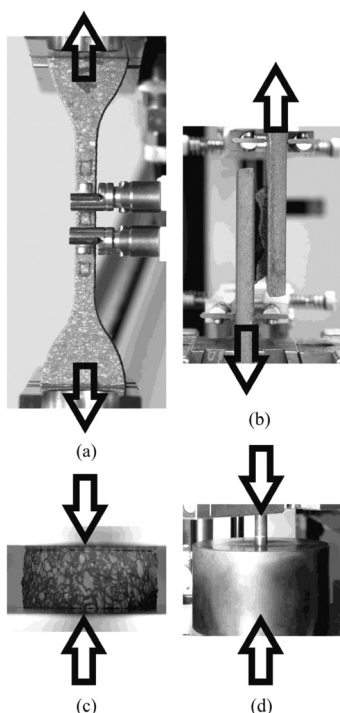


Figure 2: Performed tests: a) simple tension, b) simple shear, c) simple compression, d) volumetric compression

Slika 2: Izvedeni preizkusi: a) enostaven nateg, b) enostavno striženje, c) enostavno stiskanje, d) volumetrično tlačenje

of the parameters of a finite-strain viscoelastic constitutive model using simple tension, simple shear and simple compression tests (simple tests) according to ⁶ and, in addition, using a volumetric-compression test.

2 EXPERIMENTAL PART

Experimental samples were cut from ACM87 plates using a water jet. The plates were (2, 6 and 9) mm thick. The geometry and designation are obvious from **Figure 1**. The first symbol denotes the type of the test and the second symbol denotes the characteristic dimension. The strain rate is appended to these two symbols (e.g.,

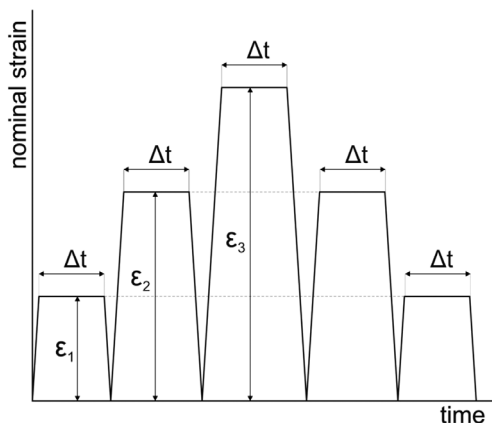


Figure 3: Applied-strain history

Slika 3: Zgodovina uporabljenega obremenjevanja

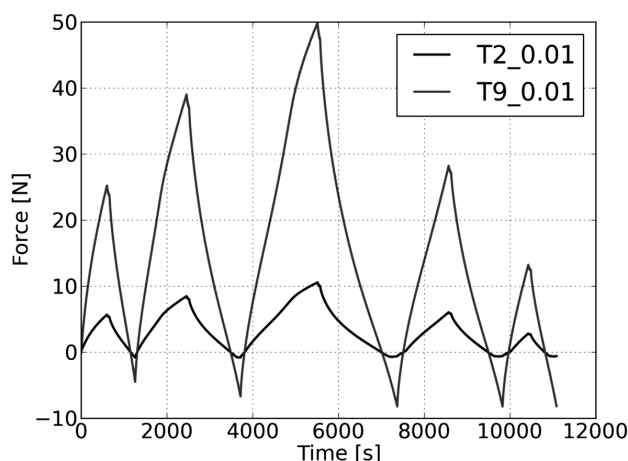


Figure 4: Force-time diagram, simple tension, strain rate of 0.01 s^{-1}
Slika 4: Diagram sila-čas enostaven nateg, hitrost obremenitve $0,01 \text{ s}^{-1}$

T2_0.10 is a tensile sample with a 2 mm thickness that was loaded at a 0.1 s^{-1} strain rate).

The tests were performed on a Zwick/Roell Z050 machine using 200 N or 50 kN load cells (**Figure 2**). A contact-type extensometer with two sensor arms was used to measure displacements under the tensile (*T*) and shear (*S*) loading. The initial gage length in the case of the T test was 10 mm. In the case of the S test, the relative displacement of the steel plates, the glue wasn't measured (it was used for the bonding of the steel plates and the samples), was measured using the Loctite 480 glue. Displacement during the compression tests was measured using an extensometer with one sensor arm that was placed on the moving platen (simple compression – C test) or on the moving grip where the piston was fixed (volumetric compression – V test).

At least three new intact samples (to enable the observation of the Mullins effect) were used for each test. The temperature was $23 \pm 1 \text{ }^\circ\text{C}$, the atmospheric moisture was $50 \pm 6 \text{ } \%$.

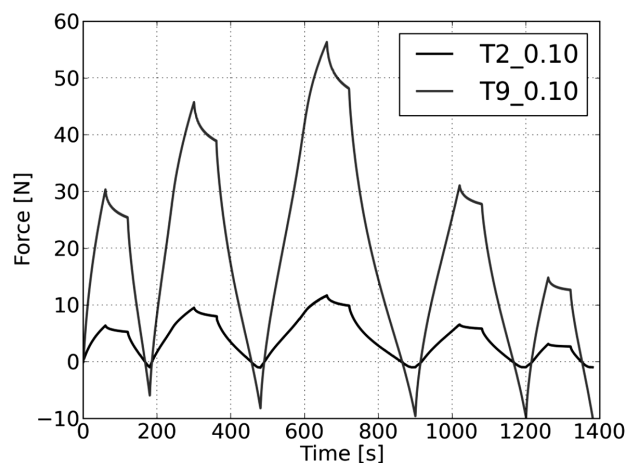


Figure 5: Force-time diagram, simple tension, strain rate of 0.1 s^{-1}

Slika 5: Diagram sila-čas, enostaven nateg, hitrost obremenjevanja $0,1 \text{ s}^{-1}$

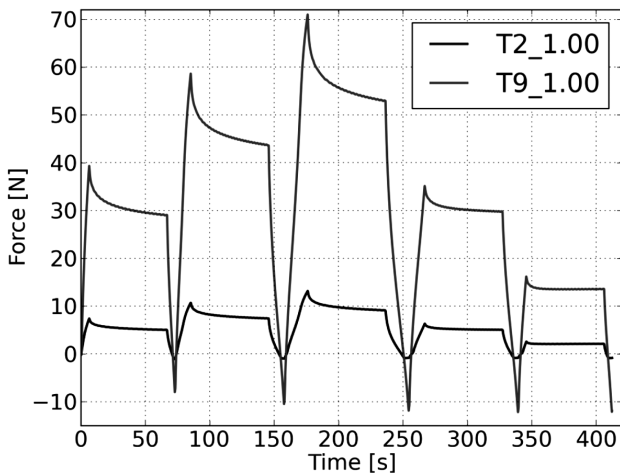


Figure 6: Force-time diagram, simple tension, strain rate of 1 s^{-1}
Slika 6: Diagram sila-čas, enostaven nateg, hitrost obremenjevanja 1 s^{-1}

The same nominal-strain history was applied in the T, S and C tests.⁶ The strain history is shown in **Figure 3**. Five loading/unloading cycles with values of the nominal strain $\varepsilon_1 = 10 \%$, $\varepsilon_2 = 20 \%$ and $\varepsilon_3 = 30 \%$ were performed. The relaxation time was $\Delta t = 60 \text{ s}$. The samples were loaded at three different nominal-strain rates: 0.01 s^{-1} , 0.1 s^{-1} , and 1 s^{-1} .

Only three cycles were performed during the V test. The maximum strain for all three cycles was 30% . The relaxation time was $\Delta t = 0 \text{ s}$. All the V samples were loaded at a 0.02 s^{-1} strain rate.

3 RESULTS AND DISCUSSION

From the minimum of three samples for each test, typical force-time/displacement curves were selected and further processed.

Figures 4 to 12 show force-time ($F-t$) curves for the simple tests. It is obvious that the forces relaxed significantly. Especially, when the strain rate was 0.1 s^{-1} , the

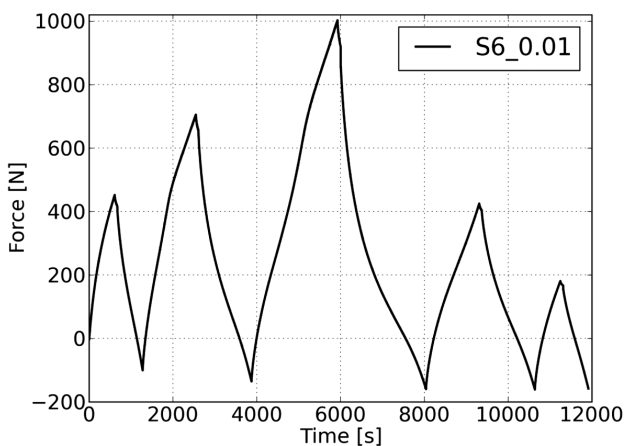


Figure 7: Force-time diagram, simple shear, strain rate of 0.01 s^{-1}
Slika 7: Diagram sila-čas, enostavno striženje, hitrost obremenjevanja $0,01 \text{ s}^{-1}$

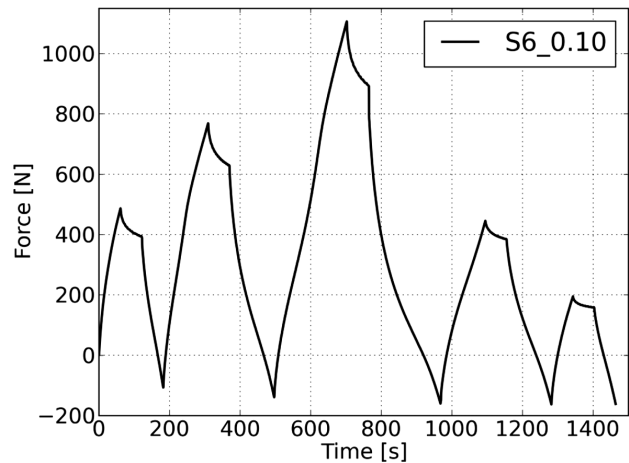


Figure 8: Force-time diagram, simple shear, strain rate of 0.1 s^{-1}
Slika 8: Diagram sila-čas, enostavno striženje, hitrost obremenjevanja $0,1 \text{ s}^{-1}$

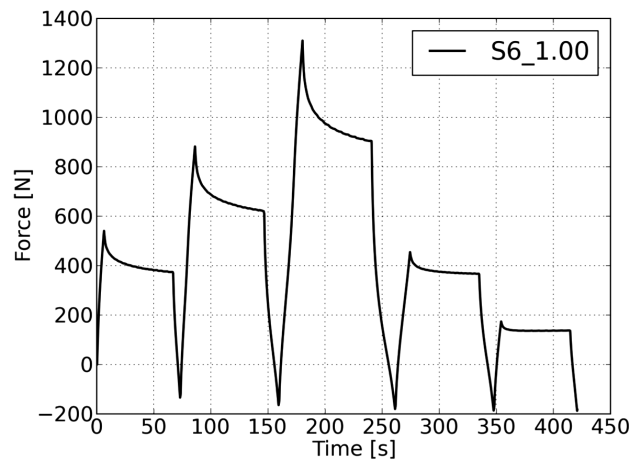


Figure 9: Force-time diagram, simple shear, strain rate of 1 s^{-1}
Slika 9: Diagram sila-čas, enostavno striženje, hitrost obremenjevanja 1 s^{-1}

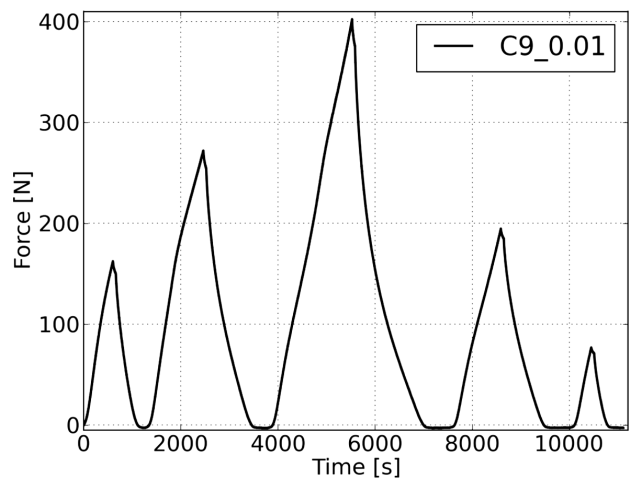


Figure 10: Force-time diagram, simple compression, strain rate of 0.01 s^{-1}
Slika 10: Diagram sila-čas, enostavno tlačenje, hitrost obremenjevanja $0,01 \text{ s}^{-1}$

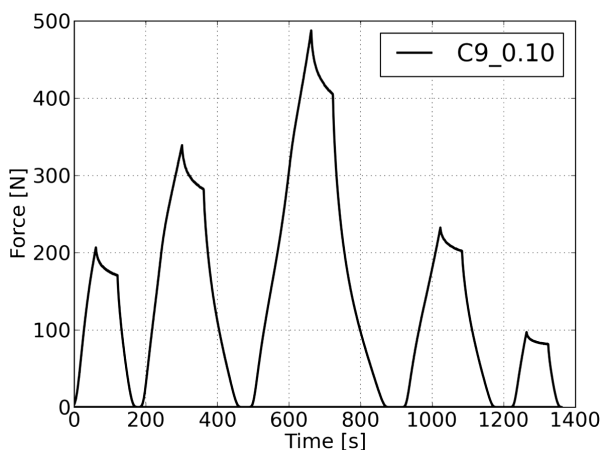


Figure 11: Force-time diagram, simple compression, strain rate of 0.1 s^{-1}
Slika 11: Diagram sila-čas, enostavno tlačenje, hitrost obremenjevanja $0,1 \text{ s}^{-1}$

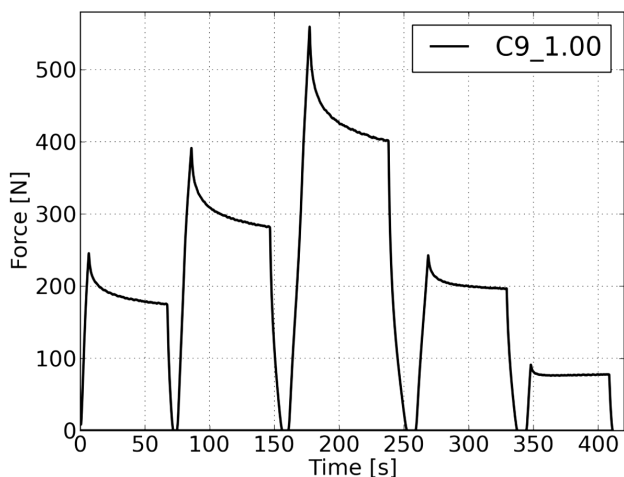


Figure 12: Force-time diagram, simple compression, strain rate of 1 s^{-1}
Slika 12: Diagram sila-čas, enostavno tlačenje, hitrost obremenjevanja 1 s^{-1}

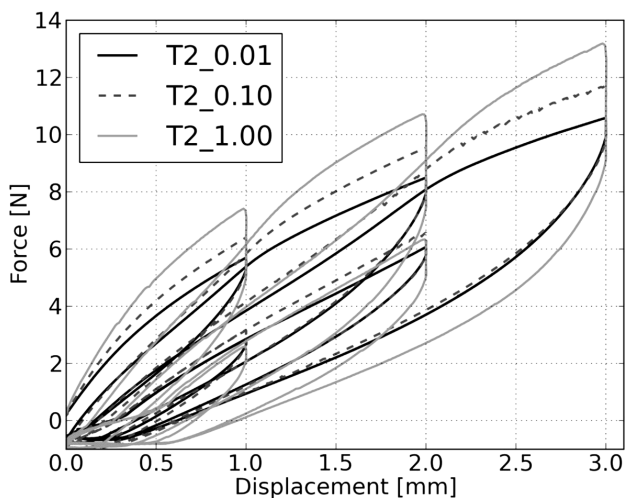


Figure 13: Force-displacement diagram, simple tension, various strain rates, sample thickness of 2 mm
Slika 13: Diagram sila-raztezek, enostaven nateg, različne hitrosti obremenjevanja, debelina vzorca 2 mm

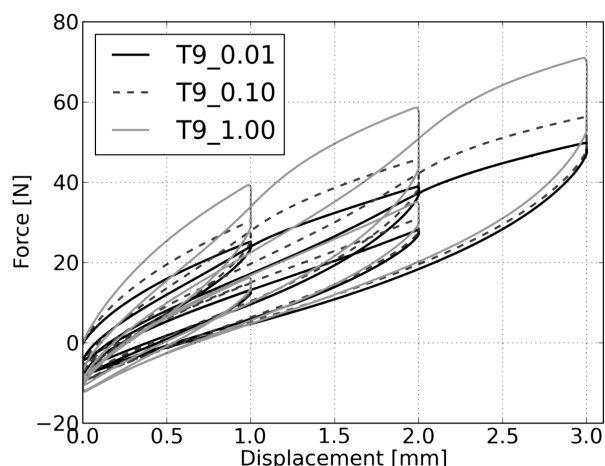


Figure 14: Force-displacement diagram, simple tension, various strain rates, sample thickness of 9 mm
Slika 14: Diagram sila-raztezek, enostaven nateg, različne hitrosti obremenjevanja, debelina vzorca 9 mm

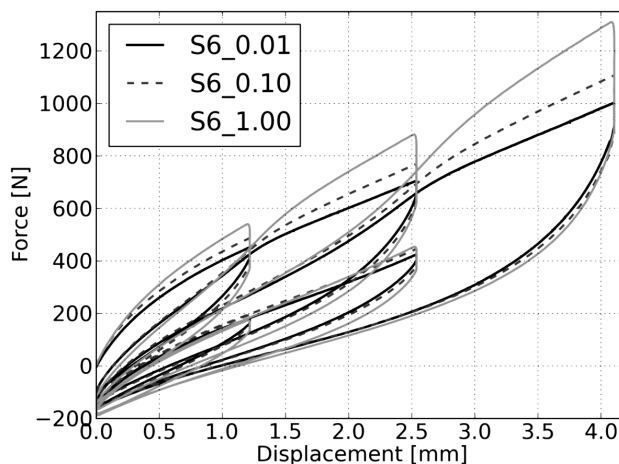


Figure 15: Force-displacement diagram, simple shear, various strain rates
Slika 15: Diagram sila-raztezek, enostavno striženje, različne hitrosti obremenjevanja

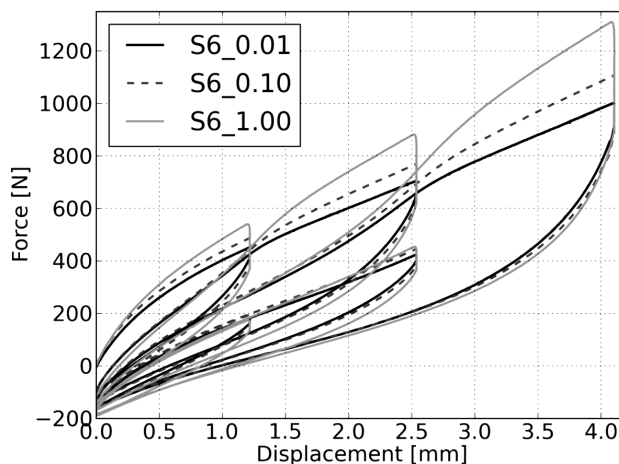


Figure 16: Force-displacement diagram, simple compression, various strain rates
Slika 16: Diagram sila-raztezek, enostavno tlačenje, različne hitrosti obremenjevanja

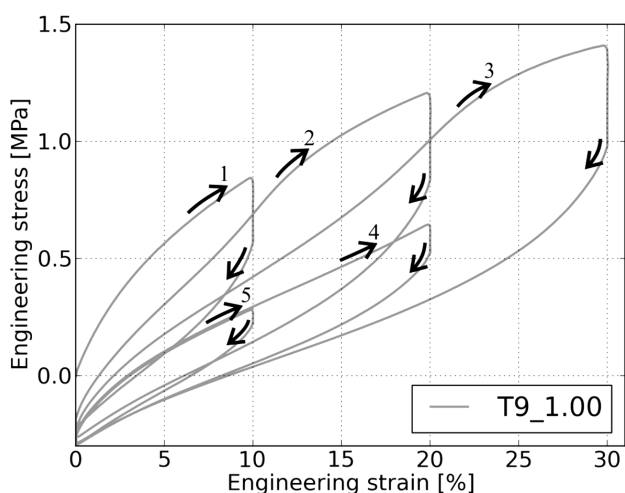


Figure 17: Stress-strain diagram, simple tension, cycle explanation
Slika 17: Diagram napetost-raztezek, enostaven nateg, razlaga ciklov

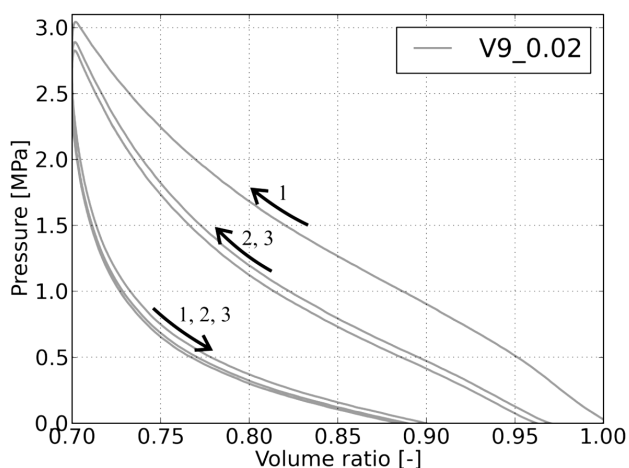


Figure 18: Volumetric compression, strain rate of 0.02 s^{-1}
Slika 18: Volumetrično tlačjenje, hitrost obremenjevanja $0,02 \text{ s}^{-1}$

force decrease was approximately 30 % during the relaxation time and if the relaxation time was longer, the force would still relax.

The force-displacement ($F-u$) curves of the simple tests are shown in **Figures 13 to 16**. The sequence of the loading/unloading cycles is obvious from the stress-strain curve of the simple tension test in **Figure 17**. A significant influence of the strain rate on the $F-u$ curves is obvious in all the performed tests. Both hysteresis and stiffness increase with the strain rate.

The observed force-time/displacement diagrams can be converted (using the mentioned geometry of the samples) into stress-time/strain diagrams. Then, a closed-form solution of the identification of the parameters of a large-strain viscoelastic constitutive model can be

performed. However, a conversion with high accuracy is possible only in the case of simple tension. In the cases of simple compression and simple shear, the strain distribution is not homogeneous. Therefore, a more accurate identification process can be done using a numerical model where the $F-t$ or $F-u$ curves of finite-element-method simulations are fitted to the experimental data.^{7,8}

Figure 18 shows a pressure-volume ratio diagram of the volumetric compression test. Assuming a hydrostatic stress field, the value of the initial bulk modulus was determined to be $K = 9.3 \text{ MPa}$.⁹

4 CONCLUSIONS

Experimental data for the identification of the parameters of the Bergstrom-Boyce model or other viscoelastic constitutive models of the ACM87 composite were obtained. Significant time-dependent behaviour of the material was proved. The amount of energy dissipated during the loading/unloading cycles (the area within the loops) demonstrates the suitability of the cork/rubber composite for damping.

Acknowledgement

This work was supported by the Ministry of Education, Youth and Sports of the Czech Republic under the project LO1506 PUNTIS, and by the Student Grant System SGS-2013-36.

5 REFERENCES

- R. Kottner, J. Vacík, R. Zemčík, *Mater. Tehnol.*, 47 (2013) 2, 189–193
- V. Lašová, J. Vacík, R. Kottner, *Procedia Engineering*, 48 (2012), 358–366, doi:10.1016/j.proeng.2012.09.526
- J. Vacík, V. Lašová, R. Kottner, J. Káňa, *Experimental determination of damping characteristics of hybrid composite structure*, Proc. of the 48th International Scientific Conference on Experimental Stress Analysis, Velké Losiny, 2010, 483–490
- J. S. Bergström, M. C. Boyce, *Mechanics of Materials*, 32 (2000) 11, 627–644, doi:10.1016/S0167-6636(00)00028-4
- A. Kossa, *Effect of the modelling of lateral stretch in the parameters identification algorithm of hyperelastic foam materials*, Proc. of the 31st Danubia-Adria Symposium on Advances in Experimental Mechanics, Kempten, 2014, 141–142
- J. S. Bergström, *Bergström-Boyce model*, *Material Models* [online] 2015, available at <https://polymerfem.com/content.php?77-bergstrom-boyce-model>
- T. Kroupa, V. Laš, R. Zemčík, *Journal of Composite Materials*, 45 (2011) 9, 1045–1057, doi:10.1177/0021998310380285
- H. Srbová, T. Kroupa, R. Zemčík, *Mater. Tehnol.*, 48 (2014) 4, 549–553
- S. Z. Qamar, M. Akhtar, T. Pervez, M. S. M. Al-Kharusi, *Materials and Design*, 45 (2013), 487–496, doi:10.1016/j.matdes.2012.09.020

FABRICATION AND PROPERTIES OF SiC REINFORCED COPPER-MATRIX-COMPOSITE CONTACT MATERIAL

IZDELAVA IN LASTNOSTI S SiC UTRJENEGA KOMPOZITNEGA MATERIALA NA OSNOVI BAKRA

Gozde Fatma Celebi Efe^{1,2}, Mediha İpek¹, Sakin Zeytin¹, Cuma Bindal^{1,2}

¹Sakarya University, Faculty of Engineering, Department of Metallurgy and Materials Engineering, Esentepe Campus, 54187 Sakarya, Turkey

²Sakarya University, Biomedical, Magnetic and Semi Conductive Materials Research Center (BIMAS-RC), Esentepe Campus, 54187 Sakarya, Turkey
gcelebi@sakarya.edu.tr

Prejem rokopisa – received: 2015-07-01; sprejem za objavo – accepted for publication: 2015-07-28

doi:10.17222/mit.2015.175

This study aims at improving mechanical properties of electrical contacts through copper and copper-matrix silicon-carbide-reinforced composites produced with powder metallurgy. Copper powder was produced with the cementation method. Pure copper and mixtures of copper with 3 % of mass fraction of SiC powder were pressed with a uniaxial pressure of 280 MPa and sintered at 700 °C for 2 h in an atmospheric environment. After the sintering, these compacts were immediately pressed at a load of 850 MPa while the samples were hot. The characterization of the samples was made with microstructural investigations, relative-density experiments, electrical-conductivity and hardness measurements. XRD analyses revealed that there are no other phases besides Cu and SiC in the sintered samples. Electrical conductivity of pure copper was reduced from 91.7±1.8 % IACS to 66.4±0.9 % IACS but the hardness of pure copper was increased from 127±1.2 HVN to 142±6.0 HVN with the addition of 3 % of mass fraction of SiC. Contact-count experiments were made with these samples to determine the contact performance for (3000, 6000, 9000, 12.000 and 21.000) turns-on/off. The loss of the contact material increased with the increasing number of turn-ons, related with the increased copper oxide amount formed on the contact surfaces.

Keywords: Cu-SiC composite, hardness, relative density, electrical conductivity, IACS, contacts test

Namen študije je izboljšanje mehanskih lastnosti električnih kontaktov iz bakra in kompozita bakra, ojačanega z delci silicijevega karbida, izdelanih iz prahov. Prah bakra je bil izdelan z metodo cementacije. Čisti baker in mešanice bakra s 3 masnimi odstotki SiC so bili enoosno stiskani s tlakom 280 MPa in sintrani 2 h na 700 °C v atmosferskem okolju. Po sintranju so bili vzorci še vroči stisnjeni z obtežbo 850 MPa. Vzorci so bili karakterizirani s preiskavo mikrostrukture, z eksperimenti relativne gostote, z meritvijo električne prevodnosti in z meritvijo trdote. Rentgenska difrakcija je odkrila, da v sintranih vzorcih ni drugih faz, razen Cu in SiC. Električna prevodnost čistega bakra se je zmanjšala iz 91,7±1,8 % IACS na 66,4±0,9 % IACS, trdota čistega bakra se je povečala iz 127±1,2 HVN na 142±6,0 HVN z dodatkom 3 masnih odstotkov SiC. Preizkusi števila kontaktov so bili izvedeni s temi vzorci za določitev zmogljivosti kotaktov pri (3.000, 6.000, 9.000, 12.000 in 21.000) vklopih in izklopih. Izguba materiala kontakta se povečuje s povečanjem števila vklopov, kar je posledica povečanega obsega tvorbe oksida bakra na kontaktni površini.

Ključne besede: Cu-SiC kompozit, trdota, relativna gostota, električna prevodnost, IACS, preizkus kontaktov

1 INTRODUCTION

There are many electrical contact materials subject to relative motions and used in a variety of applications, such as electrical switches, contactors, circuit breakers, connectors, relays, chips in cards, voltage regulators, arcing tips and switch gears.^{1,2} Electrical contact materials used in these applications must have a good combination of wear strength, high electrical conductivity, and erosion and welding resistance. On the contrary, low electrical conductivity and wear resistance cause poor contact and arcing, and thus the contacts erode. An electric arc is the form of an electric discharge with the highest current density that takes place when contacts are in the process of establishing a current flow interrupting the flow of the current. Depending on high temperature and mass flow on the contact material surface, an erratic contact resistance and a material loss occur, thus the contact material surface is severely corroded and eroded. Hence, a contact material should have a high resistance to corrosion as

well as a high arc-erosion resistance to maintain the contact integrity by having high electrical and thermal conductivity, a high melting point and also a certain strength.^{2,3} As copper has a high thermal conductivity, a low electrical resistance, a lower coefficient of thermal expansion (CTE) than aluminum and can easily be formed or machined into complicated lead frames or base plates, it is extensively used for cables, wires, electrical contacts and a wide variety of other parts that are required to pass electrical current.^{4,5}

Cu-based composites were feasible to be used as electrical-contact materials in relays, contactors, switches, circuit breaks and other switch-gear components.⁶ As SiC has a high thermal conductivity and offers good availability, low price and possible machinability, it can be used as a reinforcement in copper-based composites for high-performance heat-sink materials and packages. Dispersion of fine SiC particles improve the copper-matrix strength through impeding the dislocation movement and also prevent the grain growth of the copper

matrix at high temperature so that the composites can maintain a relatively high strength at elevated temperature.^{3,7-9} In the present work, the effects of SiC particles on the electrical, mechanical and also contact performance of Cu-SiC composites were investigated.

2 EXPERIMENTAL DETAILS

The copper powder used in this study was produced, with the cementation method, from CuSO₄ solutions using metallic-iron powder. Cemented Cu powder and 3 % mass fractions of SiC powder with a 99.5 % purity and a 1 μm particle size were mechanically mixed and cold pressed. The sintering of pure copper and copper 3 % mass fraction of SiC was performed at 700 °C for 2 h, embedded in the graphite powder. In order to increase the relative density and mechanical properties of test samples, they were hot pressed after the sintering. The presence of the phases formed within the sintered samples was determined with X-ray diffraction using Cu-K_α radiation with a wavelength of 1.5418 Å over a 2θ range of 10–90°. The relative densities of the composites were measured with a method based on Archimedes' law.

The microstructure analysis of the composites was performed with a JEOL JSM-5600 model scanning electron microscope (SEM). The microhardness of both pure copper and the composite was measured with a Leica WMHT-Mod model Vickers-hardness instrument under an applied load of 50 g. The measurements of electrical conductivity of the specimens were performed with a GE-model electrical-resistivity measurement instrument. The experimental set-up for the contact test consisted of a square 555-wave oscillator turning on/off the contactor, a counter and a contactor, on which the samples were mounted. The contact counter was adjusted to the desired number (3000, 6000, 9000, 12.000 and 21.000) before the experiment. When the selected count number was reached, the operation was automatically ended. The electrical load over the counter was 1600 W (at 220 V) for all the experiments. The experimental set-up used in this study is shown in **Figure 1**. The weight loss of the samples was determined. Subsequently, surface and oxide evaluations of the samples were carried out with SEM-EDS.

3 RESULTS AND DISCUSSION

SEM micrographs of Cu and the SiC reinforcement agent used in the experimental studies and the sintered Cu-3 % of mass fractions of SiC composite are given in **Figure 2**. It is seen from **Figure 2a** that copper powder has a spherical shape and a particle size of 5 μm; and it is seen from **Figure 2b** that SiC particles have an angular and irregular shape, and a diameter of 1 μm. In **Figure 2c** light-grey areas indicate the Cu matrix and dark-grey

and cornered shapes indicate the SiC reinforcement component.

XRD patterns of the Cu-3 % of mass fractions of SiC composite consist of copper and SiC peaks (**Figure 3**). No oxide peak was observed in the XRD analysis of the Cu-3 % of mass fractions of SiC composite sintered at 700 °C for 2 h. The relative density, hardness and % IACS (the international annealed copper standard) of the samples are given in **Table 1**. The relative density of the sintered samples decreased with the addition of SiC because SiC particles behave as an obstacle for the Cu atom diffusion. On the contrary, the hardness was found to increase with the SiC addition. The SiC addition strongly impeded the plastic flow, causing the hardness of the Cu-SiC composite to increase with the amount of reinforcing particles. It is known that the higher the relative density the higher is the electrical conductivity.

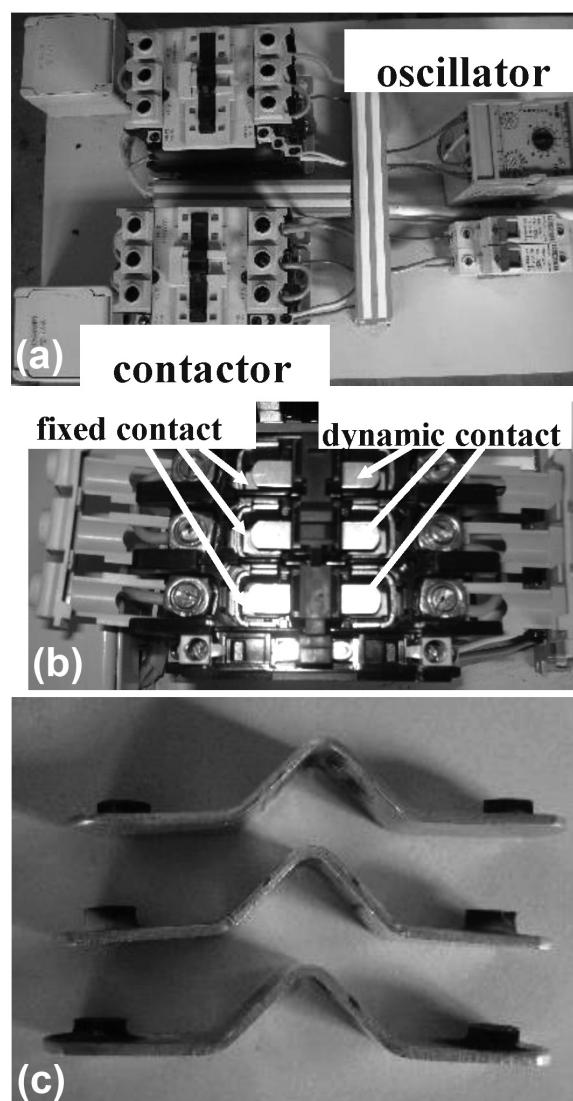


Figure 1: Images of: a) experimental set-up, b) contactor, on which samples were fixed, and contacts, c) dynamic contacts

Slika 1: Posnetki: a) eksperimentalnega sestava, b) kontaktorja, na katerem so pritrjeni vzorci in kontakti, c) dinamičnih kontaktov

The electrical conductivity of the composites decreased with the increment in the SiC content because ceramic-based SiC forms a barrier to the motion of copper electrons, providing electrical conductivity.

Generally, the weight loss increased with the increasing contact count for both Cu and Cu-3 % of mass fractions of SiC composite. But it is obvious that the material loss of the Cu-3 % of mass fractions of SiC composite is higher than that of pure Cu (Figure 4).

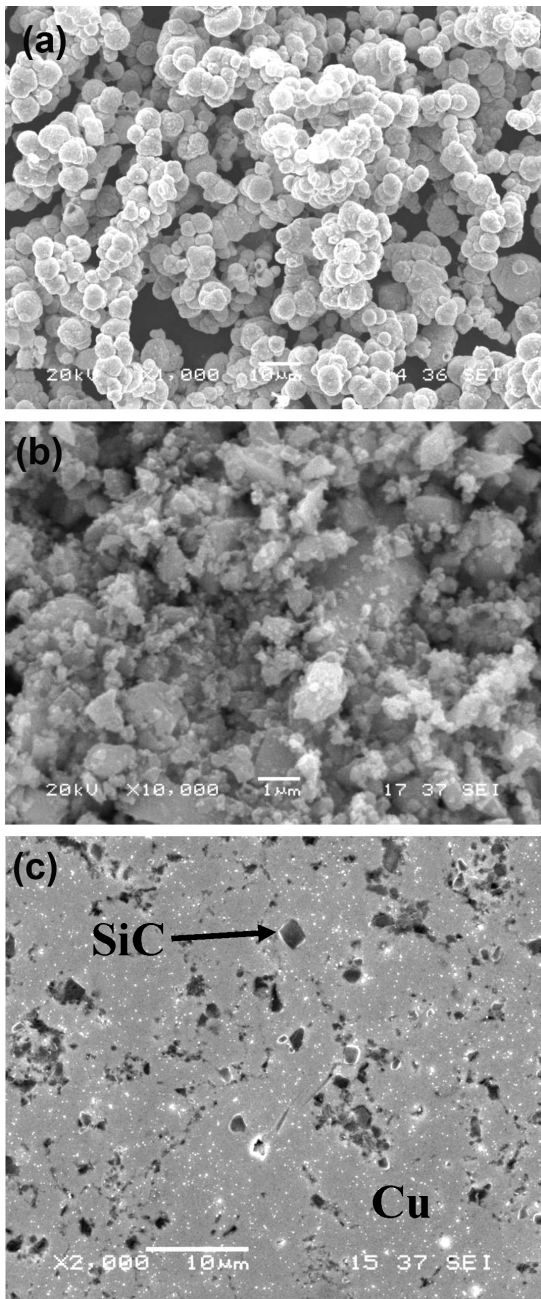


Figure 2: SEM micrographs of: a) copper powder, b) SiC particles and c) Cu-3 % of mass fractions of SiC composite
Slika 2: SEM-posnetki: a) prah bakra, b) delci SiC in c) kompozit Cu-3 % masnega deleža SiC

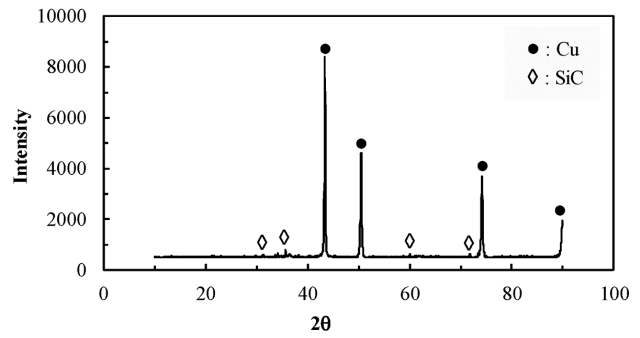


Figure 3: XRD patterns of Cu-3 % of mass fractions of SiC composite sintered at 700 °C for 2 h

Slika 3: Rentgenogram kompozita Cu-3 % masnega deleža SiC, sintranega 2 h na 700 °C

Table 1: Relative density, hardness and electrical-conductivity values of Cu and Cu-3 % of mass fractions of SiC composite sintered at 700 °C for 2 h

Tabela 1: Relativna gostota, trdota in električna prevodnost Cu in kompozita Cu-3 % masnega deleža SiC, 2 h sintranega na 700 °C

Samples	Relative density (%)	Hardness (HV)	% IACS
Cu	97.5 ± 0.8	127 ± 1.2	91.7 ± 1.8
Cu-3% of mass fractions of SiC	92.3 ± 1.1	142 ± 6	66.4 ± 0.9

SEM photographs of the sample surfaces after (3000, 6000 and 9000) turns-on/off are given in Figures 5 and 6. When SiC reinforced contact materials heat up, they have to absorb heat, cool down the contact and delay the arc formation; thus, their material loss is lower than that of pure copper.² But it can be seen from the SEM micrographs that the surface of the Cu-3 % of mass fractions of SiC composite is destroyed to a larger extent than the surface of pure Cu; in addition, spherical formations, which got smaller with the increasing contact count number, were detected on the contact surfaces. With the increasing contact count number, deformed regions

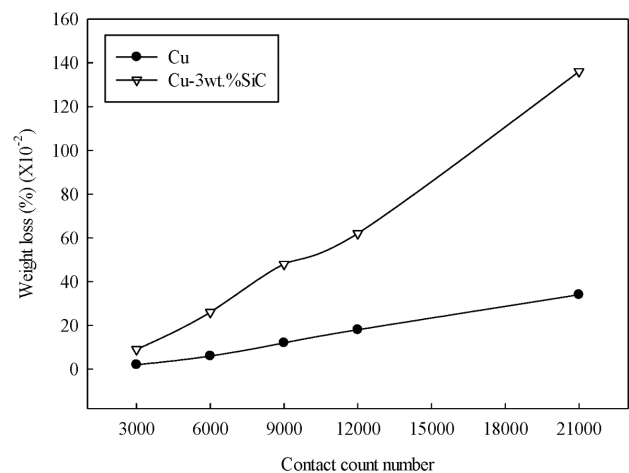


Figure 4: Weight loss of the contact via the contact count number
Slika 4: Zmanjšanje teže kontakta v odvisnosti od števila vklopov

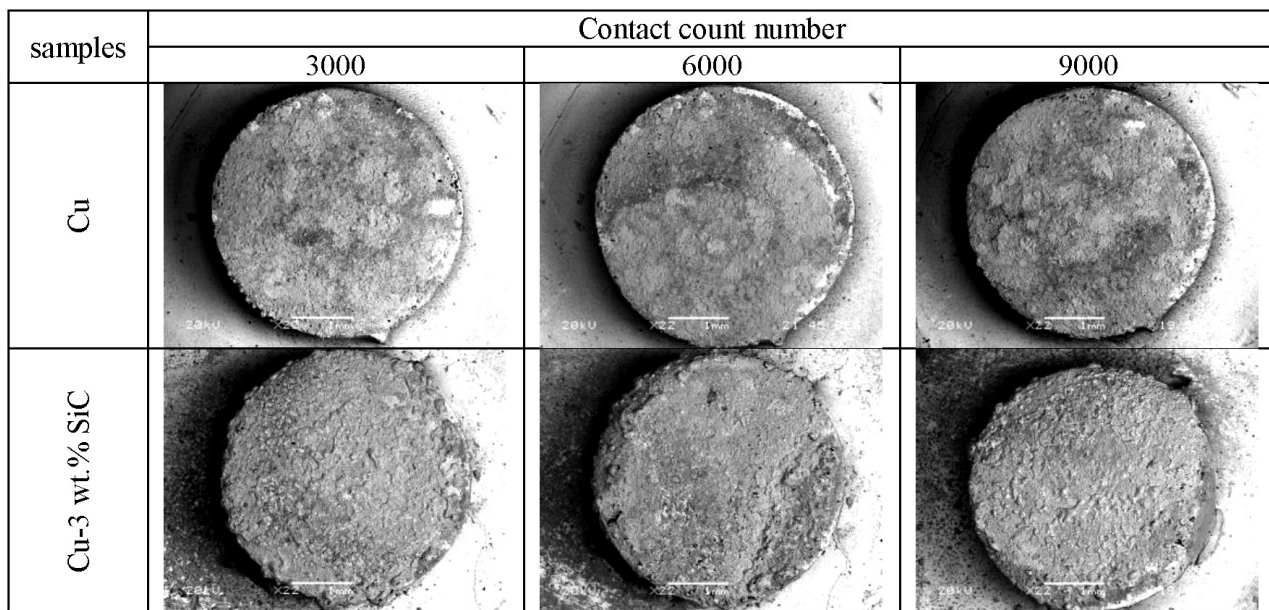


Figure 5: SEM micrographs of Cu and Cu-3 % of mass fractions of SiC composite at a low magnification after 3000, 6000 and 9000 turns on/off
Slika 5: SEM-posnetki Cu in kompozita Cu-3 % masnega deleža SiC pri majhni povečavi, po 3000, 6000 in 9000 vklopih in izklopih

increased and local melting and smearing areas were formed.

EDS result taken from the surfaces of the contact samples are given in **Figures 7 and 8**. It was found that the weight loss increased with the increasing number of turns on/off in the contact-count experiments. Surface evaluations showed that oxide increased when the number of turns on/off increased and the arc formation got easier. O. Guler and E. Evin² claimed that an increased copper oxide amount simplifies the arc formation between the contacts by increasing the contact resistance.

An increasing arc or a high resistance on a contact-material surface during a turn on/off heats up the contact surfaces. When the contact number is increased, particles on the surface become coarser. Brittle oxide layers on the contact material are broken by the impact force formed during turns on/off and removed from the surface. This causes a mass loss. This situation continues with a feedback mechanism.² The EDS analysis of the sphere formations on the pure Cu surface after 9000 contacts show that these regions are O- and Cu-rich areas (**Figure 7**). The EDS analysis shows that many Cu-rich regions

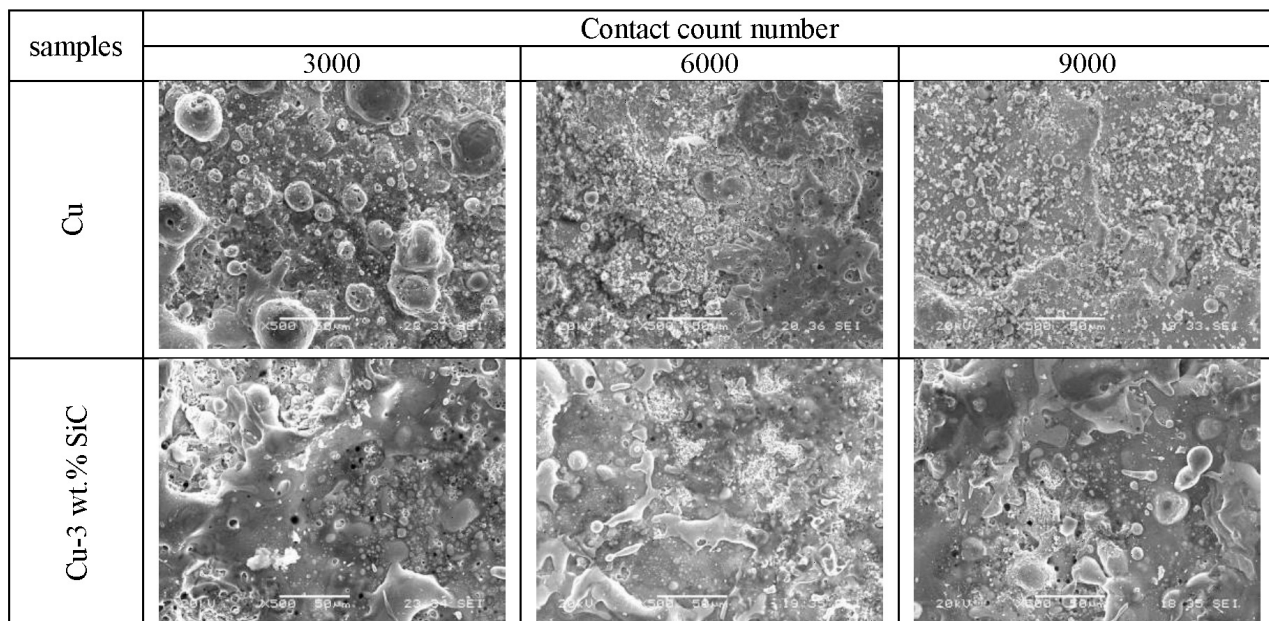


Figure 6: SEM micrographs of Cu and Cu-3 % of mass fractions of SiC composite after 3000, 6000 and 9000 turns on/off
Slika 6: SEM-posnetki Cu in kompozita Cu-3 % masnega deleža SiC po 3000, 6000 in 9000 vklopih in izklopih

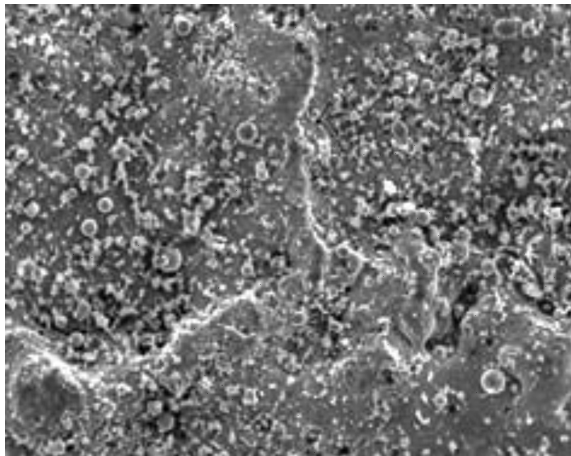


Figure 7: SEM micrograph and EDS analysis of Cu contact after 9000 turns on/off

Slika 7: SEM-posnetek in EDS-analiza Cu kontakta po 9000 vklopih in izklopih

w/%	Marks					
	1	2	3	4	5	6
C		15.66				
O	16.25	17.68	23.900	20.87	17.87	1.641
S			0.328			
Fe	1.181	0.845	1.035	1.158	0.765	0.510
Cu	82.56	65.79	74.737	77.96	81.35	97.85

remain intact because they are under the average contact level. The remaining Cu-rich areas show that the contact material can resist more turn on/off cycles.

In **Figure 8**, glassy regions rich with silicon, verified with the EDS analysis, are obvious. SiC particles probably oxidized with the increasing arc, the heat effect and/or the Cu and Si compounds formed. A. K. Kang and S. B. Kang¹⁰ indicated that SiC particles decompose into Si and C and merge with Cu. T. Schubert et al.⁵ claimed that SiC is not stable at elevated temperatures and forms Cu-Si solid solutions due to its decomposition. In **Figure 8**, Si-rich areas indicated with arrows have some bubbles and pores. These pores may result from gas reactions. It is thought that the gases in these bubbles leak towards the surface with the increasing heat/arc and bulge on the material surface. During the contact test, decomposed C reacts with O, which results in CO₂ and CO gas formations.¹⁰ The microcracks in the micrographs indicate that the contact surfaces are brittle and may be coated with a thin oxide film (**Figure 8b**).

4 CONCLUSIONS

A cemented Cu-SiC composite was manufactured successfully with the powder-metallurgy method. The presence of Cu and SiC was verified with an XRD analysis. All of the samples manufactured had a remarkably high relative density. The hardness of the composite was increased with added SiC. It was observed that the

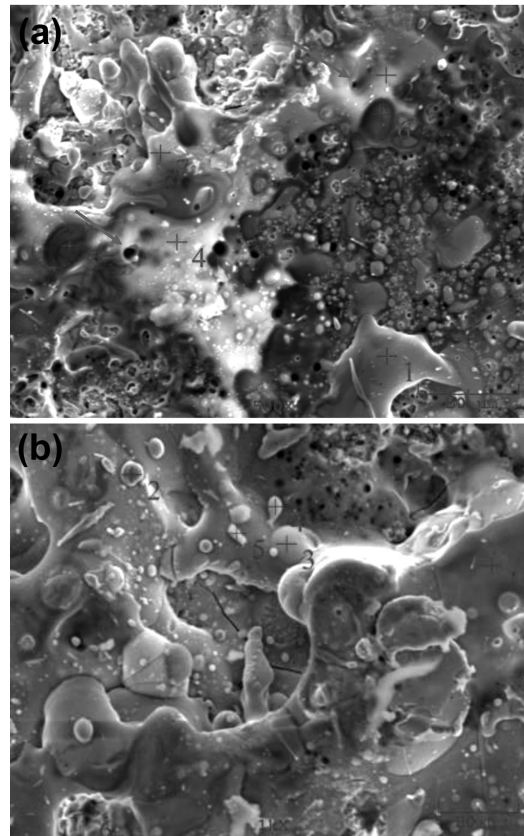


Figure 8: EDS analysis of Cu-3 % of mass fractions of SiC composite after: a) 3000, b) 9000 turns on/off

Slika 8: EDS-analiza kompozita Cu-3 % masnega deleža SiC po: a) 3000 in b) 9000 vklopih in izklopih

w/%	Marks						
	1	2	3	4	5	6	7
C	2.364						
O	8.36	42.1	16.9	39.4	31.9	24.0	21.8
Si		16.1	4.39	17.8	11.9	6.00	11.2
Fe	0.86	4.08	0.83	5.86	2.90	1.83	5.85
Cu	88.4	37.6	77.8	36.8	53.1	68.1	60.9

w/%	Marks					
	1	2	3	4	5	6
O	42.05	7.707	8.085	49.89	51.44	11.06
Si	17.77	0.939	1.630	15.83	14.76	0.219
Fe	8.527	1.152	1.024	6.112	5.813	0.226
Cu	31.64	90.20	89.26	28.15	27.97	35.09

electrical conductivity of the Cu-SiC composite is in good agreement with the literature. During the contact-count experiments, the weight loss and oxidation increased with the increasing number of turns on/off for both samples. Also, the surface of the Cu-3 % of mass fractions of SiC composite was destroyed to a larger extent than the surface of pure Cu.

Acknowledgment

The authors thank expert Fuat Kayis for performing the XRD and SEM-EDS studies and special thanks are

extended to technician Ersan Demir of the Sakarya University for assisting with the experimental studies. This work was conducted as a project supported by TUBITAK, with the contract number of 106M118.

5 REFERENCES

- ¹ J. Barrigaa, B. Fernandez-Diaza, A. Juarrosa, S. I. Ahmedb, J. L. Aranac, Microtribological analysis of gold and copper contacts, *Tribology International*, 40 (2007), 1526–1530, doi:10.1016/j.triboint.2007.01.009
- ² O. Guler, E. Evin, The investigation of contact performance of oxide reinforced copper composite via mechanical alloying, *Journal of Materials Processing Technology*, 209 (2009), 1286–1290, doi:10.1016/j.jmatprotec.2008.03.034
- ³ Z. Shi, M. Yan, The preparation of Al₂O₃-Cu composite by internal oxidation, *Applied Surface Science*, 134 (1998), 103–106, doi:10.1016/S0169-4332(98)00223-2
- ⁴ R. D. Joseph, Copper and copper alloys, *ASM International Handbook*
- ⁵ T. Schubert, A. Brendel, K. Schmid, T. Koeck, L. Ciupinski, W. Zielinski, T. Weibgarber, B. Kieback, Interfacial design of Cu-SiC composites prepared by powder metallurgy for heat sink applications, *Composites*, 38 (2007), 2398–2403, doi:10.1016/j.compositesa.2007.08.012
- ⁶ R. Zhang, L. Gao, J. Guo, Temperature-sensitivity of coating copper on sub-micron silicon carbide particles by electroless deposition in a rotation flask, *Surface and Coatings Technology*, 166 (2003), 67–71, doi:10.1016/S0257-8972(02)00748-X
- ⁷ J. Zhu, L. Liu, G. Hu, B. Shen, W. Hu, W. Ding, Study on Composite Electroforming of Cu/SiC Composites, *Materials Letters*, 58 (2004), 1634–1637, doi:10.1016/j.matlet.2003.08.040
- ⁸ R. Zhang, L. Gao, J. Guo, Effect of Cu₂O on the fabrication of SiCp/Cu nanocomposites using coated particles and conventional sintering, *Composites: Part A*, 35 (2004), 1301–1305, doi:10.1016/j.compositesa.2004.03.02
- ⁹ G. Celebi, M. Ipek, S. Zeytin, C. Bindal, An investigation of the effect of SiC particle size on Cu- SiC composites, *Composites: Part B*, 43 (2012) 4, 1813–1822, doi:10.1016/j.compositesb.2012.01.006
- ¹⁰ H. K. Kang, S. B. Kang, Thermal decomposition of silicon carbide in a plasma sprayed Cu/SiC composite deposit, *Materials Science and Engineering A*, 428 (2006), 336–345, doi:10.1016/j.msea.2006.05.054

INVESTIGATION OF THE CUTTING FORCES AND SURFACE ROUGHNESS IN MILLING CARBON-FIBER-REINFORCED POLYMER COMPOSITE MATERIAL

PREISKAVA SIL REZANJA IN HRAPAVOSTI POVRŠINE PRI REZKANJU KOMPOZITNEGA POLIMERNEGA MATERIALA, OJAČANEGA Z OGLJIKOVIMI VLAKNI

Senol Bayraktar¹, Yakup Turgut²

¹Recep Tayyip Erdogan University, 53100 Rize, Turkey

²Gazi University, Faculty of Technology, Manufacturing Engineering, 06500 Teknikokullar, Ankara, Turkey
senol.bayraktar@erdogan.edu.tr, senolbyrkr@gmail.com

Prejem rokopisa – received: 2015-07-03; sprejem za objavo – accepted for publication: 2015-07-27

doi:10.17222/mit.2015.199

In this study, milling of a carbon-fiber-reinforced polymer composite material (CFRP) was investigated experimentally using various carbide end mills. The input parameters included the spindle speed, feed rate and cutting tool, whereas the output parameters were defined as the cutting force and surface roughness. The experimental design was based on the Taguchi L_{18} ($6^1 \times 3^2$) orthogonal array. In the tests, six different carbide end mills with a 10 mm diameter were used: an uncoated two-flute 30° helix-angled one; carbide-coated two-, three- and four-flute 30° helix-angled ones; and TiAl-coated three- and four-flute 45° helix-angled ones. The cutting parameters included three different feed rates (0.03, 0.06, 0.09) mm/tooth and three different spindle speeds (3800, 4800, 5800) min^{-1} . The Taguchi method was applied to select the most appropriate cutting parameters (cutting force, feed rate) for the tests. With the analysis of variance (ANOVA), the feed-rate factor was found to be the most effective one among these parameters (cutting forces and surface roughness). The results of the experiments showed that the uncoated carbide end mill had a better performance in terms of the cutting forces and surface roughness. Besides, it was also seen that the surface roughness increases with the increasing number of flutes and helix angle.

Keywords: CFRP, cutting forces, surface roughness, Taguchi method, ANOVA

V študiji je bil eksperimentalno proučevano rezkanje polimerne kompozitnega materiala, ojačanega z ogljikovimi vlakni (CFRP) z uporabo rezkarjev z različnim karbidnimi nanosi. Vhodni parametri so vključevali hitrost vrtenja vretena, hitrost podajanja in rezalno orodje, medtem ko sta bila izhodna parametra sila rezanja in hrapavost površine. Zasnova eksperimenta je temeljila na Taguchi L_{18} ($6^1 \times 3^2$) ortogonalni matriki. Pri preskusih je bilo uporabljenih šest različnih cilindričnih rezkarjev s premerom 10 mm, dvorezni s kotom spirale 30° brez nanosa, dvo, tri in štirirezni s kotom spirale 30° prekriti s karbidi ter tri- in štirirezni rezkar s kotom spirale 45° in nanosom TiAl. Uporabljeni parametri rezanja so vključevali tri različne hitrosti podajanja (0.03, 0.06, 0.09) mm/zob in tri različne hitrosti vrtenja vretena (3800, 4800, 5800) min^{-1} . Za izbiro najprimernejših uporabljenih parametrov (sila rezanja, hitrost podajanja), je bila uporabljena Taguchi metoda. Med uporabljenimi parametri (sila rezanja in hrapavost površine) se je pokazalo, s pomočjo analize variance (ANOVA), da je hitrost podajanja najbolj vpliven faktor. Rezultati preskusov so pokazali, da ima rezkar brez nanosa karbida, boljše zmogljivosti glede na silo rezanja in hrapavost površine. Poleg tega se je pokazalo, da hrapavost površine narašča z večanjem števila utovorov in kota vijačnice.

Ključne besede: CFRP, sila rezanja, hrapavost površine, Taguchi metoda, ANOVA

1 INTRODUCTION

In the aviation and automotive industry, processing of composite materials constitutes the great majority of the machining operations. On the composite materials, machining operations such as milling, drilling, edge cutting, turning and grinding are practiced. In these applications, some undesired situations such as tool wear, delamination and fiber rupture are encountered due to non-uniform structures of composite structures. The reasons for these situations are unsuitable cutting parameters and cutting conditions.¹

Milling is a widely used process in the machining of CFRP materials. A composite material, which is taken out of the mold, cannot be used directly. Certain removals from the material surface must be made with respect to the previously specified dimensions and tolerances.

The milling process, which provides a surface of desired quality, plays a significant role in the shaping of the CFRP materials. Besides, the surface roughness also plays an effective role in the optimization of cutting parameters and tool geometries because of its significant effect on the dimension accuracy and production costs.^{2,3} The surface roughness is one of the most important factors in machining, influencing the manufacturing performance. The realization of the desired function of machine parts (in contact with each other) achieved by spending minimum energy depends on the surface roughness.⁴ In order to achieve the desired quality of a machined surface, it is necessary to understand the mechanisms of material removal and the kinetics of machining processes affecting the performance of cutting tools.^{5,6}

Previous researchers investigated the effect of the rotational speed and feed rate on the cutting forces in the milling of a polymer carbon-fiber composite material, using time series and the empirical relationship for the amplitude of the cutting force (F_x) to find the highest coefficient of delamination (R^2).⁷ However, if all three components of the total forces (F_x , F_y , F_z in the x , y , z directions, respectively) had been taken into account, the coefficient of delamination could have been calculated more precisely. The obtained vibration graphs were examined according to the test results and it was found that there was a decrease in the cutting forces with an increase in the number of revolutions, while the cutting forces increased as the feed-rate values increased. They evaluated the surface roughness and delamination in the milling of a 55 % fibered and $0^\circ/90^\circ$ angled carbon-fiber-reinforced composite material, using the Taguchi method, ANOVA and multiple regression analysis with respect to the cutting speed and feed-rate parameters. After the measurement of the maximum width of damage (W_{\max}) caused by the material, the damage normally assigned to the delamination factor (F_d) was determined. This factor is defined as the ratio between the maximum width of damage (W_{\max}) and the width of cut (W). The delamination-factor value was calculated with Equation (1):

$$F_d = \frac{W_{\max}}{W} \quad (1)$$

In their work, it was observed that the surface roughness and delamination factor increased depending on the increased feed rate and cutting speed.⁵ They also investigated the effects of the cutting-tool helix angle, the coating process and the cutting force on the delamination factor and surface roughness in their experimental study. An experimental study on the optimum machining of fiber-reinforced composite materials was made. It was specified that a higher cutting speed and a lower feed rate had to be used at a constant depth of cut in order to decrease delamination and the fiber amount and fiber angles of the material were also important to obtain the optimum results. They concluded that the upper and lower layers of fiber-reinforced composite materials have the biggest influence on the surface quality when cutting these materials.⁸ Thus, the milling of these materials requires a very sharp cutting edge, which is particularly necessary for solid carbide millig cutters. They investigated the cutting forces, created in the helical and orthogonal machining of multi-directional ($60^\circ/0^\circ/120^\circ$) and unidirectional (60°) CFRP material, using the artificial-neural-network (ANN) method. In their work, it was emphasized that mechanistic modeling approaches are valid for machining FRPs and predictive capabilities of cutting forces can be calculated for a rotating helical milling tool and for any fiber orientation using ANNs.¹ They also used different numbers of flutes/edges or helix-angled cutting tools and different fiber orientations for modelling approaches.

The effect of different cutting parameters (cutting speed, feed rate and tool geometry) on the surface roughness in the machining of glass-fiber-reinforced polymer composite material was investigated. In all of the cutting tests, depending on the increase in the feed rate, an increase in the surface roughness was observed and the best surface quality was obtained with a four-flute carbide end mill at the highest cutting speed and the lowest feed rate. Moreover, according to their study it is evident that the surface roughness increased with the increasing number of flutes.⁹ However, the surface roughness must increase with the increasing number of flutes due to the contact unit time. Thus, this situation can bring about an increase in the temperature in the cutting zone. ANOVA was used to identify significant factors using the grey relational grade value. According to the ANOVA results, it is clear that the fiber orientation angle (51.00 per cent) has the main influence on the milling of GFRP composites, followed by the helix angle (19.54 per cent), the feed rate (14.37 per cent) and the spindle speed (1.56 per cent).¹⁰ They also pointed out different optimization approaches and multiple regression analysis in their study. In this way, they were able to reveal more realistic results.

In another study, the hole delamination created during the drilling of FRP plates was shown, using a digital-analysis-based approach. Since a digital image is considered as the matrix where columns and rows identify one point of the image, the value corresponds to the luminous intensity of this point. The image processing produces satisfactory results, allowing an observation and analysis of the details from the digitalized image. Thus, in their work, the digital image of the damage area is used to characterize its extension at the hole entrance and exit. As a result, a comparison of the created delamination factors was made using the digital-analysis approach according to the cutting speed and feed rate in the tests. An increase in the delamination factor was found to depend on the increase in the cutting speed and feed rate.¹¹

This digital-analysis-based approach can also be applied to the milling of FRP materials using different cutting parameters and tool geometries. The researchers developed a delamination-prediction model using a multilayer feed-forward ANN and a training EBPT algorithm. They claimed that the developed ANN model showed a good correlation for both the training and testing data sets and that the delamination decreased with an increase in the number of revolutions, while it increased when a drill of a bigger tip angle was used.¹² Moreover, they also stated that at higher feed-rate values the drill could not function properly due to the coherence on the tool edges, causing an increase in the delamination. They developed a mathematical analysis method for the analysis of delamination in drilling FRPs. The delamination was measured using the ultrasonic C-scan method. They claimed that as the tool wear increased, the feed-rate factor increased. Furthermore, the feed-rate

factor decreased with a decrease in the number of revolutions and increased with an increase in the feed-rate values.¹³ In another study, chip-formation mechanisms were used, the Taylor tool-wear constants were determined and the surface roughness was measured with respect to the cutting speeds and feed rates. Moreover, the authors observed an increase in the tool wear and surface roughness due to the increase in the cutting speed and fiber angle, depending on the constant feed rate in turning.¹⁴ They investigated the effect of the fiber orientation on the grindability of CFRPs. They claimed that the surface roughness increased with the increase in the fiber angle and chip formation. The grinding forces and surface integrity were also found to depend on the fiber orientations in the grinding of an FRP.¹⁵

In this study, the effects of cutting parameters and cutting-tool properties (coated or uncoated, the helix angle, the number of flutes) on the cutting force and surface roughness were experimentally investigated for the 45° orientation angle in the milling of CFRP. Besides, the experimental results were optimized using the Taguchi method and the most effective cutting parameters (cutting speed and feed rate) for the cutting force and surface roughness were determined through a variance analysis (ANOVA).







2 EXPERIMENTAL PROCEDURE

2.1 Materials and method

In the milling of a CFRP material, six different carbide end mills with a 10 mm diameter were used: an uncoated two-flute 30° helix-angled mill; two-, three- and four-flute 30° helix-angled mills; and TiAl-coated, three- and four-flute 45° helix-angled carbide end mills. For the tests, coated carbide end mills of the GC1630 quality, PVD-coated with TiAl, with a coating thickness of 3–5 μ and made of fine-particle cemented carbide were used. The technical properties of the end mills used in the tests are given in **Table 1**.

Table 1: Coated and uncoated carbide end mills used in the tests

Tabela 1: Karbidni rezkarji, z nanosom in brez nanosa, uporabljeni pri preskusih

Cutting tool	Cutting-tool manufacturer code	Taguchi cutting-tool code	Diameter (mm)	Number of flutes	Helix angle	Helix length (mm)	Cutting-tool length (mm)	Cutting-tool view
TiAl-coated carbide	R216.32-10030-AC19P	(b)	10	2	30°	19	72	
Uncoated carbide	R216.32-10030-AC19A	(a)	10	2	30°	19	72	
TiAl-coated carbide	R216.33-10030-AC19P	(e)	10	3	30°	19	72	
TiAl-coated carbide	R216.33-10045-AC19P	(f)	10	3	45°	19	72	
TiAl-coated carbide	R216.34-10030-AC22N	(d)	10	4	30°	22	72	
TiAl-coated carbide	R216.34-10045-AC22N	(c)	10	4	45°	22	72	

The tests were made at three different revolutions: 3800, 4800, 5800 min⁻¹ and three different feed rates: 0.03, 0.06, 0.09 mm/tooth, and at a 1 mm depth of cut (**Table 2**).

Table 2: Cutting parameters

Tabela 2: Parametri rezanja

Spindle speed (min ⁻¹)	Feed rate (mm/tooth)	Depth of cut (mm)
3800, 4800, 5800	0.03, 0.06, 0.09	1

A CFRP composite material (polymer matrixed) was used in the tests. In accordance with ASTM D 792, the density test result as well as the mechanical, thermal and electrical properties of the CFRP material are given in **Table 3**.

Table 3: Physical properties of the material used in the tests according to ASTM D 792

Tabela 3: Fizikalne lastnosti materiala uporabljenega pri preskusih po ASTM D 792

Material	Density (gr/cm ³)	Percentage by weight of fiber	Thermal conductivity (W/Mk)	Fiber diameter (μm)	Electrical conductivity (μ-Ω-m)	Tensile modulus (GPa)	Tensile strength (GPa)
CFRP	1.59	74.6%	5	7	18	231	3.75

In **Figure 1**, the fiber orientation angles of the material used in the tests are given. The lay-up sequence of the CFRP was [0°/45°/90°/45°/-45°/90°/45°/0°]; it was created as a laminate. The CFRP composite used for the milling studies had a thickness of 15 mm.

The cutting tests were carried out on a Johnford VMC-850 CNC vertical machining center. In order to obtain the optimum results the Taguchi orthogonal array was used for specifying suitable factors and levels from the cutting parameters.

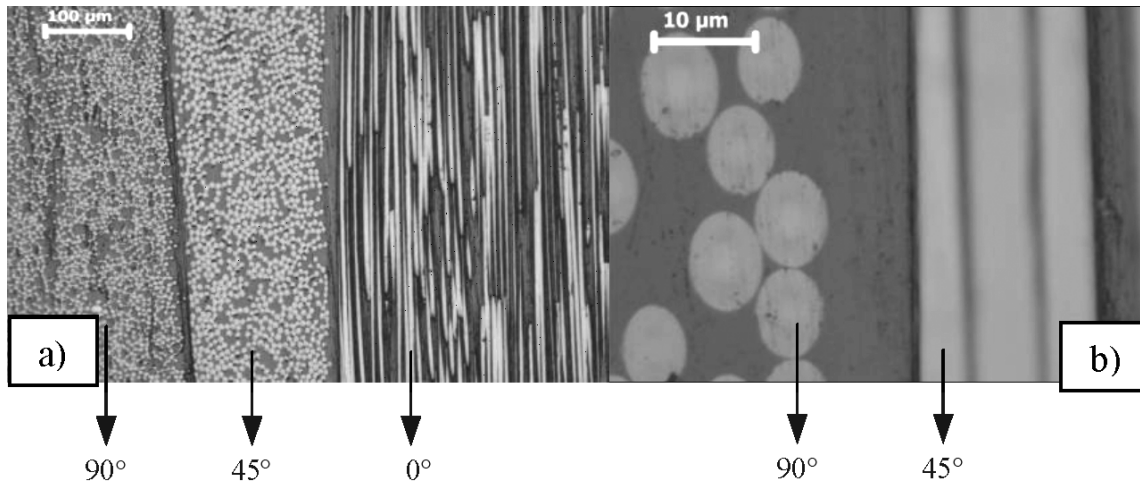


Figure 1: Scanning-electron-microscope (SEM) images of the materials used in the tests
Slika 1: Pregled materialov uporabljenih pri preskusih (SEM)

After each machining operation, surface-roughness (R_a) measurements were made using a surface-roughness measurement device called Mahr Perthometer M1. At least three points were measured to obtain the surface-roughness values. Cutting forces were measured with a KISTLER 9257B type dynamometer and a KISTLER 5070A type amplifier. The cutting-force values measured with the dynamometer were transferred to the computer digitally and graphically using the Dynaware software. The cutting and feed-rate direction used in the tests are given in **Figure 2** and a schematic representation of the experimental set-up is given in **Figure 3**.

The orientation of the resultant force with respect to the cutting direction is defined with Equation (2):

$$\lambda_e = \tan^{-1} \left(\frac{F_t}{F_c} \right) \quad (2)$$

The resultant orientation signifies the magnitudes of F_c and F_t , being relative to each other. The thrust force is greater than the principal force (the cutting force) for fiber orientation angles larger than 45° . Contrary to the cutting-force behavior in metal cutting, the thrust force is found to be higher than the corresponding principal force for fiber orientations ($0^\circ < \theta \leq 75^\circ$), except for the data

taken from some investigations.^{16,17} In general, the thrust force exhibited a more complex behavior than the principal force. An increase in the thrust force is exhibited when cutting small positive fiber orientations; then the thrust force decreases with further increase in the fiber orientation.

The chip-formation mode in cutting positive fiber orientations ($0^\circ < \theta < 90^\circ$) was described previously as the fiber-cutting mode, which consists of fiber cutting by compression shear followed by chip flow upward on the rake face by interlaminar shear along the fiber-matrix interface. It was noted that this type of chip formation is similar (only in the appearance because of the absence of plastic deformation) to the chip formation by shear in metal cutting. In these cases, the principal (cutting) force F_c and the thrust force F_t can be resolved into a shear force, F_s , acting along the shear plane, and a normal force, F_n , acting on the shear plane as shown in **Figure 4** and with Equations (3) and (4), respectively. It is noted here that the shear plane cutting FRPs is generally found to coincide with the plane of the fibers for fiber orientations ($0^\circ < \theta < 90^\circ$):

$$F_s = F_c \cos \theta - F_t \sin \theta \quad (3)$$

$$F_n = F_c \sin \theta - F_t \cos \theta \quad (4)$$

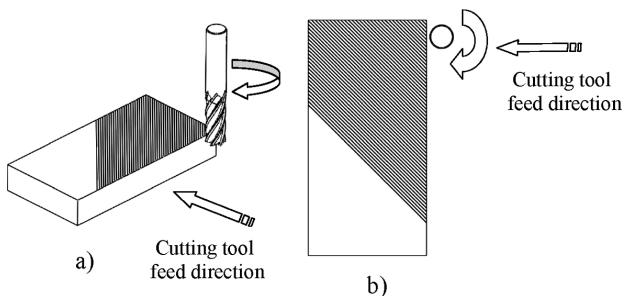


Figure 2: 45° fiber orientation and rotation direction of the cutting tool: a) isometric, b) top view

Slika 2: 45° orientacija vlaken in smer rotacije rezilnega orodja: a) izometrično, b) pogled z vrha

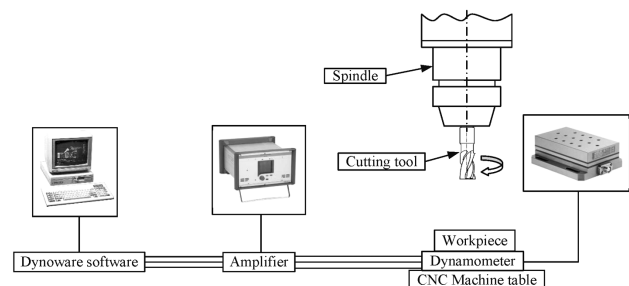


Figure 3: Experimental set-up for the milling test
Slika 3: Eksperimentalni sestav pri preskusu rezkanja

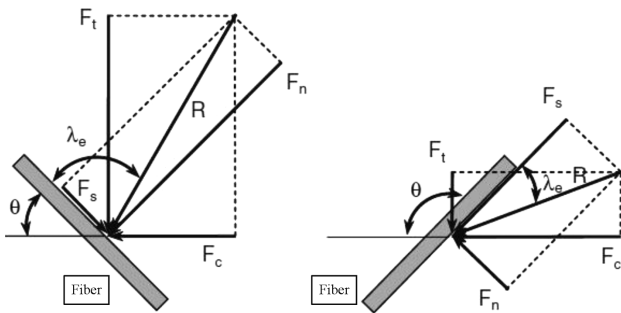


Figure 4: Cutting-force components along and perpendicular to the plane of fibers

Slika 4: Komponente sile rezanja vzdolž in pravokotno na ravnino vlaknen

It is also shown in **Figure 4** that the resultant force, R , makes an angle λ_e to the fiber orientation. The behavior of angle λ_e and normal force F_n with the fiber orientation may be linked to the chip-formation mode.⁴

2.2 Experimental design

The Taguchi experimental design was used in order to determine the control parameters that affect the cutting force and surface roughness and to minimize the time and costs with the minimum number of tests. An orthogonal array for three factors at six levels was used for describing of experimental design (**Table 4**).

Table 4: Assignment of the levels to the factors

Tabela 4: Opis nivojev in faktorjev

Symbol	Factors	Level					
		1	2	3	4	5	6
A	Cutting tool (carbide end mill)	a	b	c	d	e	f
B	Spindle speed (min ⁻¹)	3800	4800	5800	-	-	-
C	Feed rate (mm/tooth)	0.03	0.06	0.09	-	-	-

The L_{18} ($6^1 \times 3^2$) array mixed type shown in **Table 5** was determined with eighteen rows corresponding to the numbers of the tests and three columns at six levels. The factors and the interactions are designated to the columns.

The experimental design is made up of eighteen tests where the first column was designated to the test number, the second column to the carbide end mills (a,b,c,d,e,f), the third column to the spindle speed (rev/min) and the fourth column to the feed rate (mm/tooth).

An analysis of variance of the data relating to the cutting force, F_c (N) and surface roughness R_a (μm) for the CFRP material was made with the aim of analyzing the influence of the cutting tool (a carbide end mill), spindle speed (min⁻¹) and feed rate (mm/tooth) on the total variance of the results.

Table 5: Orthogonal array L_{18} ($6^1 \times 3^2$)

Tabela 5: Ortogonalna matrika L_{18} ($6^1 \times 3^2$)

L_{18} ($6^1 \times 3^2$) test	Cutting tools (Carbide end mills)	Spindle speed (min ⁻¹)	Feed rate (mm/tooth)
1	a	3800	0.03
2	a	4800	0.06
3	a	5800	0.09
4	b	3800	0.03
5	b	4800	0.06
6	b	5800	0.09
7	c	3800	0.06
8	c	4800	0.09
9	c	5800	0.03
10	d	3800	0.09
11	d	4800	0.03
12	d	5800	0.06
13	e	3800	0.06
14	e	4800	0.09
15	e	5800	0.03
16	f	3800	0.09
17	f	4800	0.03
18	f	5800	0.06

3 RESULTS AND DISCUSSION

The milling tests were conducted to evaluate the effect of the cutting parameters and cutting-tool properties (the helix angle, TiAl-coated or uncoated) on the cutting force and surface roughness for the 45° fiber orientation angle. The cutting forces were determined with Equations (3) and (4). The value of the feed rate (mm/min) was calculated with Equation (5):

$$f = f_z z n \tag{5}$$

where f_z is the feed per tooth, z is the number of flutes and n is the number of revolutions. The value of the surface roughness (μm) was calculated with Equation (6) where f is the amount of feed in mm/min, r is the cutting-tool radius in mm and R_a is the average surface roughness (μm):¹⁸

$$R_a = \frac{f^2}{32r} \tag{6}$$

In this study, the Taguchi experimental design makes it possible to isolate the effects of individual machining parameters at different levels using either the average values of experimental outputs or their corresponding S/N ratios. Herein, analyses of the effects of the machining parameters were performed on the basis of the S/N ratios of the machinability outputs using response graphs and an analysis of variance (ANOVA). ANOVA was performed to determine the relative influence of the experimental parameters on each of the machinability outputs. This can be accomplished by calculating the variability of the computed S/N ratio for each parameter and the associated error.

In the Taguchi experimental design for a variable product or process and uncontrollable factors, the most suitable combinations of controllable-factor levels are selected and the variability of the product or process is optimized for a certain purpose as the smaller-the-better (SB), the nominal-the-best (NB) and the higher-the-better (HB).¹⁹ The results obtained with the cutting tests are given in **Table 6**. The test results, obtained with the Taguchi experimental design were evaluated by converting them into the signal/noise (S/N) ratio. S/N values were calculated with the smaller-the-better Equation (7) because the stresses due to the parameters affecting the cutting force and surface roughness were desired at the lowest level. Here, Y is the performance-characteristic value (the stress), n is the number of Y values. The values with the highest S/N ratio among the levels of the factors in the tests created the best performance. Besides, the degrees of importance of the factors were investigated statistically on the test results with the variance analysis (ANOVA) and the best combination was determined with his study.²⁰

Smaller-the-better:

$$\frac{S}{N_{SB}} = -10 \lg \left(\frac{1}{n} \sum_{i=1}^n y_i^2 \right) \quad (7)$$

The cutting force is one of the most important output variables, created during the process and is directly affected by any variable. These variables, which affect the cutting forces are feed rate, depth of cut (radial and axial), cutting speed, tool and turning-chip geometry, workpiece material, tool-work interface dynamic characteristics, fixture system, development of the wear on the tool cutting surfaces, temperature and vibration. The cutting forces affecting the tool is an important data

Table 6: Taguchi experimental design

Tabela 6: Taguchi načrt preskusa

Experiment number	A	B	C	F_c (N)		R_a (μm)	
				Cutting force (N)	S/N (dB)	Surface roughness (μm)	S/N (dB)
1	a	3800	0.03	101.8	40.1550	1.147	1.19127
2	a	4800	0.06	121.6	41.6987	1.259	2.00051
3	a	5800	0.09	129.7	42.2588	1.406	2.95971
4	b	3800	0.03	113	41.0616	1.179	1.43028
5	b	4800	0.06	132.6	42.4509	1.231	1.80516
6	b	5800	0.09	139	42.8603	1.263	2.02807
7	c	3800	0.06	98	39.8245	1.400	2.92256
18	c	4800	0.09	117.8	41.4229	1.647	4.33387
9	c	5800	0.03	91.3	39.2094	1.078	0.65238
10	d	3800	0.09	130.8	42.3322	1.581	3.97864
11	d	4800	0.03	113.3	41.0846	1.093	0.77240
12	d	5800	0.06	133.2	42.4901	1.420	3.04577
13	e	3800	0.06	112.8	41.0462	1.191	1.51824
14	e	4800	0.09	96.2	39.6635	1.367	2.71537
15	e	5800	0.03	101.8	40.1550	1.181	1.44500
16	f	3800	0.09	115.9	41.2817	1.544	3.77295
17	f	4800	0.03	96.4	39.6815	1.173	1.38596
18	f	5800	0.06	160.8	44.1257	1.309	2.33879

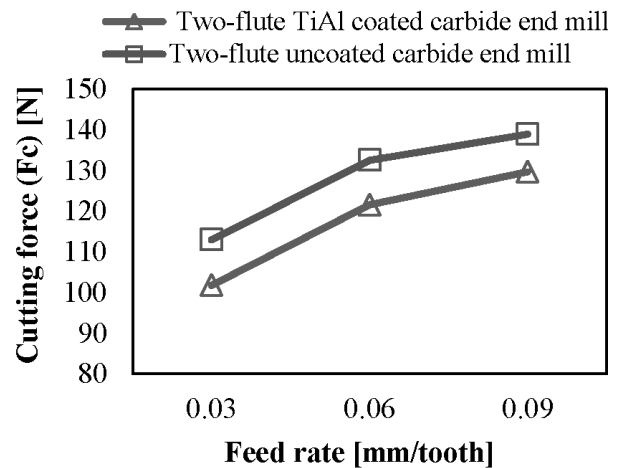


Figure 5: Variation of cutting forces depending on the cutting-tool type and feed rate

Slika 5: Spreminjanje sile rezanja v odvisnosti od vrste orodja in hitrosti podajanja

source for the condition of the tool. This information can be used for a better understanding of machinability, tool fracture, tool wear and surface integrity.^{21,22}

The cutting forces created during the milling of the CFRP material with two-flute, 30° helix-angled TiAl-coated and uncoated carbide end mills are shown in **Figure 5**.

In **Figure 5**, an increase in the cutting forces was observed for both the coated and uncoated carbide end mills, with the increasing feed rates depending on the constant depth of cut (a_p) and the number of revolutions (n). This can be explained with the increase in the turning-chip volume per unit time with the increase in the feed rate.²³ In their study²⁴, the authors explain the

impact of the axial and tangential feed rates per tooth on the process forces. They also noticed an increase in the cutting forces with the increasing feed rates. In another study, they also described an increase in the cutting temperatures with the cutting forces. As a result, undesirable thermal stresses occurred in the cutting tool and the workpiece. The maximum cutting temperature of 44°C was reported for the cutting speed of 35 m/min and feed rate of 0.178 mm/min.²⁵ It referred to a glass-fiber-reinforced laminate that was machined with a PCD tool. It is seen that at low and moderate feed rates per tooth, only slight increases in the normal force occur over a cutting-speed range of 1200–2400 m/min. In these tests, the cutting force increased due to the cutting-tool coating process. The coating on the cutting tool increased the hardness and strength of the cutting tool.²⁶ Besides, the cutting-tool coating caused a lower frictional coefficient and, as a result, the cutting forces of the coated tools were lower.²⁷ In relation with this, the lowest cutting force was determined for the coated tool at the lowest feed rate (0.03 mm/tooth).²⁶

Depending on the constant depth of cut and the number of revolutions, the surface roughness created during the milling of the CFRP material with the two-flute carbide end mill is given in **Figure 6**.

As shown in **Figure 6**, when the coated and uncoated carbide end mills were compared with respect to the surface roughness, the roughness values at the feed rates of 0.03 and 0.06 mm/tooth came out to be very close to each other whereas, at higher feed rates, a better surface quality was obtained with the uncoated carbide end mills. They also confirmed in their study that the surface roughness decreased with an increase in the cutting speed, but no critical speed could be identified. This could have been due to the fact that the cutting speed range used in these studies was below the critical cutting speed. All of the experimental studies confirm that the

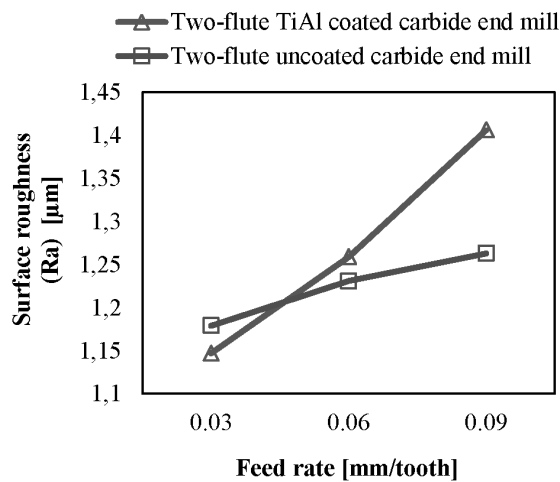


Figure 6: Variation of the surface roughness depending on the cutting-tool type and feed rate

Slika 6: Spreminjanje hrapavosti površine, v odvisnosti od vrste orodja za rezanje in hitrosti podajanja

feed rate is the most influential factor in determining the surface roughness. In these tests, the cutting-tool coating causes a thickening in the form of a cutting edge and the cutting tool ruptures the fibers rather than cutting them, which causes the coating and the workpiece to chemically react. For this reason, in the tests carried out with the coated cutting tools, the surface roughness was higher compared to the uncoated tools.²⁸ They also pointed out in their study that the feed rate is the cutting parameter which has a greater influence on the surface roughness (33.43 per cent) when milling GFRP composite materials with solid carbide coated with PCD.²⁹

Depending on the constant depth of cut and the number of revolutions, the surface roughness created during the milling of the CFRP material with all of the carbide end mills is given in **Figure 7**.

An increase in the surface roughness with the increase in the feed rates was observed for all the carbide end mills (**Figure 7**). It was specified that this was an expected result and was also present in the literature. They also found that the surface roughness increases with the increase in the feed rate. In these tests, it was also observed that there was an increase in the surface roughness with the increase in the number of flutes and the helix angle.³⁰ Depending on the increasing feed rates, the best surface quality in all the tests was obtained with the two-flute 30° helix-angled uncoated carbide end mill. It was specified that the increase in the number of flutes and helix angles adversely affected the surface quality.⁵ According to another study, the feed rate is also the most significant factor affecting the surface roughness.³¹

Even the wear of the machining edge causes a high increase in the cutting resistance, which, in turn, leads to a plastic strain of the surface layers of the sample and delamination. What may be observed here is a correlation between the delamination size and the feed rate and cutting speed. Every single growth of these quantities translates into an increase in the cutting forces and an increase in the surface roughness. **Figure 8** shows a selected microscope photograph of the milling surface (the speed of cutting is fixed, while the feed rate is changeable).

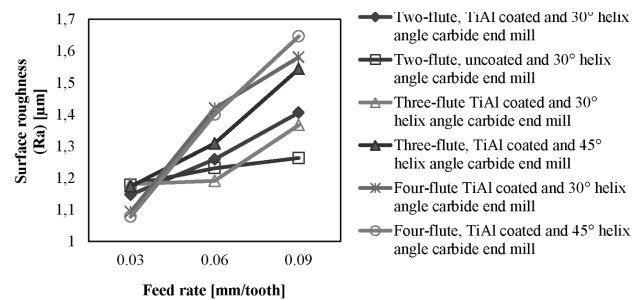


Figure 7: Feed rate/surface roughness relationship for all carbide end mills used in the tests

Slika 7: Odvisnost hitrosti podajanja in hrapavosti površine za vse karbidne rezkarje uporabljene v preskusu

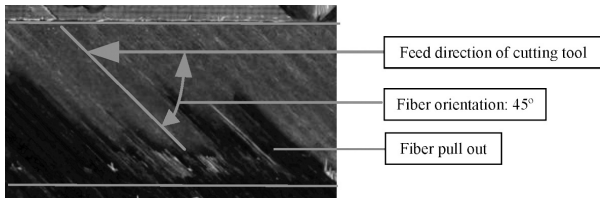


Figure 8: Cutting and feed direction for the 45° fiber orientation
 Slika 8: Smer rezanja in podajanja pri orientaciji vlaken 45°

3.1 Analysis of variance (ANOVA)

The experimental design and statistical analysis (ANOVA) were made with respect to a mixed-level design through the Minitab 15.0 software. According to the ANOVA analysis of the cutting force (Table 7), the feed rate had the highest effect with a 53.06 % ratio. The effects of the cutting tool and the number of revolutions were 22.93 % and 16.17 %, respectively. In the ANOVA analysis of the surface roughness (Table 8), the feed rate again had the highest effect with a 86.01 % ratio and the effects of the cutting tool and the number of revolutions were low.

On the basis of the test results, S/N ratios and optimum parameters were estimated. In Figures 9 and 10, the S/N ratio graphs of control factors are given depending on the cutting force and surface roughness. In Figure 9, the cutting parameters for the cutting force, obtained through the Taguchi optimization were found to be "A₃B₁C₁" (four-flute and 45° helix-angled, TiAl-coated carbide end mill, 3800 rpm and a feed rate of 0.03 mm/tooth). It was assumed that the highest S/N ratio of each parameter indicated the optimum level of that parameter.¹⁹ The obtained parameters in the optimization of the surface roughness were "A₂B₃C₁" (two-flute 30° helix-angled uncoated carbide end mill, 5800 rpm, 0.03 mm/tooth) as seen in Figure 10. When the optimization

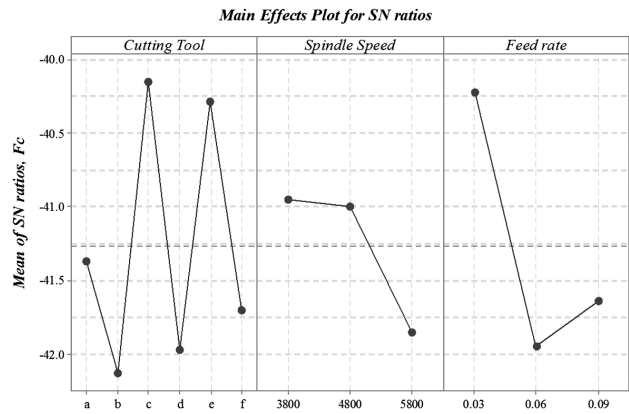


Figure 9: Signal/noise ratios for cutting forces
 Slika 9: Razmerja signal/hrup pri silah rezanja

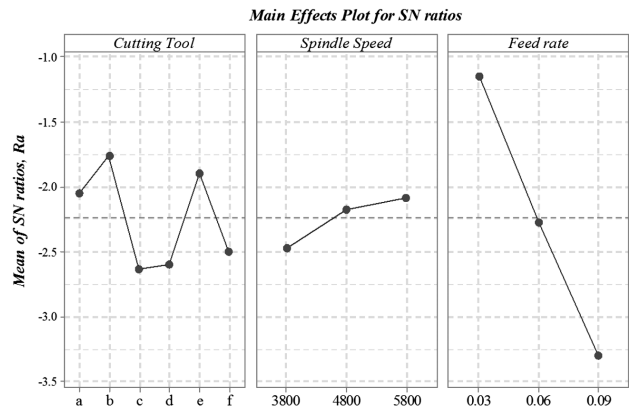


Figure 10: Signal/noise ratios for the surface roughness
 Slika 10: Razmerja signal/hrup pri hrapavosti površine

process was evaluated, it was observed that although the cutting tools with a large helix angle and many cutting edges came out to be better with respect to the cutting forces, the cutting tools with a small helix angle and few

Table 7: ANOVA results for cutting forces

Tabela 7: ANOVA rezultati sil rezanja

	Cutting parameters	Degrees of freedom	Sequential sum of squares	Average correction	Means of squares	P	Percentage contribution
A	Cutting tool	5	10.87	10.87	2.174	0.086	22.93%
B	Spindle speed	2	3.067	3.067	1.5337	0.189	16.17%
C	Feed rate	2	10.052	10.052	5.0262	0.019	53.06%
Error		8	5.945	5.945	0.7431		7.82%
Total		17	29.934				100%

Table 8: ANOVA results for surface roughness

Tabela 8: ANOVA rezultati za hrapavost površine

	Cutting parameters	Degrees of freedom	Sequential sum of squares	Average correction	Means of squares	P	Percentage contribution
A	Cutting tool	5	2.2355	2.2355	0.4471	0.477	5.44%
B	Spindle speed	2	0.5018	0.5018	0.2509	0.593	3.09%
C	Feed rate	2	13.9017	13.9017	6.9509	0.002	86.01%
Error		8	3.5904	3.5904	0.4488		5.45%
Total		17	20.2295				100%

flutes gave better results from the point of the surface roughness and delamination.

3.2 Confirmation tests

After obtaining the best estimation results for the Taguchi optimization, validation tests were made to verify the optimization. In the Taguchi experimental design, the next step after the selection of the optimum levels of the test parameters is the estimation of the measurement result for the optimum parameter and the determination of the difference by comparing it with the actual measurement.^{32,33}

The determined optimum parameters of "A₃B₁C₁" and "A₂B₃C₁" for the cutting force and surface roughness and the results of the verification tests were compared (Tables 9 and 10). There was a good consistency between the actual and estimated values for both of the two performance characteristics (the cutting force and the surface roughness). As for the optimum cutting parameters obtained with the Taguchi application, there were improvements of 0.8536 dB and 0.3249 dB for the cutting force and surface roughness according to the *S/N* ratios in comparison with the original parameters.

Table 9: Verification test results for cutting force

Tabela 9: Rezultati preskusov preverjanja sile rezanja

	Starting cutting parameters	Optimum cutting parameters	
		Prediction	Experiment
Level	A ₁ B ₂ C ₃	A ₃ B ₁ C ₁	A ₃ B ₁ C ₁
Cutting force (N)	101.5	83.35	92
<i>S/N</i> ratio (dB)	-40.1293	-38.7934	-39.2757
Improvement of <i>S/N</i> ratio	0.8536 dB		
Prediction error (dB)	0.4823		

Table 10: Verification test results for surface roughness

Tabela 10: Rezultati preskusov preverjanja hrapavosti površine

	Starting cutting parameters	Optimum cutting parameters	
		Prediction	Experiment
Level	A ₁ B ₂ C ₂	A ₂ B ₃ C ₁	A ₂ B ₃ C ₁
Surface roughness (<i>R_a</i> , μm)	1.259	1.034	1.207
<i>S/N</i> ratio (dB)	2.00	-0.5015	-1.6741
Improvement of <i>S/N</i> ratio	0.3249 dB		
Prediction error (dB)	1.1726		

According to the data obtained from the verification tests, a high consistency was observed between the estimated and experimental values in the optimization of the cutting force and surface roughness and the effectiveness of the Taguchi optimization was proved with this study.

4 CONCLUSIONS

In this study, a CFRP material was milled with several carbide end mills, and the cutting force and surface roughness for a 45° fiber orientation angle were investigated. The Taguchi optimization and ANOVA were applied to the experimental data. The conclusions from these processes can be listed as follows:

- For all of the carbide end mills, an increase in both the cutting force and surface roughness was observed depending on the increasing feed rate.
- In the tests with an uncoated carbide end mill, a better surface quality and less delamination were obtained.
- As for the cutting tools, there was an increase in the surface roughness as the number of flutes and the helix angle increased.
- At the end of the Taguchi optimization of the cutting force, suitable cutting parameters for the four-flute 45° helix-angled TiAl-coated carbide end mill (A₃B₁C₁) were found to be 3800 min⁻¹ and a feed rate of 0.03 mm/tooth.
- At the end of the Taguchi optimization, suitable cutting parameters for the two-flute 30° helix-angled uncoated carbide end mill (A₂B₃C₁) were found to be 5800 min⁻¹ and a feed rate of 0.03 mm/tooth.
- The lowest cutting forces were obtained for the cutting tools with the highest number of flutes and the largest helical angles, whereas the best surface-roughness values were obtained with the cutting tools with a low number of flutes and acute helix angles.
- At the end of the tests, when ANOVA was applied to the obtained data, the most effective parameter for the cutting force and surface roughness was the feed rate.
- The optimum parameters that were obtained as a result of the Taguchi optimization and the estimated cutting-force and surface-roughness values were compared by performing validation tests. This comparison indicated a high consistency between the values.

Acknowledgement

This study was accomplished with the support of Gazi University Scientific Research Project no 07/2010-18. Authors thank the Gazi University Scientific Research Unit for their support.

5 REFERENCES

- ¹ D. Kalla, J. Sheik-Ahmad, J. Twomey, Prediction of Cutting Forces in Helical End Milling Fiber Reinforced Polymers, International Journal of Machine Tools & Manufacture, 50 (2010) 10, 882–891, doi:10.1016/j.ijmactools.2010.06.005
- ² M. Ramulu, Characterization of surface quality in machining of composites, In: S. Jahanmir, M. Ramulu, P. Koshy (Eds.), Machining of Ceramics and Composites, Marcel Dekker, New York 1999, 575–648

- ³ E. Erisken, Influence from production parameters on the surface roughness of a machined short fibre reinforced thermoplastic, *International Journal of Machine Tools & Manufacture*, 39 (1999) 10, 1611–1618, doi:10.1016/S0890-6955(99)00017-6
- ⁴ J. Y. Sheikh-Ahmad, *Machining of Polymer Composites*, Springer, 2009
- ⁵ J. P. Davim, P. Reis, Damage and Dimensional Precision on Milling Carbon Fiber-Reinforced Plastics Using Design Experiments, *Journal of Materials Processing Technology*, 160 (2005) 2, 160–167, doi:10.1016/j.jmatprotec.2004.06.003
- ⁶ P. S. Sreejith, R. Krishnamurthy, S. K. Malhotra, K. Narayanasamy, Evaluation of PCD tool performance during machining of carbon/phenolic ablative composites, *Journal of Material Processing Technology*, 104 (2000) 1–2, 53–58, doi:10.1016/S0924-0136(00)00549-5
- ⁷ R. Rusinek, Cutting Process of Composite Materials: An Experimental Study, *International Journal of Non-Linear Mechanics*, 45 (2010) 4, 458–462, doi:10.1016/j.ijnonlinmec.2010.01.004
- ⁸ D. Berger, F. Bleicher, C. Dorn, F. Puschitz, Optimised Machining of Fibre Reinforced Material, *Daaam International Scientific Book*, 3 (2008), 27–34, doi:10.2507/daaam.scibook.2008.03
- ⁹ Ö. Erkan, B. Işık, Investigation of Cutting Parameter Effects on Surface Roughness During Machining of Glass Fiber Reinforced Plastic Composite Material, 5th International Advanced Technologies Symposium (IATS 09), Karabük, Turkey 2009, 1414–1419
- ¹⁰ N. Naresh, M. P. Jenarathanan, R. H. Prakash, Multi-objective optimisation of CNC milling process using Grey-Taguchi method in machining of GFRP composites, *Multidiscipline Modeling in Materials and Structures*, 10 (2014) 2, 265–275, doi:10.1108/MMMS-06-2013-0042
- ¹¹ J. P. Davim, J. C. Rubio, A. M. Abrao, A Novel Approach Based on Digital Image Analysis to Evaluate the Delamination Factor after Drilling Composite Laminates, *Composite Science and Technology*, 67 (2007) 9, 1939–1945, doi:10.1016/j.compscitech.2006.10.009
- ¹² S. R. Karnik, V. N. Gaitonde, J. C. Rubio, A. E. Correia, A. M. Abrao, J. P. Davim, Delamination Analysis in High Speed Drilling of Carbon Fiber Reinforced Plastics (CFRP) Using Artificial Neural Network Model, *Materials and Design*, 29 (2008) 9, 1768–1776, doi:10.1016/j.matdes.2008.03.014
- ¹³ C. C. Tsao, H. Hocheng, Effect of Tool Wear on Delamination in Drilling Composite Materials, *International Journal of Mechanical Sciences*, 49 (2007) 8, 983–988, doi:10.1016/j.ijmecsci.2007.01.001
- ¹⁴ S. K. Kim, G. D. Lee, K. Y. Kwak, S. Namgung, Machinability of Carbon Fiber-Epoxy Composite Materials in Turning, *Journal of Materials Processing Technology*, 32 (1992) 3, 553–570, doi:10.1016/0924-0136(92)90253-O
- ¹⁵ N. S. Hu, L. C. Zhang, Some Observations in Grinding Unidirectional Carbon-Fibre-Reinforced Plastics, *Journal of Materials Processing Technology*, 152 (2004) 3, 333–338, doi:10.1016/j.jmatprotec.2004.04.374
- ¹⁶ T. Kaneeda, CFRP cutting mechanism, *Transactions of the North American Manufacturing Research Institute of SME* 19, 1991, 216–221
- ¹⁷ H. Takeyama, N. Iijima, Machinability of glass-fiber-reinforced plastics and application of ultrasonic machining, *CIRP Annals – Manufacturing Technology*, 37 (1988) 1, 93–96, doi:10.1016/S0007-8506(07)61593-5
- ¹⁸ M. Stephen, *Grinding Technology*, Society of Manufacturing Engineers, Industrial Press, New York 1989
- ¹⁹ N. S. Mohan, S. M. Kulkarni, A. Ramachandra, Delamination analysis in drilling process of glass fiber reinforced plastic (GFRP) composite materials, *Journal of Materials Processing Technology*, 186 (2007) 1–3, 265–271, doi:10.1016/j.jmatprotec.2006.12.043
- ²⁰ G. Taguchi, S. Chowdhury, Y. Wu, *Taguchi's Quality Engineering Handbook*, Wiley-Interscience, New Jersey, USA 2004
- ²¹ R. A. Kishore, R. Tiwari, A. Dvivedi, I. Singh, Taguchi analysis of the residual tensile strength after drilling in glass fiber reinforced epoxy composites, *Materials and Design*, 30 (2009) 6, 2186–2190, doi:10.1016/j.matdes.2008.08.035
- ²² K. Palanikumara, J. P. Davim, Assessment of some factors influencing tool wear on the machining of glass fibre-reinforced plastics by coated cemented carbide tools, *Journal of Materials Processing Technology*, 209 (2009) 1, 511–519, doi:10.1016/j.jmatprotec.2008.02.020
- ²³ H. Hocheng, H. Y. Puw, Y. Huang, Preliminary study on milling of unidirectional carbon fibre-reinforced plastics, *Composites Manufacturing*, 4 (1993) 2, 103–108, doi:10.1016/0956-7143(93)90077-L
- ²⁴ B. Denkena, D. Boehnke, J. H. Dege, Helical milling of CFRP – titanium layer compounds, *CIRP Journal of Manufacturing Science and Technology*, 1 (2008) 2, 64–69, doi:10.1016/j.cirpj.2008.09.009
- ²⁵ M. Ucar, Y. Wang, End-milling machinability of a carbon fiber reinforced laminated composite, *Journal of Advanced Materials*, 37 (2005) 4, 46–52
- ²⁶ W. Konig, C. H. Wulf, P. Grab, H. Willerscheid, Machining of fibre reinforced plastics, *Annals of CIRP*, 34 (1985), 537–547
- ²⁷ E. P. DeGarmo, J. T. Black, R. A. Kohser, *Materials and Processes in Manufacturing*, Prentice-Hall Inc., New Jersey 1997
- ²⁸ J. P. Davim, P. Reis, Multiple regression analysis (MRA) in modelling milling of glass fiber reinforced plastics (GFRP), *International Journal of Manufacturing Technology and Management*, 6 (2004) 1–2, 185–197, doi:10.1504/IJMTM.2004.004514
- ²⁹ M. P. Jenarathanan, R. Jeyapaul, N. Naresh, Modelling and analysis of factors influencing surface roughness and delamination of milling of GFRP laminates using RSM, *Multidiscipline Modeling in Materials and Structures*, 8 (2012) 4, 489–504, doi:10.1108/15736101211281588
- ³⁰ J. R. Ferreira, N. L. Coppini, G. W. A. Miranda, Machining optimisation in carbon fibre reinforced composite materials, *Journal of Materials Processing Technology*, 92–93 (1999), 135–140, doi:10.1016/S0924-0136(99)00221-6
- ³¹ K. Ogawa, E. Aoyama, H. Inoue, T. Hirogaki, H. Nobe, Y. Kitahara, T. Katayama, M. Gunjima, Investigation on cutting mechanism in small diameter drilling for GFRP (thrust force and surface roughness at drilled hole wall), *Composite Structures*, 38 (1997) 1–4, 343–350, doi:10.1016/S0263-8223(97)00069-X
- ³² V. Krishnaraj, A. Prabukarthi, A. Ramanathan, N. Elanghovan, M. S. Kumar, R. Zitoune, J. P. Davim, Optimization of machining parameters at high speed drilling of carbon fiber reinforced plastic (CFRP) laminates, *Composites: Part B*, 43 (2012) 4, 1791–1799, doi:10.1016/j.compositesb.2012.01.007
- ³³ G. D. Babu, K. S. Babu, B. U. M. Gowd, Effect of Machining Parameters on Milled Natural-Fiber-Reinforced Plastic Composites, *Journal of Advanced Mechanical Engineering*, 1 (2013), 1–12, doi:10.7726/jame.2013.1001

DEVELOPMENT OF ALUMINIUM ALLOYS FOR AEROSOL CANS

RAZVOJ ALUMINIJEVIH ZLITIN ZA AEROSOL DOZE

Stanislav Kores¹, Jože Turk¹, Jožef Medved², Maja Vončina²

¹Talum d.d., Tovarniška cesta 10, 2325 Kidričevo, Slovenia

²University of Ljubljana, Faculty of Natural Sciences and Engineering, Department of Materials and Metallurgy, Aškerčeva 12, 1000 Ljubljana, Slovenia
stanislav.kores@talum.si

Prejem rokopisa – received: 2015-11-06; sprejem za objavo – accepted for publication: 2015-11-24

doi:10.17222/mit.2015.330

New aluminium alloys were developed for aluminium narrow strips, cast with a rotary strip caster, to produce slugs for aerosol cans. The newly developed alloys provide constant mechanical properties during the manufacturing of aerosol cans, a good transformation and high deformable and burst pressures of the aerosol cans. The problem that occurs during the manufacturing of aerosol cans is a decrease in the mechanical properties of the material up to 15 %. This is reflected in lower deformable and burst pressures for the aerosol cans. By increasing the mechanical properties of aerosol-can materials it is possible to produce aerosol cans with thinner walls, having a significant impact on the weight of the final aerosol cans. Using new aluminium alloys for aerosol cans, it is possible to increase the deformability and burst pressure by more than 10 %.

Keywords: aluminium alloys, rotary strip casting, slug, impact extrusion, aerosol cans

Razvite so bile nove aluminijeve zlitine za aluminijev ozki trak, ulit po sistemu rotary strip caster, za izdelavo surovcev za iztiskovanje aerosol doz. Nove zlitine imajo konstantne mehanske lastnosti skozi celoten proces izdelave aerosol doz, zato se dobro preoblikujejo in dosegajo visoke deformabilne in razpočne tlake. Problematika, ki se pojavlja pri izdelavi aerosol doz, je poslabšanje mehanskih lastnosti materiala, tudi do 15 %. To se kaže v nižjih deformabilnih in razpočnih tlakih aerosol doz. Z višanjem mehanskih lastnosti materiala za aerosol doze je možno izdelati aerosol doze s tanjšo steno, kar bistveno vpliva na težo končne doze. Z uporabo novih zlitin za izdelavo aerosol doz je mogoče doseči tudi več kot 10 % višje deformabilne in razpočne tlake doz.

Ključne besede: aluminijeve zlitine, sistem rotacijskega ulivanja traku, surovec, protismerno iztiskovanje, aerosol doze

1 INTRODUCTION

Aluminium aerosol cans are made either by impact extruding aluminium slugs or by deep drawing discs stamped out of an aluminium sheet. The aluminium sheet is mainly produced with the direct-chill (DC) cast technology. The continuous-casting (CC) technology, however, provides energy and economic savings, while reducing environmental emissions. Compared with the DC cast technology, the CC technology also takes advantage of high productivity.¹

Some 7.6 billion aluminium aerosol cans a year are used worldwide. Almost 80 % of the production is attributable to the cosmetics industry.² Aluminium spray cans

are not only user friendly, they also help conserve resources. Today, a typical cylindrical aerosol can (38 mm/138 mm) weighs 17 g and is about 30 % lighter than at the beginning of the 1970s, and there is still the potential for further savings. Aluminium is also readily recyclable and can be repeatedly processed to new, high-grade products without any loss in quality, and the same is true for aerosol cans.³

1.1 Aluminium narrow strip and slug production process

Aluminium aerosol cans for the cosmetics and food industries are manufactured from aluminium slugs using

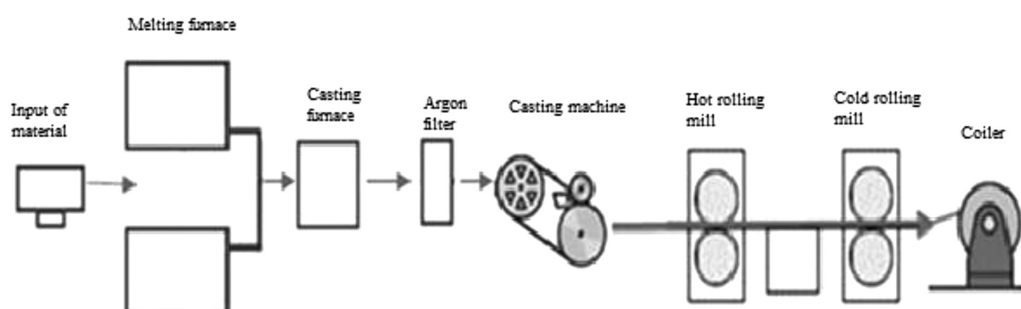


Figure 1: Production line of aluminium narrow strip

Slika 1: Proizvodna linija za izdelavo aluminijevega ozkega traku

impact extrusion. In the company Talum d.d., the aluminium slugs are semi-manufactured products stamped from an aluminium narrow strip produced by a rotary strip-casting machine (Figure 1).

An aluminium strip is usually cast with a horizontal casting system, which enables the casting of a wide spectrum of aluminium alloys. A narrow aluminium strip, which is cast using a rotary strip-caster system, is limited to the casting of the AA1XXX and AA3XXX-series aluminium alloys. The 1XXX and 3XXX-series aluminium alloys find wide applications in the transportation, food, beverage and packaging industries. In these applications, control of the plastic anisotropy of the sheet is of great importance in order to ensure the formability of the final product and to reduce the waste of the material resulting from earring behaviour.⁴ The 1XXX and 3XXX-series distinguish good formability and corrosion resistance, the AA3XXX-series aluminium alloys also have good weldability and relatively good mechanical properties.⁵ Good mechanical properties mean achieving a high deformation and burst pressure.⁶

The rotary strip-casting machine⁷ consists of a casting wheel and a steel belt. The melt flows from the casting channel into the area between the endless steel

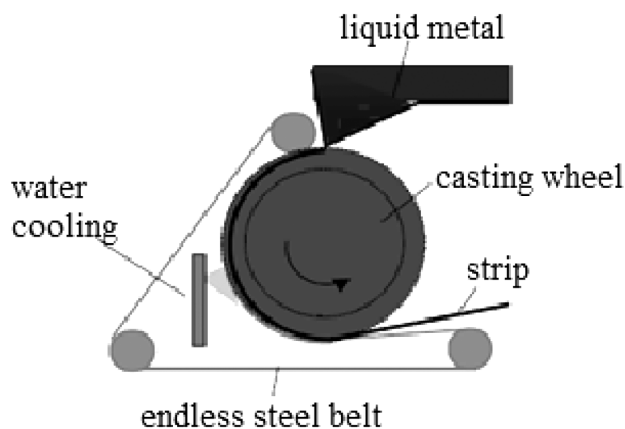


Figure 2: Rotary strip-casting system⁷

Slika 2: Sistem rotacijskega ulivanja traku⁷

belt and the water-cooled wheel (Figure 2). The casting wheel is manufactured from a copper or steel alloy.

From the casting machine the aluminium strip is led to the hot-rolling mill and then to the cold-rolling mill through a roller track. In the hot-rolling mill the strip thickness is reduced by 40–70 %, while in the cold-rolling mill it reaches 30–50 %.

The rolled narrow aluminium alloy strip then travels to the stamping line, where slugs are stamped using a stamping machine. From the stamping machine the slugs are led into annealing furnaces, where the slugs are softened and the oil remaining from the stamping is burned off. After the annealing the slugs are surface-treated by sandblasting, vibrating or tumbling.

1.2 Aerosol can manufacturing with impact extrusion

Impact extrusion is the most widely used process to manufacture aluminium aerosol cans. With impact extrusion the aerosol cans are produced as a single piece without a seam or joint from the aluminium slugs. The cold disc is placed in a steel die and a punch at high pressure is then forced into the disc. Deformation of the aluminium generates heat and the metal flows in the opposite direction to the punch and takes on the form determined by the shape of the die.³

The can blank is subsequently cut to length and washed to remove any lubricants. After drying the interior is lacquered to protect the contents from direct contact with the metal. Once the cans have been formed, an internal lacquer is applied to each can and a polymerization step is performed. Additional operations are lacquering of the outside, printing, coating with the transparent protective lacquer layer and the appropriate intermediate drying processes. The final manufacturing step is the draw in the can shoulder and – in case of shaped cans – the can body in a multi-die necking machine.³

The manufacturing process for aerosol cans consists of the following steps (Figure 3): (1) Slug → (2) impact extrusion → (3) washing and drying → (4) internal lacquering and polymerization → (5) external lacquering

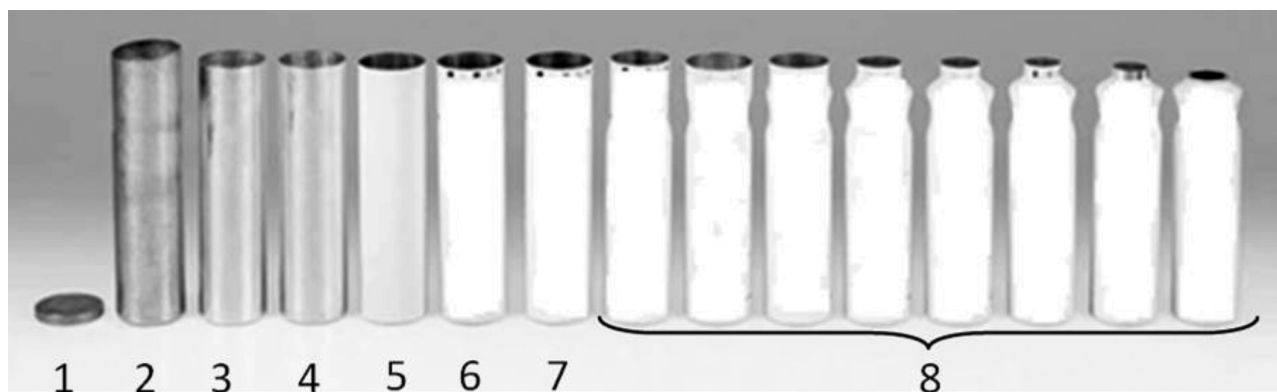


Figure 3: Sequence of aerosol can manufacturing

Slika 3: Koraki izdelave aerosol doz

→ (6) printing → (7) coating with protective lacquer layer → (8) draw in the can shoulder and body in a multi-die necking machine.

The drying of washed, externally lacquered and printed cans is performed at temperatures of 140–180 °C. The polymerization of internal lacquering occurs at temperatures around 250–280 °C.

2 EXPERIMENTAL PART

2.1 Aluminium alloys for aerosol cans

Aerosol cans are generally made from an aluminium-based alloy containing 99.5 % or 99.7 % of the mass fractions of Al. The Talum company produces slugs for aerosol cans from the alloys presented in **Table 1**.

Table 1: Mechanical properties of standard aluminium alloys for aerosol cans

Tabela 1: Mehanske lastnosti standardnih aluminijevih zlitin za izdelavo aerosol doz

Mechanical properties					
Alloy	Hardness (HB _{2.5/15.625})	R _m (MPa)	R _{p0.2} (MPa)	Elongation (%)	Grain number/mm ²
99.7	18.5	70	34	42	60-100
99.5	19.5	75	37	41	60-100
AlMn0.3	22	80	41	40	20-30
AlMn0.6	27	92	55	38	30-60

Samples from heat treated slugs

A very important factor in impact extrusion is the grain number/mm². Slugs produced from pure aluminium 99.5 % and 99.7 % have smaller grains than slugs from the AlMn0.3 and AlMn0.6 alloys (**Figure 4**).

2.2 Methods and material

First, some basic examinations with the Thermo-Calc program were made at the Faculty of Natural Sciences and Engineering, Department of Materials and Metallurgy: simple thermal analysis, DSC and observation under light and scanning electron microscopes.

For the development of aluminium alloys, standard alloys for aerosol cans (**Table 1**) were used as the base material. These alloys were modified with the combination of different alloying elements. The base of alloy T1 is pure aluminium Al99.7 %, of alloy T3 AlMn0.3 alloy and the base of T4, T4+ AlMn0.6 alloy.

The reason for the development of new aluminium alloys for aerosol cans was in the decrease of the mechanical properties during the manufacturing process. The question was how to eliminate the decrease in mechanical properties and at the same time be able to cast aluminium narrow strip on a rotary strip-casting machine.

3 RESULTS AND DISCUSSION

3.1 Material properties during the manufacturing process

During the manufacturing process for aerosol cans the mechanical properties of the material decrease by up to 15 % after polymerization. This is reflected in achieving lower deformable and burst pressures of the aerosol cans.

Figure 5 shows the mechanical properties of the aerosol can material during the manufacturing process – after extrusion and after polymerization.

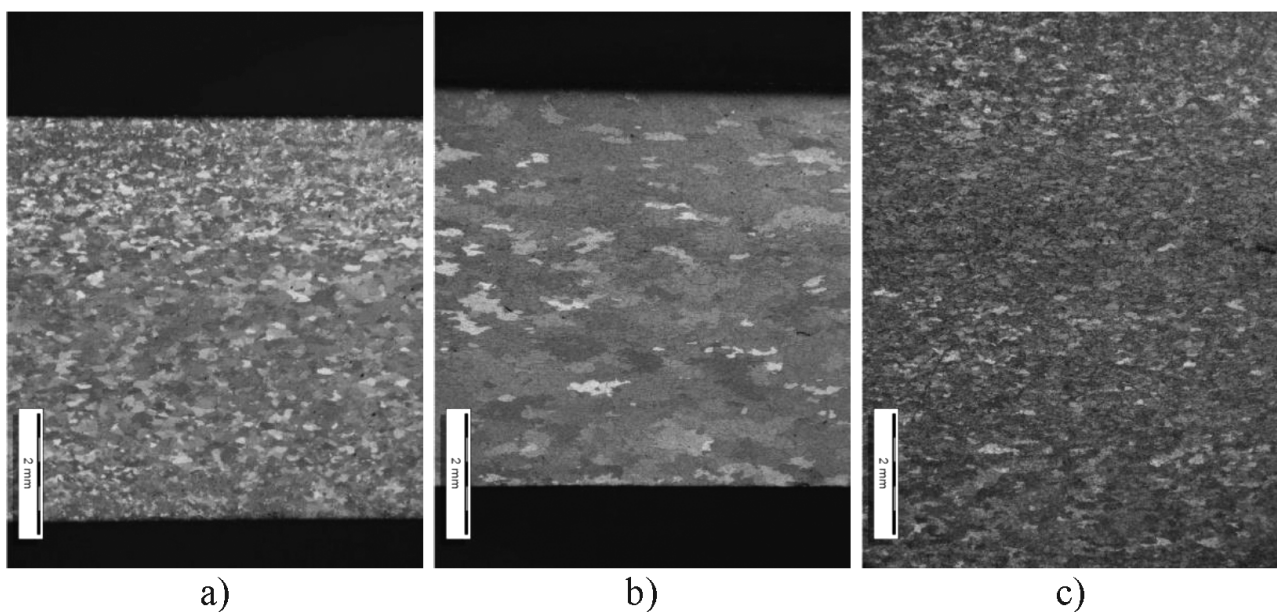


Figure 4: Grain structure of standard aluminium alloys for aerosol cans: a) Al99.5 %, b) AlMn0.3 and c) AlMn0.6 in polarized light
Slika 4: Znatost standardnih aluminijevih zlitin za izdelavo aerosol doz: a) Al99.5 %, b) AlMn0.3 in c) AlMn0.6 v polarizirani svetlobi

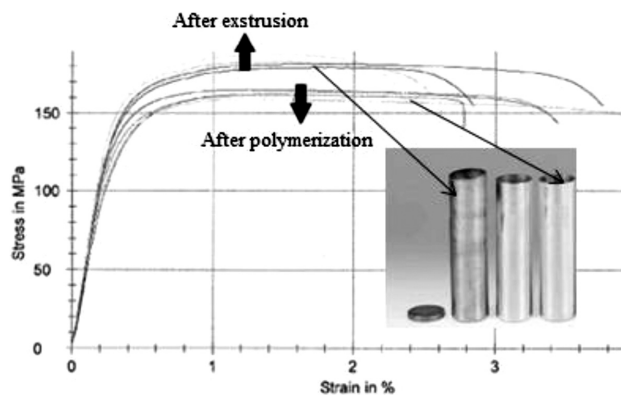


Figure 5: Mechanical properties of Al99.7 % aerosol cans after extrusion and after polymerization

Slika 5: Mehanske lastnosti aerosol doze iz Al99.7 % po izstiskovanju in polimerizaciji

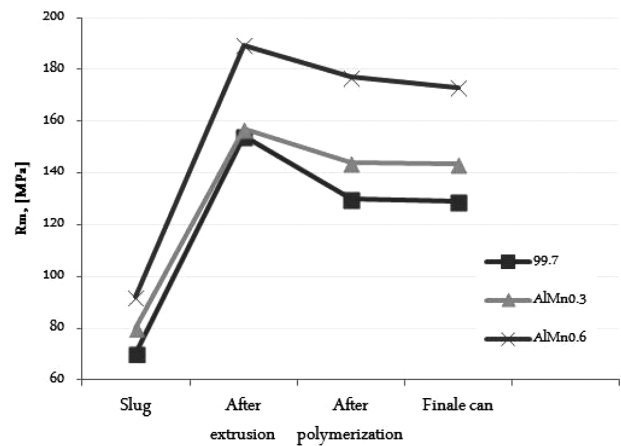


Figure 6: Mechanical properties of the aerosol can material during manufacturing

Slika 6: Mehanske lastnosti materiala aerosol doz med izdelavo

Samples of the standard material for aerosol cans were taken from the cans and with the standard tensile test the mechanical properties were measured. After polymerization the mechanical properties of the aerosol cans from the Al99.7 % decreased by 15.9 %, those of the cans from the AlMn0.3 alloy by 8.5 % and the mechanical properties of aerosol cans made from AlMn0.6 alloy decreased by 6.5 %. Figure 6 shows the tensile strength of the measured aluminium alloys at an essential step of the manufacturing process for aerosol cans.

3.2 Newly developed aluminium alloys for aerosol cans

The goal of the development of new aluminium alloys for aerosol cans was to develop such an alloy, from which it is possible to produce an aluminium narrow strip with the rotary strip-casting machine on an existing casting-rolling line.

Table 2: Mechanical properties of newly developed aluminium alloys for aerosol cans

Tabela 2: Mehanske lastnosti novo razvitih aluminijevih zlitin za aerosol doze

Mechanical properties					
Alloy	Hardness (HB _{2.5/15.625})	R _m (MPa)	R _{p0.2} (MPa)	Elongation (%)	Grain number/mm ²
T 1	21.7	78	48	36.5	16-21
T 3	23.4	80.3	52	24.9	5-7
T 4	28.9	113	82	19.9	7-14
T 4+	30.9	110.7	72.3	26.9	119

Samples from heat treated slugs

With the combination of different alloying elements a higher hardness, tensile strength and yield strength of the slugs were achieved. The elongation of the new alloy de-

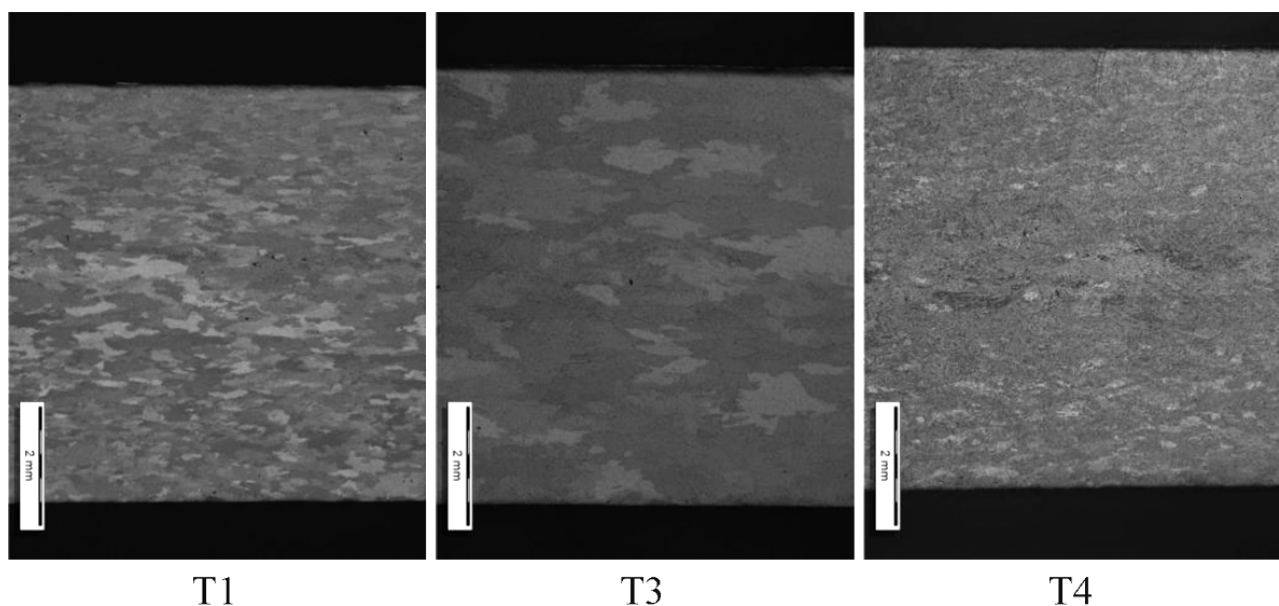


Figure 7: Grain structure of newly developed aluminium alloys for aerosol cans under polarized light

Slika 7: Zrnatost novo razvitih aluminijevih zlitin aerosol doze v polarizirani svetlobi

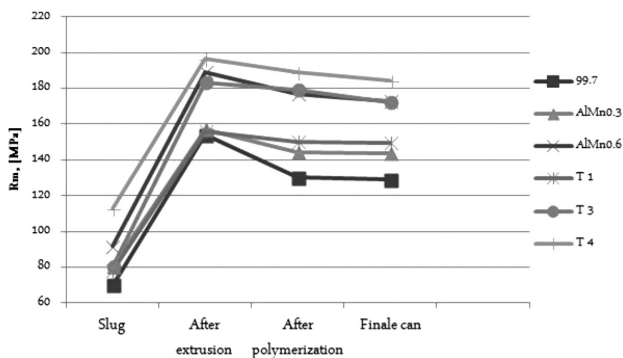


Figure 8: Comparison of mechanical properties of standard aluminium alloys and newly developed aluminium alloys for aerosol cans
Slika 8: Primerjava mehanskih lastnosti standardnih aluminijevih zlitin z novo razvitimi zlitinami za aerosol doze

creased. Moreover, the grain number/mm² decreased compared with the standard alloys.

Figure 7 shows the grain structure of the samples of new alloys taken from the slugs under polarized light. Alloy T1 has a more-or-less uniform and homogeneous grain structure, while alloy T3 has a rougher grain structure, and alloy T4 an inhomogeneous grain structure.

Figure 8 presents the tensile strengths of standard and newly developed aluminium alloys for aerosol cans. From the figure it is evident that the drop in the mechanical properties after polymerization on 2–3 % was eliminated. The mechanical properties of the alloy T1 are in the range of the AlMn0.3 alloy, but due to the lower grain number/mm² alloy T1 shows better manufacturability. With the T4 and T4+ alloy it is possible to achieve a high deformation and burst pressure, consequently this alloy shows the potential on the market where steel cans are used for packaging.

A comparison of the standard alloy Al99.7 % with the T1 alloy shows that the T1 alloy has excellent manufacturability properties, an excellent surface of the aerosol cans and a higher deformation and burst pressure. Also, a comparison of the AlMn0.3 alloy with the T3 alloy shows the same properties and the T4 alloys compared with the AlMn0.6 alloy shows a significant increase in the deformation and burst pressure, but worse manufacturability properties (**Figure 7**).

With the cooperation of aerosol can manufacturers the first test showed a 10–15 % higher deformation and burst pressure for the aerosol cans. That means it is possible to produce aerosol cans with thinner walls and thus reduce their weight and save on material.

4 CONCLUSIONS

On an existing casting-rolling line, aluminium alloys were developed to produce the aluminium narrow strip for the production of slugs, which enables:

- casting of an aluminium narrow strip with high casting speeds by using a rotary strip-caster system with an excellent surface and a minimum number of defects,
- constant mechanical properties of the material after polymerization and during the whole manufacturing process of aerosol cans, which is reflected by a more than 10 % higher burst and deformable pressures of the aerosol cans,
- good manufacturability, transformation and surface of aerosol cans from developed aluminium alloy slugs,
- improved mechanical properties of aerosol can material so as to produce aerosol cans with thinner walls and reduce their weight.

5 REFERENCES

- ¹ J. Liu, J.G. Morris, Macro-, micro- and mesotexture evolutions of continuous cast and direct chill cast AA 3015 aluminium alloy during cold rolling, *Materials Science and Engineering A*, 357 (2003) 1-2, 277-296, doi:10.1016/S0921-5093(03)00210-7
- ² Weltweite Produktion von Aluminium-Aerosoldosen wächst weiter, *Aluminium*, 5 (2015), 8
- ³ <http://www.aluinfo.de/index.php/fact-sheets.html>, 7.8.2015
- ⁴ O. Engler, Control of texture and earing in aluminium alloy AA 3105 sheet for packaging applications, *Materials Science and Engineering A*, 538 (2012), 69-80, doi:10.1016/j.msea.2012.01.015
- ⁵ L. F. Mondolfo, *Aluminium alloys: Structure and Properties*, Butterworth Co., London 1962
- ⁶ J. Medved, T. Godicelj, S. Kores, P. Mrvar, M. Vončina, Contribution of Mn content on the pressure dose properties, *RMZ-Materials and Geoenvironment*, 59 (2012) 1, 41-54
- ⁷ C. Kammer, *Continuous casting of aluminium*, Talat Lecture 3210, Goslar 1999

COMPUTER TOOLS TO DETERMINE PHYSICAL PARAMETERS IN WOODEN HOUSES

DOLOČANJE FIZIKALNIH PARAMETROV Z RAČUNALNIŠKIMI ORODJI V LESENIH HIŠAH

David Bečkovský, František Vajkay, Vladimír Tichomirov

Brno University of Technology, Faculty of Civil Engineering, Institute of Building Structures, Veveří 95, 602 00 Brno, Czech Republic
beckovsky.d@fce.vutbr.cz

Prejem rokopisa – received: 2013-10-01; sprejem za objavo – accepted for publication: 2015-06-30

doi:10.17222/mit.2013.213

Nowadays, because the number of wooden houses gradually increases and due to European regulations, a huge emphasis is put onto the aspects like energy saving and energy efficiency in family housing, which are the topic of a related ongoing research project. Hence, the paper is focused on comparing and streamlining the methods available to the engineering community in the fields of energy consumption and air-tightness measurements of buildings. The newly developed design methodologies and practical outputs of the completed research project are planned to be delivered directly to the related industry. The research project is also focused on the humidity and temperature control in wooden houses since wooden houses consist of timber structural elements, whose humidity and moisture may later cause some liability-related problems. To prevent these failures, it is necessary to investigate the quality of tools and methodologies, through which one might determine the values of humidity and temperature already within the design phase. Nevertheless, design is only one phase of the whole process; the other is the building-realisation phase. Therefore, the questions to answer are: Who is actually responsible for the failures caused by humidity and moisture? When does the water actually penetrate the structural elements? Is it in the factory or when the elements are transported or when the products are stored at the construction site?

Keywords: moisture, wooden constructions, timber structures, energy consumption, Arduino, Raspberry Pi

Dandanes se zaradi naraščanja števila lesenih hiš in tudi zaradi evropske regulative posveča veliko pozornosti prihrankom pri energiji in energijski učinkovitosti družinskih hiš, kar je tudi predmet predstavitve. Članek je usmerjen na primerjavo in usmeritev metod, s katerimi razpolaga inženiring na področju porabe energije in meritev zrakotesnosti zgradb. Novo razvite metodologije načrtovanja in praktične rešitve iz raziskovalnih projektov bodo neposredno posredovane industriji. Raziskovalni projekt je usmerjen na kontrolo temperature in vlage v lesenih hišah, ker so lesene hiše zgrajene iz lesenih strukturnih elementov pri katerih lahko vlaga povzroči problem z zdržljivostjo. Za preprečevanje takih poškodb je potrebno preiskovati kvaliteto orodij in metodologij, s katerimi je mogoče oceniti vsebnost tako vlage kot temperature, in sicer že v sami fazi načrtovanja. Načrtovanje je samo ena od faz celotnega procesa, druga pa je faza gradbene realizacije. Vprašanje na katerega je potrebno odgovoriti je: kdo je v resnici odgovoren za poškodbe, ki jih povzroči vlaga in tudi kdaj voda v resnici penetrira v gradbene elemente? Je to že v tovarni, med transportom ali pa med shranjevanjem elementov na gradbišču?

Ključne besede: vlaga, lesena konstrukcija, leseni gradbeni elementi, poraba energije, elektronska platforma Arduino, Raspberry Pi

1 INTRODUCTION

In the building industry, there are several variants of wooden houses. There are log-wood houses, wooden-frame ones, wooden houses built from cross-laminated timber panels, etc. Nevertheless, the design procedure for wooden houses is the same as that for brickwork buildings and, among other measures, it must include a thorough thermal analysis¹ since the durability and functionality of modern wooden structures depend on the humidity and moisture control. In the case of wooden houses, it is crucial to avoid condensation of water vapour in the building envelope. This affects the thermo-technical requirements given to designed structures, especially those of wall and roof cladding. The design of peripheral wall and roof cladding must also properly solve all the details, including the quality of designed materials.

However, even if the design incorporates all the design principles, there is still no guarantee that the designed structures are going to function properly when built under real-life conditions because some failures might appear during the building erection process. That is why construction works have to be regularly inspected by the construction inspector and the technical supervisor of the investor.

Supervision and monitoring throughout the construction process ensure the highest quality of the provided services and reduce the formation of defects, primarily when structural materials and elements are built in, since the initial water content can cause some problems as well. The initial water content should be checked and compared to the numbers contained in the "Technical Data Sheets" published by the manufacturers.

2 CONTAMINATION DURING THE EXECUTION

The issue of the initial mass moisture is demonstrated by T. Kalábová et al.² on mineral-fibre thermal-insulation panes, which were built into the timber joist ceilings of the EXDR1 experimental wooden house.

Within the discussed timber joist ceilings, the space between the joists is completely filled with mineral-fibre thermal-insulation boards. The built-in boards were delivered under rainy-weather conditions in summertime and were left outside to ventilate for a period of 14 days before they were unpacked and used.

Although the building material was delivered in its original packaging in shrink-wrap foils, some of the mineral-fibre boards had a significant amount of moisture content.

The moisture inside was verified with an infrared imaging camera after positioning the first layers of the thermally insulating mineral-fibre boards. Hot spots of moisture content above 70 % were localized at several locations (**Figure 1**).

With an infrared imaging camera, it is possible to:

- Determine the distribution of the surface temperature over the envelope or the distribution of the apparent radiant temperature;
- Determine the distribution of the atypical surface temperature, i.e., the temperature changes caused by some disorders such as the moisture content, insulation, or penetration of air;
- Assess the type and extent of the problem.

To determine whether the observed changes were atypical or not, the obtained thermographs were compared to the expected distributions of surface temperatures determined experimentally under the same boundary conditions in the form of building-shell variables. The estimated temperature distributions can be determined either from reference thermographs, with calculations or surveys as another possibility.

2.1 Sensing devices – a thermal imager

To take infrared images, it is necessary to fulfil one condition, which is a large temperature difference bet-

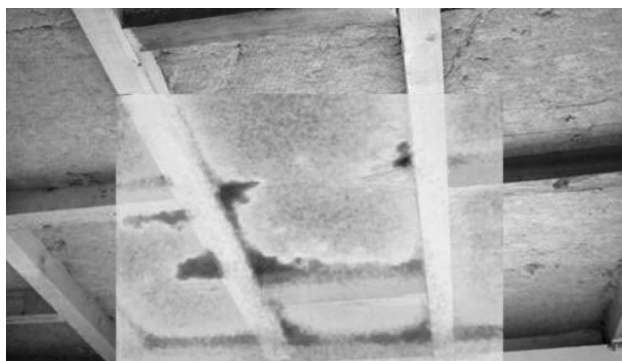


Figure 1: Moisture in the ceiling structure

Slika 1: Vlaga v konstrukciji stropa

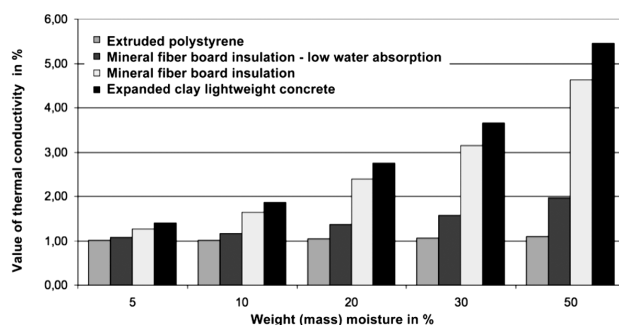


Figure 2: Thermal conductivities of different thermally insulating materials under varying moisture content

Slika 2: Toplotna prevodnost različnih materialov za toplotno izolacijo, pri različnih vsebnostih vlage

ween the inside and the outside of an envelope. The temperature difference must be big enough to allow the detection of thermal irregularities. The test cannot be conducted if the external or internal temperature varies considerably or if the structure is exposed to direct sunlight.

3 MOISTURE PREVENTION

One way to prevent the incorporation of moisture in wood-based materials susceptible to higher levels of humidity is a control mechanism and a procedure, such as the usage of stick hygrometers or infrared imaging cameras.

An application of wet materials in the course of the construction process can lead to a rapid appearance and development of wood-decaying organisms, which are very difficult and expensive to dispose of. One way for the disposal of wood-decaying organisms is to use microwave radiation,³ where electromagnetic waves oscillate at frequencies of 300 MHz to 300 GHz. These frequencies correspond to wavelengths of 1 m to 1 mm. The microwave generator is completely safe to use if treated with care. Health issues can arise only due to a long-term direct exposure from a close distance.

4 MONITORING DURING THE LIFE CYCLE

The monitoring of the physical parameters of the structures and internal environment of buildings brings significant investment costs as a large number of various sensors and data loggers are required to make such a monitoring possible. Due to individual requirements of research teams and the restlessness of developers of computing hardware and information technologies, the authors of the article (themselves researchers in the field of building physics) came up with an idea and decided to build a custom data logger with a high variability of connectable parts and sensors. The whole process is based on do-it-yourself prototyping. The data logger is made of two prototyping boards, which are cheap and relatively easy to use. Using ArduPi, it consists of a

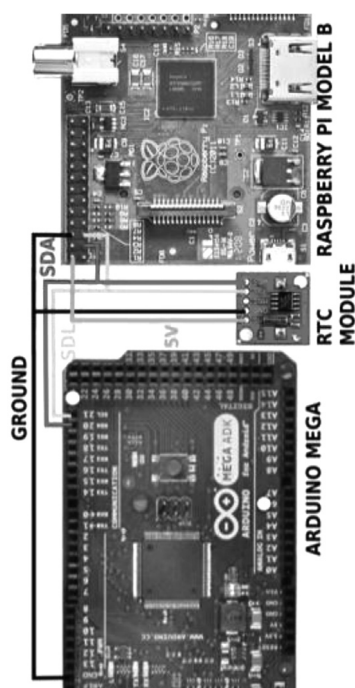


Figure 3: I2C data line between Raspberry Pi, RTC module and Arduino board

Slika 3: I2C podatkovna linija med Raspberry Pi, RTC modulom in Arduino platformo

credit-card-sized ARM-processor-based Raspberry Pi model B and an open-source microcontroller board Arduino (the correct description of the board is Arduino Mega 2560).

The boards can communicate via USB (universal serial bus), I2C (inter-integrated circuit communications) or SPI (serial peripheral interface) interfaces.⁴ A real-time clock module can be coupled to them as well as any of the available sensors. Thus, even after a power outage, the system is able to resume the task given to it.

4.1 Reasoning behind the choice of the boards

Both boards, the Raspberry Pi and the Arduino, were chosen because they can be programmed for different purposes. Both of them have a huge number of GPIO (general-purpose input/output) headers starting with USB ports and ending with analogue voltage input pins. The boards can communicate throughout the by-directional I2C communication protocol.⁵ To avoid data and speed losses, it is recommended to use a shielded cable between the two boards. Nonetheless, a by-directional voltage divider is a requirement for the I2C communication. The Raspberry Pi I2C interface works at 3.3 V, while the Arduino interface works at 5 V.

The Raspberry Pi is cheap and the first of its kind. The ARM processor with a clock speed of 700 MHz can run different processes. Thus, the Raspberry Pi can be used as a PC with Raspbian OS (a modification of Debian Linux OS) running on it. It can be hooked up with a keyboard, a mouse and a display and can run a web and

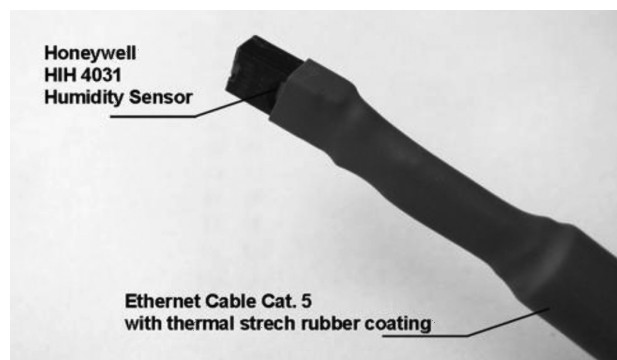


Figure 4: Close-up view of the HIH-4031 sensor

Slika 4: Podrobnejši pogled na HIH-4031 senzor

SQL server as well as displaying data. With Python^{6,7} scripting possibilities, it is suited to be used as the brain of the ArduPi.

Even though it would be possible to operate most of the sensors (1-Wire, I2C, SPI) with the Raspberry Pi, the Arduino board can do it better. Arduino boards have a 10-bit internal ADC (analogue-to-digital converter). Analogue sensors for the measurement of relative humidity, like the Honeywell HIH-4031, output electricity in place of digital data. Such readings need to be converted.

One could use ADC integrated circuits instead of an Arduino board. Nonetheless, Arduino is preferred because it can be easily programmed in the bundled IDE (Integrated Development Environment).⁸

4.2 Used sensors

When researching an indoor environment, we need to have a relatively large number of sensors: some thermal couples, relative-humidity sensors and others. The sensors that can be obtained for a reasonable price are produced by companies like Honeywell, Dallas Instruments, Panasonic and may be digital or analogue. Just to mention, the prototype of ArduPi utilizes the already mentioned analogue humidity sensors HIH-4031 (**Figure 4**) by Honeywell.

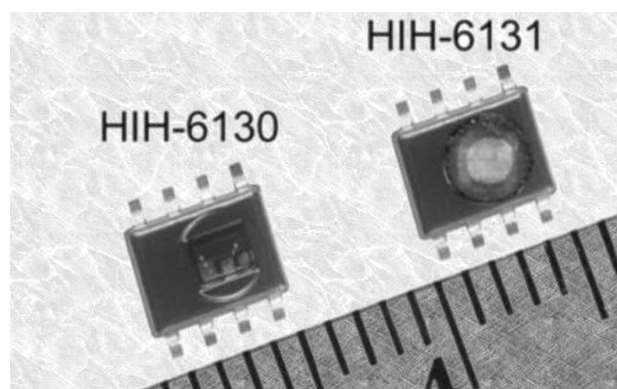


Figure 5: Close-up view of HIH-613X products

Slika 5: Podrobnejši pogled na HIH-613X proizvode

To free up the analogue input pins on the Arduino board for different sensors, the usage of combined digital sensors HIH 6131-021 is planned (**Figure 5**). These sensors are also made by Honeywell.

These sensors communicate via the already mentioned I2C communication protocol.

Energy-consumption sensors are important for monitoring an internal environment as, in the case of a power failure, they immediately record the time without electricity. Information about such conditions can be instantly delivered by GPRS or EDGE.

Analogue pins for mFi-CS sensors are available from Ubiquiti Networks and used for monitoring the energy consumption of home appliances and many others.

5 CONCLUSIONS

With the modern technologies and materials available, it is possible to put together small and cheap data loggers for experimental purposes to be used in building physics instead of the ones produced by one of the major companies. Data loggers may be customized to the needs of the user, including the software base for the operation. The choice of sensors and measuring equipment depends solely on the user. Whether the sensors hooked up are going to have an accuracy of 0.5 % or 5 % depends only on the available funds. The only requirement is their compatibility to any of the supported communication protocols. It can be said that the creation of BRESET on an ArduPi base is a major step as it brings the possibilities of research activities closer to the scientific community.

Acknowledgement

This paper was completed under project no. LO1408 "AdMaS UP – Advanced Materials, Structures and Technologies", supported by the Ministry of Education, Youth and Sports under the National Sustainability Programme I and under the Project FAST-S-15-2757 supported by Ministry of Education, Youth and Sports under "Specific University Research".

6 REFERENCES

- ¹ P. Charvat, T. Mauder, M. Ostry, Simulation of Latent-Heat Thermal Storage Integrated with Room Structures, *Mater. Tehnol.*, 46 (2012), 239–242
- ² T. Kalábová, M. Horáčková, F. Vajkay, Experimental timber framed house EXDR1, *Advanced Materials Research*, 649 (2013), 73–76, doi:10.4028/www.scientific.net/AMR.649.73
- ³ M. Novotný, J. Škramlík, K. Šuhajda, J. Sobotka, J. Gintar, T. Kalábová, Efficiency of liquidation of biotic pests using microwave radiation, *Advanced Materials Research*, 688 (2014), doi:10.4028/www.scientific.net/AMR.688.27
- ⁴ S. C. Russell, Raspberry Pi & Arduino, *The MagPi*, 7 (2012), 4–6
- ⁵ L. Oscar, Raspberry Pi and Arduino Connected Using I2C, <http://blog.oscarliang.net/raspberry-pi-arduino-connected-i2c>
- ⁶ Jaseman, The Python pit, *The MagPi*, 1 (2012), 23–29
- ⁷ M. Summerfield, *Programming in Python 3*, Pearson Education Ltd., Boston 2009
- ⁸ M. Banzl, *Getting started with Arduino*, O'Reilly Media Inc., Sebastopol 2008

IMPRESSION RELAXATION AND CREEP BEHAVIOR OF Al/SiC NANOCOMPOSITE

SPROSTITEV VTISA IN OBNAŠANJE Al/SiC NANOKOMPOZITA PRI LEZENJU

Yasaman Saberi Kakhki, Said Nategh, Tehrani Shamseddin Mirdamadi

Islamic Azad University, Tehran Science and Research Branch, Department of Materials Engineering, Tehran, Iran
s.nategh@srbiau.ac.ir

Prejem rokopisa – received: 2015-06-04; sprejem za objavo – accepted for publication: 2015-08-25

doi:10.17222/mit.2015.113

In the present study, Al-4 % of volume fractions of SiC composites were produced by mechanical alloying and the powders were gradually compacted at a pressure of 620 MPa. The post-compact samples were sintered under an argon atmosphere at 873 K and the corresponding creep results were obtained from impression-relaxation. Additionally, compression techniques were investigated at high temperature (723 K). Enforcement rates of 8.3×10^{-3} and 0.83×10^{-3} mm s⁻¹ and indenter depths of 0.5 mm and 0.8 mm were selected. Results showed a constant relation between stress relaxation and compression creep rate. Under different conditions of impression-relaxation this constant was 1000 for compression stress of 30 MPa and 32.5 MPa, and 400 for compression stress of 35 MPa, subsequently. This coefficient was affected by the porosity and was stable for different indenter depths and enforcement rates. The variations in the steady state relaxation rate were reasonable because of different nano-SiC distributions and porosities in the form of drops. Moreover, in spite of the enforcement rate decrease, the nanosized reinforcing particles caused a decrease of the relaxation rate. It should be mentioned that the constant coefficient calculated will be useful to estimate the fracture time which uses the strain rate calculated from impression-relaxation in industrial applications.

Keywords: Al-SiC, creep, impression relaxation, nanocomposite, powder processing

V študiji so bili izdelani kompoziti Al-4 % volumskega deleža SiC z mehanskim legiranjem, prahovi pa so bili postopoma stisnjeni do tlaka 620 MPa. Stisnjeni vzorci so bili nato sintrani v atmosferi argona na 873 K. Iz sprostitve pri vtiskovanju je bila dobljena povezava z rezultati lezenja. Dodatno so bile preiskovane tehnike stiskanja pri visoki temperaturi (723 K). Izbrani sta bili hitrosti vtiskovanja $8,3 \times 10^{-3}$ mm s⁻¹ kot tudi $0,83 \times 10^{-3}$ mm s⁻¹ pri globini vtiska 0,5 mm in 0,8 mm. Rezultati so pokazali konstanten koeficient med sprostitvijo napetosti in hitrostjo lezenja pri tlačenju. Vrednost konstante je bila pri različnih pogojih sprostitve vtiska 1000 pri napetostih stiskanja 30 MPa, 32,5 MPa in 400 pri napetosti stiskanja 35 MPa. Na koeficient vpliva tudi poroznost, stabilen pa je pri različnih globinah vtisa in hitrostih vtiskovanja. Tudi rezultati sprostitve so bili občutljivi zaradi različne razporeditve SiC nanodelcev in poroznosti v obliki kapljic. Poleg tega, kljub zmanjševanju hitrosti vtiskovanja, nanourtrjevalci zmanjšajo hitrost sprostitve. Pomembno je omeniti, da bo iz hitrosti obremenjevanja in sproščanja pri vtiskovanju izračunani konstantni koeficient uporaben za napovedovanje časa porušitve pri industrijski uporabi.

Ključne besede: Al-SiC, lezenje, sprostitve pri vtiskovanju, nanokompozit, obdelava prahu

1 INTRODUCTION

Powder-processed aluminum alloys reinforced with SiC particles provide significantly enhanced properties over conventional monolithic materials, such as higher specific modulus, strength and thermal stability. They are widely utilized in the aerospace and automobile industry as ground vehicle brake rotors, or combustion engine components.¹⁻³ For the goal of investigating the creep properties, methods such as uniaxial (tension and compression), impression and relaxation are often used.⁴⁻⁸ The stress relaxation test is the ideal method to investigate the creep behavior of soft materials. In such tests, specimens are subjected to impressions at a predetermined impression depth level, the cross head is arrested and the decrement in magnitude (supposed depth) as a function of time is recorded.^{5,6,8} The stress-relaxation test has the advantages of simplicity and speed over the conventional creep test.^{5,6} There have been many studies evaluating the stress exponent and activation energy of creep mechanisms in different alloys employing various

techniques.⁴⁻⁸ Furthermore, in different studies, the uniaxial creep properties of Al-SiC with micron sized reinforcements have been examined,⁹⁻¹³ but the effect of nanosized reinforcement and the evaluation of the steady state creep rate with compression and impression relaxation methods have not been investigated. Therefore, this paper aims at investigating the steady state creep rate of Al with SiC reinforcement (nanoparticles) by compression and impression relaxation tests. This approach is used to determine the correspondence of the creep results obtained through these different approaches. It is worth highlighting that the novelty of the present research is the evidence of the relaxation creep theory in these materials. The creep behavior of these composites with different methods has provided an understanding of the actual characteristics of nanocomposite. Additionally, this research aims at exploring the creep rate to evaluate the fracture time, especially in industrial cases, with porosity, with non-destructive methods.

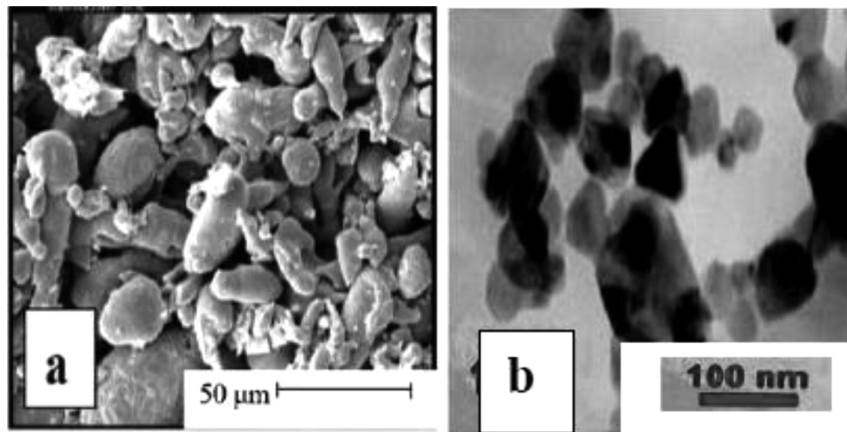


Figure 1: a) Morphology of as-received aluminum powders, b) TEM-micrograph of as-received nano-SiC powders
Slika 1: a) Morfologija dobavljenih prahov Al, b) TEM-posnetek dobljenega SiC nanoprahu

2 MATERIALS AND METHODS

The base material used in the present experimental investigation are synthesized from: atomized Al powders with a purity of 99.5 % and a particle size of less than 45 micron; reinforcing SiC powders with a purity of 99 % and a particle size from 45 nm to 65 nm (**Figure 1**); and stearic acid with purity of 97.5 % as a process control agent. Al-4 % of volume fractions SiC composites were made using a laboratory scale high-energy planetary ball mill at 260 min^{-1} with a 2 % stearic acid mass fraction as a surface active agent and a ball to powder weight ratio of 15:1. Milling was carried out under an Ar atmosphere (99.999 % purity). In order to avoid a significant temperature rise for the 4 h required to complete mixing, the ball milling process were stopped periodically for 20 min, then resumed for 45 min. The composite powders obtained by mechanical alloying, were gradually compacted uniaxially at room temperature using a cylindrical die-punch assembly (double end compaction type) to 620 MPa with a Zwick 1496-2d. The compacted samples

were sintered under Ar atmosphere (99.999 %) for 1 h at a temperature of 873 K. The density of the composite was determined by the Archimedes' principle. Compression creep measurements were made on each sample (diameter and length of 10 mm) using stresses in the range of 30–35 MPa with a Santam (STM 150) universal tensile testing machine.

Table 1 shows the sample specification (diameter of 10 mm and length of 5 mm) for the impression tests. To measure the impression relaxation creep, a primary impression of 0.5 mm depth with a speed of $8.3 \times 10^{-4} \text{ mm s}^{-1}$ was used for all specimens. Having reached this indenter depth, the crosshead was stopped and the decrease in force with time was recorded. In another test the speed was increased to $8.3 \times 10^{-3} \text{ mm s}^{-1}$ and indenter depths of 0.5 mm and 0.8 mm were selected. The stress relaxation results were also obtained.

Table 1: Porosity of samples used in impression tests

Tabela 1: Značilnosti uporabljenih vzorcev pri preizkusu vtiskovanja

Sample	Porosity (%)
1	8.5
2	13.6
3	8.1
4	10.5
5	12.2
6	11.4
7	8.9

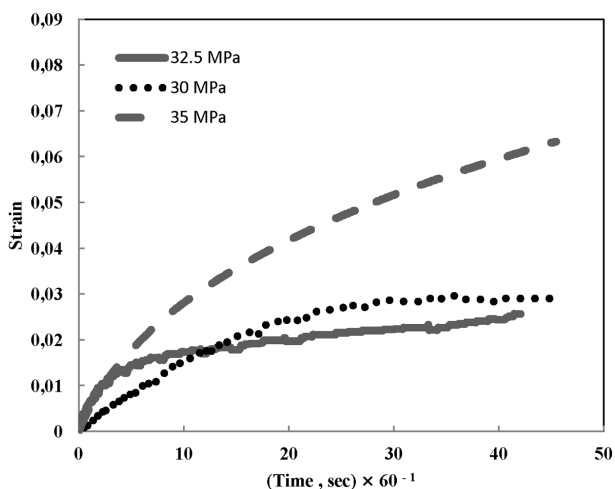


Figure 2: Compression strain as a function of time and compression stress

Slika 2: Skrček v odvisnosti od časa in napetosti pri stiskanju

3 RESULTS AND DISCUSSION

Figure 2 and **Table 2** show the compression creep data. **Figure 3** and **Table 3** show the impression stress relaxation tests in different conditions. In **Tables 4** and **5**, the relationship between stress reduction in the impression-relaxation tests and creep rate in the uniaxial creep test is shown.

Table 2: Compression steady state creep rate as a function of stress and porosity

Tabela 2: Hitrost lezenja pri stiskanju v odvisnosti od napetosti in poroznosti

Sample	Porosity (%)	$\sigma_{\text{Compression}}$ (MPa)	Compression creep rate (1/s)
1	12	30	3×10^{-6}
2	12	32.5	3×10^{-6}
3	16	35	1×10^{-5}

Table 3: Stress relaxation rate of composite samples as a function of indenter depth and enforcement rate

Tabela 3: Hitrost sproščanja kompozitnih vzorcev v odvisnosti od globine vtiska in hitrosti vtiskovanja

Sample	Indenter depth (mm), speed ($\times 10^3 \text{ mm s}^{-1}$)	$d\sigma/dt$ (MPa/s) $\times 10^3$
1	0.5, 8.3	7
2	0.5, 8.3	0.9
3	0.5, 8.3	3
4	0.8, 8.3	4
5	0.5, 0.83	6
6	0.5, 0.83	3
7	0.5, 0.83	3

Table 4: Coefficient of stress relaxation and compression creep rates (C) ($\sigma_{\text{Compression}} = 30, 32.5 \text{ MPa}$)

Tabela 4: Koeficient sproščanja napetosti in hitrost lezenja pri stiskanju (C) ($\sigma_{\text{Compression}} = 30, 32.5 \text{ MPa}$)

Sample (a)	Indenter depth (mm), speed ($\times 10^3 \text{ mm s}^{-1}$)	C(MPa) $\{\epsilon^o = (1/C)(d\sigma/dt)\}$	Average (C)
1	0.5, 8.3	2333	C=1211 (samples (1, 2, 3))
2	0.5, 8.3	300	
3	0.5, 8.3	1000	
4	0.8, 8.3	1333	C = 1333
5	0.5, 0.83	2000	C = 1333 (samples (5, 6, 7))
6	0.5, 0.83	1000	
7	0.5, 0.83	1000	

Table 5: Coefficient of stress relaxation and compression creep rates (C) ($\sigma_{\text{Compression}} = 35 \text{ MPa}$)

Tabela 5: Koeficient relaksacije napetosti in hitrost lezenja pri stiskanju (C) ($\sigma_{\text{Compression}} = 35 \text{ MPa}$)

Sample (b)	Indenter depth (mm), speed ($\times 10^3 \text{ mm s}^{-1}$)	C(MPa) $\{\epsilon^o = (1/C)(d\sigma/dt)\}$	Average (C)
1	0.5, 8.3	700	C = 363 (samples (1, 2, 3))
2	0.5, 8.3	90	
3	0.5, 8.3	300	
4	0.8, 8.3	400	C = 400
5	0.5, 0.83	600	C = 400 (samples (5, 6, 7))
6	0.5, 0.83	300	
7	0.5, 0.83	300	

It is clear that the stress relaxation is a suitable criterion of the strain rate because of the constant strain (indenter depth) during the test.^{5,14} **Figure 3** shows the positive effect of the enforcement rate of $0.83 \times 10^{-3} \text{ mm s}^{-1}$ and impression depth of 0.8 mm on recovery rate or viscoelastic coefficient decrease, relaxation ($d\sigma/dt$) or

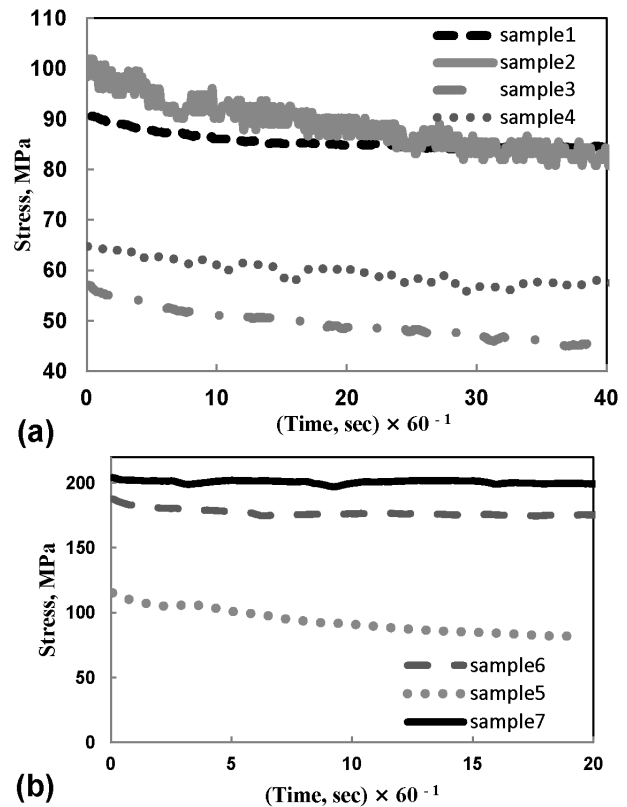


Figure 3: Stress relaxation tests as a function of impression depth and strain rate: a) samples 1, 2, 3, 4, b) samples 5, 6, 7

Slika 3: Preizkus sprostitve v odvisnosti od globine vtiskovanja in hitrosti obremenjevanja: a) vzorci 1, 2, 3, 4, b) vzorci 5, 6, 7

creep rate. In addition, the porosity and SiC distribution variations affect the movement of dislocations and threshold stress or internal friction stress. Experimental results on the creep behavior of Al composite with micron sized SiC by A. B. Pandey⁹ have emphasized the threshold stress increase with SiC content, interparticle spacing or particle size decrease. Thus, the creep resistance has been improved. Similar creep behavior has been reported in Al reinforced with nanoparticles which is the Orowan strengthening mechanism under the nano-reinforcement effect.^{15,16} In these studies the effect of oxide nanoparticles which leads to the reduction of dislocation movement has been clearly shown. Thus, in agreement with previous studies^{9,15-17}, the reinforcing phase leads to creep resistance in the composites. Also the reinforcement distribution and particle size have been shown to affect the creep behavior of composites.^{9,18} The novelty of this research in comparison with earlier work is in observation of the creep behavior of a composite using the impression-relaxation method. Initially, the speed of relaxation is high, as shown in **Figure 3**. Then the immobilized dislocations generate resistance and threshold stress. Consequently, the stress relaxation decreases until equilibrium between recovery and work hardening or the steady state condition (constant slope) is achieved. The stress relaxation behavior of materials leading to a steady state condition has been observed in

other materials.¹⁹⁻²¹ Thus, in composites with 4 % of volume fractions SiC (nano) produced by mechanical alloying, compacting with a compression force of 620 MPa, and sintering at 873 K, the primary stress relaxation rate decreases due to the creation of immobilized dislocations (pinning at the nano-reinforcement). Correspondingly, the existence of voids (depending on the indenter size) in the form of drops, or more relaxation, are observable in graphs. Considering **Tables 4** and **5**, the similarity of the coefficient of compression creep as well as the impression relaxation rates reveal minute differences of microstructure or SiC particles clustering. This issue has been proved in **Tables 1** and **2** in which the samples' densities are shown. These minute differences are illustrated in the steady state rate fluctuations of the different samples' relaxation graphs. The impression relaxation rate increases with the increase of porosity and SiC clustering. This result shows that the impression relaxation test with this indenter size can be useful for obtaining the actual composite characteristics within a short test time.

In line with earlier studies,^{5,14} correlation of the relaxation and uniaxial creep data, and the strain rate ($\dot{\epsilon}^0$) can be estimated using the stress relaxation rate ($d\sigma/dt$) and the elastic modulus (E) according to the following Equation (1):

$$\dot{\epsilon}^0 = -\frac{1}{E} \frac{d\sigma}{dt} \quad (1)$$

According to **Tables 4** and **5**, the compression and impression methods are related to each other with the approximate constant (C), (1000 MPa), even with changing indenter depth and enforcement speed, taking into account the role of porosity, **Table 1**. The stability of the coefficient is decreased with the enforcement speed or strain rate (recovery increase) and the higher strength in samples 5, 6, and 7 is justified by the effect of the nano-SiC in these composites. It means that the compression creep rate and impression stress relaxation in these composites are related by a constant of 1000 (MPa), as given in Equation (1). It is useful for the determination of the composite fracture time using equations relating the strain rate and fracture time. The determination of the compression strain rate using the impression and impression stress relaxation methods, which rapidly yields the actual composite characteristics, helps in estimating the fracture time with the safety factor. In this research, on the basis of possible applications of this composite at high temperatures and compression forces (such as in a piston), the impression relaxation test was carried out at a temperature of 723 K and with high impression depths, e.g. 0.5 mm and 0.8 mm, selected for industrial applications, and the relationship between compression rate and stress relaxation rate (coefficient) was calculated. Moreover, the stability of the coefficient (C) over different experiments has been proved. In impression relaxation tests the value of the coefficient does not change with different indenter depth or enforcement speed, which is related to the SiC content. As **Tables 4** and **5**

show, the coefficient is affected only by the porosity and nano SiC distribution. This constant coefficient can be taken to be a function of the SiC content. These findings are suitable for the evaluation of fracture times and compression creep rate for research and industrial applications.

4 CONCLUSIONS

In the present study, a constant coefficient between impression relaxation rate and compression creep rate has been shown. The results indicate that in impression-relaxation tests, the impression depth and enforcement speed have no effect on the coefficient. The SiC reinforcement nanoparticles act as work-hardening particles. The porosity and the non-symmetrical distribution of SiC led to variations of the steady state relaxation rate or creep rate. The constant coefficient was a function of SiC content, porosity and the composite's elastic modulus.

Acknowledgements

The authors would sincerely like to acknowledge the Materials Engineering Department of Ferdowsi University of Mashhad for the experimental support of the research work.

5 REFERENCES

- M. Jahedi, B. Mani, S. Shakoorian, E. Pourkhorshid, M. Hossein Paydar, Deformation rate effect on the microstructure and mechanical properties of Al – SiCp composites consolidated by hot extrusion, *Materials Science and Engineering A*, 556 (2012), 23–30, doi:10.1016/j.msea.2012.06.054
- S. Min, Effects of volume fraction of SiC particles on mechanical properties of Al/SiC composites, *Transactions of Nonferrous Metals Society of China*, 19 (2009), 1400–1404, doi:10.1016/S1003-6326(09)60040-6
- N. P. Cheng, S. M. Zeng, Z. Y. Liu, Preparation, microstructures and deformation behavior of SiC_p/6066Al composites produced by PM route, *Journal of Materials Processing Technology*, 202 (2008), 27–40, doi:10.1016/j.jmatprotec.2007.08.044
- D. Pan, I. Dutta, A mechanics-induced complication of impression creep and its solution: application to Sn–3.5Ag solder, *Materials Science and Engineering A*, 379 (2004), 154–163, doi:10.1016/j.msea.2004.01.034
- Y. I. Jung, Y. N. Seol, B. K. Choi, J. Y. Park, Behavior of stress–relaxation and the estimation of creep in Zr–1.1Nb–0.05Cu alloy, *Materials and Design*, 42 (2012), 118–123, doi:10.1016/j.matdes.2012.05.045
- L. Yinfeng, L. Zhonghua, Transverse creep and stress relaxation induced by interface diffusion in Unidirectional metal matrix composites, *Composites Science and Technology*, 72 (2012), 1608–1612, doi:10.1016/j.compscitech.2012.06.017
- S. Ansary, R. Mahmudi, M. J. Esfandyarpour, Creep of AZ31 Mg alloy: A comparison of impression and tensile behavior, *Materials Science and Engineering A*, 556 (2012), 9–14, doi:10.1016/j.msea.2012.06.052
- R. G. Raghavender, O. P. Gupta, B. Pradhan, Application of stress relaxation testing in evaluation of creep strength of a tungsten-

- alloyed 10% Cr cast steel, *International Journal of Pressure Vessels and Piping*, 88 (2011), 65–74, doi:10.1016/j.ijpvp.2011.02.005
- ⁹ A. B. Pandey, R. S. Mishra, Y. R. Mahajan, Steady state rate behavior of silicon carbide particulate reinforced aluminium composites, *Acta Metallurgica Materialia*, 40 (1992) 8, 2045–2052, doi:10.1016/0956-7151(92)90190-P
- ¹⁰ F. Moreno Mario, J. R. Carlos, Oliver. González, Compression creep of PM aluminum matrix composites reinforced with SiC short fibres, *Materials Science and Engineering A*, 418 (2006), 172–181, doi:10.1016/j.msea.2005.11.035
- ¹¹ X. U. Fu-min, W. U. Lawrence, C. M. Han, G. W. Tan. Yi, Compression creep behavior of high volume fraction of SiC particles reinforced Al composite fabricated by pressureless infiltration, *Chinese Journal of Aeronautics*, 20 (2007), 115–119, doi:10.1016/S1000-9361(07)60016-8
- ¹² K. Wakashima, T. Moriama, T. Mori, Steady state creep of a particulate SiC /6061 Al composite, *Acta Materialia*, 48 (2000), 891–901, doi:10.1016/S1359-6454(99)00386-9
- ¹³ Z. Y. Ma, S. C. Tjong, Creep deformation characteristics of discontinuously reinforced aluminium-matrix Composites, *Composites Science and Technology*, 61 (2001), 771–786, doi:10.1016/S0266-3538(01)00018-5
- ¹⁴ J. Gittus, *Creep, Viscoelasticity and creep fracture in solids*, Applied Science Publishers, England 1975
- ¹⁵ J. Cadek, S. J. Zhu, K. Milick, Threshold creep behaviour of aluminium dispersion strengthened by fine alumina particles, *Materials Science and Engineering A*, 252 (1998), 1–5, doi:10.1016/S0921-5093(98)00672-8
- ¹⁶ Z. Lin, S. L. Chan, F. A. Mohamed, Effect of nano-scale particles on the creep behavior of 2014 Al, *Materials Science and Engineering A*, 394 (2005), 103–111, doi:10.1016/j.msea.2004.11.034
- ¹⁷ W. J. Lee, S. K. Jo, I. M. Park, Y. H. Park, The effect of reinforcement clustering on the steady-state creep behaviours of discontinuous metal matrix composite: A possible origin of ‘anomalously high’ stress exponent, *Materials Science and Engineering A*, 528 (2011), 4564–4568, doi:10.1016/j.msea.2011.02.038
- ¹⁸ S. P. Deshmukh, R. S. Mishra, K. L. Kendig, Creep behavior and threshold stress of an extruded Al–6Mg–2Sc–1Zr alloy, *Materials Science and Engineering A*, 381 (2004), 381–385, doi:10.1016/j.msea.2004.05.025
- ¹⁹ R. Mahmudi, A. R. Geranmayeh, H. Noori, H. Khanbareh, N. Jahangiri, A comparison of impression, indentation and impression-relaxation creep of lead-free Sn–9Zn and Sn–8Zn–3Bi solders at room temperature, *Journal of Materials Science – Materials in Electronics*, 20 (2009), 312–318, doi:10.1007/s10854-008-9726-x
- ²⁰ L. I. Trusove, T. P. Khvostantseva, Solov’ev and V. A. Mel’nikova, Stress relaxation following heating of nanocrystalline nickel, *Nanostructured Materials*, 4 (1994) 7, 803–813, doi:10.1016/0965-9773(94)90086-8
- ²¹ S. N. G. Chu, J. C. M. Li, Localized Stress Relaxation By Impression Testing, *Materials Science and Engineering A*, 45 (1980), 167–171, doi:10.1016/0025-5416(80)90222-0

MICROSTRUCTURE AND PROPERTIES OF THE HIGH-TEMPERATURE (HAZ) OF THERMO-MECHANICALLY TREATED S700MC HIGH-YIELD-STRENGTH STEEL

MIKROSTRUKTURA IN LASTNOSTI VISOKO TEMPERATURNEGA OBMOČJA ZVARA (HAZ) TERMO-MEHANSKO OBDELANEGA JEKLA S700MC Z VISOKO MEJO PLASTIČNOSTI

Jacek Górk

Silesian University of Technology, Konarskiego Street 18a, 44-100 Gliwice, Poland
jacek.gorka@polsl.pl

Prejem rokopisa – received: 2015-06-18; sprejem za objavo – accepted for publication: 2015-07-17

doi:10.17222/mit.2015.123

The aim of the study was to determine the properties and microstructure of the high-temperature heat affected zone (HAZ) of S700MC steel heated to a temperature of 1250 °C and cooled at different speeds. The simulation of the thermal cycles was performed using a welding thermal cycles simulator. Samples with a cross-section 10 mm × 10 mm × 55 mm were submitted to metallographic analysis, impact tests, hardness measurements and tensile tests. Welding thermal cycles with cooling times $t_{8/5} = (3, 5, 10, 15, 30, 60 \text{ and } 120) \text{ s}$ and a maximum temperature cycle temperature of $T_{\max} = 1250 \text{ °C}$ were used. The welding thermal thermomechanical processing cycles differ significantly, especially with high rates of heating and cooling in the SWC, short time holding at the maximum temperature and frequent overlap of two or more cycles during the multi-layer welding. One of the elements in the evaluation of steel weldability is the analysis of the austenite phase transformation during cooling. Steel hardness tests on simulated HAZ regions cooling times increasing from 3 s to 120 s, showed reductions by approximately 40 HV, while, regardless of the length of the cooling time $t_{8/5}$, the impact resistance was very low, at the level of a few J/cm^2 . The tensile strength, hardness and toughness indicates a secondary role of austenite in the control of welded joints transformation strength and plastic properties, the analysis of the γ - α phase transition not shown to be a reliable basis for assessment of the weldability of this steel group.

Keywords: TMCP steel, welding thermal cycles, HAZ, high yield strength, impact resistance

Namen študije je bil določiti lastnosti in mikrostrukturo visokotemperaturne toplotno vplivanega območja zvara (HAZ) v jeklu S700MC, segretem na temperaturo 1250 °C in ohlajenem pri različnih hitrostih. Simulacija procesa toplotnih ciklov je bila izvedena z uporabo simulatorja toplotnih ciklov pri varjenju. Vzorci s presekom 10 mm × 10 mm × 55 mm so bili metalografsko pregledani, izveden je bil udarni preizkus, izmerjena je bila trdota in izvedeni so bili natezni preizkusi. Uporabljeni so bili toplotni cikli pri varjenju s časi ohlajanja $t_{8/5} = (3, 5, 10, 15, 30, 60 \text{ in } 120) \text{ s}$ in maksimalna temperatura toplotnega cikla je bila $T_{\max} = 1250 \text{ °C}$. Pri varjenju se cikli varilno termičnega in termomehanskega procesiranja precej razlikujejo, predvsem pri veliki hitrosti ogrevanja in ohlajanja v SWC, kratkotrajnem zadržanju na maksimalni temperaturi in pogostem prekrivanju enega ali več ciklov pri večplastnih zvarih. Eden od elementov pri ocenjevanju varivnosti jekla, je analiza premene avstenita med ohlajanjem. Pri preizkusih trdote simuliranih HAZ področij, se le ta, s povečanjem časa ohlajanja od 3 s na 120 s, zmanjša za okrog 40 HV, medtem ko je žilavost zelo nizka in na nivoju nekaj J/cm^2 ne glede na čas ohlajanja $t_{8/5}$. Natezna trdnost, trdota in žilavost kažejo drugotno vlogo pri kontroli trdnosti in plastičnosti transformiranega avstenita zvarjenih spojev. Analiza faznega prehoda γ - α ni zanesljiva osnova za ugotavljanje varljivosti te vrste jekla.

Ključne besede: TMCP jeklo, toplotni cikel pri varjenju, HAZ, visoka meja plastičnosti, odpornost na udarce

1 INTRODUCTION

Steels produced using thermomechanical treatment are characterised by a lower carbon equivalent than steels of the same yield point treated to normalisation annealing.¹ Also for yield points above 550 MPa, steels subjected to thermomechanical rolling with accelerated cooling and tempering are characterised by a lower carbon equivalent than toughened steels.²⁻⁵ Due to the significantly lower carbon equivalent, thermomechanically treated steels should have significantly better weldability in comparison to normalised or toughened steels of a similar yield point. The alloying microagents of S700MC steel, i.e. niobium, vanadium and titanium are strongly carbide and nitride-forming. If dissolved in the HAZ, they increase HAZ hardenability and steel hard-

ness after cooling. This phenomenon is considered disadvantageous. However, on the other hand, carbides and carbonitride precipitates of Nb, V, and Ti effectively impede grain growth and significantly restrict the width of the coarse-grained area of the HAZ.⁶⁻⁸ The HAZ ductility is significantly improved by Ti_2O_3 particles, which are more stable than TiN particles and insoluble even at higher temperatures and act as nuclei by the nucleation of fine-lamellar ferrite.⁹⁻¹¹ Fine-lamellar ferrite within austenite grains increases the HAZ ductility. The HAZ microstructure of a multi-run welded joint depends on the chemical composition of the steel, heat source intensity and the number of runs. Both cooling rate and heat input significantly affect the HAZ weld microstructure. By cooling welds of thermomechanically treated steels, niobium, vanadium and titanium precipitate as carbides

and carbonitrides. During cooling, these microagents precipitate in the form of carbides and carbonitrides. The amount of precipitates depends on the cooling rate. The faster the cooling, the more microagents remain in solution. A similar situation is observed in the Heat Affected Zone. The amount of microelements in solution significantly affects phase transformation during cooling and changes the properties after subsequent heat treatments.¹² This increases the content of microstructural components formed by diffusionless and indirect (bainitic) transformations. Such microstructures are the primary reason for decreased toughness, particularly in wide HAZ. This effect is even greater in welding with high linear energy and prolonged cooling times $t_{8/5}$. In the case of high cooling rates, a typical HAZ structure in thermomechanically processes steels contains lower bainite characterised by satisfactory brittle cracking resistance. A high welding heat input extends the HAZ, holds it at high temperatures and reduces the cooling rate, leading to austenite grain growth and, consequently, particularly near the fusion line, the formation of a microstructure characterised by lower plastic properties. In such case, the HAZ structure is dominated by upper bainite as well as by delta and side-lamellar ferrite.^{13,14}

2 EXPERIMENTAL PROCEDURE

HAZ areas simulated in S700 MC steel (Table 1 and Figure 1) heated up to 1250 °C and cooled at various rates, were used for testing. The thermal cycles were performed with a welding thermal cycle simulator on specimens with a cross-section of 10 mm × 10 mm × 55 mm. The specimens were then used for metallographic examination, impact strength tests, hardness measurements and tensile tests.

Table 1: The chemical composition of S700 MC steel

Tabela 1: Resnična kemijska sestava jekla S700 MC

Chemical composition, %										
C	Mn	Si	S	P	Al	Nb	Ti	V	N*	C _e
0,056	1,68	0,16	0,005	0,01	0,027	0,044	0,12	0,006	72	0,33

* - N: the amount given in ppm, the nitrogen was measured using the high temperature extraction method

The specimens were submitted to welding thermal cycles and cooling times $t_{8/5}$ = (3, 5, 10, 15, 30, 60 and 120) s, with the thermal cycle maximum temperature T_{max} = 1250 °C. The thermal cycle maximum temperature was read from a diagram recorded by means of a PC. In Table 2 (pre-set and measured) parameters of test steel thermal cycles are presented.

After the simulation, the specimens were submitted in accordance with the standard PN-EN ISO 9015-1 to Charpy V impact tests using a ZWICK/ROELL RKP 450 at a temperature of -30 °C, to metallographic examination on a NIKON ECLIPSE MA100 light microscope, and to Vickers hardness tests with a 9.81 N (HV1) load using a WILSON WOLPERT MICRO-VICKERS

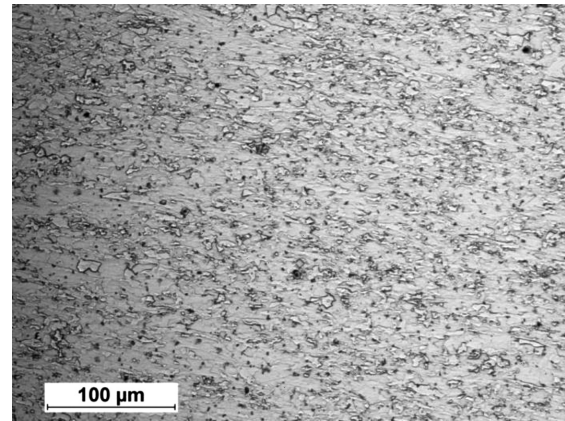


Figure 1: Microstructure of bainitic-ferritic steel S700MC with visible traces of plastic deformation

Slika 1: Mikrostruktura bainitno-feritnega jekla S700MC, z vidnimi sledovi plastične deformacije

401MVD hardness tester. Each specimen underwent 7 measurements, the two extreme values (minimum and maximum) rejected and the remaining five values averaged. The mechanical and plastic properties of round specimens were determined according to PN-EN 10002-1, using the MTS Insight testing machine.

Table 2: Input parameters and simulated thermal cycles of S700MC steel

Tabela 2: Vhodni parametri in simulirani toplotni cikli pri jeklu S700MC

No.	Types of cycles	Maximum temperature of cycles T_{max} , °C	
		Set	Real
1	3	1250	1223
2		1250	1215
3		1250	1247
4	5	1250	1231
5		1250	1234
6		1250	1217
7	10	1250	1250
8		1250	1246
9		1250	1243
10	15	1250	1257
11		1250	1262
12		1250	1255
13	30	1250	1254
14		1250	1261
15		1250	1255
16	60	1250	1262
17		1250	1258
18		1250	1265
19	120	1250	1253
20		1250	1264
21		1250	1246

3 RESULTS AND DISCUSSION

Previous tests of simulated HAZ areas heated to various maximum temperatures revealed that the HAZ were characterised by mechanical and plastic properties

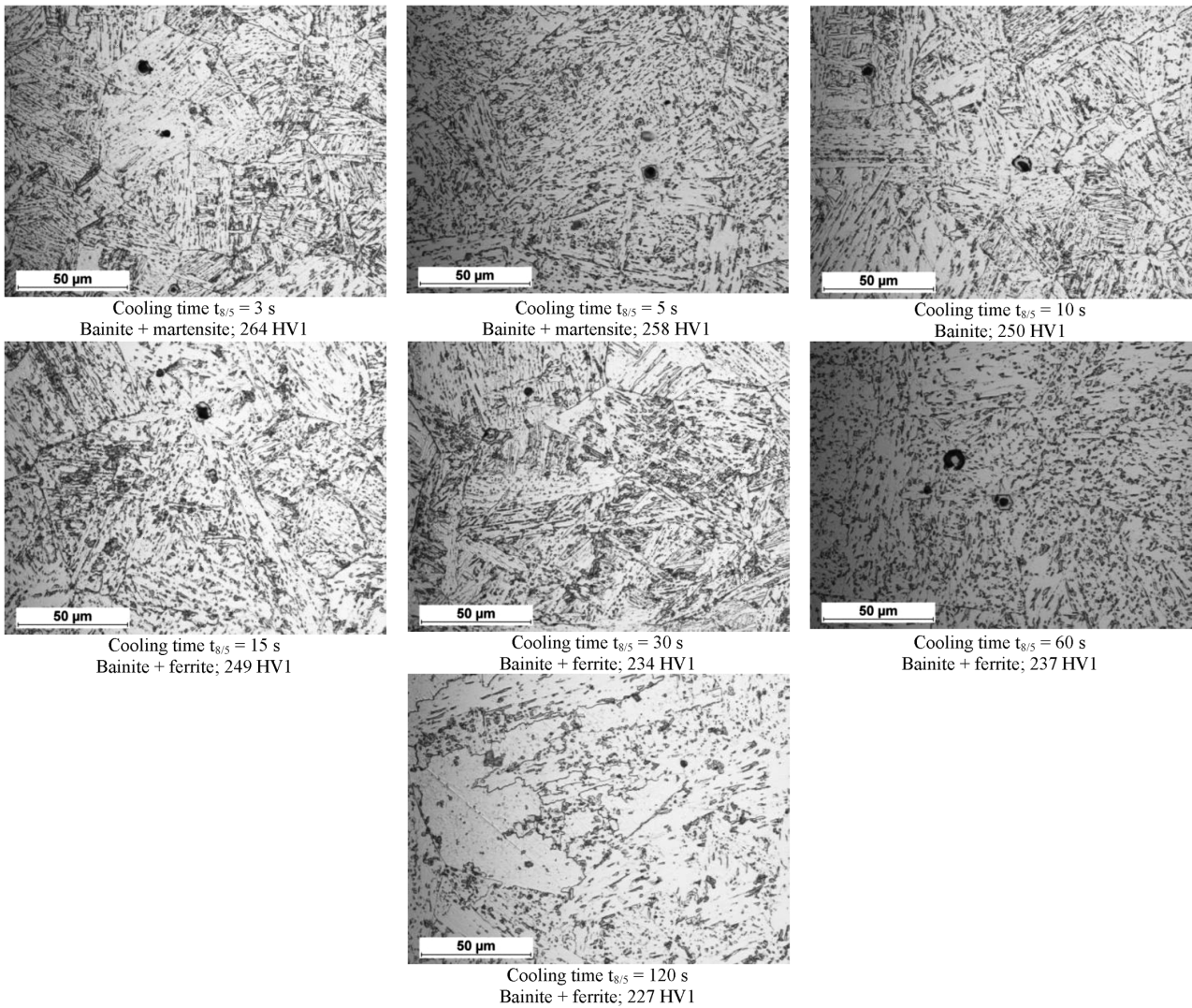


Figure 2: S700MC steel microstructure as a function of the cooling time $t_{8/5}$
Slika 2: Mikrostruktura jekla S700MC v odvisnosti od časa ohlajanja $t_{8/5}$

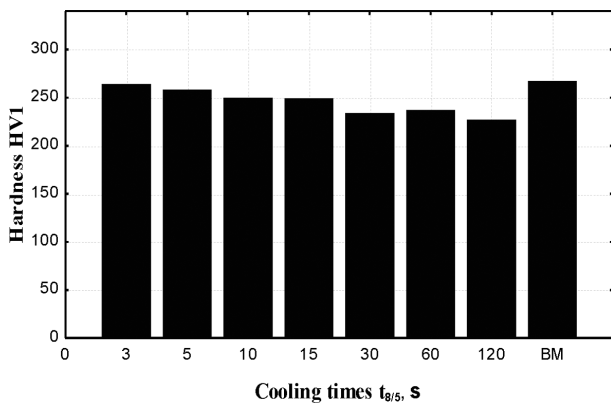


Figure 3: Hardness of simulated HAZ HV1 S700MC steel, cycle temperature 1250 °C

Slika 3: Simulirana trdota HV1 v HAZ jekla S700MC, temperatura cikla 1250 °C

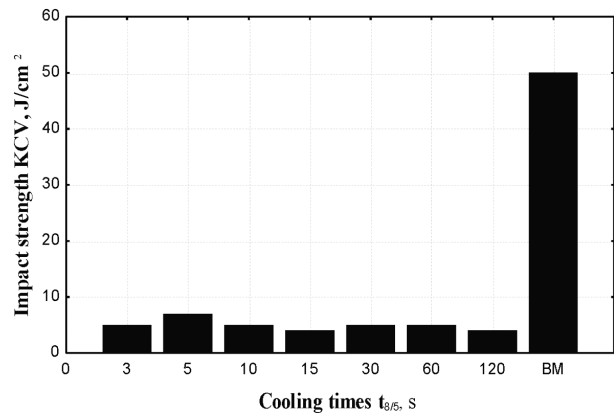


Figure 4: Toughness of simulated HAZ S700MC steel at -30 °C, cycle temperature 1250 °C

Slika 4: Simulirana žilavost HAZ jekla S700MC pri -30 °C, temperatura cikla 1250 °C

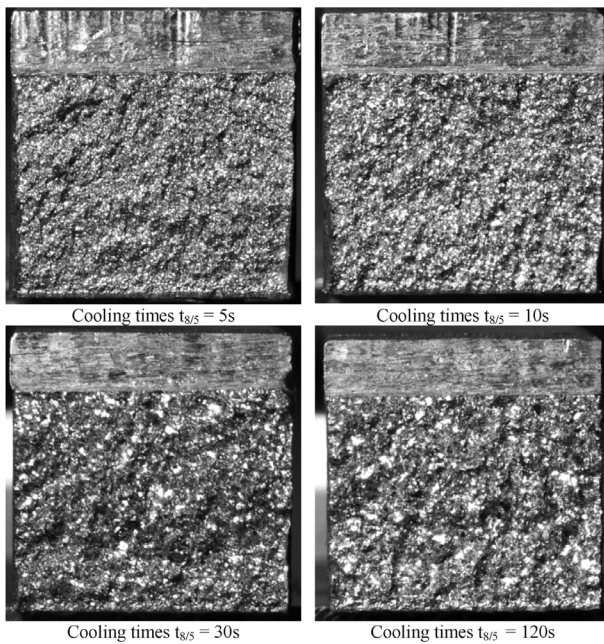


Figure 5: Brittle HAZ fracture of the specimens heated to 1250 °C, after impact test at -30 °C

Slika 5: Krhek prelom HAZ vzorcev, ogrelih na 1250 °C, po udarnem preizkusu na -30 °C

varying with cross-section. The worst changes were observed in an area heated up to 1300 °C, where the toughness dropped by several J/cm².⁹ Accordingly it was necessary to investigate the effect of cooling time $t_{8/5}$ on the microstructure and properties of the HAZ heated up to 1250 °C. For a short cooling time, i.e. below 10 s, bainite mixed with low-carbon martensite is formed in the HAZ. A cooling time in the range 10 s to 20 s forms a bainitic-ferritic microstructure closest to the initial microstructure. The further extension of cooling time increases the ferrite content in the microstructure. Cooling times exceeding 100 s lead to the formation of a ferritic-bainitic structure (Figure 2). After each cooling individual precipitates of several μm size were observed.

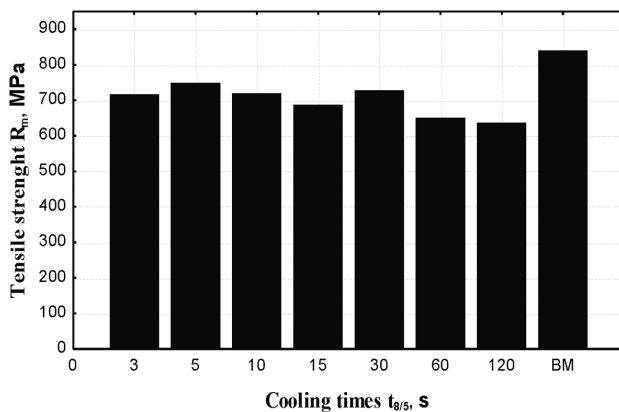


Figure 6: Tensile test of simulated HAZ S700MC steel; cycle temperature of 1250 °C

Slika 6: Natezni preizkus simulirane HAZ jekla S700MC, pri temperature cikla 1250 °C

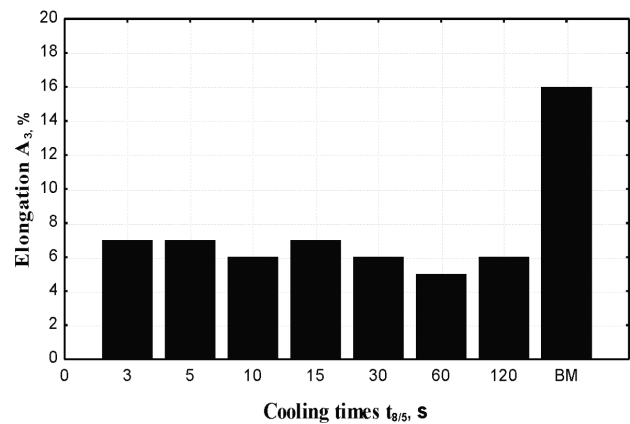


Figure 7: Elongation of the simulated HAZ S700MC steel; cycle temperature of 1250 °C

Slika 7: Raztezki simulirane HAZ jekla S700MC pri temperaturi cikla 1250 °C

The characteristic polygonal shape of the precipitates suggests the precipitates are probably (Ti,Nb)(C,N) carbonitrides. The large sizes of the precipitates do not improve steel properties; on the contrary, they could significantly reduce the mechanical and plastic properties of welded joints.

HV1 hardness measurements revealed a slight decrease in the hardness for extended cooling times $t_{8/5}$. The hardness in the HAZ area decreased from 265 HV for cooling time of several seconds to 230 HV1 for cooling times longer than 60 s (Figure 3). Regardless of cooling time, the HAZ area hardness values exceeding 270 HV did not make the area susceptible to cold cracking.

The HAZ toughness tests at -30 °C revealed a sharp drop in the mechanical properties with respect to the parent metal, irrespective of cooling time $t_{8/5}$ (Figure 4). The thermal cycle temperature of approximately 1250 °C is responsible for the properties' decrease, especially brittle fractures in impact tests as a result of thermo-mechanical treatment (Figure 5). The toughness of several J/cm² is very unsatisfactory for performance of welds with HAZ heated to the highest temperatures

The tensile tests of the round specimens of the steel subjected to thermal cycles at a temperature of 1250 °C revealed only a slight effect of cooling time $t_{8/5}$ on the mechanical properties of the S700MC steel HAZ. In the entire cooling time range of 3 s to 120 s, the tensile strength of the HAZ was lower than the tensile strength of the parent metal (Figure 6). By extending the cooling time from 3 s to 120 s, the tensile strength decreased from 720 MPa to 640 MPa. This decrease in tensile strength could primarily be ascribed to grain growth in the high-temperature HAZ area. The obtained elongation values of 7 % were significantly lower than the parent metal value of 16 % (Figure 7).

4 CONCLUSIONS

The welding thermal cycle differs significantly from a thermomechanical treatment cycle primarily by the very high heating and cooling rates in the HAZ area, short hold at a maximum temperature and the very frequent coincidence of one or more thermal cycles by multi-layer welding. The analysis of austenite phase transformations by cooling time is one of the elements for steel weldability assessment. For the steel investigated, the of the simulated HAZ (heated up to 1250 °C) hardness decreased slightly, by approximately 40 HV with the increase of cooling time from 3 s to 120 s. Regardless of the cooling time $t_{8/5}$, the toughness was very low and diminished to several J/cm². The results of the tensile and impact tests, as well as the hardness measurements suggest a secondary role for the austenite transformations in controlling the mechanical and plastic properties of welded joints. The analysis of γ - α phase transformations cannot act as the basis for the assessment of weldability in this group of steels.

Acknowledgement

The study was partially supported by the NOT Innovation Center in Gliwice and Vlassenroot Polska, under the project POIG.01.04.00-24-052/13.

5 REFERENCES

- ¹ C. Lee, H. Shin, K. Park, Evaluation of high strength TMCP steel weld for use in cold regions, *Journal of Constructional Steel Research*, 74 (2012), 134–139
- ² M. Yurioka, *Welding in the World*, TMCP steels and their welding, 35/6 (1995), 375–390
- ³ J. Górka, Weldability of thermomechanically treated steels having a high yield point, *Archives of Metallurgy and Materials*, 60/1 (2015), 469–475, doi:10.1515/amm-2015-0076
- ⁴ A. Lisiecki, Welding of Thermomechanically Rolled Fine-Grain Steel by Different Types of Lasers, *Archives of Metallurgy and Materials*, 59 (2014), 1625–1631, doi:10.2478/amm-2014-0276
- ⁵ M. Opiela, Effect of Thermomechanical Processing on the Microstructure and Mechanical Properties of Nb-Ti-V Microalloyed Steel, *Journal of Materials Engineering and Performance*, 9 (2014), 3379–3388
- ⁶ A. Lisiecki, Diode laser welding of high yield steel, *Proceedings of SPIE*, vol. 8703, *Laser Technology 2012: Applications of Lasers*, 87030S (2013), doi:10.1117/12.2013429
- ⁷ Kurc-Lisiecka A., et al, Analysis of deformation texture in AISI 304 steel sheets, *Solid State Phenomena*, 203-204 (2013), 105–110, doi:10.4028/www.scientific.net/SSP.203-204.105
- ⁸ A. Grajcar, M. Róžański, S. Stano, A. Kowalski, Microstructure characterization of laser-welded Nb-microalloyed silicon-aluminum TRIP steel, *Journal of Materials Engineering and Performance*, 23/9 (2014), 3400-3406
- ⁹ A. Lisiecki, Welding of titanium alloy by disk laser, *Proc. of SPIE*, vol. 8703, *Laser Technology 2012: Applications of Lasers*, 87030T (2013), doi:10.1117/12.2013431
- ¹⁰ D. Janicki, Disk Laser Welding of Armor Steel, *Archives of Metallurgy and Materials*, 59 (2014), 1641–1646, doi:10.2478/amm-2014-0279
- ¹¹ A. Grajcar, M. Róžański, M. Kamińska, B. Grzegorzczuk, Study on Non-Metallic Inclusions in Laser-Welded TRIP-Aided Nb-Microalloyed Steel, *Archives of Metallurgy and Materials*, 59 (2014), 1163–1169, doi:10.2478/amm-2014-0203
- ¹² M. Charleux, W-J. Poole, M. Militzer, Precipitation behavior and its effect on strengthening of an HSLA-Nb/Ti steel, *Metallurgical and Materials Transactions A*, 32 (2001), 1635–1647
- ¹³ J. Górka, Analysis of simulated welding thermal cycles S700MC using a thermal imaging camera, *Advanced Material Research*, 1036 (2014), 111–116
- ¹⁴ Y. Crowther, M. Green, P. Mitchell, The Effect of Vanadium and Niobium on the Properties and Microstructure of the Intercritically Reheated CoarseGrained Heat Affected Zone in Low Carbon Microalloyed Steels, *ISIJ International*, 41 (2001), 46–55

NEW CONCEPT FOR MANUFACTURING CLOSED DIE FORGINGS OF HIGH STRENGTH STEELS

NOV KONCEPT IZDELAVE ODKOVKOV IZ VISOKOTRDNOSTNIH JEKEL V ZAPRTIH UTOPIH

Khodr Ibrahim, Ivan Vorel, Dagmar Bublíková, Bohuslav Mašek

University of West Bohemia, Fortech Research Centre, Univerzitní 8, 306 14 Plzeň, Czech Republic
ibrahim@kmm.zcu.cz

Prejem rokopisa – received: 2015-06-18; sprejem za objavo – accepted for publication: 2015-08-25

doi:10.17222/mit.2015.122

In the automotive industry, there is an ever growing demand for steel components with enhanced mechanical properties. Typically, this involves steels with high strength combined with adequate ductility. With improved properties, the structural components of these steels can be less bulky, requiring less material, energy and lower costs. Processing a material to obtain high strength and high ductility at the same time used to be rather difficult. Today, it can be accomplished by incorporating retained austenite in a martensitic matrix. A new heat-treatment method for closed-die forgings, termed Q&P process (quenching and partitioning), leads to a combination of martensite and retained austenite with strengths above 2000 MPa and an elongation of 10-15 %.

Keywords: Q&P process, retained austenite, AHSS, closed-die forgings

V avtomobilski industriji narašča zahteva po komponentah iz jekla z izboljšanimi mehanskimi lastnostmi. Ta zadeva tudi jekla z visoko trdnostjo, v kombinaciji s primerno duktilnostjo. Zahvaljujoč izboljšanim lastnostim so te komponente iz jekel dimenzijsko manjše, ker je zanje potrebnega manj materiala, manj energije in tudi stroški so manjši. Izdelava materiala, ki bi istočasno imel visoko trdnost in dobro duktilnost je težavna. Danes je to mogoče doseči in sicer z vključitvijo zaostalega avstenita v martenzitno osnovo. Nova metoda toplotne obdelave odkovkov iz utopov je Q&P postopek ali kaljenje in delitev, kar povzroči kombinacijo martenzita in zaostalega avstenita, s trdnostjo nad 2000 MPa in raztežkom 10–15 %.

Ključne besede: Q&P postopek, zaostali avstenit, AHSS, odkovki iz utopov

1 INTRODUCTION

Closed-die steel forgings produced by hot forging are made from preforms, which are converted into the desired part shape using plastic deformation in impression dies. Then, the workpiece microstructure must be altered to obtain the desired mechanical properties. A typical microstructure upon quenching consists of martensite. It exhibits high strength but very poor ductility. This causes problems in parts which may fail in service under their operating load. Hence, parts that contain martensite are normally tempered after quenching. Today, a handful of modern metallurgical procedures are available for achieving higher ductility. They include long-time low-temperature austempering, intercritical processing of TRIP steels, and the Q&P process. Long-time low-temperature austempering can produce tensile strengths of up to 1500 MPa and hardness levels of 600-670 HV10.¹ Long-time low-temperature austempering is characterised by holding times of several tens of hours at low temperatures. The resulting microstructure consists of very fine bainitic ferrite (**Figure 1**).² Due to the long processing times, this method has failed to find industrial use. The concept of TRIP steels relies on a mixture of bainite, ferrite and retained austenite formed by intercritical annealing and isothermal holding at the bainitic

transformation temperature during a controlled cooling process³ (**Figure 2**). The third method is the Quenching and Partitioning (Q&P) process, which allows strengths of more than 2000 MPa to be obtained, together with an elongation of about 10 %. An important factor in this process is the stabilisation of austenite in the martensitic matrix (**Figure 3**). One of the ways of obtaining a martensitic structure with the desired fraction of retained austenite is a special heat treatment procedure described

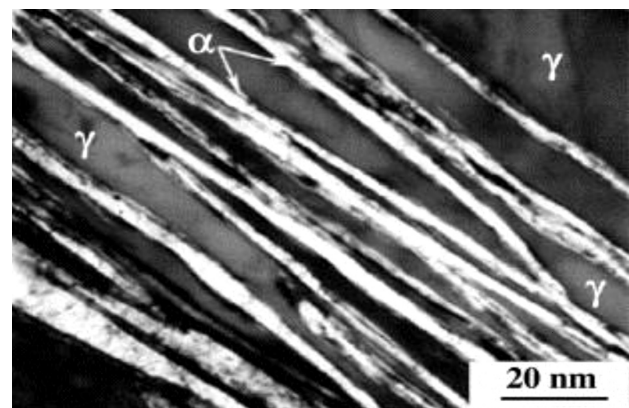


Figure 1: Microstructure produced by long-time austempering¹
Slika 1: Mikrostruktura nastala pri dolgotrajnem austempranju¹

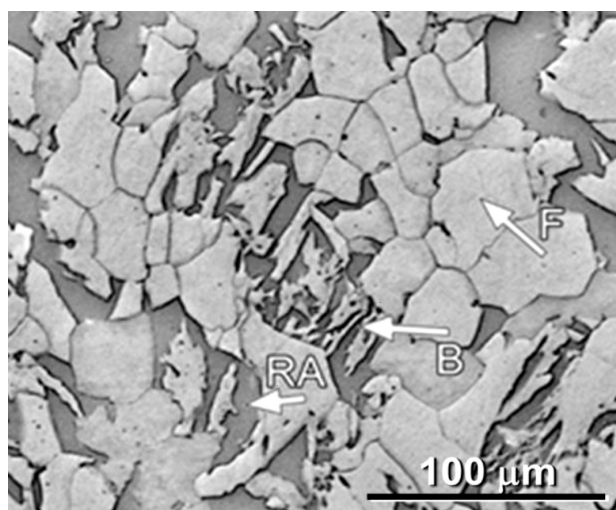


Figure 2: Typical microstructure of TRIP steel produced by intercritical annealing

Slika 2: Značilna struktura TRIP jekla po interkritičnem žarjenju

below. It is characterised by rapid cooling from the austenite region to a temperature between the M_s and M_f . During such cooling, martensite forms, whereas a portion of austenite remains untransformed. During subsequent isothermal holding, the retained austenite becomes stabilised thanks to carbon which migrates from the super-saturated martensite to austenite. According to current knowledge, this austenite exists primarily in the form of thin films between martensite laths or plates.⁴⁻⁶ The present paper focuses predominantly on the Q&P process, a novel metallurgical procedure for heat treating forged parts. So far, this process has led to the best mechanical properties.

2 EXPERIMENTAL PROCEDURE

A major issue that affects the use of the Q&P process in practice is the necessity to interrupt the quenching between the M_s and M_f temperatures. With this challenge in mind, four new experimental steels have been proposed. Their particular compositions were designed to reduce the M_s and M_f temperatures (**Table 1**). In all of these experimental steels, the M_s and M_f temperatures were depressed through the addition of manganese. To increase the material's strength, silicon and chromium have been added as well. Silicon was chosen in order to prevent carbide formation and thus to provide adequate super-saturation of martensite with carbon. Molybdenum was employed to both reduce the M_s and M_f temperatures and shift the start of ferritic and pearlitic transformations towards lower cooling rates. Nickel was added in small amounts to stabilise austenite during cooling, to enhance hardenability and to provide solid solution strengthening. The carbon content was the same in all steels: between 0.42 % and 0.43 %.

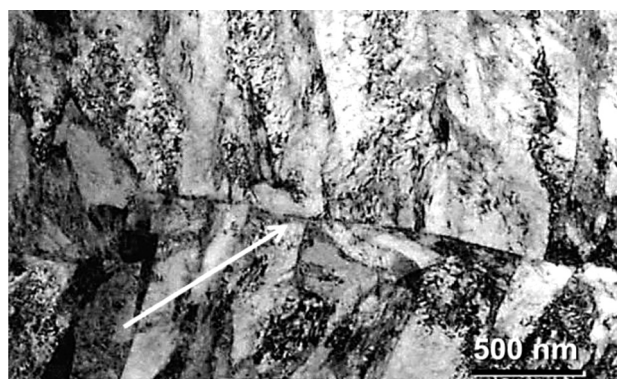


Figure 3: Prior austenite grain identified in martensitic matrix

Slika 3: Prvotna meja avstenitnih zrn, odkritih v martenzitni osnovi

In the AHSS-1 steel, the manganese level was 2.5 % and the silicon level was 2 %. The JMatPro software was used for calculating the approximate transformation temperatures. The calculated M_s and M_f temperatures in this steel were 218 °C and 88 °C, respectively. In order to map the effect of molybdenum on microstructural evolution and the shift in transformation temperatures in the AHSS-2 steel, its content was increased to 0.16 %. This increase in molybdenum content, however, has not altered the M_s and M_f temperatures in any substantial way. The M_s temperature was 214 °C and the M_f was 83 °C. In AHSS-3, the nickel level was set at 0.5 %, to achieve the desired hardenability and to depress the martensitic transformation temperatures. The M_s and M_f temperatures were 209 °C and 78 °C, respectively. In the AHSS-4 experimental steel, the molybdenum content was increased along with the nickel content. The combination of these elements led to the lowest transformation temperatures: $M_s = 204$ °C and $M_f = 73$ °C.

Table 1: Chemical compositions of experimental steels AHSS-1-4, in weight percents (w/%)

Tabela 1: Kemijska sestava eksperimentalnih jekel AHSS-1-4, v utežnih odstotkih (w/%)

	C	Mn	Si	Cr	Ni	Mo
AHSS-1	0.43	2.5	2.03	1.33	0.07	0.03
AHSS-2	0.428	2.48	2.03	1.46	0.08	0.16
AHSS-3	0.419	2.45	2.09	1.34	0.56	0.04
AHSS-4	0.426	2.46	1.99	1.33	0.56	0.15

2.1 Application of Q&P process to heat treatment of closed-die forgings

First, a heat treatment schedule for the forged parts has been developed. The development involved testing of various austenitising temperatures (T_A), two different quenching temperatures (QT), and various carbon partitioning temperatures (PT), using small specimens in a thermomechanical simulator MTS 810 (Material Test System). **Table 2** lists the parameters of the physical simulation, the resulting elongation values A_{5mm} and the fractions of retained austenite (RA) in the matrix.

Based on the results of this modelling, two experimental steels were chosen: AHSS-2 and AHSS-3. To verify the process, two complex-shaped closed-die forgings were made of these steels (Figure 4) by three forging steps. Two different bar dimensions were used for the forging process, with diameters of 45 mm, 31 mm and length of 160 mm, 180 mm. The forging was done at an automotive industry forging factory. These forgings were then heat-treated and their microstructures and mechanical properties evaluated using small flat specimens for tensile test machined from the forged parts with dimensions of 5 mm reduced section and a cross section 2 mm × 1.2 mm.

Table 2: Processing parameters of closed-die forgings in the physical simulation

Tabela 2: Parametri predelave odkovkov pri fizikalni simulaciji

$T_A(^{\circ}\text{C})/$ t_A (s)	Cooling rate ($^{\circ}\text{C}/\text{s}$)	QT ($^{\circ}\text{C}$)	PT ($^{\circ}\text{C}$) $/t_{PT}$ (s)	$A_{5\text{mm}}$ (%)	RA (%)
850/300	1	150	200/600	15	18
850/100	1	150	200/600	10	10
850/100	1	100	150/900	15	14
850/100	16	125	175/600	6	9
850/100	16	150	200/600	8	11
850/100	16	100	150/600	4	8

3 RESULTS AND DISCUSSION

The best results of the physical simulation were obtained with the cooling rate of 1 $^{\circ}\text{C}/\text{s}$. The ultimate



Figure 4: Demonstration products: AHSS steels forgings heat-treated using the Q&P process

Slika 4: Demonstracijski proizvodi: odkovki iz AHSS jekla, toplotno obdelani z uporabo Q&P postopka

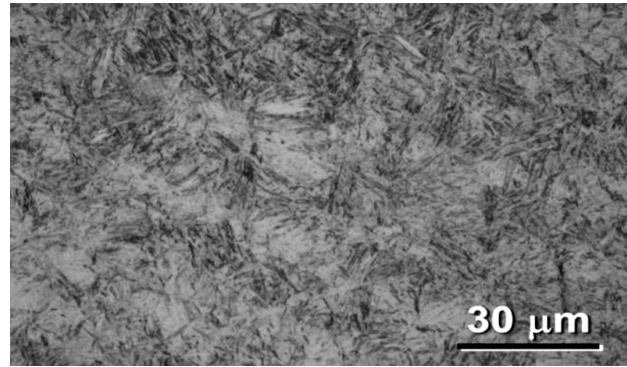


Figure 5: Light micrograph of martensitic structure with a small proportion of bainite. The processing sequence involved quenching in an oil bath at a temperature of 150 $^{\circ}\text{C}$ and austenite stabilisation in a furnace at 200 $^{\circ}\text{C}$

Slika 5: Svetlobni posnetek martenzitne strukture z majhnim deležem bainita. Sekvenca obdelave je vključevala kaljenje v oljni kopeli pri temperaturi 150 $^{\circ}\text{C}$ in stabilizacijo avstenita v peči na 200 $^{\circ}\text{C}$

strength was in the range of 2000–2400 MPa; the elongation was 15 % which corresponds to the higher volume fraction of retained austenite in the martensitic matrix, up to 18 % by volume.

Based on these findings, a low cooling rate has been recommended for processing the forgings. Heating to the austenite region was carried out in a furnace; the temperature was approx. 850 $^{\circ}\text{C}$. Subsequent quenching in hot oil finished at 150 $^{\circ}\text{C}$. Austenite was stabilised at 200 $^{\circ}\text{C}$, thanks to the carbon which migrates from the super-saturated martensite to austenite. After the forgings heat treatment, the microstructure was examined and mechanical tests were carried out. Electron microscopy revealed the presence of a martensitic microstructure with a small amount of bainite (Figures 5 and 6). Quenching with hot oil led to an ultimate strength of up to 2300 MPa and an elongation of approximately 12 %. The retained austenite fraction in the martensitic matrix was 15 %.

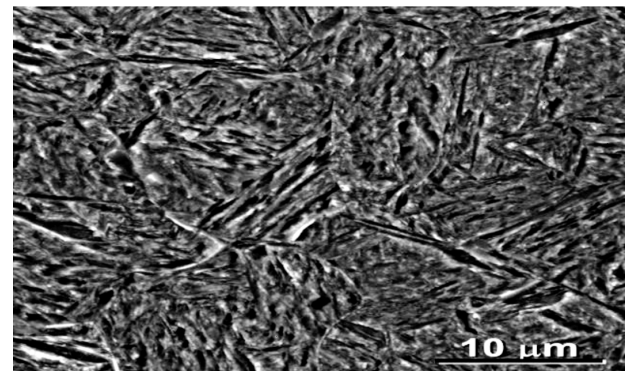


Figure 6: Scanning electron micrograph of a martensitic structure with a small proportion of bainite. The processing sequence involved quenching in an oil bath at a temperature of 150 $^{\circ}\text{C}$ and austenite stabilisation in a furnace at 200 $^{\circ}\text{C}$.

Slika 6: SEM-posnetek martenzitne strukture z majhnim deležem bainita. Sekvenca obdelave je vključevala kaljenje v oljni kopeli pri temperaturi 150 $^{\circ}\text{C}$ in stabilizacijo avstenita v peči na 200 $^{\circ}\text{C}$.

4 CONCLUSION

Heat treatment of forgings made of newly-developed experimental steels led to martensitic microstructures with a fraction of stabilised retained austenite. The heat-treating sequence was based on the quenching and partitioning process (Q&P).

First, physical simulation was carried out on specimens. The findings were then translated into the processing of real-life demonstration forgings. The physical simulation led to strengths of up to 2300 MPa and A_{5mm} elongation levels of approximately 12 %. As the amount, morphology and distribution of retained austenite have decisive impact on the resulting mechanical properties, an X-ray diffraction examination has been conducted. The retained austenite fraction was up to 15 %.

After the findings and parameters were translated into a real-life process, a simple heat treatment of actual forgings led to equivalent values of mechanical properties. The processing was carried out with hot quenching in oil to 150 °C and a furnace at a partitioning temperature of 200 °C.

The results of both physical simulation and real-life processing open new opportunities for closed-die forging. The key tasks for the future involve an optimisation of the cooling rate, a correct choice of cooling media and, where relevant, their unconventional application. High ultimate and fatigue strengths will permit the designs of forged parts to be altered towards thinner walls and more complex shapes. As a result, the utilization of material will improve and the weight of forgings will decrease, while the desired specifications of the product will still be met.

Acknowledgments

This paper includes results created within the projects SGS-2014-022 New Martensitic Structures - Process Parameters and Properties and CZ.1.05/2.1.00/03.0093 Regional Technological Institute. The projects are subsidised by the Ministry of Education, Youth and Sports from resources of the state budget of the Czech Republic and European Regional Development Fund.

5 REFERENCES

- ¹ H. K. D. H. Bhadeshia, S. R. Honeycombe, The Bainite Reaction, In Steels: Microstructure and Properties, 3rd ed., Butterworth-Heinemann, Oxford 2006, 129–154
- ² X. Y. Long, F. C. Zhang, J. Kang, Low-temperature bainite in low-carbon steel, *Materials and Science Engineering*, 594 (2014), 344–351, doi:10.1016/j.msea.2013.11.089
- ³ F. G. Caballero, H. K. D. H. Bhadeshia, Very strong bainite, *Current Opinion in Solid state and Materials Science*, 8 (2004) 3–4, 251–257, doi:10.1016/j.cossms.2004.09.005
- ⁴ B. Mašek, H. Jirková, D. Hauserová, L. Kučerová, D. Klauberová, The Effect of Mn and Si on the Properties of Advanced High Strength Steels Processed by Quenching and Partitioning, *Materials Science Forum*, 654–656 (2010), 94–97, doi:10.4028/www.scientific.net/MSF.654-656.94
- ⁵ H. Jirková, L. Kučerová, B. Mašek, Effect of Quenching and Partitioning Temperatures in the Q-P Process on the Properties of AHSS with Various Amounts of Manganese and Silicon, *Materials Science Forum*, 706–709 (2012), 2734–2739, doi:10.4028/www.scientific.net/MSF.706-709.2734
- ⁶ H. Jirková, B. Mašek, M. Wagner, D. Langmajerová, M. Tremel, D. Kiener, Influence of metastable retained austenite on macro and micromechanical properties of steel processed by the Q-P process, *Journal of Alloys and Compounds*, 615 (2014), 163–168, doi:10.1016/j.jallcom.2013.12.028

HELIUM ATOM SCATTERING – A VERSATILE TECHNIQUE IN STUDYING NANOSTRUCTURES

SIPANJE ATOMOV HELIJA – VSESTRANSKA TEHNIKA ZA ŠTUDIJE NANOSTRUKTUR

Gregor Bavdek¹, Dean Cvetko²

¹Univerza v Ljubljani, Pedagoška fakulteta, Kardeljeva ploščad 16, 1000 Ljubljana, Slovenija

²Univerza v Ljubljani, Fakulteta za matematiko in fiziko, Oddelek za fiziko, Jadranska ulica 19, 1000 Ljubljana, Slovenija
gregor.bavdek@pef.uni-lj.si

Prejem rokopisa – received: 2015-03-30; sprejem za objavo – accepted for publication: 2015-07-28

doi:10.17222/mit2015.069

In this paper we present helium atom scattering – a non-destructive technique used to study the surface structure and lattice dynamics (phonons) of clean and adsorbate-covered surfaces. We review the fundamentals of elastic and inelastic helium scattering theory and describe the basic components of the He scattering apparatus as well as its operation. We then demonstrate the use of the technique in three areas of surface analysis: clean surface structure determination of Ge(001) surface, study of overlayer lattice dynamics in Pb/Ge(001) thin film, and morphology/structure examination of organic overlayers in pentacene/Au(110).

Keywords: helium atom scattering, thermal atom diffraction, surface structure, thin films, nanostructures

Članek predstavlja sipanje atomov helija – nedestruktivno tehniko, ki se uporablja pri študiju strukture in mrežne dinamike (fononov) na čistih in z adsorbatom prekritih površinah. V članku so obravnavane osnove teorije elastičnega in neelastičnega sipanja atomov helija in opisani osnovni sestavni deli naprave za sipanje atomov helija kot tudi njihovo delovanje. V nadaljevanju sledi prikaz uporabe predstavljene tehnike na treh področjih analize površin: ugotavljanje strukture čiste površine Ge(001), študij mrežne dinamike v tankem nanosu Pb/Ge(001) in raziskava morfologije/strukture v organskih nanosih pentacena/Au(110).

Ključne besede: sipanje atomov helija, uklon termičnih atomov, struktura površin, tanke plasti, nanostrukture

1 UVOD

Prvi poskusi s sipanjem termičnih atomov helija segajo v pozna dvajseta leta preteklega stoletja, vendar pa so prve uporabne meritve s to metodo postale možne šele z uporabo mikronskih šob, ki so jih razvili v sedemdesetih letih. Te so zagotavljale intenziven in visoko monokromatski curek atomov ali molekul, ki je po sipanju na kristalnih površinah ustvaril oster uklonski vzorec, v katerem se je odražala struktura površine.

Plini, katerih atomi ali molekule se najpogosteje uporabljajo za sipanje so: He, Ne in H₂. Glede na njihovo maso jim lahko pripišemo odgovarjajočo De Brogliejevo valovno dolžino, ki pa je odvisna še od kinetične energije delcev.

Molekule H₂ zaradi svojih vibracijskih in rotacijskih prostostnih stopenj niso najbolj posrečena izbira za študij površin, omogočajo pa študij podrobnosti interakcijskega potenciala s površinami in spremljajoče interne molekulske ekscitacije. Dodatna težava vodika je tudi njegova relativno visoka reaktivnost, zaradi katere lahko na površini pride bodisi do kemijske reakcije bodisi do adsorpcije in vezave molekule.

Z vidika reaktivnosti je omejitev na zgolj žlahtne pline dokaj logična. Kljub temu izbira plina z visoko atomsko maso zaplete sipalne poskuse, saj ob trku atomov s površino pride do večfononskih površinskih

vzbujenih stanj, zaradi katerih je analiza mrežne dinamike močno otežena. Neobvladljivo postane tudi število vibracijskih nivojev v prečno izpovprečeni potencialni jami, ki se pojavi ob interakciji molekula–površina, in število preostalih sipalnih kanalov.

Glede na vse naštetе težave z molekulami in težjimi žlahtnimi plini se zdi helij najobetavnejši kandidat za poskuse s sipanjem. Curek helijevega atomov ima tako pri sobni temperaturi valovno dolžino okoli desetinke nanometra, kar je primerljivo z medatomske razdaljami trdnih površin in omogoča interferenčne poskuse. Obenem je kinetična energija curka termičnih He-atomov nekaj deset meV, kar sovпада z energijskim območjem tipičnih fononskih nihanj trdnih površin. Z neelastičnim sipanjem He-atomov zato lahko otipamo kolektivna nihanja akustične in optične veje preko več Brillouinovih con kristalne površine, česar ne moremo doseči z nobeno drugo eksperimentalno tehniko.

Zaradi svoje nizke energije je curek nevtralnih termičnih He-atomov povsem nedestruktiven, saj na površini prodre le v območje nizke gostote elektronskega oblaka, tipično nekaj desetink nm nad ravnino najbolj zunanjih atomov površine. S tem je sipanje termičnih He-atomov primerno tudi za študij mehkih organskih nanosov, ki so zelo občutljivi na druge tehnike otipanja površin, kot so sipanje elektronov in rentgenskih žarkov.

Zaradi izjemno velikega sipalnega preseka za nepravilnosti in napake na kristalnih površinah je sipanje He-atomov po drugi strani močno odvisno od urejenosti struktur na površinah. Omogoča neposredno opazovanje razvoja neurejenih struktur, ki se na primer pojavijo med nanašanjem organskih in anorganskih materialov na kristalne podlage, in njihovo termično urejevanje. Z direktnim merjenjem površinske reflektivnosti ali uklona He-atomov je tako možno *in-situ* opazovati in nadzorovati rast in (samo)urejevanje organskih in anorganskih plasti. Z metodo lahko v realnem času sledimo časovnemu razvoju urejevanja in morebitni vzpostavitvi reda dolgega dosega, kar je ključnega pomena pri razumevanju procesov medmolekularskih interakcij ter interakcij s podlago, ki določajo samousklajeno formiranje nanoarhitektur in pri snovanju visoko zmogljivih komponent za razvoj elektronskih in katalitskih elementov.

2 METODA SIPANJA He-ATOMOV

Tehniki uklona He atomov (angl. Helium diffraction, HeD) in spektroskopija izgubljene energije He atomov (angl. Helium energy loss spectroscopy, HeELS) sta konkurenčni in komplementarni uveljavljenima tehnikama uklona nizkoenergijskih elektronov (angl. Low energy electron diffraction, LEED) in spektroskopije izgubljene energije elektronov (angl. Electron energy loss spectroscopy, EELS). Glavna prednost He-atomov je njihova nevtralnost in zaradi velike mase v primerjavi z elektroni relativno majhna hitrost (in torej energija) za atomske valovne dolžine. Zaradi teh enkratnih lastnosti je uklon atomov He povsem nedestruktivna tehnika. Za razliko od nje prihaja pri uporabi tehnik LEED, RHEED in uklona RTG žarkov ob nastanku obilja sekundarnih elektronov do znatnih poškodb podlage ali tankih plasti, še posebej organskih.

Tipična kinetična energija He-atomov z valovno dolžino medatomskih razdalj v kristalu leži v območju nekaj deset milielektronvoltov, zaradi česar se termični He-atomji sipajo na skrajno zunanji gostoti elektronov (~ 1 elektron/nm³), tehnika pa je izključno površinsko občutljiva (Slika 1).

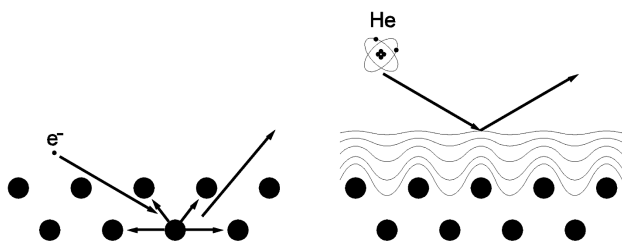


Figure 1: Electrons penetrate the material, undergoing multiple scattering and bulk diffraction. He-atoms scatter on the outer valence electron density.

Slika 1: Elektroni prodrejo globoko v snov, pri čemer se večkratno sipajo in uklanjajo v globini kristala. He-atomji pa se sipajo na zunanji gostoti valenčnih elektronov.

Sipanje He-atomov je močno občutljivo na površinske nepravilnosti, torej na odstopanja od translacijske periodičnosti zaradi adatomov, vrzeli, točkastih in linearnih nepravilnosti ipd., ki povzročajo difuzno sipanje in s tem zmanjšanje uklonskega signala. Ravno po zaslugi velikega sipalnega preseka za neperiodične površinske in adsorbirane strukture pa je sipanja He po drugi strani zelo uporabno orodje za sledenje nanešenega materiala pri adsorpciji iz plinaste faze, kot je pokazano v nadaljevanju. Dejansko je gostota valenčnih elektronov zaradi nepravilnosti na površini, ki popačijo interakcijski potencial za koherentno sipanje He-atomov prizadeta na razdaljah, ki daleč presegajo velikost same nepravilnosti. Tipični sipalni presek za difuzno sipanje helija na dodatnem atomu ali vrzeli, na sicer idealni kristalni površini, lahko presega nekaj nm², medtem ko je geometrijski presek dodatnega atoma-vrzeli le nekaj stotin nm².¹

Z vidika kinematike je sipanje He-atomov na površinah zelo podobno sipanju nevtronov v kristalih, ki so prav tako nevtralni in imajo primerljivo maso. Najpogostejša geometrija postavitve izvira helija, vzorca in detektorja, je prikazana na **Sliki 2**.² Vzorec je običajno pričvrščen na manipulator z različnim številom prostostnih stopenj, kar omogoča poravnavo normale na površino vzorca s sipalno ravnino. Vpadni kot θ in sipalni kot θ' sta povezana z enačbo $\theta + \theta' = \theta_{\text{tot}}$. V nekaterih napravah je θ_{tot} fiksni (tipično od 90° do 120°).

Kinematiko elastičnega sipanja opišemo tako, da najprej zapišemo vpadni (\vec{k}) in sipani (\vec{k}') valovni vektor:¹

$$\vec{k} = (\vec{K}, k_z), \quad \vec{k}' = (\vec{K}', k_z')$$

kjer K in k_z ponazarjata gibalno količino vzporedno s površino oziroma pravokotno nanjo. Vpadni in sipani vektor povezujeta enačbi za ohranitev energije in paralelne komponente gibalne količine:

$$k'^2 = k^2, \quad \vec{K}' = \vec{K} + \vec{G}$$

kjer je \vec{G} vektor recipročne mreže na površini. Sprememba valovnega vektorja v ravnini površine je torej

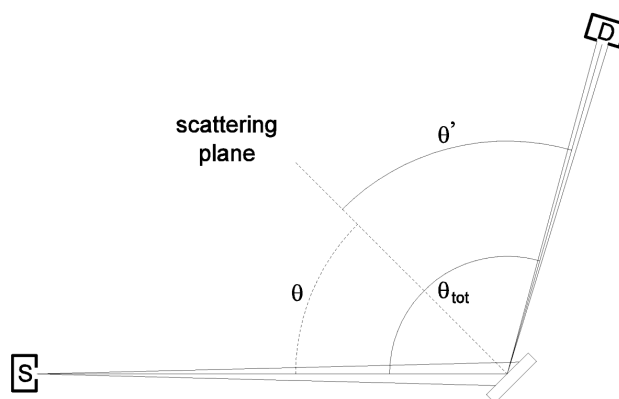


Figure 2: Schematic experimental arrangement. Here S denotes beam source and D detector. The incident angle is θ and the scattering angle θ' , while θ_{tot} denotes their sum.

Slika 2: Shema eksperimentalne postavitve. S na sliki predstavlja vir in D detektor. Vpadni kot je θ , sipalni kot θ' , θ_{tot} pa njuna vsota.

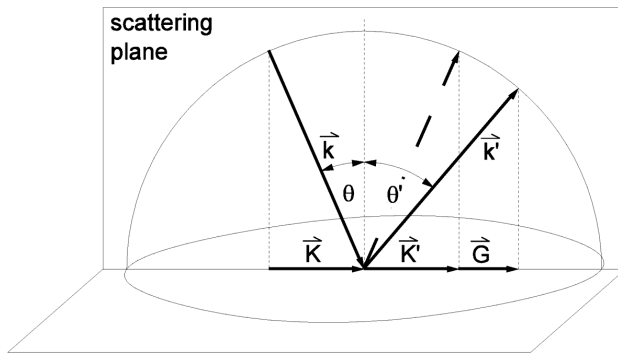


Figure 3: The scattering geometry in the case of in-plane elastic scattering. The incident beam scatters into the specular peak ($G = 0$, dashed arrow) and a series of diffracted peaks with $G \neq 0$ (continuous arrow). The Ewald sphere construction is used.

Slika 3: Siplna geometrija za elastično sipanje v ravnini. Vpadni žarek se sipa v zrcalni vrh ($G = 0$, črtkana puščica) in v vrsto uklonjenih vrhov z $G \neq 0$ (neprekinjena puščica). Pri konstrukciji je uporabljen model Ewaldove sfere.

kvantizirana po modulu vektorjev recipročne mreže, medtem ko se pravokotna komponenta ne ohranja. Poleg tega se pri elastičnem sipanju He-atomov ohranja tudi skupna kinetična energija:

$$\Delta \vec{K} = \vec{K}' - \vec{K} = \vec{G}, \quad \Delta E = \frac{\hbar^2 k'^2}{2m} - \frac{\hbar^2 k^2}{2m} = 0$$

Mehanizem elastičnega sipanja grafično ponazorimo z modelom dvodimenzionalne Ewaldove sfere (**Slika 3**).

Pri neelastičnem sipanju vključuje vzporedno s površino izmenjana gibalna količina tudi kreacijo/anihilacijo fonona z gibalno količino P in energijo $\hbar\omega$:

$$\Delta \vec{K} = \vec{K}' - \vec{K} = \vec{G} \pm \vec{P}, \quad \Delta E = \frac{\hbar^2 k'^2}{2m} - \frac{\hbar^2 k^2}{2m} = \pm \hbar\omega$$

Za opis neelastičnega dogodka, ki vključuje izmenjavo površinskih fononov, moramo pri eksperimentu dodatno pomeriti tudi porazdelitev sipanih atomov po kinetični energiji. Začetno hitrost atomov in s tem valovni vektor k določa temperatura zadrževalne komore s helijem pred ekspanzijo, hitrost elastično in neelastično sipanih atomov pa lahko neposredno določimo z merjenjem časa preleta (angl. time of flight, TOF).

2.1 Interakcija He-atoma s površino

Interakcijo helija s površino sestavlja odbojni potencial z zelo kratkim in privlačni potencial z dolgim dosegom. Odbojni potencial je skoraj izključno posledica vrhnje atomske plasti, kjer na He-atome deluje močna odbojna sila zaradi prekrivanja elektronskih valovnih funkcij na površini z zapolnjenimi He-orbitalami. Privlačni potencial pa gre pretežno na račun disperzijskih sil.

Interakcijo atom–površina zapišemo povsem splošno tako, da celotni potencial razstavimo na privlačni in odbojni del. Vzemimo, da sta smeri x in y v ravnini površine, smer z pa pravokotna nanjo. Potem lahko vektor \vec{r} od izbranega izhodišča do vsake točke na površini zapišemo

kot $\vec{r} = (\vec{R}, z)$. Za odbojno interakcijo, ki je posledica prekrivanja atomskih orbital, je dober približek, če vzamemo, da je potencial kar sorazmeren z elektronsko gostoto (ρ):

$$V_{\text{odb}} \propto \rho(\vec{R}, z) \propto e^{-\beta z} \quad (1)$$

Glavni prispevek privlačnih disperzijskih sil pri razvoju v vrsto pa je:

$$V_{\text{privl}} = -\frac{C_3}{z^3} \quad (2)$$

kjer je C_3 dan z Lifshitzovo formulo:²

$$C_3 = -\frac{\hbar}{4\pi} \int_0^\infty \frac{\varepsilon(i\omega) - 1}{\varepsilon(i\omega) + 1} \alpha_{\text{He}}(i\omega) d\omega \quad (3)$$

Pri tem je ε dielektrična funkcija snovi na površini in α_{He} atomska polarizabilnost helija. V zapisani formuli ponazarja ulomek pod integralom efektivno senčenje polja dipola pri frekvenci ω in predstavlja interakcijo trenutnega dipola helija z njegovo zrcalno sliko na površini. Enačbo (2) oziroma potenčno odvisnost $1/z^3$ je moč izpeljati z razvojem atomskega parskega potenciala med helijem in atomi v trdni površini. Prispevke parskega potenciala nato seštejemo po semineskončnem prostoru vrhnjih plasti kristala.²

Skupni potencial lahko končno napišemo v obliki:

$$V = V_{\text{odb}} + V_{\text{privl}} \propto \rho(\vec{R}, z) - \frac{C_3}{z^3} \quad (4)$$

2.2 Model toge stene

V preprostem modelu nagubane toge stene (angl. corrugated hard wall, CHW) upoštevamo le odbojni potencial, šibki privlačni potencial pa zanemarimo. V bližini površine je namreč privlačni potencial – drugi člen v Enačbi (4) – mnogo šibkejši od odbojnega, daleč od nje pa zanemarljivo majhen. Z omenjenim približkom enostavno pridemo do kvantitativne analize uklonskih intenzitet helija na površinah z majhno nagubanostjo (angl. corrugation), približek pa odpove pri močno nagubanih površinah polprevodnikov in rekonstruiranih kovinskih površinah. Pri tem so malo nagubane površine tiste, pri katerih se relief spreminja dosti manj od velikosti osnovne celice, $\zeta_0 < a$.

Togo steno ponazorimo s potencialom oblike:

$$V(\vec{R}, z) = 0 \quad \text{za } z > \zeta(\vec{R})$$

$$\text{in} \quad V(\vec{R}, z) = \infty \quad \text{za } z \leq \zeta(\vec{R}) \quad (5)$$

Pri tem funkcija nagubanosti $\zeta(\vec{R})$ natančno opisuje dvodimenzionalno ploskev – relief klasičnih obračalnih točk, kjer pride do odboja atomov He. Če se omejimo le na najnižjo Fourierovo komponento, zapišemo nagubanost površine kot:

$$\zeta(\vec{R}) = \zeta_0 \left[\cos\left(\frac{2\pi x}{a_1}\right) + \cos\left(\frac{2\pi y}{a_2}\right) \right] \quad (6)$$

kjer sta a_1 in a_2 dimenziji površinske osnovne celice, $4\zeta_0$ pa amplituda nagubanosti površine.

Sipanje na togi steni obravnavamo semiklasično, s čimer privzamemo, da k sipalni amplitudi prispevajo vsi deli osnovne celice enako. To je možno takrat, kadar sta nagubanost površine in vpadni kot dovolj majhna, da je osnovna celica enakomerno osvetljena z žarkom He. Prispevek osnovne celice k obliki uklonskega vzorca opisuje oblikovni faktor (angl. form factor). Zapis spremembe valovnega vektorja za atom He pri sipanju je torej:

$$\vec{k}' - \vec{k} = \Delta \vec{k} = (\Delta \vec{K}, \Delta k_z(\Delta \vec{K}, \omega)) \quad (7)$$

Oblikovni faktor dobimo z integracijo delnih valov po celotni osnovni celici:

$$F_{\vec{G}} = \frac{1}{a_1 a_2} \int_{o.c.} e^{-i[\vec{G}\vec{R} + \Delta k_z \zeta(\vec{R})]} d\vec{R} \propto \propto J_{|m|}(\zeta_0 \Delta k_z) J_{|n|}(\zeta_0 \Delta k_z) \quad (8)$$

Pri tem sta $J_{|m|}$ in $J_{|n|}$ Besslovi funkciji reda $|m|$ in $|n|$, \vec{G} pa vektor recipročne mreže, ki ga zapišemo v obliki:

$$\vec{G} = \left(m \frac{2\pi}{a_1}, n \frac{2\pi}{a_2} \right) \quad (9)$$

V Enačbi (8) smo že upoštevali, da dobimo prispevek k oblikovnemu faktorju le, ko je $\Delta \vec{K} = \vec{G}$.

Oblikovni faktor odraža porazdelitev gostote naboja znotraj posamezne enotske celice in prispeva k skupni ovojnici, s katero so modulirani uklonski vrhovi zaradi strukturne periodičnosti površine. Ta ovojnica se imenuje površinska mavrica (angl. surface rainbow).^{3,4} Do modulacije intenzitete uklonskih vrhov pride zaradi končne velikosti sipajočih atomov in njihovega položaja znotraj enotske celice (torej oblikovnega faktorja). Iz omenjene modulacije lahko izluščimo informacije o korugaciji površine.

Če želimo upoštevati celotno površino, je potrebno sešteti prispevke vseh enotskih celic, ki sodelujejo pri sipanju. Pri seštevanju bomo upoštevali tudi mrežno dinamiko, pri kateri se atomi lahko gibajo okrog svoje ravnovesne lege. Z uporabo modela toge stene zapišemo trenutno obliko stene v dinamični sliki z enačbo:

$$\vec{r} = (\vec{R}, \zeta(\vec{R}) + u_z(t)) \quad (10)$$

kjer je $u_z(t)$ premik površinskega atoma v bližini \vec{R} v smeri pravokotno na površino. Sipalna amplituda je torej sorazmerna:

$$M \propto \int_A e^{-i\Delta \vec{k} \cdot \vec{r}(t)} d\vec{R} \propto \sum_{\vec{R}_j} e^{-i\Delta k_z u_z(\vec{R}_j, t)} e^{-i\Delta \vec{K} \cdot \vec{R}_j} F_{\vec{G}} \quad (11)$$

kjer \vec{R}_j teče po vseh površinskih enotskih celicah v "osvetljenem" območju A. Pri tem drugi eksponent v vsoti predstavlja strukturni faktor (angl. structure factor), $S(\Delta \vec{K})$. Če se omejimo zgolj na elastično sipanje se celotna vsota poenostavi v produkt strukturnega in oblikovnega faktorja:

$$M \propto \delta(\Delta \vec{K} - \vec{G}) F_{\vec{G}} \quad (12)$$

Oglejmo si nekoliko podrobneje še prvi eksponent v vsoti prejšnje enačbe. Ta s svojo časovno odvisnostjo predstavlja dinamični strukturni faktor⁵ – to je neelastični del, kjer pride med površino in He-atomom do izmenjave energije. Intenziteta sipanja je sorazmerna termodinamični pričakovani vrednosti:

$$I \propto \int_{-\infty}^{\infty} e^{i\omega t} \langle M(0)M^*(t) \rangle dt \propto \int_{-\infty}^{\infty} e^{i\omega t} \langle e^{-i\Delta k_z u_z(\vec{R}_j, 0)} e^{i\Delta k_z u_z(\vec{R}_j, t)} \rangle dt \quad (13)$$

V harmoničnem približku je lega atoma v vsakem trenutku linearna funkcija položajev in gibalnih količin vseh ostalih ionov v kristalu ob času 0. Tedaj velja enačba:

$$\langle e^A e^B \rangle = e^{1/2 \langle A^2 + 2AB + B^2 \rangle} \quad (14)$$

Potem je intenziteta sipanja sorazmerna:

$$I \propto \sum_{\vec{R}_j} e^{-1/2 \langle [\Delta k_z u_z(\vec{R}_j, 0)]^2 \rangle - 1/2 \langle [\Delta k_z u_z(\vec{R}_j, t)]^2 \rangle + \langle [\Delta k_z u_z(\vec{R}_j, 0)] [\Delta k_z u_z(\vec{R}_j, t)] \rangle} \quad (15)$$

Pri tem sta prva dva člena v eksponentu enaka in predstavljata Debye-Wallerjev koeficient:

$$\begin{aligned} \langle [\Delta k_z u_z(\vec{R}_j, 0)]^2 \rangle &= \langle [\Delta k_z u_z(\vec{R}_j, t)]^2 \rangle = \\ &= (\Delta k_z) \langle [u_z(\vec{R}_j)]^2 \rangle = 2W \end{aligned} \quad (16)$$

Ta opisuje atenuacijo sipanega signala na račun termičnih vibracij kristalne mreže. Ob naraščajoči temperaturi je namreč sipanje v neelastične kanale vse močnejše, zato se delež intenzitete sipanja v izbrani kanal zmanjšuje.

Tretji člen v eksponentu enačbe za intenziteto sipanja pa predstavlja sipalni dogodek, pri katerem lahko pride do kreacije ali anihilacije enega ali več fononov. Z razvojem eksponenta v Taylorjevo vrsto dobimo:

$$\begin{aligned} e^{\langle [\Delta k_z u_z(\vec{R}_j, 0)]^2 \rangle \langle [\Delta k_z u_z(\vec{R}_j, t)]^2 \rangle} &= \\ = \sum_{m=0}^{\infty} \frac{1}{m!} \left(\langle [\Delta k_z u_z(\vec{R}_j, 0)] [\Delta k_z u_z(\vec{R}_j, t)] \rangle \right)^m \end{aligned} \quad (17)$$

Pri tem m -ti člen v razvoju predstavlja proces, kjer je atom He pri sipanju na površini udeležen v kreacijo/anihilacijo m fononov. Ker je pri sipanju termičnih He-atomov verjetnost za večfononske procese zelo majhna, se omejimo na enofononski prispevek:

$$\begin{aligned} e^{\langle [\Delta k_z u_z(\vec{R}_j, 0)]^2 \rangle \langle [\Delta k_z u_z(\vec{R}_j, t)]^2 \rangle} &\approx \\ \approx \langle [\Delta k_z u_z(\vec{R}_j, 0)] [\Delta k_z u_z(\vec{R}_j, t)] \rangle \end{aligned} \quad (18)$$

Z integracijo po času dobimo, da je prispevek enofononskega procesa k sipalni intenziteti enak:

$$I \propto (\vec{\epsilon}_{k_0} \cdot \Delta \vec{k}_z)^2 \quad (19)$$

kjer je $\vec{\epsilon}_{kw}$ polarizacijski vektor mrežnega nihanja pri načinu ω_{kw} .⁶

Če povzamemo: uklonski vzorec je sestavljen iz maksimumov mrežne periodičnosti (strukturni faktor), moduliran z ovojnico "oblike" enotske celice (oblikovni faktor), oslavljen za faktor termičnih vibracij (Debye-Wallerjev faktor) in obogaten z neelastičnimi vrhovi kreacije ali anihilacije fononov:

$$I \propto |S(\Delta\vec{K})|^2 \left| F_G^- \right|^2 e^{-2W} (\vec{\epsilon}_{kw} \cdot \Delta\vec{k}_z)^2 \quad (20)$$

2.3 Resonančno ujetje atoma He

Opisani semiklasični model ni dober približek za močno nagubane površine, kot je na primer površina (110) z manjkajočo vrsto (angl. missing row) nekaterih plemenitih kovin (npr. Au, Pt, Rh, Ir). Ker nagubanost površine (t.j. amplituda vertikalnega premika iona) dosega vrednosti okrog 0,1 nm, pride do večkratnega sipanja, ki zahteva kvantnomehansko obravnavo.

Najprej rešimo Schrödingerjevo enačbo za vpadni atom He:

$$\left(-\frac{\hbar^2}{2M} \nabla^2 + V(r) - E \right) \psi(r) = 0$$

Potencial smo že prej zapisali v obliki Fourierove vrste, zato lahko v enaki obliki zapišemo tudi rešitev:

$$\psi_{\vec{k}}(r) = \sum_{\vec{G}'} e^{i(\vec{k} + \vec{G}')\vec{r}} \psi_{\vec{G}'}(z)$$

Ko nastavek za rešitev vstavimo v Schrödingerjevo enačbo, dobimo sistem sklopljenih diferencialnih enačb, ki jih rešimo za dane robne pogoje. Rešitev Schrödingerjeve enačbe opisuje sipanje (za $E > 0$) kot tudi vezana stanja (za $E < 0$). Kot samousklajene rešitve za $E > 0$ dobimo vrednosti $|\psi_{\vec{G}'}|^2$, ki nam predstavljajo intenzitete sipanih uklonskih vrhov $I_{\vec{G}'}$, te pa lahko primerjamo z eksperimentalnimi vrednostmi. Tako lahko modelsko natančno določimo strukturo površine.

Če površina ni premočno nagubana, lahko višje člene Fourierove vrste za potencial zanemarimo in privzamemo, da je za vezano stanje odgovoren le prvi člen, V_0 . Za določitev vezanih stanj ($E < 0$) v tem primeru zadošča enodimenzionalna Schrödingerjeva enačba, v kateri upoševamo ohranitev energije in gibalne količine:

$$\left[\frac{\hbar}{2M} \frac{d^2}{dz^2} + V_0(z) - \left(E - \frac{\hbar}{2M} |\vec{k} + \vec{G}|^2 \right) \right] \psi_{\vec{G}}(z) = 0$$

Če negativne energije vezanih stanj označimo z ϵ_m , se enačba prepíše v:

$$\left[\frac{\hbar}{2M} \frac{d^2}{dz^2} + V_0(z) - \epsilon_m \right] f_m(z) = 0$$

Lastne funkcije in lastne energije Schrödingerjeve enačbe za atom He v interakciji z manj valovito površino so torej:

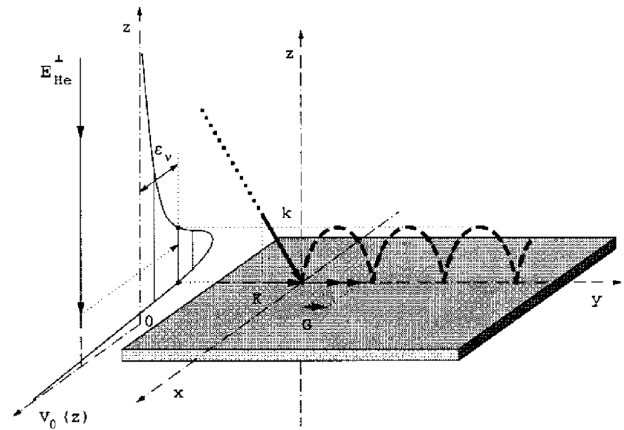


Figure 4: He atom, captured in one of the bound states of potential V_0
Slika 4: Resonančno ujetje helijevega atoma v eno izmed vezanih stanj potenciala V_0

$$\psi_{\vec{G}, \vec{k}_m}(\vec{R}) = f_m(z) e^{i(\vec{k} + \vec{G})\vec{r}} \quad \text{in} \quad E_{m\vec{G}} = \epsilon_m + \frac{\hbar^2}{2M} (\vec{K} + \vec{G})^2$$

Rešitve f_m ponazarjajo povsem prosto gibanje He-atoma po površini kristala. Vpadli atom se ujame v enega izmed lastnih stanj potenciala V_0 z lastno energijo ϵ_m . Komponenta gibalne količine v smeri pravokotno na površino se pri tem »prelije« v komponento, vzporedno s površino. Atom se v takšnem kvazistacionarnem stanju s hitrostjo, ki je večja od vpadne, nekaj časa giblje po površini, dokler je slednjič ne zapusti. Pojav se imenuje resonančno ujetje helijevega atoma ali selektivna adsorpcija (**Slika 4**). Z meritvijo teh procesov lahko precej natančno določimo vezana stanja ϵ_m in s tem obliko potenciala $V_0(z)$.

3 NAPRAVA ZA SIPANJE He-ATOMOV

Najpomembnejši del izvira monokromatskega curka He-atomov je mikronska šoba v kombinaciji z močnim črpalnim sistemom, ki omogoča, da se atomi helija adiabatsno razširijo v prostor z visokim vakuumom. Močan sistem črpanja⁷ zagotavlja, da je razmerje med tlakom v zadrževalni komori in okoliškimi pritiskom v vakuumski komori z žarkom velikostnega reda 10^7 . Žarek He-atomov, ki ga dobimo na tak način, odlikuje velika intenziteta, visoka enobarvnost in odlična prostorska koherenca. Žarek iz takšne šobe prekaša efuzijske izvire v vseh treh lastnostih za več redov velikosti. Odkritje mikronskih šob je za raziskave površin podobnega pomena kot odkritje laserja za elektrooptiko.

Atomi se iz zadrževalne komore pred šobo, kjer ima plin tlak p_0 , adiabatsno razširijo v vakuum, kjer je tlak p_1 . Na poti se po ekspanziji gostota curka močno zmanjša, trki med atomi pa postanejo zelo redki. S tem Bernoullijev tok termičnih atomov preide v molekularni tok. Curek pri ekspanziji v vakuum v smislu energijske razpršenosti tako rekoč "zamrzne". Hitrost zvoka oziroma udarnih valov je mnogo manjša od hitrosti atomov v curku. Pri velikem pretoku skozi šobo govorimo o masnem pretoku v smeri curka, pri čemer se entalpija pretvori v kinetično energijo atomov, kar pri ekspanziji skozi šobo

povzroči "zamrznitev" plina oz. močno zmanjšanje razpršenosti atomov po hitrosti.

Pri širjenju plina skozi šobo v vakuum se spremenita tako tlak kot volumen plina. Primer obravnavamo kot Lavalovo šobo, pri kateri se plinu entropija med gibanjem vzdolž šobe ne spreminja. Gibanje plina v nepredolgi šobi, ki je na koncu ustrezno razširjena, je v strženu dejansko adiabatno. Če se torej entropija ohranja, preostane v diferencialu specifične entalpije:

$$dh = Tds + \frac{dp}{\rho}$$

le drugi člen, iz česar sledi:

$$h = \int \frac{dp}{\rho}$$

Če upoštevamo, da je specifična toplota plina v danem območju konstantna, lahko h zapišemo še enostavneje:

$$h = c_p T + \text{konst}$$

Tega vstavimo v Bernoullijevo enačbo in dobimo:

$$h + \frac{v^2}{2} = c_p T + \frac{v^2}{2} = \text{konst}$$

Iz tega sledi, da je:

$$v^2 = c_p (T_0 - T)$$

Pri raztezanju v vakuum se plin močno ohladi, $T < T_0$, namesto termičnega gibanja atomov pa dobimo molekularni tok, v katerem je asimptotična hitrost atomov enaka:

$$v = \sqrt{c_p T_0}$$

Ta je torej odvisna le od temperature plina v zadrževalni komori pred šobo. Asimptotična hitrost je dosežena kmalu za šobo, medatomskih trkov je zanemarljivo malo. Vzdolž curka se posameznim atomom zato ne spreminja ne smer ne hitrost. Ker je temperatura plina po ekspanziji v območju nekaj mK, je širina porazdelitve atomov po hitrosti zelo majhna. Energija nadzvočnih He-atomov po nadzvočni ekspanziji je tako enaka:

$$E_{\text{kin}} = \frac{1}{2}mv^2 = \frac{1}{2}mc_p T_0 = \frac{5}{2}k_B T_0$$

V raziskovalni komori, ki jo uporabljamo v laboratoriju IOM-CNR v Trstu, lahko pritisk helija v zadrževalni komori nastavljammo med 10 bar in 100 bar, kar določi pretok in monokromatičnost He-žarka. Energijo žarka lahko nastavljammo v območju nekaj deset meV tako, da vzdržujemo zadrževalno komoro pri izbrani temperaturi; če jo hladimo s tekočim dušikom, imajo atomi v žarku $E_{\text{kin}} = 19$ meV, $v = 960$ m/s, $k = 60,0$ nm⁻¹ in $\lambda = 0,105$ nm. Če zadrževalno komoro pustimo pri sobni temperaturi, so lastnosti atomov v žarku naslednje: $E_{\text{kin}} = 62$ meV, $v = 1700$ m/s, $k = 109$ nm⁻¹, $\lambda = 0,058$ nm. Zadrževalno komoro lahko z vgrajenim grelcem tudi dodatno segrevamo, s čimer je možno temperaturo med omenjenima točkama zvezno nastavljanje ali pa jo celo

dvigniti nad sobno temperaturo. Izmerjena širna vrha na polovični višini (angl. Full Width at Half Maximum, FWHM) v porazdelitvi po hitrosti $\Delta v/v$ je v območju med $1 \cdot 10^{-2}$ in $1,5 \cdot 10^{-2}$. Tako ostro distribucijo lahko dosežemo z razmerjem pritiskov $p_0/p_1 \sim 10^{10}$, kar je mogoče z uporabo turbočrpalk z zelo veliko hitrostjo črpanja (~ 2000 L/s).

Na poti žarka je približno 25 mm za šobo nameščen kolimator v obliki prisekanega stožca (angl. skimmer) s premerom odprtine 0,5 mm. Ta "olupi" curek vseh atomov, ki pri ekspanziji skozi šobo v vakuum preveč divergirajo. S svojo obliko preprečuje, da bi se divergentni atomi odbili nazaj v sredino curka. Kolimator definira tudi kotno divergenco žarka, ki je v tem primeru enaka $8 \cdot 10^{-6}$ sr. Kolimatorju sledi sekalec (angl. chopper), ki zvezni He-žarek naseka na kratke gruče. Te potrebujemo za meritve časa preleta pri opazovanju neelastičnih procesov na površini. Sekalec je mogoče vstaviti ali izvleči, tako da meritve lahko potekajo v kontinuiranem ali pulznem načinu – razmerje intenzitet med enim in drugim načinom (angl. duty cycle) je 1:200. Sekalcu na prehodu v glavno merilno komoro z vzorcem sledi še en kolimator, tako da je velikost s He "osvetljenega" področja na vzorcu približno 0,7 mm. Sipani žarek potuje skozi nadaljnja dva kolimatorja v detekcijski del naprave. V njem se nevtralni He-atomski na poti skozi prečni žarek elektronov najprej ionizirajo. Učinkovitost ionizacije je kljub izbiri energije elektronov, pri kateri je verjetnost za ionizacijo največja (~ 100 eV), sorazmerno majhna: $\sim 10^{-5}$. Ioni nato vstopijo kvadrupolni masni spektrometer, ki prepusti le atome z izbranim razmerjem med maso in nabojem – v našem primeru $m/e_0 = 4/e_0$. Nazadnje prepuščene ione pospešimo do fotopomnoževalke, ki posamezne ione detektira v obliki sunkov naboja. Te zbere večkanalni časovni števec in jih prikaže ter shrani v obliki histograma v odvisnosti od časa preleta.

Vzorec (kristalinična podlaga z dobro definirano površino) je pričvrščen na manipulator s tremi rotacijskimi prostostnimi stopnjami (**Slika 5**). Manipulator omogoča tako segrevanje vzorca do ~ 1000 °C kot tudi hlajenje do temperature tekočega dušika ali helija.

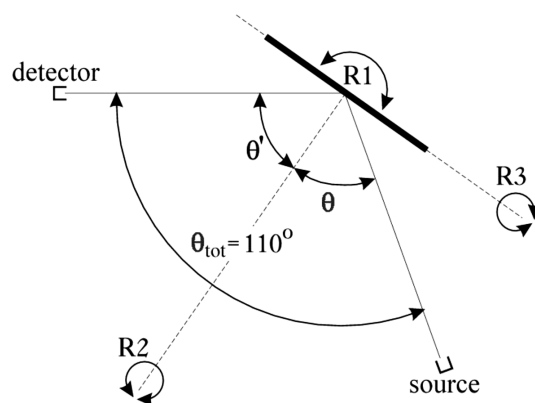


Figure 5: The three rotational degrees of freedom of the manipulator: R1, R2 and R3

Slika 5: Tri rotacijske prostostne stopnje manipulatorja: R1, R2 in R3

Zmogljivost opisane eksperimentalne komore za sipanje He-atomov dobimo z merjenjem širine uklonskih vrhov na idealno urejeni površini in jo imenujemo instrumentalna širina (angl. transfer width).⁷ Je merilo sposobnosti naprave za detekcijo površinskih struktur, koreliranih na dolge razdalje. Ključno vlogo pri tem ima prav monokromatičnost žarka – od nje je odvisna tako kvaliteta uklonskih meritev, s katerimi določamo strukturo površine, kot tudi neelastični eksperimenti pri določanju mrežne dinamike. Pri opisani napravi je za žarek helija, ohlajen s tekočim dušikom ($E_{\text{kin}} = 19$ meV), instrumentalna širina enaka $0,135^\circ$. To pomeni, da bi na površini lahko zaznali le prostorsko korelacijo struktur na razdaljah, manjših od 45 nm. Ker pa je v praksi mogoče izmeriti že razširitev vrhov od $0,135^\circ$ do $0,145^\circ$ ali celo manj, lahko učinkovito opazujemo strukturne korelacije do ~ 120 nm.

4 UPORABA METODE SIPANJA ATOMOV He V KONKRETNIH PRIMERIH

4.1 Struktura površine Ge(111)

Germanij kristalizira v diamantni strukturi z mrežno konstanto $a = 0,566$ nm. Struktura je ekvivalentna dvema ploskovno centriranim mrežama, ki sta med seboj zamaknjeni vzdolž diagonale enotske celice za četrtno njene dolžine. Osnovna celica na površini (001), katere velikost je $a_s = a/\sqrt{2} = 0,400$ nm, je prikazana na **Sliki 6a**. Ekvivalentne vrste, ki sodelujejo pri nastanku uklonskega vzorca, so skupaj s površinsko osnovno celico prikazane na **Sliki 6b**. V ravnovesju struktura površine Ge(001) ni preprosto enaka strukturi površine odrezanega kristala; ker je vsak atom Ge na površini izgubil po dva najbližja sosedra, iz njega štrli po dve reaktivni prosti vezi. Prosta energija površine se minimizira s prerazporeditvijo atomov (rekonstrukcijo) v novo konfiguracijo, ki zmanjša število prostih vezi na posamezen atom, kjer se sosednji atomi Ge premaknejo in povežejo v dimere. Translacijska perioda v smeri [1-10] je podvojena, kar pripelje do nižje translacijske simetrije (2×1). To strukturo ima površina Ge(001) pri sobni temperaturi.

Posamičen dimer ni simetričen, ampak je nagnjen in lahko zavzame dve ekvivalentni konfiguraciji (gor/dol), kar opišemo z lokalnim kvazispinom. Sosednji dimeri se pri nizki temperaturi ($T < 220$ K) nadalje prerazporedijo v "antiferomagnetno" fazo kvazispinov, kar dodatno zniža simetrijo osnovne celice v $c(2 \times 4)$. To je osnovno stanje površine Ge(001) pri nizki temperaturi.

Strukturo površine Ge(001) pri nizki temperaturi smo opazovali s sipanjem He-atomov.⁸ Uklonski vzorec je bil zajet na očiščeni in dobro urejeni površini, ohlajeni na 120 K, vzdolž simetrijske smeri [100]. Spektra, ki sta prikazana na **Sliki 7**, sta bila zajeta pri dveh temperaturah He-žarka: pri temperaturi tekočega dušika in pri sobni temperaturi. Pripadajoči valovni vektor je 60 nm⁻¹ oziroma 110 nm⁻¹. Uklonski vrh, ki je najbližji zrcalnemu vrhu, se v spektru pojavi pri $6,5^\circ$ oziroma $3,6^\circ$. Opazimo lahko, da sta vrhova v vzorcu, ki je bil zajet s

"toplejšim" He-žarkom, nekoliko širša od odgovarjajočih vrhov v spektru, zajetem s "hladnim" He-žarkom. Razlog za to tiči v slabši monokromatskosti "toplejšega" žarka. Opozoriti velja, da sta zaradi simetrije C_4 na površini (001) prisotni dve ekvivalentni domeni, med seboj zasukani za 90° (vstavek na **Sliki 7**). Dobljeni uklonski vzorec je zato preprosta superpozicija prispevkov obeh struktur, torej $c(4 \times 2)$ in $c(2 \times 4)$. Ekvivalentne vrste v takšni strukturi, ki povzročijo zrcalnemu vrhu najbližji uklonski vrh, so narazen $0,8$ nm, kar ustreza vektorju recipročne mreže $7,7$ nm⁻¹.

4.2 Študij rasti in mrežne dinamike v tanki plasti Pb/Ge(001)

Spektroskopija energije, ki jo pri trku s površino izgubijo He-atom, je ena najustreznejših metod za

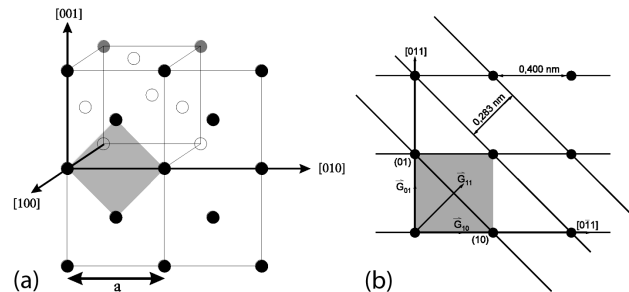


Figure 6: a) Unreconstructed Ge(001) surface model with dashed unit cell of size $a_s = 0,400$ nm, b) Ge unit cell on the surface and the nearest equivalent rows

Slika 6: a) Model nerekonstruirane površine Ge(001) z osenčeno enotsko celico velikosti $a_s = 0,400$ nm, b) površinska enotska celica Ge in najbližje ekvivalentne vrste

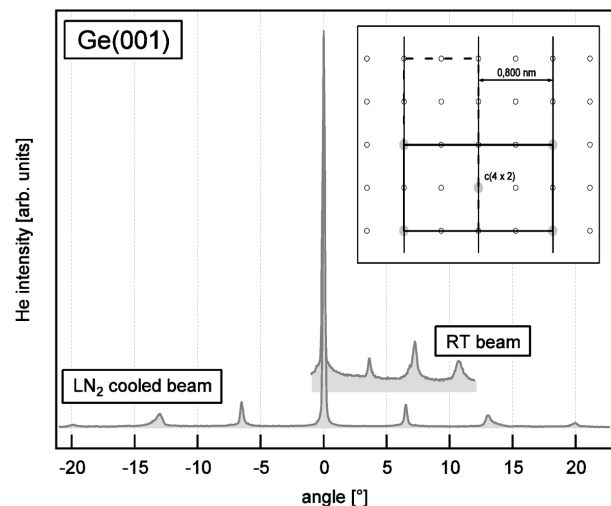


Figure 7: HAS diffraction pattern of the clean $c(4 \times 2)$ reconstructed surface acquired along [100] substrate direction at two helium atom wavelengths (0.104 nm and 0.057 nm) on the substrate Ge(001), held at 120 K. Inset: the realization of the surface for the present diffraction pattern.

Slika 7: Helijev uklonski vzorec čiste rekonstruirane površine $c(4 \times 2)$, zajet vzdolž [100] smeri podlage pri dveh valovnih dolžinah He-atomov (0,104 nm in 0,057 nm) na podlagi Ge(001), ohlajenem na 120 K. Vstavek: shema površinske strukture, ki ustreza prikazanemu uklonskemu vzorcu.

raziskovanje površinskih fononov in vibracijskih stanj adsorbiranih plasti. Kadar se He-atom na površini siplje neelastično, pride do kreacije ali anihilacije fonona. Z merjenjem časa preleta je mogoče direktno izračunati energijo, ki jo je He-atom izgubil ali pridobil, ta pa je enaka energiji anihiliranega oziroma kreiranega fonona. Če pri tem spreminjamo sipalni kot, lahko s podatkom o kotu in s prej dobljeno energijo izračunamo še gibalno količino, izmenjano vzdolž izbrane smeri na površini. Z nanašanjem energije fonona kot funkcijo izmenjane gibalne količine vzdolž površine dobimo graf, ki ponazarja disperzijsko relacijo fononov za dani sistem.

Z eksperimentom smo izmerili »trdoto«
površinskih nihanj v različni debeli plasti Pb/Ge(001).⁹ Med naprevanjem Pb na podlago Ge(001) pri nizki temperaturi ($T < 120$ K) smo merili intenziteto zrcalnega uklonskega vrha pri sipanju He z $E_{\text{kin}} = 19$ meV in $k_{\text{He}} = 60$ nm⁻¹. Izmerjena intenziteta, ki je prikazana na **Sliki 8** in je direktno merilo reda na površini, začne po ~500 s naprevanja (pri pokritosti približno 4 monoplasi) močno oscilirati, kar kaže na plastno rast Pb. Zapolnjene plasti so namreč bolj gladke od nezapolnjenih, zato je sipanje v zrcalni vrh močnejše.

Disperzijsko relacijo za površinska nihanja smo pomerili pri različnih pokritostih podlage. Heksagonalna Pb mreža je na Ge podlagi prisotna v dveh med seboj pravokotnih smereh, kar je posledica dveh med seboj pravokotnih domen, prisotnih na čisti površini Ge(001). Ker je struktura Pb-plasti heksagonalna, pri meritvah učinkovito vidimo dve heksagonalni mreži, ki sta med seboj zasukani za 30°. Pri zajemanju spektra časa preleta z večkanalnim časovnim analizatorjem zato hkrati opazujemo mrežna nihanja vzdolž dveh smeri, ΓK in ΓM .

Tipičen spekter časa preleta je prikazan v vstavku na **Sliki 9**. Posnet je s hladnim žarkom ($E_{\text{kin}} = 19$ meV in $k_{\text{He}} = 60$ nm⁻¹) pri kotu $R_1 = -3^\circ$ in stopnji nanosa c (**Slika 8**). V njem najdemo pri času preleta 962 μ s elastični vrh, preostali trije vrhovi pa pripadajo neelastičnim sipalnim dogodkom, kjer je He-atom s površino izmenjal

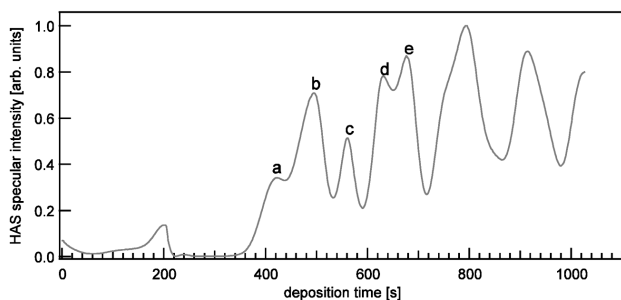


Figure 8: Specular intensity of HAS acquired during Pb deposition on Ge(001) substrate held at 120 K. Spectrum has been acquired with cold He beam, $k_{\text{He}} = 60$ nm⁻¹. The stop points where measurements of inelastic scattering have been taken (a - e) are also denoted.

Slika 8: Zrcalna intenziteta pri sipanju He-atomov med naprevanjem Pb na podlago Ge(001), ohlajen na 120 K (desno). Spekter je bil zajet z ohlajenim helijevim žarkom, $E_{\text{kin}} = 19$ meV in $k_{\text{He}} = 60$ nm⁻¹. Označene so tudi točke zaustavitve naprevanja (a - e), v katerih so bili zajeti spektri časa preleta.

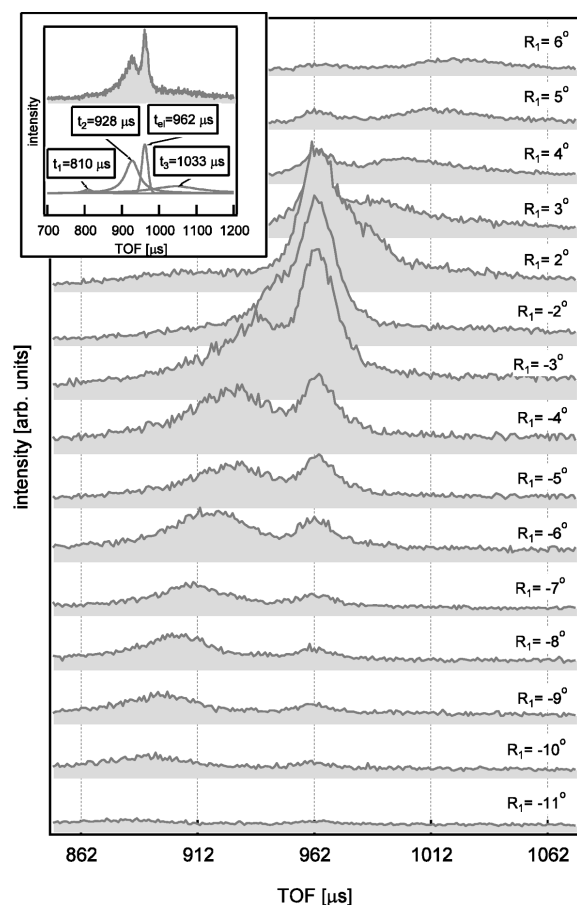


Figure 9: The time shift of the phonon in the TOF spectrum as a function of scattering angle R_1 . The phonon spectra are acquired at the fourth maximum (d) in the deposition graph (**Figure 8**). Inset: decomposition of a single phonon spectrum to inelastic and elastic peaks.

Slika 9: Premik fonona po spektru časa preleta v odvisnosti od sipalnega kota R_1 . Fononski spektri so posneti pri četrtem maksimumu (d) v naporitvenem grafu na **Sliki 8**. Vstavek: dekompozicija enega fononskega spektra na posamezne fonone in elastični vrh.

kvant energije mrežnega nihanja. Vrhova 1 in 2 ob časih 810 μ s in 928 μ s ustrezata anihilaciji fononov, vrh 3 ob času 1044 μ s pa njegovi kreaciji. Na **Sliki 9** so zbrani spektri časov preleta, zajeti pri različnih kotih sipanja (R_1), kjer je lepo vidna disperzija pri anihilaciji. Izmerjeni spektri vsebujejo med 1 in 4 milijoni zajetij.

Neelastično sipanje He-atomov, pomerjeno pri različnih debelinah Pb-plasti, smo skrbno analizirali. Natančen čas preleta je bil vsakokrat določen s prilaganjem krivulje posameznemu vrhu. Zbrane vrhove smo potem vnesli na ustrezno mesto v grafu $\Delta E(\Delta K)$. Na ta način smo dobili celotno disperzijsko relacijo površinskih nihanj (**Slika 10**). V njej je vidna tako akustična kot optična veja nihanj. Hitrost širjenja valovanja po površini je bila določena s prilaganjem premice točkam v akustični veji v bližini ničle in znaša 740 m/s ($1 \pm 0,1$). "Trdota" površinskih nihanj je le malo odvisna od debeline plasti (kvečjemu ~10 %), kolikor znaša tudi eksperimentalna napaka.

4.3 Nanostrukture organskih materialov: struktura tanke plasti pentacen/Au(110)

Kadar naporjamo na kristalne površine velike organske molekule, kot so policiklični ogljikovodiki in aminokisljine, lahko pogosto opazimo samourejevanje molekul. To je v največji meri odvisno od mobilnosti molekul na površini in od njihove sposobnosti za formiranje urejenih struktur v prisotnosti določene podlage.

Samourejevanje molekul smo opazili pri sistemu pentacen/Au(110) površini z manjkajočo vrsto. Zaradi majhne kinetične energije je sipanje He-atomov nadvse primerna tehnika za opazovanje nastalih nanostruktur, saj ostanejo z osvetlitvijo površine s He-žarkom pogoji na njej povsem nespremenjeni, prav tako niso moteni procesi, ki se na površini odvijajo.

Strukturo tanke plasti pentacena smo določili z uporabo sipanja He-atomov.¹⁰ He-žarek je imel temperaturo tekočega dušika ($E_{\text{kin}} = 19$ meV, $k_{\text{He}} = 60$ nm⁻¹). Iz Knudsenove evaporacijske celice smo molekule pentacena naparovali na podlago Au(110) pri različnih temperaturah v območju med sobno temperaturo in 470 K. Opazili smo, da je kinetika molekulske rasti na Au(110) v tem temperaturnem območju zelo raznolika.

Morfologijo površine smo podrobneje analizirali tako, da smo med naporjevanjem zajemali celotne uklonske vzorce. Razvoj strukture tanke plasti pentacena smo opazovali na podlagi pri temperaturi 470 K z zajemanjem uklonskih vzorcev vzdolž smeri [001], kar v recipročnem prostoru sovпада s smerjo ΓY . Spektri so prikazani na **Sliki 11**. Vodoravna os je v enotah recipročne mreže podlage vzdolž smeri ΓY , s črtami pa so nakazane lege za vrhove v spektru, ki pripadajo periodi v velikosti šestkratne osnovne celice. Na začetku nana-

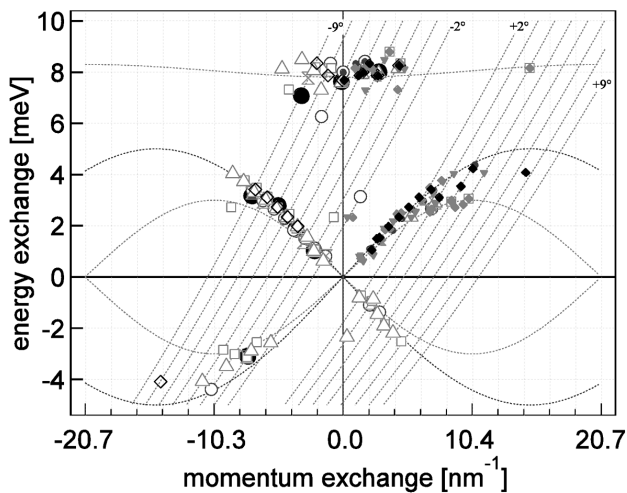


Figure 10: The measured dispersion relation of the surface vibrations in the Pb/Ge(001) film with different thickness, acquired along ΓK and GM directions. The points with filled markers are obtained by folding the upper left quadrant to the upper right quadrant.

Slika 10: Izmerjena disperzijska relacija površinskih nihanj v različno debeli plasti Pb/Ge(001), zajeta vzdolž smeri ΓK and ΓM . Točke s polnimi znaki so dobljene s prepogibanjem levega v desni zgornji kvadrant.

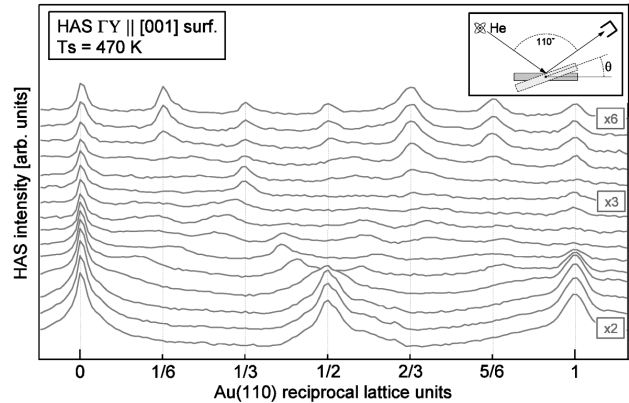


Figure 11: HAS angular diffraction scans during deposition at a substrate temperature of 470 K. The spectra have been obtained along ΓY surface direction with He atom wavevector $k_{\text{He}} = 60$ nm⁻¹. The vertical axis has a logarithmic scale.

Slika 11: Zaporedje uklonskih vzorcev sipanja He-atomov med nanašanjem pentacena pri temperaturi podlage 470 K. Spektri so bili zajeti vzdolž površinske smeri ΓY z valovnim vektorjem atomov He $k_{\text{He}} = 60$ nm⁻¹. Navpična os ima logaritemsko skalo.

šanja (spekter na dnu grafa) vidimo uklonski vzorec za dvoštevno simetrijo čiste površine Au(110). Struktura tanke plasti se preko šibko izražene trištevne simetrije razvije v fazo s šestštevno simetrijo, ki se je izkazala za najstabilnejšo in je hkrati saturacijska struktura pri tej temperaturi podlage.

Raziskava strukture tanke plasti pri nižji temperaturi podlage (420 K) pokaže še več različnih struktur vzdolž smeri ΓY . Razvoj uklonskega vzorca med nanašanjem pentacena je prikazan na **Sliki 12**. Vsak spekter v zaporedju je bil posebej normiran na velikost zrcalnega vrha. V zgodnjih spektrih razvoja lahko opazimo razcep uklonskega vrha (0, 1/2), ki je sočasen s pojavom satelitskih vrhov okrog zrcalnega vrha. Zmeren premik satelitskih vrhov vodi do prehodne kvazi-sedemštevne sime-

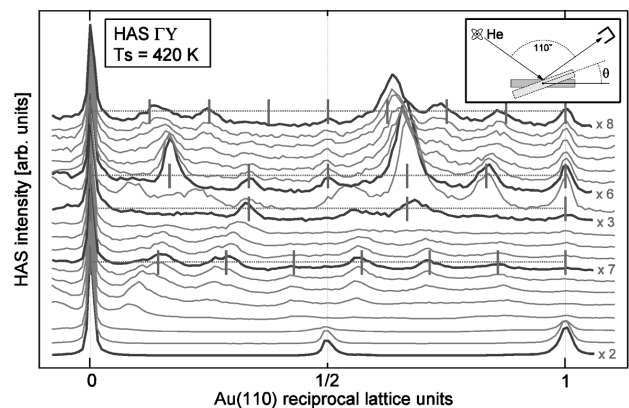


Figure 12: The evolution of HAS diffraction spectra during deposition of pentacene at a substrate temperature of 420 K. Spectra have been taken along ΓY surface direction with He atom wavevector $k_{\text{He}} = 60$ nm⁻¹.

Slika 12: Razvoj helijevega uklonskega vzorca med nanašanjem pentacena na podlago pri temperaturi 420 K. Spektri so bili zajeti vzdolž površinske smeri ΓY z valovnim vektorjem atomov He $k_{\text{He}} = 60$ nm⁻¹.

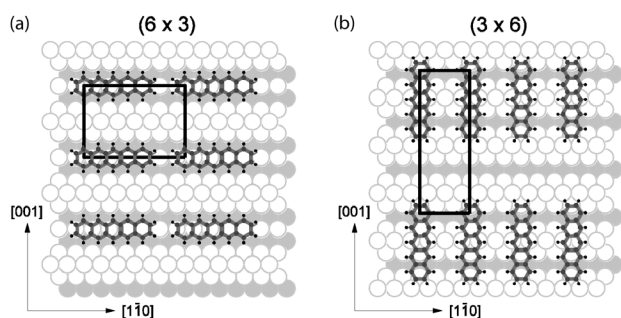


Figure 13: The pentacene/Au(110) thin film model with structures (6×3) (left) and (3×6) (right) structure. The unit cell is denoted by a black rectangle. Black arrows shows the corresponding substrate directions.

Slika 13: Model tanke plasti pentacena/Au(110) s strukturama (6×3) (levo) in (3×6) (desno). Enotska celica je označena s črnim pravokotnikom. S puščicami so nakazane ustrezne smeri podlage.

trije, ki ji sledi trištevna. To nakazuje, da se začne dvoštevna simetrija podlage rušiti zaradi nastajanja domenskih sten izven faze, ki izvirajo iz korelacije med površinskimi defekti Au, te pa inducirajo adsorbirane molekule. Oblika ovojnice (površinska mavrica) je pri teh dveh simetrijah precej drugačna kot pri fazah, ki sledita, torej šest- in osemštevni, in kaže na precej različno korugacijo površinske gostote naboja v različnih fazah pentacena, kar sovпада z različno molekulsko orientacijo.

Faza (3 × 6), ki jo odraža vrhnji uklonski vzorec v zaporedju na **Sliki 11**, se ob nadaljevanju naprejevanja ne spreminja, zato je to saturacijska faza v rasti pentacena na Au(110) pri visoki temperaturi, torej pri 470 K. Je najstabilnejša faza pentacena na tej podlagi. Pripisemo ji nominalno pokritost ene monoplasti (angl. monolayer, ML). Razvoj strukture v območju pokritosti ene monoplasti se v celoti ujema z objavljenimi meritvami s tunnelskim mikroskopom.¹¹ Molekule pentacena se v zgodnjih fazah rasti adsorbirajo med vrste atomov zlata vzdolž smeri [1-10], staknjene po dolžini, kar najprej povzroči trištevno rekonstrukcijo površine vzdolž te smeri. To je v skladu z opaženo strukturo (6 × 3), ki po velikosti ustreza dolžini molekule vzdolž smeri [1-10], in sicer 6 × 0,288 nm = 1,73 nm. Model takšne površine je prikazan na **Sliki 13a**. Korugacija površinske gostote naboja je pri tako poravnanih molekulah zelo majhna, kar povzroči zelo šibke uklonske vrhove – to pa se sklada z opaženo površinsko mavrico v strukturi (6 × 3) vzdolž smeri GX. Strukture (6 × 3) nismo opazili pri dekompoziciji faz z večjo pokritostjo, kar kaže na neravnovesno naravo te faze. Nadaljevanje nanašanja pri 470 K nepovratno vodi v visoko stabilno in dobro urejeno fazo (3 × 6). Ta simetrija je v skladu s fazo, za katero je bilo objavljeno, da so v njej molekule staknjene po širini in tvorijo široko razmaknjene (2,45 nm) verige vzdolž smeri [1-10].¹¹ V tem primeru so molekule azimutno zasukane za 90° glede na smer v fazi (6 × 3). Pripadajoči model z eno molekulo na enotsko celico je prikazan na **Sliki 13b**.

5 ZAKLJUČEK

Po več kot 30 letih teoretičnih prizadevanj in eksperimentalnih izboljšav je tehnika sipanja atomov helija dozorela, saj je iz fizikalnega eksperimenta prerasla v uporabno orodje. Je nepogrešljiva pri raziskovanju občutljivih sistemov, ki bi jih konvencionalne merse metode zmotile do te mere, da njihovi rezultati ne bi več kazali dejanske slike dogajanja na površini.

V kratkem popotovanju po lastnostih predstavljene tehnike smo pokazali, da je šele razvoj mikronskih šob skupaj z močnimi črpalnimi sistemi omogočil ustvariti intenziven curek atomov z ostro energijsko porazdelitvijo, ki je bil zmožen pridelati bogat in uporaben uklonski vzorec. Naj gre za določanje strukture, urejene na velike razdalje, ali samo meritve zrcalne reflektivnosti – z uklonom atomov helija, lahko eksperiment opravimo, ne da bi opazno posegli v strukturo in vezavo molekul na površini. To je še posebej dragoceno, kadar imamo opravka z zapletenimi in občutljivimi sistemi, kot so organsko/anorganske nanostrukture, pri katerih druge merilne tehnike pogosto povzročijo opustošenje, ki precej zakrije dejansko sliko površine.

Z uklonom termičnih atomov helija ne iščemo koščic v notranjosti češnjeve pite, pač pa tipamo njeno skorjo – površino kristala oziroma adsorbata, ki je v stiku z okolico in je zato odgovorna za množico uporabnih lastnosti, ki jih lahko s pridom izkoristimo pri proizvodnji naprednih elementov in naprav.

6 REFERENCE

- B. Poelsema, G. Comsa, Scattering of Thermal Energy Atoms from Disordered Surfaces, Springer Verlag, Berlin 1989
- F. Tommasini, Molecular beam-surface scattering, Vacuum, 31 (1981) 10–12, 647–657, doi:10.1016/0042-207X(81)90085-3
- U. Garibaldi, A. C. Levi, R. Spadacini, G. E. Tommei, Quantum Theory of Surface Rainbow, Japanese Journal of Applied Physics, 13 (1974) 2, 549–552, doi:10.7567/JJAPS.2S2.549
- G. Boato, P. Cantini, U. Garibaldi, A. C. Levi, L. Mattera, R. Spadacini, G. E. Tommei, Journal of Physics C: Solide State Physics, 6 (1973) 21, L394–L398, doi:10.1088/0022-3719/6/21/003
- E. Hulpke, Helium Atom Scattering from Surfaces, Springer Verlag, Berlin 1992
- P. Prelovšek, Teorija trdne snovi, DMFA, Ljubljana 1999
- D. Cvetko, A. Lausi, A. Morgante, F. Tommasini, K. C. Prince, M. Sastry, Measurement Science and Technology, 3 (1992) 10, 997–1000, doi:10.1088/0957-0233/3/10/011
- D. Cvetko, L. Floreano, A. Crottini, A. Morgante, F. Tommasini, Surface Science, 447 (2000) 1–3, L147–L151, doi:10.1016/S0039-6028(99)01205-4
- L. Floreano, D. Cvetko, F. Bruno, G. Bavdek, A. Cossaro, R. Gotter, A. Verdini, A. Morgante, Progress in Surface Science, 72 (2003) 5–8, 135–159, doi:10.1016/S0079-6816(03)00021-2
- L. Floreano, A. Cossaro, D. Cvetko, G. Bavdek, A. Morgante, The Journal of Physical Chemistry B, 110 (2006) 10, 4908–4913, doi:10.1021/jp055516p
- Ph. Guaino, D. Carty, G. Hughes, O. McDonald, A. A. Cafolla, Applied Physics Letters, 85 (2004) 14, 2777–2779, doi:10.1063/1.1786655